FOSSIL PALAEOWEATHERING PROFILES AND THEIR RELATION TO DEFORMATION AT BASEMENT-COVER-INTERFACES

Case studies from
Israel, Sweden and Spain

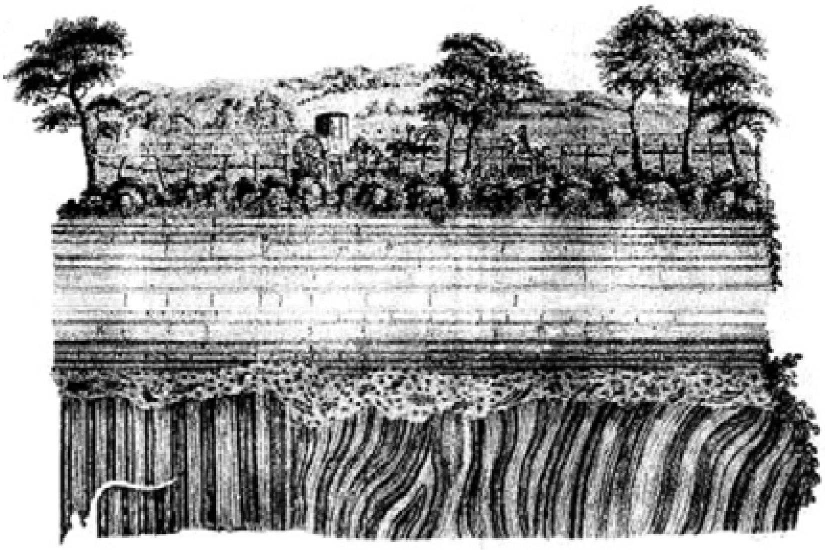

Diplom-Geologe Thomas Angerer

Inaugural-Dissertation
zur Erlangung der Doktorwürde
der Naturwissenschaftlich-Mathematischen Gesamtfakultät
der Ruprecht-Karls-Universität Heidelberg

Heidelberg, März 2007

Front page / Titelblatt: Hutton Unconformity at Jedburgh, Scotland, illustrated by John Clerk in 1787.

Gutachter: Prof. Dr. Reinhard O. Greiling
Geologisch-Paläontologisches Institut
Ruprecht-Karls-Universität
Im Neuenheimer Feld 234
69120 Heidelberg

Prof. Dr. Helga de Wall
Institut für Geologie
Julius-Maximilians-Universität
Pleicherwall 1
97070 Würzburg

Promotionsprüfung: 25. Mai 2007

Hiermit erkläre ich, dass ich die vorliegende Dissertationsarbeit selbst verfasst und mich dabei keiner anderen als der von mir ausdrücklich bezeichneten Quellen und Hilfen bedient habe.
Ich erkläre, dass ich an keiner anderen Stelle ein Prüfungsverfahren beantragt bzw. die Dissertation in dieser oder anderer Form bereits anderweitig als Prüfungsarbeit verwendet oder einer andren Fakultät als Dissertation vorgelegt habe.

Heidelberg, den 20. März 2007

Thomas Angerer

IPP Geofluids, Gases and Aerosols in System Earth

"FLUID-ROCK-INTERACTION" GRK 273

Strukturgeologie, Tektonophysik

ACKNOWLEDGMENT / DANKSAGUNG

This doctoral thesis was undertaken from April 2002 to January 2007 in the Geological-Palaeontological Institute, University of Heidelberg. I would like to thank the institutions and all Persons who supported my efforts to finish the thesis: In the first place, I thank Deutsche Forschungsgemeinschaft for three years of financial support provided as a stipend of the Graduiertenkolleg 273 “Fluid-Rock-Interaction” and Prof. Reinhard Greiling for initiation and supervision of my work and for his efforts in improving the manuscript. Prof. Helga de Wall being the second referee and for her important input regarding the Magnetic Susceptibility part.

Diese Doktorarbeit wurde zwischen April 2002 und Januar 2007 am Geologisch-Paläontologischen Institut der Ruprecht-Karls-Universität angefertigt. Ich möchte den Institutionen und allen Personen danken, die diese Arbeit ermöglichten und mich dabei unterstützten, sie fertig zu stellen. Ich danke der Deutschen Forschungsgemeinschaft für das Stipendium über drei Jahre im Rahmen des Graduiertenkollegs 273 “Fluid-Rock-Interaction” und ich danke meinem Doktorvater Prof. Reinhard Greiling für die Initiierung und Betreuung der Arbeit und seine Bemühungen zur Erhöhung der inhaltlichen und sprachlichen Qualität des Manuskriptes. Prof. Helga de Wall danke ich für ihre Bereitschaft, das Zweitgutachten zu erstellen und für die Unterstützung bei der Interpretation der Magnetischen Suszeptibilitäts-Untersuchungen.

Die Geländearbeiten in Spanien und Israel wurden erst möglich gemacht durch die Unterstützung vor Ort durch Prof. Gabriel Gutiérrez-Alonso, Universität Salamanca, sowie Prof. Dov Avigad, Hebrew University, Jerusalem. Ihnen gebührt mein besonderer Dank. Ebenso möchte ich dem Team der SGU in Måla, Schweden, danken für Bereitstellung der Långviken und Hara Bohrkerne und ihrer Unterstützung bei der Beprobung.

Den Angehörigen des Geologisch-Paläontologischen und des Umweltgeochemischen Instituts gilt mein Dank, insbesondere dem Organisationsteam vom Graduiertenkolleg und Internationalen Promotions-Projekt (IPP) Prof. Thilo Bechstädt, Roswitha Marioth, Tanja van der Beek, Friederike Busse und Francisco Cueto, sowie den hilfreichen Wissenschaftlern Agnes Kontny, Laurence Warr, Ulrich Glasmacher, Prof. William Shotyk, Carsten Vahle, Jana Just, Jens Grimmer, Guy Spence und Johanna Kontny. Auch meinen beiden Hiwis Nathan Kang und Oliver Günzenberger, sowie Hans Ebert, Odile Wallerrath, Marcus Thiel und Joachim Fillauer von den Kellerwerkstätten, Michael Bühler und Susanne Pätzold von der Bibliothek und Elfriede Hofmann und Ayten Eicher vom Sekretariat und Buchhaltung sei gedankt.

Meinen Mitstreitern im GRK und IPP danke ich für Diskussion und Zerstreuung, sowohl im Institut als auch außerhalb, wo immer wir auch zusammen waren: Ibolya Györösi, Emmanuel Laverret, Margarita Koroleva, Gaël Le Roux, Kirsten Maciejczyk, Asher Whishkerman, Ellen Roberts, Anja Schleicher, Heiko Hofmann, Jana Just, Guy Spence, Amogne Gelaye, Marta Gasparrini, Fernando Ayllon, Gesine Lorenz, Christina Reindl, Jochen Schneider, Hartwig Schröder, Zbynek Veselovsky, Axel Emmerich, Birgit Dietrich, Michael Seeling, Jorham Contreras, Friederike Bauer, Sonja Pabst, Iris Sonntag, Luca Nano und Frauke Kubischta.

Danke fürs Korrekturlesen, Nick McArthur, Raffaella di Sylvestro, Iris Koban und die bereits genannten.

Meinen engsten Freunden hier in Institut, Carsten Laukamp, Fabio Lapponi und Kevin Carrière, danke ich vor allem für die super Zeit, nicht nur im „Sozialraum 108“. Die Zukunft soll Euch das Beste bescheren.

Zu letzt, vielen Dank, liebe Eltern, für die Unterstützung während der etwas länger andauernden Endphase.

“No vestige of a beginning, no prospect of an end” – James Hutton

ABSTRACT

Detachment horizons are associated with basement-cover-interfaces in many regions of compressive or extensional regimes. The fabric evolution and alteration of ancient fossil palaeoweathering profiles and their relation to deformation at basement-cover-interfaces are the object of this thesis. Three cases of palaeoweathered granite and one case of folded sedimentary basement rocks are investigated by means of structural, mineralogical, whole-rock geochemical and magnetic susceptibility analyses.

In the case study *Negev*, South Israel, the deformed Roded Granite (Pan-African basement) weathered under warm and humid to (semi-) arid conditions to a saprock-saprolite-laterite sequence, buried beneath Cambrian red beds. The laterite was compacted beneath 2.8 ± 0.1 km overburden to 73% of its original thickness (plane strain). In the case studies *Långviken* and *Hara*, Central Swedish Caledonian margin, the deformed Revsund Granite (Fennoscandian basement) weathered in a temperate to cold climate to weathering-breccias, which were buried beneath sequences of Vendian conglomerates and Cambrian black shales, respectively. Caledonian detachment tectonics overprinted and duplicated the autochthonous weathering-breccia in basement slices under anchizonal cataclasis. In the case study *Narcea Antiform*, Cantabrian Mountains in North Spain, sedimentary basement rocks, folded during the Cadomian orogeny, weathered moderately without significant textural changes in an arid climate and were buried beneath Cambrian siliciclastics. The Variscan Orogeny overprinted the rocks under regional anchimetamorphic conditions. It reactivated the angular unconformity, locally under higher metamorphic conditions causing ductile quartz deformation.

The intensity of weathering features, which are preserved in all cases, is a function of proximity to the unconformity. Hydrolysis of Na-feldspar and chlorite is the predominant chemical weathering process, leading to clay precipitation, whole-rock Al-enrichment and Na-, Ca-leaching. SiO_2-dissolution and partly reprecipitation is locally observed, as well as magnetite dissolution (Långviken, Negev), martitization of magnetite (Negev) and microcrystalline haematite precipitation (Negev and Narcea Antiform).

The bulk susceptibility (κ_{bulk}) can be used as a tracer of weathering intensity. However, the alteration of magnetic carriers has to be known. The particular weathering of ferrimagnetic lithologies led to a decrease of κ_{bulk}, whereas weathering of paramagnetic lithologies caused a κ_{bulk}-increase. κ_{bulk} was overprinted in particular horizons, e.g. by the passive enrichment of Fe-phases during compaction of the Negev laterite and by ferrimagnetic pyrrhotite precipitation in Långviken cataclasite. The magnetic field dependence of pyrrhotite-bearing rocks is dependent on pyrrhotite grain size, but also on its modal fraction. A corrected field dependence parameter is calculated, in order to eliminate the influence of the matrix susceptibility.

The obliteration of primary petrofabrics by palaeoweathering mainly depends on the intensity of physical brecciation and not necessarily on the intensity of chemical alteration. Fabrics have been lost in the Swedish cases due to weathering-brecciation and associated grain size reduction. Granitic foliations are preserved in the absence of grain size reduction (Narcea Antiform) and even in a laterite, where extreme hydrolysis and dissolution processes took place (Negev).

Unconformity-parallel compaction fabrics developed by pressure solution and rotation of phyllosilicates in clay-rich weathering-zones during the diagenetic stage. Intensity of compaction depends on the burial depth, the weathering mineralogy (clay-richness) and the porosity. A general positive covariance between the intensities of palaeoweathering and horizontal fabric is suggested, which is reflected by a stronger horizontal fabric imprint with proximity to the unconformity. AMS fabrics are results of the superposition of the compaction fabric with primary (older than compaction) or secondary (younger than compaction) fabrics. The gradual change of compaction fabrics is quantified in the AMS by a systematic decrease of the magnetic anisotropy P'. Flat-lying magnetic lineations, associated with unconformity-parallel fabrics, appear to be a common feature in fossil palaeoweathering profiles, which were subject to at least moderate textural rearrangement.

Primary and secondary contrasts of lithologies above and beneath the unconformity developed during the evolution of the basement-cover-interfaces. Primary refers to the lithological differences (palaeoweathering, sedimentary lithology) and the unconformity topography, whereas secondary refers to texture-modification and mineral alterations related to diagenesis and later processes (e.g. by compaction, fluid flow). Collectively, most of the contrasts lowered the shear strength of the palaeoweathering zones and created a permeability-anisotropy along the unconformity. Overpressured fluids beneath the "sealed" unconformities and increased horizontal shear stresses enabled (approximately unconformity-parallel) rock failure in the palaeoweathering zone (Sweden) or frictional sliding along the unconformity (Narcea A.). Showing common characteristics of textural evolution, fluid-rock-interaction and associated shear-strength weakening, this thesis demonstrates the importance of fossil palaeoweathering zones for upper crustal detachment tectonics, as well as for the characteristics of fluid-flow in the basement and related element mobilization and potential ore formation.

ZUSAMMENFASSUNG

In Regionen kompressiver und extensionaler Regimes sind Abscherhorizonte häufig an Grundgebirgs-Deckgebirgs-Grenzen lokalisiert. Objekt der Studie sind die Gefügeentwicklung und Alterationen fossiler Paläoverwitterungszonen sowie deren Zusammenhang mit Deformationen an Grundgebirgs-Deckgebirgs-Grenzen. Drei Fälle von paläoverwittertem Granit und ein Fall von verfaltetem sedimentärem Grundgebirge wurden anhand gefügekundlicher, mineralogischer, geochemischer und magnetischer Suszeptibilitäts-Messungen untersucht.

Im *Negev* Fall, Israel, verwitterte der deformierte panafrikanische Roded Granit unter warm-humid bis (semi-) ariden Bedingungen zu einer Saprock-Saprolit-Laterit Abfolge und wurde von kambrischen Rotsedimenten überdeckt. Dabei wurde der Laterit unter 2.8 ± 0.1 km Überdeckung auf 73% des Orginalmächtigkeit kompaktiert („plane strain“). In den Fällen *Hara* und *Långviken* vom mittelschwedischen Rand der Kaledoniden, verwitterte der deformierte fennoskandische Revsund Granit in temperiertem bis kühlem Klima und wurde von einer Abfolge von vendischen Konglomeraten und kambrischen Schwarzschiefern überdeckt. Teile der Verwitterungsbrekzie wurden im Zuge der Kaledonischen Überschiebungstektonik dupliziert und anchizonal kataklastisch überprägt. Im Fall *Narcea Antiform*, im Kantabrischem Gebirge Nordspaniens, verwitterte Cadomisch-verfaltetes sedimentäres Grundgebirge schwach in aridem Klima ohne Texturüberprägung und wurde von kambrischen klastischen Sedimenten überlagert. Die Variszische Orogenese führte zu regionaler anchizonaler Gesteinsüberprägung und Reaktivierung der Diskordanz, mit lokal erhöhten Temperaturen, die duktile Quarzdeformation hervorriefen.

Verwitterungsmerkmale sind in allen Fällen erhalten und zeigen eine generelle Abnahme der Intensität mit zunehmender Entfernung zur Diskordanz. Die wichtigsten chemischen Verwitterungsreaktionen sind die Umwandlungen von Na-Feldspat und Chlorit, welche zur Anreicherung von Tonmineralen und Al sowie einer Abreicherung von Na und Ca führt. Untergeordnete Reaktionen sind SiO_2-Lösung und dessen lokale Wiederanreicherung sowie magnetomineralogisch interessante Magnetitlösung (Långviken, Negev), Martitisierung von Magnetit (Negev) sowie Anreicherung von mikrokristallinem Hämatiten (Negev and Narcea Antiform).

Prinzipiell ist die magnetische Suszeptibilität ein Tracer des Verwitterungsgrades, jedoch nur unter Kenntnis der magnetischen Phase zu interpretieren. So führte die Verwitterung paramagnetischer Lithologien zur Erhöhung der κ_{bulk}, während die Verwitterung von ferrimagnetischen Gesteinen eine Senkung zur Folge hatte. Zudem ist κ_{bulk} durch Überprägung einzelner Horizonte angestiegen (Laterit-Kompaktion in Negev, Pyrrhotin-Anreicherung im Långviken-Kataklasit). Die magnetische Feldabhängigkeit von Pyrrhotin-führenden Gesteinen ist abhängig von der Korngröße Pyrrhotins aber auch von dessem Modalbestand. Ein korrigierter Feldabhängigkeits-Parameter wurde berechnet, um den Einfluss der paramagnetischen Matrix zu eleminieren.

Die Zerstörung primärer Gefüge im Grundgebirgsgestein durch die Verwitterung ist von der Intensität der physikalischen Verwitterung abhängig, nicht aber unbedingt von der chemischen. So sind durch die intensive Kornzerkleinerung in den schwedischen Verwitterung-Brekzien primäre Texturen weitestgehend nicht mehr vorhanden. Andererseits, wenn Kornzerkleinerung keine große Rolle spielte (Narcea Antiform), können Primärtexturen bis in die Zone extremer chemischer Verwitterung erhalten sein (Negev-Laterit).

Während der diagenetischen Überprägung sind in den tonreichen Verwitterungszonen durch Drucklösung und Mineraleinregelung Diskordanz-parallele Kompaktionsgefüge entstanden. Die Ausprägung dieser Gefüge ist abhängig von der Versenkungstiefe, der Verwitterungsmineralogie (Tonreichtum) und der Porosität. Eine generelle Kovarianz zwischen den Intensitäten von Paläoverwitterung und Kompaktionsgefüge ist anzunehmen. Sie führt zu ausgeprägteren horizontalen Gefügen nahe der Diskordanz. AMS-Gefüge resultieren aus der Überlagerung des Kompaktionsgefüges mit einer primären (älter als Kompaktion) oder sekundären (jünger) Gesteinsfoliation. Mit der AMS ist die graduelle Entwicklung der Kompaktionsgefüge durch systematische Anisotropiesenkung (P’) quantifizierbar. Die Entwickung Diskordanz-paralleler magnetischer Lineationen ist in Paläoverwitterungszonen, die mindestens eine moderate Texturänderung aufweisen, ein allgemeines Merkmal.

Während der Genese der Grundgebirgs-Deckgebirgs-Grenzen entstanden *primäre* und *sekundäre* Kontraste zwischen den Gesteinen oberhalb und unterhalb der Diskordanz. Primäre Kontraste sind anhand der Lithologien (Sedimente, Verwitterungsmaterial) und der Diskordanz-Topographie definiert. Die sekundären Kontraste ergeben sich durch Texturänderungen und Alterationen (z.B. Kompaktion, Fluidfluss). Die meisten primären und sekundären Kontraste führten zu einer Verringerung der Scherfestigkeit und zu einer Permeabilitäts-Anisotropie entlang der Diskordanz. Ein gespannter Fluidfluss (Überdruck) unterhalb der „versiegelten“ Diskordanz und erhöhte horizontale Scherspannung führten zu Gesteinsversagen in der Verwitterungszone (Hara, Långviken) oder zur Abscherung der Diskordanz (Narcea Antiform). Die texturelle Entwicklung, Fluid-Gesteins-Wechselwirkung und assoziierte Verringerung der Scherfestigkeit zeigt, wie wichtig fossile Paläoverwitterungprofile der oberen Kruste sind bezüglich der Lokalisierung von Abscherungen sowie des Fluidfluss und daran gebundene Elementmobilisierung und Vererzungen im Grundgebirge.

CONTENT

1 INTRODUCTION 10

1.1 Motivation 10
1.2 Weathering and palaeoweathering profiles – terminology and genesis 12
  1.2.1 Chemical weathering 14
1.3 Methods 16
  1.3.1 X-ray diffraction 16
  1.3.2 Whole-rock geochemistry (ICP-E/MS) 17
  1.3.3 Scanning Electron Microscopy and Chlorite geothermometry by microprobe analyses 18
  1.3.4 Determination of bulk rock density and porosity 18
  1.3.5 Image analysis of mineral modal fraction, shape distribution and SPO 19
  1.3.6 Correction-rotation of unoriented drill core sections 21
  1.3.7 Magnetic susceptibility and AMS 22

2 CASE STUDY NEGEV, ISRAEL 28

2.1 Introduction 28
  2.1.1 Regional Geology 28
  2.1.2 Sampling and applied methods 29
2.2 Description of the weathering zones 29
  2.2.1 Unweathered granite 31
  2.2.2 Saprock (moderately weathered granite) 32
  2.2.3 Saprolite (intensely weathered granite) 33
  2.2.4 Laterite 34
  2.2.5 Determination of laterite compaction by means of image analysis 35
  2.2.6 Density and porosity of the laterite 37
  2.2.7 Cataclasis zones 37
  2.2.8 Late brittle structures 38
  2.2.9 Cover rocks 38
  2.2.10 XRD 38
  2.2.11 Whole-rock geochemistry results 41
  2.2.12 Magnetomineralogy 45
2.3 Magnetic susceptibility analyses 48
  2.3.1 Bulk susceptibility κ_{bulk} *48*
  2.3.2 Temperature dependent susceptibility $\kappa(T)$ *48*
  2.3.3 Ratio of κ_{bulk} */ total iron content 50*
  2.3.4 Modelling of κ_{bulk} *and the contribution of the main magnetic carriers 50*
  2.3.5 AMS 52
2.4 Image analyses of chlorite and martite SPO 54
  2.4.1 3D-SPO fabric of a granite 54
  2.4.2 Sectional SPO of a laterite 57
  2.4.3 Sectional SPO of a cataclasite 58
2.5 Discussion of alteration, weathering and deformation in the weathering profile 59
  2.5.1 Sub-surface physical weathering 59
  2.5.2 Mineralogical processes and their relation to alteration phases 60
  2.5.3 Geochemical processes and their relation to alteration phases 61
  2.5.4 Magnetomineralogy 63
  2.5.5 Saprolitic pallid zone and transition to lateritic ferricrete 64
  2.5.6 Laterite morphology as a result of weathering and compaction 65
  2.5.7 Cataclasis 69
2.6 Association of κ_{BULK} and AMS with alteration and deformation 70
  2.6.1 Magnetic susceptibility 70
  2.6.2 Magnetite / martite-ratio in $\kappa(T)$*-curves 71*
  2.6.3 Relation of AMS to petrofabrics - implications from image analyses 71
  2.6.4 AMS fabrics 76
2.7 Alteration and fabric evolution of the Roded weathering profile 81
  2.7.1 Late Pan-African emplacement, autometasomatism and subsequent deformation 83
  2.7.2 Cambrian peneplanation and subaerial weathering (palaeoclimatic implications) 84

2.7.3 Burial stage and compaction 86
2.7.4 Tertiary tectonics and related fluid flow 86
2.8 CONCLUSIONS 87

3 CASE STUDY HARA, SWEDEN 94

3.1 INTRODUCTION 94
3.1.1 Regional geology 94
3.1.2 Sampling and applied methods 96
3.2 DESCRIPTION OF THE LITHOLOGIES 96
3.2.1 Unweathered granite (SD-2.c) 97
3.2.2 Weathering-breccia (SD-2.b) 98
3.2.3 Weathered granite (SD-1.c, SD-2.b/c) 98
3.2.4 Foliated black siltstone (SD-1.a) 99
3.3 XRD RESULTS 99
3.4 BULK SUSCEPTIBILITY κ_{BULK} AND TEMPERATURE DEPENDENT SUSCEPTIBILITY $\kappa(T)$ 101
3.5 AMS RESULTS 105
3.5.1 Trends through the section 105
3.5.2 AMS-types 106
3.6 DATA INTERPRETATION AND ESTABLISHING AN ALTERATION AND DEFORMATION SEQUENCE 107
3.6.1 D_1 *- vertical foliation in the granite and early metamorphism (stage 1) 108*
3.6.2 Palaeoweathering (stage 2) 108
3.6.3 D_2 *- burial compaction (stage 3) 110*
3.6.4 D_3 *- vertical cleavage and related fluid-rock-interaction (stage 4) 110*
3.6.5 D_4 *- lower fault and related fluid-rock-interaction (stage 5) 111*
3.6.6 D_5 *- upper fault and related fluid-rock-interaction (stage 6) 111*
3.7 DEVELOPMENT OF κ_{BULK} AND AMS AND THEIR RELATION TO THE PETROGENESIS 112
3.7.1 Bulk susceptibility 112
3.7.2 AMS fabrics 112
3.8 CONCLUSIONS 117

4 CASE STUDY LÅNGVIKEN, SWEDEN 120

4.1 INTRODUCTION 120
4.1.1 Sampling and applied methods 120
4.2 DESCRIPTION OF THE LITHOLOGIES 120
4.2.1 Autochthonous section 121
4.2.2 Lower Allochthon section 123
4.3 XRD RESULTS 125
4.3.1 Autochthonous section 125
4.3.2 Lower Allochthonous section 126
4.4 WHOLE-ROCK GEOCHEMISTRY RESULTS 127
4.4.1 Autochthonous section 127
4.4.2 Lower Allochthonous section 127
4.4.3 Fe_2O_3 / S *- ratio 128*
4.5 MAGNETIC SUSCEPTIBILITY ANALYSES 128
4.5.1 Bulk susceptibility κ_{bulk} *and temperature dependent susceptibility* $\kappa(T)$ *128*
4.5.2 Calculation of the magnetite grain number in the autochthonous granite 132
4.5.3 κ *-field dependence of pyrrhotite in the allochthonous slice 134*
4.6 AMS RESULTS 138
4.6.1 Autochthonous section 138
4.6.2 Lower Allochthonous section 142
4.7 DATA INTERPRETATION AND ESTABLISHING AN ALTERATION AND DEFORMATION SEQUENCE 144
4.7.1 D_1 *- granite deformation and metamorphism in the Autochthon (stage 1) 144*
4.7.2 Palaeoweathering (stage 2) 144
4.7.3 D_2 *- unconformity parallel compaction in the Autochthon (stage 3) 146*
4.7.4 D_3 *- vertical cleavage in the weathering breccia and lower cover (stage 4) 146*
4.7.5 D_4 *- slice formation and cataclasis within the allochthonous slice (stages 5a-c) 146*
4.7.6 Evolution of the magnetomineralogy 147
4.7.7 Genetic relation of the autochthonous and allochthonous basement parts 149
4.8 DEVELOPMENT OF κ_{BULK} AND AMS IN RELATION TO PETROGENESIS 150
4.8.1 Evolution of κ_{bulk} *150*

- *4.8.2 Factors defining the field dependency of κ_{bulk} in the allochthonous slice* — *151*
- *4.8.3 AMS fabrics* — *152*
- 4.9 CONCLUSIONS — 156

5 CASE STUDY NARCEA ANTIFORM, SPAIN — 162

- 5.1 INTRODUCTION — 162
  - *5.1.1 Regional setting* — *162*
  - *5.1.2 Sampling and applied methods* — *165*
- 5.2 DESCRIPTION OF LITHOLOGIES — 166
  - *5.2.1 Mora Formation* — *166*
  - *5.2.2 Herrería Formation* — *166*
- 5.3 DESCRIPTION OF STRUCTURES — 168
  - *5.3.1 Folding of Mora Fm. - B_{1M}* — *168*
  - *5.3.2 Bedding-parallel cleavage - S_{1M}* — *168*
  - *5.3.3 Isoclinal folding of the Mora Fm. bedding - B_{2M}* — *172*
  - *5.3.4 Cleavage in Mora and Herrería Fm. - S_2* — *172*
  - *5.3.5 Subhorizontal folding in the Mora Fm. (Luna region) - B_{3M}* — *172*
  - *5.3.6 Fracture cleavage in Mora and Herrería Fm. (Luna region) - S_3* — *173*
  - *5.3.7 Vertical folding - B_4* — *173*
  - *5.3.8 Deformation at the unconformity in the Luna region* — *173*
  - *5.3.9 Deformation at the unconformity in the Narcea region* — *174*
- 5.4 CHARACTERIZATION OF THE WEATHERING PROFILE IN THE MORA FORMATION — 175
  - *5.4.1 Petrography* — *175*
  - *5.4.2 XRD* — *175*
  - *5.4.3 Whole-rock geochemistry* — *177*
  - *5.4.4 Bulk susceptibility κ_{bulk}* — *178*
- 5.5 ILLITE- AND CHLORITE CRYSTALLINITY (IC, CHC) — 179
  - *5.5.1 IC and ChC section across the NA in the Luna region* — *179*
  - *5.5.2 XRD-spectra and IC of the clayey gouge zone in outcrop MH 7* — *179*
  - *5.5.3 Illite crystallinity in a bedding-plane slickenside* — *180*
- 5.6 CHLORITE CLASSIFICATION AND GEOTHERMOMETRY — 180
- 5.7 DATA INTERPRETATION AND ESTABLISHING A TECTONOMETAMORPHIC AND ALTERATION SEQUENCE — 182
  - *5.7.1 Cadomian deformation in the Mora Fm. - D_{1M}* — *182*
  - *5.7.2 Palaeoweathering in Neoproterozoic-Cambrian time (climatic indications)* — *184*
  - *5.7.3 Main Variscan E-W compression and unconformity reactivation - D_2 and peak metamorphism* — *185*
  - *5.7.4 Fluid-flow during D_2-reactivation of the unconformity* — *188*
  - *5.7.5 Second phase of Variscan compression and unconformity reactivation - D_3* — *189*
  - *5.7.6 Oroclinal bending and related unconformity reactivation - D_4* — *190*
- 5.8 CONCLUSIONS — 191

6 SUMMARY OF CASE STUDIES AND DISCUSSION — 197

- 6.1 COMMON PALAEOWEATHERING FEATURES AND TRENDS — 197
- 6.2 BULK SUSCEPTIBILITY AS A TRACER OF WEATHERING — 199
- 6.3 TEXTURAL REARRANGEMENT AND UNCONFORMITY-PARALLEL FABRICS — 200
- 6.4 AMS AS A TRACER OF FABRICS RELATED TO WEATHERING AND COMPACTION — 201
- 6.5 STRUCTURAL STRENGTH OF PALAEOWEATHERING ZONES AND SHEAR ALONG THE UNCONFORMITY — 202
  - *6.5.1 Primary contrasts and related processes* — *203*
  - *6.5.2 Secondary contrasts and related processes* — *204*
  - *6.5.3 Physicochemical conditions* — *205*

7 FINAL CONCLUSIONS — 208

LITERATURE — 210

SYMBOLS, ABBREVIATIONS, EQUATIONS — 223

APPENDIX — 224

1 INTRODUCTION

1.1 Motivation

This dissertation is about the geological significance of basement-cover-interfaces in the upper crust with respect to fabric evolution and rock alteration (especially palaeoweathering). As a ubiquitous feature in the upper crust, basement-cover-interfaces (or basement-cover-unconformities) have a key importance with respect to continent evolution: major decollement surfaces are associated with these interfaces in many orogenic regions. A comprehensive examination of this distinctive aspect of the geological record, however, is still missing. The present thesis was initiated to tackle this problem. The study comprises structural (field work, petrography), mineralogical (XRD), geochemical (ICP-ES, Microprobe) and magnetic susceptibility (AMS, field and temperature dependent susceptibility) analyses on several sections across the erosional unconformity between palaeoweathered basement rocks (fossil palaeoweathering zones) and overlying cover sediments.

A geological basement is defined as the older crystalline and/or metamorphic rocks beneath a sedimentary cover. The definition of basement at a regional scale is extended to a major body of deformed and metamorphosed sedimentary rocks, which are unconformably overlain by the cover rocks (e.g. case study Narcea Antiform in this thesis). Basement-cover-unconformities can be categorized by their following characteristics: (1) basement lithology, (2) cover lithology, (3) age and (4) style of the palaeoweathering, (5) alteration and (6) tectonometamorphic overprint. Three examples of granitic basement were chosen, in order to obtain a comprehensive view on the aspects of one typical category. They are characterized by weathering in late Neoproterozoic to Cambrian time under different climatic conditions (see below), and covered by Neoproterozoic or Cambrian siliciclastic sediments. In an additional example a Neoproterozoic sedimentary basement (encountered late Neoproterozoic weathering) is investigated. Important characteristic of all case studies is the overprint of the fossil palaeoweathering zone either by burial diagenesis or orogenic deformation, which caused a vertical compaction and/or led to a detachment along the unconformity.

The following case studies were chosen and implemented in this thesis (Figure 1.1):

- Case study Negev, South Israel. Here, a deformed granite of Neoproterozoic age, the Roded Granite (Pan-African basement), weathered to a saprock-saprolite-laterite profile and was buried beneath red beds. This is an example without orogenic overprint. The Roded Granite is mainly ferrimagnetic, its weathering rocks comprise ferrimagnetic, antiferromagnetic and paramagnetic magnetic carriers.
- Case study Hara, Central Sweden. At the eastern margin of the Scandinavian Caledonides deformed Revsund Granite (Fennoscandian basement) weathered in a cold climate and was buried beneath black shales. Caledonian thrust tectonics overprinted the rocks, duplicating the contact by imbrication. Both parent and weathered rocks are paramagnetic.
- Case study Långviken, Central Sweden. Here, a deformed and weathered Revsund Granite is overlain by quartzitic siliciclastic sequences. The Caledonian thrust tectonics overprinted the rocks, duplicating the weathering zone and interface in a sheared basement slice. Parent granite is ferrimagnetic and weathered rock paramagnetic. Rocks in the basement slice are ferrimagnetic and paramagnetic.
- Case study Narcea Antiform, North Spain. Folded turbidite sequences (Cadomian meta-sedimentary basement) weathered in an arid climate and were buried beneath siliciclastic sequences. Variscan Orogeny overprinted the rocks and reactivated the angular unconformity.

The aim, which is pursued by this approach of case studies and their comparison, is to discover significant similarities and differences in rock characteristics across comparable basement-cover settings.

The following key questions are addressed.

- Is Neoproterozoic weathering in the rocks traceable by geochemistry and mineralogy, as well as distinguishable from overprinting alterations?

- Are there specific rock fabrics, such as preferred orientation of minerals, created by palaeoweathering, and are they distinguishable from overprinting deformation?
- How do magnetic susceptibility signatures change during palaeoweathering? Are there general relations to specific alterations and fabrics? The magnetic susceptibility and its anisotropy (AMS), considered as sensitive markers of rock alteration and fabrics, respectively, are a key element in the present studies of the granitic palaeoweathering zones.
- Are palaeoweathering and diagenetic features important factors modifying shear strength of rocks in the fossil palaeoweathering profile and along the unconformity?

The localization of regional scale decollement surfaces along basement-cover-interfaces is a frequently observed phenomenon in the crust, both in extensional and compressional regimes. There are many examples of detachments along basement-cover interfaces, e.g. in cratons (Alkmim et al. 1999, Bleeker et al. 1999, Riller et al. 1998); in the Caledonian orogen (Gee 1980, Hartz & Andresen 1995), in the Variscan foreland fold-and-thrust belts (Alonso 1989, Gutiérrez Alonso 1996, Gutiérrez-Alonso 1992), in the Alps (e.g. Schönborn 1994, Slack et al. 1996). Deeper crustal examples are found in extensional metamorphic core complexes (e.g Hartz et al. 1994) or below accretionary wedges (e.g. Housen et al. 1996).

The basement-cover-interface, as a discontinuity between two rock bodies, is considered susceptible to strain localization, if major differences in the rheological behaviours between the bodies exist. These rheological differences may be primary due to different lithologies (e.g. basement granite below cover shale); they may also be a result of secondary rock alteration and deformation. Lithological modification during palaeoweathering, mainly massive clay precipitation through feldspar decomposition (see following chapter) and diagenetic compaction may be substantial factors leading to a shear strength weakening in the basement rocks just beneath the unconformity. It has been proposed for fault zones, that not only the phyllosilicate (clay) content, but also the preferred orientation (SPO/LPO) of phyllosilicates and the associated permeability-anisotropy causing fluid overpressure are important factors lowering the frictional strength in fault zones (Wintsch et al. 1995 and references therein).

Palaeoweathering has been studied for a long time (e.g. Goldich 1938, Jenny 1994, Taylor & Eggleton 2001, White & Brantley 1995a) and from a geochemical point of view pedogenetic processes are understood quite well (see following chapter). However, studies about deformation and fluid activity in fossil

Vendian - Cambrian boundary interval (at ca. 550 Ma)

Figure 1.1: Palaeogeographic reconstruction for the Vendian - Cambrian boundary interval with locations of the four case studies. GON: Gondwana, BAL: Baltica,

palaeoweathering profiles are rare (e.g. Migon & Lidmar 2001, Nesbitt & Young 1989, Retallack 1991). Several studies focused on geochemical alteration at unconformities (e.g. Behr 1989, Braendlein et al. 1994, Craw 1994, Sutton & Maynard 1996). The compaction of palaeosoils due to sedimentary overburden has been investigated quantitatively (Caudill et al. 1997, Retallack 1991, Sheldon & Retallack 2001). The relation of magnetomineralogy and related magnetic susceptibility to pedogenetic processes are a point of discussion (Dearing et al. 1996, Liu et al. 2001, Liu et al. 2003, Maher 1998, Maher et al. 2003, Retallack et al. 2003, Vidic et al. 2004). Very few AMS studies have been carried out on weathering profiles. In a nodular iron crusts in soils, ferromagnetic neo-formation led to horizontal fabrics and lowered anisotropy degrees (Mathe et al. 1997). In another case, large deviations of the principal susceptibility directions are caused by bioturbation (Hus 2003). Magnetic fabrics in soils are used to test the calculation of volumetric strain by immobile element mass balancing (Mathe et al. 1999).

In this thesis, the studied palaeoweathering profiles are from the Neoproterozoic-Cambrian boundary interval. Palaeoweathering in that time (e.g. Avigad et al. 2005, German et al. 1996, Ziegler & Longstaffe 2000) is regarded as an important indication for the worldwide climatic change that took place at the dawn of the Palaeozoic. This change was a greenhouse-like warming after Vendian (Cryogenian) glaciations and coincided with the opening of ocean basins and sea level rise, which eventually led to the biological radiation in the Cambrian (Brasier 1992). Palaeoweathering zones are considered to provide valuable information about the palaeoclimatic conditions in which the weathering took place. This has been inferred from the global distribution, the *zonality*, of modern soil equivalents (Martini & Chesworth 1992).

As indicated in Figure 1.1, the chosen case studies were located at different latitudes during the time interval, when palaeoweathering took place. According to the palaeographic reconstruction, the profile of the case study Negev was situated at a low latitude of approximately 10° N. Here, close to the Equator at the northern continental margin of Gondwana, a (sub-) tropical climate can be assumed (Avigad et al. 2005). The laterite, which is observed in the Negev weathering profile, is a characteristic soil in these climates. The case study Narcea Antiform was located near 30° S on a microcontinent at the Northern margin of Gondwana during the Neoproterozoic-Cambrian time (Gutiérrez-Alonso et al. 2003). An arid climate is considered to be predominant during weathering (Gutiérrez-Alonso et al. 2004a, van den Bosch 1969b).

The two Swedish case studies, Hara and Långviken, were located at high latitudes, ca. 60° S (e.g. Bingen et al. 2005, Buchan et al. 2000, Elming et al. 1993, Vidal & Bylund 1981). This latitude implies a temperate to cold climate prevailing during palaeoweathering in Neoproterozoic-Cambrian time, which is supported by glacigene sediments of the Cryogenian age in that region (e.g. Kumpulainen & Nystuen 1985).

Although weathering signatures in the case studies are an key topic in this thesis, the determination of palaeoweathering conditions (palaeoclimate) is of secondary importance. Although geochemical trends can be preserved up to lower greenschist facies metamorphism (Retallack 1991), reconstructing palaeoclimatic conditions by such old weathering profiles is not straightforward. It has to be considered that physiochemical conditions in the rocks of the profiles changed during the approximately 600 Ma lifetime, and geochemical signatures were subject to change (Nesbitt 1992). For example, subsequent hydrolysis reactions may occurred under the influence of formation waters during the Phanerozoic time (Barshad 1966) or metasomatism modifies the geochemistry (e.g. Fedo 1995).

1.2 Weathering and palaeoweathering profiles – terminology and genesis

The term palaeosoil (or palaeosol, paleosol, Greek *palaios* = ancient, + Latin *solum* = ground) is widely used for a soil “formed in a landscape of the past” (Ruhe 1956). There are two principal types of palaeosoils: (1) a buried or *fossil* palaeosoil and (2) a *relic* soil, which began forming in the past, but still continues to form today under different climatic conditions (Bronger & Catt 1989). This thesis deals only with the fossil palaeosoils.

The formation of weathering profiles is dependant on five major factors (Jenny 1994): (a) climate, (b) relief, (c) parent material, (d) time and (e) organisms (including man). These factors cause the following soil-forming processes (Bronger & Catt 1989): (1) physical weathering, the disintegration of a rock into smaller fragments, each with the same properties as the original; it is mainly a result of repeated temperature and pressure changes, (2) chemical weathering of minerals including hydrolysis (leading to clay formation), mineral dissolution and redox processes (3) downward leaching of soluble materials by percolating of rain water in humid regions, (4) concentration of soluble salts in upper soil layers by surface evaporation in arid regions, (5) downward translocation of solid particles as clay, (6) disturbance processes leading mostly to homogenization of the weathered material (shrink-swell movements: argilliturbation; freeze-thaw movements: cryoturbation, root penetration or faunal activity: bioturbation).

Acting individually or in combination, the soil forming processes produce a *weathering profile*, a sequence of weathering horizons approximately parallel with the land surface (exceptions are e.g. some vertisoils: Smith 1999). The relative importance of each weathering process depends on the interplay of the soil-forming factors and defines the characteristics of the weathering profile. Weathering and palaeoweathering profiles formed in tropical regions reach extreme thicknesses of more than 100 metres (Migon & Lidmar 2001).

The velocity of weathering processes and its dependence on the factors of soil formation has been studied. For example, Freyssinet & Farah (2000) estimated 17 Ma (3 metres / Ma) for a ca. 50 metres thick laterite profile developed on the ultramafic Paramaca Schist in French Guiana. The fastest documented chemical weathering rates, thick weathering profiles on crystalline igneous and metamorphic rock take on the order of 10^5 - 10^6 years to form (White & Brantley 1995b).

Generally, four zones are distinguished in a weathering profile. These are from top to bottom: (1) *soil horizons*, a series of intensely weathered horizons dominated by secondary soil minerals and/or organic material and soil textures, (2) *saprolite*, intensely in-situ weathered material with an almost intact primary texture, (3) *saprock*, slightly in-situ weathered rock with an intact primary texture, and (4) unweathered *parent rock*. The boundary between unweathered and weathered rock is called the *weathering front*. The term *weathering crust* is commonly employed to describe a *weathering profile*, which shows predominantly in-situ formed weathering zones (i.e. saprock, saprolite, lateritic saprolite) (Migon & Lidmar 2001). The in-situ (or *autochthonous*) weathering zones may be eroded and subsequently replaced by an *allochthonous soil-sediment*. Soil-sediments are transported soil materials originated from different parent rocks, commonly mixed with other detrital material. Soil-sediments typically have a breccia-like texture (e.g. Migon & Lidmar

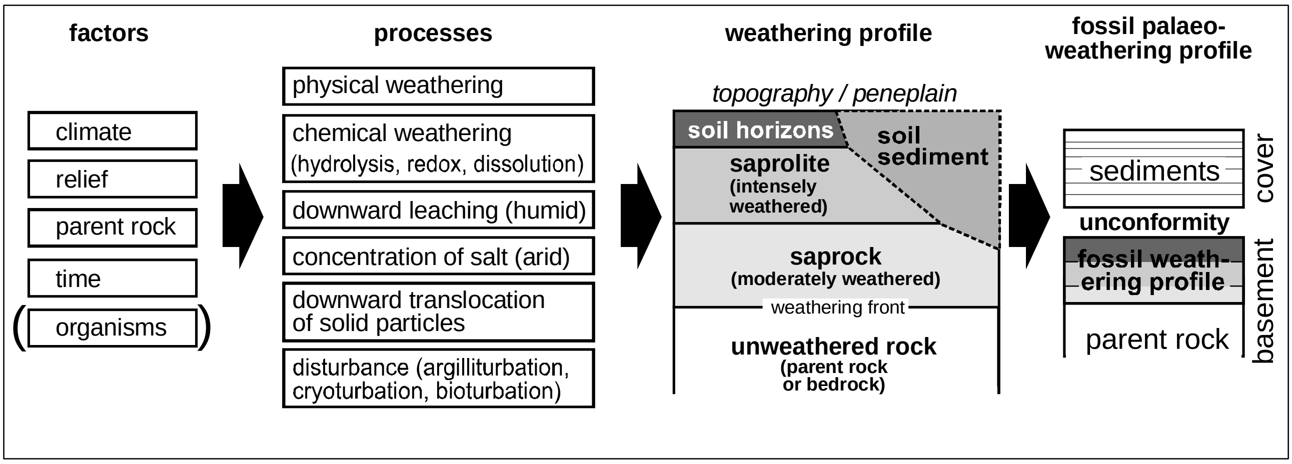

Figure 1.2: Key factors and processes for soil formation, the typical zones of weathering profiles and fossil palaeoweathering profiles.

2001).

Saprolite and saprock also often appear as brecciated (densely cracked at the hand specimen- to microscale), due to sub-surface disintegration processes (argilliturbation, cryoturbation, bioturbation). Some authors use the term *grus* to describe this disintegration zone in weakly to moderately in-situ weathered rocks (Migon & Lidmar 2001). The term grus is used by other authors to describe a coarse-grained soil-sediment. This term is not referred to in this thesis. Instead, the term *weathering-breccia* is favoured, not referring to a specific weathering zone, such as soil-sediment, saprock or saprolite. The term weathering-breccia should not be confused with the term *regolith breccia*, which is widely used in planetary sciences to describe the unconsolidated and fragment-rich material in the uppermost metres on planet or moon surfaces.

In Figure 1.2 the key points of palaeosoil formation are summarized.

The fossilization of the weathering profile, i.e. preservation beneath a sedimentary cover, depends on regional geological processes subsequent to weathering. Typically, the uppermost soil horizons are eroded during *peneplanation*, or with the initial stage of cover sedimentation. The remaining weathering profile beneath the (erosional) unconformity and the basal cover sediments is subject to textural, mineralogical and geochemical modifications, which are dependent on many factors, such as the pre-existing texture of the weathered material, fluid-rock interaction, burial depth and the tectonometamorphic circumstances.

1.2.1 Chemical weathering

Chemical weathering of silicate minerals is the most important process in the production of weathering profiles in silicate basement rocks. The Goldich series describes the order in which silicate minerals weather chemically (Goldich 1938). Minerals forming at high temperatures and pressures are least stable, and weather most quickly because they are farther from their "zone of stability". Minerals which form at lower temperatures and pressures are most stable. Hence, the order of mineral stability in the weathering environment is the opposite order as Bowen's reaction series:

- Iron- and aluminium-hydroxides (mostly goethite, haematite, gibbsite)
- Quartz
- Clay Minerals (mostly illite, smectite, kaolinite)
- Muscovite
- K-Feldspar
- Na-Plagioclase
- mafic minerals (Biotite, Amphiboles, Pyroxenes, Ca-rich plagioclase, Olivine)

Aluminium is the most important immobile element with respect to silicate weathering, and soils of most intense silicate weathering (so-called *bauxites*) are dominated by Al-oxides (gibbsite, boehmite, diaspor). Also the enrichment of iron (in hardly soluble ferric ion modification, Fe^{III}) is often observed in intense weathering zones. Iron- and aluminium-enriched soils are called *feralitic* soil. Understanding the immobility of specific elements (in addition to Al, Fe^{III}, typically also Ti, Zr, Hf) during chemical weathering helps to interpret the mass and volume balance (geochemical enrichment and depletion) during soil development (e.g. White 1995).

The weathering-induced formation of clay minerals is the result of incongruent chemical dissolution of silicates. This characteristic alteration reaction is known as *hydrolysis*, which means the attack of the primary mineral by H^+ or OH^- derived from the weathering agent (e.g. meteoric water infiltrating the rock or groundwater). Ions of the primary mineral are subject of mobilization and mostly depletion in the weathering system (leaching). The following sequence: *primary silicate – illite (and smectite) – kaolinite – Al-oxides (e.g. gibbsite)* reflects typically the progression of weathering. It corresponds to the enrichment of aluminium in the secondary minerals, thus in the weathering material. Although, pure illite is discussed as being a weathering product under certain chemical conditions (Meunier and Velde, 2004), a mixed-layering of illite

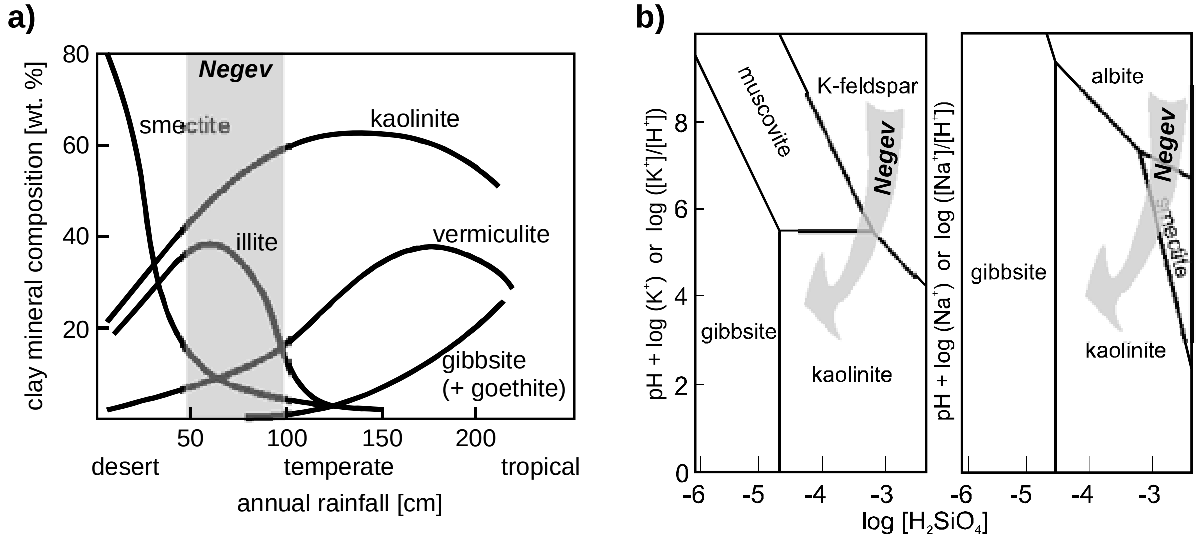

Figure 1.3: Indicative secondary minerals for estimating climatic environment during weathering. a) The clay mineral content indicates the possible conditions during the weathering (modified after D.F. Sherman, University of Bristol; b) Phase stability diagrams of primary K- (left) and Na-minerals (right), and weathering products (Tardy 1971). The grey zones refer to the Negev case (chapter 2).

with smectite (I/S) is more common in the weathering zone. The occurrence of smectite, kaolinite and Al-oxides are climatic indicators (Figure 1.3.a). The dominance of kaolinite + smectite in a soil indicates a warm climate with rather temperate rainfall conditions (Barshad 1966). In Figure 1.3.b it is shown that ultimately, at a very advanced level of weathering, kaolinite hydrolyses to gibbsite, often accompanied by SiO_2 leaching.

Some common weathering reactions associated with the weathering from primary feldspar to gibbsite is summarized here:

The “illitization” reactions for plagioclase (1) and for K-feldspar (2), respectively are:

(1a) $3\ NaAlSi_3O_8 + 2H^+_{aq} + K^+_{aq} = K_{(1-x)}Al_3Si_3O_{10}(OH)_2\ (illite) + 6SiO_{2\,aq} + 3Na^+_{aq}$

(1b) $3\ KAlSi_3O_8 + 2H^+_{aq} = K_{(1-x)}Al_3Si_3O_{10}(OH)_2\ (Illite) + 6SiO_{2\,aq} + 2K^+_{aq}$

This hydrolysis is considered as equivalent to “sericitization” under hydrothermal conditions (Meunier & Velde 2004).

The illite-to-smectite reaction is an intermediate weathering process involving hydration and exchange of alkali and alkaline earth element ions. It can be written as:

(2) $K_{1-x}Al_3Si_3O_{10}(OH)_2 + X_{aq} + H_20 = X_{0.3}Al_2Si_4O_{10}(OH)_2 \cdot 10(H_2O) + K^+_{aq}$

X_{aq} is Na^+ and Ca^{2+} in case of montmorillonite, which is the most abundant smectite type in weathering clays.

The “kaolinization” reaction of K-feldspar and Na-plagioclase (3), for illite (4) and for montmorillonite (5) can be written as:

(3) $2\ (Na,K)AlSi_3O_8 + 2H^+_{aq} + 9H_2O = Al_2Si_2O_5(OH)_4 + 4H_4SiO_{4(aq)} + 2(Na,K)^+_{aq}$

(4) $2\ KAl_3Si_3O_{10}(OH)_2 + 2H^+_{aq} + 3\ H_20 = 3\ Al_2Si_2O_5(OH)_4 + 2\ K^+_{aq}$

(5) $(Na, Ca)_{0.3}Al_2Si_4O_{10}(OH)_2 \cdot 10(H_2O) + 5\ H^+_{aq} = Al_2Si_2O_5(OH)_4 + 2\ H_4SiO_{4(aq)} + 0.3\ (Na^{+,}\ Ca^{2+})_{aq}$

The “final” kaolinite-to-gibbsite reaction is:

(6) $Al_2Si_2O_5(OH)_4 + 5H_2O = 2Al(OH)_3 + 2H_4SiO_{4aq}$

Whereas illite alteration to smectite and kaolinite does not involve SiO_2 mobilization, hydrolyses of feldspar, smectite and kaolinite do involve mobilization of SiO_2.

The iron content in silicates is generally mobilized during hydrolysis. Together with iron of primary Fe-oxides or Fe-hydroxides, the mobilized iron is commonly subject of oxidation or reduction, hydration and/or dissolution during weathering. Phase transitions mainly depend on the Eh-pH conditions of the fluid-rock system (Figure 1.4). The oxidation of primary iron-II-bearing phases (e.g. magnetite) to iron-III phases (e.g.

haematite) is frequently observed under aerobic (oxidizing and acidic) conditions:

(7) $2\ Fe^{II}Fe^{III}{}_2O_4\ (magnetite) + ½O_2 = 3\ Fe^{III}{}_2O_3\ (haematite)$

Hydration may come along with, or follow oxidation, forming hydroxides, such as ferric hydroxide or goethite:

(8a) $4\ Fe^{II}O\ (ferrous\ oxide) + 6\ H_2O + O_2 = 4\ Fe^{III}(OH)_3\ (ferric\ hydroxide)$

(8b) $Fe^{II}Fe^{III}{}_2O_4 + H^+{}_{aq} + 2\ H_2O = 3\ Fe^{III}OOH\ (goethite)$

Dehydration of the hydroxides to haematite may follow subsequently to oxidation and hydration:

(9a) $2Fe^{III}OOH = Fe^{III}{}_2O_3 + H_2O$

(9b) $2Fe^{III}(OH)_3 = Fe^{III}{}_2O_3 + 3\ H_2O$

Reduction of iron occurs in anaerobic conditions (waterlogged). The reduced iron compounds are segregated out as blue-green coloured mottles or concretions in the soil, so-called *gleying* zones. The reduction reactions are basically reversed oxidations, therefore not explained in detailed here.

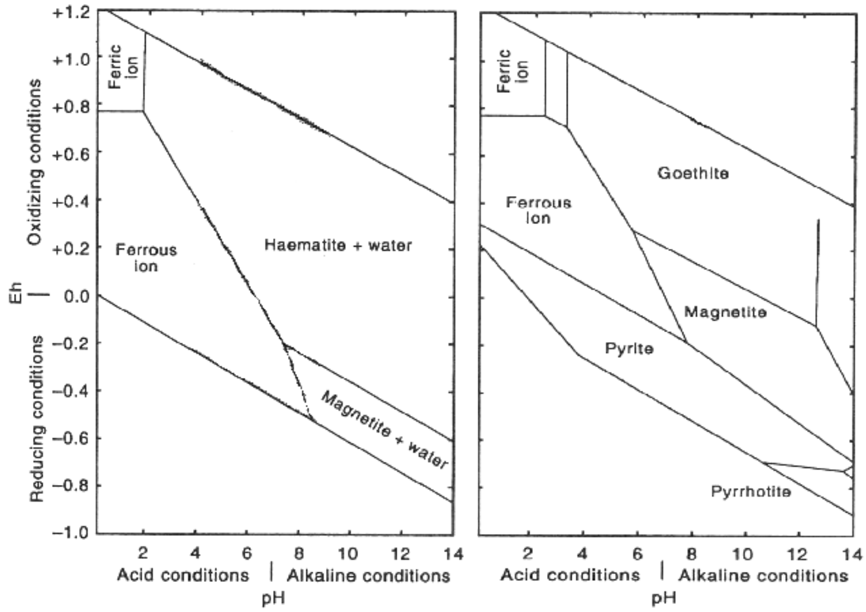

Figure 1.4: Eh-pH-diagrams with the stability fields of iron oxides and sulphides at room temperature.

Gradual changes in geochemical signatures are commonly observed in weathering profiles (e.g Brown et al. 2003, Middelburg et al. 1988, Price & Velbel 2002). Weathering indices, based on the mobility of certain elements, are established as tools to quantify weathering degree (Price & Velbel 2002). Three indices are calculated for the case studies: *CIA* (Nesbitt & Young 1982), *CIW* (Harnois 1988) and *PIA* (Fedo et al. 1995) according to following equations:

(10) $CIA = [Al_2O_3/\ (Al_2O_3+CaO+Na_2O+\ K_2O)\cdot 100]$

(11) $CIW = [Al_2O_3)/(Al_2O_3+CaO+Na_2O)\cdot 100]$

(12) $PIA = [(Al_2O_3-K_2O)/(Al_2O_3+CaO+Na_2O-K_2O)\cdot 100]$

1.3 Methods

1.3.1 X-ray diffraction

X-ray diffraction (XRD) on unoriented whole-rock powder and oriented preparation of the clay fraction (<2 μm) is performed in order to identify mineral alteration and precipitation throughout the granite weathering profile. Since calibrations with mineral standards are not carried out in the studies, all XRD measurements are semi-quantitative. Consequently, spectra do not indicate absolute mineral contents, but relative differences of peak parameters (d-spacing, intensity, full width at half maximum (FWHM)) of indicative peaks in a spectra and their variation between samples are used for mineralogical interpretation.

The measurements are performed with a *Siemens D 500* instrument at the Geological-Palaeontological Institute of the University of Heidelberg. Measuring conditions are 40 kV / 30 mA, using CuKα radiation.

The steps of whole-rock sample preparation are cleaning, grinding with hammer, and milling 40-50 seconds in a tungsten rotary mill in dampened conditions (by adding de-ionized water) to obtain a fine powder. The pulverized and dried whole-rock samples are scanned from 2° to 70° 2θ at a step-scan-rate of 0.02°/s.

The < 2 μm clay fraction is separated and mounted pursuing the following steps: first, about 50 g of wet whole-rock material is milled for 5 seconds. Milling wet material for a short time disaggregates the rock matrix and therefore optimizes the yield of clays and minimizes grinding of larger minerals down to the clay fraction, i.e. minimizes contamination of the clay size fraction by non-clay minerals. Then, this fine-grained wet “paste” is filled up with ca 1.5 ltr de-ionized water and disaggregated during a 30 min ultra-sonic bath. The disaggregated suspension is centrifuged 4 min at 1000 U/min, to settle down the >2 μm particles. The <2 μm particle suspension is evaporated at 60 °C, without any chemical treatment. Texture mounts (3 x 3 cm glass mounts) are made with suspensions of 45 mg of the <2 μm powder in 1 ml de-ionized water, treated 5 min in an ultra-sonic bath. The mounts are air-dried at room temperature. Diffraction measurements are performed at a step-scan-rate of 0.02°/0.5s, first in air-dried state (from 2° to 50° 2Θ) and then ethylene glycol-solvated (from 2 to 32° 2θ). For spectra analyses and peak decomposition the software MacDiff© (by Dr. Rainer Petschick) is used.

The crystallinity of illite and chlorite are considered to be dependent on the metamorphic grade in the diagenetic to low grade metamorphic zone (Arkai 1991, Kübler 1967, Warr & Rice 1994). By XRD on oriented preparation the illite and chlorite crystallinity (IC and ChC, respectively) in the clay fraction (< 2 μm) can be estimated. The illite crystallinity is defined as the FWHM [Δ2θ] of the illite 001 peak and referred to as the Kübler Index (Kübler 1967). The Kübler Index (KI) attributed to the boundary between late diagenesis to lower anchimetamorphism is 0.42 and the KI defining the boundary between anchizone to greenschist facies is 0.25.

Only shales and siltstones are used for crystallinity determination. In fine-grained siliciclastic rocks the clay fraction is considered as largely authigenic, however, a certain portion of clay-sized detrital mica (contamination) decreases the FWHM indicating misleadingly slightly higher metamorphism grades. This has to be considered when interpreting IC and ChC data. Coarse-grained rocks (greywackes, sandstones and conglomerates) may not give appropriate results, because of the stronger influence of detrital mica contamination and the pore space facilitating illite growth.

The FWHM values are determined from fitted peaks (with Split-Pearson IIV functions). Data calibration is performed with the CIS sample set, which was kindly provided by L. Warr of the Geological-Palaeontological Institute, University Heidelberg (calibration details in Warr & Rice 1994). A combined calibration equation for illite and chlorite is calculated from 11 CIS measurements (data and regression in Appendix IV.d):

$$(1) \qquad IC_{CIS} = 1.1463 \cdot IC_{Lab} - 0.0066 \; (R^2 = 0.9554).$$

Up to three mounts of a sample are measured and the standard deviation σ for IC and ChC is calculated. The error of IC and ChC is defined as

$$(2) \qquad IC, ChC\text{-}error\ [\%] = \sigma / mean\ IC, ChC\text{-}value \cdot 100$$

1.3.2 Whole-rock geochemistry (ICP-E/MS)

To gain information about element mobilization through the weathering profiles, whole-rock major elements of a representative sample selection are measured. The analyses are performed by ACME Analytical

Laboratories Ltd., Canada. For major element oxides an Inductive Coupled Plasma Emission Spectrometer, ICP-ES, after $LiBO_2$ fusion is used (ACME whole-rock package 4A). Procedure details can be obtained from ACME-Lab (*www.acmelab.com*).

1.3.3 Scanning Electron Microscopy and Chlorite geothermometry by microprobe analyses

Scanning Electron Microscopy (SEM) backscatter imaging is employed on carbon-coated thin sections to study the structures and mineralogy in the microscale. The element distribution in minerals is qualitatively analysed with energy dispersive X-Ray diffraction (*SEM-EDX; LINK-ISIS, Oxford Instruments*).

Microprobe studies for exact element distribution of chlorites, white mica and Fe-Mg-carbonates is carried out for specific samples (carbon-coated thin sections).

Two chlorite geothermometers are applied (Cathelineau 1988, de Caritat et al. 1993). They are based on the distribution of cations in chlorite-layer vacancies, which is indicative for the thermal conditions in which the chlorites were crystallized. Principally, with higher metamorphism or hydrothermal alteration a decrease of Si^{IV} and Al^{VI} together with an increase of Al^{IV} and $(Fe + Mg)^{VI}$ occurs (de Caritat et al. 1993). Al^{IV}-contents are directly disproportional to the Si^{IV}-contents, because both elements are substituting each other at the tetrahedral vacancy positions.

A “proto”-thermometer by Cathelineau (1988) based on empirical data calculates the temperature depending on the Al^{IV} content with the function

$$T\,[°C] = -61.93 + 321.98 \cdot Al^{IV}.$$

The revision of de Caritat et al. (1993) pointed to the fact that the Al^{IV} content is depending on the total Al-content, which is itself lithology-dependent. Therefore, the thermometer by Cathelineau (1988) is not valid in all settings. Consequently, a better correlation between temperature and Al^{IV}- or Si^{IV}-content is given, when comparing chlorites of similar total Al-content. Total Al-content is expressed as the hypothetical Al-end member $Al_{12}Si_{-2}O_{10}(OH)_8$ and can be calculated as the ratio of Al^{VI} and the sum of all octahedral vacancy members: $[Al^{VI} / (Al^{VI} + Fe + Mg + Mn)]$ (Marioth 2001). For simplicity, all iron is considered a substitute at the octahedral vacancy (i.e. Fe^{2+}), the ratio Fe^{2+}/Fe^{3+} could not be determined, but is close to one. De Caritat (1993) published empirical thermometers for three different chlorite types, i.e. “Al-chlorites”- contents:

“Al-chlorites” < 0.2 : **$Si^{IV} = -0.0021 \cdot T\,[°C] + 3.6061$**; [$R^2 = 0.9477$]
“Al-chlorites” 0.2 to 0.24: **$Si^{IV} = -0.0013 \cdot T\,[°C] + 3.2208$**; [$R^2 = 0.9919$]
“Al-chlorites” > 0.24 : **$Si^{IV} = -0.0005 \cdot T\,[°C] + 2.7895$**; [$R^2 = 0.8929$]

1.3.4 Determination of bulk rock density and porosity

The bulk rock density ρ and the porosity ϕ of the rocks from the weathering profile in case study Negev are determined. The bulk rock density is measured by the weight and volume of the standardized AMS cylinders with the basis .

$$\rho = \frac{mass_{AMS}}{volume_{AMS}} \qquad (2)$$

where $volume_{AMS} = \pi \cdot (½ \cdot 2.5\ mm)^2 \cdot 2.2\ mm = 10.8\ mm^2$).

For calculating the porosity, the solid density ρ_{solid}, which is the density of the rock powder, has to be determined. This is done employing the method described in Hölting (1996): A vessel filled with the rock powder of $mass_{dry}$ is filled up with a quantity of water ($mass_{V2}$, equal V_2, since the density of water is 1) and this quantity is subtracted from the defined vessel volume ($mass_{V1}$ or V_1). ρ_{solid} is calculated with:

$$\rho_{solid} = \frac{mass_{dry}}{V_1 - V_2} \qquad (3)$$

The determination of the rock porosity is based on following equation:

$$(4) \qquad \phi = \frac{\rho_{solid} - \rho}{\rho}$$

1.3.5 Image analysis of mineral modal fraction, shape distribution and SPO

Image analyses are carried out on selected thin sections of case studies Israel and Långviken. Investigated are the modal fraction, shape distribution and shape preferred orientation (SPO) of specific minerals.

To quantify the cryptic granitic petrofabrics in the unweathered and macroscopically undeformed granite (sample RA3-1) and determine their relation to the AMS fabrics, the three-dimensional (3D) SPO of relevant components for rock and magnetic fabric are determined by image analyses of thin sections. The following phases are analysed: a) chlorite (actually chlorite/mica-stacks), b) all single martite grains and c) all martite clusters. Martite clusters are the combination of martite grains that are spatially very closely located (maximum distance half diameter) and all remnant martite grains that are disseminated (see Appendix V.a for micrographs).

In addition, two-dimensional (2D) martite image analysis of a moderately weathered cataclasite and a laterite sample (sample RA1-4.a and RA2-1.b respectively) is carried out. Both lithologies comprise a different petrographic fabric with respect to the granite, hence the relation of single martite shapes and martite cluster shapes with the new petrographic fabric and the AMS has to be determined. Technical reasons permit only the use of two thin sections (cut perpendicular) for each sample, but this is enough to estimate the relation with AMS directions and the form factor of the 3D-SPO.

The thin sections are cut from one of the measured AMS-cylinder and are oriented with respect to the principal AMS-surfaces $\kappa_1\kappa_2$, $\kappa_1\kappa_3$ and $\kappa_2\kappa_3$. This allows a direct comparison of SPO with principal AMS axes and may provide information about maximum fabric anisotropy. A possible misfit of ± 5° of the section orientations is due to the cutting process. In case of the cataclasite and laterite sample only $\kappa_1\kappa_2$ and $\kappa_2\kappa_3$ sections were used.

For the chlorite analysis, the polished thin sections are scanned with 3200 dpi, which provides a sufficiently high resolution of 7.9 µm/pixel. For the martite analysis, photo-micrographs in reflected light of every martite grain and martite grain-cluster are taken (with a digital microscopy camera *Leica Digital DFC 480*). The photo-micrographs are compiled in a large image of 600 dpi, providing a resolution of 3.1 µm/pixel.

The images are “classified” using the image analysis software *DIana* (© 1991-2003 J. Duyster). “Classification” means to assign specific colours or grey-values to the phases of interest. The single martite grains are automatically classified, because of their high colour contrast to the matrix (in reflected light micrographs). Martite clusters and chlorites are classified manually.

The classified images are imported into *SPO2003* (© 2003 Patrick Launeau & Pierre-Yves F. Robin). This program uses the inertia tensor method (Launeau & Cruden 1998) to calculate the shape tensor of each particle in the classified image and ultimately the SPO (mean inertia tensor) of a phase population in the entire section. The mean inertia tensor is expressed as an ellipse with absolute lengths of the long axis *a* and short axis *b*, the shape ratio R and the long axis direction, ϕ, in relation to a reference direction. The mean tensor is calculated by weighted single tensors. This weight-factor corresponds to the area of each particle in the image (Launeau & Robin 2005) and is crucial for interpreting the SPO with respect to AMS, since it takes the influence of particle size into account. Rose diagrams are used to visualize the preferred orientation ψ of the population independent of size or shape ratio: ψ is the greatest eigenvector of the direction cosine dispersion matrix defines (Harvey & Laxton 1980). The intensity Rf½ of the preferred orientation is defined

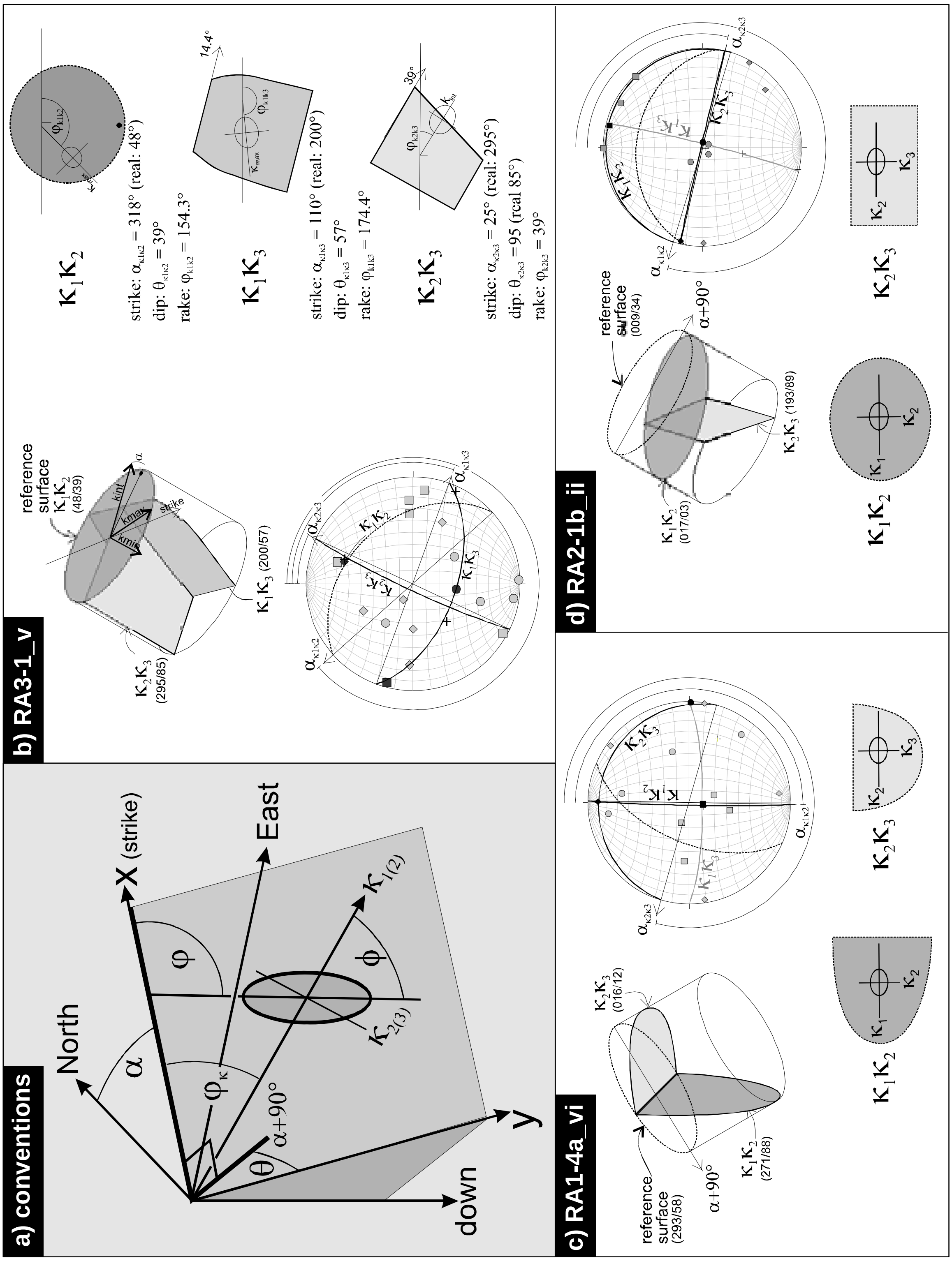

Figure 1.5: Thin section orientations for image analyses of mineral SPO. a) Conventions for directions and angles of thin sections and SPO for the use in ELLIPSOID (changed from Launeau & Robin 2005); b) unweathered granite sample RA3-1_v (three section for 3D-SPO and best-fit-ellipsoid determination); c) cataclastic sample RA1-4b_vi; d) laterite sample RA2-1b_ii. The angle α between section strike and North is defined by a right hand rule, i.e. measure starts from N in right direction (dip may be higher than 90°; in this case *real* dip inclination is also displayed).

by Launeau & Robin (1996) as the square root of ratio of eigenvalues of Harvey & Laxton’s direction cosine dispersion matrix.

The AMS long-axes in the principal surfaces (κ_1 in $\kappa_1\kappa_2$ and $\kappa_1\kappa_3$ and κ_2 in $\kappa_2\kappa_3$) are defined as the reference direction in each sectional image. These reference directions have their distinct geographical orientations, which are defined by the conventions given by Launeau & Robin (2005) (see also Figure 1.5.a.): The section surface itself is described by strike ϕ and dip θ. In cases of overturned section faces, the dip angle θ will be greater than 90°. The rake of the reference direction on this surface (from horizontal) is φ_κ. The determined

SPO ellipse long axis on the section has the angle ϕ with the reference line. The rake φ from horizontal is therefore exactly defined and can be calculated with the angles φ_κ and ϕ. All angle definitions follow a right-hand rule, i.e. angles are measured from right (clockwise) of the azimuth direction. The reference lines are displayed horizontally in the figures.

The SPO data (lengths of ellipse's axes *a* and *b*, rake φ of the long axis and orientations of the three sections) of sample RA3-1 are imported into *ELLIPSOID* (© Patrick Launeau & Pierre-Yves Robin 2003). This program calculates best-fitting ellipsoids of at least three ellipses (tensors) of mutually perpendicular sections. *ELLIPSOID* calculates the orientations and lengths of the three principal axes *A*, *B*, *C*, the shape parameters (L/F, P' and T allowing direct comparison with AMS parameters) and provides misfit measures for the ellipsoids and for the particular sections tensors, so-called "incompatibility indices" $\sqrt{\tilde{F}}$ and F½, respectively (see Robin 2002) for equation). $\sqrt{\tilde{F}}$ is an estimate of the standard deviation of the population of sectional ellipses (Launeau & Robin 2005). The smaller $\sqrt{\tilde{F}}$ is, the more compatible are the data. The best-fitting ellipsoids are determined in two different ways: a) with scale and b) without scale (Robin 2002). Scale refers here to the mean tensor sizes of the sections, which is mainly dependent on the absolute particle size distribution in each section. The scale of the mean tensor is defined by the absolute lengths of the long and short axes of the ellipse, *a* and *b* respectively. The ellipsoid determination without scale just uses the ratio of *a* and *b*, not their absolute lengths.

The volume content and grain size distribution of pyrrhotite in selected samples of the case study Långviken are estimated. For the high amount of grains in sample st-j an automated digital counting of classified images is employed. Manual counting is carried out for the low amount of grains in st-e.

1.3.6 Correction-rotation of unoriented drill core sections

The drill cores of the Swedish case studies, Hara and Långviken, are not oriented regarding their declination.

Rotation axis is 0/90 (drill-axis). The dominant steep planar fabric (gneissic foliation in the deformed granite or mica cleavage in weathering breccia) in each sample are stably oriented through the drill core sections and thus represent a reference for the angle of correction-rotation. The sampling and correction-rotation procedure is shown in Figure 1.6. Broken parts of drill cores are reassembled until a break occurs, where a reassembling is not possible (e.g. due to missing parts). The x-axes of the cylinder specimens point to North ("N") in the

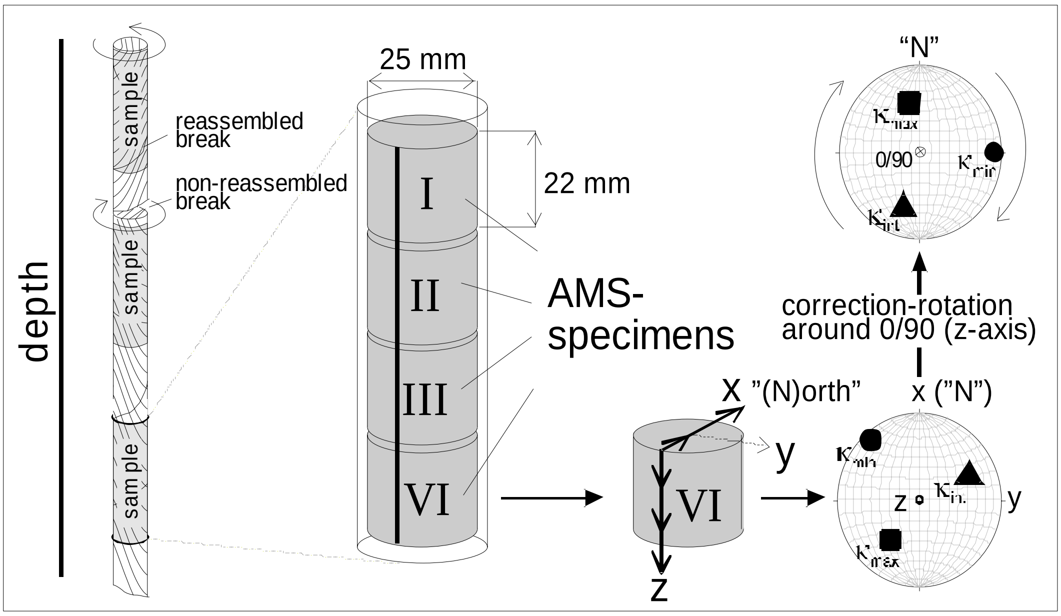

Figure 1.6: Sampling method and correction-rotation for the Hara and Långviken drill cores.

stereonet. The AMS data in the stereoplots were rotated around vertical z-axis (0/90) by angles, which are determined to match the continuity of the orientation of the foliations. For interpretations of AMS fabrics the corrected orientations are used

1.3.7 Magnetic susceptibility and AMS

1.3.7.1 Introduction

As a key analytical method for tracing alteration and fabric changes in the granitic weathering profiles, the magnetic susceptibility and its anisotropy is applied. The AMS of the weathered sedimentary basement, case study Narcea Antiform, is not discussed in this thesis, because the influence of bedding and cleavage on AMS is too strong to gain any information concerning weathering-induced alteration and fabric changes. These data are summarized in Appendix II.d.

All material, including minerals, possesses the property of becoming magnetized in the presence of an applied magnetic field. This property is called magnetic susceptibility (e.g. Dunlop & Özdemir 1997, Tarling & Hrouda 1993). The magnetic susceptibility κ is a material property. In weak fields, like the Earth's magnetic field, the magnetization is approximately linearly proportional to the magnetising field:

$$(2) \qquad \vec{M} = \frac{\vec{J}}{\mu_0} = \kappa \cdot \vec{H}$$

where *M* is the magnetic dipole moment per unit volume, *J* is the magnetic polarization or magnetization, *H* is the (applied) magnetic field, μ_0 is the magnetic permeability and κ is the magnetic susceptibility. The magnetic behaviour within an applied magnetic field depends on the atomic magnetic moments, which show orbital and spin motions of electrons, and on the relative position of these moments in the mineral lattice resulting in dia-, para-, and ferromagnetic behaviour.

Diamagnetism

Diamagnetic minerals are e.g. quartz, feldspars, calcite, in principal minerals without incorporated iron. Without the influence of a magnetic field diamagnetic minerals show completely compensated magnetic moments. Within a magnetic field, all magnetic moments align anti-parallel to the applied field, which cause low induced magnetization and negative values of the magnetic susceptibility. Diamagnetic susceptibility shows no temperature dependent behaviour.

Paramagnetism

The paramagnetic materials (e.g. chlorite, biotite, amphibole, Fe-bearing carbonates) show partially uncompensated spin-moments. Without an applied field at room temperature none of the magnetic moments show interactions, and thus, their alignment is statistically irregular. Applying a magnetic field, magnetic moments align parallel with the field, which causes positive values of the magnetic susceptibility. Paramagnetic susceptibility displays temperature-dependent behaviour according to the Curie law:

$$(3) \qquad \kappa_{para} = C / T$$

where C is the Curie constant and T is the temperature. Paramagnetic minerals show a distinct variation of κ, which is mainly caused by the iron-content.

Ferromagnetism

Strongly interacting paramagnetic moments cause a distinct orientation of the uncompensated spin-moments within a crystal lattice and leading to residual magnetic moments. This is called ferromagnetism. Aligned parallel with the applied field, ferromagnetic moments persist also in absence of the magnetic field. There are several possibilities of the orientation of the magnetic moments within a crystal lattice.

Pure Ferromagnetism (iron, cobalt, nickel) is characterized by a parallel alignment of all uncompensated magnetic moments. This is realized in nature in Fe-Ni alloys, e.g. in meteorites. Ferromagnetic minerals are characterized by paired anti-parallel alignment of the magnetic moments, which do or do not compensate each other, resulting in two principal magnetic characteristics: Antiferromagnetism and Ferrimagnetism, respectively.

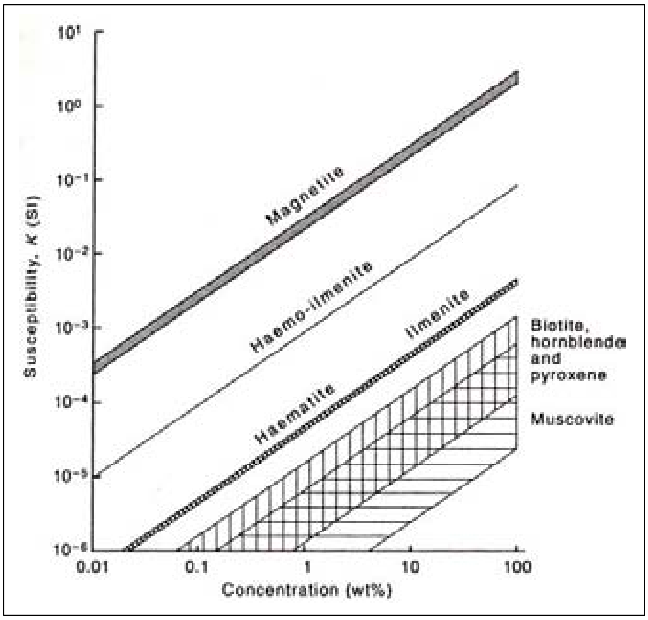

Figure 1.7: The relation between susceptibility κ and modal fraction (wt%) of important magnetic carriers in rocks (Tarling & Hrouda 1993)

Antiferromagnetism: When paired and anti-parallel magnetic moments compensate each other, the sum of the magnetic moments is zero and the minerals show antiferromagnetic behaviour (e.g. haematite, ilmenite,). When applying a magnetic field, the induced magnetization is parallel with this field and the magnetic susceptibility shows positive values. At a distinct temperature, the *Néel temperature* ($T_{\text{Néel}}$), which is characteristic for each mineral, the order of the magnetic moments disappears passing into a statistically randomized, i.e. paramagnetic order. The antiferromagnetic κ is therefore temperature-dependant according to the Curie-Weiss law. Antiferromagnetic minerals show a steep increase of magnetic susceptibility just below their T_{Curie}, which is called *Hopkinson peak*. A transition specific to haematite (α-Fe_2O_3) in which there is a change in the direction of the atomic magnetic moments in the antiferromagnetic state from parallel to perpendicular to the c-axis is called *Morin transition*.

Ferrimagnetism: In some natural minerals (e.g. magnetite, titanomagnetite, monoclinic pyrrhotite) the paired and anti-parallel magnetic moments do not compensate each other. Consequently, a resulting magnetic moment exists also outside a magnetic field, which is referred to as remanent magnetization. Similar to the antiferromagnetic order, the ferrimagnetic order passes into a paramagnetic order above a distinct temperature, which is called the Curie temperature (T_{Curie}). Above the T_{Curie}, the ferrimagnetic minerals show a temperature dependent behaviour according to the Curie-Weiss law. The Hopkinson peak is typical for ferrimagnetic minerals, as well. Mixed-valent mineral systems encounter an ordering of ions at low temperatures. In case of ferrimagnetic magnetite ($Fe^{III}_2Fe^{II}O_4$), the ordering of Fe^{III} and Fe^{II} ions within octahedral sites changes the magnetic behaviour. The *Verwey transition* (T_{Verwey}) of magnetite occurs at ca. -150 °C.

Field dependence of ferrimagnetic minerals: For some ferromagnetic minerals (haematite, titanomagnetite and monoclinic pyrrhotite), the relationship between magnetic field and susceptibility is non-linear with increasing field amplitude. These minerals show a field dependence of magnetic susceptibility. Field dependence of haematite (e.g. Hrouda et al. 1998) and titanomagnetite (e.g. de Wall 2000a, Jackson et al. 1998) have been documented. The field dependence of pyrrhotite has been described (Clark 1984, de Wall & Worm 1993, Dekkers 1988, Kontny et al. 2000, Worm 1991, Worm 1995, Worm et al. 1993). In case of pyrrhotite, the susceptibility increases at fields above 10 A/m by a power law function $k \sim H^{0.25}$; and the grain size is an important controlling factor for the field dependence of pyrrhotite (Worm et al. 1993). The significance of field dependence of pyrrhotite for magnetic anisotropy has been investigated (de Wall & Worm 1993, Hrouda et al. 2000, Pokorny et al. 2004).

The intrinsic susceptibilities of important minerals (susceptibility carriers) in the present case studies are displayed in Table 1.1 and Figure 1.7. The magnetic susceptibility of ferrimagnetic minerals are orders of magnitudes higher than of para- and antiferromagnetic minerals. Diamagnetic susceptibilities are very small and have negative values.

Table 1.1: Intrinsic volume susceptibility κ and anisotropy parameters P' and T of minerals, which are the important magnetic carriers in the present case studies. * (Hunt et al. 1995); ** (Tarling & Hrouda 1993)

Mineral	**Volume Susceptibility κ[10^{-6} SI]**	**Anisotropy degree P'**	**Shape factor T**
Magnetite (ferrimagnetic)	1,000,000 - 5,700,000*		
Pyrrhotite (ferrimagnetic)	3,200,000* at 300A/m, field dependend		
Pyrrhotite (antiferromagnetic)	1,000 - 170,000*		
Haematite (antiferromagnetic)	500 - 40,000* (field dependent!)		
Goethite	1,100 – 12,000		
Chlorite (paramagnetic)	70 to 1,550**	1.154 to 1.753**	0.26 to 0.74**
Biotite (paramagnetic)	998 to 1,290**	1.198 to 1.372**	0.90 to 0.99**
Muscovite (paramagnetic)	122 to 165**	1.1393 to 1.413**	0.44 to 0.67**
Fe-Illite (paramagnetic)	410*		
Pyrite (paramagnetic)	35 – 5,000*		
Quartz (diamagnetic)	-13 to - 17*	1.01**	1**
Oligoclase (diamagnetic)	-13 to - 17*		
Calcite (diamagnetic)	-7.5 to -39*	1.11**	1**
Graphite (diamagnetic)	-80 to -200*		

1.3.7.2 Anisotropy of the magnetic susceptibility

Ferri-, antiferro-, para- and diamagnetic minerals show a directional dependence of the magnetic susceptibility corresponding to their crystallographic axes or shapes (e.g. Tarling & Hrouda 1993)). The resulting anisotropy of the magnetic susceptibility can be described as a second order tensor, which is displayed as a susceptibility ellipsoid with a maximum, intermediate and a minimum principal axis (κ_1, κ_2, κ_3) (Figure 1.8). The maximum principal axis κ_1 represents the magnetic lineation and the surface defined by κ_1 and κ_2 is referred to as the magnetic foliation. The bulk AMS is commonly measured in a low magnetic field (300 A/m) and is the sum of the magnetic anisotropies of all contributing minerals in a sample specimen. The measurement of AMS is commonly used for the quantitative evaluation of petrofabrics (SPO or LPO). The measuring method is rapid and non-destructive, it is applicable to all rock types and it has a very high sensitivity. It is possible to identify bulk strain in rocks with the AMS-ellipsoid, even though macroscopic strain indicators, like foliation and lineation, are missing (Pares et al. 1999). A correlation of orientation and eccentricity of the strain-ellipsoid and the AMS-ellipsoid has been carried out for many case studies but its coincidence is proofed in few examples. The relationship between strain and AMS is more complex in rocks bearing petrographic subfabrics, such as crenulated cleavages or SC-fabrics. This is also the case for subfabrics defined by differently oriented sets of magnetic carriers, such as magnetites and micas. In both cases, the AMS tensor is the product of the superposition of the subfabrics and can lead to bulk magnetic anisotropies differing from strain directions (Borradaile 1988, Housen et al. 1993, Pares & van der Pluijm 2000, Pares & van der Pluijm 2002a, Tarling & Hrouda 1993). Some theoretical cases of AMS fabric caused by superposition of subfabrics are shown in Figure 1.9. According to these cases, superposition of differently oriented oblate subfabrics can result to isotropic or even prolate AMS, analogously, overprinting prolate subfabrics can result in isotropic or oblate AMS fabrics. There is a dependency of

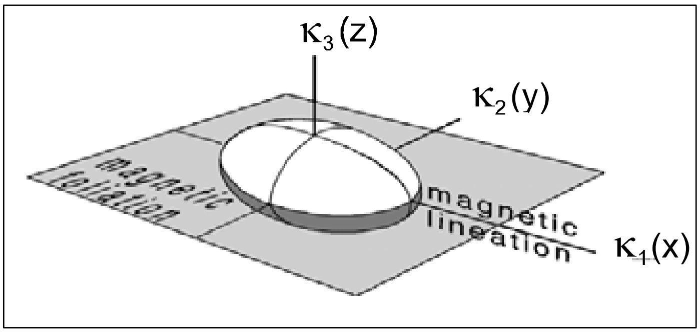

Figure 1.8. The magnetic susceptibility ellipsoid with its principal axes κ_1, κ_2 and κ_3. The maximum axis (κ_1) represents the magnetic lineation. The surface defined by κ_1 and κ_2 is referred to as the magnetic foliation.

ellipsoid parameters and axis distribution of specimens on the scale of rock fabric. Large scale fabrics with respect to the specimen dimension, such as a folded foliation, can produce a pattern which appears to be prolate (clustered κ_1 and girdling κ_3), although specimens AMS are oblate (Figure 1.9.d). Is the foliation folded in sub-specimen scale (crenulated), producing prolate magnetic fabrics, the resulting AMS may show clustered κ_3 distribution, typically a feature of oblate fabrics.

1.3.7.3 AMS measurements

The low-field anisotropy of magnetic susceptibility (AMS) of the samples of case studies Negev and Narcea Antiform is measured with a *KLY-2 Kappabridge* (AGICO, Brno, Czech Republic) at the Geological-Palaeontological Institute of the University of Heidelberg. For the samples from Sweden (case studies Hara

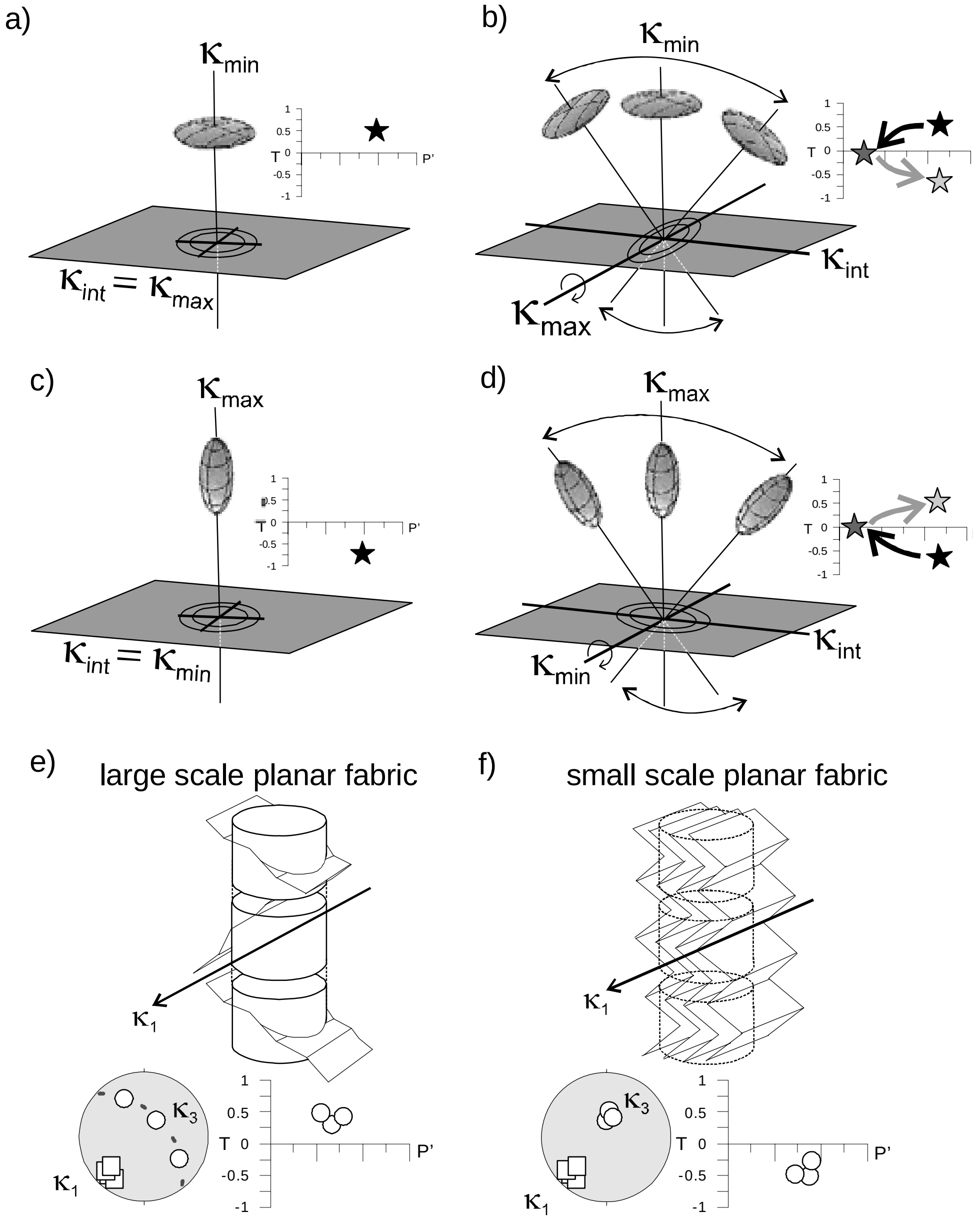

Figure 1.9: Composite magnetic fabrics and the effect of fabric scale on AMS. a) oblate AMS ellipsoid; b) composite magnetic fabric by superposition of differently oriented oblate subfabrics resulting in a decrease of T and P' and progressively a the formation of a prolate T; c)+d) analogue superposition effects with primary prolate shapes (a-d after de Wall et al. 2000). e+f) general dependency of ellipsoid parameters and axis distribution of specimens on rock fabric scale (see text).

and Långviken) the *KLY-4S Kappabridge* is used. Three to six standardized cylinder with the dimensions: 25 mm (base) 22 mm (height) are taken. The applied magnetic field in both instruments is 300 A/m at room temperature. Sensitivity of the KLY-4S is $0.03 \cdot 10^{-6}$ (SI) for bulk susceptibility measurements and $0.02 \cdot 10^{-6}$ (SI) for spinning-specimen anisotropy measurements. The KLY-2 has a slightly higher detection limit.

The resulting data for each specimen are the bulk susceptibility tensor (volume susceptibility κ_{bulk} in SI units) and three principal axes ($\kappa_1 \geq \kappa_2 \geq \kappa_3$) of an AMS-ellipsoid with their geographically corrected orientations. κ_{bulk} is a measure for the susceptibility of all magnetic components in the sample. It is defined with sufficient accuracy as the sum of susceptibilities contributed by dia-, para- and ferrimagnetic phases in a rock volume (Daly & Henry 1983):

$$(4) \qquad \kappa_{bulk} = c_f \kappa_f + c_p \kappa_p + c_d \kappa_d,$$

where c_f, c_p, c_d are the volume percentages and κ_f, κ_p, κ_d their specific susceptibility, respectively. Two anisotropy parameters, corrected anisotropy degree P' and shape factor T are calculated from κ_{bulk} and the principal axes (Jelinek 1981, Tarling & Hrouda 1993):

$$(5) \qquad P' = \exp\,[2(\ln \kappa_1 - \ln \kappa_{bulk})^2 + 2(\ln \kappa_2 - \ln \kappa_{bulk})^2 + 2(\ln \kappa_3 - \ln \kappa_{bulk})^2]^{1/2}$$

$$(6) \qquad T = (2 \ln \kappa_2 - \ln \kappa_1 - \ln \kappa_3)\,(\ln \kappa_1 - \ln \kappa_3)^{-1}$$

P' expresses the degree of anisotropy (eccentricity or ellipticity) with values ≥ 1, where 1 represents a perfect sphere.

Factor T ranges between +1 and -1 and indicates the ellipsoids' shape, positive values show oblate geometry, negative values prolate geometry.

From each sample up to six AMS cylinders are measured. The arithmetic mean values and standard deviations σ of κ_{bulk}, P' and T are calculated.

1.3.7.4 Field dependence measurements

A rapid determination of the field dependence of magnetic susceptibility is carried out with the *Minikappabridge KLY-3* (AGICO). This experiment is important to determine, whether the rocks show any field dependence due to the presence of the minerals titanomagnetite, haematite or monoclinic pyrrhotite.

A more accurate measurement of the field dependence is performed with the *Kappabridge KLY-4S*. Two steps of investigation are carried out: (1) the field dependence of the bulk susceptibility is measured in alternating fields ranging from 2 to 450 A/m. (2) The field dependence of the AMS is studied by measurements in two field strengths: 30 A/m and 300 A/m.

The field dependence parameter κ_{HD} (de Wall 2000a) is calculated for interpretations.

$$(7) \qquad \kappa_{Hd}\,[\%] = \frac{(\kappa_{300} - \kappa_{30})}{\kappa_{300}} \cdot 100$$

1.3.7.5 Temperature dependence measurements

The temperature dependence of magnetic susceptibility $\kappa(T)$ of a selection of whole-rock samples (ca. 0.25 cm^3 of fine granulate) is measured using the *KLY-2* Kappabridge (300 A/m at 920 Hz) combined with CS-2 (for high temperature) and CS-L (for low temperature) units (AGICO). The temperature rage is -192 to 700 °C. Measuring in that temperature range indicative susceptibility characteristics (curve progression, $T_{Néel}$, T_{Curie} and Hopkinson peak) of all common magnetic minerals can be recorded. Measurements are performed in an Argon atmosphere to reduce oxidation during heating.

Granulate is obtained by crushing a sample piece with a hammer, without direct contact of the hammer metal to prevent contamination. Moderate grain destruction by crushing is favoured over milling, because of the possibility of changes of magnetic properties due to grain size dependency. Thus, the granulate has a broad grain size spectrum from powder up to 0.5 mm. Measurements are performed in a two-step heating run and one-step cooling run: (1) from -192 °C to ambient temperature with the CS-L unit, (2) from ambient temperature to 700 °C with the CS-2 unit, and (3) cooling phase from 700 °C down to ambient temperature with the CS-2 unit. Detailed description of analysis procedures are given in Just (2005).

2 CASE STUDY NEGEV, ISRAEL

A fossil saprock-saprolite-laterite sequence in the Roded Granite (Dead Sea Rift shoulder, South Israel)

2.1 Introduction

This case study examines a fossil lateritic palaeoweathering profile, which was not subject to orogenic deformation. The weathering profile was formed in the Roded Granite, South Israel, during late Neoproterozoic (Vendian) to early Cambrian time and buried subsequently below Cambrian red-bed sediments. Structures and alterations in the Roded Granite are studied by means of structural, mineralogical and geochemical data. The vertical compaction of the laterite horizon and the related volume strain is determined by image analysis of primary quartz vein deformation. The relationship to weathering and compaction of the laterite soil aspects density, porosity, R_{0_loss} (White 1995) and immobile element mass balance are investigated. The weathering indications are evaluated with respect to the palaeoclimatic conditions, under which weathering took place.

The magnetomineralogy and the AMS is studied in detail and evaluated in the light of the other data. The changes of magnetic minerals and associated magnetic fabrics during hydrothermal alteration, pedogenesis, diagenesis and brittle tectonics are a key object. Employing image analyses at the microscale, the relation between AMS and the primary (granitic) and secondary petrofabrics is established. The usage of magnetic susceptibility for understanding geological processes, which took place in fossil lateritic profiles, is evaluated.

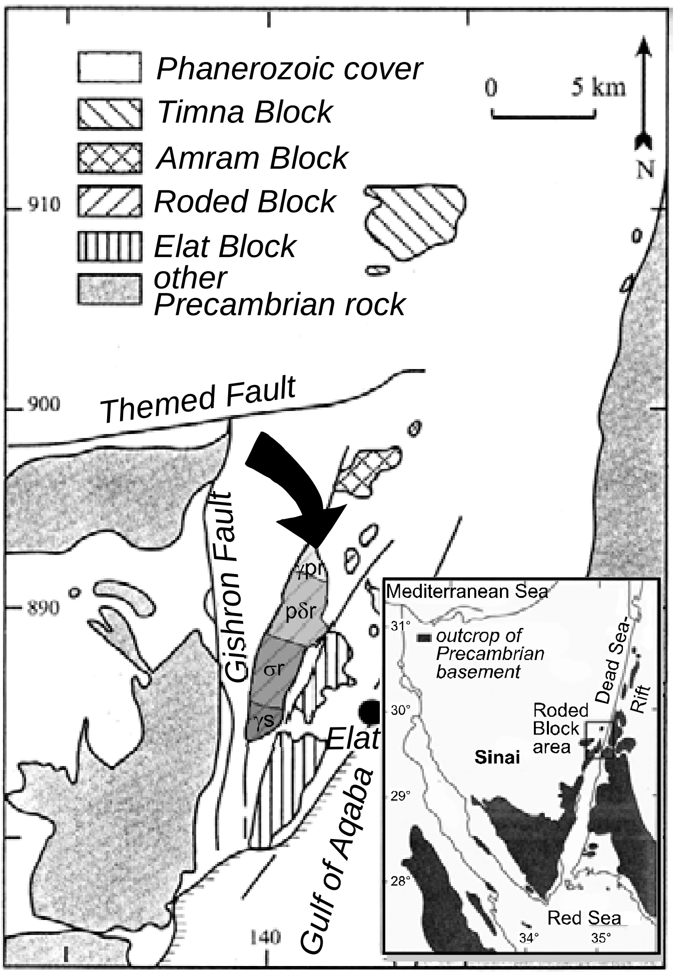

Figure 2.1. Geological map of the Roded Block region (Arrow points to sampling area). The Roded Block is divided from North to South into: *γpr:* Roded Granite, *pδr:* Roded Quartz Diorite, *σr:* Roded Schist, Gneiss, Migmatite, *γs:* Shahmon Granite. The inset shows the locality of the Roded Block region (square) in the Sinai. (modified after Garfunkel (1980) and Gutkin & Eyal (1998)

2.1.1 Regional Geology

The Roded Granite is a part of the Roded Block, located in the western shoulder of the Dead Sea Transform (DST) in the Negev Desert in South Israel. The Roded Block is one of the northernmost Precambrian basement outcrops of the Sinai and is part the Arabian-Nubian Shield (Figure 2.1). It consists of granites, quartz diorites and metamorphic schists, gneisses and migmatite. The major intrusion in the vicinity of the Roded Granite, the Roded Quartz Diorite, has an intrusion age of 634 ± 2 Ma (U/Pb on zircons: Katz et al. 1998) and both Roded Granite and Roded Quartz Diorite are supposed to be approximately of the same (Pan-African) age and tectonic setting (Avigad *pers. comm.*). Subsequent late orogenic tectonometamorphic overprint took place over a period of 100 Ma and its retrograde path marks the exhumation of the orogen

(Katz et al. 1998). Weathering and peneplanation took place after the Pan-African orogeny (Garfunkel 1999, 2002, Stern 2002), dating back to 530 ± 10 Ma (Jarrar et al. 1993). The feralitic pedogenesis produced a saprolite (Avigad et al. 2005), its top-horizon is referred to as laterite in the present study. There are only few palaeoclimatic indicators of Vendian-Cambrian time in the Arabian-Nubian Shield (Avigad et al. 2005, German et al. 1996). They all point to a tropical to subtropical climate.

The burial during Palaeozoic time began with the Cambrian red-bed ‘Amudai Shelomo Formation, which covers the weathered granite (Avigad et al. 2003). The mass-production of Cambrian sandstones, sub-arkoses (approximately 300 m thick: Druckman et al. 1993) in the region is considered as a consequence of the intense silicate weathering, accommodated by high atmospheric $p\mathrm{CO}_2$ due to widespread volcanism (Avigad et al. 2005). Palaeozoic sedimentation occurring later than Cambrian age is not documented in the geological record. The Cambrian siliciclastics in this area are unconformably overlain by thick piles of marine Cretaceous to Pleistocene sediments. The total thickness of the Cambrian to Pleistocene stratigraphic column is ca. 1000 to 2300 metres thick (Druckman et al. 1993).

During the Phanerozoic time until the Early Neogene, the basement blocks in the northern Arabian-Nubian Shield, including the Roded block, remained tectonically relatively stable. Beginning from 14-18 Ma, the area has been involved into the tectonics of the Dead Sea Transform (e.g Ben & Lazar 2006, Sobolev et al. 2005). The DST defines the boundary between the Arabian plate and the Sinai sub-plate of the African plate. Neogene to recent features in the geological record of the basement, such as volcanism, sinistral strike slip zones and earth quakes are associated with the DST (Eyal et al. 1981).

2.1.2 Sampling and applied methods

The studied palaeoweathering profile and the erosional unconformity between the Roded Granite and the ‘Amudai Shelomo Formation is exposed in an outcrop in a dry valley, situated directly in the North of the Shehoret Canyon (about 8 km NNW of Elat). Sampling of 18 oriented hand specimens along the profile is carried out with a sampling space increasing roughly at logarithmic scale. Below the unconformity, the profile of the weathered granite reaches 15 m vertically down. Palaeoweathering reaches deeper than the bottom of the dry valley, i.e. the weathering front is below surface. Therefore, sampling of the unweathered granite is carried out in a locality nearby (some 100 metres SSE), inside the Shehoret Canyon. The exact distance to the unconformity of that sample is unknown, but is estimated as more than 50 m.

X-ray diffraction (XRD) on the whole-rock powder and on oriented preparation of the clay fraction (<2 µm) is carried out for all samples. For a selection of 10 samples the whole-rock geochemistry (major and trace elements) is analysed. The AMS of 17 samples throughout the weathering profile are measured. The temperature dependence of magnetic susceptibility $\kappa(T)$ of a selection of 9 samples are investigated and a field dependence test is rapidly performed. By means of image analysis at the microscale, the relation between AMS and the primary (granitic) and secondary petrofabrics is studies.

2.2 Description of the weathering zones

The weathering profile is divided into four weathering zones, which are described in this chapter (Figure 2.2). A distinction of the weathering zones was already achieved in the field and, concerning the saprolite and laterite, supported by Avigad et al. (2005). The nomenclature is based on the four general zones of a weathering profiles described in chapter 1.2: (1) unweathered, (2) saprock, (3) saprolite, (4) soil, in this case a laterite horizon.

The freshest rock in the profile (sample RA3-1) is referred to as the unweathered granite (parent rock) (see chapter 2.2.1). This sample is used as a reference for the weathering degree.

From at least 15 up to 3 metres beneath the unconformity the granite is affected by moderate weathering, referred to as saprock (sample sequence RA1-1 to 1-5). Parts of this lithology are characterized by a slight

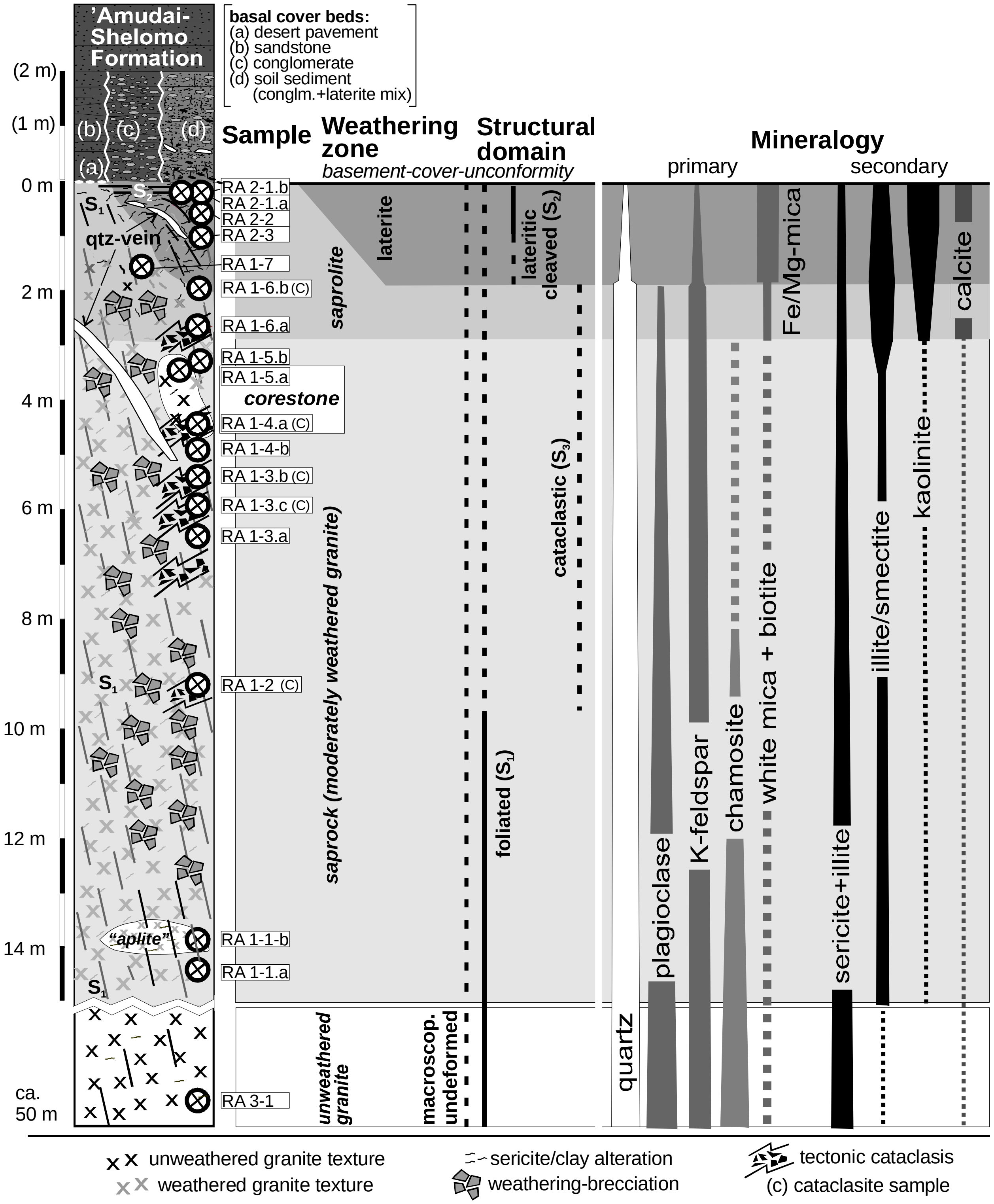

Figure 2.2: The Roded weathering profile, with sample locations, weathering zones, structural domains and main primary and secondary mineralogy, as determined by petrography and XRD analyses.

brecciation (weathering-brecciation, see chapter 2.2.2). A body (lens or dyke) of slightly finer grained granite, here referred to as "aplite", is located inside the saprock zone (sample RA 1-1.b at 14 metre profile depth).

A one to three metre thick saprolite zone (partly also weathering-brecciated) follows on top of the saprock (samples RA1-6.a,b to 1-7) (see chapter 2.2.3). The unweathered granite, saprock and saprolite are macroscopically undeformed or (gneissic) foliated (see chapter 2.2.1.1 and 2.2.1.2). Either the saprolite is cut by the unconformity or it changes through a transitional zone into a purple-red laterite. The laterite horizon has a maximum thickness of 2.5 metres (sample sequence RA2-x) and is characterized by a flaky texture and by variously inclined cleavages, relics of the “primary” (gneissic) foliation and a secondary unconformity-parallel cleavage (chapter 2.2.4).

The boundaries between the weathering stages are diffuse and thicknesses of the weathering zones vary within the outcrop. Locally, lenses of fresher rock occur inside the weathered saprock (RA 1-5.a). A zone of cataclasis between 2 and 10 m beneath the unconformity locally overprints the saprock and saprolite (see chapter 2.2.5). As it is described below, cataclasis can be distinguished from weathering-brecciation by petrography and magnetic fabrics.

2.2.1 Unweathered granite

The Roded Granite varies slightly throughout the sampling area in grain size, deformation and colour; however, it was mapped and considered as one calc-alkaline granite (Druckman et al. 1993). In comparison to all other rocks described below, the macroscopic impression of the granite sample is fresh, therefore it is referred to as unweathered granite. Sample RA1-5.a is from a lens of unweathered granite within the saprock zone (assumed a so-called *corestone*). It shows same alterations as sample RA3-1. Generally, the grey to flesh-coloured granite has a sub-equigranular texture with crystal sizes of 2 to 10 mm. The texture is either isotropic (“macroscopically undeformed granite”; Plate 2.1.a), or it is defined by a steep gneissic foliation (“foliated granite”; Plate 2.1.b). Domain-sizes of these two textures within the outcrops are at metre to decametres scale. Locally, quartz veins are parallel with this foliation.

Components are mainly plagioclase, quartz and K-feldspar. In some cases, plagioclase displays a zoning of oligoclase cores and albite rims. K-feldspar is mainly microcline, occasionally micro-perthite and micro-antiperthite. Minor components in the matrix are biotite, chlorite and white mica, commonly present as chlorite-mica stacks (together ca. 20 vol%; chlorite-dominated, with intercalated biotite and white mica, Plate 2.2.d). Furthermore, there are subhedral, less often anhedral martite, small rutile, titanite, and calcite. Martite is a coarse grained haematite, pseudomorphously grown after magnetite and titanomagnetite (Ramdohr 1975); see chapter 2.2.12). Accessory phases are epidote, apatite and zircon. The minor and accessory phases are accumulated in interparticle space between quartz and feldspar.

A profound sericitization of feldspars is observed at the microscale (equations *1a*, *1b* in chapter 1.2; see Plate 2.2.a). Oligoclase cores of zoned plagioclases are clouded by a dense impregnation with sericite (“sericitization” - The term “sericite” is used to describe a well-crystallized illite (Hunziker et al. 1986), which is detectable with optical microscopy due to its size larger than the clay fraction). The cloudy cores indicating sericitization in plagioclase crystals, are not evident in K-feldspar crystals.

Chlorite is the dominating mineral in the mica-stacks (Plate 2.2.d). Chlorites are partially altered, brownish coloured and impregnated with red microcrystalline haematite crystals, rutile and titanite (Plate 2.2.d-f). Secondary haematite occurs as fillings of fissure-like interparticle space and in cleavage fissures of feldspars. The magnetomineralogical observations are described in chapter 2.2.12.

2.2.1.1 Texture of the macroscopically undeformed granite

The macroscopically undeformed granite, defined by its isotropic texture, reveals under the microscope a weak preferred orientation of the chlorite-mica stacks. White micas are partially recrystallized to sericite. Quartz and feldspar are rarely elongated. Quartz shows intracrystalline deformation, mostly undulatory extinction, less frequently subgrains and recrystallization. The undulatory extinction of quartz is often chessboard like, thus prism- and basal-parallel slip was important, indicating deformation at high temperatures (Kruhl 1996, Okudaira et al. 1998). Feldspars are undulating (Plate 2.2.c) and their grain boundary to quartz are moderately bulged. These are results of diffusion creep, demonstrating that deformation took place at least at medium temperatures (Passchier & Trouw 1996). Subhedral titaniferous martite grains are often flattened and elongated. The SPO of martite and chlorites of the macroscopically undeformed granite are determined in chapter 2.4.

2.2.1.2 Texture of the foliated granite

In the (gneissic) foliated granite a macroscopic foliation, referred to as S_1, is well defined by the orientation of chlorite-mica stacks (Plate 2.1.b). Chlorite and mica content is higher than in the macroscopically undeformed granite. Quartz grains are mostly elongated defining also the foliation surfaces. Feldspars have no distinct shape preferred orientation. Intracrystalline deformation of quartz and feldspar is similar to the macroscopically undeformed granite, however, dynamic recrystallization is more abundant in foliated granite.

The orientation of S_1 is generally SW-NE striking with a steep dip of 50-80 ° (Figure 2.3.b). Two different sets of foliation dominate throughout the outcrop, a SE and a NW dipping. A set of quartz-veins parallels the S_1-foliation. S_1 is interpreted as being the late orogenic Pan-African foliation, described throughout the Roded Block (Katz et al. 1998).

The corestone granite is deformed by two sets of similarly developed foliations but differently oriented (chlorite SPO), which produce a weakly defined L-tectonite-like fabric (Figure 2.30.a).

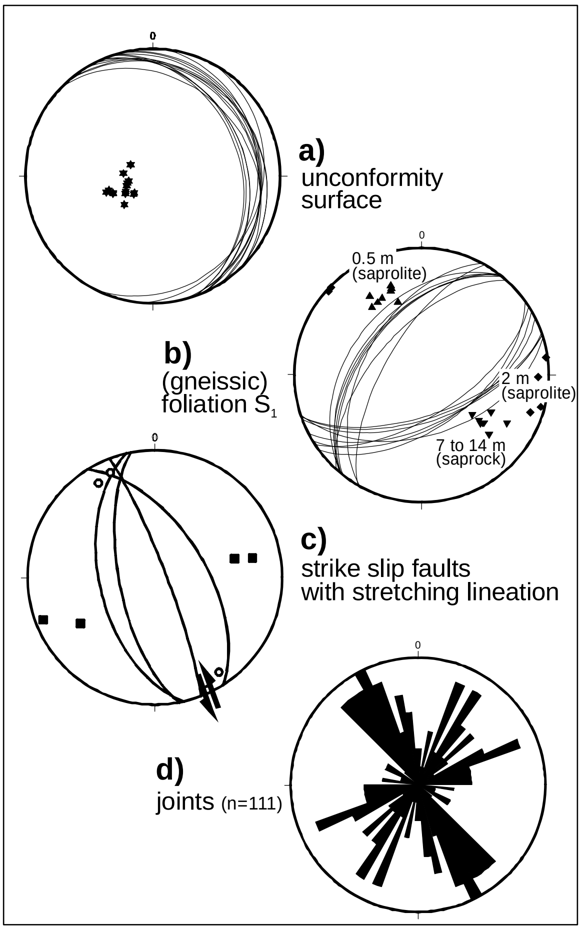

Figure 2.3: Structural elements in the weathering profile; a) unconformity surface between capped weathered granite and basal Cambrian sandstone; b) (gneissic) foliation at different depths (indicated by different symbols); c) strike slip faults (squares) with stretching lineation (circles) and sinistral displacement kinematics (arrows); d) joint sets (strike direction). (a-c: equal area projection of the lower hemisphere, with poles and associated great circles, indicating surfaces)

2.2.2 Saprock (moderately weathered granite)

The dominant zone of weathering in the profile is the moderately weathered, or saprock zone. The present saprocks are characterized by various rock colours, mostly brownish to reddish, and textures similar to the unweathered granite (see chapters 2.2.1.1 and 2.2.1.2). The texture cohesion of large parts of the saprocks is slightly reduced due to rock fragmentation (Plate 2.1.c). This “brecciation” can be described as a dense jointing at the cm-scale. Along the joints, grain-size reduction of primary minerals by brecciation and also minor precipitation of secondary clayey material is observed. The texture between the joint sets is the granitic texture without showing brecciation-related grain size reduction. Consequently, S_1, in the foliated saprocks, is preserved in the saprock zone (see the cluster “7 to 14 m (saprock)” in Figure 2.3.b). An additional cataclastic foliation is not observed in the “brecciated” saprocks. These observation allows a petrographic distinction of the saprock “breccias” from cataclastic saprock (see chapter 2.2.5). The described “brecciation” is considered by the author as a “weathering-brecciation”. It corresponds to the sub-surface weathering typical for saprocks and saprolites (see chapter 1.2).

It is partly observed in the saprock zone, that the chlorite-mica stacks altered to kaolinite and a mix of haematite/titanite/TiO_2 (Plate 2.2.g,h). The titaniferous oxide may be rutile, considering a hydrothermal formation or anatase, considering a weathering-related formation (Deer et al. 1966).

The brown to reddish colour of the rocks in the saprock zone results from (1) the flesh K-feldspars, and the alteration products (2) sericite/illite, (3) the mix of haematite/titanite/ TiO_2 in the matrix and (4) clay, which is located mostly along joints.

2.2.2.1 *"Aplite" in the saprock zone*

A lens or dyke of an "aplite" (sample RA1-1.b) is located in the lower part of the saprock zone. This rock has an equigranular texture with grain sizes of ca. 2 mm (Plate 2.2.b). The rock has is reddish colour and shows similar alteration products as the moderately weathered wall rock granite (Plate 2.2.b); sericite is predominant secondary mineral. The "aplite" is harder than the wall rock (foliated granite), due to a higher quartz content, and it is not affected by weathering-brecciation. The mineral deformation at the microscale is similar to the foliated granite. However, the foliation S_1 is less pronounced. It is measured in the field (within cluster "7 to 14 m (saprock)" in Figure 2.3.b) and has an orientation corresponding to the granite foliation S_1.

2.2.3 *Saprolite (intensely weathered granite)*

The saprolite zone is characterized by strongly altered granite with an almost white colour (Plate 2.1.d). The primary granitic texture is generally intact (see chapter 2.2.1.1 and 2.2.1.2), however, large parts of the rock is friable due to dense fracturing, similar to the "brecciation" in the saprock zone ("weathering-brecciation"; see chapters 2.2.2), and/or profound alteration of feldspar. S_1, if developed, is preserved in the saprolite (cluster "2 m (saprolite)" and "0.5 m (saprolite)" in Figure 2.3.b). This colourless saprolitic refers to *pallid zone,* which is typically located in a lateritic weathering profile just underneath indurated (sub-)soil material (Stephens 1946, Tardy 1992). This is observede here, where the laterite is preserved. Kaolinization is much more abundant in the saprolite than in the saprock. Kaolinite, together with quartz and microcline, are the main saprolite constituents. A microcrystalline calcite generation is a minor secondary component of the kaolinite-enriched matrix (Plate 2.3.b). Plagioclase and K-feldspar are intensely kaolinized in the saprolite zone (equation *3* in chapter 1.2). Plagioclase is almost not evident in the saprolite, presumable due to the combination of sericitization / illitization and kaolinization. Remnants of sericitized plagioclase are observed locally in

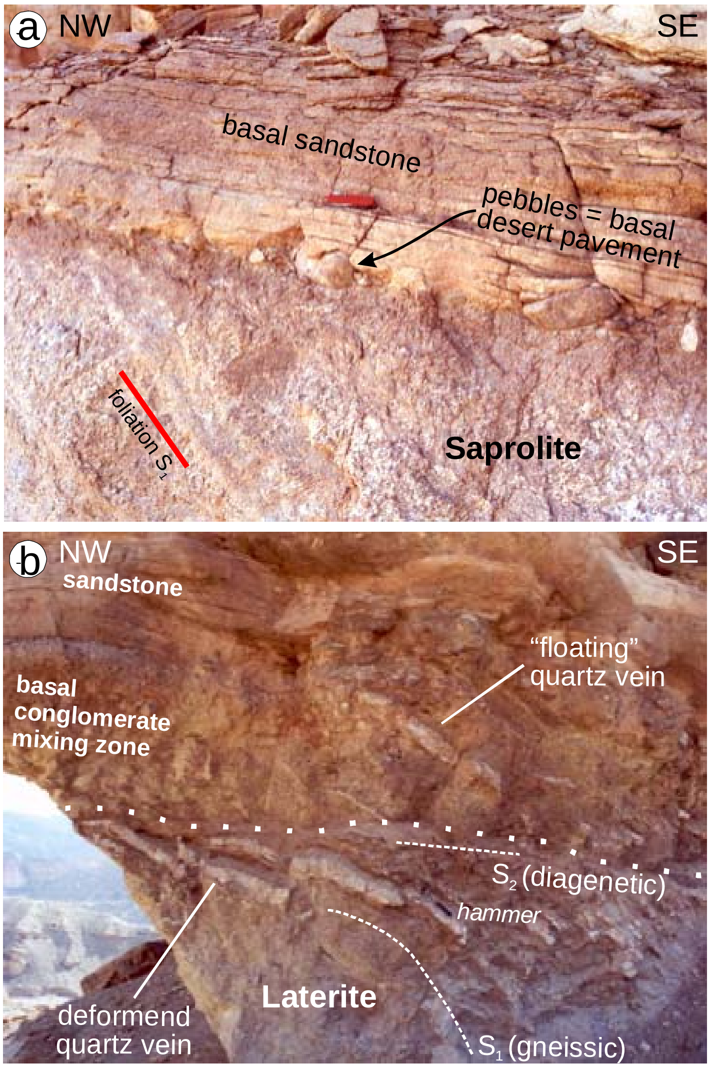

Figure 2.4: a) Outcrop photograph showing the gneissic foliated saprolite unconformably overlain by a sandstone of the 'Amudai Shelomo Fm. A layer of loose pebbles marks the unconformity. This is a desert pavement. b) Outcrop photograph showing the laterite and the sedimentary cover. The laterite shows relics of primary granite foliation and unconformity-parallel texture. A quartz vein is rotated and normal-faulted. The basal cover bed is a mix of lateritic and conglomeratic material (including "floating" parts of quartz vein).

the matrix. Although K-feldspar is partly kaolinized in the saprolite, it appears macroscopically as relatively fresh. This is due to the direction of replacement, from the rim towards the centre of the feldspar crystals, leaving behind a relatively fresh crystal core in cases of uncompleted alteration (Plate 2.3.a). The intense alteration of chlorite is another important change from the moderately to intense weathering zone. Chlorite break-down, observed in an incipient stage in the saprock zone, is advanced in the saprolite to a degree of almost entire chlorite decomposition. Chlorite is replaced by kaolinite and a mixture of haematite/titanite/TiO_2. The residual mineral of the altered chlorite-mica stacks is a mica-kaolinite-stack, enriched in secondary Fe-oxides (mainly haematite) and TiO_2, presumably anatase (Plate 2.3.b). This mica is referred to as Fe/Mg-mica; it has a “dirty” optical appearance due to the dense impregnation with mineral inclusions (Plate 2.3.d). These microcrystalline inclusions parallel the basal surfaces of the Fe/Mg-mica (Plate 2.3.c). The abundant occurrence of haematite and titaniferous minerals in the Fe/Mg-micas are the sum of (1) the inclusions observed in chlorite of the unweathered granite, and (2) the by-product of the saprolitic kaolinization of chlorite.

2.2.4 Laterite

A purple-red coloured, weakly indurated clayey horizon represent the uppermost part of the preserved palaeoweathering profile, reaching 2 metres beneath the unconformity. (Plate 2.1.e,f). This lithology is dominated by Fe/Mg-mica and clay minerals (Plate 2.3.d), whereas quartz and K-feldspar content are reduced in contrast to the saprolitic stage. The main component of the matrix is kaolinite impregnated with haematite, which causes the purple-red colour (Plate 2.3.e). The clay material, supported by calcite, acts as a weak cement. By these basic petrographic characteristics (red colour, clayey, Al-Fe-enriched) the lithology can be referred to as laterite *sensu lato*. To be more precise, it is be termed as a (lateritic) *ferricrete* (Bourman et al. 1987), which is a sub-soil horizon of laterite profiles typically developed on top of the saprolitic *pallid zone* (see above) (Tardy 1992).

Most prominent mineral between the clay matrix, are the Fe/Mg-mica stacks (30 vol%); quartz and K-feldspar are minor components (together 10 vol%). Quartz occurs as primary crystals, as well as small exsolution rods (Figure 2.5). These quartz rods are considered as a secondary (weathering?) product, being a feature exclusively observed the laterite. The rods are deformed, without showing crystalplastic deformation of the quartz crystals. K-feldspars are mostly kaolinized, but relic cores are disseminated in the matrix. Chlorite is not observed, as it already vanished in the saprolite stage.

The petrographic transitional zone from saprolitic pallid zone to lateritic ferricrete is gradual and can reach some decimetre thickness. It is referred to as *mottled zone* (e.g. Stephens 1946, Tardy 1992), characterized by red clay-mica concretions in a pale saprolite matrix with granitic texture. The content of these concretions increases upwards, until white rock fractions are vanished (Figure 2.5). This zoning is typical for the sub-soil

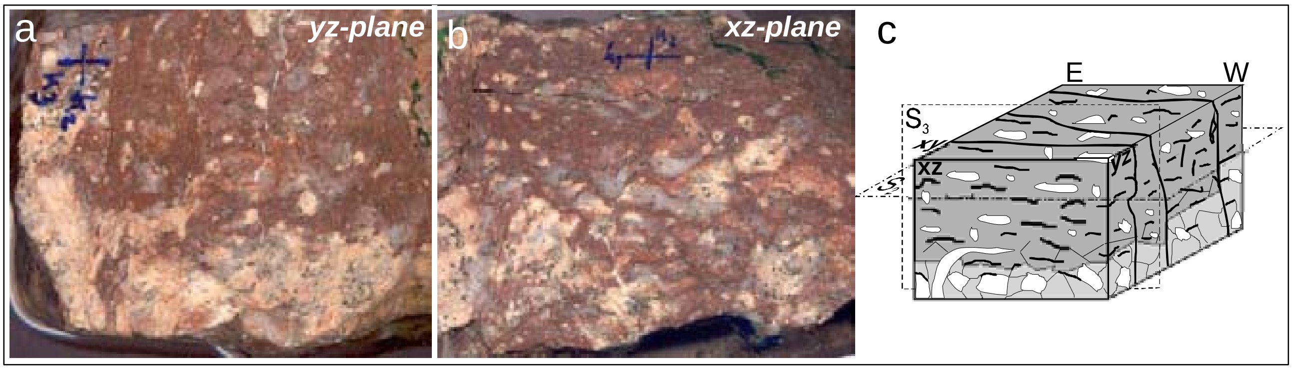

Figure 2.5: a-b) Hand specimen photographs (sample RA1-6b) showing textures and fabrics of the upper part of the mottle zone between saprolitic pallid and lateritic ferricrete zone. The preferred oriented phyllosilicates and flattened quartz rods are evident. c) Sketch showing the relation of lateritic S_2 (compaction) and overprinting cataclastic S_3. (long side of both photographs: 12 cm)

part of a lateritic profile (Tardy 1992).

The lateritic texture appears as planar and flaky, primarily defined by the parallel orientation (SPO/LPO) of Fe/Mg-mica stacks, which “anastomize” around “porphyroclastic” relic or partly reprecipitated quartz (rods) and relic K-feldspar grains (Figure 2.5). The preferred orientation of Fe/Mg-mica and quartz rods changes within the laterite horizon, defining a depth-dependent gradient of fabric inclination. Locally at the base of the laterite, it is observed that the planar fabric is steeply inclined and with proximity to the unconformity, a shallow to unconformity-parallel inclination is ubiquitously developed. This shallow inclined fabric is not observed in the weathering stages beneath the laterite. The shallow SPO is locally also observed in the basal laterite zones (as shown in Figure 2.5). The fabric gradient is indicated in Figure 2.2 and Figure 2.4.b. It is also observed that a quartz vein in the laterite, comparable to the quartz veins of the unweathered granite, mimics this gradient. The vein is broken into several parts and these parts are rotated from a steep inclination at the base, towards a shallow inclination at the unconformity.

The lower steep and the higher shallow SPO are in fact two different fabrics, one overprinting the other, as revealed by SEM observations (Plate 2.1.f). It is displayed that surfaces of an earlier steep cleavage are crenulated in microlithons between surfaces of a later shallow cleavage. Both cleavages are defined by the Fe/Mg-micas. This fabric configuration is seldomly observed in the microscale, because the weak consolidation of the laterite causes a destruction, especially of the early fabric. The macroscopically observed gradient of fabric inclination is an effect of progressively increased overprint of the younger cleavage approaching the unconformity. Although not measurable in the laterite, the steep orientation of the “primary” cleavage resembles quite well the orientation of the SE-dipping set of the gneissic foliation S_1 (Figure 2.3.b). The lateritic steep cleavage is the relic foliation of the foliated granite.

It is evidenced that a secondary cleavage was formed, defined by Fe/Mg-mica SPO. Apparently, this cleavage, which is referred to as S_2, is related to the unconformity, because of its flat-lying orientation and its increased intensity towards the unconformity. S_2 is considered as the result of a vertical compaction (see following chapter).

2.2.5 Determination of laterite compaction by means of image analysis

Compaction of the laterite is indicated by the following structural features: a) an unconformity parallel foliation S_2, which crenulated a primary gneissic foliation S_1, and b) a rotated and faulted quartz vein. In this chapter, the amount of vertical compaction is determined by strain analysis, based on the deformation of the quartz vein (Figure 2.4.b). It has been established that the amount of compaction of buried palaeosoils can be calculated by strain analyses of deformed features, such as vertical clastic veins (Caudill et al. 1997) or quartz veins.

A geometrical technique of restoration to an assumed pre-deformation state is applied. The determination is based on following assumptions: a) the initial orientation of the vein is known, b) the vein was rotated and faulted passively without changing its aspect ratio and c) the deformation of the quartz vein is a result exclusively of vertical compression. In the upper metre of the laterite, the quartz vein is clearly deformed by vertical compression, indicated by normal faulting and rotation towards small inclinations. Petrographic observations (undeformed primary foliation) and geochemical volume strain calculation (chapter 2.2.11) demonstrate that rocks below the laterite are not compacted. The quartz vein is not visible in the lower metre of the laterite, but S_1 surfaces can be traced macroscopically and appears to have a relatively undisturbed inclination. It is therefore inferred that compaction in the lower part is not as intense as in the upper part, and consequently, a compaction gradient within two metres of the palaeosoil profile is developed. To trace this gradient, the laterite horizon is divided into four sections showing different strain increments. The upper three sections (section 2-4) show parts of the quartz-vein, and their specific compaction is determined by the rotation and offset of the vein. A compaction curve constructed from results of the upper three sections. In the lowermost section (section 1) the quartz vein is not observed and the section compaction is determined by the curve. Figure 2.6 shows the geometrical determination of each section compaction, referred to as C_1 to C_4. C is the measured *thickness* divided by the *initial thickness* (after Caudill et al. 1997, Sheldon & Retallack 2001):

$$(6a) \qquad C = \text{thickness} / \text{initial thickness}$$

The *initial thickness* is the sum of the compacted *thickness* and the *rotational* and *faulting increment* of strain:

$$(7) \qquad \text{initial thickness} = \text{thickness} + \text{rotational increment} + \text{faulting increment}$$

hence:

$$(6b) \qquad C_{section} = \text{thickness} / (\text{thickness} + \text{rotational increment} + \text{faulting increment})$$

or

$$C_{section} = z_w / z_i$$

which is the same equation with respect to a coordinate system (z = vertical direction, index w means weathering and i initial). The bulk compaction of the laterite is the weighed mean of the section compaction, i.e. the sum of the products $C_{section} \cdot z_{w(section)}$, divided by the thickness of the entire laterite, which is the sum of z_w of each section:

$$(8) \qquad C_{laterite} = [\Sigma(C_{section} \cdot z_{w(section)})] / \Sigma z_{w(section)}$$

Results: The gradual increasing compaction follows a logarithmic compaction curve. The compaction in section 1 is very low (C_1 = 0.93), in section 2 it is higher (C_2 = 0.70), in section 3 very high (C_3 = 0.29) and in section 4, compaction is at a maximum (C_4 = 0.08). The quartz vein fraction in section 4, just beneath the unconformity, is almost paralleling the unconformity and may be a collapse feature due to the pedogenesis or early cover sedimentation. Bulk compaction $C_{laterite}$ is 0.73. Just the quartz vein section, without the lower part of the laterite, is compacted to 0.42 of the initial thickness. For comparison with sample data, the compactions at 0.2 and 1 m are determined, using the constructed compaction curve (RA2-1.a: $C_{0.2\,m}$ = 0.22; RA2-3: $C_{1\,m}$ =

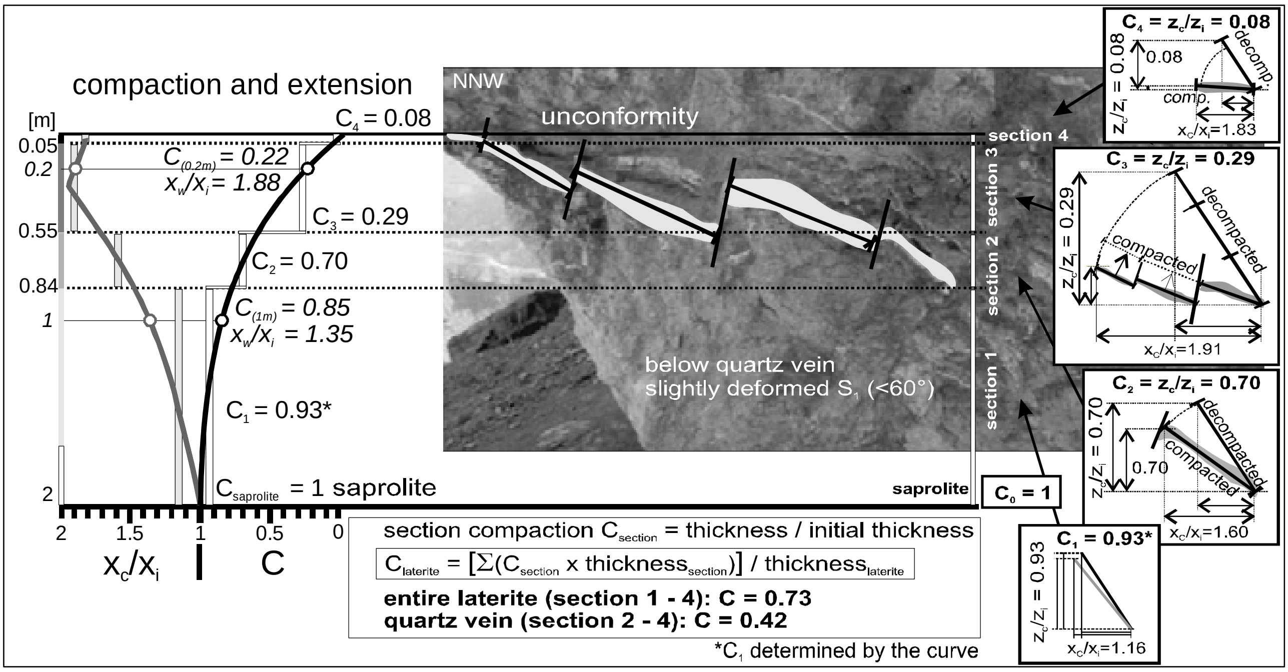

Figure 2.6: Geometric determination of vertical compaction (z_w/z_i = C, ratio of measured thickness / initial thickness) and horizontal extension (x_w/x_i) of the laterite by a faulted and rotated quartz vein. Four sections with different strain increments $C_{section}$ are used to construct z-compaction and x-extension curves. C and x_w/x_i are considered as 1 (no deformation) at the saprolite-laterite boundary (ca. 2 metres). The bulk compaction $C_{laterite}$ is the weighted mean of all measured thicknesses in the sections. The z-compaction and x-extension at metre 0.2 and 1 are indicated for comparison with other data of samples RA2-1a and RA2-3, respectively.

0.85).

The volume of the laterite due to the compaction relative to its initial volume can be calculated using the equation

$$(9) \qquad V_w/V_i = x_w/x_i \cdot y_w/y_i \cdot z_w/z_i$$

According to the applied method of compaction determination, vertical compaction z_w/z_i leads to extension in horizontal direction x_w/x_i. The extension in y direction, y_w/y_i is not known, but can be estimated as a value between x_w/x_i and 1. A higher extension, $x_w/x_i < y_w/y_i$, is unlikely, as the volume will increase enormously. The geometrical volume strain V_w/V_i is calculated assuming two extreme situations of horizontal extension: (1) “plane strain”, where $y_w/y_i = 1$, thus no extension in y direction, and (2) “oblate pure shear”, where $y_w/y_i = x_w/x_i$, thus same extension in both directions. In both “plane strain” and “oblate pure shear” conditions, volume increase (dilatation) is calculated for the lower part (0.55 - 2 m:) and volume decrease for the upper part of the laterite (0 - 0.55 m) (Table 2.2 and Figure 2.24). The “plane strain” condition shows less maximum dilatation (< 1.14) than “pure shear” (< 1.79). The average volume strain in the entire laterite is calculated according to the following equation (modified from equation 8):

$$(10) \qquad V_{laterite} = [\Sigma(V_{section} \cdot z_{w(section)})] \,/\, \Sigma\, z_{w(section)}$$

$V_{laterite} = 0.88$, thus indicating general volume compaction in the laterite.

The data are summarized in Table 2.2 and discussed in chapter 2.5.6.

2.2.6 Density and porosity of the laterite

In order to understand the impact of weathering and compaction on the laterite, the density and porosity are determined. Methods of determination are described in chapter 1.3.4. The trends of the entire weathering profile are shown in Figure 2.9. (See Appendix I.a for data). The bulk density ρ decreases from the unweathered granite (2.46 g/cm^3) to the saprolite (2.32 g/cm^3). It does not change significantly across the saprolite-laterite boundary and increases within the laterite only slightly (from 2.31 to 2.38 g/cm^3). Within the entire weathering profile, porosity increases with degree of weathering. Porosity in the unweathered is as low as 0.04. Highest porosity (0.34) is measured in the lower laterite sample. The saprolite has a value of 0.27. A decrease is observed in the upper laterite sample (0.24).

The data are summarized in Table 2.2 and discussed in chapter 2.5.6.

2.2.7 Cataclasis zones

Some of the samples within the saprock and saprolite stage show a texture, which is not exclusively associated with weathering-brecciation. These texture characteristics are (1) a replacement of the granitic texture by a fine-grained matrix supported texture (Plate 2.2.g), (2) a dark reddish matrix colour (Plate 2.2.g), (3) the formation of a vertical cleavage (Plate 2.2.h) and (4) the occurrence of small calcite veins (Plate 2.3.f-h). These texture characteristics point to cataclastic overprint, therefore those rocks are referred to as cataclasites. The cataclastic matrix is strongly consolidated, presumable due to a cementation of haematite, sericite/illite and quartz remobilization and precipitation.

The rock matrix consists of cataclastically destroyed fine-grained primary minerals (quartz, feldspar, mica), and secondary chlorite, sericite/illite and opaque phases such as haematite and rutile. The colour is a result of martite cataclasis and microcrystalline haematite precipitation (Plate 2.5.b,c). Larger brecciated minerals, mainly quartz and feldspar, also martite, are partly elongated and aligned indicating a cataclastic flow fabric. Sets of incipient discrete foliations are observed in the zones of cataclasis Plate 2.1.g,h). The foliations are vertically orientated, trending approximately WSW-ENE and NNW-SSE. They are mainly defined by microcrystalline particles (haematite, rutile), which are apparently residual minerals of a pressure solution process. Partly, hollandite veins ($BaMn_8O_{16}$) define the foliation. Both pressure solution and cataclastic flow are the processes of foliation development.

There are no indications for a direct relation of cataclasis and the formation of S_1. Both structural features are presumable products of different deformation phases, the cataclasis overprinted earlier S_1 fabrics. The vertical cataclastic foliation affected the saprolite texture and the clayey texture in the lower part of the laterite (Figure 2.5.b,c): As a result, small offsets of laterite and saprolite domains and deflection of the horizontal compaction fabric S_2 into parallelism with cataclastic foliation is evident. This demonstrates the late development of cataclasis with respect to weathering. The cataclastic cleavage is therefore referred to as S_3.

Deformed calcite veins (Plate 2.3.f) and calcitic domains in the matrix (Plate 2.3.g) are observed exclusively in cataclasites. In the veins, there are two distinguishable generations of calcite fillings. Partly, the vein calcite and the calcite in the matrix are recrystallized (Plate 2.3.h).

2.2.8 Late brittle structures

Late structures are strike-slip faults and joints, which overprint all other structures. Strike-slip faults are developed as metre scale vertical surfaces, trending NNW to SSE. Slickensides are developed as surfaces of phyllosilicates. In at least one fault, the displacement sown by the slickensides has sinistral kinematics (arrows in Figure 2.3.c).

The occurrence of joints in unweathered granite is relatively rare. The weathering-breccias of saprock and saprolite zones are heavily fractured by joints. Here, weathering-induced and tectonic-induced joint may have been accumulated to form a dense and complex network. In the laterite there are no joints of tectonic origin and this is because of the weakly cemented clayey matrix. Rocks in the cataclastic zone are only moderately jointed, which may be a further indication for its late genesis. Mineral precipitation in joint spaces is abundant, comprising mainly calcite and haematite. Joints are grouped in a major NNW to SSE striking set and in a minor SSW/SW to NNE/NE set (Figure 2.3.d).

The major joint set and the strike-slip faults have similar orientations coinciding with the NNW-SSE trend of the outcrop-valley.

A late horizontal rotation caused the gentle tilt of the unconformity and Cambrian strata (Druckman et al. 1993) (see following chapter).

2.2.9 Cover rocks

Both the unconformity and overlying Cambrian beds dip 10° NE (Figure 2.3.a). The cover rocks of the ‘Amudai Shelomo Fm. are thick red-beds of conglomerates and well stratified coarse-grained sandstones. These lithologies are laterally intercalated and both can be the basal beds on top of the weathered granite. Locally, the lowermost 2 metres of cover rocks on top of the laterite is a poorly stratified mixture of red clay material and conglomerate material (pebbles, sand); also “floating” quartz vein relics are observed (Figure 2.4.b). This sediment can be interpreted as a reworked laterite, mixed with conglomeratic material. It is therefore considered as a soil-sediment, genetically belonging to the cover, because of its autochthonous nature. The sandstone/conglomerate strata of the ‘Amudai Shelomo Fm. follows on top of this soil-sediment. The lateral occurrence of the soil-sediment is lens-shaped (length of ca. 5-10 metres in the outcrop) and presumable the infill of a channel or valley. Aside of the soil-sediment lens, the saprolite is capped by the unconformity. Here, a thin basal layer of well rounded pebbles is observed (Figure 2.4.a) “coating” the unconformity, which is interpreted as a desert pavement (e.g. Wood et al. 2005).

2.2.10 XRD

2.2.10.1 Whole-rock samples

The presence of primary and secondary rock constituents, as determined by petrography, are in general supported by XRD. Most remarkable changes through the weathering profile are the variation of feldspars

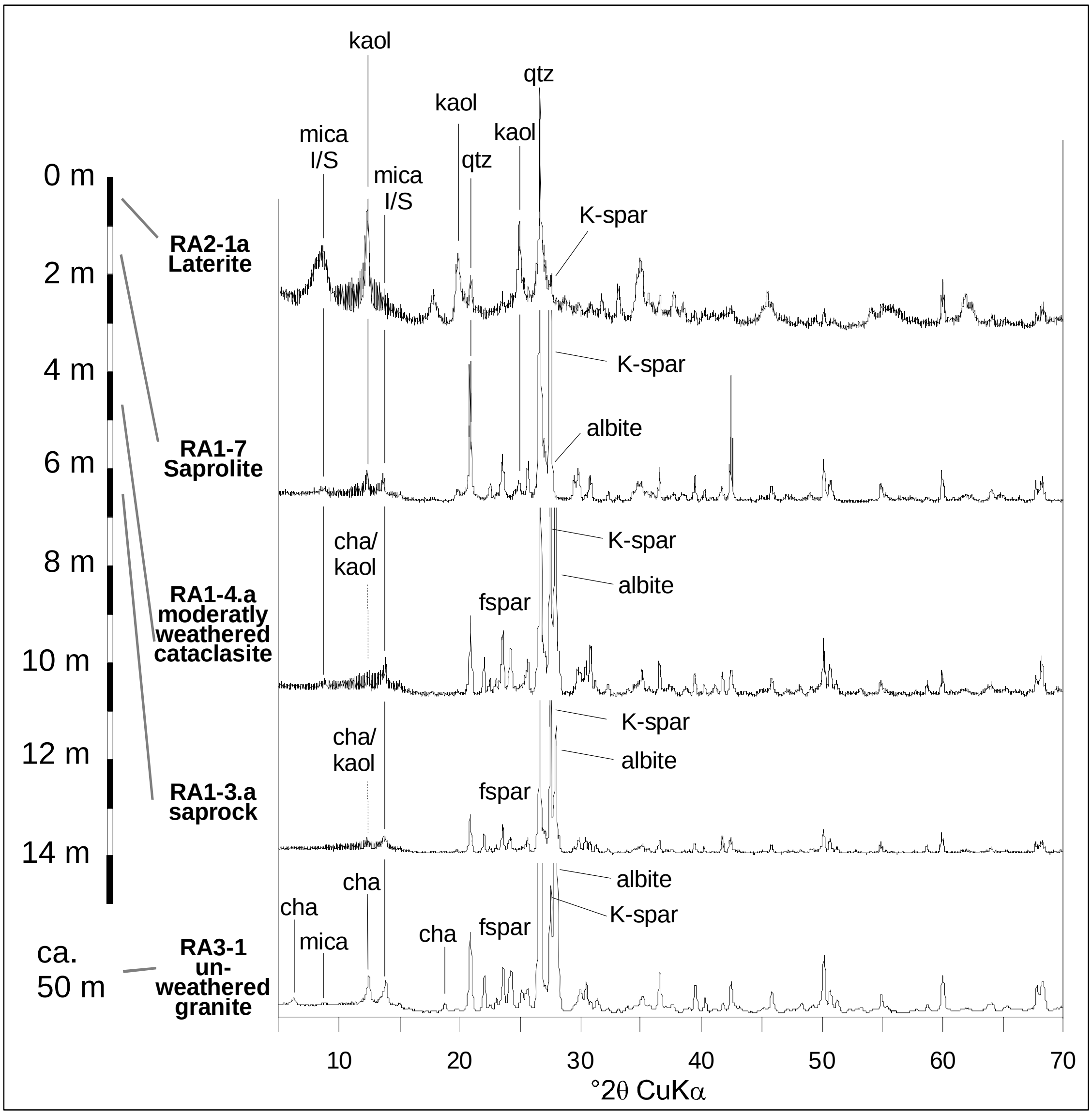

Figure 2.7: XRD spectra of the whole-rock. A selection of representative samples from each weathering zone and from the cataclasis zone is displayed. The peaks of quartz and feldspar are capped.

and phyllosilicates. Petrographic and XRD observations lead to a compilation of all important mineralogical changes through the profile, shown in Figure 2.2.

The selection of XRD whole-rock spectra in Figure 2.7 shows a dominance of quartz and feldspar variations in the zones beneath the laterite. Due to this dominance by quartz and feldspars, the variations of the phyllosilicates (chlorite, white mica, biotite), having much lower modal fractions, are not as good detectable. Chlorite is clearly detectable by its 14 Å peak of (001 *hkl* surface) only in the unweathered granite. The 001 peak may just be masked in the upper weathering zones; a high Fe-content leads to a small 001 peak, compared to the 002 peak (Moore & Reynolds 1997). The 7 Å (chlorite 002 and kaolinite 001) peak is well defined in the entire profile, however dominated by kaolinite in the saprolite and laterite. This is evident, because in saprolite and laterite the distinctive 3.58 Å peak of kaolinite (002) is clearly developed. A 7 Å peak interference of chlorite and kaolinite may be present already in the saprock, since kaolinite occurrence in saprocks is indicated by petrography.

The mineralogical changes are most significant between the saprolite and laterite. The increase of kaolinite and mica against quartz and K-feldspar is evident. Mica modifications are Fe/Mg-mica, illite and I/S mixed-layer mineral. The broad peak at ca. 10 Å (001) indicate the complexity of the mica phases and the importance of smectite.

A comparison between sample RA1-3.a and RA1-4.a shows that there are no significant differences between “undisturbed” saprock and cataclastic saprock in the whole-rock XRD spectra.

The ratio between Na-plagioclase and K-feldspar is traceable by significant whole-rock XRD peaks at ca. 3.24 Å (orthoclase and microcline) and at ca. 3.19 Å (albite, calcian albite). A half-quantitative determination of this ratio is achieved by dividing the peak intensities (Figure 2.9.q). With proximity to the unconformity, the ratio gets smaller, indicating that K-feldspar dominates over plagioclase. In the laterite, plagioclase is not detected at all, whereas microcline is relatively abundant. The trend confirms the petrographic observations.

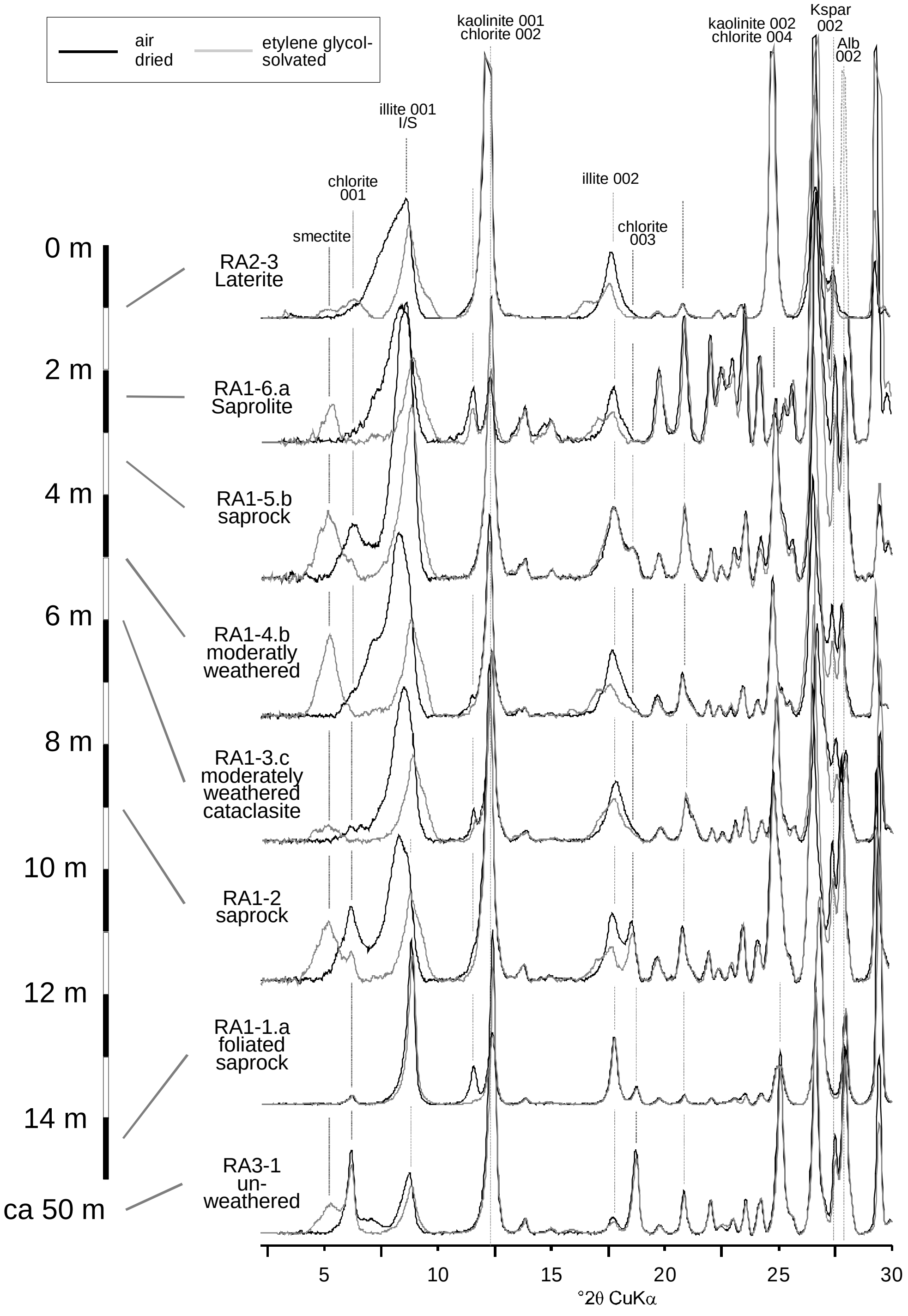

Figure 2.8: XRD spectra of the clay fraction (<2 μm).

The Na-plagioclase / K-feldspar ratio must be considered as qualitative, because (1) XRD measurements are not calibrated with standards, which is necessary for quantitative determination of mineral contents and (2) the peaks of other mineral may interfere with the chosen feldspar peaks.

2.2.10.2 Clay fraction (<2μm)

XRD spectra of the oriented preparation of clay fraction provide a better insight of phyllosilicate types and their changes through the profile. In the granite, main components of the clay fraction (<2 μm) is illite and illite/smectite (I/S) mixed-layer phases. In the unweathered granite and in the lowermost saprock, the illite 10 and 5 Å peaks are symmetric and remain stable when measured after ethylene glycol-solvation (Figure 2.8). This shows the absence of I/S mixed-layer and coexistence of illite and smectite in these samples. In all other granite samples mixed-layering of I/S, indicated by displaced, broad and asymmetrical ca. 10 Å peaks, is evident. Illite polytype determination is not performed. The <2μm fraction of illite produced by sericitization (“sericite”, see chapter 2.2.1) is assigned to the illite group. Therefore, the products of sericitization and illitization associated with weathering or diagenesis (Meunier & Velde 2004) are not distinguished here by XRD.

Exact identification of smectite-types is not carried out, but the existence of montmorillonite (hydrated and Na, Ca, ± Mg bearing) is likely, indicated by 17 or 18 Å peaks after ethylene glycol-solvation.

Fe-Mg-chamosite is the dominant chlorite modification in all samples. A low concentration of clay-sized chamosite can be traced through the profile up to the lower boundary of the saprolite stage. In the saprolite and laterite, chamosite is absent.

Approaching the unconformity, the content of kaolinite increases from below detection limit in the unweathered granite to dominant in the laterite samples. Kaolinite is very well crystallized in the laterite, which is indicated by sharp, narrow peaks. The ratio between I/S and kaolinite is high in the unweathered granite, saprock and saprolite and low in the laterite. This is only a rough estimation for samples beneath the saprolite and laterite zone, due to the interference of the 7 Å peaks of kaolinite and chlorite.

The qualitative feldspar variation, as determined by whole-rock XRD, is also displayed in the clay fraction by (002) peaks of feldspars.

Comparable to the whole-rock spectra, also the clay fraction spectra do not point to major mineralogical changes associated with cataclasis.

2.2.11 Whole-rock geochemistry results

A selection of 10 representative samples is taken to determine the changes in the whole-rock geochemical composition through all weathering stages. A selection of major element (oxides), which show trends of depletion or enrichment is displayed in Figure 2.9.a-k. (entire data set in Appendix I.a).

In the profile section below the laterite, only a few major element (oxides) and trace elements show a trend of depletion (Na_2O, CaO, Ba, Zn, Sr, Co) or enrichment (K_2O, Rb). The mobilization and depletion of Na, down to an almost absolute absence in the saprolite and laterite horizons is observed. Potassium trend is complex: beginning with a value of ca. 2.5 wt% in the unweathered granite, it shows an enrichment with proximity to the unconformity up to a maximum value of ca. 9 wt% in the lower saprolite, and than a decreases down to ca. 6 wt% through the saprolite and laterite. The elements U, V and Zr are stable until the lower saprolite boundary, above this point they show a depletion trend.

A significant change of the composition occurs in the transition to the lateritic zone. A decrease is observed only in SiO_2, Ba, Th, Cu. SiO_2 is strongly depleted in the laterite, unlike most other major elements. The loss of SiO_2 equals the sum of enrichment of the other major element oxides plus volatiles (Figure 2.10.a).

Element (oxides) that increase their concentration at this boundary are Al_2O_3, Fe_2O_3, MgO, TiO_2, P_2O_5, Hf,

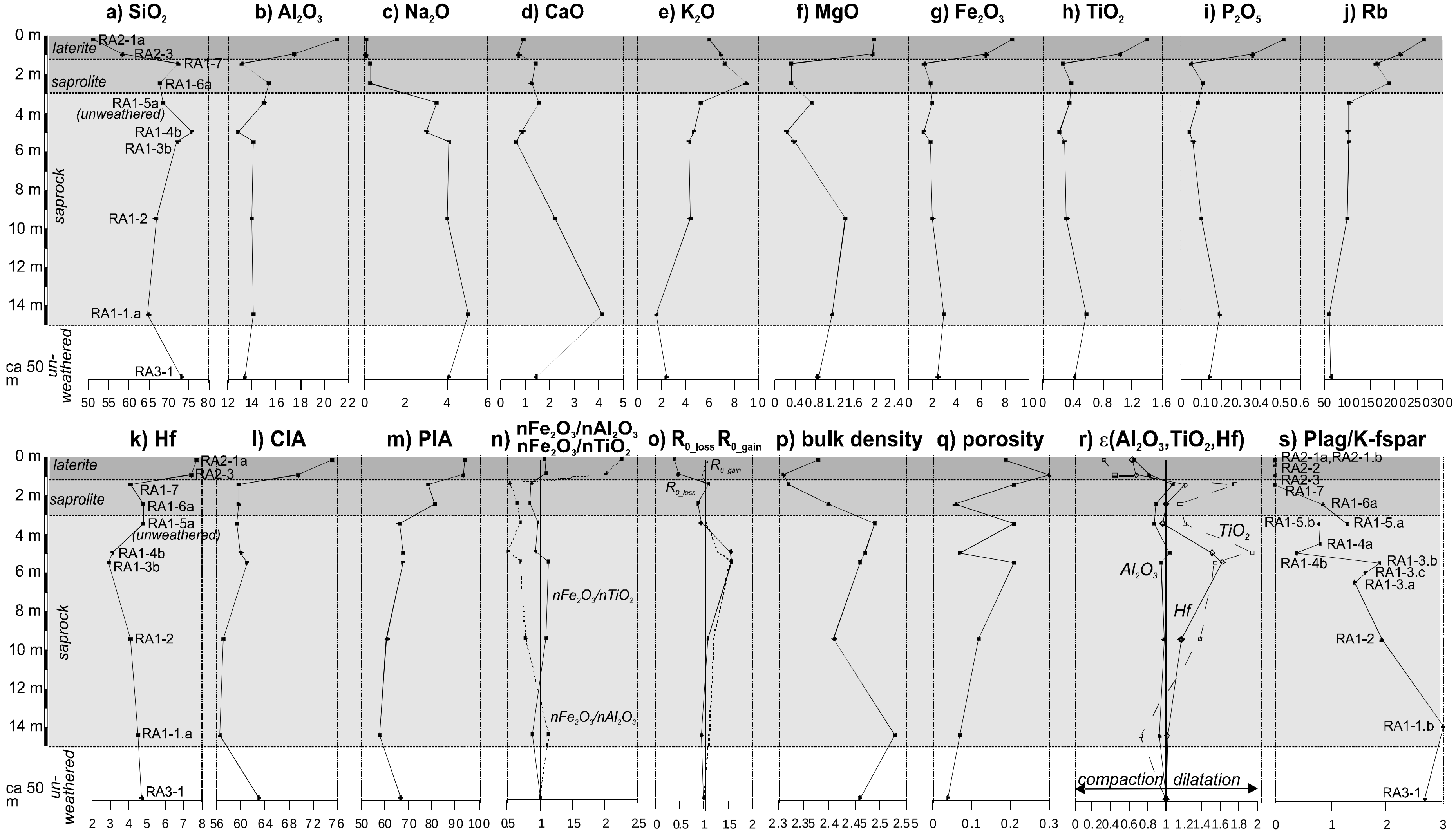

Figure 2.9: a-h) major element oxides; i-k) trace elements; l-m) geochemical alteration indices; n) ratios of normalized oxides (normalized to unweathered parent rock RA3-1); o) R_{0_loss}, , depletion-factor of mobilized elements and R_{0_gain}, enrichment-factor, both normalized to Ti,Hf; p) bulk rock density [g/cm^3]; q) porosity; r) volume strain ε by immobile element mass balancing (Al. Ti, Hf); s) intensity ratio of indicative XRD-peaks (whole-rock) of plagioclase and K-feldspar. See text for details.

Pb, As, Cs, Ga. In the laterite there is a remarkable jump in Al_2O_3 concentration, it almost doubles its concentration from 13 wt% (unweathered granite) to 21 wt% (in the upper laterite sample RA2-1a). The concentration trend of volatile substances (loss on ignition - LOI) is similar to the Al_2O_3 trend. Fe_2O_3, TiO_2 and P_2O_5 show even stronger increases by up to four times of the concentration in the unweathered granite. The ratios nFe_2O_3/nAl_2O_3 and $nFe_2O_3/nTiO_2$ (n means *normalized* to unweathered granite*)* are plotted in Figure 2.9.n. The ratios are calculated as follows:

$$(1) \qquad nX / nY = (X_w/X_p) / (Y_w/Y_p)$$

X and Y are the specific element oxides, indices w and p refer to weathered and parent rock, respectively. Normalized Fe increases more than normalized Al in the laterite, shown by an increase of the ratio of ca. 2.3. A very high correlation between Fe and Ti throughout the entire profile is indicated by the stable ratio of ca. 1 and evidences by the linear regression ($R^2 = 0.991$; Figure 2.11).

Whereas most element are subject to change within the laterite, either showing an increase or a decrease from the lower (RA2-3) to the upper laterite sample (RA2-1a), only Hf remains quite stable within the laterite. The CaO concentration scatters, but an approximately stable trend of Ca concentration through the profile is observed.

All other measured elements do not show significant trends, either because of too low concentrations or geochemical inhomogeneities of the primary lithology.

Following Nesbitt (1992), the ternary plots *Al-CaNa-K*, *Al-CaNa-FeMg* and *Si-Al-Fe* are plotted to characterize the trends of major element concentration Figure 2.12. In the first two ternary plat (a, b) the distinction between a saprock-saprolitic and a lateritic trend can be made. The saprolitic trend is characterized by a path from plagioclase to K-feldspar constitution, which corresponds to the microscopically observed plagioclase depletion. In the laterite, the depletion of K is visible by the path towards illitic composition. This illitic composition is the average from existing micas, illite, and K-feldspars. The saprock-saprolitic trend in the *Al-CaNa-FeMg* plot is indicated the aluminium enrichment, whereas in the laterite the enrichment of Fe and Mg is stronger than Al enrichment, which can also be seen in the *nFe_2O_3/nAl_2O_3* plot (Figure 2.9.n.). In the Si-Al-Fe (c) plot the saprock-saprolite trend is not developed, which is an effect of the relative stability of the elements beneath the laterite. The lateritic trend, however, is illustrated and is associated with the SiO_2 depletion and coincident Al_2O_3 and Fe_2O_3 enrichment.

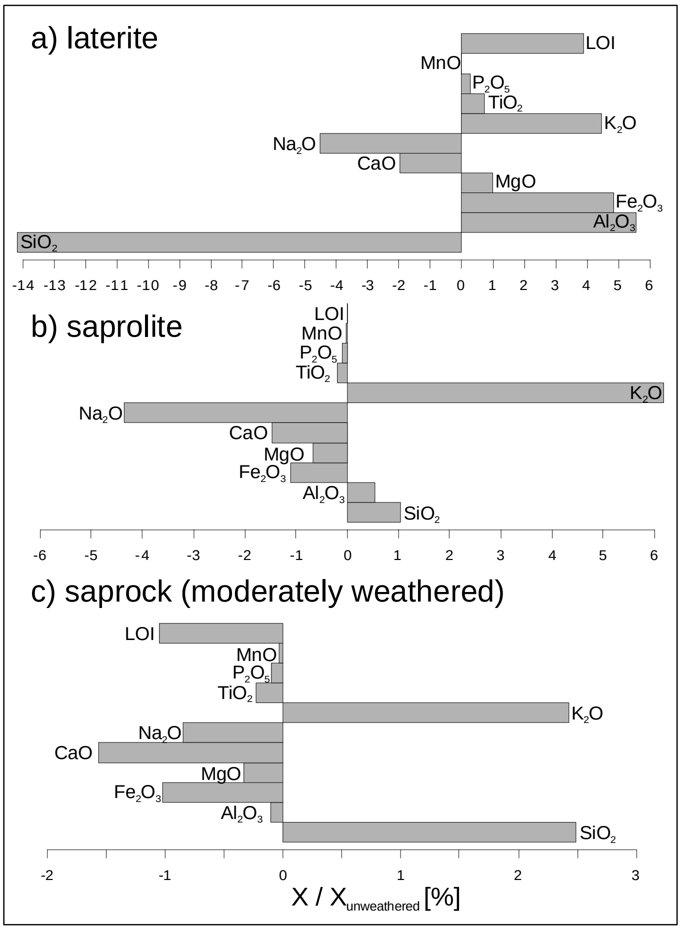

Figure 2.10: Geochemical enrichment-depletion diagrams of element-oxides in the weathering stages a) laterite, b) saprolite and c) moderately weathered granite. Elements of the unweathered granite (RA3-1) are used for normalization. X refers to the specific element-oxide.

Two chemical indices of alteration are plotted. The inversely proportional relation between K_2O (increase until saprolite) and Na_2O and CaO (decrease) is visualized with *PIA* (Fedo et

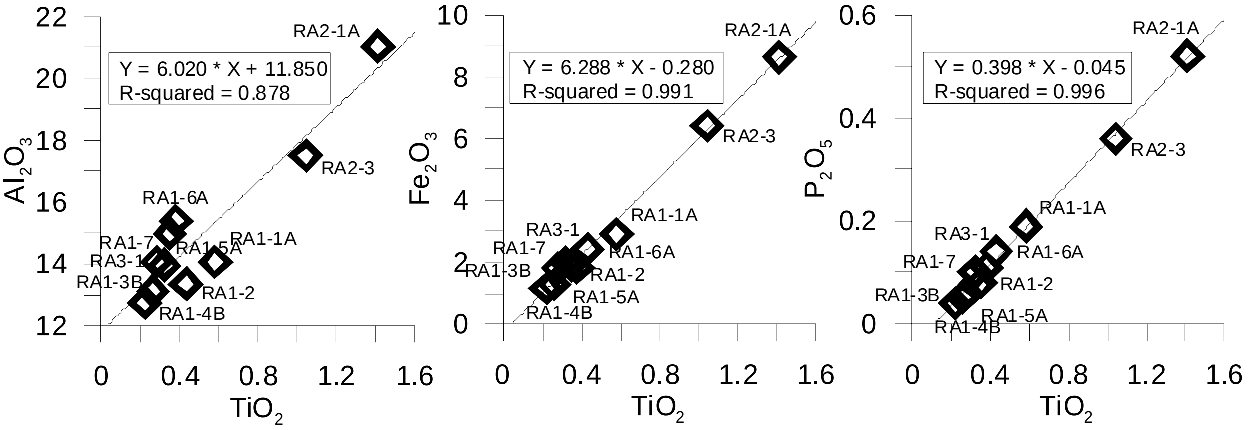

Figure 2.11: TiO_2 versus Al_2O_3, Fe_2O_3 and P_2O_5. The correlations between TiO_2 and Fe_2O_3, and TiO_2 and P_2O_5 are very good ($R^2 > 0.99$), whereas Al_2O_3 is less good correlated ($R^2 = 0.88$) with Ti.

al. 1995) (Figure 2.9.m; equations 11 and 12 in chapter 1.2.1). According to *PIA*, alteration (weathering) increases strongly in the saprolite (*PIA* values of ca. 57 % to 80 %), below, it is relatively stable (between 57 and 68 %). In the laterite, *PIA* values are as high as 94 %, indicating highest degree of weathering. For comparison, *CIA* (Nesbitt & Young 1982) is plotted (Figure 2.9.l, equation 10 in chapter 1.2.1). The *CIA* shows an increase only in the laterite, which strongly corresponds to the Al_2O_3 trend. In comparison to *PIA*, *CIA* does not differentiate between K and the other alkali and alkaline earth elements.

Volumetric strain calculations are carried out with a mass balance method using assumed immobile elements (1) aluminium, (2) titanium and (3) hafnium (Brown et al. 2003, Mathe et al. 1999, White 1995). Other “immobile” elements, e.g. Th and Zr, are not suitable here because of leg den their low and variable content in the samples. This method calculates the volume change ε between parent and weathered rock (changed from White 1995):

$$(4a) \qquad \varepsilon = V_w / V_p$$

Indices p and w mean parent and weathered rock, respectively. Substituting V with bulk-rock density ρ and concentration of the immobile element C the equation can be written as:

$$(4b) \qquad \varepsilon = (\rho_p \cdot C_p) / (\rho_w \cdot C_w)$$

Both parameters, density ρ and concentration *C*, can be measured, hence ε calculated (Figure 2.9.p). All mass balance calculations show $\varepsilon < 1$ in the laterite horizon (Al_2O_3: 0.67; TiO_2: 0.32; Hf: 0.63) and thus suggest a volume decrease (compaction). A decrease of volume with proximity to the unconformity is indicated by ε_{Al} and ε_{Ti}, whereas ε_{Hf} does not change within the laterite. Below the laterite, the discrepancy of volume stain between the “immobile” elements is very high. Whereas ε_{Al} and ε_{Hf} remains relatively stable between 0.9 and 1.05, indicating no significant volume strain, ε_{Ti} locally shows dilatation, which are unrealistically high (up to 2). ε_{Hf} and ε_{Al} are similar below the laterite, except deviations in the cataclastic samples RA1-3b and RA1-4b. Hafnium is associated with zircon; comparing the Hf concentration with Zr (and associated U, see Appendix I.a), it is evident that discrepancy is related to a locally changed zircon content. The reliability of the elements regarding their immobility will be discussed in chapter 2.5.3.3. Ti and Hf seem to be more reliable than Al and an arithmetic mean of ε_{Ti} and ε_{Hf} is calculated ($\varepsilon_{Ti.Hf}$) to represent the best geochemical volume strain indicator in the laterite.

The depletion factor R_{0_loss} is calculated. It represents a measure for the depletion of easy soluble major elements (SiO_2, Na_2O) normalized to the arithmetic mean of immobile elements Ti and Hf, and is calculated with the following equation (changed after White 1995):

$$(5) \qquad R_{0\_loss} = [\Sigma(C_{w(loss)})\, C_{p(Ti,Hf)}) / (C_{w(Ti,Hf)} \cdot \Sigma(C_{p(loss)})]$$

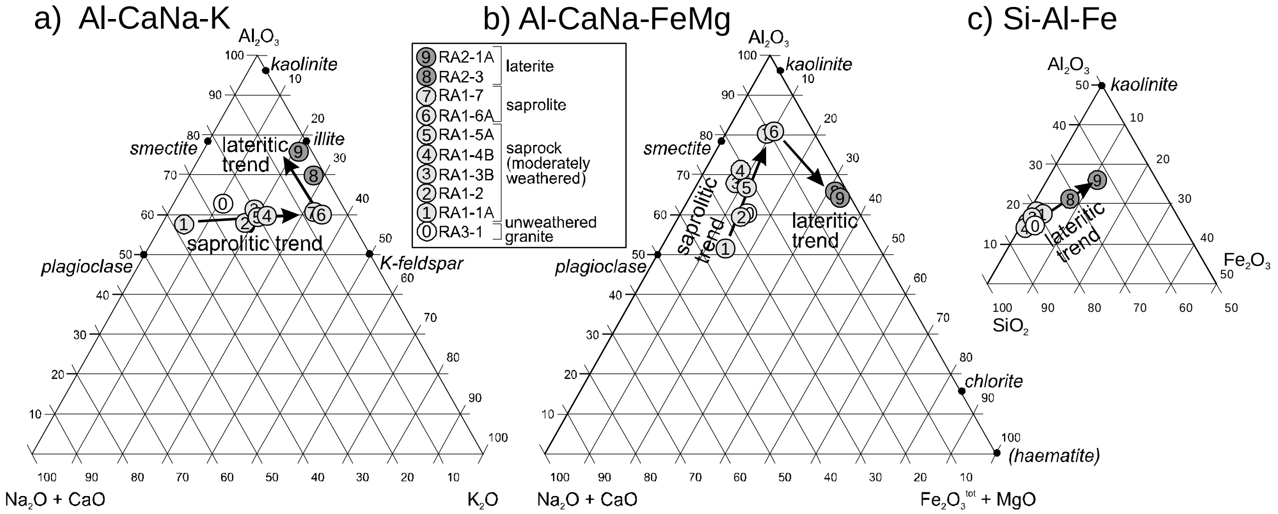

Figure 2.12: Ternary diagrams displaying a saprolitic and a lateritic weathering trends. a) Al-CaNa-K shows substantial Na_2O (and minor CaO) depletion while relative stable K_2O content, b) Al-CaNa-FeMg shows Fe_2O_3+MgO enrichment in comparison to Al_2O_3 and c) Si-Al-Fe indicates only a lateritic trend characterized by SiO_2 depletion. Mineral compositions are plotted for comparison in the diagrams.

where $\Sigma(C_{w(loss)})$ is the sum of concentrations in weathered rock and $\Sigma(C_{P(loss)})$ is the sum of concentration in the parent rock. Analogously, the normalized enrichment factor, R_{0_gain}, of elements Al_2O_3, Fe_2O_3, MgO, TiO_2, P_2O_5, MnO is calculated by:

$$(6) \qquad R_{0\_gain} = [\Sigma(C_{w(gain)})\, C_{p(Ti,Hf)}) / (C_{w(Ti,Hf)} \cdot \Sigma(C_{p(gain)})]$$

The calculations display the strong depletion of SiO_2, Na_2O (R_{0_loss} = 0.46) in the lower laterite and only a moderately advanced depletion in the upper laterite (R_{0_loss} = 0.37) (Figure 2.9.o). The gain of the relatively enriched elements is well correlated with the relative gain of immobile Hf and Ti, shown by the stable ratio R_{0_gain} of ca. 1 ± 0.1.

2.2.12 *Magnetomineralogy*

Important ferromagnetic minerals in the profile are antiferromagnetic iron oxides (microcrystalline haematite and (titaniferous) *martite*) and ferrimagnetic magnetite as inclusions in martite. Martite is a coarse grained haematite (Dunlop & Özdemir 1997, Ramdohr 1975). Goethite is rarely observed in the laterite. Low amounts of titanium are frequently present in the martites (detected by SEM-EDX). The magnetomineralogy in the rocks is part of the $Fe^{II}Fe^{III}Ti$ system (Figure 2.13). Dominant paramagnetic mineral in the granite and saprock is chlorite (less important are white mica and biotite); and in saprolite and laterite Fe/Mg-mica.

Martite (coarse-grained haematite): Martite appears mostly in cubic subhedral grains of less than 0.5 mm size in those samples where the granitic texture is not destroyed by cataclasis or lateritic weathering. Martite grains are accumulated in clusters or are disseminated in the matrix. A preferred distribution of martite grains along with chlorite-mica-stacks is often observed (Plate 2.4 a,e,f). With reflected light under crossed nicols, most martite grains reveal a serrate lamellae-pattern due to their pleochroism. The lamellae are

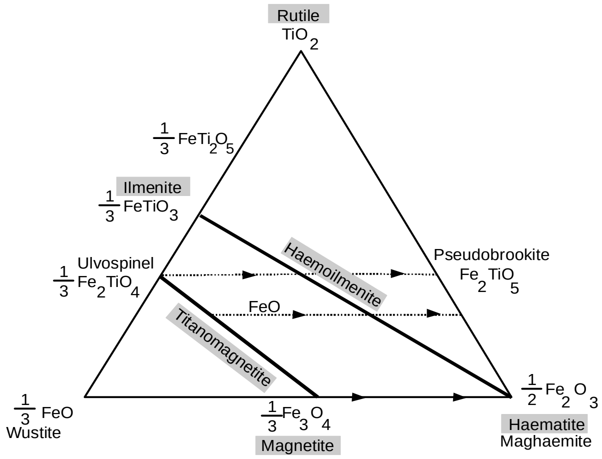

Figure 2.13: Ternary plot of titaniferous iron oxides. Arrows indicate the oxidation path towards Fe^{3+}-phases. The phases in the Roded Granite profile are grey (modified from Lindsley 1991)

parallel with the pre-existing cubic magnetite crystallography ({111} or {110} surfaces). In some cases, the pleochroism reveals an irregular patchy martite crystal pattern. Geochemical variations between the lamellae or between the patches are not observed. Martite is in all weathering stages an accessory component (< 1.2 %, see chapter 2.2.12.1). Petrographic observations show that martite content decreases with proximity to the unconformity. It has a minimum in the saprolite samples (only very few grains per thin section RA1-7). The number of martites is highest in the laterite, although their modal fraction is lower than in the granite due to their reduced grain sizes (Figure 2.14). The martite shapes are modified from euhedral to anhedral with serrate boundaries in the laterite (Plate 2.5.a). In such anhedral martites, magnetite remnants define locally the edges of martite. In the cataclasite, martite grains are smaller than in the granite and have a higher degree of dissemination. The amount of grains which form clusters is low in the cataclasite. Smaller grains are typically disseminated, whereas larger grains build the cluster. The appearance of martite clusters in the granite can be divided into three groups: (1) mechanically disintegrated large primary crystals (Plate 2.4.g and Plate 2.5.e); (2) accumulation of smaller single grains generated by the crystallization process and (3) presumable the result of chemical disintegration, leading to anhedral grains with serrate boundaries, as observed in the laterite.

In several cases, martite grains are enriched in titanium towards the grain boundary. This may indicate the presence of primary ilmenite or titanomagnetite. Occasionally, these titaniferous martite rims are altered to a skeleton-like dissolution pattern (Plate 2.4.d). In rare cases, single lamellae in martites are altered to microcrystalline haematite and rutile (TiO_2), indicating a primary titaniferous chemistry of lamellae (Plate 2.4.c).

Haematite in chlorite: Haematite inclusions in chlorite-mica stacks and Fe/Mg-mica are observed in all samples (Plate 2.2.e,f). These haematites are highly elongated parallel with basal surfaces of the phyllosilicates.

Microcrystalline haematite: Clay-sized haematite densely impregnates the kaolinite matrix in the purple-red coloured laterite. Commonly, this microcrystalline haematites is highly concentrated in the direct vicinity of martites (Plate 2.5.a). At least a part of this haematite generation nucleated at goethite surfaces (Plate 2.5.i).

In cataclasites, microcrystalline haematite is abundant, and causes the typical red colour of the lithology. It appears that this generation is, at least partly, the result of cataclasis of iron oxides (martite or magnetite) (Plate 2.5.b,c). To some extend, nucleation of haematite is possible, too.

Haematite in veins: Haematite is a major fissure and joint filling in the granite, saprock, saprolite and cataclasites. Haematite fissures crosscut quartz and feldspar along its cleavage surfaces and haematite-rich joints cut through the rock texture (Plate 2.4.f).

Magnetite: Magnetite is detected as poicilitic inclusions in most martite grains. Both magnetite and martite are distinguishable due to the pleochroism of haematite under reflected light with crossed nicols, and after applying *ferrofluid (G 100)* on thin sections. The distribution and shapes of the magnetite inclusions are mostly parallel with a cubic crystal lattice apparent in most martites. (Plate 2.4.e,f,g). In other martite grains, magnetite inclusions are irregular. Since the haematite structure is not cubic, but hexagonal, it can be inferred that martite is actually a crystallography-controlled pseudomorphic replacement product after cubic magnetite, a process called *martitization* (Dunlop & Özdemir 1997, Ramdohr 1975). The magnetite inclusions are considered as remnants of the primary magnetite crystals (Lagoeiro 1998).

The unweathered granite and the cataclasite indicate a high ratio of magnetite within martite (magnetite area / entire martite area ca. 0.3). A slight decrease of magnetite remnants in the martite grains can be observed approaching the laterite. The larger a martite grain is the higher is the content of relic magnetite; very small grains are typically deficient in magnetite remnants. This observation is valid for all studied rocks. In a laterite sample, a magnetite / martite ratio of 0.0366 is determined by modelling (see chapter 2.3.4).

Iron hydroxides: A very small fraction of the observed iron phase in the laterite are hydrated iron oxides, such as goethite and ferrihydrite. Qualitative determination of the iron content is carried out with SEM-EDX, but exact mineral identification is not performed. These phases are distinguished from martite and magnetite by crystal habits and dissolution patterns, which are unusual with respect to the iron oxides. A selection of these iron hydroxides is shown in Plate 2.5.e-i. Often, relics of primary (euhedral) grain boundaries are evident (Plate 2.5.e), thus it is likely that hydrated iron phases are pseudomorphs, formed after magnetite or martite. The needle-like habit displayed in Plate 2.5.h,i may point to goethite. Here, it is observed that microcrystalline haematite nucleated on the surfaces of these needles and ultimately replaced goethite(?).

Leucoxene: Titaniferous minerals (euhedral rutile and titanite) are often associated with martite. They build secondary concretions, which are referred to as leucoxene. Leucoxene is either in the vicinity of euhedral or subhedral martites (Plate 2.5.a) or it replaces in situ the titaniferous iron oxide, preserving partly the iron oxide lattice and showing sharp boundaries with the matrix (Plate 2.5.d). The euhedral rutile crystals can be quite large (0.2 mm). Carbonates are often associated with leucoxene. Leucoxene typically occurs in laterite, and less often in granite, saprock, saprolite. In the cataclastic zones leucoxene relics are disseminated in the matrix without spatial association with martites. This points to a relative age relation between older leucoxene formation and younger cataclasis.

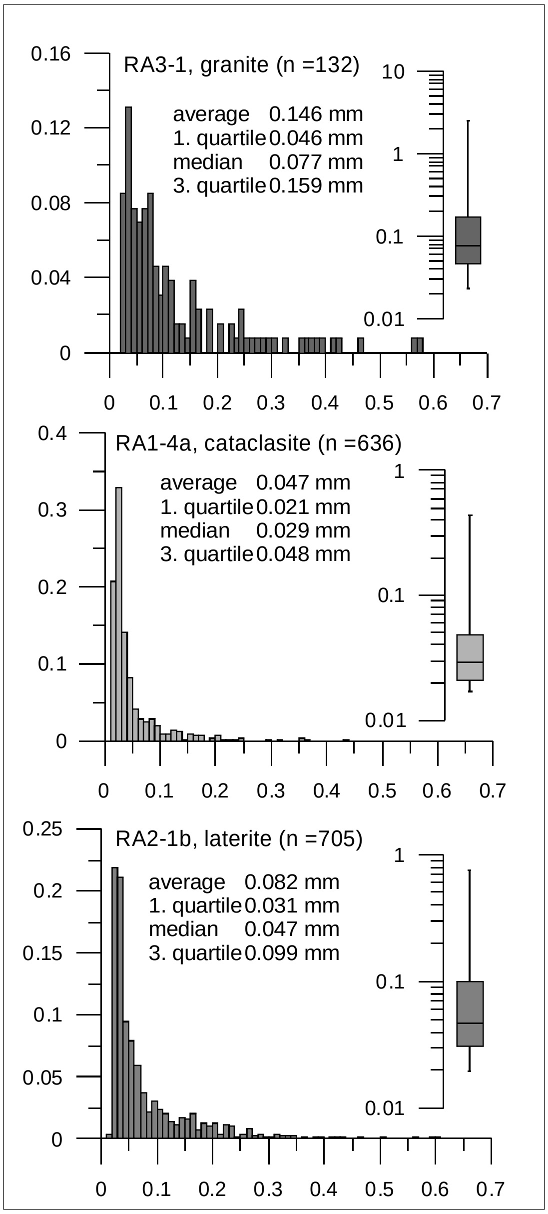

Figure 2.14: Grain sizes (diameters) of martite cluster + single martites determined by image analysis. The results of the thin sections are combined for each histogram. The corresponding box-whisker plot show minimal, maximal, 1. quartile, median and 3. quartile values.

2.2.12.1 *Martite modal fraction and grain shape distribution*

The modal fraction of martites is estimated for three samples by image analysis of thin sections by summing up the classified area of the phases (method see chapter 1.3.4). The martite fraction in the granite sample is 0.012, in the cataclastic sample 0.00314, and in the lateritic sample 0.0085.

The grain shape distribution of martite cluster + single martite is calculated by image analysis using the program SPO (by Launeau & Robin). Only the shapes of the clusters are considered here. For granite, cataclasite and laterite the distribution are binomial and skewed to the right (Figure 2.14). Differences in grain sizes are distinct: the granite bears the highest grain sizes with an average of 0.146 mm and a maximum size of about 0.57 mm. The cataclasite is characterized by a much smaller grain size (average: 0.047 mm, maximum: about 0.45 mm). The laterite has a medium grain size spectrum with an average size of 0.082 mm and a maximum size of about 0.6 mm.

2.3 Magnetic susceptibility analyses

2.3.1 Bulk susceptibility κ_{bulk}

To test a field dependence of the bulk susceptibility, one specimen of each sample is measured in two different low-fields (30 and 300 mA). The specimens do not show any field dependence of κ_{bulk}. The influence of petrographically detected titanomagnetite on κ_{bulk} can therefore be ruled out.

The development of κ_{bulk} throughout the weathering profile is shown in Figure 2.17.a. κ_{bulk} shows a clear relation to the weathering stages. The unweathered granite has the highest κ_{bulk} reaching $2800 \cdot 10^{-6}$ SI. κ_{bulk} decreases (ranging from 200 to $1095 \cdot 10^{-6}$ SI; maximum $1500 \cdot 10^{-6}$ SI) through the saprock zone. The unweathered samples of a corestone inside the saprock zone show higher κ_{bulk} (RA1-4.a: ca. $1115 \cdot 10^{-6}$ SI, RA1-5.a: ca. $1067 \cdot 10^{-6}$ SI) than the wall rock samples. As sample RA1-4.a is a cataclasite, a significant relation of κ_{bulk} and cataclasis is not recognized. However, it should be taken into account that cataclasis affected rocks in both weathering stages, saprock and saprolite, therefore potential effects on κ_{bulk} of weathering and cataclasis may be superimposed. The lowest values ($\kappa_{\text{bulk}} = 50$ to $105 \cdot 10^{-6}$ SI) are measured in the saprolite. κ_{bulk} increases in the laterite to a values ranging between 400 and $1000 \cdot 10^{-6}$ SI.

Standard deviations σ of κ_{bulk} between the specimens of each sample, displayed by the error bars in Figure 2.17.a, change systematically through the profile. σ is generally higher in the unweathered granite and saprock than in the saprolite and laterite. σ is low also in the cataclasites.

2.3.2 Temperature dependent susceptibility $\kappa(T)$

To determine whether the main contributors are the abundant low susceptible paramagnetic and anti-ferromagnetic (Fe-phyllosilicates, haematite) minerals, or the scarce high susceptible ferrimagnetic magnetite, temperature dependent susceptibility measurements $\kappa(T)$ are carried out. Normalized magnetic susceptibility (normalized to κ at room temperature) is used for evaluation (Figure 2.15).

Magnetite is indicated by the significant drop of the susceptibility at the characteristic Curie temperature (T_{Curie}), in the range between 570 to 590 °C. The Verwey transition (T_{Verwey}) at ca. -150 °C in magnetite, indicated by a susceptibility increase, is well pronounced. Magnetite is evident in all weathering stages and structural domains (Figure 2.15.a-e). The Hopkinson peaks (HP) are pronounced in the saprolite and laterite samples (Figure 2.15.d,e). It has been described that Hopkinson peaks are most pronounced in samples with a high ratio of single-domain / multi-domain state of magnetite (e.g. Just 2005). Although not exactly defined, ca. 0.05 µm is considered as the grain size representing the transition between single- and multi-domain state (Harrison & Putnis 1996). The sizes of relic magnetites in martite are in the granite sample generally larger, ranging between ca. 1 to 50 µm (Figure 2.14). This size range represents multi-domain state of magnetite. With proximity to the unconformity, a general grain size reduction of relic (poicilitic) magnetite by advanced oxidation to martite is evident, but a consequential predominance of single-domain magnetite in the saprolite and laterites can not be confirmed.

Haematite is detected by its T_{Curie} at ca 670 °C in the saprolitic and lateritic sample. The T_{Curie} of haematite is weakly pronounced in the saprolite and very well in the laterite. The characteristic Morin transition (T_{Morin}), taking place in the vicinity of -12 °C is not (clearly) displayed. This can either be caused by impurities in haematite, probably the incorporation of aluminium, or by the haematite grain size which is smaller than ca. 0.02-0.03 µm (de Boer et al. 2001). Haematite grain size spectra are not determined, but haematite pigments are to be found in the clay-fraction.

Further magnetic carriers: The low-temperature curve of the laterite has a hyperbolic gradient typically indicating paramagnetic susceptibility. These paramagnetic phases contributing significantly to the

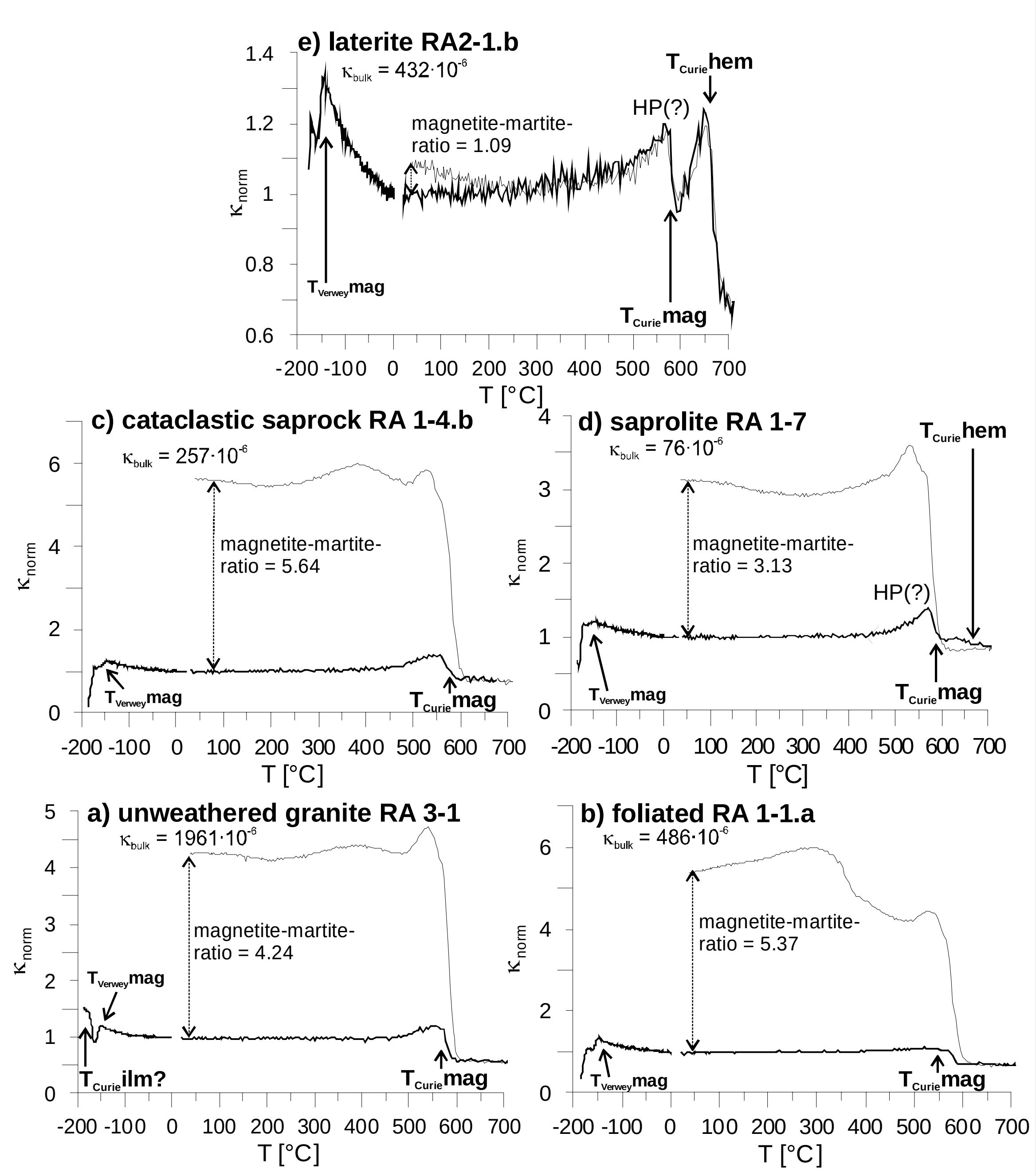

Figure 2.15: Temperature dependence of bulk susceptibility $\kappa_{norm}(T)$ (normalized to κ at room temperature) of samples from the weathering profile of the Roded Granite. Bold lines are heating curves, thin lines are cooling curves. a) unweathered granite, sample RA 3-1; b) foliated granite, RA 1-1.a; c) cataclastic granite, RA 1-4.b; d) saprolite, RA 1-7; e) laterite, RA 2-1.b. The magnetite/martite-ratio is calculated from $\kappa(T_{room})$ after cooling / $\kappa(T_{room})$ before heating.

susceptibility are Fe/Mg-micas and probably iron-bearing illite and kaolinite.

Granite, saprock and saprolite samples show at the cooling run in the temperature range of ca. 300 to 400 °C an increased susceptibility. These undefined carriers of susceptibility, probably iron bearing carbonates, are experimentally produced and not of concern for the interpretation.

Reversibility: The κ(T)-curves of all granite, saprock and saprolite samples are not reversible, i.e. curves of the heating and cooling run are different. An increase of susceptibility (by the factor 2.5 to 5.5) occurs during the cooling run at about 590 °C.

This indicates magnetite formation and can be interpreted as a reduction of martite to magnetite during the experiment (e.g. Just 2005). The κ(T)-curve of the laterite is reversible. During the cooling run, this reaction does not occur in the laterite, although martite is observed with a content similar, mostly even higher, to other samples. It appears that microcrystalline haematite does not reduce to magnetite like martite does, an observation also documented by Just (2005).

2.3.3 Ratio of κ_{bulk} / total iron content

The total iron content in the profile beneath the laterite has a relatively stable value of 2 wt% (oxide) (Figure 2.9.f). Iron content increases up to ca. 9 wt% in the laterite. The iron content in the profile is mostly bound to those minerals that carry κ_{bulk}. These minerals are magnetite, martite, microcrystalline haematite and Fe/Mg-mica (+ iron-bearing clays, such as chlorite, phengitic illite, kaolinite). Specific phase transitions between these carriers (particularly, the magnetite to martite oxidation) are associated with variation of κ_{bulk}, without a change of iron content. Therefore, the ratio κ_{bulk} / $Fe_2O_3^{total}$ provides information about these phase transitions and their occurrence in specific zones of the profile (Figure 2.17.d). The unweathered samples (RA 3-1 and RA 1-5.a) show a high ratio of $\kappa_{bulk} > 500\ 10^{-6}$ SI. Medium ratios of 160 to 250 are evident in the saprock and smallest ratios of 50 to 134 are shown in the saprolite. The ratio does not increase significantly in the laterite (κ_{bulk} = 65 to 110).

2.3.4 Modelling of κ_{bulk} and the contribution of the main magnetic carriers

The chlorite-mica stacks (Fe/Mg-mica in saprolite and laterite), martite and magnetite are the main magnetic carriers in the rocks. With the modal fractions of these magnetic carriers, a theoretical κ_{bulk} of the sample can be calculated and compared with the measured κ_{bulk}. This helps to gather information about the actual intrinsic susceptibility of the magnetic carriers, which can vary considerably with structural and chemical impurities and grain size (Hunt et al. 1995). From κ(T) results it is evident that κ_{bulk} is dominantly influenced by magnetite, but in the saprolite and laterite a considerable contribution derives from haematite. A closer look to the relative influence of phases on κ_{bulk} and its change across the profile seems to be necessary and leads to an improved assessment of the AMS fabrics. This relative influence is best expressed by the ratios $c_{chl}k_{chl}/\kappa_{bulk}$; $c_{hem}\kappa_{hem}/\kappa_{bulk}$ and $c_{mag}\kappa_{mag}/\kappa_{bulk}$. The modelled κ_{bulk} is calculated with the equation of (Daly & Henry 1983):

$$(1) \qquad \kappa_{bulk} = c_f\kappa_f + c_p\kappa_p + c_d\kappa_d,$$

where c_f, c_p, c_d are the modal fractions and κ_f, κ_p, κ_d the intrinsic volume susceptibilities of ferromagnetic, paramagnetic and diamagnetic carriers, respectively. With this model, an idealized alteration trend with respect to the magnetic carriers is established, from non-altered granite (oxides are 100 % magnetite) to "ideally altered" saprolite (100 % martite).

An unweathered granite (RA3-1), a cataclasite from the corestone (RA1-4.a) and a laterite sample (RA2-1.b) are investigated. Their modal fractions are determined by image analyses (in chapter 2.2.12.1). It is indicated by geochemical observations (chapter 2.2.11), that the total amount of iron did not change significantly in the weathering stages beneath the laterite, thus a total content of all iron-oxides ($c_{mag}+c_{mar}+c_{hem}$) are considered as stable. However, the absolute content of iron-oxides is strongly increased in the laterite due to the advanced weathering. At the depth of sample RA2-1.b (0.2 metres), Fe_2O_3 concentration increased by the factor 3.55 in comparison to the granite (Figure 2.9.g). An additional enhancement of total Fe-oxide in the laterite content is expected from the volume collapse during compaction (chapter 2.2.12). For the sample RA2-1.b, the ratio between strained volume and original volume ranges between 0.41 and 0.78 (in "plane strain" and "pure shear" situation, respectively; Table 2.2). Taking the average volume collapse of 0.6 as an approximation for the actual value, the reciprocal 1.67 represents the factor for compaction-related iron enrichment. Multiplying

Table 2.1: Modal fractions and modelled κ_{bulk} for three samples. Calculation of κ_{bulk} is carried out with different intrinsic susceptibilities of haematite κ_{hem}. The last two rows show the modelled "ideally unaltered" fresh granite and the "ideally weathered" saprolite). (* assumed but not measured; ** modal fraction of microcrystalline haematite was estimated under the assumption that total haematite (martite + microcrystalline) remains stable; *** initial sum multiplied with the Fe-enrichment factor 5.93 (see text)

	c_{chl}	c_{mar}	c_{mag}	c_{hem}	$c_{mag}+c_{mar}$	$c_{mag}+c_{mar}+c_{hem}$	c_{mag}/c_{hem}	intrinsic κ_{hem}	κ_{bulk}	$c_{chl}\kappa_{chl}$ / κ_{bulk} [%]	$c_{hem}\kappa_{hem}$ / κ_{bulk} [%]	$c_{mag}\kappa_{mag}$ / κ_{bulk} [%]
RA3-1_v	0.07	0.0092	0.0028	0	0.012	0.012	0.3043	5.00E-04	2.875E-03	2.44	0.16	97.4
measured κ_{bulk}	0.07	0.0092	0.0028	0	0.012	0.012	0.3043	1.00E-03	2.879E-03	2.43	0.32	97.25
$2.810\cdot10^{-3}$	0.07	0.0092	0.0028	0	0.012	0.012	0.3043	5.00E-03	2.916E-03	2.4	1.58	96.02
	0.07	0.0092	0.0028	0	0.012	0.012	0.3043	1.00E-02	2.962E-03	2.36	3.11	94.53
	0.07	0.0092	0.0028	0	0.012	0.012	0.3043	5.00E-02	3.330E-03	2.1	13.81	84.08
RA1-4a_vi	0.07*	0.0024	0.00074	0.00886**	0.00314	0.012	0.3083	5.00E-04	8.156E-04	8.58	0.69	90.73
measured κ_{bulk}:	0.07*	0.0024	0.00074	0.00886**	0.00314	0.012	0.3083	1.00E-03	8.213E-04	8.52	1.37	90.11
$1.242\cdot10^{-3}$	0.07*	0.0024	0.00074	0.00886**	0.00314	0.012	0.3083	5.00E-03	8.663E-04	8.08	6.5	85.42
	0.07*	0.0024	0.00074	0.00886**	0.00314	0.012	0.3083	1.00E-02	9.226E-04	7.59	12.2	80.21
	0.07*	0.0024	0.00074	0.00886**	0.00314	0.012	0.3083	5.00E-02	1.373E-03	5.1	41.01	53.9
RA2-1b	0.1	0.0082	0.0003	0.06266**	0.0085	0.07116***	0.0366	5.00E-04	4.354E-04	22.97	8.14	68.9
measured κ_{bulk}	0.1	0.0082	0.0003	0.06266**	0.0085	0.07116***	0.0366	1.00E-03	4.709E-04	21.24	15.05	63.71
$4.33\cdot10^{-4}$	0.1	0.0082	0.0003	0.06266**	0.0085	0.07116***	0.0366	5.00E-03	7.543E-04	13.26	46.97	39.77
	0.1	0.0082	0.0003	0.06266**	0.0085	0.07116***	0.0366	1.00E-02	1.109E-03	9.02	63.92	27.06
	0.1	0.0082	0.0003	0.06266**	0.0085	0.07116***	0.0366	5.00E-02	3.943E-03	2.54	89.86	7.61
fresh Granite	*0.07*	*0*	*0.012*	*0*	--	*0.012*			*1.207E-02*	*0.58*	*0*	*99.42*
Saprolite	*0.02*	*0.0025*	*0*	*0.00935*	*0.012*	*0.01185*	*0*	5.00E-04	*2.593E-05*	*77.15*	*22.85*	*0*

this value with the weathering-induced concentration enrichment factor 3.55, a total Fe-enrichment factor for sample RA2-1.b of 5.93 is determined (5.93 = 3.55 · 1.67).

The results of the κ_{bulk} calculations are summarized in Table 2.1. Chlorite and Fe/Mg-mica are considered as having similar intrinsic susceptibility of $1000 \cdot 10^{-6}$ SI. For magnetite an intrinsic susceptibilities of 1 SI is most likely, because any higher intrinsic susceptibilities causes unrealistic high κ_{bulk} (at least 1 order of magnitude higher than the measured κ_{bulk} values). For calculating the best-fitting κ_{bulk} of the granite, which respect to the measured κ_{bulk}, a variety of intrinsic susceptibilities of haematite is assumed (Hunt et al. 1995). Best results for the granite and the laterite are calculated with an intrinsic haematite susceptibility value of $1000 \cdot 10^{-6}$ SI. The calculation of κ_{bulk} of the cataclasite RA1-4a gives too small κ_{bulk}-values. This is probably due to additional magnetic carriers such as Fe-bearing carbonates, which are not taken into account in the model (Plate 2.3.e-h).

The κ_{bulk}-model suggests that magnetite is the main magnetic carrier ($c_{mag}\kappa_{mag}/\kappa_{bulk}$ > 70 – 97 %) in all weathering stages and structural domains. However, in the laterite ca. 23 % of the bulk susceptibility are carried by the iron bearing phyllosilicates and 8 % by microcrystalline haematite. This has to be kept in mind, when evaluating the AMS of the laterite in chapter 2.6.

The modelled "ideally unaltered" fresh granite has a κ_{bulk} of $1.207 \cdot 10^{-2}$ SI. The calculation of the "ideally altered" saprolite is based on the total martitization of magnetite. As demonstrated by geochemical mass balancing (chapter 2.2.11), the saprolitic alteration was iso-volumetric and without major mobilization of iron. Thus, the total haematite content (martite + microcrystalline) is considered as stable at the level of the granite (0.012 vol%, determined by image analysis, chapter 2.2.12.1). The magnetite-free saprolite has a modelled κ_{bulk} of $26 \cdot 10^{-6}$ SI, which resembles more or less the measured κ_{bulk} of the "real" saprolite samples RA1-7 ($76 \cdot 10^{-6} \pm 21$ SI). Adding a small amount of magnetite (magnetite: $2 \cdot 10^{-4}$ vol%), which is realistic and constrained by microscopy and κ(T), leads to a value of $50 \cdot 10^{-6}$ SI. Very small amounts of magnetite can double κ_{bulk}. In the "ideal" saprolite without relic magnetite, chlorite and Fe/Mg-mica have the strongest influence on κ_{bulk} ($c_{chl}k_{chl}/\kappa_{bulk} = 77$ %).

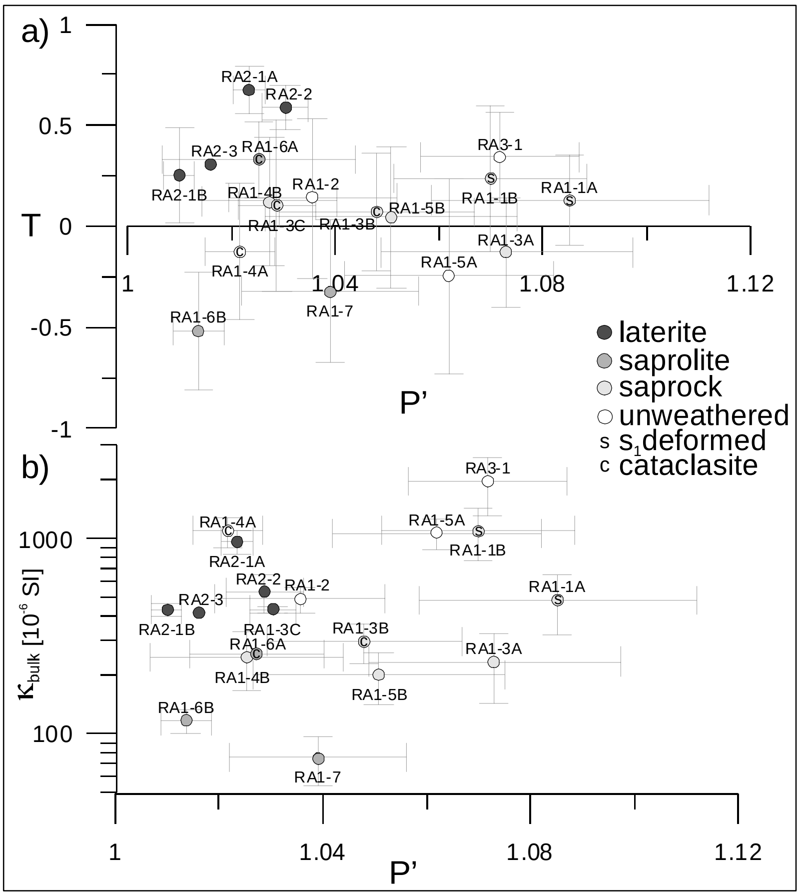

Figure 2.16: AMS parameters: a) "Jelinek" diagram P` vs. T; b) P' vs. κ_{bulk}.

2.3.5 *AMS*

The anisotropy degree P' varies in unweathered and macroscopically undeformed granite between 1.04 and 1.09 with a standard deviation of ± 0.01 or 0.02 (Figure 2.16). Shapes are mainly oblate (T > 0.34 ± 0.22). AMS parameters of the saprocks highly scatter across the entire T(P') field. P' is low (< 1.033 ± 0.02) and T highly scatters between -0.5 and 0.5 in the saprolite. Laterite samples have small

P’ values (< 1.04 ± 0.005) and exclusively oblate shapes. Samples showing a macroscopic S_1 foliation reach with P’ = 0.11 highest eccentricities in the profile. Shapes are oblate ($0 < T < 0.5$, two specimen with $T < 0$). Rocks that suffered cataclastic deformation through the weathering stages, generally show a low P’ ranging between 1 and 1.07 ± 0.02 and T is scattered throughout oblate and prolate fields ($-0.4 < T < 0.4$).

The diagram P’ vs. depth shows a general decrease with proximity to the unconformity (Figure 2.17.b). The trend correlates positively with the κ_{bulk} vs. depth curve. Such positive correlation of κ_{bulk} and P’ is visualized in (Figure 2.16.b). P’ changes significantly through structural domains and weathering zones. In the corestone, the cataclastically deformed unweathered granite shows much lower P’ than the intact unweathered granite, There is no clear dependence of shape factor T on depth and weathering stage.

The AMS ellipsoid axes are heterogeneously oriented. Distinct axes patterns within the weathering zones are almost not developed (sample stereoplots see Appendix II.a). The unweathered and macroscopically undeformed granite sample (RA3-1) has shallowly to moderately towards N-S plunging poles of magnetic foliation (κ_3) and horizontal W-E trending magnetic lineations (κ_1) (SPO image analysis in chapter 2.4.1). Alternatively, the unweathered granite corestone (RA1-5.a) shows a girdle distribution of κ_3 around a moderately inclined and NE trending κ_1. The weathering breccias of the saprock and saprolite zones have a similar pattern to RA1-5.a, and a few of them resemble the axes distribution as seen in RA3-1. Laterite samples (RA2-1.b, RA2-2) have steep inclined κ_3 and N-S trending flat-lying κ_1. This magnetic fabric resembles relatively well the petrographic fabric defined by the SPO of Fe/Mg-micas (SPO image analysis in chapter 2.4.2). One laterite sample (RA2-1.a) shows an AMS pattern quite similar to patterns observed in unweathered and saprolite samples. The samples that show clearly S_1 deformations (RA1-1-a, b) are defined

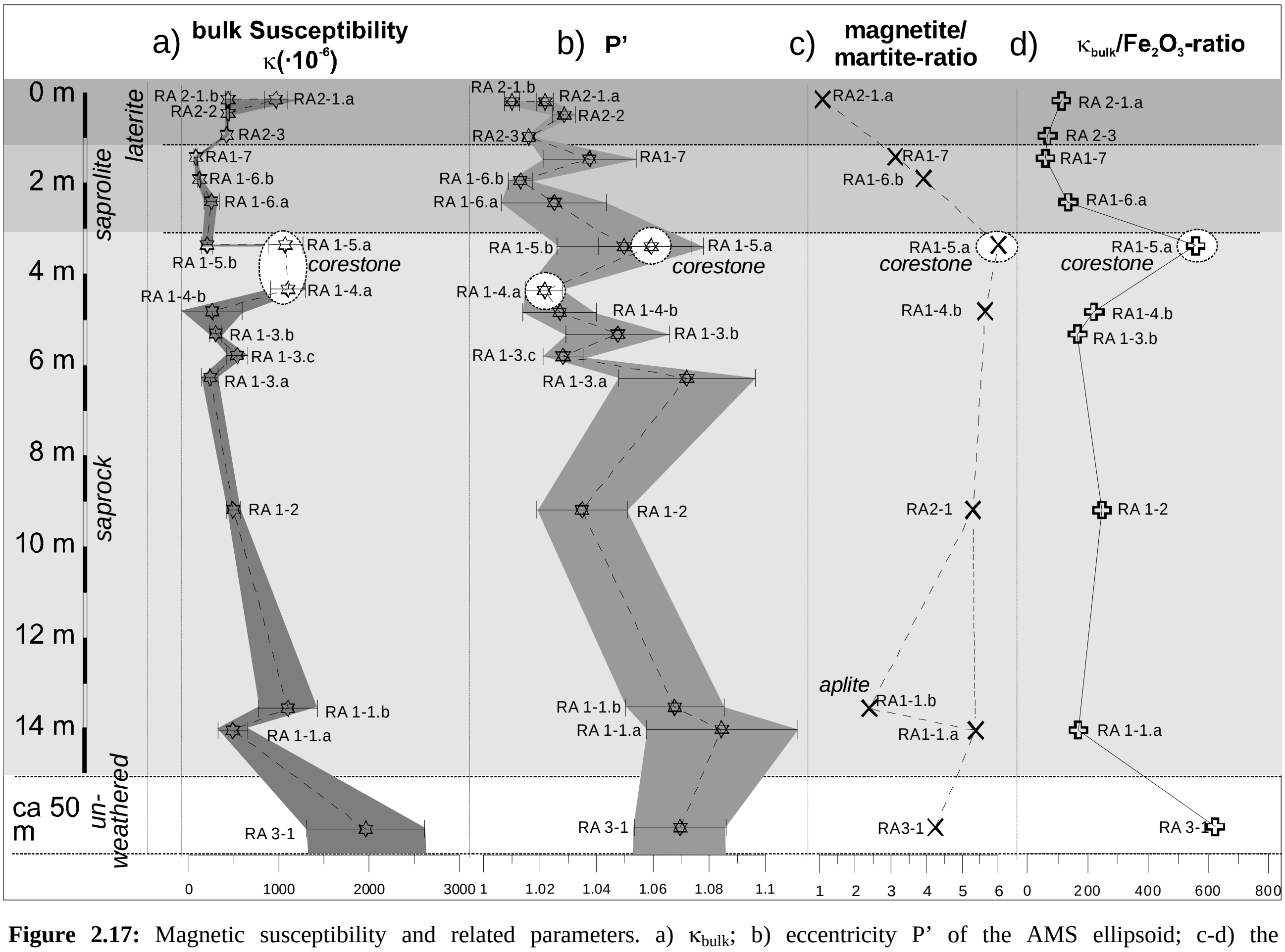

Figure 2.17: Magnetic susceptibility and related parameters. a) κ_{bulk}; b) eccentricity P’ of the AMS ellipsoid; c-d) the magnetite/martite-ratio and the κ_{bulk}/Fe_2O_3-ratio, respectively, represent indicators for the magnetically important phase transition from magnetite to martite (martitization). See text for details.

by shallow inclined κ_3 dipping towards NW or SE. Magnetic lineations plunge shallowly towards SW, indicating an association to the petrofabric. AMS patterns associated with cataclastic rocks are heterogeneously defined, but a preferred subvertical κ_1 can be observed. There is no apparent relation between petrographic and AMS fabric in the cataclasites, however, the relatively steep magnetic foliations are comparable to the steep planar cataclastic structures (cataclastic flow and cleavage) (SPO image analysis in chapter 2.4.3). A determination of AMS fabric types and their assignment to petrofabrics is carried out in chapter 2.6.4.

Specimens with AMS anisotropies with P’ less than 1.02 or 1.01 shows a random axes distribution and are not taken into account. The specimen data loss is ca. 4 % high. These deleted specimens are without exceptions from the weathering-breccia and cataclasis zone.

2.4 Image analyses of chlorite and martite SPO

2.4.1 3D-SPO fabric of a granite

2.4.1.1 Sectional SPO

The granite sample specimen RA3-1_v is investigated by means of image analysis. The petrographic fabric of the granite sample RA3-1 is incipiently developed (macroscopically undeformed). The SPO of the chlorites displays this weak fabric, therefore it is quantitatively analysed here for comparison with the AMS fabric. It is established that the magnetic anisotropy of chlorite is defined by its LPO (Tarling & Hrouda 1993). However, a major influence of chlorite LPO on the AMS can be excluded for the granite, as inferred by modelling of the bulk susceptibility (chapter 2.3.3). Therefore the LPO of chlorite can be neglected and is outside the scope of this study.

The abbreviations $\kappa_1\kappa_2$; $\kappa_1\kappa_3$ and $\kappa_2\kappa_3$ refer to the thin section surfaces.

Chlorites: The weighted SPO long axes of the chlorite stacks corresponds well to the principal magnetic axes on thin section surfaces $\kappa_1\kappa_2$ ($\phi_{\kappa1\kappa2}$=7.16°) and $\kappa_1\kappa_3$ ($\phi_{\kappa1\kappa3}$=11.72°), less well on surface $\kappa_2\kappa_3$ ($\phi_{\kappa2\kappa3}$=35.69°) Figure 2.18.a). The SPO anisotropies are well defined in $\kappa_1\kappa_2$ with $R_{\kappa1\kappa2}$=1.407. In $\kappa_1\kappa_3$ and $\kappa_2\kappa_3$ SPO anisotropies are less well defined, but still substantial with $R_{\kappa1\kappa3}$=1.201 and $R_{\kappa2\kappa3}$=1.176. The anisotropy of the rose diagram is high (Rf½=1.344) showing the relative uniform orientation of the chlorite crystals. This implies a homogeneous chlorite deformation, however, anisotropies in $\kappa_1\kappa_3$ and $\kappa_2\kappa_3$ (Rf½=1.175 and 1.167 respectively) are less defined. Angles between unweighted SPO long axes and AMS direction ($\psi_{\kappa1\kappa2}$=27.1°; $\psi_{\kappa1\kappa3}$=1.16°; $\psi_{\kappa2\kappa3}$=34.29°) are similar to the weighted long axes to AMS angles. This indicates that particle SPO and grain size are independent variables.

Martites: The SPO of the single martite grains does not correspond to the principal AMS directions, only section $\kappa_1\kappa_2$ bears a SPO distribution with long axes comparable to the κ_1 direction ($\phi_{\kappa1\kappa2}$=151.01°; $\phi_{\kappa1\kappa3}$=78.94°; $\phi_{\kappa2\kappa3}$=40.06°) (Figure 2.18.b). The mean axes-ratios of martite particles in the principal surfaces are small ($R_{\kappa1\kappa2}$=1.096, $R_{\kappa1\kappa3}$=1.117, $R_{\kappa2\kappa3}$=1.246). Like in the chlorites, the directions of the unweighted mean long axes of martites are in all sections very similar to the weighted mean directions ($\psi_{\kappa1\kappa2}$=158.71°; $\psi_{\kappa1\kappa3}$=72.46°; $\psi_{\kappa2\kappa3}$=41.38°), indicating again no link between martite SPO and grain size.

The martite cluster SPO (including single disseminated martites) shows a remarkable good correlation with the AMS directions ($\phi_{\kappa1\kappa2}$=0.2°; $\phi_{\kappa1\kappa3}$=6.79°; $\phi_{\kappa2\kappa3}$=21.11°) and the shape ratios are strongly defined ($R_{\kappa1\kappa2}$=1.463, $R_{\kappa1\kappa3}$=1.413, $R_{\kappa2\kappa3}$=1.270) (Figure 2.18.c). The non-weighted distribution of axes-directions remains similar to the single martites case ($\psi_{\kappa1\kappa2}$=168.63°; $\psi_{\kappa1\kappa3}$=114.28°; $\psi_{\kappa2\kappa3}$=36.89°). Different SPO of martite cluster and single martites are evident. The effect of the large clusters on defining the mean tensor is stronger, because of the area-dependent weight-factor. In the sections $\kappa_1\kappa_2$ and $\kappa_1\kappa_3$ clusters have a high shape-anisotropy, whereas section $\kappa_2\kappa_3$ bears irregular shapes without preferred orientation. The relatively small tensor axes ratio in $\kappa_2\kappa_3$ expresses this fact.

Comparing the mean tensor of single martites and clusters in section $\kappa_1\kappa_3$ a long axis angles difference of 72.15° is evident. This strong deviation originates in one extreme large cluster, which incorporates 174 single grains, separated mostly by brecciation fissures. A detailed SPO study of this cluster with its constituents is carried out (large cluster in Figure 2.18.b,c) and shows that the cluster's SPO long axis orientation is very close to the AMS directions ($\phi_{\text{cluster}} = 5.92°$ vs. $\phi_{\text{single martite}} = 80.12°$; angle difference 74.2°). The absolute area of the tensor ellipse ($3.462\text{ mm} \cdot 2.179\text{ mm} / 2 \cdot \pi = 11.849\text{ mm}^2$) is much larger than the mean tensor area of its constituents ($0.1926\text{ mm} \cdot 0.1728\text{ mm} / 2 \cdot \pi = 0.0523\text{ mm}^2$). The dominant influence of the cluster on the mean tensor of the entire section is evident. Subtracting the large cluster shape from the cluster SPO, the resulting mean SPO is similar to the single martite shape SPO and has no relation to the AMS direction.

2.4.1.2 SPO ellipsoids

The orientations of section $\kappa_1\kappa_2$, $\kappa_1\kappa_3$ and $\kappa_2\kappa_3$ and the corresponding SPO data of sample RA3-1_v are analysed using *ELLIPSOID* (© Launeau & Robin 2003). Both solutions of best-fit ellipsoids (with scale and without scale) lead to contradicting results. Therefore, this problem has to be discussed first, before interpreting the results.

The best-fit ellipsoids without scale factor are well constrained as indicated by the low "incompatibility indices" $\sqrt{\tilde{F}}$ (chlorites: 7.1 %, single martites: 4.6 %, martite clusters: 8.5 %). The chlorite SPO-ellipsoid with scale factor bears a higher misfit ($\sqrt{\tilde{F}} = 18.3$ %), but corresponds in orientation very well to the SPO-ellipsoid without scale factor. The SPO-ellipsoids with scale factor of single martites and martite clusters are very uncertain ($\sqrt{\tilde{F}} = 23.3$ % and 45.7 % respectively) and differ from the SPO-ellipsoid without scale factors. This is clearly a result of the scale heterogeneity between the mean tensors of the sections, which is very low in the case of the chlorites; high in the case of the single martite; and highest in the case of the martite clusters. The reason for the high heterogeneity of tensor scales in the case of martite clusters is the extreme "particle" size variations in the $\kappa_1\kappa_3$-section (bearing one extreme large cluster). Although this large cluster has to be included in the calculation of the section's mean tensor, since it obviously influences the bulk AMS, its effect on 3D should be neglected, because it is not represented in the two other sections. In the case of single martite SPO-ellipsoids, the high difference of particle number ($\kappa_1\kappa_2$: n = 102, $\kappa_1\kappa_3$: n = 223, $\kappa_2\kappa_3$: n = 101) might be a reason for the heterogeneity (c.f. Launeau & Robin 2005). These heterogeneities within and between the sections do limit the value of ellipsoids with scale for interpretation. These results do not necessarily represent the true 3D-SPO.

This leads to a preferred usage of the ellipsoids without scale for interpretation. The scale of the martites is considered in each of the three sectional SPO. The huge size heterogeneity of the clusters raises the possibility that a major cluster may have been missed in the thin section. Another general limitation of determining 3D-SPO by multiple 2D-images is that the actual 3D-shapes of the particles are never observable. Due to these facts, the following description of results just refers to the ellipsoids without scale.

The SPO of chlorite stacks define a cryptic strain fabric, which can be quantified by image analysis. The strain ellipsoid defined by chlorite shapes is prolate with a long axis to short axis quotient L/F = 1.206 (P' = 1.407, T = -0.088). The foliation pole (short axis C) has an orientation of 200.2/8.2, the lineation (long axis A) 107.9/15.4 and the intermediate axis B 317.2/72.4 (Figure 2.19).

The ellipsoid produced by the single martite SPO has similar short axis orientations to the chlorite ellipsoid (C = 211.8/7.0), but its long and intermediate axes are reversed (A = 90.9/76.6 and B = 303.2/11.4). The prolate shape is strongly defined (L/F = 2.714; P' = 1.283; T = -0.442). The ellipsoid long axis is steeply plunging. In their axes orientation and aspect-ratio the martite-cluster ellipsoid resembles the chlorite

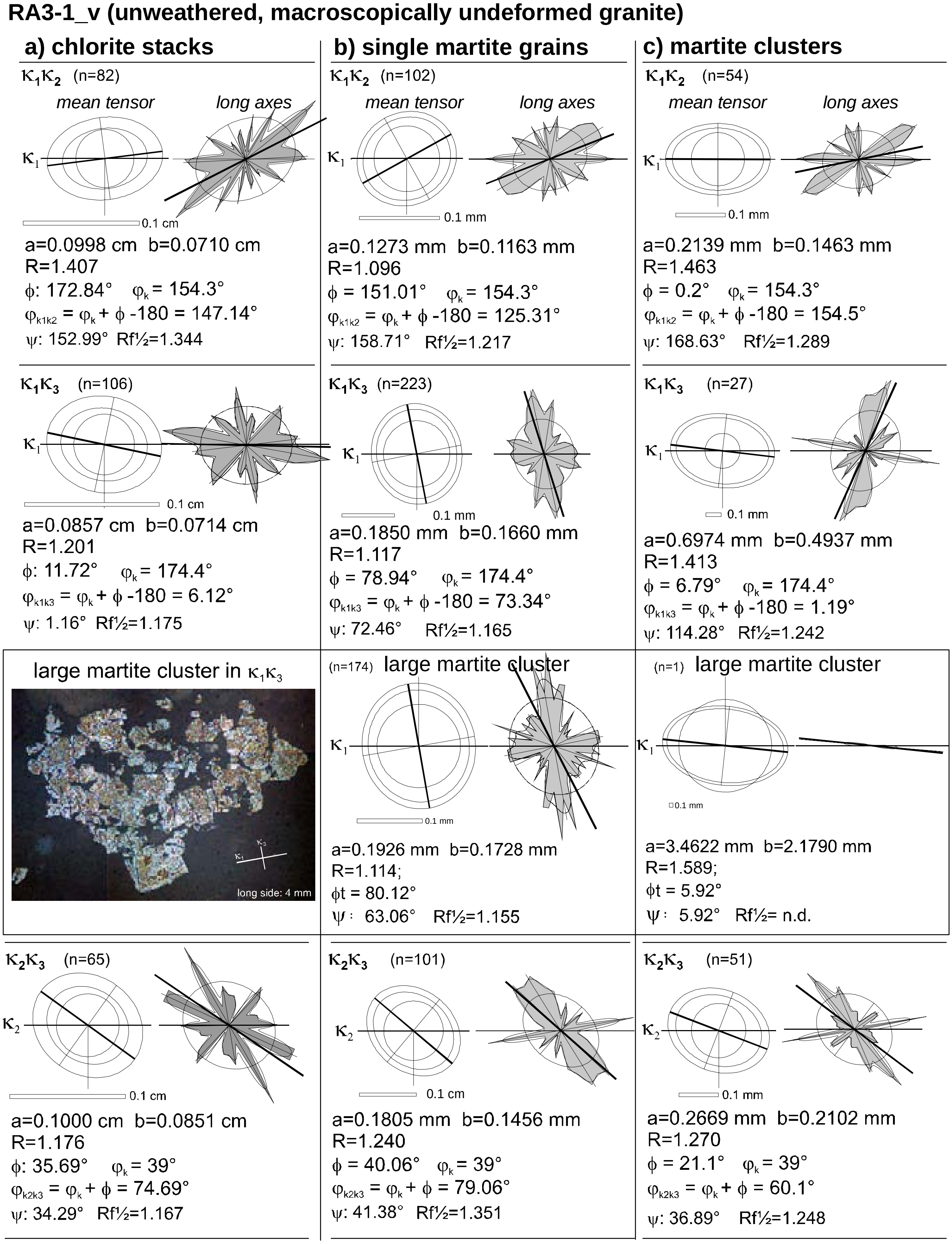

Figure 2.18: Sectional SPO results of the image analysis in RA3-1 (unweathered, macroscopically undeformed granite); a) chlorite stacks; b) single martite grains; c) martite clusters. The microphotograph of the cluster is shown.

ellipsoid. The prolate shape (L/F = 1.244; P’ = 1.612; T = -0.090) is moderately defined and very similar to the chlorite fabric. Long axis A is horizontally oriented (113.7/0.7) and short axis C is shallowly inclined with 204.0/26.2. In all three determined ellipsoids the SPO foliation poles are similarly oriented (subhorizontal to SSW). Single martite SPO shows a conversion of long and intermediate axes compared to the chlorite and martite cluster fabric ellipsoids.

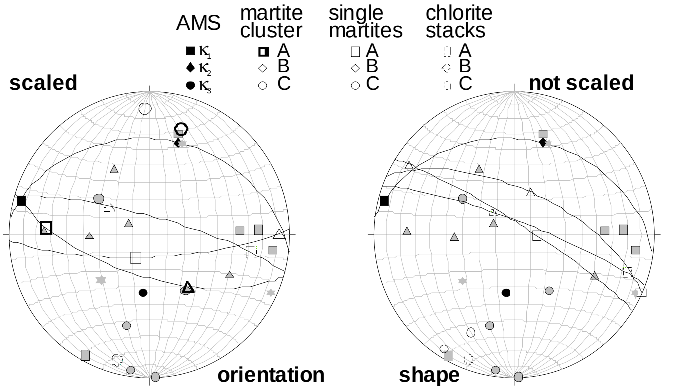

AMS	κ_1	284.0/05.0	L/F = 0.969
	κ_2	17.8/33.1	P’ = 1.067
	κ_3	186.9/56.4	T = 0.506

phase	with scale		without scale	
	orientation	shape	orientation	shape
chlorite stacks	A 99.8/26.8	L/F = 1.398	A 107.9/15.4	L/F = 1.208
	B 304.6/60.9	P’ = 1.250	B 317.2/72.4	P’ = 1.407
	C 195.1/10.5	T = -0.156	C 200.2/8.2	T = -0.088
	$\sqrt{\tilde{F}}$ = 18.3%		$\sqrt{\tilde{F}}$ = 7.1%	
single martites	A 211.6/75.0	L/F = 1.794	A 90.9/76.6	L/F = 2.714
	B 89.6/8.0	P’ = 1.386	B 303.2/11.4	P’ = 1.283
	C 357.8/12.5	T = -0.263	C 211.8/7.0	T = -0.442
	$\sqrt{\tilde{F}}$ = 23.3%		$\sqrt{\tilde{F}}$ = 4.6%	
martite cluster	A 273.9/26.7	L/F = 0.307	A 113.7/0.7	L/F = 1.244
	B 142.6/52.7	P’ = 1.831	B 22.3/63.8	P’ = 1.612
	C 16.9/24.0	T = 0.477	C 204.0/26.2	T = -0.090
	$\sqrt{\tilde{F}}$ = 45.7%		$\sqrt{\tilde{F}}$ = 8.5%	

Figure 2.19: Compilation of the measured AMS axes of sample cylinder RA3-1_v and the calculated best-fit-ellipsoids (with scale and without scale *sensu* Launeau & Robin 2005) of chlorite stacks SPO, of single martite grains SPO and martite cluster SPO. Squared F is the “incompatibility index” (Robin 2002; Launeau & Robin 2005). Stereonets are projections of the lower hemisphere.

2.4.2 *Sectional SPO of a laterite*

An image analysis is carried out to investigate the relation between petrographic fabric and martite and magnetite SPO in the laterite (RA2-1.b). In this laterite, the petrographic fabric is very well defined by the phyllosilicates and correlates well with the AMS. In the laterite sequence a first moderately steep inclined sub-fabric (S_1) is overprinted by a subhorizontal (unconformity parallel) compaction fabric. In this sample (0.2 metres below the unconformity), the compaction fabric is dominating the texture and causes a horizontal AMS fabric with N-trending k_1. Chlorite is almost not detectable and the phyllosilicate are not important magnetic carrier. Section $\kappa_1\kappa_3$ is not prepared and no SPO data is produced.

Martite grains are moderately small, representing a size distribution between granite and cataclasite. The amount of clusters is relatively high. Both small and large grains form clusters. Besides the cataclastic cluster type, which is the normal type in granite and cataclasite, a second type of cluster is abundant: the dissolution cluster. This type is a weathering feature and characterized by an accumulation of rather small irregular shaped martite grains.

The SPO of the single martite grains does not correspond to the principal AMS directions ($\phi_{\kappa1\kappa2}$=37.36°; $\phi_{\kappa2\kappa3}$=149.63°) (Figure 2.20.a). The mean axes-ratios of martite particles in the principal surfaces are very small ($R_{\kappa1\kappa2}$=1.098, $R_{\kappa2\kappa3}$=1.060). The non-weighted distribution of axes-directions does not show significant preferred directions (weak correspondence with AMS directions; $\psi_{\kappa1\kappa2}$=18.63°; $\psi_{\kappa2\kappa3}$=176.44°).

SPO of the martite clusters (+ single martites) correlates very well with the AMS directions ($\phi_{\kappa1\kappa2}$=178.11°; $\phi_{\kappa2\kappa3}$=167.60°) and the shape ratios are better defined only in $\kappa_2\kappa_3$ ($R_{\kappa1\kappa2}$=1.083, $R_{\kappa2\kappa3}$=1.126) (Figure 2.20.a). Although the AMS can be traced with the weighted SPO axes, the non-weighted distribution of axes-directions scatters intensely ($Rf½_{\kappa1\kappa2}$=1.037, ($Rf½_{\kappa2\kappa3}$=1.065) showing only a weak statistical preferred direction, but corresponding to the AMS-directions ($\psi_{\kappa1\kappa2}$=175.98°; $\psi_{\kappa2\kappa3}$=172.59°).

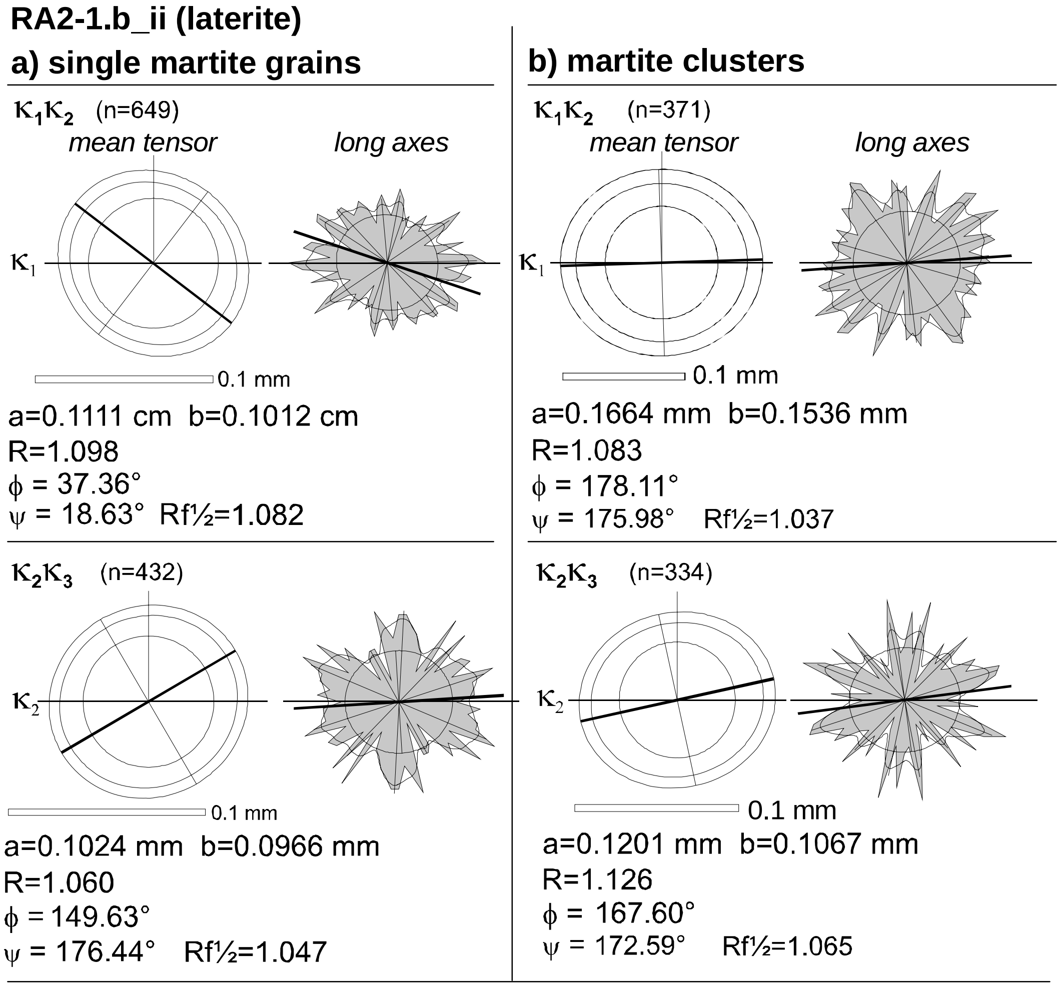

Figure 2.20. Sectional SPO results of the image analysis of a laterite (sample RA2-1.b). a) single martite grains, b) martite clusters.

The 3D-SPO fabric has presumable an oblate shape (no $\kappa_1\kappa_3$ information!), with L/F = 0.96. This resembles more or less the corresponding (weak) oblate AMS fabric (L/F = 0.998). Like in the cataclasite, here the SPO-L/F ratio is stronger developed than the corresponding AMS-L/F ratio.

The image analysis of the laterite shows that martite cluster SPO are clearly related to the AMS.

2.4.3 Sectional SPO of a cataclasite

SPO of the martite single shapes and clusters were determined. Chlorite could not be detected for image analysis, presumable due to the intense cataclastic grain size reduction.

The SPO of the single martite grains does not clearly correspond to the principal AMS directions ($\phi_{\kappa1\kappa2}$=29.5°; $\phi_{\kappa2\kappa3}$=163.09°). The mean aspect ratios of martite particles in the principal surfaces are very small ($R_{\kappa1\kappa2}$=1.056, $R_{\kappa2\kappa3}$=1.102) (Figure 2.21.a). The preferred orientation of long axes fit well to the AMS directions in the $\kappa_1\kappa_2$ section ($\psi_{\kappa1\kappa2}$=10.37°), less well in the $\kappa_2\kappa_3$ section ($\psi_{\kappa2\kappa3}$=147.90°).

The martite cluster SPO shows a very good correlation with the AMS directions ($\phi_{\kappa1\kappa2}$=2.48°; $\phi_{\kappa2\kappa3}$=1.49°) and the shape ratios are better defined ($R_{\kappa1\kappa2}$=1.149, $R_{\kappa2\kappa3}$=1.086) (Figure 2.21.b). The unweighted directions of mean axes fit well to the AMS directions ($\psi_{\kappa1\kappa2}$=8.64°; $\psi_{\kappa2\kappa3}$=156.11°).

It is shown that the SPO of martite cluster and single martites are different. The effect of the SPO of large clusters on defining the mean tensor is evident, although the actual content of clusters is low. Clusters are very homogeneous oriented in the cataclasite, paralleling AMS directions. Although section $\kappa_1\kappa_3$ is missing,

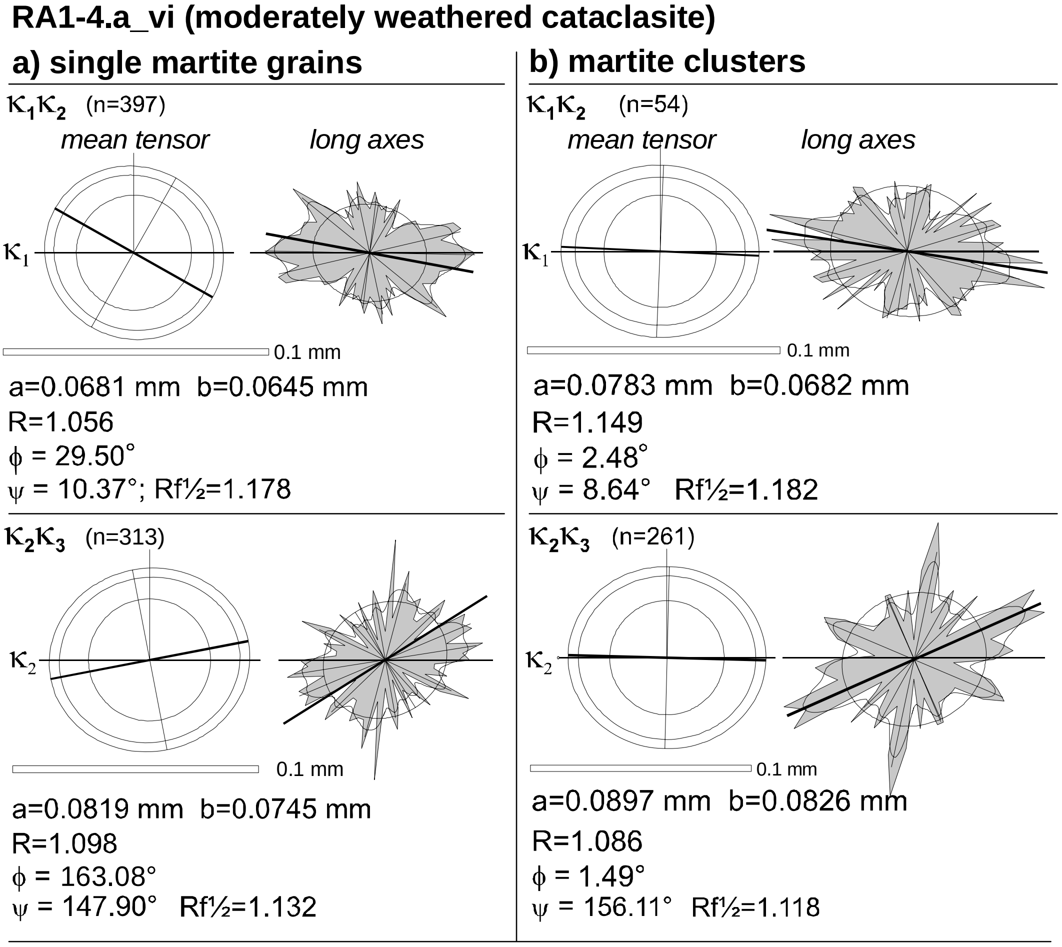

Figure 2.21. Sectional SPO results of the image analysis of a cataclasite (sample RA1-4.a). a) single martite grains, b) martite clusters.

the ratio L/F = $\kappa_1\kappa_2$ / $\kappa_2\kappa_3$ can be calculated: L/F = 1.054, indicating a weak prolate 3D-SPO defined by martite cluster. The AMS fabric is also prolate (L/F = 1.008; P’ = 1.029 and T = -0.301), but the L/F ratio is even lower than the corresponding SPO-L/F ratio.

2.5 Discussion of alteration, weathering and deformation in the weathering profile

The division of the Roded weathering profile into three zones of increasing weathering intensity, saprock, saprolite and laterite, made by field observations, is confirmed by petrography, mineralogical and geochemical trends, as it will be shown in the following chapters.

2.5.1 Sub-surface physical weathering

The most prominent weathering process in the Roded profile below the laterite is weathering-brecciation (see chapter 2.2.2). This form of brecciation is a dense micro-cracking with preservation of primary granitic textures. Weathering-brecciation, as a physical sub-surface weathering feature, might have been a result of different processes. Erosion by infiltration of meteoric water is one likely process, which may have been intensified by the (seasonal) change of infiltration. Pre-existing joints facilitated the fluid flow. An additional process is argilliturbation, a repeated shrink-and-swell movement of clays, which is associated with (seasonal) changes of water infiltration. Argilliturbation is indicated by illite located along micro-cracks, which is, however, not a common characteristic. This illite may have been smectite-rich, which is susceptible for shrink-and-swell movement.

Alternatively, cryoturbation is a possible process for brecciation. The shrink-and-swell movement associated with volume change of water as a result of the seasonal depth-variations of the permafrost zone cannot be confirmed. Bioturbation processes can be excluded due to the high age of the weathering. For climatic implications, refer to chapter 2.7.2.

A further investigation of the fabric preservation in the zone of weathering-brecciation by means of AMS follows below.

The preservation of primary rock fabric features (S_1) in the laterite is documented (Plate 2.1.f) and evidences the autochthonous nature of the laterite. The lack of rounded particles indicating that particles have not been transported, and the gradual transition of mineralogy and morphology from saprolite to laterite are further indications. The primary rock fabric resisted the textural destruction and collapse related to intense chemical weathering, typically occurring in laterites (Retallack 1991). The in-situ nature of the weathering zones saprock, saprolite and laterite is the base for all interpretations concerning mineralogical and geochemical weathering trend in the profile.

2.5.2 Mineralogical processes and their relation to alteration phases

A sequence of distinct mineral alterations associated with each weathering zones is developed.

In the unweathered granite (parent rock), serizitisation of plagioclase and chloritization are the main alteration processes. Chlorite, dominating over biotite and muscovite in chlorite-mica stacks, points to a replacement process of biotite (and muscovite?) by chlorite. This is supported by the ubiquitous presence of titaniferous minerals at the rim of the stacks (Plate 2.2.d), which are considered as residual minerals of the replaced biotite (Eggleton & Banfield 1985). Chloritization is commonly observed as a feature of *propylitic* alteration under hydrothermal conditions (Wimmenauer 1985). Accompanying or following the propylitic chloritization, chlorite (chamosite) altered to haematite. Chamosite is an “oxidized” chlorite, bearing more than 4 wt% of Fe^{III} (of Fe^{total}) (Deer et al. 1966). Secondary haematite ($Fe^{III}_2O_3$) in chlorite indicates this “oxidized” state (petrographic observation; Plate 2.2.e,f).

The XRD patterns indicate a generation of illite (sericite) in unweathered granites (see chapter 2.2.10). The sericitization of feldspars is a hydrolysis reaction, similar to reactions during weathering (Meunier & Velde 2004) (equations 1a,b in chapter 1.2). Pure illite is only observed in the unweathered granite and in the lowermost saprock sample, indicated by relative symmetric 10 and 5 Å peaks, which remain stable after ethylene glycol-solvation. Sericitization of feldspars is a process of the hydrothermal stage (Wimmenauer 1985). A first hydrothermal alteration commonly takes place subsequent to granite emplacement during the cooling stage.

Within the saprock zone, I/S mixed-layer mineral or coexistent illite and smectite become progressively important with proximity to the unconformity. Considering illite (sericite) as present in the rocks due to earlier hydrothermal alteration, the conversion of illite to I/S was an important chemical weathering process in all weathering zones (Meunier & Velde 2004). Pure illite is discussed as a weathering product (Meunier & Velde 2004). A coexistence of illite and I/S mixed-layer phases is suggested, which implies a) an incomplete illite-to-I/S conversion during weathering and/or b) a prograde *illitization* of I/S mixed-layer mineral during Palaeozoic burial stage.

The saprolite and laterite is characterized by the conversion of primary chlorite/mica-stacks to Fe/Mg-mica and by major kaolinite precipitation. Kaolinite is a progressive product of feldspar, mica, illite and I/S hydrolysis (see chapter 1.2). In the XRD-spectra (clay fraction) of the laterite illite and I/S is less important than kaolinite. Plagioclase and K-feldspar are subject of replacement by kaolinite in the saprolite and laterite. All hydrolysis processes are maximized in the laterite. The minerals produced by chlorite breakdown during weathering are much smaller than hydrothermal alteration products. Kaolinite and microcrystalline haematite, as a replacement of chlorite, is observed in some chlorite-mica stacks in the unweathered granite (Plate 2.2.f). However, this alteration is more typical for the weathered rocks. It can be inferred that the intensified decomposition of chlorite in the profile to its complete absence from the upper parts of the medium weathered granite/cataclasite upwards (see XRD spectra, Figure 2.7 and Figure 2.8) was driven by the palaeoweathering as a continuation of hydrothermal alteration.

The following sequence of weathering products in the Roded weathering profile is inferred (Figure 2.22): (1) illite, (2) I/S mixed-layered mineral, (3) kaolinite and perhaps (4) gibbsite. Gibbsite, a final products of hydrolysis during weathering (chapter 1.2), is not observed in the profile. According to (Rebertus et al. 1986), the kaolinization of Fe/Mg-bearing mica in the saprolite and laterite may be responsible for a strong so-called anti-gibbsite effect. The soils in which Fe/Mg-mica alter to kaolinite are characterized by a low content of gibbsite. It may be that gibbsite was formed in an upper laterite zone, which was eroded. This sequence may be a function of water infiltration, which continuously decreases with profile depth. The minor occurrence of I/S mixed-layered minerals and kaolinite in the unweathered granite is negligible and is interpreted as a result of recent weathering or circulation of formation waters.

An important alteration factor is the pH of the soil agents (Hamer et al. 2003). Chlorite may break down to swelling mixed-layer intermediate mineral or to vermiculite in neutral or slightly acidic soils. However, chlorite weathering in soils with very low pH results in a hydrolysis directly to kaolinite, Al- or Fe-oxides.

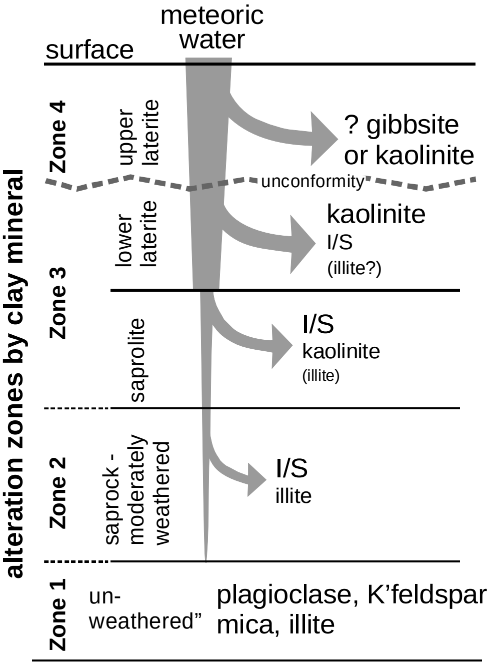

Figure 2.22: Alteration zones by the dominant occurrence of clay minerals. Infiltration of meteoric water decreased with depth of the weathering profile and caused a downward sequence of hydrolysis reactions. The upper gibbsite zone is not observed. If it developed, it has been eroded subsequently.

2.5.3 Geochemical processes and their relation to alteration phases

2.5.3.1 Mobile elements and weathering indices

The whole-rock geochemical trends resemble mostly the observed mineralogical alteration trends and thus allow a quantification of alteration.

Sodium is bound almost completely to plagioclase in the rocks. A mobilization of Na is due to the incongruent dissolution of plagioclase (albite and oligoclase cores).

Calcium is associated with plagioclase, mostly oligoclase cores of zoned plagioclase and to calcite. Calcite is a constituent of the kaolinite-dominated matrix in saprolite and laterite. Calcite-enriched fluids infiltrated the granite producing veins in most of the structural domains, except in the laterite. Primary Ca concentrations seem to vary throughout the profile, therefore an interpretation is not straightforward. The stability of Ca may be an effect of two subsequent processes, mobilization due to plagioclase hydrolysis and reprecipitation as calcite, mostly in the intense weathered zones. Calcium mobilized by plagioclase hydrolysis may have been the source of carbonate in weathered matrix. The calcite veins may be associated with the matrix-calcite above, as a result of downward leaching during weathering or later processes. The veins are slightly deformed and show calcite recrystallization. Therefore, a pre- or syn-cataclasis precipitation of these calcite veins is inferred giving a minimum relative age. Its exact timing relative to weathering and burial compaction remains unsolved.

The balance of SiO_2 vs. most other major elements is a result of profound mineralogical changes at the boundary between saprolite and laterite. These changes are the mobilization of primary quartz grains and K-feldspar hydrolysis (see equation in chapter 1.2). SiO_2 was removed as dissolved silicic acid $H_4SiO_{4(aq)}$. The remaining SiO_2 is bound to phyllosilicates (Fe/Mg-mica and clays) and to the secondary quartz rods in the laterite (Figure 2.5).

According to the Plagioclase alteration index *PIA* (Fedo et al. 1995), chemical weathering is significant only in the saprolite (ca. 81 %) and laterite (up to 94 %) (Figure 2.9.m). Below the saprolite, in the saprock, chemical weathering, mainly associated with plagioclase decomposition, is only weakly described by *PIA*. *PIA* takes the enrichment of K into account (see following chapter), with K being part of numerator and denominator (equation 12 in chapter 1.2.1). Thus, *PIA* represents a more accurate weathering index than the chemical alteration index *CIA* (Nesbitt & Young 1982). The *Al-CaNa-K* ternary plots visualize quite well the plagioclase decomposition in the saprock weathering trend, (Figure 2.12.a).

2.5.3.2 Indications for K-metasomatism

The trend of K is complicated. K_2O shows, unlike Na_2O, an increase from the unweathered granite up to the lower saprolite. Then, K_2O reduces from a maximum value of 9 wt% to a value of 6 wt% in the uppermost laterite part (Figure 2.9.e). This concentration is still higher than the concentration in the unweathered granite, thus a net-enrichment is inferred. Potassium is bound to K-feldspars and to white micas (muscovite, Fe/Mg-mica, sericite, illite). K-feldspar is not as intensely hydrolysed as plagioclase below the saprolite; consequently, K is not decreased. Smectite formation during illite-to-smectite transformation, beginning in the saprock, caused a mobilization of K (Meunier & Velde 2004). This had, however, no effect on the whole-rock geochemistry, as not associated decrease is observed. The decreasing trend in saprolite and laterite is attributed to kaolinization of K-feldspar. The relative enrichment of illite and Fe/Mg-micas in the laterite seems to have not much influence on the K concentration.

The general K_2O-enrichment below the upper saprolite is partly a result of relative concentration enrichment by loss of Na_2O, which, however, should not be as high. Therefore, a secondary input of K into the system by fluid flow is suggested. The increase of K_2O in the moderately weathered zone and a maximum value in the saprolite points to that. The K_2O-depletion within the laterite, representing the relic weathering trend of K-feldspar depletion, points to an absence of the secondary K-enriching alteration.

Such an enrichment of K is reported from several “ancient” basement-cover-interface (of at least Palaeozoic age) (Dott Jr. 2003, Medaris et al. 2003, Sutton & Maynard 1996, Ziegler & Longstaffe 2000) and has been interpreted as a feature of metasomatism during burial evolution (Fedo et al. 1995). The potassium signature is the most significant difference between recent and ancient soils (Dott Jr. 2003, Bobrov & Shchipakina 1990, Fedo et al. 1995).

2.5.3.3 Immobile elements and mass balancing

Regarding major element oxides, Fe_2O_3, TiO_2 and P_2O_5 are enriched in the laterite and do not change their relative concentration to each other, which is indicated by the very high correlation coefficients (Figure 2.11; P_2O_5 is not displayed here, see Figure 2.9.i for comparison). Since a simultaneous mobilization of all three elements by the same degree seems to be unlikely, the high correlations are interpreted as an evidence of immobility of these elements and associated (predominantly primary) minerals. These insoluble minerals are oxidized iron oxides (martite, microcrystalline haematite), iron hydroxides (goethite), titanium-oxides (primary rutile, secondary anatase) and apatite. The enrichment of these minerals is not an absolute enrichment due to secondary precipitation from external fluids, but the result of the loss of soluble mineral (mostly feldspar, quartz).

Although Al_2O_3 displays the same trend through the entire profile as Fe_2O_3, TiO_2 and P_2O_5 (Figure 2.11), Al_2O_3 enriches less than the other three element oxides in the laterite. This is displayed by an increase of the $Fe_2O_{3_{norm}}/Al_2O_{3_{norm}}$-ratio from 1 up to 2.3. A minor Al_2O_3 decrease in comparison to Fe_2O_3+MgO is also shown by the lateritic trend in the *Al-CaNa-FeMg* ternary system (Figure 2.12.b). Therefore, aluminium seems to be slightly mobilized in the laterite, although by many authors considered as an immobile element with respect to weathering (e.g. Fedo et al. 1995, Mathe et al. 1999, Nesbitt & Young 1982). Below the laterite, Al may be immobile. Titanium, on the other hand, appears to be a immobile element within the laterite, indicated by the stable ratio to Fe and P. Additionally, hafnium is considered as a very robust immobile element due to its high field strength as a tetravalent cation and its association with zircon, which is very resistant during weathering (Brown et al. 2003). Therefore, Hf (Figure 2.9.k) is additionally considered here as an immobile element.

Al_2O_3-related mass balance, $\varepsilon_{\mathrm{Al}}$, shows an iso-volumetric weathering below the laterite (Figure 2.9.r). The usability of TiO_2 below the laterite horizon is questionable because the $\varepsilon_{\mathrm{Ti}}$ suggests far too high dilatation values in some samples ($\varepsilon_{\mathrm{Ti}}$ is almost 2). Hf-based mass balancing, $\varepsilon_{\mathrm{Hf}}$, shows iso-volumetric weathering, except for weathering-brecciated and cataclastic samples RA1-3.b and RA1-4.b. Volume increase, shown by $\varepsilon_{\mathrm{Hf}}$ and $\varepsilon_{\mathrm{Ti}}$, is due to a decrease of bulk rock density ρ or Ti- or Hf-concentration (see equation 4b in chapter 2.2.11). It is possible that weathering brecciation resulted in bulk rock density decrease (by enhanced jointing) and cataclasis to minor mobilization of Al. The latter is evidenced for RA1-7 and RA1-4.b, showing lower Al_2O_3 concentration than neighbouring samples (Figure 2.9.b). The geochemical compaction estimated in the laterite with TiO_2 is 0.44 (at 1 m) and 0.32 (at 0.2 m). Hf-based mass balance is 0.68 (at 1 m) and 0.63 (at 0.2 m).

The iso-volumetric weathering in the saprock and saprolite is indicated petrographically by the preserved textures observed in the unweathered granite. Hence, the Al- and Hf-based mass balancing show reliable iso-volumetric results beneath the laterite. Titanium appears to have a too low concentration in saprock and saprolite to get reliable calculations. Therefore, Ti-based mass balancing cannot be used through the entire profile. In the laterite, where it shows no mobilization, Ti may be used as for calculations. Also Hf, although immobile, may not be consistently distributed through the profile. This is inferred by the highly varying Zr content (not shown, data see Appendix I.a), which indicates primary zircon variation in the profile. Hence, Hf-based mass balancing is questioned, as well. Conclusively, it has to be stated that no element exists in the profile providing a reliable constancy and immobility. Nevertheless, for the purpose of tracing qualitative trends, the results of Al-based mass balancing is used for saprock and saprolite samples, and Ti+Hf-based (arithmetic mean of Hf and Ti, see Table 2.2) mass balancing for the laterite samples. Primary concentration variations of Ti and Hf may under- or over estimate volume strain in the laterite.

2.5.4 Magnetomineralogy

The content of titanium in martite (primarily magnetite, as shown in chapter 2.2.12) in the Roded Granite is very low, but it was originally higher, considering the abundance of titaniferous phases (leucoxene) adjacent to martite grains. An almost complete exsolution process of titanomagnetite [$Fe_{(3-x)}Ti_xO_4$] to ilmenite and magnetite (Ramdohr 1975) can be inferred. Exsolution follows this equation:

$$(1) \qquad 6\,Fe_2TiO_4 + O_2 = 6\,FeTiO_3$$

This reaction commonly takes place during the earliest stage of granite cooling after emplacement (Ramdohr 1975).

The entire primary population of (titaniferous) iron oxides is martitized. Martitization is a result of a pervasive hydrothermal alteration (Just et al. 2004, Ramdohr 1975). The Fe^{II} to Fe^{III} transition during oxidation of magnetite into haematite (*first* stage of martitization – *hydrothermal martitization*) occurred under oxidising (high Eh) environments (Figure 1.4).

Petrographic observations imply a hydrothermal chlorite-to-haematite alteration (Plate 2.2.e). Nevertheless, it is possible that magnetite was the direct alteration product of the chlorite alteration. Magnetite precipitation during biotite-to-chlorite alteration is described by Eggleton & Banfield (1985). In this case, martitization took place subsequently in an oxidising milieu.

The titaniferous iron oxides were increasingly affected in two ways by palaeoweathering with proximity to the unconformity: a) the number of grains decreases until the saprolite-laterite boundary, followed by an increase in the laterite due to the compaction and b) increased martitization. The periodic infiltration of oxidising meteoric waters likely caused a martitization of magnetite (*second* stage of martitization - *weathering martitization*). In the laterite, some martite grains are still euhedral-subhedral and others have serrate boundaries as an effect of dissolution. Magnetite remnants subsisted specifically along edges of martites that display serrate boundaries. Magnetite dissolves much easier than haematite. Thermodynamic calculations (Florindo et al. 2003) indicate that magnetite is unstable under conditions of elevated dissolved silica concentrations, which leads to acidic conditions. Conditions for hydrating Fe^{III} had to be extremely acidic, thus dissolving haematite may have been less important. Although minor depletion hardly dissolvable Al is evident, extreme acidic conditions can be ruled out, because other relic minerals such as rutile, anatase and apatite do not show any significant dissolution patterns.

These observations point to a preferred dissolution of magnetite, before the residual part oxidized to martite. Euhedral-subhedral shaped grains are remnants of the (hydrothermal) first stage martitization, before the weathering agent dissolved them. The mobilization of Fe^{II} due to dissolution of magnetite has to be in accord with the observed stability of total iron oxide concentration, related to immobile Ti, throughout the profile. This can be explained by the frequently observed haematite veins neighbouring martites, the area of dissolution (Plate 2.4.f). This occurrence evidences the local reprecipitation of iron. In the laterite, iron locally reprecipitated as microcrystalline haematite in the vicinity of martites (the area of dissolution; Plate 2.5.a). This process may be directly associated with martitization of the remaining magnetite (Lagoeiro 1998). In the cataclasite, both reprecipitation processes are developed (Plate 2.5.b).

The occurrence of goethite, pseudomorphously replacing magnetite, is an indication of hydration process, possibly as an intermediate stage before dissolution took place. It is possible that haematite formed, as pseudomorphs replacing goethite, by dehydration during diagenesis (van Houten 1973). Iron mobilization during weathering of chlorite can form nanometre-scaled haematite, goethite and magnetite crystals, which are coated on clay minerals such as smectite or kaolinite (Ji et al. 2002). These Fe-oxyhydroxides possibly were the precursors of microcrystalline iron oxides in the laterite matrix.

A sequence of alteration is suggested, beginning with magnetite or martite alteration to goethite(?)-pseudomorphs, followed by precipitation of microcrystalline haematite (replacing or nucleating at magnetite and goethite).

Haematite precipitation as inclusions in iron rich minerals is a function of temperature (Shotyk *pers. comm.*); thus, it most likely occurred under hydrothermal conditions. However, special weathering conditions (Ca- or Mg- bearing fluids in a pH 4-5 environment) are also favourable (Tröger 1969). The extensive hydrolysis in the matrix and Al-dissolution indicates that those conditions might have been realized in the saprolite and laterite.

A common increasing ratio of *martite / (magnetite + ilmenite)* with age of rocks has been described for sedimentary red beds (van Houten 1973). The buried laterite may have encountered similar conditions, leading to a significant martitization process taken place during diagenesis in Phanerozoic time. This would have been the *third* stage of martitization (*burial martitization*). The towards the unconformity increasing gradient of martitization-“infection”, interpreted as a characteristic of the weathering martitization, is not eliminated by burial martitization.

2.5.5 Saprolitic pallid zone and transition to lateritic ferricrete

Pallid zones in soil profiles are commonly Fe-leached (Tardy 1992) leading to the characteristic decolourization. The present pallid zone of the Roded Granite is not Fe-leached, as indicated by whole-rock geochemistry. Iron is bound to abundant haematite veins cutting the weathered granitic texture. Haematite richness is also evidenced by a red colour of the rock powder. As discussed in the previous chapter, Fe^{II} was mobilized by magnetite dissolution and reprecipitated as goethite and/or haematite without significant transport in the weathered rocks. This process was apparently maximized in the pallid zone, inferred by lowest martite content and lowest magnetic susceptibilities of the profile (Figure 2.17.a). Pallid zones are characteristically located beneath indurated clay rich sub-soils, occasionally with a mottle zone in-between (Tardy 1992). The mottle zone represents the downwards advancing laterite formation.

The formation of pallid zones beneath the clay horizon is generally interpreted as the result of lateral flow of a confined groundwater, often accompanied by extensive leaching of Fe. Reduced chemical conditions are usually attributed to the formation of pallid zones (Tardy 1992), however, this is not indicated in the present pallid zone. The immediate reprecipitation of dissolved iron as goethite and/or haematite requires oxidizing conditions.

The pallid zone shows the maximum enrichment of K (see chapter 2.5.3.1) and maximum burial martitization (see previous chapter). Both events may have been related to each other, or were different processes with the same lateral fluid-flow-pattern. Presumably, in both post-weathering fluid-flow events, flow direction was unconformity-parallel, comparable to confined groundwater flow during formation of the pallid zone. Whereas fluid-rock-interaction was maximized in the saprolite, as the lateritic ferricrete behaved more or less as an aquitard. The overall geochemical trends through the weathering profile are functions of weathering and thus suggest a lateral flow of the fluids. A vertical flow would have caused a mixing of elements and consequently, an obliteration of most geochemical trends.

2.5.6 Laterite morphology as a result of weathering and compaction

The morphology of the lateritic ferricrete is a result of two major geological episodes: weathering and compaction during burial stage. Thus, most (physicochemical) soil parameters must be considered as results of a weathering increment and compaction increment. The increments of following soil parameters are discussed here: a) volumetric strain, b) normalized element concentrations of depleted elements, depletion-factor R_{0_loss}, c) porosity ϕ, d) rock density ρ and e) geochemical volume strain ε.

The laterite compaction C ($=z_c/z_i$), associated horizontal extension in x direction x_c/x_i and volume strain V_c/V_i are geometrically determined by image analysis (chapter 2.2.5).

The vertical compaction of the laterite (Table 2.2, Figure 2.24.a) describes a logarithmic depth function. The compaction is a compressional deformation due to the sedimentary load and petrographically indicated by the unconformity-parallel crenulation cleavage S_2. It is likely, that a minor collapse of void space during weathering occurred (c.f. Retallack 1991). However, this collapse is considered to be minor, since S_1 surfaces are generally well preserved inside microlithons between S_2 surfaces.

Significant volume decrease associated with compaction down to $V_w/V_i = 0.41$ in the upper part of the laterite is suggested by the volumetric strain calculation (Table 2.2, Figure 2.24.b). The extreme volume decrease of $V_w/V_i = 0.15$ in section 4 may be result of progressive deformation (see below).

Bulk volume decrease during compaction of porous soil material is accompanied by void space (porosity) decrease (Boivin et al. 2005 and references therein). Compaction of a porous material leads generally to bulk volume compaction, as long as there are no chemical reactions associated leading to volume increase at the mineral scale. Those chemical reactions are minimized during burial compaction, as interpreted beforehand. A volume dilatation, as determined for the lower part of the laterite, is not compatible with the observed porosity in the rock. Therefore, the intense dilatation in the “pure shear” scenario below ca. 0.5 m is implausible. Considering some variations due to measuring errors, the calculated dilatation of 1.14 in the “plane strain” scenario may represent almost isochoric strain ($V_w/V_i = 1$) for the lower laterite part.

Table 2.2: Laterite compaction and soil characteristics by depth-sections and samples. (*average* is the calculated average from the laterite data, following equation 10 in chapter 2.2.5. * estimated, not calculated.)

	$C=z_c/z_i$ (x_c/x_i)	**V_c/V_i "plane" ("pure")**	***Bulk density*** **ρ [g/cm^3]**	***Porosity*** **ϕ**	***volume strain*** **ε**	**R_{0_loss}**
Entire laterite (average)	*0.73 (1.36)*	*0.88 (1.33)*	*2.34*	*0.29*	*0.53 (Hf, Ti)*	*0.43*
Section 4 (0-0.05 m)	0.08 (1.83)	0.15 (0.27)	--	--	--	--
at RA2-1a (0.2 m)	0.22 (1.88)	0.41 (0.78)	2.38	0.24	0.47 (Hf, Ti)	0.37
Section 3 (0.05–0.55 m)	0.29 (1.91)	0.55 (1.06)	--	--	--	--
Section 2 (0.55-0.84 m)	0.70 (1.60)	1.12 (1.79)	--	--	--	--
at RA2-3 (1 m)	0.85 (1.35)	1.14 (1.53)	2.31	0.34	0.56(Hf, Ti)	0.46
Section 1 (0.84-2 m)	0.93* (1.04)*	1.08 (1.25)	--	--	--	--
Saprolite (RA1-7) (1.5 m)	1* (1)*	1*	2.32	0.27	1.08 (Al)	1.11
unweathered granite	1* (1)*	1*	2.46	0.04	1 (1)	1

Consequently, extension dominantly in x-direction ("plane strain") accompanied the vertical compaction. This uniaxial extension is accommodated by normal faulting affecting the quartz-veins (Figure 2.4) and equals the dip direction of the quartz-vein and S_1 (NW-SE). To establish an extension in the lateritic basement, while no (or minor) compaction-related horizontal extension took place in the cover beds, a minor unconformity-parallel reactivation of the basement-cover-interface in x-direction must have taken place (displacement arrows in Figure 2.23). It is likely that the uppermost centimetres (section 4) of the remaining laterite were directly affected by this horizontal shear, thus showing such an intense compaction (C_4 = 0.08). Excluding section 4 from calculation, the bulk compaction and related volume strain does not change significantly ($C_{1\text{-}3}$ = 0.73).

Changes of soil characteristcs are generally dependent on mineral alterations and deformation. Mineral alterations during chemical weathering (hydrolysis, dissolution and oxidation) cause changes of volume, density and porosity at the mineral scale. An element mobilization is associated with alteration, probably leading to element leaching. The element transport is mainly dependent on permeability: if permeability is low, reprecipitation is likely to take place very near the mobilization area. Otherwise, the element is transported away. The fluid chemistry is also an important factor regarding reprecipitation ability. Deformation, in this case vertical compaction and horizontal extension, causes a rearrangement of minerals, which effects the volume, porosity and density at the sample scale. Whether geochemical changes, i.e. loss of elements, occurred during compaction within the laterite has to be determined, in order to understand the soil parameters correctly. If no loss took place, the concentration of elements are not affected by compaction.

Mobilization of quartz may have occurred during compaction, indicated by the existence of quartz-rods in the laterite texture, paralleling the compaction fabric S_2 (Figure 2.5). These rods are not necessarily indicative for SiO_2 loss at the sample scale, since immediate reprecipitation is likely in the laterite due to the clayey texture with low permeability. The concentrations of most elements changed generally more across the saprolite-laterite boundary than within the laterite (as shown by *PIA*, Figure 2.9.m). For example, the difference of *PIA* between saprolite and lower laterite is 13 %, whereas the difference between lower and higher laterite sample is < 1 %. Such a pattern is also shown by Hf and, less intensely, by SiO_2, Fe_2O_3, TiO_2 and P_2O_5 (Figure 2.9). The immobile element Ti shows an increase from 0.26 to 1.04 wt% (increase by the factor 4) across the boundary, and a minor increase to 1.41 % (factor 1.36) within the laterite. Considering the present section compactions in section 3 (where the upper laterite sample RA2-1a is located) of C_3 = 0.29 (fraction of the initial thickness), C_1 = 0.93 in section 1 (lower laterite sample RA2-3) and 1 (no compaction) in the saprolite, the observed geochemical gradients within the laterite become even less stronger (Figure 2.6). This is because the initial, i.e. pre-compaction distance between lower and upper sample increases significantly, while the distance between saprolite sample and lower laterite sample remains almost unchanged. The different

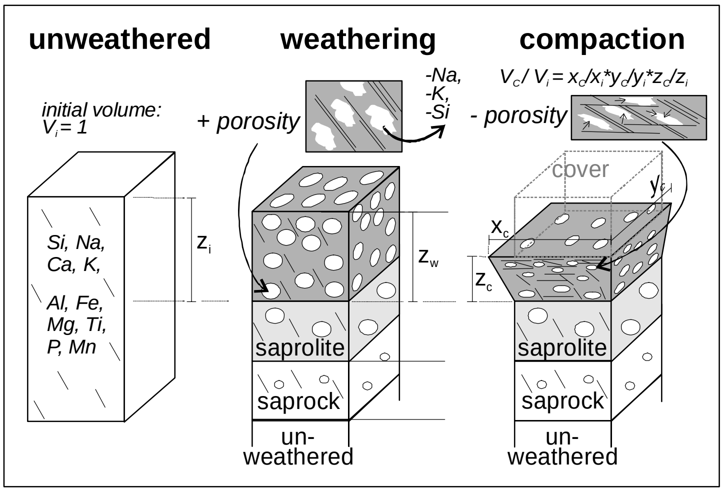

Figure 2.23: Morphological changes of the laterite resulting from weathering and compaction.

gradients described here are related to different relative geochemical changes induced by weathering and compaction. The intense change of element concentrations within the lower laterite section, which was hardly influenced by compaction ($C_1 > 0.93$), was almost completely caused by weathering. The additional minor changes of element concentration within the laterite zone are due to progressive weathering. Effective, but minor loss of e.g. Si might have occurred during compaction. This may explain the slightly stronger concentration increase of the elements Al, Ti, Fe and P through the laterite, in comparison to the *PIA* or Hf gradients, which show only minor increases (Figure 2.9). The gradients of soil parameters are interpreted under the assumption that almost the entire geochemical balance in the laterite is due to weathering and only a minor loss of Si is due to compaction.

According to that assumption, the parameter R_{0_loss} is almost exclusively affected by mineral alterations during the weathering period. Therefore, it provides information about the mass balance resulting from weathering in the laterite. The strong initial decrease of R_{0_loss} from 1.1 to 0.46 across the saprolite-laterite boundary is an indication for a weathering-related trend (Figure 2.24.f). A moderate decrease within the laterite is in accordance to the progressive, but less pronounced weathering trend towards the upper soil.

The porosity ϕ is a critical parameter with respect to volume strain, bulk density and permeability characteristics of the laterite. In soil morphology, a general distinction is made between micro- and macro-porosity (Boivin et al. 2005). Micro-porosity (< 10 μm), or inter-particle porosity, refers to the void space between clayey to sandy particles defining the soil matrix. Macro-porosity (> 50-100 μm) is genetically related to void space left behind by dissolution of large primary minerals such as feldspar and quartz. The porosity of the present laterite has a high macro-porosity, produced by the “framework-like” crenulation fabric of S_1-surfaces and S_2-surfaces (Plate 2.1.f). This fabric prevented a collapse of larger voids.

Within the entire weathering profile, porosity increases with degree of weathering (Figure 2.24.c). Highest porosity is measured in the lower laterite sample ($\phi = 0.34$), whereas a decrease is observed in the upper laterite sample (0.24). This value is lower than the value saprolite (0.27). Porosities of ca. 0.27 to 0.5 are commonly observed in modern or relic laterites, which were not subject of burial compaction (e.g. Mathe et al. 1999, McCrea et al. 1990, Sheldon & Retallack 2001). Porosity induced by weathering, named ϕ_w, increases with dissolution intensity and thus is a function of weathering degree. From this, it follows that ϕ_w is inversely proportional to R_{0_loss}. The increase of ϕ in the lower laterite part reflects this relation to dissolution intensity. The observed decrease of ϕ in the upper laterite part, however, displays that porosity is not only associated with advanced chemical weathering. Here, ϕ shows a qualitative correlation with the gradient of laterite compaction. The decrease of porosity in the upper part of the laterite is in accordance to the volume strain calculations ($V_c/V_i < 1$). The macro-porosity is reduced by the vertical compaction and extension in horizontal x-direction, by crenulation, as illustrated in the small sketches in Figure 2.23. This shows that the porosity of the laterite is a complex parameter, i.e. it is dependent on both degree of weathering and degree of compaction.

The bulk density ρ decreases within the saprock and saprolite from 2.46 to 2.32 g/cm^3 (Figure 2.24.d). ρ does

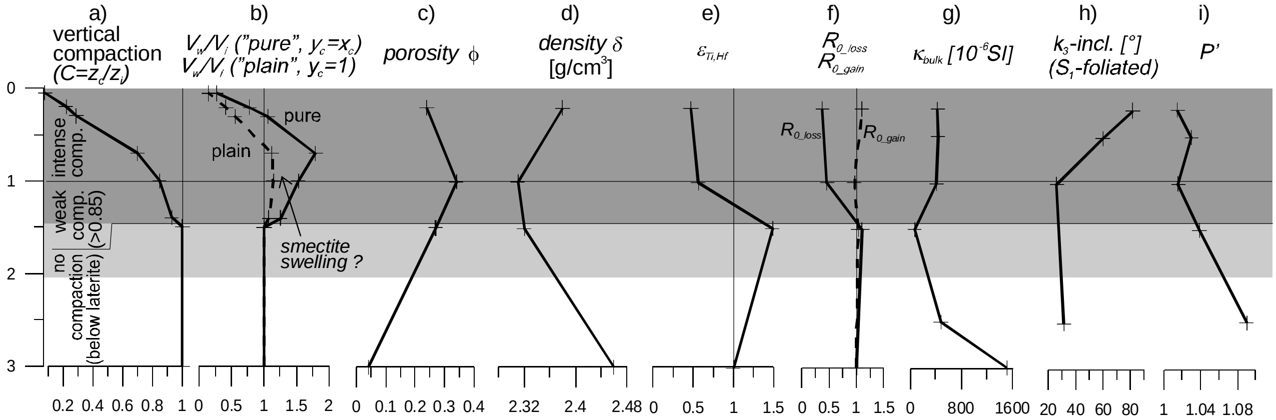

Figure 2.24: Compilation of laterite aspects determined by compaction and volume determination (a-b), density (c), porosity measurements (d), geochemistry (e-f) and magnetic susceptibility (g-i).

not change across the saprolite-laterite boundary (saprolite: 2.32 g/cm^3, lower laterite 2.31 g/cm^3), whereas it increases within the laterite slightly to 2.38 g/cm^3. Laterite densities from the literature are usually lower (1.75 g/cm^3: McCrea et al. 1990) due to their higher porosity. The decrease of density within the saprock and saprolite is associated with leaching and hence, the porosity increase. The relative stable bulk density within the saprolite-laterite transition zone is a result of a) a strong increase of porosity with a decreasing effect on ρ and b) an increase of residual heavy minerals leading to an increase of ρ. The slight increase of ρ from the lower to the upper laterite part is attributed to the burial compaction. Bulk density is therefore a complex parameter, comparable to porosity.

Geochemical volume strain $\varepsilon_{Ti,Hf}$ is by definition inversely proportional to the product of ρ and $c_{Ti,Hf}$ (see equation 4b in chapter 2.2.11). Therefore, it is a complex parameter. Within the saprock and saprolite, ε is influenced exclusively by weathering and thus, showing values of 1 to 1.08, indicates approximately iso-volumetric weathering (Figure 2.24.g). This is in accordance to petrographic observations. Crossing the saprolite-laterite boundary, $\varepsilon_{Ti,Hf}$ decreases considerably to a value of 0.56, displaying volume loss. Since ρ does not change significantly across the saprolite-laterite boundary, the decrease of $\varepsilon_{Ti,Hf}$ is due to major concentration increase of Ti and Hf, therefore dominantly influenced by weathering. A slight decrease of $\varepsilon_{Ti,Hf}$ (0.47) towards the upper laterite is observed because of minor increases of bulk density and immobile element concentration. Comparing both volume strain results, V_c/V_i and e (Table 2.2), differences are observed in the less compacted lower part of the laterite: here, V_c/V_i shows isochoric deformation and ε significant volume collapse due to $c_{Ti,Hf}$ increase at stable ρ. In the compacted upper laterite, the increase of both $c_{Ti,Hf}$ and ρ led to an $\varepsilon_{Ti,Hf}$ value comparable to the geometric volume strain.

ε may be an applicable tool for volumetric strain determination in fossil palaeolaterites, which underwent burial compaction, because it integrates the density increase caused by the compaction. However, the relations between element mobilization and porosity and their influence on bulk density ρ are complicated. It can be summarized that changes of parameters by weathering show different symmetries within the profile that changes induced by compaction: change of weathering is very strong at the basis and remains relatively stable through the laterite, and compaction becomes stronger going upwards.

2.5.6.1 Calculation of laterite burial depth by a compaction curve

The degree of compaction in the laterite is dependent on the sedimentary load, thus it is described by a depth-function (Caudill et al. 1997, Sheldon & Retallack 2001). The overburden on top of the laterite is unknown; its minimum thickness of 1 to 2.3 km is estimated by the stratigraphic record (Duckman et al. 1993). The theoretical maximum burial depth of the weathering profile is estimated by mineralogical indications: the preserved main weathering products kaolinite and smectite and their distribution in the profile characterized by a depth function (as described in chapter 2.2.10), indicate maximum temperatures below the anchizone (maximum 150-200 °C). A theoretical maximum of ca. 5-6 km can be inferred assuming a geothermal gradient of 30 °C/km. With the bulk compaction of the laterite ($C_{laterite}$ = 0.73, as the average of all section compactions) the burial depth can be calculated employing a published palaeosoil compaction curve. To do this, the equation of Caudill et al. (1997) and Sheldon & Retallack (2001) is used:

$$(4) \qquad C_{S\&R} = (1-F_0) / [(F_0/e^{Dk})-1]$$

D is the burial depth. F_0 is the porosity produced by weathering (as a fraction of 1) and k is an empirical parameter, both depending on the soil type. An adjustment of $C_{S\&R}$ for the present laterite would be possible, if F_0, which equals ϕ_w is known, whereas k does not have much effect on the results. A value of 0.29 for k is supposed to be typical values for feralitic soils (Caudill et al. 1997, Sheldon & Retallack 2001). The "pre-compaction"-porosity ϕ_w cannot be exactly quantified but approximated by the measured ϕ multiplied with a factor that is associated with the compaction degree $C_{laterite}$ = 0.73 (Figure 2.6).

$$(5) \qquad \phi_w = \phi / C_{laterite}$$

ϕ = 0.29 and $C_{laterite}$ = 0.73 (Table 2.2), i.e. ϕ_w = 0.29 / 0.73 = 0.40. It follows from equation 4 that D is 2.8 ± 0.1 km (with $F_0 = \phi_w = 0.37$). The calculation is very sensitive to changes of F_0: a value of 0.5 for F_0, considered as a typical value of feralitic soil (Caudill et al. 1997, Sheldon & Retallack 2001), results in a much lower burial depth of 1.6 km.

2.5.6.2 Evaluation of hydraulic properties in the laterite

The hydraulic properties of the laterite are not quantified. The water content, permeability and hydraulic conductivity of the laterite are important parameters with respect to fluid-rock-interaction during weathering and burial history. The void space in microlithons between cleavage domains in the laterite, representing a macro-porosity, has a high water capacity. However, permeability and hydraulic conductivity is considered as very low in the laterite, as the specific morphology and relatively low "concentration" of the macro-porosity may reduce the interconnectivity of voids. A joint system, increasing the hydraulic conductivity, is not developed. The porosity in the laterite decreased during compaction (c.f. Richard et al. 2001). With the degree of compaction and the associated higher density of subhorizontal S_2 cleavage domains, a horizontal petrographic anisotropy developed reducing the vertical conductivity (permeability-anisotropy). An enhancement of horizontal permeability is not likely. With proximity to the unconformity, the hydraulic parameters porosity, permeability, water content and conductivity are lowered. Beneath the laterite, in the pallid zone, the permeability is much higher than in the laterite, due to intensive jointing from weathering-brecciation. As discussed in chapter 2.5.5, several phases of lateral flow of a confined groundwater took place beneath the laterite. Although permeability is low, relatively high water content in the laterite cannot be excluded, considering fluid-flow with overpressure beneath.

2.5.7 Cataclasis

As is it observed by relative fabric overprints, cataclasis post-dated the fabric, induced by the burial compaction (Figure 2.5). The much smaller grain size in the matrix of the cataclasites, compared to the granite (Plate 2.1.g,h) is a result of intense mechanical destruction. The laterite did not encounter this intense cataclasis, which is demonstrated by the large mean grain size of relic quartz, feldspar and Fe/Mg-mica, and maximum grain sizes similar to the granite (martite grain-size distribution: Figure 2.14).

Mobilization of Fe accompanied the massive grain-size reduction in the cataclastic zones. A reprecipitation as microcrystalline haematite caused a reddening of the fine-grained matrix. Haematite is present in the matrix and in veins. The Fe mobilization did not change the whole-rock content of Fe, indicated by the quite stable correlation of Fe with Ti and P (Figure 2.11). In total, no significant mineralogical reactions (phase transitions) accompanied the grain-size reduction during cataclasis, as it is deduced from XRD (see chapter 2.2.10), geochemistry (chapter 2.2.11) and κ_{bulk}/Fe ratio (Figure 2.17.d).

Hollandite ($BaMn_8O_{16}$) in veins, defining occasionally the cataclastic cleavage S_3, indicate oxidising fluid (Deer et al. 1966).

2.6 Association of κ_{bulk} and AMS with alteration and deformation

2.6.1 Magnetic susceptibility

From κ(T) curves and κ_{bulk} modelling (chapter 2.3.2 and 2.3.3, respectively) it is inferred that relic magnetite in martite grains is the main carrier in the unweathered granite, saprock and cataclasite ($c_{mag} \cdot \kappa_{mag} / \kappa_{bulk} > 90$ %). In the saprolite and laterite magnetite is important, as well, but microcrystalline haematite and Fe/Mg-micas increase its influence on magnetic susceptibility ($c_{mag} \cdot \kappa_{mag} / \kappa_{bulk} < 70$ %). Primary, unaltered magnetite grains are not observed in the rocks due to the stages of martitization (*hydrothermal, weathering and burial martitization*: chapter 2.5.4).

The susceptibility of a hypothetically fresh granite (without martitization) is modelled as $1.21 \cdot 10^{-2}$ SI (see chapter 2.3.3). Measured bulk susceptibilities are generally lower due to martitization. Highest κ_{bulk} is measured in the unweathered granite, attributed to highest content of martite grains and relic magnetite in martite. The unweathered rock is solely affected by *hydrothermal martitization*, possibly also by “burial martitization”. The high κ_{bulk}/Fe_2O_3-ratio (Figure 2.17.d) of the fresh rocks (beneath the weathering front and in the corestone) implies a high content of magnetite in these rocks.

With proximity to the unconformity up to the mottle zone, κ_{bulk} is reduced to 1/10th to 1/50th of the value of the unweathered granite. This is a combined effect of (1) magnetite dissolution during weathering and (2) second stage of martitization (*weathering martitization*) (see chapter 2.5.4). The decrease of the κ_{bulk}/Fe_2O_3-ratio toward the saprolites is attributed to the advanced magnetite dissolution and martitization.

Crossing the saprolite-laterite boundary, the κ_{bulk}/Fe_2O_3-ratio does not change significantly, because the shifts of κ_{bulk} and of Fe_2O_3 are approximately proportional. That demonstrates that the degree of martitization in saprolite and laterite is similar. Considering the different hydraulic conductivity in both lithologies (see chapter 2.5.6.2), present after compaction event, it is suggested that *burial martitization* took place before compaction, probably already started with initial burial. Otherwise, a distinct difference of the degree of martitization would be observed, most likely a higher degree of martitization in the higher permeable saprolite. Furthermore, these results also suggest that coarse-grained martites and microcrystalline haematites have rather similar intrinsic susceptibilities.

The increased susceptibility in laterite, correlating with the increase of iron content, is due to the passive enrichment of Fe-oxides and Fe/Mg-micas, attributed to advanced chemical weathering. κ_{bulk} remains relatively stable within the laterite (Figure 2.24). This is due to two subsequent processes affecting κ_{bulk} in an opposing manner in the upper laterite: (1) advanced magnetite dissolution lowered κ_{bulk} and (2) volume loss during compaction increased κ_{bulk}. This demonstrates that κ_{bulk} is a complex soil-parameter, following the definition in chapter 2.5.6). Goethite precipitation may have been an intermediate stage before the formation of microcrystalline haematite. In this case, the susceptibility may have been temporary increased, before it decreased again with the dehydration to haematite (as indicated by the intrinsic susceptibilities of the minerals: Table 1.1).

The cataclasis does not show any effect on the κ_{bulk}/Fe_2O_3-ratio.

The high standard deviation of κ_{bulk} in the unweathered granite (Figure 2.17.a) is related to a heterogeneous distribution of magnetite at the sample scale. In a coarse-grained texture, κ_{bulk} changes significantly with the variation of a few grains of magnetite. Both weathered and cataclastic samples show lower κ_{bulk}, and smaller standard deviations with respect to κ_{bulk}. A low standard deviation with respect to κ_{bulk} implies a high degree of homogenization of main magnetic carriers in the texture at the sample scale. Two petrographic factors lowered the degree of homogenization of magnetic carriers in these lithologies: (1) a homogenized distribution of magnetite, which is particularly observed in the cataclasites by grain size reduction of martite (Figure 2.14) and (2) a lowered difference between $c_{mag}\cdot\kappa_{mag}/\kappa_{bulk}$, $c_{hem}\cdot\kappa_{hem}/\kappa_{bulk}$ and $c_{mica}\cdot\kappa_{mica}/\kappa_{bulk}$ (from κ_{bulk}-modelling: Table 2.1) in the highly weathered saprolite and laterite.

2.6.2 Magnetite / martite-ratio in κ(T)-curves

The irreversibility during the κ(T)-cooling run is assumed to be directly related to the reduction of martite to magnetite during the heating run. Under this assumption, the ratio of $\kappa(T_{room\ after\ heating})$ and $\kappa(T_{room\ before\ heating})$, referred to as *magnetite/martite-ratio*, is calculated to estimate the oxidation state of magnetite and its change through the profile (Figure 2.17.c and Figure 2.15). The magnetite/martite-ratio does not take magnetic carriers other than iron oxides into account. A significant amount of Fe-bearing calcite in the samples, for instance, may influence κ_{bulk}. For this reason, the ratio only approximates the oxidation state of magnetite.

The variation of the magnetite/martite-ratio reflects the decreasing trend of κ_{bulk} through the weathering zones. In the unweathered granite, the magnetite/martite-ratio is 4.2. It increases slightly in the moderately weathered granite and cataclasite below the saprolite (5 to 6). In the saprolite, the ratio decreases to < 4 and in the laterite to ca. 1. The aplite vein (RA1-1.b) shows an anomalous value, which is due to the lithology.

A simple model shows, how κ(T)-curves directly reflect the progressive alteration of rocks (Figure 2.25). Generally, high ratios are due to high degree of martite reduction during the experimental heating and therefore indicate intense natural martite generation in relation to the initial magnetite content in the rocks. Low values, on the other hand, point to less intense martite reduction and indicate low martite generation in comparison to the initial magnetite content. A very low ratio points to no significant martite reduction. A reversible curve, which would be accomplished in absolute fresh granite, is not present in the profile (stage a). Such a curve is shown in the granite of case study Långviken (Figure 4.7.d). A stage b curve with a medium magnetite/martite-ratio is developed in the unweathered granite. A martite generation with relatively high amount of magnetite remnants is present in this rock. The moderately weathered granite and cataclasites with an advanced martitization, but low microcrystalline haematite content, features a high ratio (stage c). The ratio decreases in saprolites (and saprolitic cataclasites) because intensified weathering forced magnetite to dissolve to form ultimately microcrystalline haematite, rather than oxidize to martite (stage d). The almost reversible curve in the laterite with a very low ratio (stage e) shows clearly the dominance of microcrystalline haematite and the most advanced magnetite breakdown.

2.6.3 Relation of AMS to petrofabrics - implications from image analyses

2.6.3.1 Macroscopically undeformed granite

The prolate 3D-SPO of chlorite of the macroscopically undeformed granite defines a fabric represented by a foliation, dipping steeply to the N, and a horizontal lineation in E-W direction (Figure 2.19). The orientation of this fabric does not correspond to the SW-NE striking S_1, observed in the foliated granite, consequently, the fabric of the macroscopically undeformed granite and its weathered rock equivalents is a result of another deformation phase. The intracrystalline deformations of quartz and feldspar indicate medium to high temperatures in the granite under which the petrofabric developed. The fabric can therefore be interpreted as the primary magmatic fabric, formed during syn-kinematic emplacement. AMS as a marker for weakly developed primary granitic fabric is well established (e.g. Archanjo et al. 1995a, Ferre & Ameglio 2000,

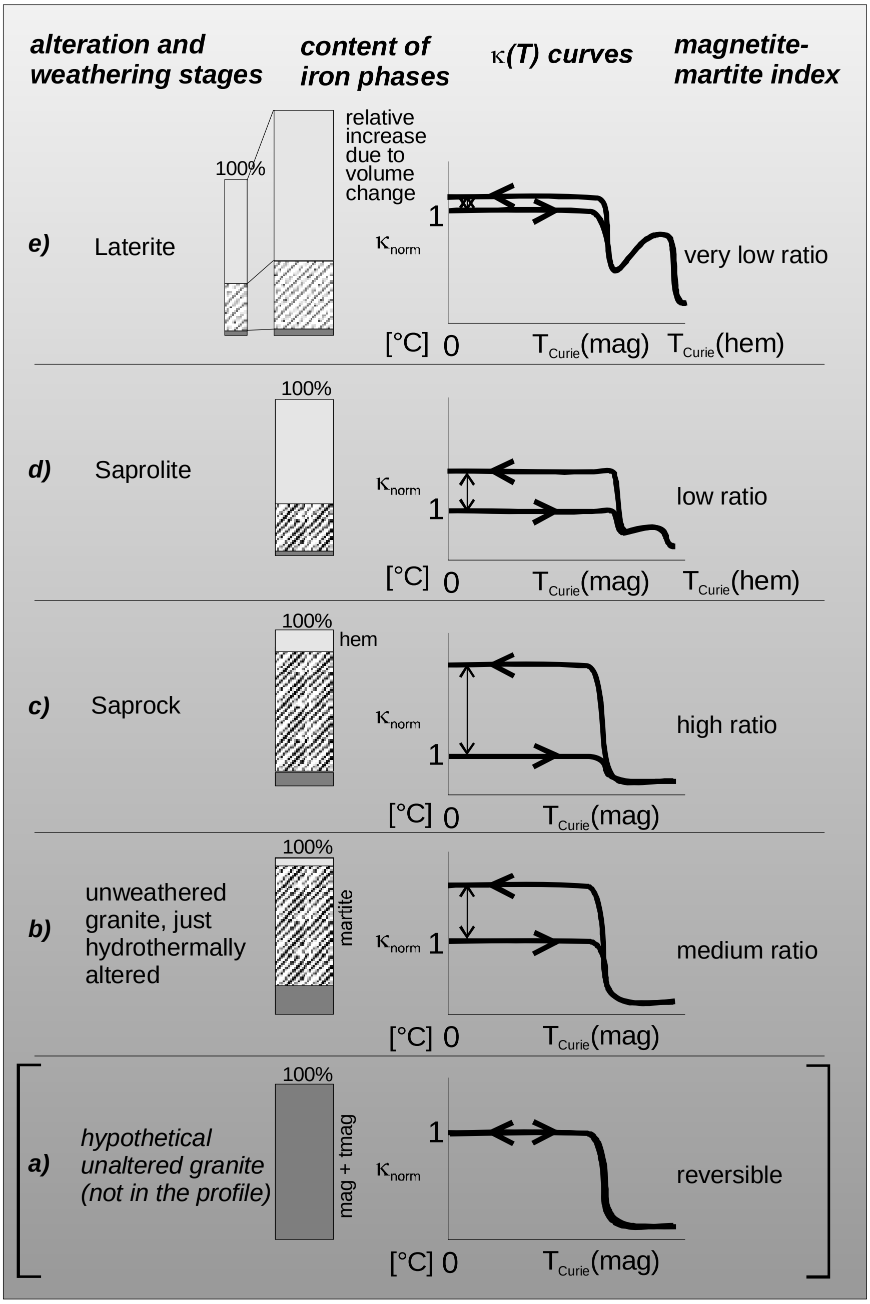

Figure 2.25: Model correlating the evolution of the κ(T) with alteration of magnetite through alteration and weathering stages. It illustrates the ability of temperature dependent susceptibility to match alteration processes within a simple system of iron oxides (magnetite, martite, microcrystalline haematite.)

Gattacceca et al. 2004, Greiling & Verma 2000, Henry 1988). The weak steep foliation of this primary fabric is referred to as S_0 to point out an earlier formation than S_1.

The image analysis results suggest a close genetic relation of martite cluster shapes to the petrographic fabric represented by chlorite SPO (Figure 2.19). The single martite SPO is different, showing a steeply plunging lineation but similarly orientated ellipsoid short axis C. The difference of single and cluster SPO is best observed in the very large cluster of section $\kappa_1\kappa_3$ (microphotograph in Figure 2.18). Here, the long axes (A) of single and cluster SPO show an almost perpendicular orientation. The single martite sub-fabric with its orthogonally oriented lineation to the cluster elongation is an expression of a distinctively anisotropic micro-crack pattern of the large primary martites. The fragmentation is almost exclusively restricted to martites

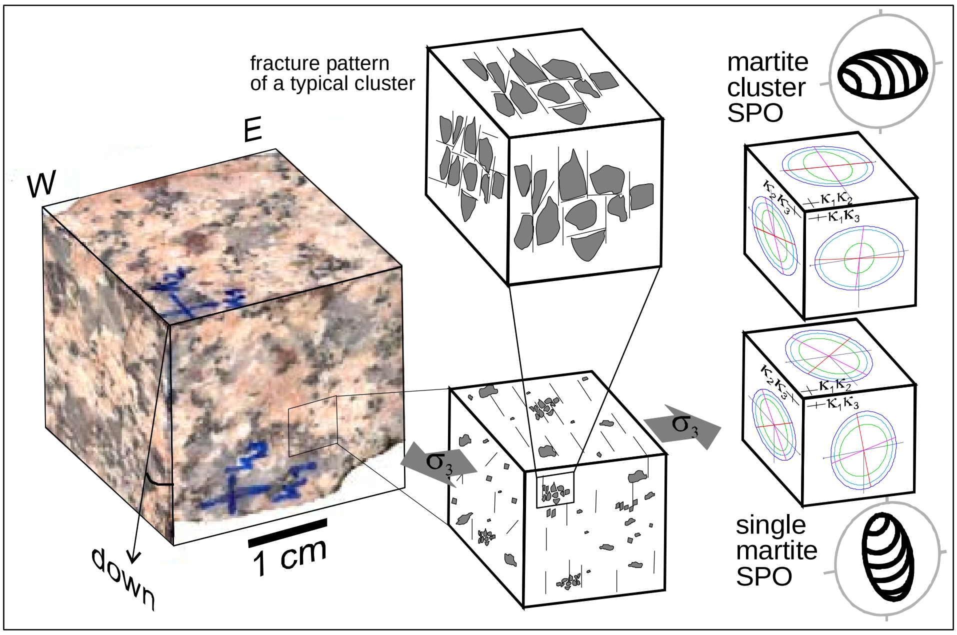

Figure 2.26: Granite fabric (sample RA3-1) and comparison of prolate SPO of single martites and martite clusters. The fracture pattern is anisotropic and was generated as a relaxation process subsequent to the development of early fabrics.

(Figure 2.26), therefore it is not directly related to the texture-forming deformation. The fragmentation shows rather characteristics of relaxation cracking, probably induced subsequently to a deformation during temperature decrease.

Martitization of the cluster is a later process, which can be deduced from the typical seams along the martite grain rims, dividing magnetite remnant from neighbouring intra-cluster-martites or matrix.

It is striking that the oblate AMS fabric (L/F = 0.969; P’ = 1.067; T = 0.506: Figure 2.19) is not reproduced by any of the SPO. Nevertheless, a good correspondence of the long axes with κ_1 is evident for chlorites (20.3° angle difference) and for martite cluster (11.2°). Single martites long axis shows an almost perpendicular orientation to κ_1 (81.9°). The declination of the AMS foliation pole κ_3 and the SPO foliation poles (C) are similar, but considerable deviation of the inclination of 32.6° (cluster) up to 53.1° (single martites) are present. Intermediate and short SPO axes, lie on a great circle with κ_2 and κ_3. This deviation can be related to the misfit of sectional SPO axes and AMS directions in $\kappa_2\kappa_3$ and directly influences the inclination of intermediate and short ellipsoid axes. An explanation for this deviation is discussed below.

Relic magnetite in martite, as the actual magnetic carrier of the AMS in the granite, is not discussed in terms of SPO, because its anisotropy cannot be determined employing image analysis. It is demonstrated in chapter 2.3.3 that the influence of magnetite dominates against martite and chlorite ($c_{mag}\kappa_{mag}/\kappa_{bulk} > 95$ %) in the granite. Thus, the measured bulk AMS must be a direct expression of the AMS of magnetite.

The determination of the martite SPO is important for the evaluation of shapes and distribution of magnetites. It is established that purely magnetite crystal shape carries the AMS as long as the crystal does not interact significantly with a neighbouring magnetite crystal. The latter case will produce a distribution-anisotropy (Archanjo et al. 1995a, Archanjo et al. 1995b, Cañon-Tapia 2001, Gaillot et al. 2006, Grégoire et al. 1998, Grégoire et al. 1995, Hargraves et al. 1991, Stephenson 1994). The image analysis demonstrated a close relationship of martite cluster shapes with the petrographic fabric and with the AMS fabric. It is therefore very likely that magnetite shapes and distribution, which defines the AMS, are strongly dependent on martite clusters shapes. Otherwise, such a good correlation of the petrographic fabric and the AMS would not have been established. Instead, the AMS would bear no relation to the petrographic fabric. How does the AMS of the small magnetite remnants reproduce the martite SPO and how does the interaction between martite neighbours influence the AMS? As described beforehand, the magnetite shapes do not display a distinct anisotropy, at least none that correlates with the martite shapes (Plate 2.4). This should lead to an AMS defined by magnetite shapes. However, if there is considerable magnetic interaction between the relic magnetites, the shape of the martite is important for defining the anisotropy of that interaction. Possible theoretical cases of magnetic interaction of magnetite in martite grains are summarized in Figure 2.27.a. An important case is 2b in Figure 2.27.a, where an AMS similar to the martite-shape is generated by mostly interacting, equant-shaped and randomly or cubically distributed magnetites. According to (Grégoire et al. 1995), the distance of magnetite and their shapes are important factors defining a resulting AMS (Figure 2.27.b).

Only in rare cases, magnetite remnants do touch each other between neighbouring martite grains. More

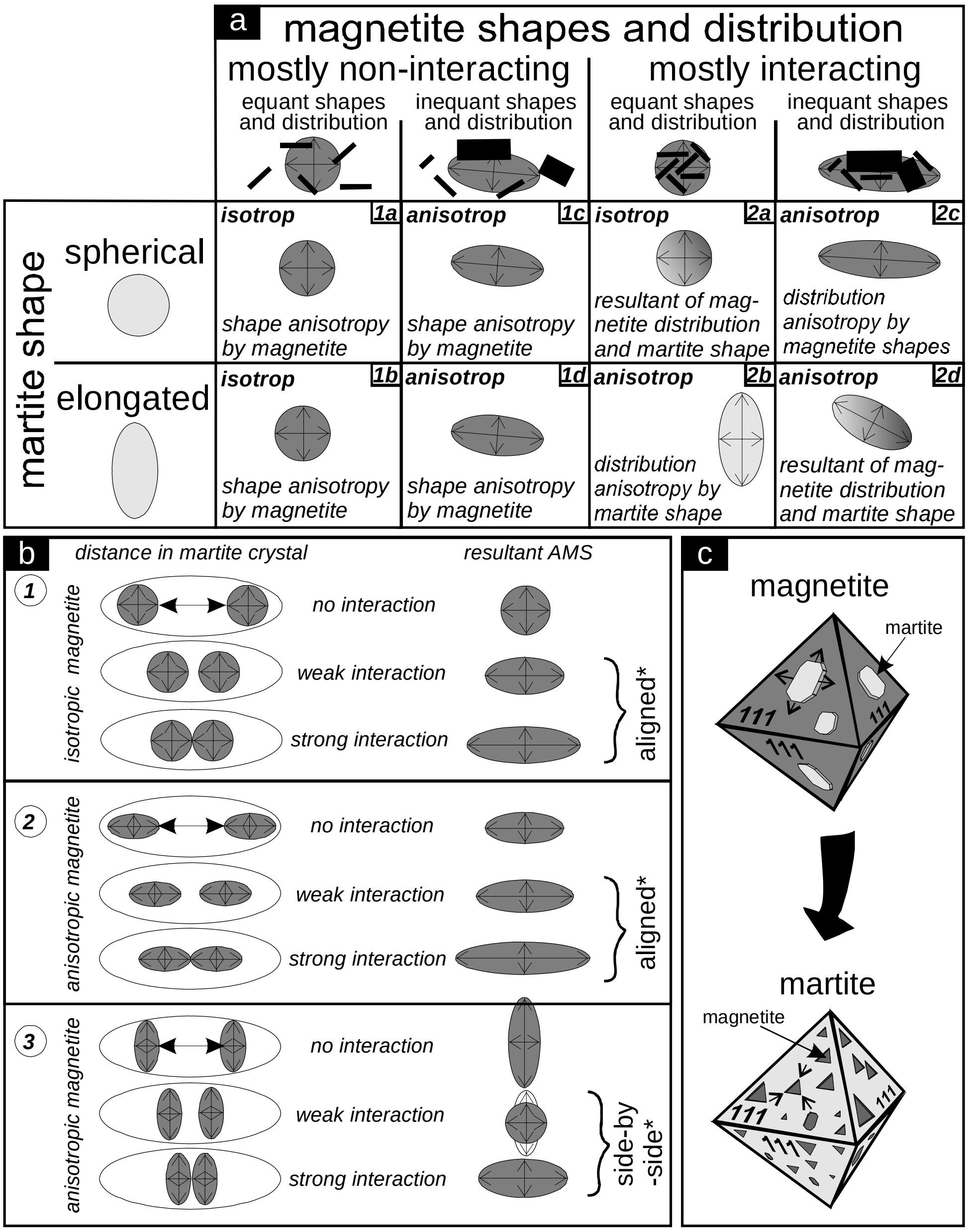

Figure 2.27: Magnetic interaction of magnetite. a) Possible cases of magnetic interaction of relic magnetite in martite grains and the theoretically resulting intrinsic AMS of a martite grain. b) the effects of magnetite distance on the resulting martite AMS, with "side-by-side and "aligned" cases (Grégoire et al. 1995). c) Propagation of pseudomorphous martitization in cubic magnetite.

typical are seams of martite (Figure 2.18.d), which are a result of martitization subsequent to the fragmentation of martites. It has to be considered that the magnetite remnants in neighbouring martites interact magnetically.

In some cases, a side-by-side or aligned configuration (Grégoire et al. 1998) of at least two single martites form a cluster. This arrangement can result in a switch of principal magnetic axes, when magnetic interaction is strong enough to overcome the intrinsic susceptibility anisotropy of the single grains (Cañon-Tapia 2001, Gaillot et al. 2006, Grégoire et al. 1998). The large cluster in section $\kappa_1\kappa_3$ rich in magnetite remnants mimicking the single martite shapes gives a good example for a side-by-side configuration (Figure 2.18.d). Whereas the statistical SPO of the single grains constituents is almost perpendicular to the AMS direction, the shape of the cluster itself parallels the AMS. The magnetite remnants are large and close enough to interact magnetically with each other across martite grain boundaries. This implies the importance of a high fraction of magnetite remnants inside martite grains for defining AMS. It is inferred that magnetic interaction between the magnetite remnants in the martites is important in defining the bulk AMS.

It is likely that the present AMS fabric of the altered granite did not change significantly, with respect to axis distribution, compared to the unaltered granite (before martitization). (Just et al. 2004) showed both preservation of primary magnetic fabrics and profound modification of AMS axes distribution by martitization in granites.

Apparently, the two SPO fabrics, although both prolate, correlate quite well with the oblate AMS fabric. Considering both SPO fabrics as AMS sub-fabrics, they produce a resultant AMS fabric by superposition (as shown in Figure 1.9). A simple geometric addition is employed here to investigate this composite fabric. For simplicity, the small angles of deviation between the principal axes of the two ellipsoids are not taken into account, i.e. the principal axes are paralleling each other. Consequently, just three small vector additions have to be carried out:

$$A_C+B_S = A_{CS} = 1.281 + 0.965 = 2.246$$
$$A_S+B_C = B_{CS} = 1.148 + 0.992 = 2.14$$
$$C_S+C_C = C_{CS} = 0.787 + 0.902 = 1.689$$
$$L = 2.246 / 2.14 = 1.05$$
$$F = 2.14 / 1.689 = 1.267$$

The resultant ellipsoid is oblate (L/F = 0.829), where A is horizontal, B subvertical and C is subhorizontal (Figure 2.28). The ellipsoid resembles quite well the AMS tensor. It is important that the measured oblate AMS fabric can be reproduced by the composition of two perpendicular prolate SPO ellipsoids. By this calculation the importance of both sub-fabrics, single martites and clusters, in defining the AMS can be supported. Their relative contribution directly affects the ratio of A_C+B_S to A_S+B_C and is therefore significant. A lower ratio (< 1) will result in an exchange of A_{CS} and B_{CS}, i.e. the long axis is vertical and the intermediate axis horizontal. The addition of cluster SPO and single martite SPO is a simplification, because the rest of single martites subsumed in the cluster fabric are counted twice. However, this is not a problem for a qualitative determination of the oblate shape of the resultant fabric.

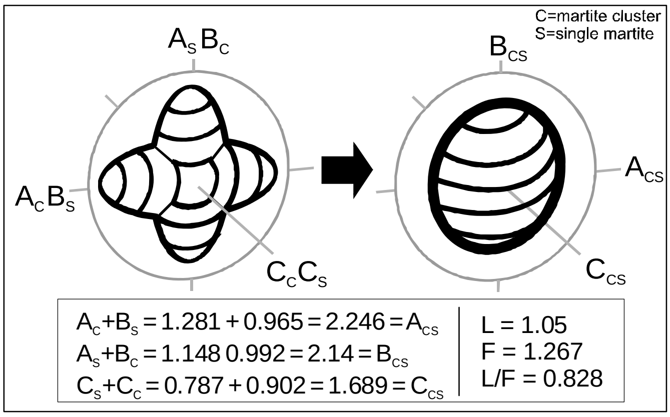

Figure 2.28: Addition of ellipsoid axes of two prolate sub-fabrics determined by SPO and sketch showing the oblate compositional fabric. The oblate superposition fabric resembles well the AMS fabric of that sample (also refer to Figure 1.9).

The deviation of the SPO and AMS foliations poles, which are caused by the misfit of the SPO ellipse with respect to the AMS directions in section $\kappa_2\kappa_3$ is problematic. There are two possibilities for explaining this misfit: a) The section $\kappa_2\kappa_3$ does not show a representative petrographic fabric or b) the AMS is influenced by another important source of anisotropic susceptibility, such as another large cluster, which is not represented in the $\kappa_2\kappa_3$ section. As it is revealed by the SPO of section $\kappa_1\kappa_3$, the effect of one single large cluster can be very high. The other AMS specimens of sample RA3-1 show κ_3-axes, which plunge more shallowly and thus, fit quite well the measured SPO (Figure 2.19). If a homogeneous deformation is considered throughout the sample (excluding cylinder iv and vi, which represent another AMS-type, see below), an influence of the AMS by some hidden clusters is likely.

2.6.3.2 Laterite

Magnetite is an important magnetic carrier ($c_{mag}\kappa_{mag}/\kappa_{bulk}$ = 68 %) in the laterite, although the modelled c_{mag}/c_{mar}-ratio of 0.0366 is very small (Table 2.1). An increased influence of the paramagnetic and antiferromagnetic carriers (Fe/Mg-mica, microcrystalline haematite, respectively) is evident. The lower content of magnetite inclusions in martite causes inevitably an increase of the spatial distance between remaining magnetites. It has to be investigated, whether the spatial distance between the magnetites has an effect on their magnetic interaction. It has been shown by modelling that magnetic interaction becomes insignificant with distances higher than the mean diameter of the interacting grains (Cañon-Tapia 2001, Gaillot et al. 2006). Microscopic observations demonstrate generally high distances between relic magnetites inside a martite grain (e.g. Plate 2.5.a), suggesting no significant distribution-anisotropy.

The AMS of all cylinders of sample RA2-1b show a uniform axes distribution, although the eccentricity (P’) with about 1.01 is very low (Figure 2.17). The axes distribution is attributed to the combination of two factors: a) the rotation to horizontal of the phyllosilicate-rich matrix during the vertical compaction and b) the “averaging out effect” (Hrouda & Ježek 1999b) of a high number of small low-susceptible phases (kaolinite-haematite matrix and Fe/Mg-mica) in contrast to a small number of high susceptible phases (martite + magnetite). It is inferred that the paramagnetic petrofabric influences the AMS fabric and martite cluster emphasize the fabric, due to their rotation parallel with the petrofabric. A destruction of the large martites into smaller grains took place during or subsequently to the rotation, inferred from the good correspondence of cluster SPO with the compaction fabric. This interpretation shows the difference between granite AMS, which is based on the dominance of magnetic interaction, and laterite AMS.

2.6.3.3 Cataclasite

The results from the cataclastic sample are comparable with the granite image analysis; in both samples, the correlation of cluster SPO with AMS directions is striking (Figure 2.21). This correlation of AMS and SPO in the cataclasite is comparable to the results of the granite example. The c_{mag}/c_{mar} ratio of 0.31 (petrographic observation; Table 2.1) is as high as in the unweathered granite sample and thus supports the interpretation involving magnetic interaction. The uniformly shaped magnetites and their dense distribution within martite grains and the martite distribution in clusters define the magnetic anisotropy. In the cataclasite, both AMS and SPO fabrics are prolate. Therefore, the model of superposition of sub-fabrics, as it is inferred for the granite, cannot be transferred to the cataclasite. A deeper investigation is not possible without having information of the $\kappa_1\kappa_3$-section.

2.6.4 AMS fabrics

Magnetic fabrics are heterogeneously distributed at the sample scale, i.e. the magnetic fabrics of specimens of a sample are not homogeneously representing one specific AMS fabric with respect to axes orientation and AMS parameters. This demonstrates that rocks in the weathering profile can incorporate more than one

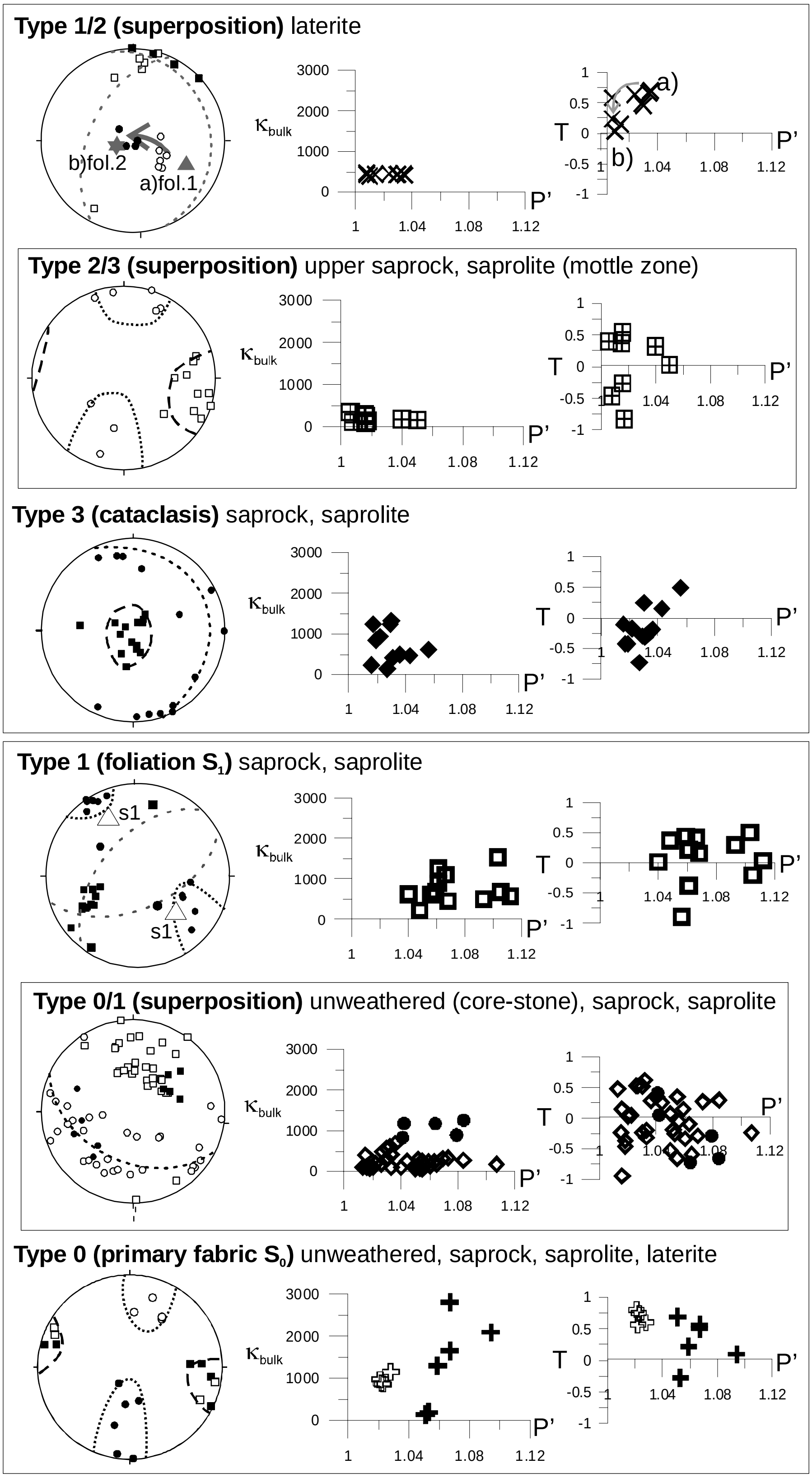

Figure 2.29: Types of AMS-pattern in the Roded profile. Early fabrics in granite are type 0 (primary granitic fabric) and type 1 (foliated granite) persist in all weathering stages. Type 0/1 is a superposition fabric in unweathered granite (corestone) and weathering-breccias. Type 1/2 occur in laterite and in the uppermost saprolite (mottle zone); it reveals a progressive imprint of diagenetic foliation S_2. Type 3 corresponds to the cataclastic fabrics. Type 2/3 results from overprint of cataclastic foliation S_3 on the compaction texture S_2.

magnetic fabric at the sample scale, which either interchange or superimpose each other. As a result, a simple correlation of magnetic fabrics with petrographic types at the sample scale is not straightforward. A discrimination method at the specimen scale has to be applied in order to correlate magnetic fabrics to petrographic fabrics. To do this, the AMS ellipsoid of each specimen is evaluated regarding its petrography, axes orientations (magnetic lineation, pole of magnetic foliation) and AMS parameters (κ_{bulk}, P' and T) and grouped into types of AMS fabrics.

Relating the AMS-types to petrographic characteristics of the rocks in the weathering profile shows that these AMS fabrics, especially their axes orientation, represent relatively well the different structural domains (S_1-foliation, laterite compaction and cataclasis). Weathering degree, on the other hand, is indeed an important factor changing the intensity and shape of AMS ellipsoids, but a secondary factor (Figure 2.29) concerning changes of axes directions.

2.6.4.1 Type 0 – primary magmatic fabric (S_0)

AMS-type 0 is developed in samples of the unweathered, moderately weathered and lateritic zones, as well as different structural domains (macroscopically undeformed granite and cataclasite) (type 0 section of Figure 2.29; black symbols represent granite, saprock and saprolite samples, white symbols represents laterite). This AMS pattern has subhorizontal κ_1, which trends in a WNW-ESE direction. κ_3 is NNE-SSW trending with a subhorizontal to medium steep inclination. P' and κ_{bulk} values are high in the unweathered granite and low in more weathered parts of the profile. This is partly related to the generally positive correlation of P' and κ_{bulk} (Figure 2.16.b and Figure 2.17.a,b), but also to the overprint by weathering-brecciation (see below). Ellipsoid shapes of type 0 are mostly oblate ($0 < T < 0.8$). Structural overprint at the specimen scale by S_1, S_2 or S_3-foliations leads to changes of the AMS pattern. AMS-type 0 exhibits relatively high T (mostly positive), therefore a composite magnetic fabric, usually characterized by lowered T (e.g. Borradaile 1988, Debacker et al. 2004), is unlikely, taking into account that in all other AMS-types within the profile, T is lower than in type 0.

As interpreted from image analysis (see chapter 2.6.3.1), martite cluster shapes with poicilitic relic magnetites define a distribution-AMS *sensu* Hargraves et al. (1991). AMS-type 0 is associated with S_0 (primary granitic fabric in the macroscopically undeformed granite). Probably, the superposition of the two AMS subfabrics defined by single martite and martite cluster led to an oblate AMS in the unweathered granite. The decrease of ellipsoid definition in those weathered granites showing AMS-type 0 (low-κ_{bulk} black symbols in type 0 of Figure 2.29), indicates that the oblate martite shapes still define the bulk AMS, but with a significant reduction of intensity. Here, shape anisotropies of non-interacting magnetite particles, which are randomly oriented relative to the preferred martite orientation, increase their influence and cause weaker anisotropies.

In the lateritic samples representing AMS-type 0 (RA2-1a, RA2-3), the compaction cleavage S_2 overprints the primary texture, but (and remarkable so) an AMS fabric resembling AMS-type 0, with respect to axes orientations, is observed. This may be a different magnetic fabric induced by fabrics other than S_0. However, there are no specific petrofabrics associated with the magnetic fabric. It is therefore likely that magnetic fabrics induced by compaction did not overprint the primary AMS fabric in this case. This phenomenon can be explained in light of the significantly higher κ_{bulk} (ca. $1000 \cdot 10^{-6}$ SI: white symbols of type 0 in Figure 2.29) compared to the other laterite samples with ca. $400 \cdot 10^{-6}$ SI (type 1/2, referring to RA2-2 and RA2-1b). A higher κ_{bulk} is due to a higher magnetite content (increased $c_{mag} \cdot \kappa_{mag}/\kappa_{bulk}$ to a value of > 90 %; Table 2.1). The abundant magnetite remnants in martite may cause a distribution-anisotropy, which is reduced in the other laterite samples due to the advanced magnetite oxidation. Two competing processes play a role in generating the lateritic AMS-type 0: (1) Martite rearrangement by crenulation due to vertical compaction is negligible and (2) the high inherent AMS intensity of the magnetite-carried (ferrimagnetic) primary fabric S_0 dominates, whereas the overprinting S_2-related (paramagnetic) AMS is weak.

It is concluded that neither the advanced martitization, nor the martite shape alteration due to dissolution are important factors changing AMS axes distribution in the laterite.

2.6.4.2 *Type 1 – foliated granite (S_1)*

Type 1 is characteristic for the S_1-foliated granites in the lower part of the profile. κ_3 is subparallel with the NW-SE trending and shallowly inclined S_1-foliation poles. κ_1 plunges medium steeply in SW direction. The magnetic lineation parallels the SW plunging constructed intersection lineation of S_1 sets (Figure 2.3.b). AMS ellipsoid shapes are mostly oblate ($T < 0.5$) and eccentricity is high in comparison to other types (P' = 1.07 to 1.12).

As observed for AMS-type 0, type 1 is also preserved up to the lateritic horizons. Type 1 is differentiated from type 0 by a ca. 30° differing declination of the axes and the stronger oblate (1.04 to 1.12) ellipsoid shapes. The correlation between κ_1 and the constructed intersection lineation is interpreted as being induced by superposition of similar oblate subfabrics (e.g. Borradaile 1988); also Figure 1.9.b). In case of superimposing planar fabrics, a magnetic lineation develops pointing in the direction of the intersection lineation of the two planar fabrics (Figure 1.9.a,b). As in type 0, magnetite interaction of magnetites inside and between martite grains define these subfabrics. Although image analysis is not carried out on AMS-type 1 sample, this conclusion is drawn, because there are no magnetomineralogical differences between granites of type 0 and 1, with respect to magnetite. SPO of the weakly flattened martites parallels the tectonic foliation surfaces (S_1). This preferred orientation of martites parallel with S_1-surface increased the eccentricity P' of the AMS ellipsoids.

Diagenetic compaction fabrics affected the magnetic fabric in lateritic samples and consequently, a composite AMS pattern developed (AMS-type 1/2: chapter 2.6.4.4).

2.6.4.3 *Type 0/1 – S_1-fabric overprinting S_0-fabric*

AMS-type 0/1 represents a magnetic fabric that displays characteristics of the first two fabrics, type 0 and 1. This type is established in unweathered granite inside the corestone (RA1-5a) and in weathering-breccias throughout the saprock and saprolite zone. The magnetic lineation κ_1 dips to the NE in AMS-type 0/1 and the magnetic foliation poles κ_3, located in the SW and NW quadrants of the stereonet, slightly girdle on the great circle of κ_1 (Figure 2.30.b). The high κ_{bulk} of > $600 \cdot 10^{-6}$ SI in the unweathered corestone granite implies, as determined for type 0, that martite shapes influence the distribution-anisotropy of magnetite remnants. The "L-tectonite"-like fabric of the corestone granite is defined by two sets of differently oriented but similarly developed foliations (Figure 2.30.a). κ_1

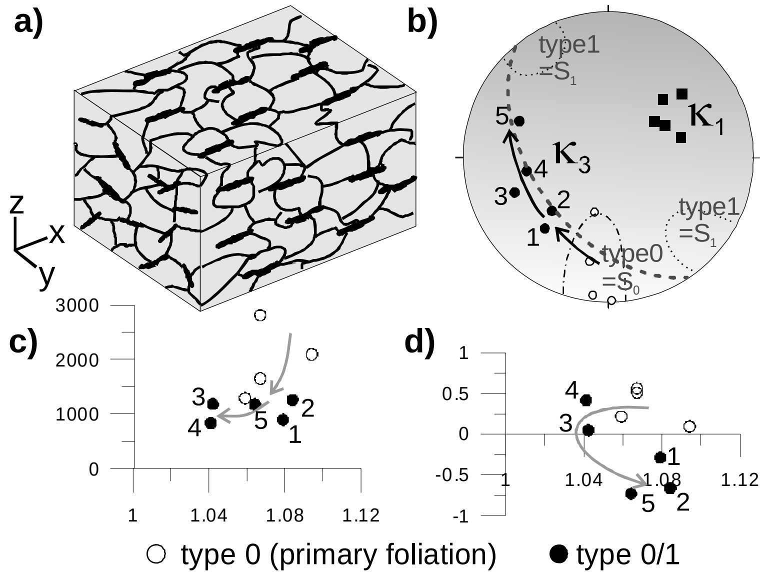

Figure 2.30: AMS-type 0/1, as it is developed in fresh granite from the corestone (sample RA1-5a), interpreting the magnetic fabric as a composite fabric defined by AMS-type 0 and 1. a) displays the granite texture dominated by intersection lineation of subfabrics S_0 and S_1 (petrographic lineations exaggerated); b) is the AMS projection (lower hemisphere) with κ_3 of type 0/1 between κ_3 of type 0 and 1; c+d) are the ellipsoid parameters indicating superposition by low P' and low to negative T. The arrows follow path from type 0 to type 0/1.

correlates geometrically with the x-axis (lineation) of the composite rock fabric. Foliations incorporated in the rock show a distribution of poles on the same great circle of κ_1. Consequently, the generation of a magnetic superposition fabric of "primary" rock foliations is likely. These foliations are S_0, the primary granitic foliation (subvertical E-W) and S_1 (subvertical SW-NE). The proposed evolution of the superposition of S_0 with S_1 surfaces is shown in Figure 2.30.c,d. Superposition is indicated comparing the ellipsoid parameters of type 0/1 with the parameters of the AMS-types 0 and 1: P' values are small and shapes are spherical to prolate ($T < 0$), whereas both type 0 and type 1, show high P' values and oblate shapes ($T > 0$). The decreasing parameter path, which is commonly observed in composite fabrics (Borradaile 1988; and Figure 1.9.a,b) is displayed.

Comparing the AMS of weathering-brecciated rocks with the corestone granite of AMS-type 0/1, a similarity of AMS axes distribution is observed: κ_3 scatter along a great circle of the well-clustered NE-NNE trending κ_1-axis. It is inferred that the AMS-type 0/1 is the precursor of the magnetic fabric of weathering-breccias. The relative imprint intensity of type 0 and type 1 differs between the weathering-brecciated samples leading to a girdling of κ_3 on the great circle. The well-clustered κ_1 of the generally oblate AMS fabrics is a result of the superposition of two fabrics. The κ_3-girdling of oblate specimen is interpreted to be a result of the scale of fabrics exceeding the specimen size (Figure 1.9.e,f).

2.6.4.4 Type 1/2 – lateritic compaction cleavage S_2 overprinting S_1

AMS-type 1/2 is a magnetic fabric, which occurs exclusively in the laterite. κ_1 is horizontally NNE oriented and κ_3 changes gradually between the poles of foliation S_1 and the unconformity parallel compaction fabric S_2 (Figure 2.29). This specific AMS fabric is the result of the superposition of S_1 and S_2 surfaces (Plate 2.1.f). Anisotropy degrees are very low ($P' < 1.04$) although shapes are distinctively oblate ($0 < T < 0.6$). Ellipsoid shapes scatter between oblate and prolate ($-0.7 < T < 0.7$).

Martitization is advanced in the laterites (as discussed in 2.5.4 and 2.6.1), thus the density of magnetic remnants in each martite is reduced. The combination of a weak magnetite anisotropy and high paramagnetic anisotropy characterizes the AMS ellipsoids in type 1/2. This results in low eccentricities ($P' = 1.01$ to 1.02) but well defined oblate ellipsoid shapes and distinct κ-axes distribution.

The samples showing AMS-types 1/2 indicate a deformation sequence, in which the rock fabric of the uppermost decimetres of the lateritic zone changes. In RA2-2 (0.5 metres beneath the unconformity), foliation S_1 dominates the magnetic foliation, whereas in RA2-1 (0.2 metres), the subhorizontal diagenetic foliation S_2 influences the orientation of κ_3-axes. Foliation S_2 overprints S_1 causing one stable resulting magnetic lineation in the direction of the intersection lineation. The AMS parameters κ_3-inclination and P' can be compared with the compaction gradient within the laterite (Figure 2.24.h). The AMS data are associated with the S_1-foliation, which is undeformed beneath the laterite (RA1-1a) and deformed by compaction within the laterite (RA2-1b, RA2-2, RA2-3). According to this, κ_3 is shallowly plunging in the saprock up to the lower laterite. A gradient of κ_3-inclination (i.e. decreasing inclination of the magnetic foliation) within the laterite corresponds well to the gradient of vertical compaction. It appears that P' is not linked to the variation of κ_3-inclination, showing a decrease in the saprolite-laterite transition, but no significant change from lower to upper laterite. This is attributed to the complex relation of the AMS ellipsoid shape to the superposition of subfabrics (Figure 1.9.a,b) and, as mentioned, to κ_{bulk}.

2.6.4.5 Type 3 – cataclasis

AMS-type 3 is the magnetic fabric developed in the cataclasites. Characteristically, this AMS fabric has a girdle distribution of κ_3-axes and vertically clustered κ_1-axes (Figure 2.29). A high scattering of ellipsoid shapes between oblate and prolate ($-0.7 < T < 0.7$) and a moderate to low anisotropy degree ($P' < 1.08$) is evident. As inferred by petrographic, κ(T) and image analyses, the main magnetic carriers are magnetite (comparable to the granite). Cataclasis is characterized by matrix supported texture and the development of discrete subvertical foliation surfaces (Plate 2.1.g,h). Pre-cataclastic fabrics are not preserved in the fine-grained cataclastic matrix. Martite suffered cracking or total destruction (Plate 2.5.b,c). Grain size reduction of martite and accompanied reordering of magnetite particles led to a change of the AMS fabric during cataclasis.

Generally, cataclasis initially leads to an obliteration of magnetic anisotropies (Just et al. 2004, Nakamura & Nagahama 2001). Subsequently, clasts alignment (cataclastic flow) or pressure solution causes the formation of secondary planar fabrics and consequently new AMS fabrics.

AMS-type 3 is interpreted by a model, in which subvertical cataclastic foliation surfaces superpose each other. The SPO of martites are preferentially oriented parallel with the cataclastic flow direction and pressure solution seams (S_3). Consequently, a combination of a shape-anisotropy by non-interacting magnetite and distribution-anisotropy by interacting magnetite in martite defines the vertical magnetic foliation, which parallels rock foliation surfaces or is located in an intermediate position. One major set of cataclastic foliation developed, striking about E-W. This set is reflected by predominantly N-S trending κ_3. Microcrystalline haematite accumulated along the S_3 foliation surfaces and may influence the magnetic anisotropy.

2.6.4.6 Type 2/3 – superposition in the mottle zone

Cataclasites and rocks with significant imprint of cataclastic foliations in the uppermost saprock zone and the saprolite-laterite boundary (mottle zone) predominately incorporate a magnetic fabric that is different from cataclastic AMS-type 3. This AMS-type 2/3 is characterized by steep magnetic foliations, similar to type 3, and subhorizontally oriented and E-W trending magnetic lineations (Figure 2.29). Although axes distribution is remarkably similar to AMS-type 0, both types are not directly related, since AMS-type 0 is not affected by cataclasis. Bulk susceptibility and P’ of type 2/3 is much lower ($\kappa_{bulk} < 500 \cdot 10^{-6}$ SI; $P' < 1.05$) than in the type 0 granite. T-values strongly scatter between -0.5 to +0.5, showing a systematic change from oblate to prolate with proximity to the upper saprolite boundary.

Compaction and cataclasis destroyed the primary granitic texture. The cataclasis-induces cataclastic flow and shear surfaces and the subhorizontal compaction cleavage, locally preserved between the oblique cataclastic foliation (Figure 2.5.a), create a composite fabric, which is reflected by the AMS fabric. The horizontal direction of the magnetic lineations is not related to a horizontal cataclastic flow, since kinematics markers indicate rather a vertical movement. The orientation of κ_1 is rather an effect of superposition of horizontal compaction (S_2) and a dominant vertical E-W trending cataclastic foliation (S_3). The gradient of T from oblate to prolate reflects the increasing imprint of the horizontal compaction fabric on bulk AMS. This increasing imprint leads to a more pronounced intersection lineation and consequently magnetic lineation, although significant changes of axes orientation are missing.

To summarize, the AMS reveals that the imprint of the diagenetic compaction reaches down to the lower saprolitic boundary, showing a decrease in influence. Ccataclasis led to the development of new magnetic fabrics related to sets of cataclastic foliations, which dominantly parallel primary foliation surfaces S_0 and S_1 Thus, reactivation of these granitic foliations may have played an role during cataclasis.

2.7 Alteration and fabric evolution of the Roded weathering profile

This chapter summarizes the timing of the alteration and deformation events observed in the weathering profile of the Roded Granite. Figure 2.31 summarizes the evolution of mineral alterations. The associated changes in the κ_{bulk} and AMS are shown in Figure 2.32.

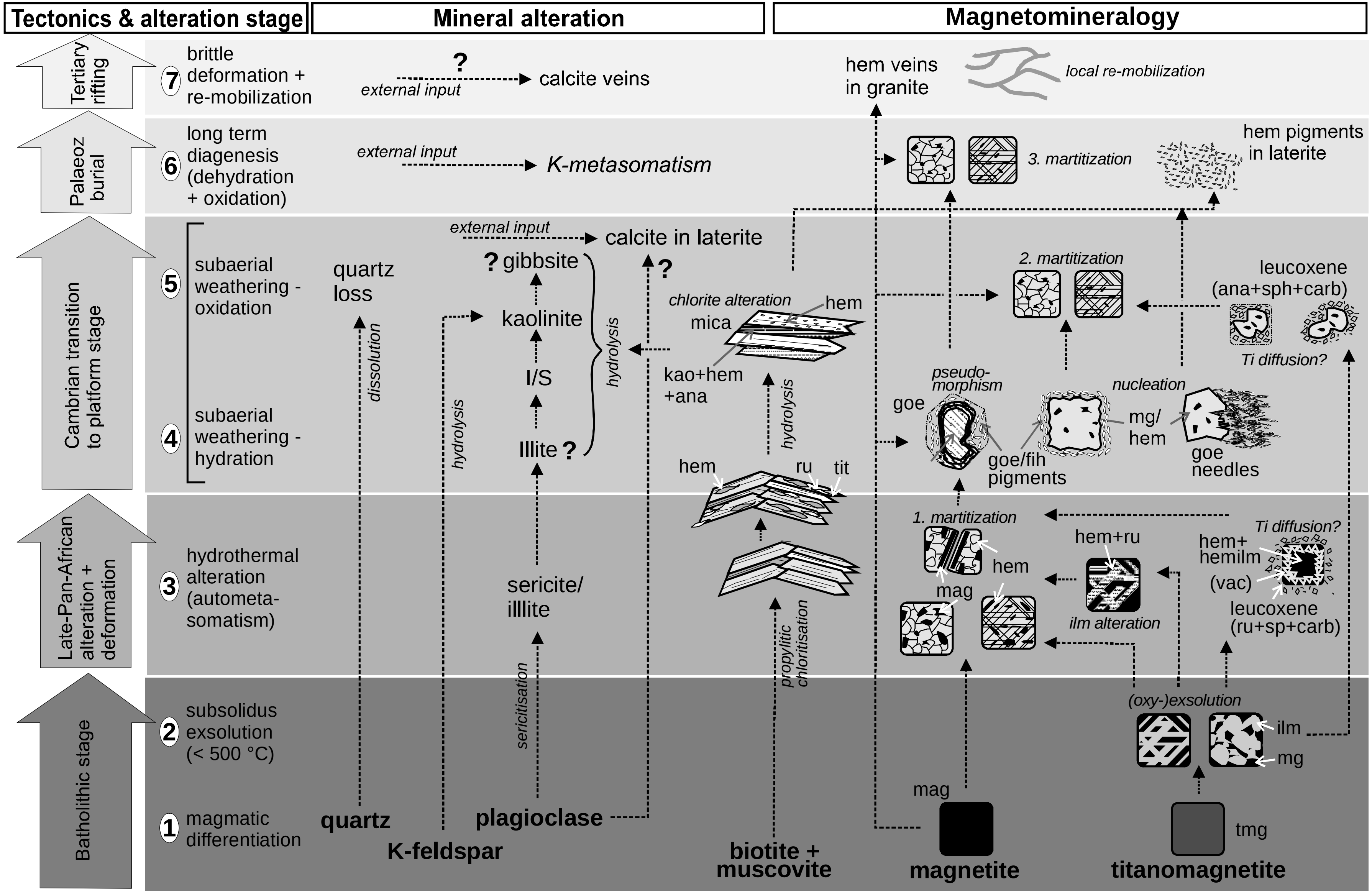

Figure 2.31: The stages of mineral alteration in the Roded weathering profile. mag=magnetite, hem=hematite, tmg=titanomagnetite. ilm=ilmenite, goe=goethite, fih=ferrihydrite, kao=kaolinite, ana=anatase, bio=biotite, chl=chlorite, mus=muscovite, ru=rutile, tit=titanite, carb=carbonate, (vac)=vacancy.

2.7.1 *Late Pan-African emplacement, autometasomatism and subsequent deformation*

The Roded Granite was emplaced during the late Pan-African orogenesis (stage 1 in Figure 2.31). Four pervasive alterations observed in the granite are considered as related to early processes: a) exsolution of titanomagnetite to ilmenite and magnetite (stage 2), b) chloritization, c) sericitization and d) martitization (all stage 3). All described reactions may have been realized simultaneously or subsequently under the same hydrothermal conditions. The dissolution of oligoclase enriched the fluid with Ca, which possibly was incorporated, together with Ti from biotite, into titanite (Eggleton & Banfield 1985); and Plate 2.2.d). K-cations probably deriving from the biotite alteration were used for illite formation during sericitization. Since no external sources of elements were needed for reaction, the system can be considered as an autometasomatic (deuteric) system (Wimmenauer 1985). These deuteric conditions existed during the cooling phase of the pluton (300 °C or higher).

During the phase of hydrothermal martitization, magnetic susceptibility decreased from a (modelled) initial value of $1.2 \cdot 10^{-2}$ SI down to values observed in the unweathered granite ($> 1000 \cdot 10^{-6}$ SI). Later martitization led to further decrease of κ_{bulk} in the unweathered granite.

The exhumation setting of the Roded block intrusions, dominated by retrograde metamorphism, is associated with a shallow intrusion (5-9 km) during the latest orogenic phase of the Arabian-Nubian Shield (Katz et al. 1998). The minimum upper greenschist facies deformation in the Roded Granite indicates a very high geothermal gradient in those shallow crustal depths. Deformation took place in all intrusions of the Roded Block during the initial pluton cooling (Katz et al. 1998) and persisted during the exhumation path with decreasing P/T-conditions, outlasting perhaps the entire hydrothermal stage. The final stage occurred at the minimum temperature for static quartz recrystallization (ca. 270 °C).

In the macroscopically undeformed granite, the revealed S_0 is interpreted as a cryptic magmatic flow fabric generated during syn-kinematic crystallization. AMS-type 0 is the result of this process (Figure 2.32). According to the steep chlorite and martite cluster SPO (see chapter 2.6.3.1), flow direction was in horizontal E-W direction and accompanied by a minor horizontal compression. The intracrystalline deformation features in the granite indicate that magmatic flow was still in progress when subsolidus temperatures were reached. Horizontal compression continued, with slightly changed directions, resulting in the development of NW-SE striking S_1. Deformation occurred non-pervasively, leading to partial preservation of S_0. The aplite dyke (see chapter 2.2.2.1), which intruded into the granite, was deformed by S_1. Therefore, D_1 foliation can be considered truly post-intrusive. A horizontal E-W shortening of the late Pan-African deformation has been demonstrated in the Roded block (Katz et al. 1998). S_1 orientation in the rocks supports this regional Pan-African stress pattern. The AMS-type 1 is associated with this foliation (Figure 2.32).

Similar two-stage configuration revealed by AMS and field observations is reported for other regions (e.g. Egleton granite: Henry 1988).

Alternatively, S_0 and S_1 could have been realized simultaneously in a strike-slip regime. In this case, the subvertical magnetic foliation of type 0 represents a weak C-surface, with its subhorizontal shear direction (WNW-ESE) represented by the subhorizontal magnetic foliation κ_1. S_1 surfaces inclined with ca. 30 to 40° to S_0 (C-surfaces), represent the S-surfaces. In this case, compression direction did not change during the entire deformation process and kinematics of this strike-slip shear zone would be dextral. Ductile dextral strike-slip features are reported for the Roded block, in form of E-W trending discordant schistose dykes intruding syn-kinematically into the late Roded quartz-diorite (Bogoch et al. 2002). Pervasive ductile strike-slip deformation is assumed for the Roded Granite and quartz-diorite, but remains undemonstrated (*pers. comm.* Dov Avigad). Other syn-kinematic granitoid intrusions in transpressional regimes show similar domain-like distributed transcurrent and compressional features (e.g. Pyrenees: Gleizes et al. 2001, Gleizes et al. 1998), elsewhere revealed by means of AMS (e.g. Variscan crystalline: Greiling & Verma 2000).

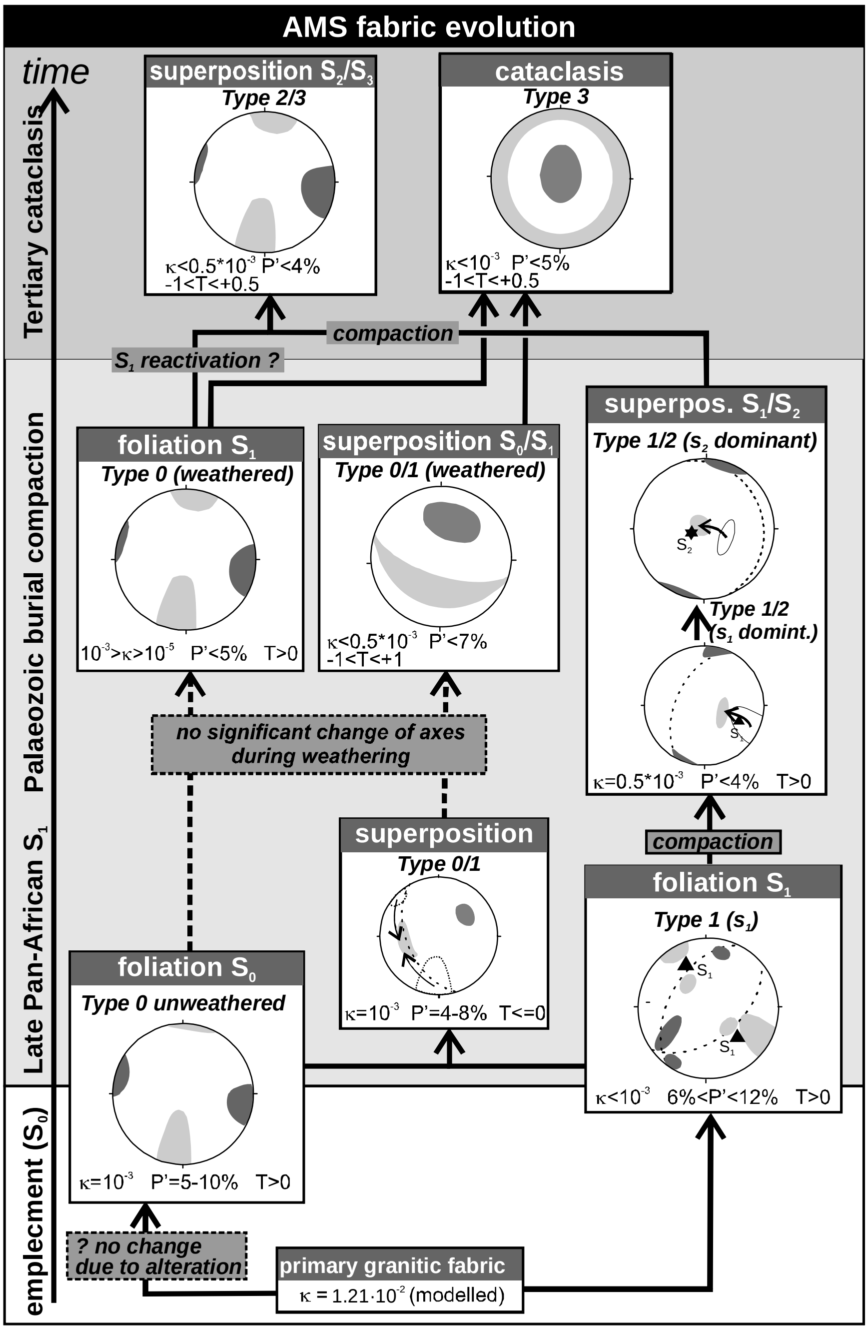

Figure 2.32: The evolution of the AMS in the Roded palaeoweathering profile. The magnetic fabric of the primary unaltered granite is not preserved; its κ_{bulk} is modelled (chapter 2.3.3).

2.7.2 Cambrian peneplanation and subaerial weathering (palaeoclimatic implications)

Sub-aerial weathering and peneplanation of the Roded Granite (stages 4 and 5) followed the transition from the orogenic to platform stage in the early Cambrian time (Garfunkel 1999, 2002). A weathering profile consisting of moderately weathered saprock (>15m to), saprolite (with pallid and mottle zone) (4 m to 0 m) and laterite (2.5 m to 0 m) is developed.

The following alteration products, approaching the unconformity from below, are attributed to the Cambrian subaerial weathering: (a) smectite due to hydrolysis of plagioclase in illite/smectite mixed-layer minerals (I/S), (b) Kaolinite due to hydrolysis of feldspars and chlorite, (c) microcrystalline anatase along basal surfaces of Fe/Mg-mica, (d) microcrystalline haematite by progressive chlorite and magnetite breakdown and (e) titaniferous leucoxene rims around martite.

All interpretations concerning climatic conditions during palaeoweathering have to be taken with care, since alterations during Phanerozoic time occurred and partially changed geochemical signatures, K-metasomatism, calcification and Fe-mobilization. The lateritic ferricrete with associated pallid zone underneath are indications for a warm and humid climate during weathering (Das 1982, Raja 2001, Stephens 1946, Subramanian 2002, Tardy 1993, Tardy et al. 1995), but are also described from arid to semi-arid zones (e.g. Firman 1994). An acidic and oxidizing meteoric fluid led to silicate hydrolysis and magnetite dissolution. The lateral groundwater flow beneath the laterite produced the pallid zone and presumably the zone of weathering-brecciation beneath with repeated infiltration of water. This repeated infiltration may be the result of periodical rainfall (Watson 1992) or major vertical fluctuations of the groundwater level. Those (seasonal?) groundwater level variations are typical for semi-arid climates. It may therefore indicate a change of climatic conditions from a tropic to (semi-) arid climate. The haematite and calcite precipitation in the laterite (Plate 2.3.e-h), the desert pavement on top of the eroded saprolite (Figure 2.4.a) and the laterite-conglomerate mixing zone on top of the remaining laterite (Figure 2.4.b) may be expressions of a (semi-) arid or arid climate following the humid climate forming the laterite. Haematite is commonly observed as a dehydration product of goethite under higher temperature and lower or stable water activity (Tardy et al. 1990). Calcite (allochthonous) in the laterite matrix may derived from evaporates (Watson 1992). The surficial formation of loose pebble layers (desert pavement) is understood as a feature on peneplains in arid climates (e.g. McFadden et al. 2005, Wood et al. 2005). The laterite-conglomerate mixing zone (soil-sediment) may be interpreted as a wadi-type deposit, which commonly is observed in deserts valley after sporadic but intense rainfall (Al Faraj & Harvey 1997).

As discussed in chapter 2.5.1, cryoturbation might have been a possible process leading to weathering-brecciation. In this case, it has to be considered that a major change of climate from cold to tropic during the time interval of subaerial exposure of the granite occurred. In terms of the worldwide climatic changes during the late Neoproterozoic time, a cold climate can be discussed (see chapter 1.2). The opposite climate trend (warm to cold) is less likely, since the laterite on top of the weathering-breccia does not show any profound change due to cryoturbation.

The unconformity crosscuts the saprolite-laterite boundary, i.e. the entire laterite horizon was locally eroded. Adjacent to the unconformity, saprolites have mineralogical and geochemical signatures different from laterites. This shows that the intensity of alteration and fabric development in the weathering profile is related in the first place to the weathering stage (lithology) and secondarily to the distance to the unconformity.

Weathering-induced dissolution of magnetite is an important factor for changing κ_{bulk}. A general decrease of κ_{bulk} is associated with increasing weathering intensity beneath the laterite. The κ_{bulk} of the “ideally altered”, magnetite-free saprolite is $25 \cdot 10^{-6}$ SI (Table 2.1). Measured susceptibilities of the pallid zone are slightly higher due to minimum relics of magnetite (ca. $50 \cdot 10^{-6}$ SI). Alteration processes affecting magnetite intensified in the laterite, however, the passive enrichment of magnetite (or martite) and Fe/Mg-mica causes a net increase of κ_{bulk}. Martitization which effectively lowered κ_{bulk} (see chapter 2.5.4), occurred during weathering, but is a process that began earlier (hydrothermal stage) and presumably continued during early burial stage (van Houten 1973).

The possibility of a preservation of granitic fabrics and related ferrimagnetic AMS through the weathering profile is demonstrated (chapters 2.6.4.1, 2.6.4.2, 2.6.4.3). Parameters defining the shape of the AMS ellipsoids (P’, T) are subject of change, mostly because of weathering-brecciation, magnetite dissolution and martitization. Sub-surface physical weathering (weathering-brecciation) in saprock and saprolite led to a dissemination (girdling) of magnetic foliation on a great circle of the magnetic lineation. Chemical weathering in saprock, saprolite (including pallid and mottle zone) and laterite, however, has a minor influence on the principal AMS axes orientation (Figure 2.32).

2.7.3 Burial stage and compaction

With the onset of the Cambrian sedimentation, basal conglomerates and sandstones were sedimented on top of the weathered basement (stage 6).

Microcrystalline haematite may be a product of aggregation, dehydration, and internal structural rearrangement of goethite (or other Fe-hydroxides, such as ferrihydrite) under diagenetic conditions (van Houten 1973). Diagenetic conditions facilitated this dehydration process.

During burial stage, the laterite was compacted to 0.73 of the original thickness (see chapter 2.2.5). According to the burial-depth-curve of (Sheldon & Retallack 2001), a maximum burial depth of 2.8 ± 0.1 km was reached under the assumption that the initial (“pre-compaction”) porosity ϕ_w was 0.40 (see chapter 2.5.6.1).

K-metasomatism, as indicated by the absolute enrichment of rocks with K, took place during burial stage (e.g. Nesbitt & Young 1989 and references therein). K-enrichment increased with proximity to the unconformity and maximum enrichment is observed in the pallid zone. Because of its clayey texture, the laterite horizon itself was only slightly influenced, because of the reduced porosity and assumable very low permeability and hydraulic conductivity.

Burial compaction did not effectively influence κ_{bulk} (Figure 2.24.g), which is possibly an indication that κ_{bulk} is exclusively defined by weathering processes. The burial compaction in the laterite influenced the AMS, as described in chapter 2.6.4.4 (Figure 2.32).

2.7.4 Tertiary tectonics and related fluid flow

The cataclasis (and accompanied jointing) in the Roded weathering profile, as the latest pervasive structural overprint in granite evolution (see chapters 2.2.7, 2.2.8, 2.5.7), is related to the Tertiary Dead Sea Rift. Cataclasis, strike-slip faulting and jointing have approximately same structural orientations. A simultaneous development has to be considered. All these brittle deformation features overprint and therefore postdate the burial compaction of the laterite (Figure 2.5.b,c). Steep primary foliations S_1 was reactivated during cataclasis.

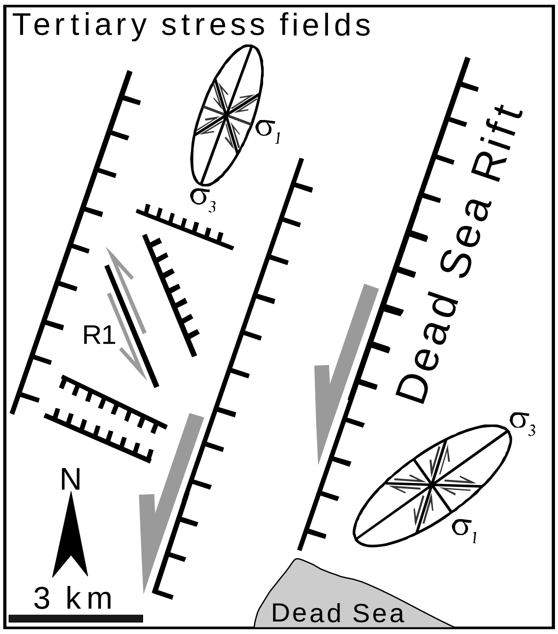

Figure 2.33: Possible transtensional palaeostress fields in the western shoulder of the Dead Sea Rift with corresponding tectonic features observed in the Roded outcrop and taken from Eyal et al. 1981.

The NNW-SSE trend of the main joint set and the strike slip faults are features of the structural regional Tertiary tectonic pattern (Eyal et al. 1981). The vertical displacement and shear-sense indicators on surfaces, such as reactivated S_3, suggest normal faulting (Figure 2.5.a, c). A transtensional palaeostress field can be inferred by a NNE-SSW directed extensional component and a SSE to NNW directed strike-slip component. Sinistral strike slip faulting accompanied by normal faulting is described as a major tectonic pattern for the Dead Sea Rift (Eyal et al. 1981). The transtensional palaeostress may be related to the overall Dead Sea Rift probably as a second order Riedel-shear pattern (R1 in Figure 2.33).

The vertical magnetic lineation associated with the cataclasite is unique in the profile (Figure 2.32). The orientation is attributed to superimposed sets of vertically oriented S_3-cleavage surfaces and parallel cataclastic flow domains. Partly, these planar fabrics re-activated S_0 (and S_1) surfaces.

A late stage fluid flow pervasively infiltrating the rocks through veins is supposed to be cogenetic to cataclasis (stage 7). The fluid mobilized iron and possibly other element, but a significant change of the whole-rock geochemistry did not occur, as local reprecipitation took place (see chapter 2.5.4).

There are no evidences of a late hydrothermal overprint in the weathering profile of the Roded Granite. However, Tertiary (13-15 Ma) hydrothermal alteration, induced by the infiltration of basinal brines, has been reported from the Timna block, 15 km north of the Roded Granite (Beyth et al. 1997). The surrounding Palaeozoic sediments are the assumed source of the fluids are. Crustal thinning during the Dead Sea Rift probably generated fluid temperatures of 250-300 °C, which may have affected also the Roded block (Beyth et al. 1997).

2.8 Conclusions

Four main stages of evolution are observed in the weathering profile of the Roded Granite:

1) Syn-kinematic emplacement: A cryptic subvertical E-W trending foliation S_0 developed under at least higher greenschist facies metamorphism, followed by a post-intrusive steep vertical SW-NE trending gneissic foliation S_1. This indicates a two phased late syn-intrusive to post-intrusive deformation succession, probably within a transpressional deformation regime. Autometasomatic hydrothermal alteration comprised propylitic chloritization, sericitization and a first martitization phase (*hydrothermal martitization*).

2) Late Neoproterozoic to Early Cambrian weathering: weathering conditions were initially warm and humid and changed to (semi-) arid. The saprock is characterized by sub-surface physical weathering-brecciation. Chemical weathering, attributed to the humid and warm stage, is important above the saprock, producing a sequence of saprolite with pallid zone, mottle zone and ferricrete laterite. Main processes were hydrolysis of silicates, SiO_2- and partly Al-leaching and dissolution of magnetite. A downward sequence of kaolinite - I/S mixed-layered clays - illite developed during weathering. A subsequent arid stage produced calcite and haematite precipitation in the laterite matrix, martitization (*weathering martitization*) and the basal cover rocks (wadi-deposit and desert pavement).

3) During burial stage, the laterite was vertically compacted to 73 % of its original thickness under a sedimentary load of 2.8 ± 0.1 km (calculated with burial-depth-compaction curve). This compaction was accommodated by a macro-porosity decrease and by a development of an unconformity-parallel cleavage (S_2). The S_2-imprint increases its intensity with proximity to the unconformity; locally it reaches down to the lower saprolitic boundary, facilitated by the disintegration due to weathering-brecciation. The compaction is of plane strain nature, involving volume decrease of the upper laterite part and horizontal extension in NW-SE direction, perpendicular to the strike of the primary fabrics S_1. This horizontal extension caused a minor reactivation of the basement-cover-interface, or at least a pronunciation of unconformity-parallel fabric in the upper dm of the laterite. During the entire burial stage diagenetic conditions have never been exceeded. Long-term diagenesis led to an almost complete martitization (*burial martitization*) of magnetite. K-metasomatism is displayed by a gradient of K-enrichment with proximity to the unconformity, whereas the clay-rich laterite was not involved, as it acted as an aquitard characterized by lower permeability.

4) Tertiary cataclastic deformation and alteration are presumably related to the Dead Sea Rift. In the western graben shoulder, a transtensional palaeostress field might have been the reason for simultaneous formation of NNW-SSE strike slip faults and W-E trending normal faults (with related cataclasis in granite, saprolite and laterite). Fluid controlled alterations comprised mobilization and local reprecipitation of iron, as well as carbonate precipitation in rock matrix and veins.

A ferrimagnetic κ_{bulk} dominates in rocks beneath the laterite. A general decreasing trend of κ_{bulk}, from an assumed primary value of $> 10^{-2}$ SI in the hypothetically unaltered granite down to $< 100 \cdot 10^{-6}$ SI in the pallid zone, is due to magnetite dissolution associated with weathering and progressive martitization (three stages). In the laterite, κ_{bulk} increased with weathering and burial compaction, because both processes caused an enrichment of magnetic carriers, mostly antiferromagnetic haematite and relic paramagnetic Fe-Mg-mica. Brecciation and laterite-formation are weathering processes, which do not directly influence the AMS-axes but do modify κ_{bulk} and AMS-ellipsoid shapes. A correlation between P' and weathering intensity is observed. The main influencing factor for the AMS evolution is the structural overprint (S_1 to S_3) causing specific AMS fabric types. Locally, magnetic subfabrics superpose each other. In the laterite, superposition of the relic primary foliation and the unconformity-parallel compaction-cleavage led to flat-lying κ_1-orientations and rotation of κ_3 to a vertical position. Magnetic interaction of magnetites, which carry κ_{bulk} and AMS, is a significant fabric-defining characteristic in less martitized rocks (unweathered granite). Magnetite distribution-anisotropy can mimic the SPO of martite clusters, which parallel the dominant petrofabrics (foliations).

Plate 2.1: (Textures, page 89) a) hand specimen photograph of macroscopically undeformed granite (RA3-1, long side 8 cm); **b)** AMS-cylinder of the foliated granite (RA1-1a, 2.8 cm); **c)** hand specimen of the weathering-breccia, with relatively fresh microcline (flesh colour) in weathered plagioclase (brown) matrix (RA1-5b, 10 cm); d**)** AMS-cylinder of a saprolite, which shows a weak foliation (RA1-7, 2.8 cm); **e)** the laterite texture with a preferred orientation of micas (RA2.1b, 4.85 mm); **f)** SEM-micrograph of a laterite zone with preserved crenulation cleavage, flat-lying S_2 overprinting steep S_1 (RA2-1b); g) hand specimen of a red cataclasite (RA1-4a, 11 cm); h) micrograph of the haematite-rich cataclastic texture with vertical S_3-seams (RA1-4a, 4.85 mm)

Plate 2.2: (Alterations 1, page 90) a) micrograph of the texture of the unweathered granite (sample RA3-1; long side: 4.85 mm); **b)** texture of the aplite lens/dyke (RA1-1.b, 4.85 mm); **c)** fresh microcline with twinning and undulatory extinction (RA3-1, 1.4 mm); **d)** SEM-micrograph of a chlorite-mica-stack (RA3-1), light grey is biotite, darker grey is chlorite; **e)** micrograph of chlorite with haematite inclusions (RA3-1, 0.54 mm); **f)** SEM-micrograph of chlorite with haematite inclusions (RA3-1); **g)** chlorite alteration (weathering) to layers of kaolinite and haematite-rutile/anatase-titanite symplectites (RA1-2, SEM); **h)** detail of g (SEM)

Plate 2.3: (Alterations 2, page 91) a) micrograph of texture of a saprolite with fresh microcline and kaolinite matrix (sample RA1-7, long side: 4.85 mm); **b)** SEM-micrograph of the “weathering-brecciated” saprolite texture, mainly consisting of a kaolinite + $CaCO_3$ matrix, Fe/Mg-mica-kaolinite stacks, quartz and relic K-feldspar (RA1-7); **c)** detail of (c) showing a rutile/anatase inclusion in Fe/Mg-mica (SEM); **d)** laterite texture dominated by Fe/Mg-mica and kaolinite (RA2-1b; 1.4 mm); **e)** kaolinite-haematite matrix in the laterite (RA2-1b, SEM); **f)** micrograph of deformed calcite vein in cataclasite (RA1-4a, 4.85 mm); **g)** detail of recrystallized calcite in a vein (RA1-4a, 1.4 mm); **h)** cement calcite (RA1.4a, 1.4 mm)

Plate 2.4: (Magnetomineralogy 1, page 92) a) martite cluster in chlorite-mica stacks (chlorite is red due to haematite inclusions), (sample RA1-4a, long side is 1.4 mm, crossed nicols); **b)** single euhedral martite in the laterite displaying optical anisotropy under reflected light and crossed nicols (RA2-1b, 0.69 mm); **c)** SEM-micrograph of a martite with altered Ti-rich lamellae (RA3-1); **d)** SEM-micrograph (high contrast) of a martite with altered zones due to Ti-diffusion(?), vicinity (black) is leucoxene (RA-3-1); **e)** martite cluster with applied ferrofluid indicating magnetite remnants, which parallel crystallographic orientation (RA3-1; 0.54 mm); **f)** same under crossed nicols, demonstrating optical anisotropy of martite and related leucoxene and haematite veins (RA3-1, 0.54 mm); **g)** detail of a martite with irregular magnetite distribution (RA3-1, 0.54 mm); **h-j)** examples of martite shapes and magnetite remnants.

Plate 2.5: (Magnetomineralogy 2, page 93) a) texture of martite (after magnetite dissolution), leucoxene and microcrystalline haematite in a lateritic kaolinite matrix (sample RA2-1b, long side 0.69 mm); **b+c)** cataclastically deformed martite in a saprolite (RA1-7, 1.4 mm); **d)** advanced martitization of magnetite in the saprolite (RA1-7, 1.4 mm); **e)** SEM-micrograph of goethite after magnetite alteration in the laterite (RA2-1b, SEM); **f)** titaniferous Fe-hydroxide (goethite?) with myrmekite-like alteration (RA2-1b, SEM); **g)** detail of f; **h)** needle-shaped goethite (RA2-1b, SEM); **i)** detail of h, revealing haematite crystallization at the goethite crystal-rims

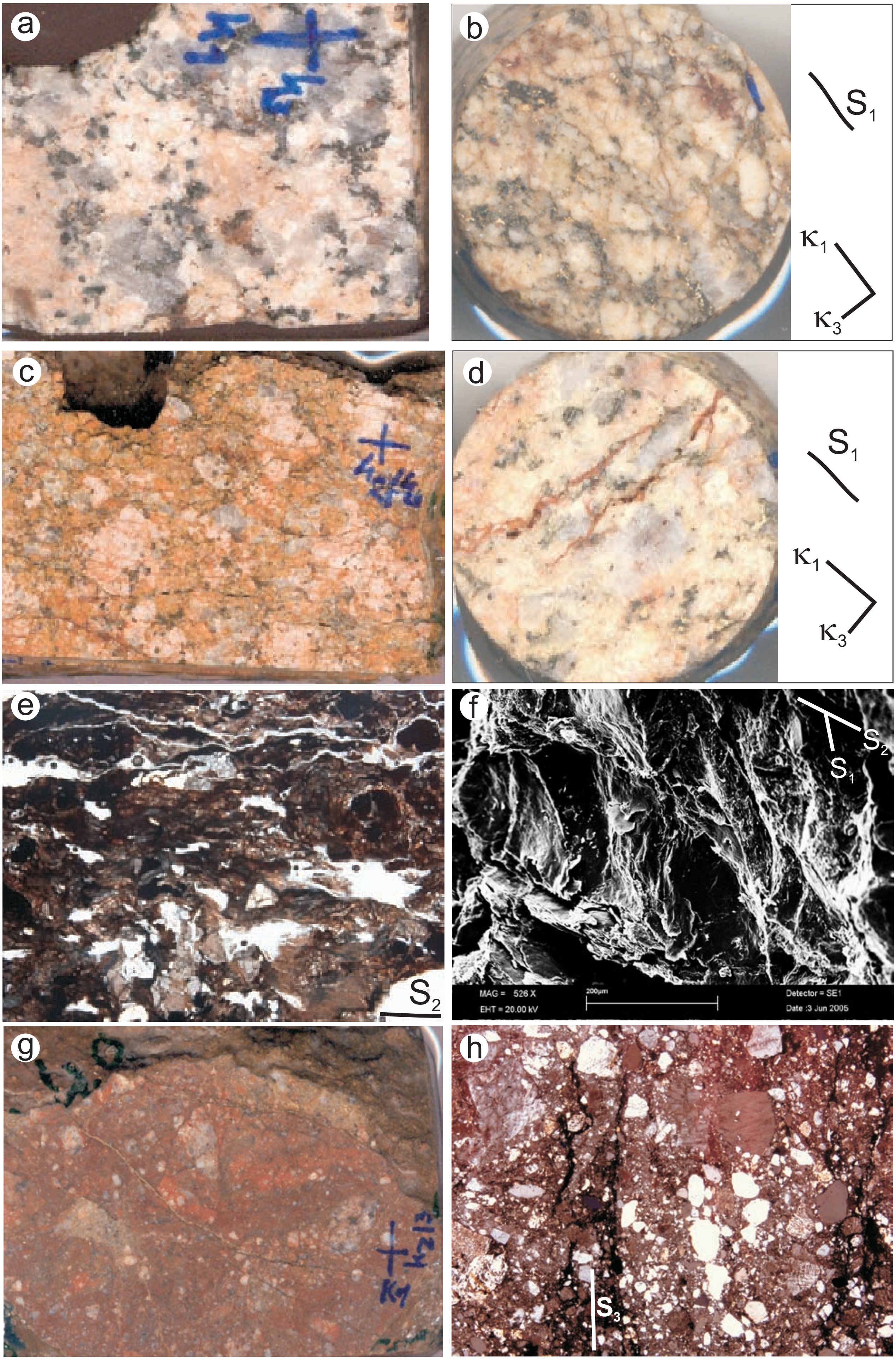

Plate 2.1.a-h (Textures, caption see page 88)

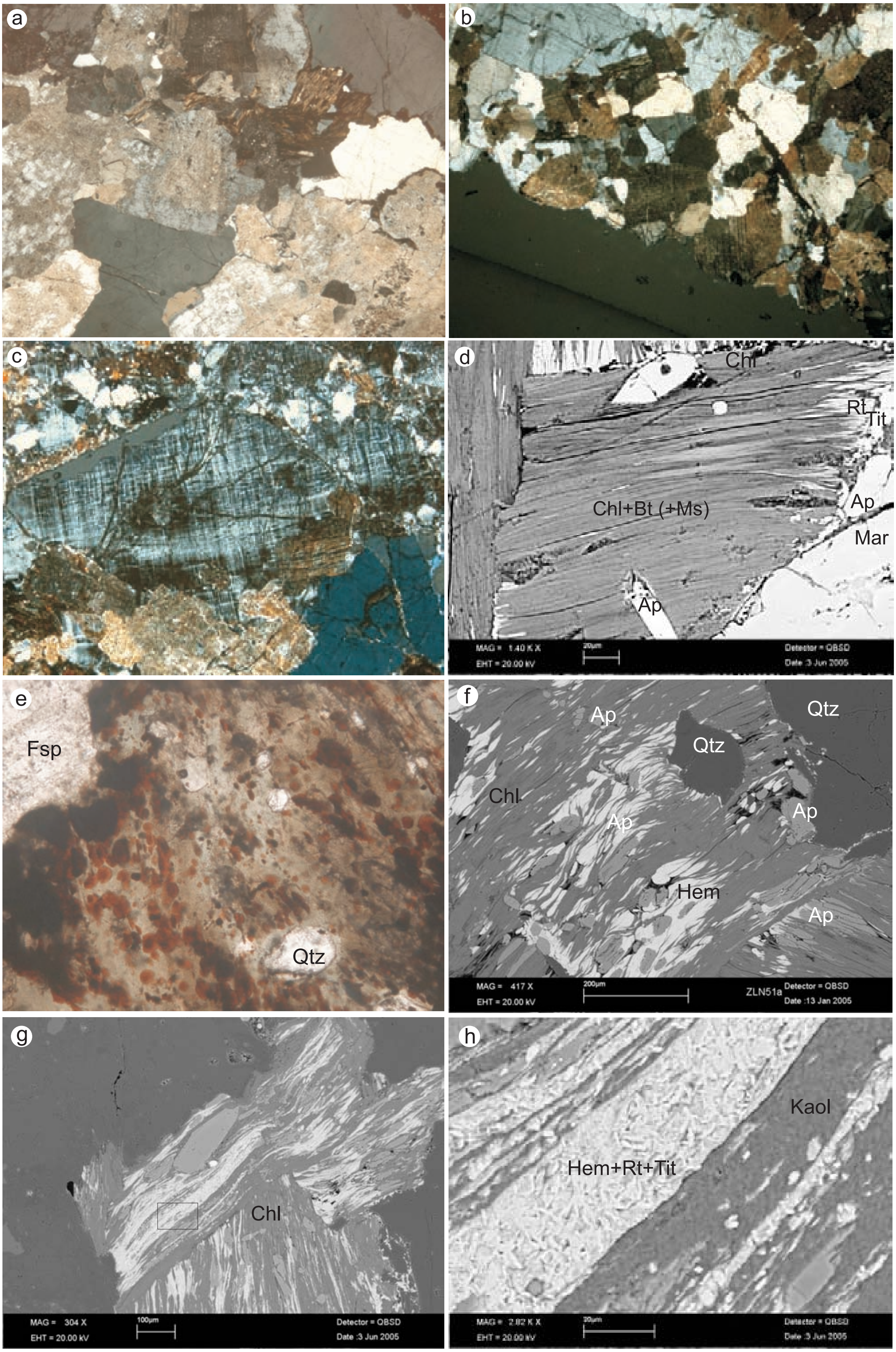

Plate 2.2.a-h (Alteration 1, caption see page 88)

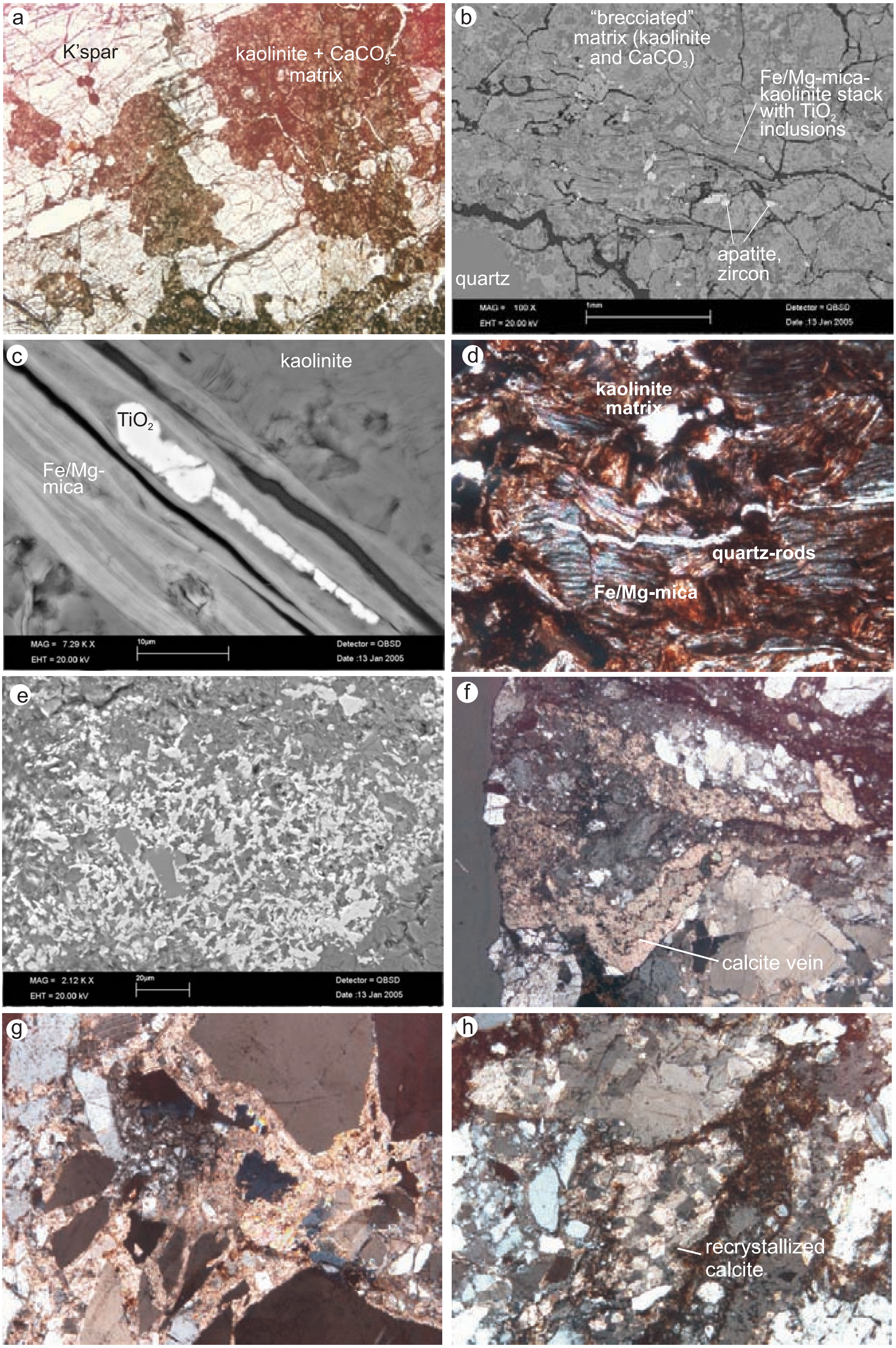

Plate 2.3.a-h (Alteration 2, caption see page 88)

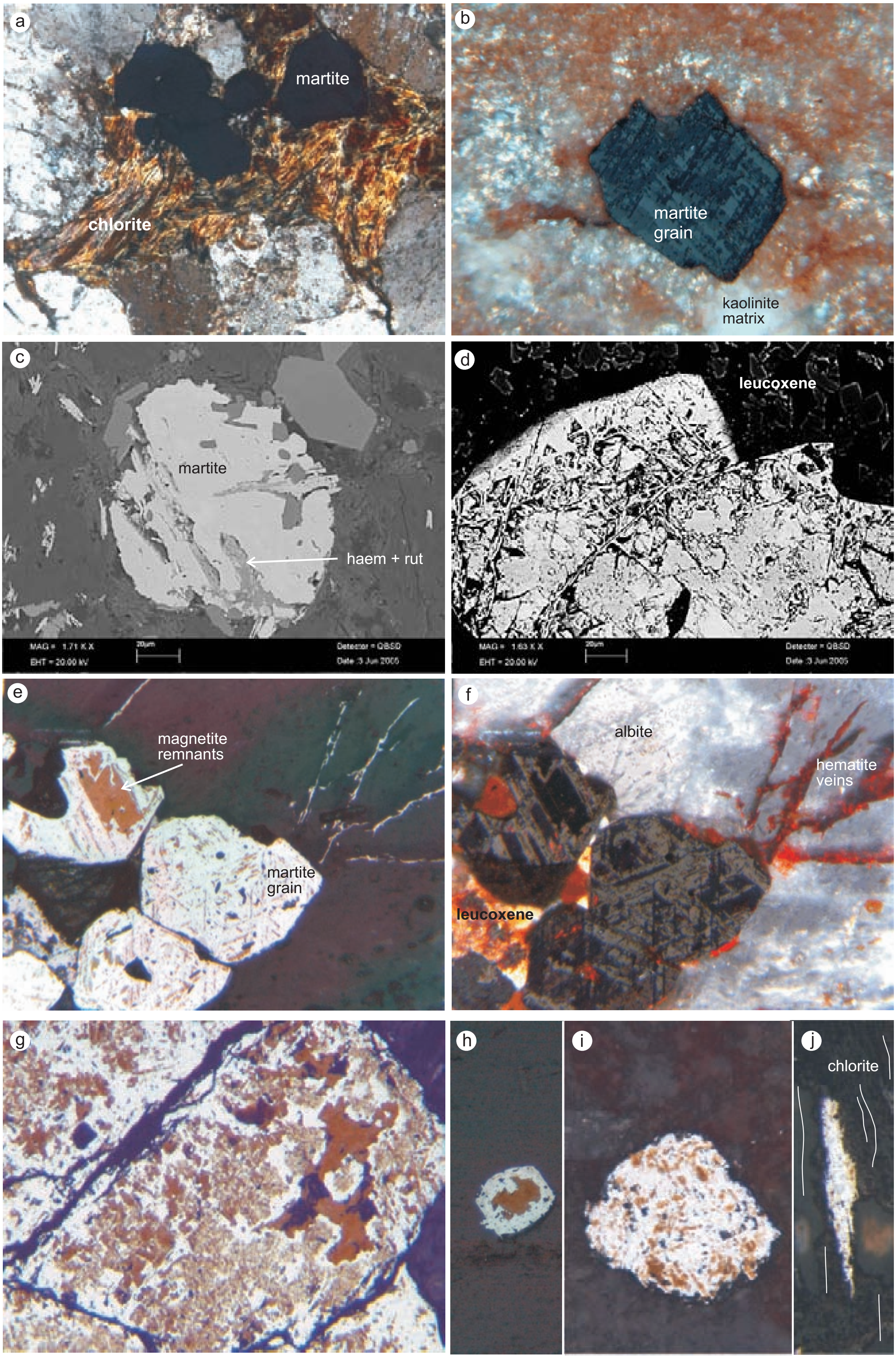

Plate 2.4.a-j (Magnetomineraloigy 1, caption see page 88)

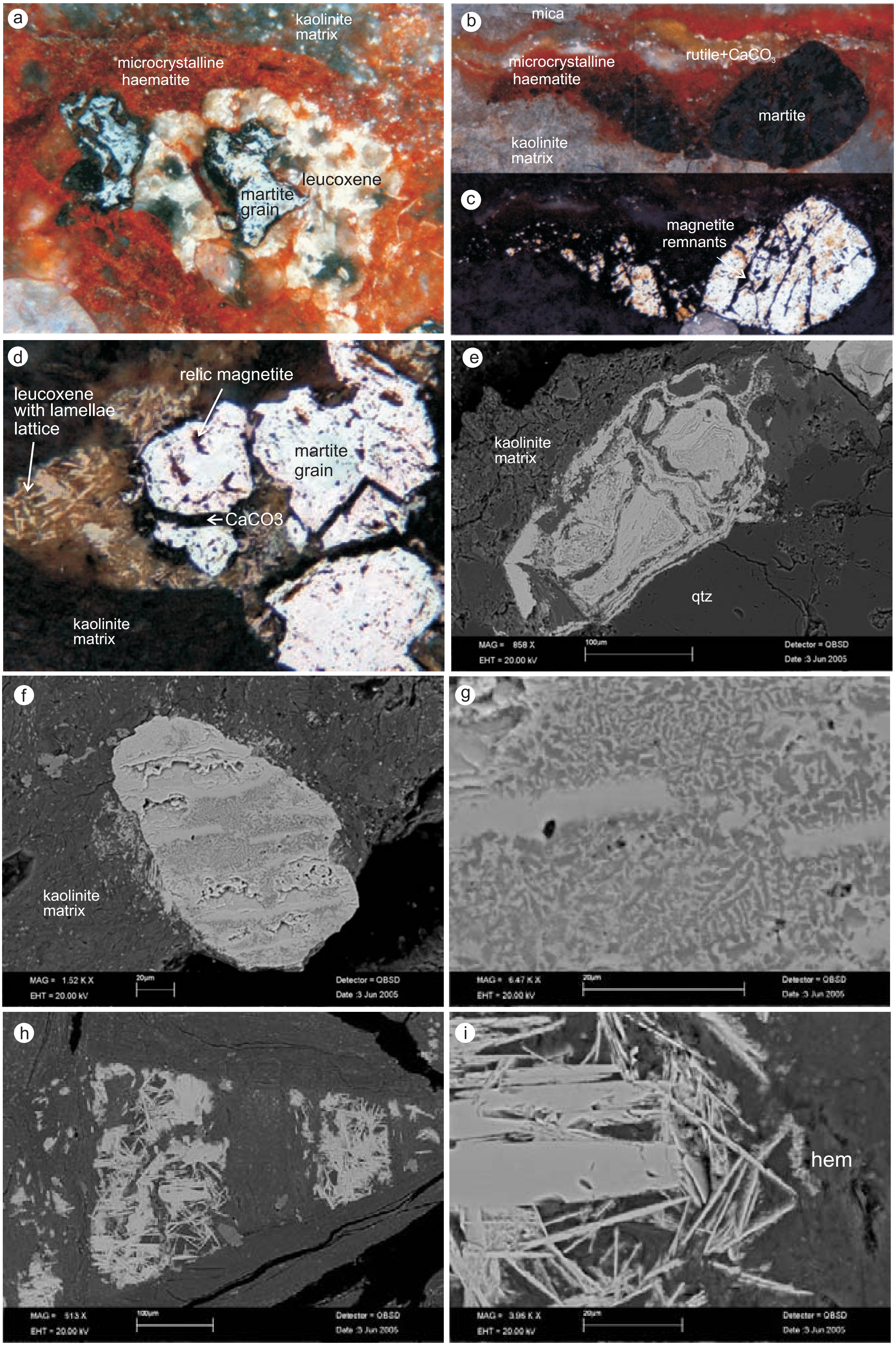

Plate 2.5.a-h (Magnetomineralogy 2, caption see page 88)

3 CASE STUDY HARA, SWEDEN

Weathering-brecciated Revsund Granite at the Caledonian margin (Central Swedish Caledonides)

3.1 Introduction

This case study deals with a drill core section from the Caledonian margin across the basal unconformity of Cambrian cover sediments overlying weathered Proterozoic Revsund Granite. Fresh and weathered rocks of this section show deformation. The aim of this case study is to reconstruct changes in mineralogical composition, fabrics, as well as magnetomineralogy and related magnetic fabric, produced by weathering processes and post-weathering deformations. The Hara location is situated near Lake Storsjön, 30 km south of Östersund (Jämtland) (Figure 3.1). The drill core SGU Hara 79002 (Gee et al. 1982) was studied and sampled at the SGU (Swedish Geological Survey) department in Malå.

3.1.1 Regional geology

The SGU 79002 Hara drill hole is situated in the Jämtland nappe region (e.g. Kumpulainen & Nystuen 1985). The drilling intersects parts of the Lower Allochthon (Norråker and Fjällbränna Formations (Fm.)) and the Autochthon, consisting here of Alum shales and the underlying granitic basement (Figure 3.2). The autochthonous basement granite represents the Fennoscandian Revsund Granite, as described by (Gee et al. 1982). This porphyritic granite has an intrusion age of ca. 1.80 Ga (U-Pb: Claesson & Lundqvist 1995). It is documented from the Svecofennian Domain (Baltic Shield east of the Caledonian margin), that some parts of the basement underwent metamorphism up to the greenschist facies (Kousa et al. 2000). NW-SE trending regional shear zones of Proterozoic age cut through the Proterozoic rocks in the Svecofennian Domain. One of these zones, the Storsjön-Edsbyn deformation zone SE of Östersund (Mattsson & Elming 2001), possibly affected early granitic fabrics in the studied granite.

A regional palaeoweathering of the granitic basement is manifested by an erosional unconformity along the eastern Caledonian margin beneath overlying sediments and a locally developed weathering crust reaching several metres down into the basement. Palaeoweathering took place between Late Vendian and Middle Cambrian times and according to Kumpulainen & Nystuen

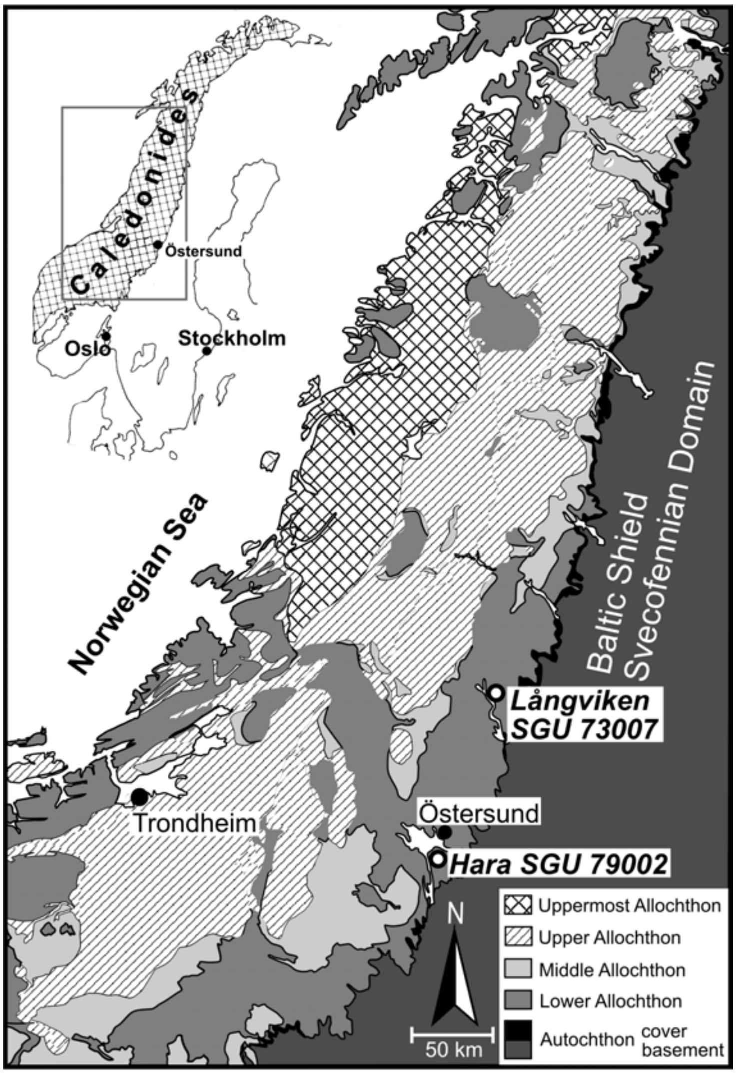

Figure 3.1: Geological overview of the Central Caledonides with the drill hole localities of SGU 79002 Hara (case study Hara) and SGU 73007 Långviken (case study Långviken) (in courtesy of R.O. Greiling, modified)

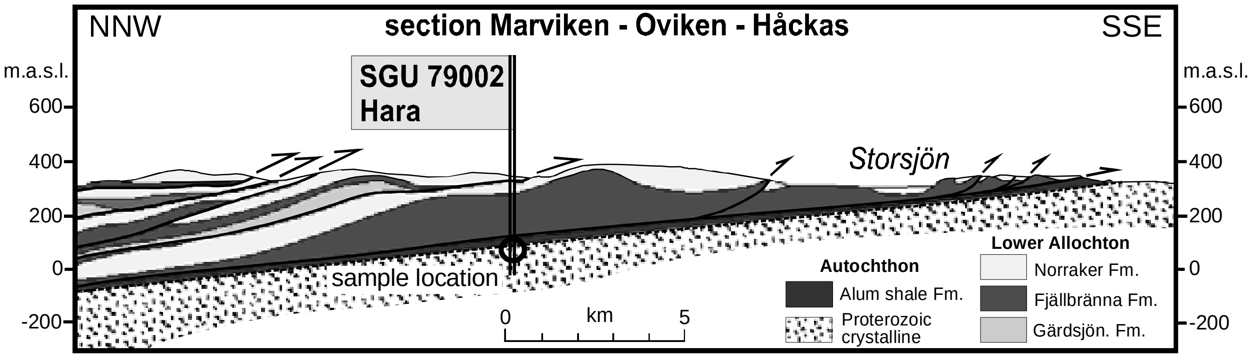

Figure 3.2: Section of the Caledonian front in Central Sweden showing the Hara drill core location (near Lake Storsjön, 30 km South of Östersund, Jämtland). Section modified after Gee (1982). m.a.s.l. = metres above sea level.

(1985) weathering was enhanced and accompanied by a progressively lowered basement relief. By several studies on Vendian cover sediments and paleosoils, it is indicated that climatic conditions during the peneplanation interval were subject to profound variations: thin crusts of kaolinite-rich weathered basement, interpreted as indicator for warm and humid climate, were described from beneath the contact to Cambrian sediments in the Svecofennian domain (Elvhage & Lidmar-Bergström 1987); also Hanken & Owen (1982) concluded warm and humid conditions. Alternatively, (Willdén 1980) inferred a temperate climate with moderate rainfall. A period of cold climate during Cryogenian time is documented by tillites of the Varanger Ice age, deposited at the base of the cover sequence on top of the basement (e.g. Torsvik et al. 1996), summarized in Kumpulainen & Nystuen 1985). A rapid climate cooling is suggested by the occurrence of red beds (0.75 Ga), which are just slightly older than the Varanger tillites (0.65-0.62 Ga) (Elming et al. 1993). This cooling trend corresponded with the Vendian drift of the Fennoscandian plate towards a polar position (Elming et al. 1993). The drift towards high latitudes is inferred from palaeomagnetic data (e.g. Bingen et al. 2005, Buchan et al. 2000, Elming et al. 1993, Vidal & Bylund 1981).

The oldest autochthonous strata overlying the basement granite along the eastern Caledonian margin are Cryogenian siliciclastics (including locally the Varanger tillites). Lateral changes of the basal lithologies are due to a well developed morphological basement relief (“basement high”: Willdén 1980). Following the Cryogenian, a successive transgression began with submergence of the western Baltoscandian Platform (Kumpulainen & Nysten 1985). This is documented by four flooding events of Ediacaran to Cambrian age along the central to northern Swedish Caledonian margin (Greiling et al. 1999b, Vidal & Moczydlowska 1996). The transgression stages are indications of temporarily higher sedimentation rates, although subsidence decreased with time corresponding to (modelled) lithospheric stretching and subsequent thermal subsidence (Greiling et al. 1999a). In most parts along the Caledonian margin, the Middle to Upper Cambrian Alum Shale Fm. (Andersson et al. 1985, Gee et al. 1974) represents the stratigraphically highest autochthonous unit. The original thickness of the Alum Shale Fm. is obscured due to tectonic reduction associated with Caledonian overthrusting of the Lower Allochthon (Bierlein & Greiling 1993, Gee et al. 1974). A 2.4 to 3.1 kilometres thick Neoproterozoic to Palaeozoic cover sequence on top of the crystalline has been modelled by Middleton et al. 1996). Detachment horizons along the Alum shales are abundant in the Lower Allochthon, because of the low strength and friction of that lithology (e.g. Greiling et al. 1998). The initial phase of the Caledonian orogeny began in Early Ordovician time (e.g. Essex et al. 1997), and the main orogenic phases begin during Silurian time (e.g. Essex & Gromet 2000, Gee et al. 1978). A sequential, mainly East directed, compressive nappe stacking, of the tectonostratigraphic units Lower, Middle, Upper and Uppermost Allochthon, took place (Gee 1978, Roberts 2003, Roberts & Gee 1985, Roberts & Stephens 2000). The Lower Allochthon is stratigraphically strongly related to the Autochthon and incorporates tectonic slices, which lithologically resemble the basement and cover rocks below the sole thrust (Roberts 2003). The geometry of the eastern part of Caledonian Orogen is considered as a wedge, tapering towards the eastern Caledonian margin (Garfunkel & Greiling 1996, Garfunkel & Greiling 1998, Greiling et al. 1998, 1999a). An inclination of 1.5 to 2° to the WNW (towards the hinterland) of the basal decollement between Autochthon and Lower Allochthon (Figure 3.2), has been determined by mapping (Bierlein & Greiling 1993, Gee et al. 1978), drilling and geophysical data. The top surface of the wedge was constrained to dip ca. 5° to the ESE (Greiling et al. 1993, Warr et al. 1996). This geometry explains the gradient of decreasing metamorphism observed in the Autochthon and Lower Allochthon towards the eastern margin. The present eastern Caledonian erosional margin encountered anchimetamorphic conditions, revealed by illite crystallinity (Garfunkel & Greiling 1998, Warr et al. 1996) and fluid inclusion thermometry. By constrained maximum temperatures of 150 °C, a burial depth of 5 km (assuming a geothermal gradient of 30 °C/km) by sedimentary and thrust loading is calculated for the present eastern Caledonian margin (“cover effect”: Warr et al. 1996).

3.1.2 Sampling and applied methods

The lowermost cover sediment and a sequence of 20 m of the underlying granitic basement are sampled from the drill core. The sampling interval increases approximately logarithmically with distance from the unconformity. Each sample is a 10 to 20 cm long piece of drill core. Three to five oriented standardized AMS cylinders are drilled from each of the samples. A correction-rotation of each sample stereoplot is carried out. In this case study the following methods are used: thin section petrography, optical microscopy and SEM backscattering in combination with EDX analyses, X-ray diffraction (XRD) on the whole-rock powder and on oriented preparation of the clay fraction (<2 μm), AMS and temperature dependence of magnetic susceptibility. Each method is described in chapter 1.3.

3.2 Description of the lithologies

According to Gee et al. (1982), basement rock alteration in the drill core section is mainly attributed to palaeoweathering. The rock terminology anticipates interpretations, which are discussed farther below. The drill core section can be divided into two main structural domains (SD), which are separated by a black shale (Figure 3.3). The black shale is considered as a tectonic boundary between both structural domains, as it is discussed in chapter 3.6.5. Above the black shale, a sequence of fault-brecciated and moderately weathered granite is present, and below the black shale, a matrix-supported breccia (interpreted as a weathering-breccia) and a lower intact granite are observed. A thin transition zone of weathered granite is located in between.

The sediments on top of the basement are mainly dark Alum shales of Cambrian age (Gee et al. 1982). The sequence is some 10s of metres thick. The sediments directly above comprise silty black shales and sandy arkoses of the Alum Shale Fm.

The drill core section reveals two times a basement-cover-contact (upper and lower unconformity). The upper unconformity is located at a drill depth of 183.85 metre. The contact to the granite is a narrow and steep fault zone. The fault character of that contact is defined by a few centimetres of foliated black siltstone, which is calcite rich (“mylonite” of Gee et al. 1982) (SD-1.a). Beneath the foliated black siltstone, a granitic succession of 7.5 metres follows, which comprises an almost undeformed granite (SD-1.b), weathered and brecciated granite (SD-1.c) and intensely brecciated weathered granite (SD-1.d).

The lower unconformity is marked by a black shale horizon, located between metres 189.45 and 190.15. It is unconsolidated, presumably destroyed by drilling. A thick zone of dark grey matrix-supported breccia (metres 190.15 to ca. 201) follows beneath this horizon (SD-2.a, b). It is here referred to as a weathering-breccia (“basal arkose” of Gee et al. 1982). In a quite narrow transition zone between metres 195 and 196, the breccia passes into intact and weathered granite (SD-2.c). At 10 metres below the black shale, intact and unweathered granite is reached. Locally, there are thin brecciated zones in the intact granite.

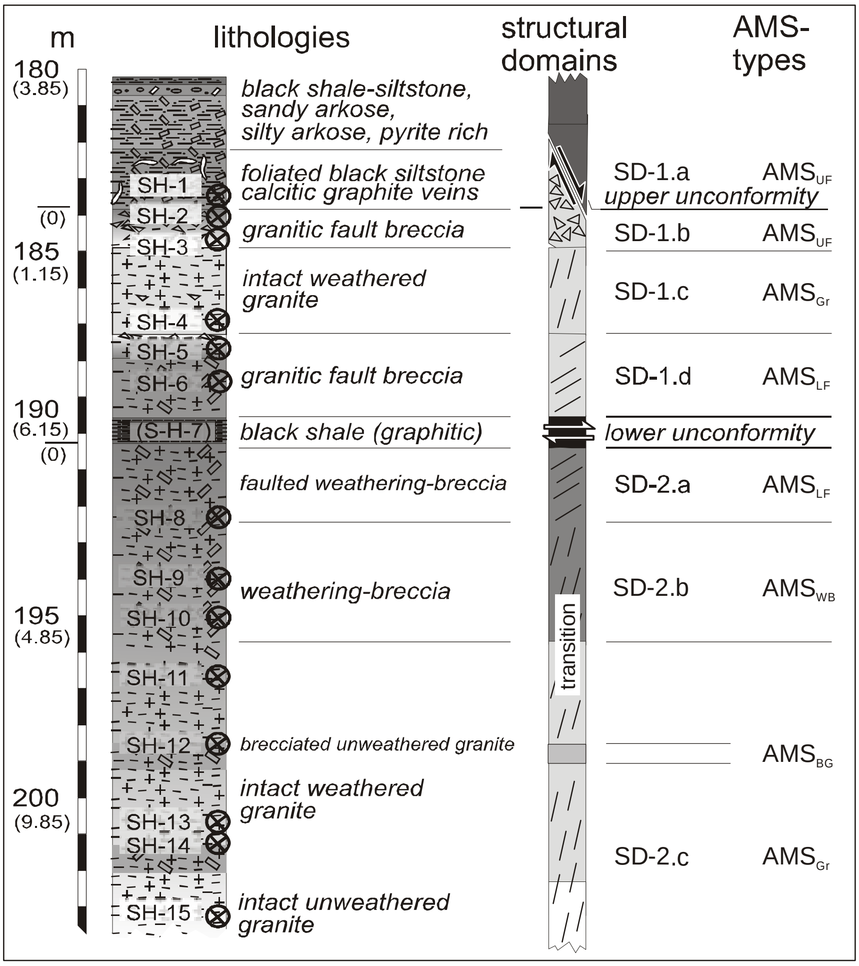

Figure 3.3: SGU 79002 Hara drill core section with lithologies, sample locations, structural domains and AMS-types.(metres in brackets mean distance from unconformity)

3.2.1 Unweathered granite (SD-2.c)

The unweathered intact granite is coarse crystalline and light grey to greenish coloured. Its main constituents are anhedral quartz, albite, chlorite and subhedral microcline phenocrysts. These microclines (< 1 cm, microcline twinning) dominate the texture with up to 50 vol%. Chlorite builds large crystal stacks (mm size).

All parts of the intact granite are deformed by sets of subvertically oriented gneissic schistosities (Plate 3.1.a). One foliation set is dominant. The schistosity domains are dark-grey-coloured and defined by a preferred orientation of chlorites. Rutile, titanite, graphite and epidote impregnate chlorite. Locally, large primary quartz crystals (< 0.5 cm) are affected by intracrystalline deformation, comprising grain size reduction by dynamic recrystallization and subsequent static recrystallization. Dynamic recrystallization of quartz is indicated by bulging, and static recrystallization is indicated by straight boundaries.

The unweathered granite is the least altered granite in the drill core section. Indications of alteration are biotite remnants in chlorite and an intense sericitization causing a white and friable feldspar appearance at the macroscale. Albite crystals are cloudy or partly completely sericitized, whereas microcline phenocrysts are typically affected by sericitization along the crystal cleavages (Plate 3.1.c). Albite veins cutting through the rock. Veins and rock matrix show same epidote-chlorite-albite assemblage. Chlorites and veins are impregnated with microcrystalline graphite.

3.2.2 *Weathering-breccia (SD-2.b)*

The breccia in SD-2 is characterized by a dark-grey and fine-grained matrix with domains of coarse-grained granite, resembling the unweathered granite. The volume relation of matrix and granitic remnants increases approaching the black shale. The main matrix constituents are illite, chlorite and quartz (see also chapter 3.3). These minerals are also the cement of the matrix. Locally, quartz or very large intact and subhedral microclines are disseminated in the fine-grained matrix (Plate 3.1.e). Dynamic recrystallization of quartz is apparent in clastic domains, indicated by weak, but distinct crystal elongation (mimicking the surrounding oriented sericites) and by a uniform orientation of quartz c-axes (qualitative estimation by interference colours). These recrystallization domains may be inherited components of the granite, as similar features are observed in the granite (see previous chapter).

The breccia is partly subvertically foliated. Declinations of this weakly defined cleavage vary considerably, without showing distinct sets (Plate 3.1.d). A subvertical granitic schistosity is observed in parts, where primary textures are preserved. A horizontal compaction cleavage is petrographically not recognized but can be identified by means of AMS (chapter 3.5.2.2). Such a fabric is evident in a similar weathering profile (case study Långviken: Plate 4.1.g).

The breccia is the most intensely altered (weathered) granitic rock type in the profile. Plagioclase is intensely altered to illite, locally plagioclase is entirely replaced by clayey material. K-feldspar is much fresher than albite. Chlorite is impregnated densely with rutile and titanite. Alteration products in the brecciated matrix are brownish carbonate flakes and a mixture of illite, chlorite, graphite and carbonate, here referred to as "alteration symplectites", together reaching ca. 20 vol%.

The weathering-breccia in the two metres beneath the black shale is cataclastically deformed and deficient in granitic relics.

3.2.3 *Weathered granite (SD-1.c, SD-2.b/c)*

A transitional zone between the unweathered granite and weathering-breccia is observed. The petrographic characteristics of the weathered granite are similar to those in the unweathered granite, however, albite alteration is advanced and carbonate content is enhanced. Weathering degree, with respect to formation of the clayey matrix, is weaker in comparison to the weathering-breccia. Here, the weathering-related phases, brownish carbonate accumulation and alterations symplectite, reach maximal 10 vol% of the matrix content.

3.2.3.1 *Fault-brecciated weathered granite (SD-1.b,d)*

Directly above the black shale, in SD-1, weathered granite is brecciated. Especially, quartz, albite and K-feldspars are intensively fractured, which is not as clearly observed in the weathering-breccia. It shows the cataclastic nature of the breccias in SD-1 in opposition to weathering-breccia in SD-2. Rocks in SD-1.b and SD-1.d are referred to as fault-breccia. The following differences define fault- and weathering-breccias: (1) weathering-breccia is stronger altered than fault-breccia, with respect to illitization of plagioclase, content of alteration symplectites and carbonates; (2) weathering-breccias bear a lower content of quartz clasts and show the imprint of subvertical cleavage. In the fault-breccia, this vertical cleavage is not present; (3) moderately inclined discrete black shear surfaces, defined mostly by chlorite and graphite, are present in the *lower* fault-breccia (SD-1.d). Stretching lineation of a fine graphite-chlorite-mica association is observed on these shear surfaces. The downward transition from intact granite to lower fault-breccia (SD1-c to d) resembles a trend of increasing intensity of cataclasis.

The *upper* fault-breccia (SD-1.b) has a uniform subvertical slaty cleavage, paralleling the steep inclination of the fault, which defines the upper contact to the sediments (in SD-1.a). The upper fault-breccia shows crenulated remnants of moderately inclined shear surfaces attributed to the deformation of the lower fault zone. This implies that the lower fault zone is an earlier deformation than the upper fault. Both sets of surfaces parallel each other, therefore, the intersection lineation of both surfaces, which is not developed petrographically in the specimen, is considered as subhorizontal.

3.2.4 Foliated black siltstone (SD-1.a)

The foliated black siltstone is considered as a part of the cover sequences (SD-1.a). Biotite and chlorite are the main matrix constituents. These minerals generate a penetrative steep slaty cleavage. As in the upper fault zone (SD-1.b), this cleavage parallels the steep inclination of a fault. This fault defines the upper boundary between granite and cover. The matrix of the foliated black siltstone is interlaced with white to grey calcite-graphite veins, parallel with the foliation.

These calcite-graphite veins in the fault zone consist of two to three generations of calcite. An early generation of medium-sized (< 0.4 mm) calcites defines the vein rims. The crystal-SPO is parallel with the vein rim. A second generation in the rim-centre is coarse crystalline (< 5 mm) and hardly deformed (only few deformation twins). A third generation is a very fine (< 0.05 mm) one in strain-shadows of large graphite crystals (flakes), which are boudinaged and partly brecciated (Plate 3.1.g). These coarse-crystalline graphite flakes (sub-mm long) are dominantly located in the rim area and their basis-surfaces parallel the fault-zone foliation and the vein-rim. In addition to the large graphite flakes, a considerable amount of microcrystalline graphite impregnate calcite grain-boundary and the wall rock matrix. Some coarse crystalline (0.5 mm) and perfectly idiomorphic quartz porphyroblasts are disseminated at the vein rim (Plate 3.1.h). They bear graphite and calcite inclusions parallel to the crystal surfaces, indicating several growth stages.

A shear deformation is evident in the matrix and in the vein rim, whereas minor brittle deformation affected the vein centre (Plate 3.1.g).

The black siltstones directly above the fault zone are densely impregnated with pyrite or marcasite and graphite. The sediments above SD-1are not clearly cleaved.

3.3 XRD results

Well-crystallized illite and chlorite are the main clay minerals in the whole section (Figure 3.5). Quartz, feldspars and calcite are also present. The modal fraction of the clay-size-minerals in the weathering-breccia (SH-8) and fault-breccia (SH-2, SH-5) is much higher than in the intact weathered granites (SH-11) and unweathered granite (SH-15) (not quantified). The abundance of two feldspar types, albite and microcline, are high in the unweathered granite, whereas in the weathered granite and in the weathering-breccia, albite peaks are almost not developed due to the advanced alteration (sericite / illite precipitation). Lowest content of feldspar in the clay fraction is documented close to the lower unconformity, in SH-8. Slightly enhanced feldspar content, compared to the weathering-breccia, is recognized in the weathered granite of SD-1 (especially in SH-5).

Illite 10 Å peaks are weakly asymmetric in air-dried conditions (AD) and have FWHM values of ranging between 0.42 and 0.8 (Figure 3.6.d). The presence of mixed-layer phases (I/S) is suspected as a reason for peak

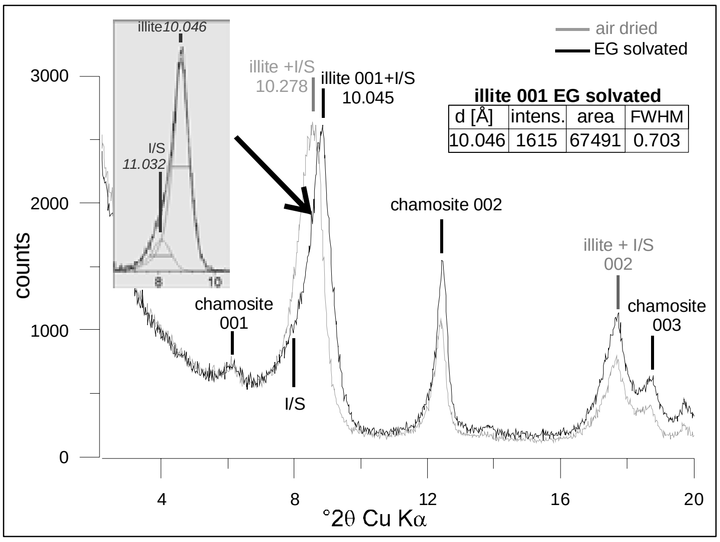

illite 001 EG solvated

d [Å]	intens.	area	FWHM
10.046	1615	67491	0.703

Figure 3.4: XRD-spectrum (°2θ peaks, low angles) of the clay fraction of an upper fault-breccia, just below the foliated black siltstone.

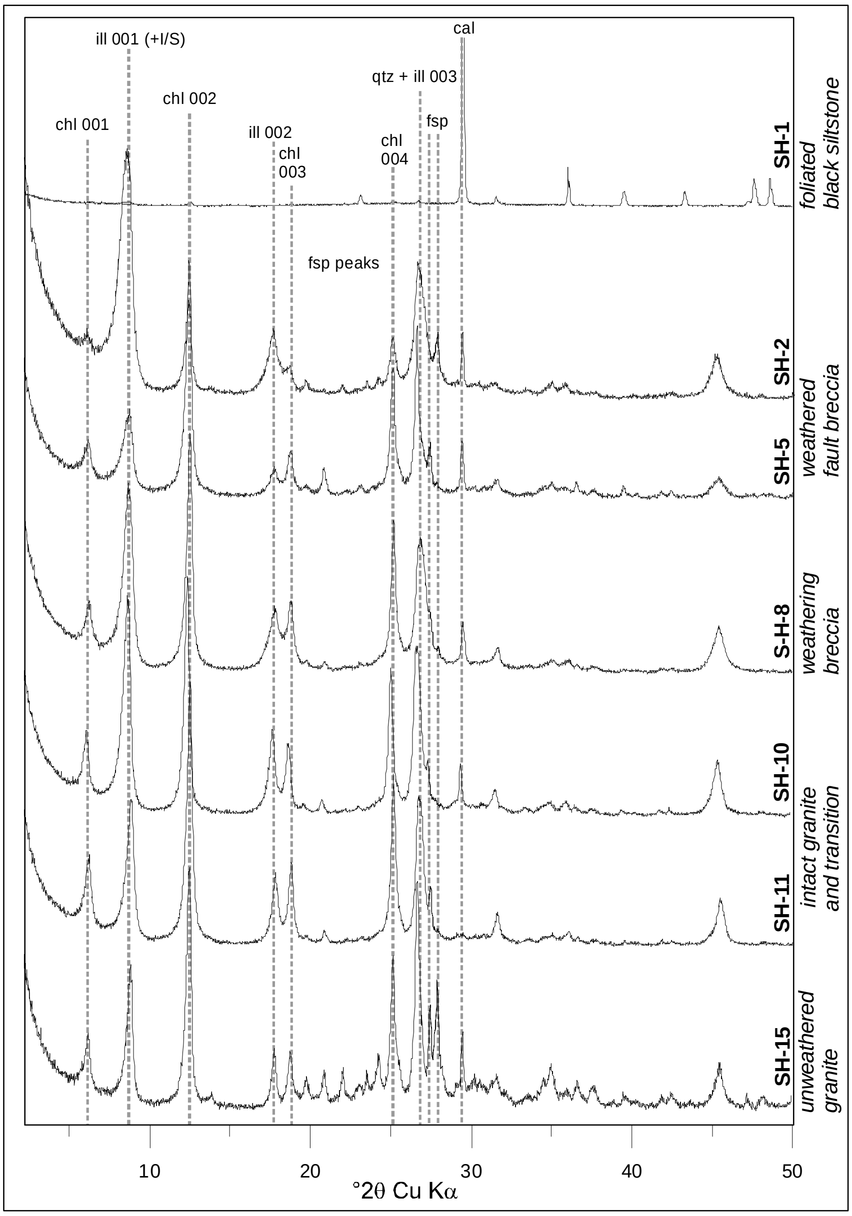

Figure 3.5: XRD-spectra of the clay fraction (< 2 µm) of selected samples from the Hara drill core. Samples SH-5, SH-2 and SH-1 are taken from SD-1, the others represent SD-2.

broadening. Therefore, a repeated measuring after ethylene glycol-solvation (EG) is carried out with sample SH-2, which showed the broadest illite 001 peak (FWHM = 0.793 °2θ). The EG-measurement results in a weak shape modification and slight shift towards higher angle (from d = 10.278 Å in AD to 10.045 Å in EG) of the illite 10 Å peak (Figure 3.4). This points to the presence of an I/S mixed-layered mineral. After peak decomposition of the EG spectrum, the pure “illite” 001 peak establishes at d = 10.045 Å with a FWHM of 0.703 °2θ. This high FWHM (compared to well-crystallized illite peaks (< 0.42 °2θ)) points to a compositional peak of pure illite and I/S mixed-layered mineral. However, the content of I/S-phases in the sample can be considered as very low (less than 5 %), by the relative sharp pure “illite + smectite” peak and the minor shape and d-spacing modification between AD and EG spectra.

The distances (Δd-spacing) between “illite + I/S” 10 Å and 5 Å peak positions give a measure of relative changes of the illite/smectite ratio within the profile (Meunier & Velde 2004, Moore & Reynolds 1997). This is associated with a slight shift of the peak position occurring with the incorporation of smectite. An increase

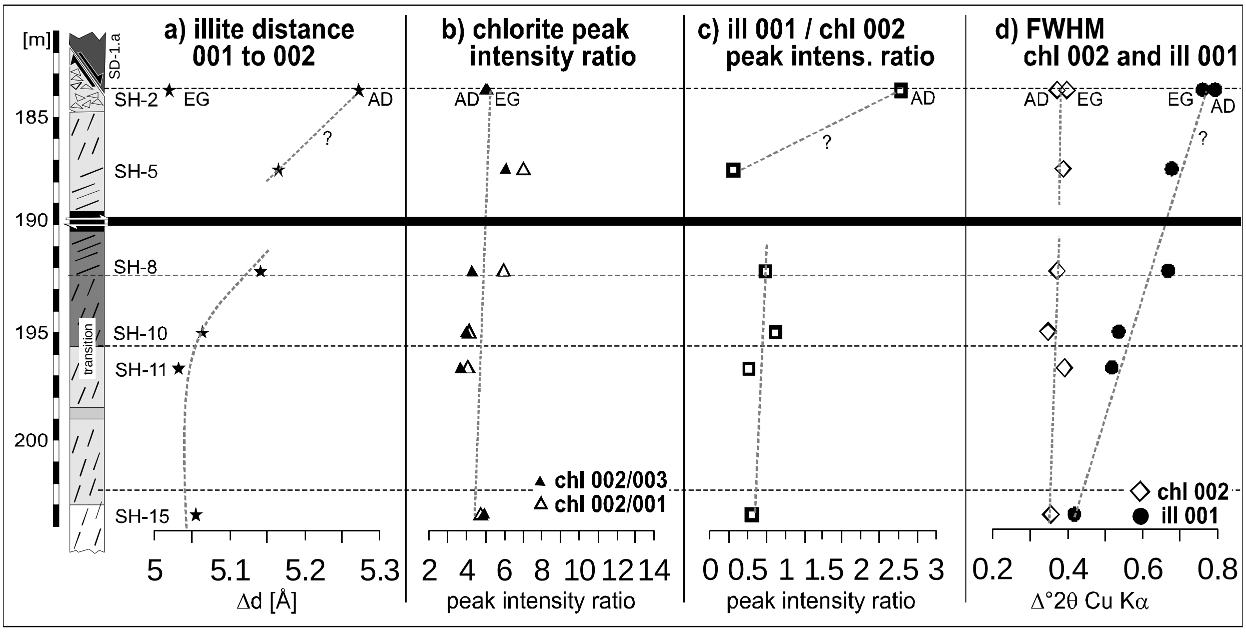

Figure 3.6: XRD parameters (clay fraction, < 2 μm) of illite and chlorite. a) d-value distances of illite 10 Å (001) and illite 5 Å (002) peaks; b) chlorite peak intensity ratio (002/003 and 002/001); c) illite 10 Å (001) / chlorite 7 Å (002) peak intensity ratios; d) Full width at half maximum (FWHM) values of illite 001 and chlorite 002.

of the Δd-spacing with brecciation degree is evident (Figure 3.6.a), pointing to an increased influence of an I/S phase. It cannot be stated with certainty, whether the results show an elevated smectite content in the I/S-phase or a relative increase of I/S phase in comparison to well-crystallized illite, or both. Δd are higher in the fault-breccia than the weathering-breccia.

Chamosite is the only chlorite phase, which is deduced by weakly developed chlorite-001 and -003 peak in comparison to the 002 peaks (Moore & Reynolds 1997). The chlorite 002/003 peak intensity ratio is ca. 4 and stays stable through the entire drill core section (Figure 3.6.b).

The illite 001 / chlorite 002 peak ratio is a qualitative expression of changes in the modal fraction of clays in the matrix (Figure 3.6.c). The ratio stays almost stable with the degree of weathering-brecciation. An increase with degree of fault-brecciation is indicated.

A comparison of FWHM of the low-angle illite (10 Å) and chlorite (7 Å) peaks provides information about growth conditions throughout the section (Figure 3.6.d). Chamosite FWHM varies between 0.35 and 0.4 °2θ. Illite 001 FWHM, however, changes significantly in the weathering profile below the black shale. Well-crystallized illites with lowest FWHM are present in the unweathered granite (FWHM = 0.418 °2θ); illites FWHM resembles almost the chamosite FWHM of 0.355. A broadening of illite peaks with proximity to the unconformity is evident (0.667 °2θ in SH-8), which is either due to an enhanced I/S content, or due to an increase of the mixing ratio of poorly to well-crystallized illites. The clay-sized chlorite, on the other hand, does not show any unconformity-related trend of XRD parameters. In SD-1, peak FWHM of both chamosite and illite resemble those of the weathering-breccia.

3.4 Bulk susceptibility κ_{bulk} and temperature dependent susceptibility $\kappa(T)$

Bulk susceptibility (κ_{bulk}) values are low, reaching from 100 to $350 \cdot 10^{-6}$ [SI] (Figure 3.7). Highest values (average $248 \cdot 10^{-6}$ SI) are observed in the weathering-breccia. The unweathered granite (in D-2) and the brecciated weathered granite in SD-1 show similar κ_{bulk} values ($193 \cdot 10^{-6}$ and $172 \cdot 10^{-6}$, respectively).

Temperature dependent susceptibility measurements κ(T) show in all samples paramagnetic minerals, i.e. κ(T) curves are proportional to the unction $\kappa(T) = 1/T$ (*T* is temperature) and no Curie temperatures were

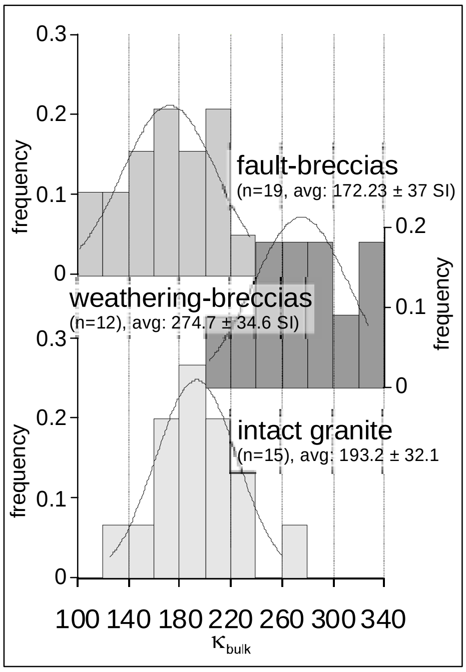

Figure 3.7: κ_{bulk} histograms of the main lithologies (unweathered granite, weathering-breccia in SD-2 and fault-breccia in SD-1). The Gaussian regression curves indicate the differences in κ_{bulk}. The relative frequencies of the values are plotted (y-axis).

detected (Figure 3.9). These paramagnetic minerals are Fe-chamosite, relic biotite (in chlorite-stacks) and white mica. White mica comprises primary mica stacks, interlayered with chlorite, secondary sericite in feldspar (illite polytype: Meunier & Velde 2004) and matrix-illite+I/S (see chapter 3.3). White mica may be phengitic, i.e. it bears Fe^{III} as a substitute of Al^{VI} (Deer et al. 1966). In general, intrinsic susceptibility of paramagnetic minerals increases with their Fe-content (Tarling & Hrouda 1993). The present accessory para- or antiferromagnetic iron-sulphides, pyrite and chalcopyrite, do not influence κ_{bulk} significantly, having low paramagnetic intrinsic susceptibilities. Carbonates are quite abundant in weathered rock types and are possibly enriched in iron, which is indicated by their brown colours.

The cooling curves show an irreversibility with respect to the heating curves. Two distinct increasing steps of susceptibility are displayed during the cooling runs, related to magnetite (T_{Curie} at about 575 °C) and at least one additional ferrimagnetic phase (T_{Curie} ranging between 350 and 450 °C). These phases are reaction products during experimental heating and do not represent original phases. Because T_{Curie} are indicated only in the cooling runs, transformations take place above the specific T_{Curie}. Thus, magnetite generation occurs above T_{Curie} of magnetite (575 °C), and the second ferrimagnetic phase above ca. 450 °C. The latter may be a ferrite modification incorporating Mg and/or Mn, $(Mn, Mg, Fe)_3O_4$ with T_{Curie} down to 400 °C (e.g. Just 2005), which can be formed from Fe-Mg-Mn-carbonates at about 500 °C and are stable up to the maximum T of 700 °C (Isambert et al. 2003, Just 2005). Magnetite may be generated by Fe-bearing chlorite, phengitic illite and/or Fe-bearing carbonates. Phengitic illite, although stable with heating to 700 °C, may segregate small amounts of iron from crystal-

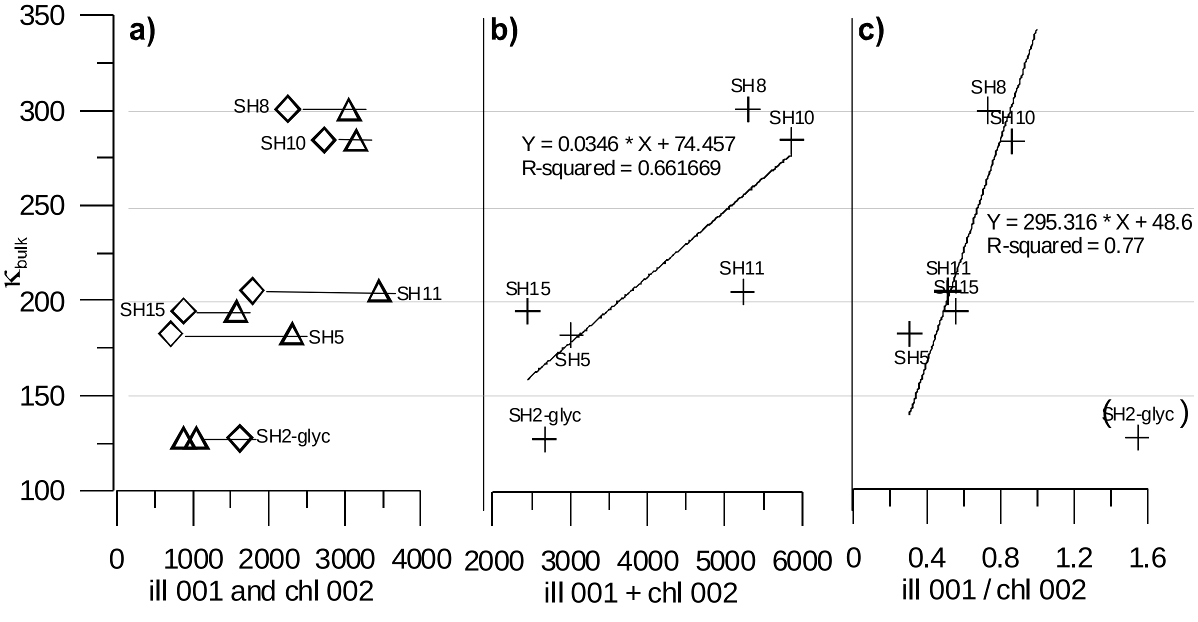

Figure 3.8: Diagrams showing κ_{bulk} vs. XRD peak parameters of illite and chlorite in the clay fraction a) peak intensities of illite and chlorite (triangle: illite, diamond: chlorite); b) sum of peak intensity clay content (illite + chlorite) and c) illite/chlorite-ratio.

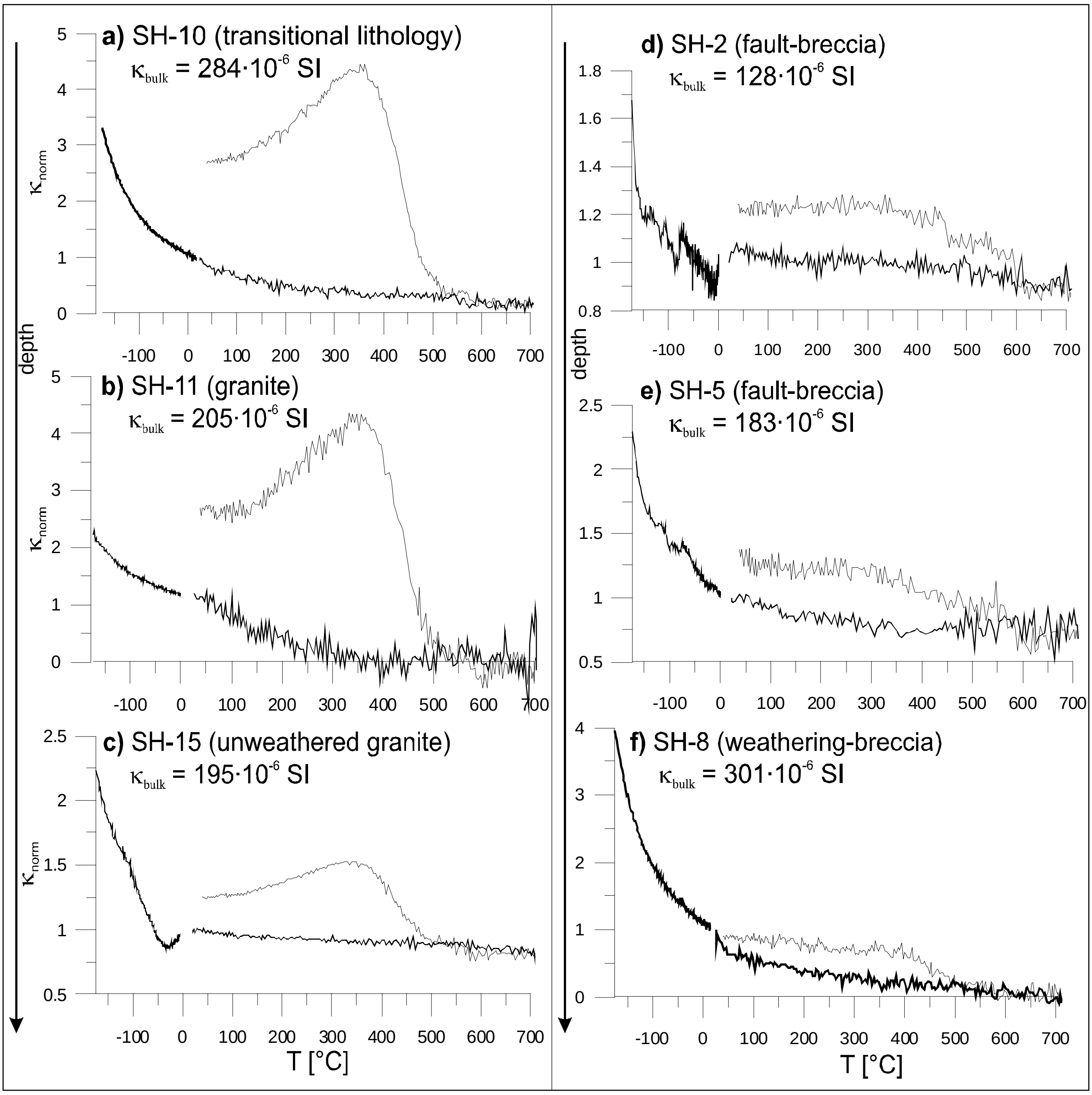

Figure 3.9: Temperature-dependence of bulk susceptibility, normalized to the κ-value at T = 0 °C. κ_{norm}(T) of the granite, weathering-breccia and fault-breccia. a-c) show the unweathered and weathered granite and the transition lithology, d-f) show fault- and weathering-breccias.

edges to form magnetite (Warr *pers. comm.*). The magnetite precipitation during experiment heating is incipient. The oxidation of iron sulphides into magnetite is a commonly observed conversion, known to be completed below 575 °C (e.g. Just 2005, Kontny et al. 2000). And in general, oxidation is minimized since measurements were performed in Argon atmosphere, but even though minor reactions may occur (Kontny et al. 2000).

The κ(T) curves display that only insignificant susceptibility-relevant phase-transitions occurred through the entire weathering profile.

A positive correlation between κ_{bulk} and the proximity to the black shale unconformity is significant (Figure 3.10). An immediate κ_{bulk} decrease by ¼ ($\Delta\kappa_{bulk} = 80 \cdot 10^{-6}$ [SI]) is evident when passing from the weathering-breccia of SD-2.b into weathered granite in SD-2.c.

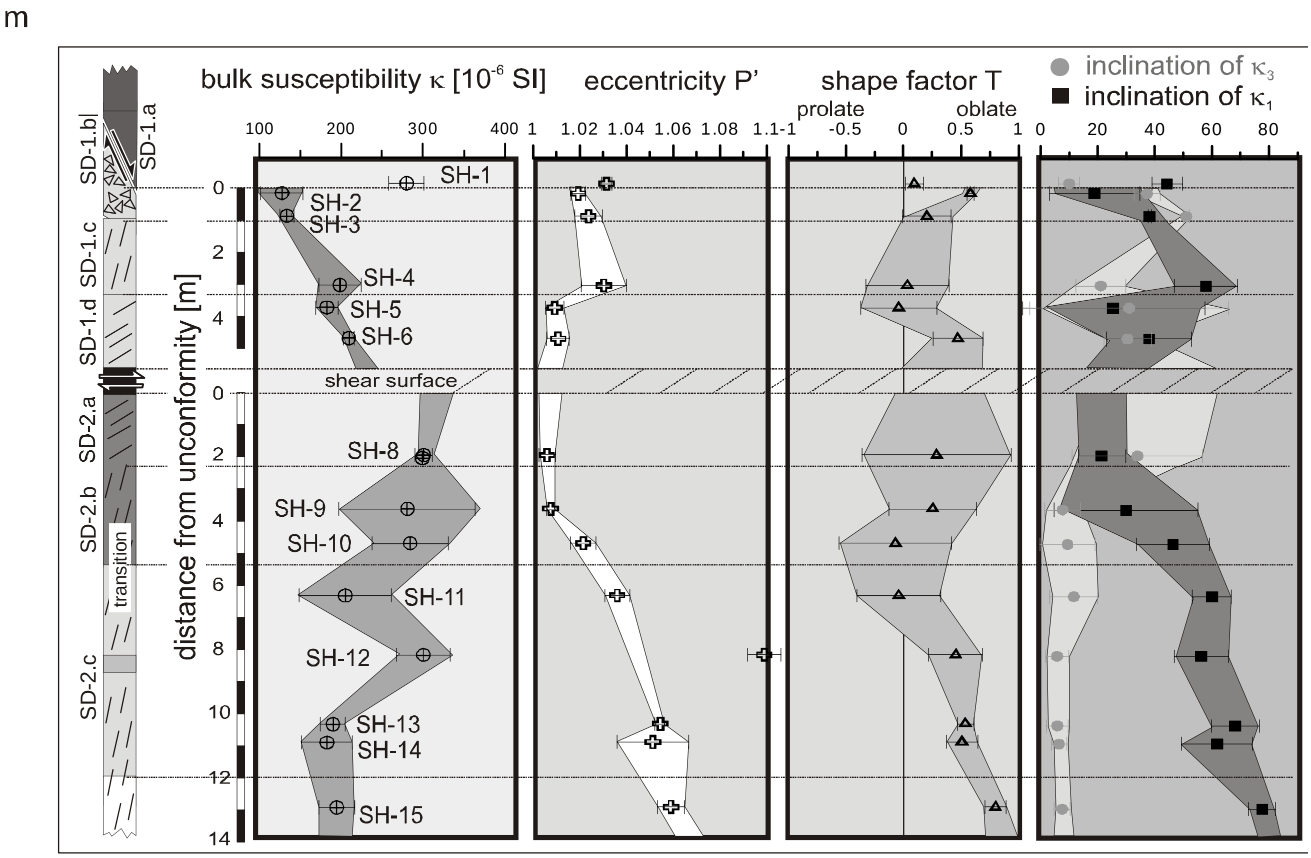

Sample SH-12 represents a brecciated zone alternating with unweathered granite in SD-2.c and shows higher κ_{bulk} due to the increased content of the fine-grained cataclastic matrix.

The fault-breccia in SD-1 has a lower κ_{bulk} compared to weathering-breccias below the shale. In fact, the values are comparable to those of the weathered granites above and below the black shale.

The characteristic increase of κ_{bulk} with weathering intensity points to the dependency of magnetic susceptibility to the matrix clay-content, which can be semi-quantified by the peak intensities of illite 001 and chlorite 002 from the clay-fraction XRD-spectra (Figure 3.8.a) and by the sum of both peak intensities (Figure 3.8.b). The illite/chlorite-ratio displays a positive correlation with κ_{bulk}, too (Figure 3.8.c). Considering that Fe-chamosite is higher susceptible than illite (Figure 1.8, Table 1.1), this may give evidence for a susceptibility-increasing chlorite alteration, presumably to the higher susceptible Fe-carbonates (or symplectites) (see chapter 3.2.2).

Paramagnetic κ_{bulk} as a function of modal fraction of clays has been proposed by Potter et al. (2004), according to the susceptibility addition (equation 4 in chapter 1.3.7.3). The modal fraction of mica can be calculated by this dependency, having two restrictions in mind: (1) there is no difference possible between clay and coarse-grained mica and (2) other Fe-phases are not considered. The equation 4 in chapter 1.3.7.3 can be written as:

$$(1) \qquad c_{para} = (\kappa_{bulk} - \kappa_{dia}) / (\kappa_{para} - \kappa_{dia})$$

c_{para} is the modal fraction of paramagnetic clay mix (illite + chlorite); κ_{para} is the intrinsic volume susceptibility of the clay mix and κ_{dia} is the intrinsic volume susceptibility carried by diamagnetic quartz-feldspar mix. c_{para} can be calculated with the known intrinsic volume susceptibilities (Figure 1.8) and measured $\kappa_{bulk} \cdot c_{para}$ is 74.3 % for sample SH-8 ($\kappa_{bulk} = 300.77 \cdot 10^{-6}$ SI). For sample SH-10 ($\kappa_{bulk} = 284.43 \cdot 10^{-6}$ SI) calculated c_{para} is 70.5 %. The latter value may be about 10 % too high, because of coarse-grained mica content.

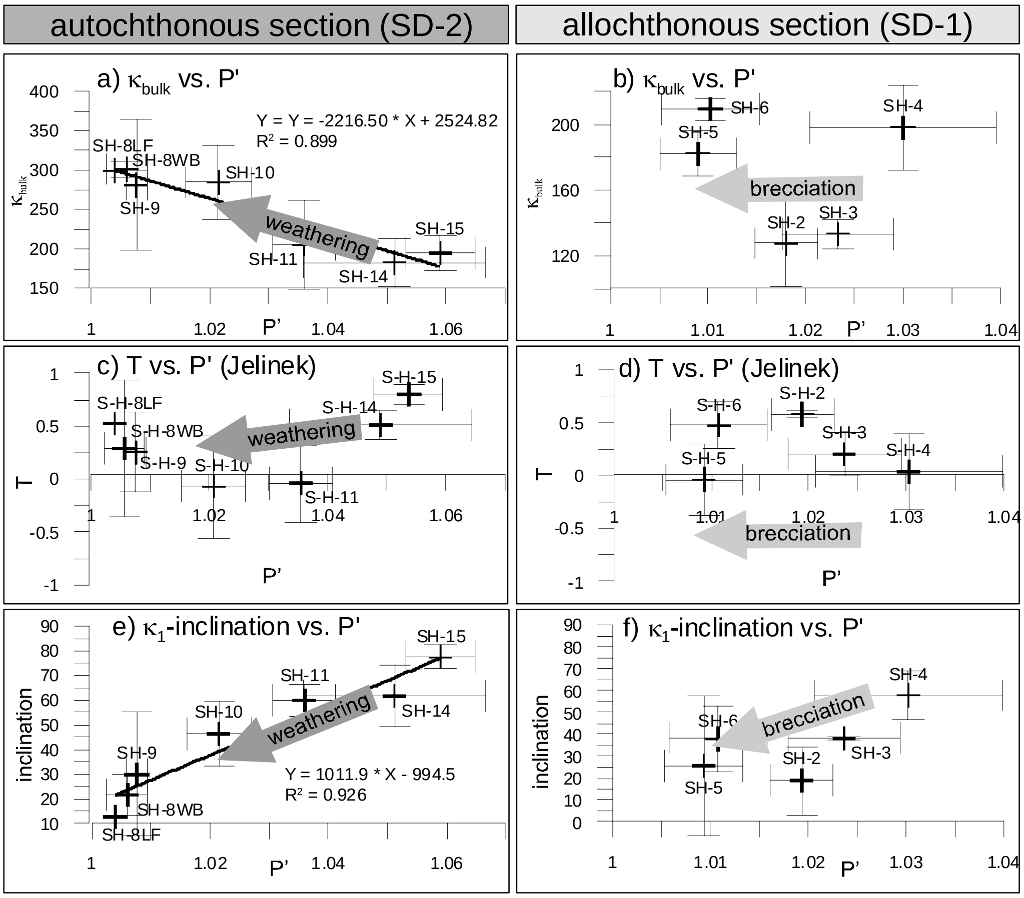

Figure 3.11: P’ vs. T, P’ vs. κ_{bulk} and P’ vs. κ_1-inclination. Average sample values are considered. In sample SH-8, it is distinguished between lower fault (LF) and weathering-breccia (WB).

3.5 AMS results

3.5.1 Trends through the section

The anisotropies of magnetic ellipsoid are low in the entire drill core section. Intact granite samples (unweathered or weathered) have higher P’ values (1.02 to 1.07) than weathering-breccias (1.01 to 1.03) (Figure 3.10). This implies a general inversely proportional correlation between κ_{bulk} and P’, well observed in SD-2 with a high squared correlation coefficient ($R^2 = 0.899$) (Figure 3.11.a). Fault-breccias in SD-1 do not show such a general inversely proportional correlation (Figure 3.11.b). Ellipsoid shapes are mostly oblate ($T > 0$); some prolate shapes ($T < 0$) are present, especially in the weathered granite (SD-1 and SD-2) (Figure 3.10). The Jelinek diagrams do no point to a good correlation between P’ and shape factor T (Figure 3.11.c,d). With increasing P’, the inclination of κ_1 increases in SD-2 ($R^2 = 0.926$) (Figure 3.11.e). Beginning in an upright position (75-80°) in the unweathered granite, κ_1-inclination decreases slightly in the moderately weathered granite to 50-70° and then, after the transition to the weathering-breccia, κ_1-inclination decreases steeply and continuously down to 20°. The scattering of values in the breccias is high, showing standard deviations up to 30°.

The positive correlation between P’ and κ_1 is not distinct in the allochthonous section (Figure 3.11.f). κ_3 remain stable in a sub-horizontal position in SD-2, except in SD-2.a, where κ_3 inclination scatter between 15 and 65° (Figure 3.10).

3.5.2 *AMS-types*

The systematic distribution of AMS axes orientation in the drill core section, combined with characteristic AMS parameters, leads to a categorization of AMS fabric types (Figure 3.12). AMS patterns specimens SH-8 and SH-5 are heterogeneous and can be sub-divided by their axes orientation and by ellipsoid shapes into AMS_{LF}, AMS_{S1} and AMS_{WB} types. Principally, such heterogeneities can occur and indicate non-uniformly distributed fabric imprints through the samples specimens (see case study Negev).

3.5.2.1 AMS_{S1}

This AMS fabric is developed in the unweathered granite in SD-2.c and in a part above the black-shale unconformity (SD-1.c) (Figure 3.12.d). The AMS fabric type is characterized by shallow κ_3 axes (<11°) and high oblate eccentricities. AMS_{S1} in the unweathered intact granite (SH-15) shows a well defined oblate shape (P' 1.06; $T > 0.5$) and a vertical position of κ_1. AMS-ellipsoids are slightly more flat-lying in the unweathered granite sample above the black shale (SH-4 and single specimens of SH-5).

3.5.2.2 AMS_{WB}

P' are very low (< 0.01) in the weathering-breccia (WB) (Figure 3.12.b). Shapes tend to be oblate (ca. $-0.2 < T < 0.6$) but a high scattering is evident. This is an effect of the very low anisotropy degree (P' < 0.01). A scattering of T is an effect of the extremely weak defined ellipsoids. AMS_{WB} is similar to $AMS_{S1}$with respect to κ_3. κ_1 are shallower inclined in AMS_{WB} than in AMS_{S1} (down to 20°) (Figure 3.12.b).

3.5.2.3 AMS_{BG}

In a brecciated granite (BG), a magnetic fabric is developed, which bears characteristics of both, AMS_{S1} and AMS_{WB} (Figure 3.12.c). κ_{bulk} is as high as in the weathering-breccias, which points to a similar alteration stage. P' of 1.09 to 1.1 is higher than in the unweathered granite. The petrographic and magnetic foliation is well developed, but differs in declination by about 60° from those in the wall rock granite (AMS_{S1}). This is interpreted as a local deviation. With respect to the inclination of the principal anisotropy axes, there is no deviation detectable: κ_3 is steep and κ_1 moderately steep inclined.

3.5.2.4 AMS_{LF}

AMS_{LF} is the magnetic fabric characteristic for samples adjacent to the black-shale unconformity (LF = lower fault). This AMS fabric is developed in weathered granite (SH-5, SH-6) above the black shale and in a weathering-breccia (SH-8) beneath the black shale. Eccentricity values are low (P' = 1.01), shape factor is oblate to prolate. κ_3 of AMS_{LF} is generally medium inclined (average 35°) (open symbols in Figure 3.12.b). The moderately inclined magnetic foliation corresponds to the inclined shear surfaces. The magnetic lineation is oriented in dip direction of the magnetic foliation, paralleling the graphite-chlorite-mica stretching lineation on the shear surfaces.

3.5.2.5 AMS_{UF}

In the foliated black siltstone and in the fault-breccia beneath, dominating structures are related to the upper fault deformation (UF). κ_3 is flat-lying (10°) in the siltstone and steeper (up to 40°) in the fault-breccia. The small trend is indicated by arrows in Figure 3.12.a. Ellipsoid shapes are oblate and anisotropy degrees are low (P' = 1.02 to 1.03). Magnetic lineation κ_1 has a shallow inclination (< 39°) in the brecciated granite. It either parallels shear direction, i.e. inclination of κ_3 (SH-3) or lies perpendicular to it (SH-2). The sedimentary hanging wall of the upper fault (SH-1) shows a κ_1-inclination of 40 - 50°.

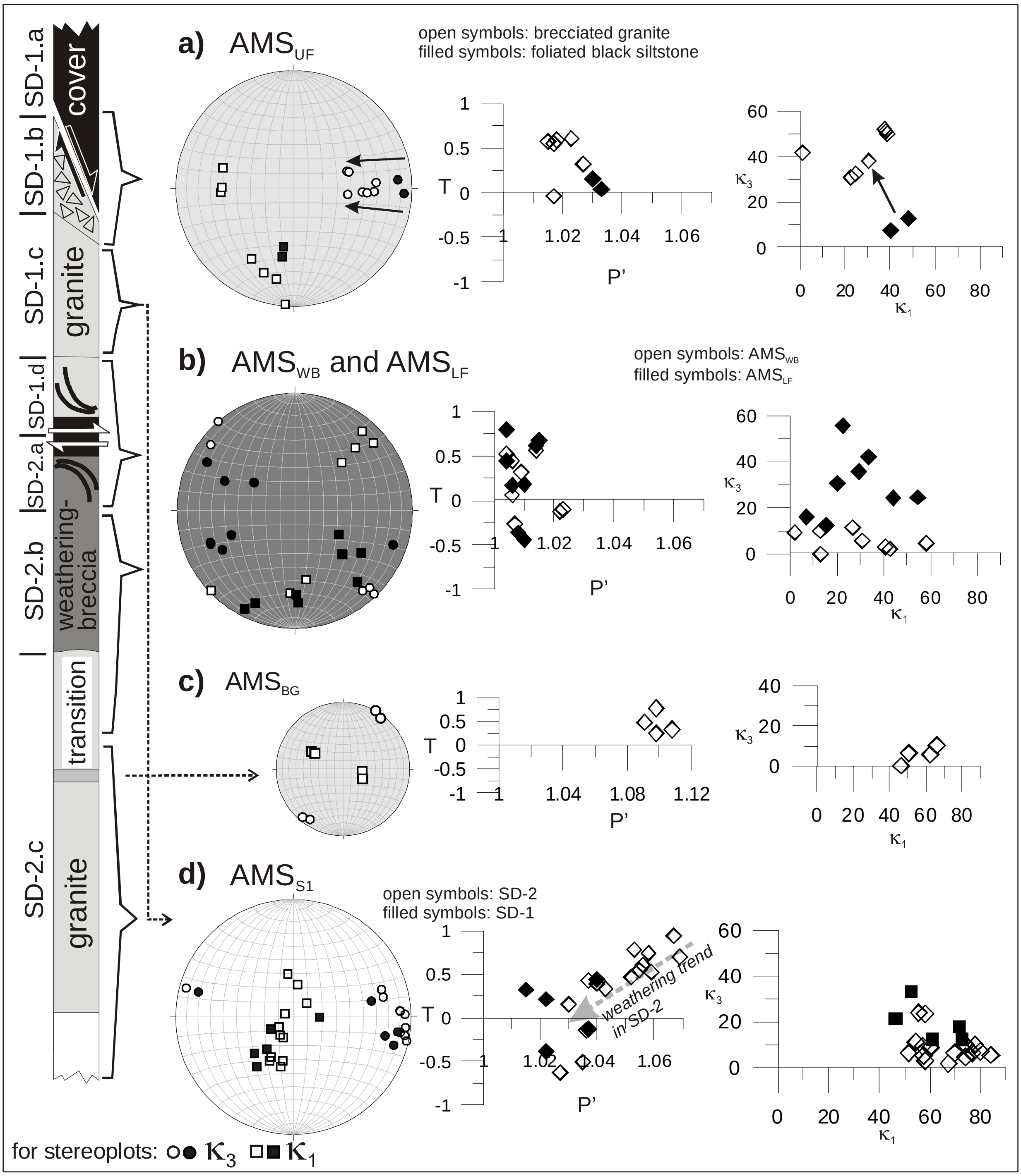

Figure 3.12: The main AMS fabrics types and their occurrence in the profile. Discrimination is made by the anisotropy parameters P' and T and κ_1 and κ_3 orientations.

3.6 Data interpretation and establishing an alteration and deformation sequence

Five stages of granite deformation and alteration are observed in the drill core section (Figure 3.13 and Figure 3.14). This sequence is discussed in this chapter. (stage 1) formation of an early schistosity in the granite, accompanied by an early hydrothermal stage with pervasive propylitic alteration of phyllosilicates and sericitization of feldspar; (stage 2) palaeoweathering in upper Vendian to Cambrian time, possibly with burial silicification of the weathered matrix; (stage 3) burial compaction with incipient horizontal foliation (D_2), possibly accompanied by burial silicification of the weathered matrix. Caledonian deformations are documented as: (stage 4) development (possibly induced by reactivation) of a vertical tectonic cleavage in the weathering-breccia (S_3), accompanied by a very-low-grade hydrothermal alteration; (stage 5) detachment along the black shale with basement duplication in a tectonic slice (D_4) and (stage 6) the upper (normal) fault with reactivation of vertical planar surfaces (D_5).

3.6.1 D_1 - vertical foliation in the granite and early metamorphism (stage 1)

The subvertical schistosity, mainly defined by chlorite SPO, is observed in the (unweathered and weathered) granite but not throughout the entire weathering-breccia; therefore, foliation is attributed to an early deformation, taking place before weathering-brecciation (Figure 3.13.a). The two foliation sets (Plate 3.1.a) are referred to as S_{1a} and S_{1b}, whereas S_{1a} is by definition stronger developed. Remnants of S_1 are observed in those parts of the weathering breccia, where primary textures are preserved.

The epidote-chlorite-assemblage in the granite and the quartz-recrystallization evidences a low-grade metamorphism during that deformation. Chlorite may be a product of retrograde biotite alteration, as titanite is present (c.f. case study Negev, Plate 2.2.d). Biotite was supposedly the main primary phyllosilicate in the granite. The sericitization of plagioclase in the granites was initiated during early metamorphism, as it is a typical feature of deuteric alteration. Sericitization may have taken place also during later very-low grade alteration (see below). Rutile and titanite impregnation inside chlorite may be a feature of the early hydrothermal alteration.

Regionally, deformation and metamorphism up to the greenschist facies have been observed in the Revsund granite (Kousa et al. 2000). The tectonometamorphic overprint of the studied granite can be attributed to the NW-SE trending Storsjön-Edsbyn shear zone SESZ (Mattsson & Elming 2001), which is observed in the basement SE of Östersund. The extension of the SESZ at least to the Hara location is very likely. A similar metamorphic overprint comparable to the SESZ (brittle-plastic to mostly plastic and retrograde: (Mattsson & Elming 2001) is evident by the very-low grade mineral assemblage and the subvertical schistosity fits to the mainly transpressional regime, in which basement rocks were overprinted within the SESZ (Mattsson & Elming 2001). The age of the SESZ is younger than the Revsund Granite intrusion (slightly younger than ca. 1.8 Ga: (Mattsson & Elming 2001), and therefore the oldest tectonometamorphic overprint in the studied granite.

3.6.2 Palaeoweathering (stage 2)

Subaerial weathering led to a destruction of the granitic texture (Figure 3.13.b). Processes causing a textural breakdown were chemical weathering of almost total albite content and minor K-feldspar and mechanical fragmentation (weathering-brecciation). The modal fraction of the clay-size-minerals is much higher in the weathering-breccia than in the intact weathered granites below; it is a function of weathering degree. The alteration and mechanical destruction of chlorite is the second important process that took place during weathering. This is inferred by the absence of chlorite clasts in the matrix. Chamosite in the clay fraction (chapter 3.3) may be a mixture of a primary type, mechanically destructed during weathering-brecciation, and a secondary type, formed authigenically later than weathering (see below). Alteration of primary chlorite led to the formation of illite and smectite phases and the “alteration-symplectites”.

Illite and smectite are the main clay phase in the weathering-breccia and precipitation is related to the hydrolysis of plagioclase and chlorite. A broadening of illite peaks with proximity to the unconformity (Figure 3.6.d) is due to an enhanced I/S mixed-layer mineral content or to an increase of the mixing ratio of poorly to well-crystallized illites (Meunier & Velde 2004). Both are attributed to palaeoweathering. Although pure illite is discussed as a primary weathering clay mineral (Meunier & Velde 2004) and smectite content in the I/S mixed-layer minerals is minor (< 5 %), it is likely that the clayey weathering products were predominantly smectite phases, as the more typical weathering product in many weathering zones. Illite precipitation itself may have been a result of subsequent prograde transformation during burial diagenesis (Meunier & Velde 2004).

Quartz is the main cement of all breccias in the drill core section. Quartz may derive from Na-hydrolysis (see equation 1a in chapter 1.2.1). Primary quartz could have been mobilized during weathering, as well. A rapid and local reprecipitation may have produced the quartz-cementation in the weathering-breccia.

A weathering profile developed, characterized by progressive brecciation and enrichment of clay and alteration-symplectite towards the unconformity. The maximum of chemical decomposition of feldspar and chlorite is recognized by XRD just beneath the unconformity (see chapter 3.3). Alteration degree of feldspar and chlorite is lower and weathering-brecciation less developed in the breccias of the SD-1 (at least in sample SH-5). The gradually increasing grain-size-reduction in the weathering-breccia is a function of plagioclase alteration (illitization) and weathering-brecciation. This suggests an autochthonous (in-situ) formation of the breccia. The clastic material, resembling the granite mineralogy from below (except diminished albite and chlorite), may support an in-situ formation, but may also point to proximal material transport. The partly rounded clasts suggest that the breccia is a soil-sediment (see chapter 1.2). The angularly shaped K-feldspar clasts indicate a proximal transportation of the material. AMS support an in-situ formation, at least for the lower weathering-brecciation section (until 2-3 metres beneath the black shale) (see chapter 3.7.2.4).

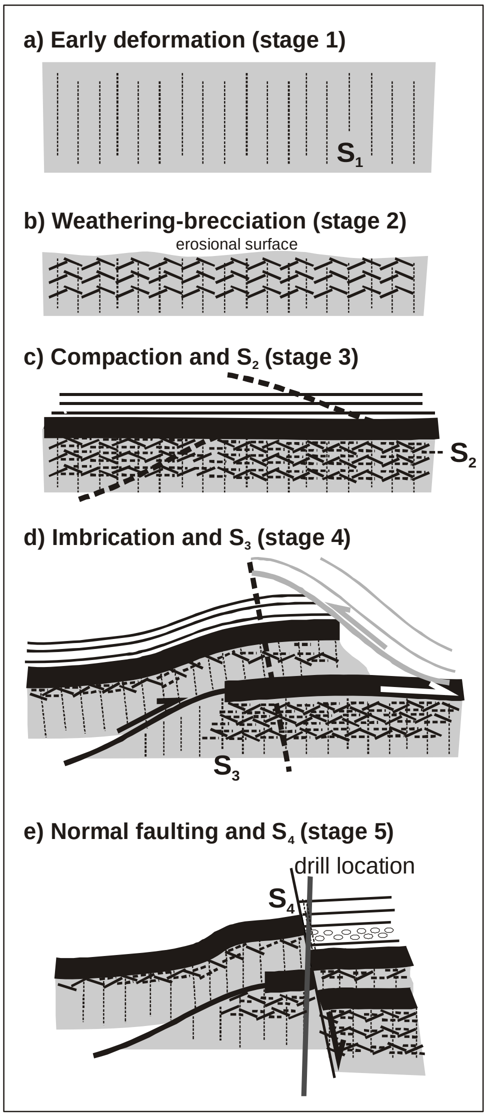

Figure 3.13: Sketch sequence explaining the structural development of the studied drill core section.

3.6.2.1 Palaeoclimatic implications

Implications regarding the palaeoclimate during weathering are difficult to ascertain. Chemical weathering accompanied by weathering-brecciation is not indicative for climatic conditions (Retallack 1991). As discussed in chapter 2.7.2 (case study Negev), weathering-brecciation in the weathering profile can either occur in warm and humid weathering conditions, when rock forming minerals are altered (by hydrolysis) and dissolved (see case study Israel) or during frost weathering (cryoturbation or congelifraction) in a temperate to cold climates.

The absence of kaolinite, as an indicator for warm and humid conditions, may point to rather cold environment. Silicate weathering, such as feldspar hydrolysis, can be considerably high in cold and wet climate (West et al. 2002). Enhancing factors are the presence of carbonate or dissolved (organic) carbon and high pH and $p\mathrm{CO}_2$ conditions in the rocks (Williams & Walter 2004, Williams et al. 2003). Na-plagioclase decomposition, together with the alteration symplectites bearing carbonate and graphite are petrographic indicators that may be point to intensified silicate weathering in a temperate or cold climate.

Precipitation of SiO_2 from soil solutions is observed in repeated freeze-thaw cycles (Dietzel 2005 and references therein). The present quartz-cemented weathering-breccia could represent a permafrost zone.

The most likely period for the palaeoweathering was the latest Cryogenian, which is characterized by a cold

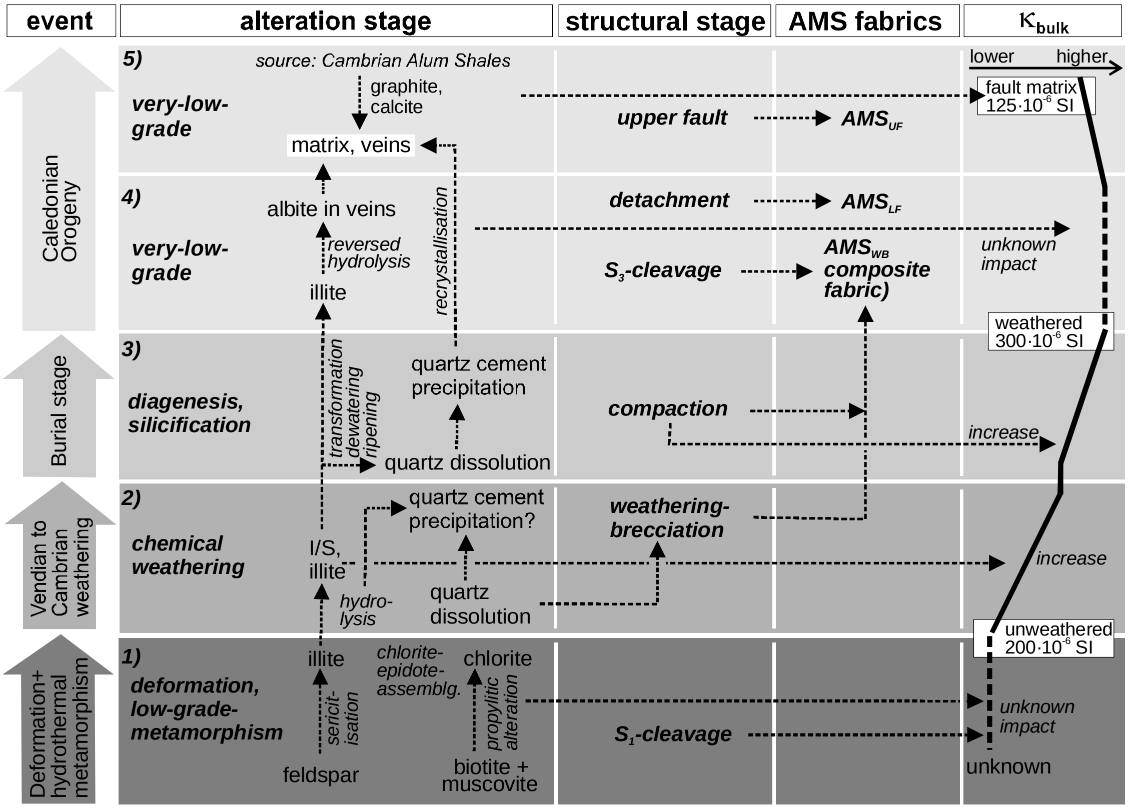

Figure 3.14: Synthesis of tectonometamorphic and alteration stages and corresponding AMS-type and κ_{bulk} evolution in the Hara drill core at the basement-cover-interface. Numbers refer to alteration and deformation stages, see text.

climate in the region and pre-dated the first flooding horizon, associated with the beginning Ediacaran time at 590 Ma (Greiling et al. 1999b) (see chapter 3.1.1).

Regarding the completeness of the weathering profile, there is the likelihood that abrasion of the top-horizons occurred during the Cambrian flooding event, which caused the Alum Shale Fm. sedimentation (Vidal & Moczydlowska 1996). A tectonic reactivation (horizontal shear) of the unconformity may have obscured the situation by tectonically reducing the erosional contact between basement and cover beds (see chapter 3.6.5).

3.6.3 D_2 - burial compaction (stage 3)

Compaction features are not observed in the weathering-breccia. Considering the textural disintegration during weathering-brecciation, a compaction can be expected. The deformation is referred to as D_2 (Figure 3.13.c). With the AMS results, this can be better investigated (see chapter 3.7.2.4).

Burial diagenesis in the core reversed the mineralogical effects of weathering in the sense that the relic soil clay content (smectite, I/S mixed-layer minerals) transformed prograde to illite (Meunier & Velde 2004). Illite is presently the dominant clay phase exceeding chlorite and smectite contents. Illite-forming reactions involved de-watering in the matrix and may have facilitated the dissolution of quartz (Weaver 1989). Primary quartz may have been remobilized during the burial stage and reprecipitated locally. Due to this, quartz is the main cement of all granitic breccias in the drill core section. The absence of a clear compaction cleavage may be attributed to the quartz cementation during weathering hydrolysis of plagioclase. Quartz precipitation resulting from feldspar hydrolysis as a reaction-hardening process is discussed by Wibberley (1999). D_2 might have reached into an early phase of Caledonian nappe stacking.

3.6.4 D_3 - vertical cleavage and related fluid-rock-interaction (stage 4)

The subvertical cleavage that is observed in the weathering-breccia is named S_3 (Figure 3.13.d). S_3 is restricted to the autochthonous basement (SD-2) and the lower allochthonous basement slice (SD-1). It is not developed in the cover rocks. S_3 was accompanied by elevated temperatures up to 270 to 300 °C (sub-greenschist facies), which is indicated by a) incipient quartz recrystallization, b) stable chamosite 002 FWHM throughout the profile section (Figure 3.6) and c) an epidote-chlorite-assemblage in veins. These veins crosscutting the matrix of weathering-breccia and intact granite, demonstrating a post-weathering and late to post-deformational hydrothermal overprint. Albite veins may have originated during prograde “reversed hydrolysis” at the expense of I/S or sericites in the rock. D_3 occurred after D_2 during a prograde change of metamorphic grade reaching here maximum sub-greenschist facies conditions. S_3 is similarly inclined as S_1; the cleavage may have been induced by reactivation of S_1 surfaces in the granite beneath.

Setting for D_3 is the main phase of Caledonian nappe stacking involving the emplacement of the Lower Allochthon on top of the autochthonous basement (Gee 1978, Roberts 2003, Roberts & Gee 1985, Roberts & Stephens 2000). According to the orogenic wedge model (e.g. Greiling et al. 1999a), peak conditions of metamorphism near the present Caledonian front were at most anchizonal (Warr et al. 1996).

3.6.5 *D_4 - lower fault and related fluid-rock-interaction (stage 5)*

SD-1 is a repeated section of the weathered granite. This is interpreted by the (sheared) black shale between both domains and by the mineralogy in the granite of SD-1, which is comparable to the weathered granite in SD-2 (e.g. similar FWHM of both chamosite and illite XRD-peaks in the tectonic slice and weathering-breccia: Figure 3.6.d). SD-1 can be referred to as the basement part of a tectonic slice, and therefore this slice is considered as a part of the Lower Allochthon, which typically incorporates underlying basement rocks in slices (Roberts 2003). The repeated basement-cover-contact (upper unconformity) is a result of this structural duplication. The black shale represents the shear-horizon. The brecciation zones, adjacent to the black shale (above and below), are tectonically induced by the faulting.

The Palaeoweathering in the core took place prior to D_4-fault propagation. The part of the weathering-brecciation is tectonically reduced in SD-2, which is due to the upper fault (see below). The lower fault zone has reverse kinematics (thrust), causing the basement repetition (thrust slice) (Figure 3.13.d).

The downward transition in the lower part of the tectonic slice from intact granite to breccia is not a weathering trend, but a trend of increasing intensity of fault-brecciation. S_3 is not developed in the fault-breccia of SD-1. Apparently, S_3 developed prior to the lower fault propagation, presumable as an initial deformation of the D_4-detachment tectonics. Moderately inclined discrete black shear surfaces with a stretching lineation are associated with the lower fault (detachment) and are interpreted as secondary shear surfaces (Riedel-shear surfaces?). These brittle deformations features indicate that subsequent to D_3 temperatures decreased.

The XRD Δd-spacing indicates that brittle deformation in SD-1 caused smectite precipitation (Figure 3.6.a). This can be inferred by the similar and increased Δd-spacing in the fault-brecciated rock, compared to the weathering-breccia. Moore & Reynolds (1997) question the reliability of absolute d-spacing of I/S peaks in AD conditions. Nevertheless, the results can be considered as reliable with respect to relative changes of I/S content within the sections.

3.6.6 *D_5 - upper fault and related fluid-rock-interaction (stage 6)*

The upper fault deformation is the latest texture-defining deformation in the core section (D_5). This is interpreted from crenulated D_4-fabrics. D_5 produced a uniformly subvertical slaty cleavage in the foliated black siltstone, paralleling the steep inclination of the (upper) D_5-fault. The D_5-fault caused the rather steep tectonic contact between basement-rocks (brecciated granite) and foliated black siltstone (cover) (Figure 3.13.e). The D_5-fault tectonically reduced the upper part of the basement slice with presumable normal kinematics. The normal kinematics of the upper fault zone is a consequence of the hanging wall - footwall relation, and the graphite-calcite-veins in the foliated black siltstone, showing boudinaged graphite flakes (Plate 3.1.g), may indicate an extensional character of the fault zone.

The idiomorphic quartz porphyroblasts at the vein rim show graphite and calcite inclusions parallel with the crystal surfaces, indicating several stages of growth (Plate 3.1.h). This quartz is a relatively late generation in the vein evolution, as it is not deformed and overprinted all calcite generations.

The growth of the coarse-crystalline graphite required moderately elevated temperatures and high differential stress and/or highly C-enriched fluid compositions (Bonijoly et al. 1982, Pitcairn et al. 2005). The fluids infiltrating the veins were indeed enriched in C and calcite. Calcite may have originated in the organic and carbonate rich cover sediments (Alum Shale Fm.).

Fault-related alterations in the tectonic slice during D_5 took place under “warm” temperature conditions (temperatures below 200 °C). This is indicated by the advanced I/S precipitation (in sample SH-2, see chapter 3.3) and by chamosite, which did not undergo alteration (stable FWHM: Figure 3.6.d). Cover sediments are not clearly cleaved, above SD-1, pointing to a local imprint of D_5-fabrics. Here, dense pyrite or marcasite precipitation may be related to the fluid infiltration and indicate that these fluids were reducing in nature.

A second pulse of C-enriched fluids reached parts of the autochthonous granite, impregnating chlorites and all types of veins with microcrystalline graphite. The microcrystalline graphite is likely associated with a cooler fluid temperature than the first, syn-D_5-fluid. This evidences a general path of decreasing temperatures accompanying deformations D_3, D_4 and D_5.

3.7 Development of κ_{bulk} and AMS and their relation to the petrogenesis

3.7.1 Bulk susceptibility

Bulk susceptibility of the rocks was modified during the alteration and deformation stages. Figure 3.14 summarizes a reconstruction of the evolution of κ_{bulk}. The primary susceptibility was carried mainly by biotite, after chloritization κ_{bulk} is carried by chlorite. κ_{bulk} values of the studied Revsund Granite are similar to those described from the SEDZ (Mattsson & Elming 2001). Main factor for an increase of κ_{bulk} is the illite and smectite precipitation, which is maximized in the weathering-breccia. The impact of fault-brecciation is minor, but precipitation of diamagnetic graphite and calcite led to a decrease of κ_{bulk}.

The amount of experimentally formed Mn-Mg-ferrite in the κ(T)-curves (Figure 3.9), increases from unweathered granite to the lower boundary of the weathering-breccia and may therefore indirectly show a progressive Fe-carbonate precipitation during progressive chemical weathering. In the weathering-breccia and fault-breccias, however, the susceptibility-enhancing effect of Fe-bearing carbonates is negligible. Since XRD-results show no significant change in carbonate content within the entire profile, the changes are explained by a decrease of Fe-content in carbonates in the breccias rather than a decrease of carbonate content itself.

Silicification of the matrix during burial stage is a process, which replaces paramagnetic by diamagnetic material. Hence, it had a negative effect on κ_{bulk} in the profile. Petrographic observation shows that silicification is a feature of all brecciated matrixes.

3.7.2 AMS fabrics

3.7.2.1 Reliability of the AMS data set

The low P’ values in the paramagnetic granite, respectively breccia, are typical considering the absence of strongly developed S- or L-fabrics (Pares & van der Pluijm 2002b). Anisotropy may have been additionally lowered by superposition of magnetic subfabric (e.g. Housen et al. 1993); compare also Figure 1.9.b, d).

The reliability of the anisotropy has to be discussed, since the anisotropies in the paramagnetic samples are quite low. It is recommended by Pueyo et al. (2004) to statistically discriminate the data (at sample scale) into groups of reliable and non-reliable AMS orientation. The reliability of the present data set is considered as low, according to the discrimination methods suggested by Pueyo et al. (2004). However, the clearly developed trends of the P' and κ_1-inclination in SD-2 (Figure 3.15) suggest a reliable data set, at least for the weathering profile in SD-2.

3.7.2.2 Relation of AMS to minerals and brecciation

The evolution of shapes and principal-axes orientations of the AMS ellipsoids are a result of the change in crystallographic orientation (SPO/LPO) of Fe-bearing phyllosilicates chlorite and (phengitic?) illite (Pares & van der Pluijm 2002b, Tarling & Hrouda 1993). This follows by the paramagnetic nature of the rocks, evidenced by κ(T) measurements (Figure 3.9). Chlorite is the carrier in the granites. Chamosite (determined by intensity relation of XRD-peaks: chapter 3.3) and illite, as well as relic primary chlorite, are the main carriers of AMS in the weathering-breccias. Relic primary chlorite is considered as an important carrier in the fault-breccias, which did not show as much of clayey transformation as the weathering-breccia.

A principal relation of rock texture and AMS fabric is evident: granitic textures are related to strong anisotropic and clearly oblate shapes, whereas brecciation texture are characterized by a weak anisotropy with less oblate shapes (Figure 3.12).

A negative κ_{bulk}-to-P' correlation, is observed beneath the lower unconformity, but not in the allochthonous slice (Figure 3.11.c,d). This has to be attributed to a different contribution of the both brecciation processes (weathering in SD-2 and faulting in SD-1) on κ_{bulk}, as stated in the previous chapter. On the other hand, a general dependency of P' on brecciation degree is evident, independent from the brecciation processes. A loss of ellipsoid eccentricity (P') is a general observation in brecciated rocks, which did not undergo cataclastic flow or cleavage formation (Nakamura & Nagahama 2001); see also case study Negev).

3.7.2.3 Foliated granite - AMS$_{S1}$

The AMS$_{S1}$ fabric reflects the uniform subvertical rock foliation in the granite. The phyllosilicates-foliation S$_{1a}$, locally, a secondary set is developed (S$_{1b}$) (Plate 3.1.a), define the sub-vertical magnetic foliation. S$_{1a}$ is stronger developed than S$_{1b}$, therefore the former is more important than the latter in defining the declination of κ_3. A weak vertical intersection lineation of the two sets of phyllosilicates-foliation result in a vertical κ_1 orientation (as displayed in Plate 3.1.a). κ_3 is slightly more inclined in the weathered granite of the allochthonous slice (SD-1), which is likely a result of passive rotation during thrusting (Figure 3.12.d), since rocks were already foliated by the time D$_3$-detachment took place.

The formation of S$_1$ in the granite was very likely associated with the SEDZ, as discussed in chapter 3.6.1. As the investigation of Mattsson & Elming (2001) on the SEDZ and its undeformed wall rocks features an AMS fabrics study, a correlation with those patterns can be carried out here. Considering a linear extension of the SEDZ towards the Hara drill location in the NW, it is likely that the present basement rocks are in the NE transitional zone between undeformed and highly sheared Revsund Granite (locations ST01 to ST07 of (Mattsson & Elming 2001). A comparison of the AMS data confirm this. The rocks in the transitional zone show steep magnetic foliations and P' values ranging mainly between 1.05 and 1.1, generally increasing with deformation intensity. The magnetic lineation gradually becomes steeper with proximity to the SEDZ, thus with deformation degree. The fabric, characterized by vertical κ_1 and horizontally clustered κ_3, is associated with the pure-shear dominated transpressional regime, in which the SEDZ formed (Mattsson & Elming 2001 and references therein). AMS$_{S1}$ resembles the AMS pattern from the transitional zone between undeformed and deformed Revsund Granite, and thus can be correlated with the zone. The slightly lower P' and κ_{bulk} can be attributed to the chloritization of biotite, which has a higher intrinsic susceptibility than chlorite. Chloritization is not observed in the region E of the Caledonian front (Mattsson & Elming 2001). This may suggest that chloritization is a late stage alteration, associated with thrust tectonics (D_3), thus restricted to zones near thrust surfaces, as it is the case in the drill core section. These zones were eroded E of the Caledonian front. The uniform FWHM values of clay-sized chamosite throughout the drill core section (Figure 3.6.d) supports this late stage formation of chlorite.

3.7.2.4 Overprinted weathering-breccia - AMS_{WB}

The weathering-brecciation destroyed earlier textures to form a matrix supported texture. The matrix-supported domains are deformed by S_3. Relic granitic domains with S_1 are present. The shallowly plunging κ_3 are a product of the subvertical relic S_1 and secondary S_3 (Plate 3.1.d). κ_3 stays stable across the weathering profile beneath SD-2.a (Figure 3.15). This is due to a strong influence of mica and chlorite, which define S_3 and S_1, respectively (see chapter 3.2.2 and 3.4).

The clay formation and accompanied disintegration of the matrix in the weathered intact granite advanced during the burial stage and must have caused the development of a flat-lying compaction fabric by mineral reorientation. This flat-lying D_2-fabric is most likely defined by cryptic clay mineral SPO (not observed by optical microscopy). The existence of the D_2-fabric is investigated by AMS.

In Figure 3.15, the degree of weathering-brecciation is marked from *a* to *e*: *a* is the fresh intact granite and *e* the strongest weathered breccia; *(e)* represents the theoretical upper end-member of AMS_{WB}, which is not preserved due to the cataclastic overprint of D_3. This cataclastic overprint is observed in SH-8, which shows a deviation of κ_3 from a shallow inclination to a medium steep inclination (excluding specimen SH-8LF).

κ_1-inclination decreases systematically from the granite towards the lower unconformity. This distinct κ_1-

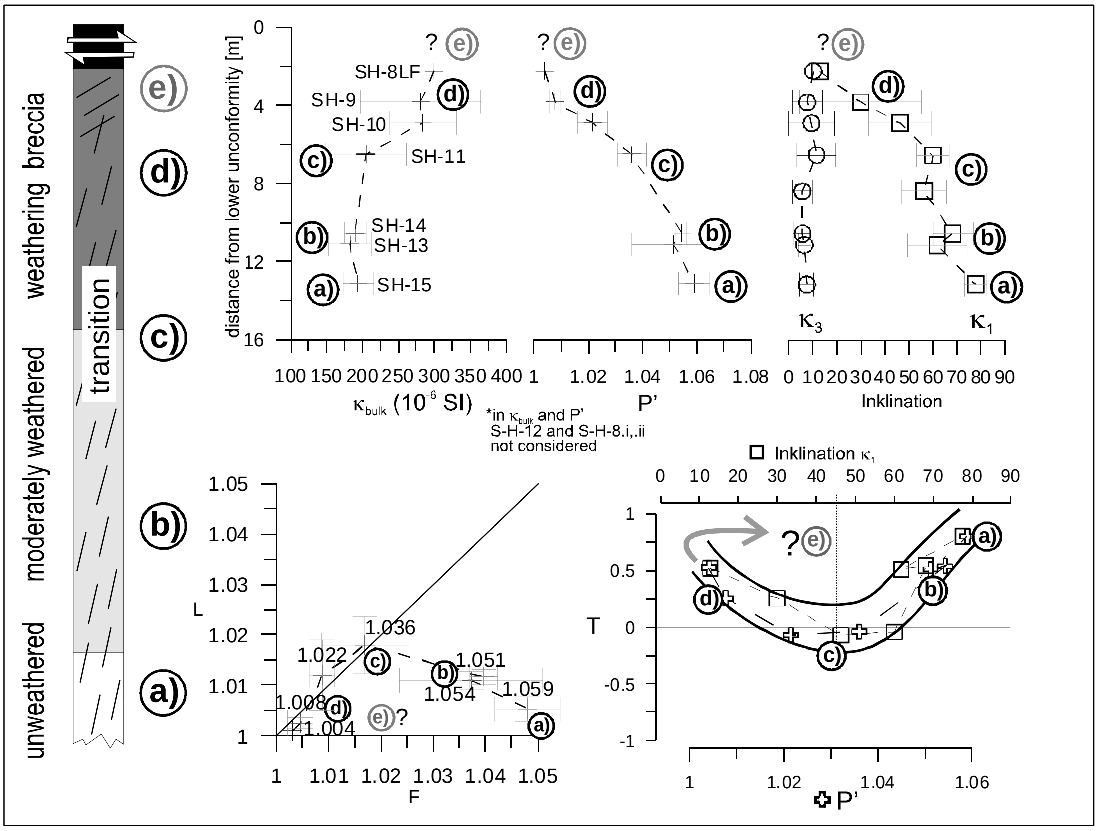

Figure 3.15: Compilation of AMS-data of SD-2 showing the distinct AMS-trend in the weathering profile below the lower unconformity (black shale). Stages of weathering-brecciation are marked with letters a to e. e is the hypothetical stage of AMS_{WB}. SH-8LF is a subset of SH-8.

inclination trend correlates well with P' (positive correlation, $R^2 = 0.926$) Figure 3.11.e). Together with the good κ_{bulk}-to-P' correlation ($R^2 = 0.899$), it indicates a simultaneous generation of rock alteration (increase of κ_{bulk}), ellipsoid shape (decrease of P') and orientation of magnetic (shallowing of κ_1-inclination).

The data point to superposition of magnetic sub-fabrics, considering the unique pattern of a stable κ_3 and changing κ_1/κ_2 axes. An overprint of the flat-lying D_2-fabric by the steep S_3-surfaces has to be discussed as the cause for the composite AMS fabric in the weathering breccia and the superposition of the S_1 by S_2 in the weathered granite. The horizontal magnetic lineation is an expression of the rock's intersection lineation of both fabrics (Pares & van der Pluijm 2002a; also Figure 1.9). The gradual decrease of κ_1-inclination towards the unconformity in accord to the gradual decrease of P' is attributed to the increasing intensity of the horizontal D_2-fabric. D_2-fabric intensifies with proximity to the unconformity as a function of brecciation-

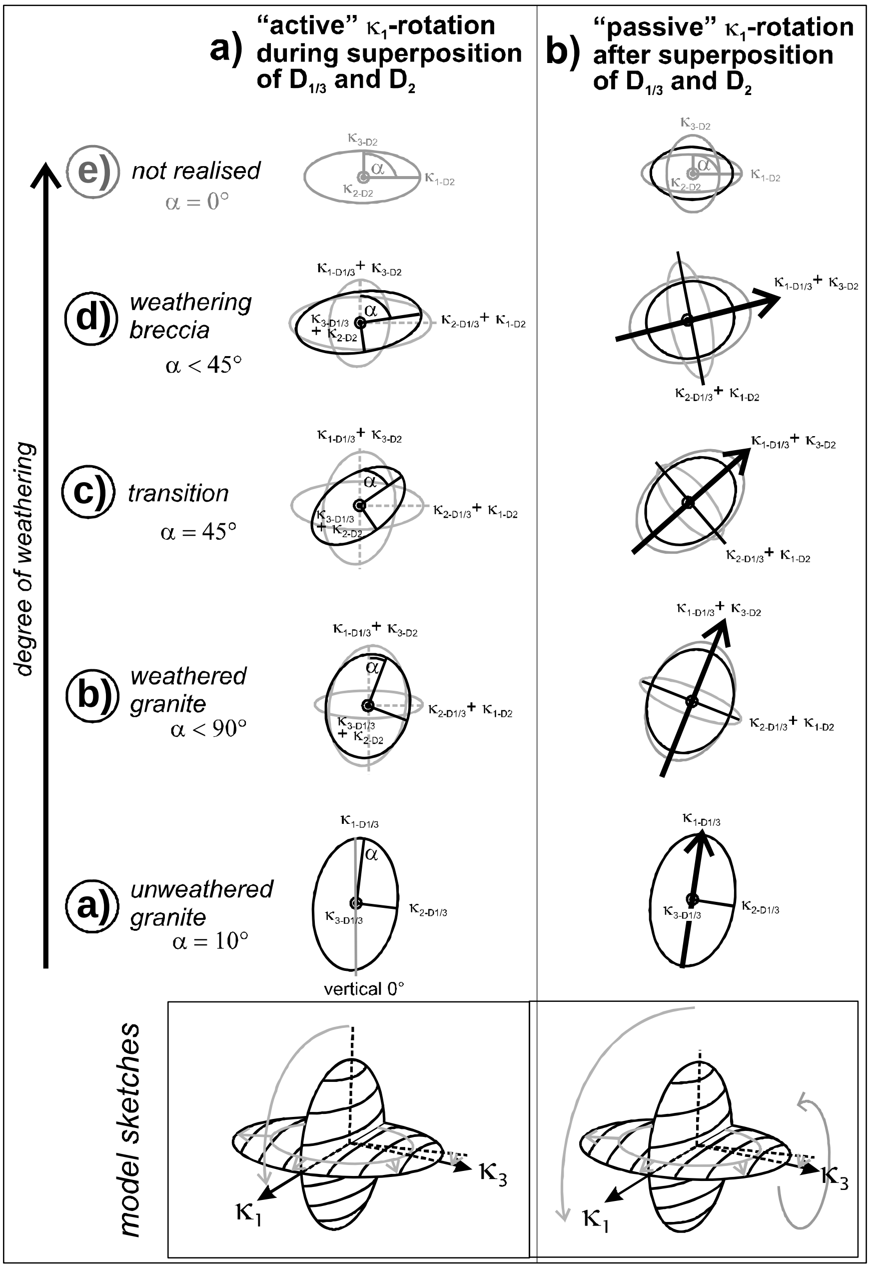

Figure 3.16: Rotation of κ_1. Two scenarios are possible: a) "active" rotation, occurring simultaneously to modifications of the ellipsoid shape during overprint of D_2 with D_3, and b) "passive" rotation after the occurrence of changes in ellipsoid shape (supposedly during D_3). Stages a to e refer to Figure 3.14. Indices D1, D2, D1/3 refer to deformation stages.

intensity and clay-precipitation. Oblate and bedding-parallel AMS fabrics induced by diagenesis have been described and modelled for sediments (Hrouda & Ježek 1999b). In total, the D_2-fabric is the weaker AMS subfabric compared to the S_1- and S_3-fabrics in the granite and weathering breccia, respectively. This is shown by the stable subhorizontal κ_3, defined by the vertical S_1- and S_3-surfaces

A simplified two-dimensional model using vector addition may elucidate the results of the superposition (Figure 3.16.a). It is based on the assumption that there is a small angle between κ_3 of D_1-fabric (parallel to the main compressional axis) and κ_1 of D_2, which is confirmed by the measurements. By this, a rotation of κ_1 occurs, as the axis is the resultant vector of both subfabrics. The observed rotation of κ_1 is termed here as "*active*", because it occurs simultaneously to the changing relative superposition of both subfabrics. Contrary to that, a "*passive*" κ_1-rotation, without changing the ellipsoid shape, would be the result of a rotation of the entire AMS-ellipsoid around κ_3 during a subsequent rotational deformation (Figure 3.16.b). The D_3-shear parallel with the unconformity would be the rotational deformation. In this case, the progressively lowered P' is either a superposition effect (*sensu* Housen et al. 1993), or due the decreasing anisotropy of the progressively brecciated texture. The second model requires D_3-related shear-features across the weathering-breccia, which, however, are missing. Only the part adjacent to the lower unconformity, SD-2.a with sample SH-8, shows such brittle deformation features (as described in chapter 3.2.2). Here, however, is the AMS_{WB} partly destroyed and modified to AMS_{LF}, as observed by the abruptly changed κ_3-inclination. Therefore, the first (active) superposition model is preferred: burial compaction fabric (D_2) and vertical tectonic foliations (S_1 and S_3) produced AMS_{WB}.

In accordance to Hrouda (*pers. comm.*), it is inferred that gradual κ_1-modification can be generated in a composite fabric of such sub-fabrics, which are not perfectly oblate and having their κ_1 oriented in an angle less than 90°. The author is not aware of literature examples describing gradual κ_1-modifications in oblate

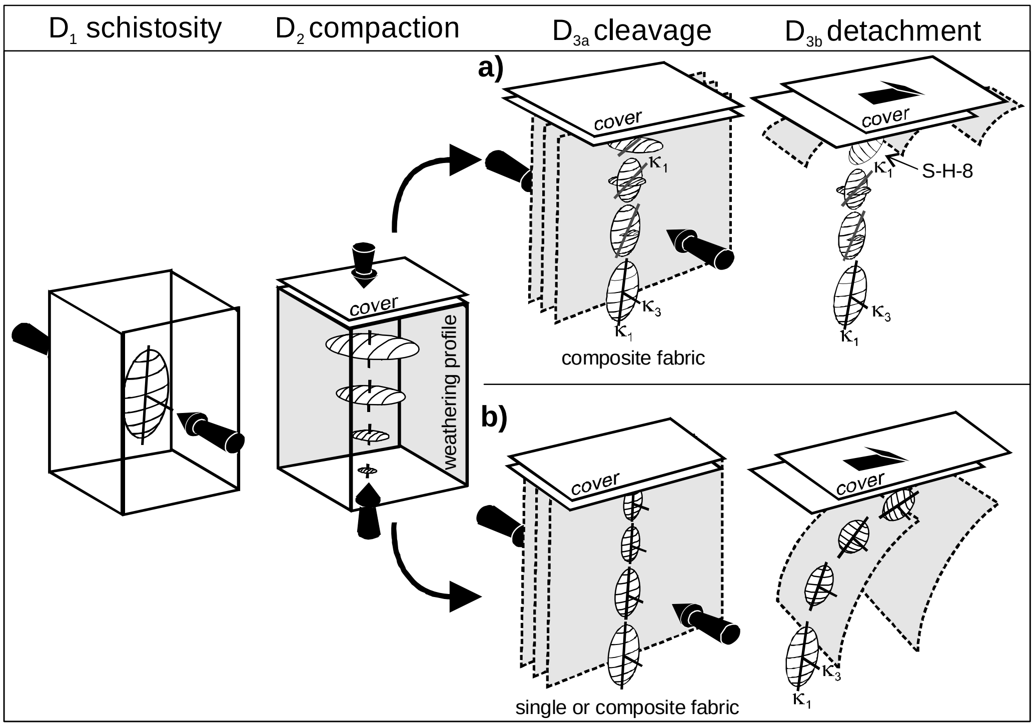

Figure 3.17: Sketches showing the two possible deformation sequences, which may have led to the observed trend of AMS fabrics in the weathering profile. In a) a composite AMS fabric with "active" rotation of κ_1 is carried by S_1 and S_3 (vertical schistosity and cleavage, respectively) and D_2-fabric (horizontal burial compaction). Horizontal shear with rotation of the AMS fabric is only in the uppermost part important. b) AMS is defined by S_1 and S_3 and horizontal D_3-fabric causing a rather "passive" rotation of the ellipsoid.

subfabrics. In most AMS studies on the superposition of oblate sub-fabrics in sediments (e.g. Anderson & Morris 2004, Debacker et al. 2004, Housen & van der Pluijm 1991, Pares & Dinares-Turell 1993, Pares & van der Pluijm 2002a, Saint-Bezar et al. 2002), κ_1 modifies strictly by the direction exchange with κ_2. The same is reported from granitic SC-fabrics examples (e.g. Aranguren 1996, Tomezzoli et al. 2003). For deformed black shales, Aubourg et al. (1995) showed a transition of κ_1, caused by competing orthogonally oriented prolate subfabrics. Similarly, Callot & Guichet (2003) described intermediate κ_1-positions in dykes created by superposition if magnetite subfabrics. However, these are examples of prolate subfabrics. An extension of the theory about superposition of oblate magnetic subfabrics, which essentially is based on perfect model situations with respect to fabric shape and angles (e.g. Housen et al. 1993) seems to be necessary.

3.7.2.5 Lower fault - AMS$_{LF}$

Cataclasis is the main texture-defining process in the thin deformed zones above and below the black shale (SD1.d and SD-2.a, respectively). This process led to a decrease of P’ in the fault-brecciated weathered granite (samples SH-5, SH-6) and to a further decrease of P’ in sample SH-8 in the weathering-breccia. Here, the ellipsoid anisotropy are extreme low (P’1.01). κ_3 are medium steeply inclined and appear to be related to the discrete D$_3$-shear surfaces.

The “passive” rotation of κ_1-inclination is related to D$_3$. This scenario is visualized in Figure 3.17.b. As discussed in the previous chapter, the influence of D$_3$-shear is petrographically evident in the SD-2.a, but not beneath.

3.7.2.6 Upper fault - AMS$_{UF}$

The poles of magnetic foliation, κ_3, are flat-lying (10°) in the foliated black siltstone due to the subvertical slaty cleavage, and steeper (up to 40°) in the upper fault-breccia, where slightly shallower shear-bands exist. The higher P’ in the foliated black siltstone must be attributed to the elevated κ_{bulk}. κ_1 either parallels the shear direction, i.e. the inclination of κ_3 (SH-3) or lies perpendicular to it (SH-2). The former may be the result of stretching lineations, the latter may results from a composite fabric-induced by the shear bands, which developed by the superposition of subvertical D$_4$-surfaces on shallow inclined detachment-related D$_3$ surfaces. The sedimentary hanging wall of the upper fault (SH-1) shows a κ_1-inclination of 40 - 50°, which may be related to the cryptic remnants of the sedimentary fabric.

3.8 Conclusions

In the drill core section, six stages of granite alteration and deformation are observed. (Stage 1) early schistosity in the Revsund Granite, accompanied by a hydrothermal stage with pervasive sericitization of feldspar and probably chloritization of biotite, (stage 2) palaeoweathering in upper Vendian (Cryogenian) time, (stage 3) vertical burial compaction, D$_2$, with an incipient flat-lying, thus unconformity-parallel diagenetic compaction fabric and accompanied by burial silicification of the weathered matrix. Caledonian deformations are documented as: (stage 4) development of a vertical tectonic cleavage S$_3$ in the weathering-breccia, possibly related to reactivations of S$_1$ and (stage 5) detachment along the black shale with basement duplication in a tectonic slice, D$_4$, and (stage 6) the upper (normal) fault, D$_4$, with reactivation of vertical planar surfaces.

Peak metamorphosis is related to stage 1. Sedimentary overburden and Caledonian thrusts led to a maximum anchizonal facies overprint during stages 4 and 5, followed by a decrease to sub-anchizonal conditions during stage 6. The early deformation and related AMS fabric in the deformed granite are related to the Storsjön-Edsbyn deformation zone (SEDZ) and the rock represents the transitional zone between shear zone and undeformed wall rock. Therefore, age (1.8 Ga, slightly younger than the Revsund Granite itself) and pure-shear dominated transpressional stress regime are constrained. The study confirms the interpretation of Gee et al. (1982), regarding subaerial weathering of the autochthonous basement beneath the lower unconformity. In the drill core, the weathering crust reaches pervasively 6 metres below the black shale unconformity, but weathering-breccia relics are also observable at ca. 9 metres depth. Soil development involved texture-collapse due to weathering-brecciation. Climatic conditions during Cryogenian weathering were presumably moderate to cold and caused extensive silicate weathering to smectite (and illite) and presumably quartz-dissolution with immediate reprecipitation as quartzitic matrix cement.

The erosional unconformity was tectonically reactivated during Caledonian orogeny, producing a tectonic slice repeating parts of the weathered granite (Lower Allochthon). The upper basement-cover-interface developed by normal faulting, which paralleled and reactivated the steep cleavage of the granites. Calcite veins with coarse-grained graphite and idiomorphic quartz are associated with the deformations.

Chlorite is the paramagnetic magnetic carrier in the granites and Fe-bearing clay minerals (phengitic illite and chamosite) together with relic primary mica in the weathering-breccia. κ_{bulk} is causally dependent on the intensity of the chemical weathering, which increased the content of the magnetic carriers. Fault-brecciation did not substantially modify κ_{bulk}. Phyllosilicate SPO/LPO fabrics are displayed by AMS fabrics. The unconformity-parallel diagenetic compaction fabric (S_2) is only detected by means of AMS, which shows a trend of vertical to flat-lying κ_1-inclination defined by the superposition of S_2 (showing intrinsic horizontal κ_1) with subvertical S_3 (showing intrinsic subvertical κ_1). κ_3 are parallel with the poles of the dominant S_3-rock foliation. The high linear correlation of the κ_1-inclination and anisotropy degree P’ is causally dependent on the change of the relative overprinting strength of S_2 and S_3. Orientation of magnetic lineation and P’, are a measure for relative changes of intensity in a system of superimposed phyllosilicate fabrics, one with a vertical κ_1. As far as the author is aware, this case study discusses for the first time a natural example of a superposition of oblate paramagnetic subfabrics, resulting in a gradual κ_1-modification.

Plate 3.1: **a)** AMS cylinder of an unweathered granite, κ_3 is ca. parallel with pole of S_1 (sample SH-15); **b)** micrograph of an unweathered granite with sericitization of Na-feldspar and incipient alteration of K-feldspar (SH-15, long side 4.85 mm); **c)** pattern of sericitization in K-feldspar along crystallographic surfaces (SH-15, 4.85 mm); **d)** texture of a weathering-breccia, dark matrix is illite rich I/S, chamosite and graphite rich (SH-9; AMS); **e)** micrograph of the texture of an weathered breccia (SH-9, 4.85 mm); **f)** texture of the tectonic breccia with quartz-rich cement (SH-5; 4.85 mm); **g)** vein-matrix in the upper fault (D_4), graphite “swims” in calcite matrix and is boudinaged parallel with the vein boundary (SH-1; 2 mm); **h)** SEM-micrograph of an idiomorphic quartz in the calcite-graphite vein (SH-1).

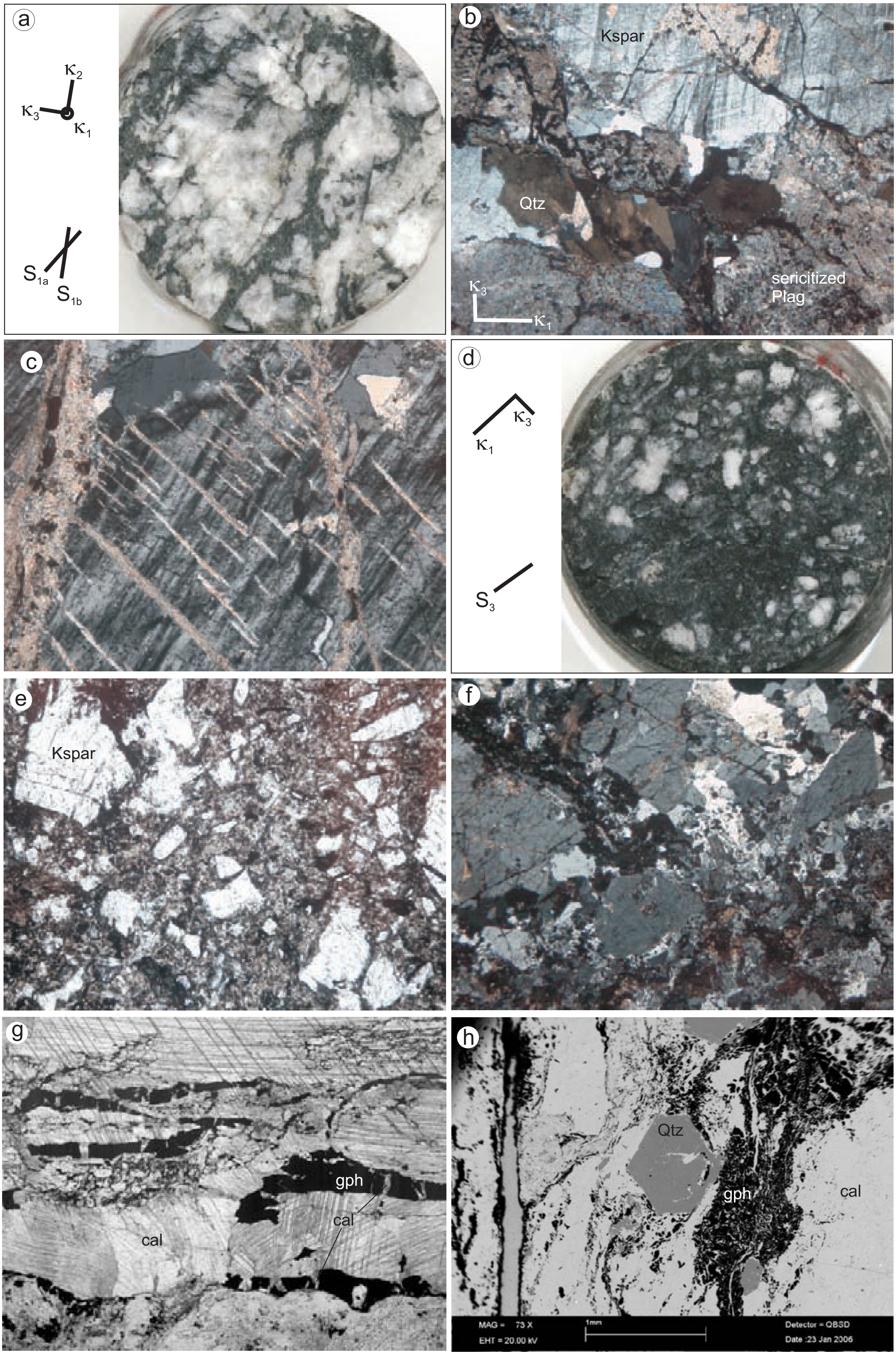

Plate 3.1.a-h (caption see previous page)

4 Case study Långviken, Sweden

Weathering-brecciated Revsund Granite and a sheared allochthonous equivalent (Caledonian margin in Central Sweden)

4.1 Introduction

Two sections from a drill core exhibiting the erosional unconformity between Revsund Granite and siliciclastic Vendian to lower Cambrian Gärdsjön Formation (Gee et al. 1974, Gee et al. 1978) are studied. These two sections are a) the autochthonous part and b) a tectonic slice 11 metres above, belonging to the Lower Allochthon. The aim of this study is to track changes in mineralogy, petrofabrics as well as magnetomineralogy and magnetic fabrics across a fossil and deformed autochthonous weathering profile and to compare these observations with the sheared equivalent in the allochthonous tectonic slice. Applied methods are petrography, geochemistry, XRD and magnetic susceptibility analyses (AMS, temperature and field dependent susceptibility). A geological overview of the region is given in chapter 3.1.1. The drill core SGU Långviken 73007 was studied and sampled at the SGU (Swedish Geological Survey) department in Malå. The drill location is situated in the Tasjön-Ormsjön area (Jämtland nappe region; e.g. Kumpulainen & Nystuen 1985; see Figure 3.1 and Figure 4.1). A petrographic description of the entire drill core can be found in Gee et al. (1978).

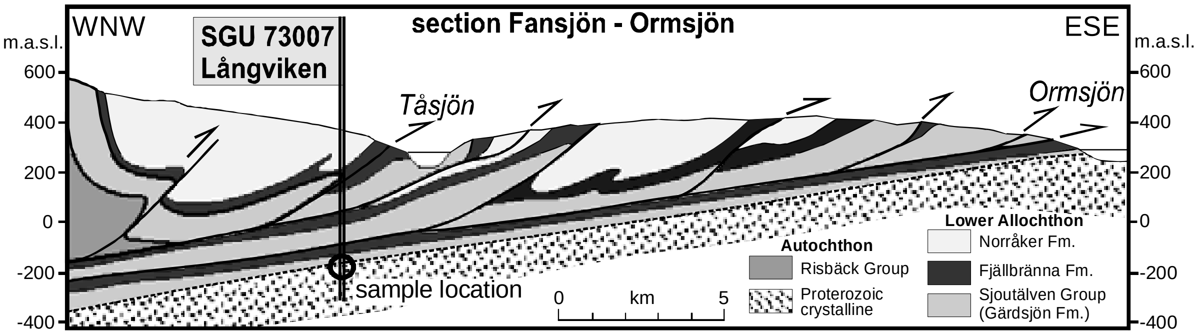

Figure 4.1: SGU 73007 Långviken drill core location at the Caledonian front in Central Sweden (Tasjön-Ormsjön area, Jämtland). Section modified after Gee et al. (1978). m.a.s.l = metres above sea level.

4.1.1 Sampling and applied methods

The lower section of the drill core reaches from the lowermost cover beds down 29 metres into the autochthonous granite. The upper section is from an allochthonous tectonic slice with a 7 metres thick basement part and the directly overlying cover sediment. The sampling interval increases approximately logarithmically with distance from the unconformity. Each sample is a 10 to 20 cm long piece of drill core. Three to five oriented standardized AMS-cylinders are drilled from the collected parts of the drill core.

Following methods are used in this case study: thin section petrography employing optical and backscattering scanning electron microscopy in combination with EDX analyses, XRD of the whole-rock and of the clay fraction (< 2μm) and whole-rock geochemistry employing ICP-MS. The magnetic studies comprises measurements of bulk susceptibility κ_{bulk} in a measuring range of 2 to 450 A/m, of AMS in magnetic fields of 300 A/m and of 30 A/m and of temperature dependent magnetic susceptibility in 300 A/m. Each method is described in chapter 1.3.

4.2 Description of the lithologies

The entire drill core section with both autochthonous and allochthonous sections is displayed in Figure 4.2.

The drill core exhibits a basement-cover-interface in the Autochthon and a second interface in the Lower Allochthonous slice (Gee et al. 1978). There is no indication observable for a structural reactivation of the autochthonous unconformity.

4.2.1 *Autochthonous section*

Two key structural domains in the autochthonous section below the autochthonous unconformity are present: 1) a 7.5 m thick brecciated zone between metre 436.59 and 441.50 and 2) an intact granite, continuing to the lower end of the sampled section (at metre 449.79). A thin transition zone between both structural domains is about 1 metre thick (ca. metre 441.50 to 442.50). There are some thin zones of brecciation present within the upper metres of the intact granite.

4.2.1.1 *Foliated Revsund Granite*

The intact Revsund Granite is coarse crystalline, with an average grain size of about 1 centimetre (samples ST-9 to -15). Major rock forming minerals are quartz, albite and microcline. Stacks of rather pure chlorites, locally intergrowing with biotite-muscovite, have a modal fraction of about 20 vol%. Most important accessory phase is magnetite.

The granite is pervasively overprinted by two sets of subvertical tectonic foliation, S_{2a} and S_{2b}. These continuous schistosities give a gneissic appearance to the intact granite.

Intracrystalline deformation of rock forming minerals is evident in the granite. Quartz is pervasively recrystallized under both dynamic (LPO) and static (straight grain boundaries and 120° triple points) conditions. The recrystallized quartz displays undulatory extinction under crossed nicols; locally grains are elongated parallel with the schistosity surface, and bear a second generation of subgrains by bulging (Plate 4.1.b). Feldspars display undulatory extinction and locally thin core-and-mantle structures. Microcline, when adjacent to albite, exhibits a distinctively increased undulation.

Chlorite, as the abundant phyllosilicate in the granite, defines the foliation surfaces.

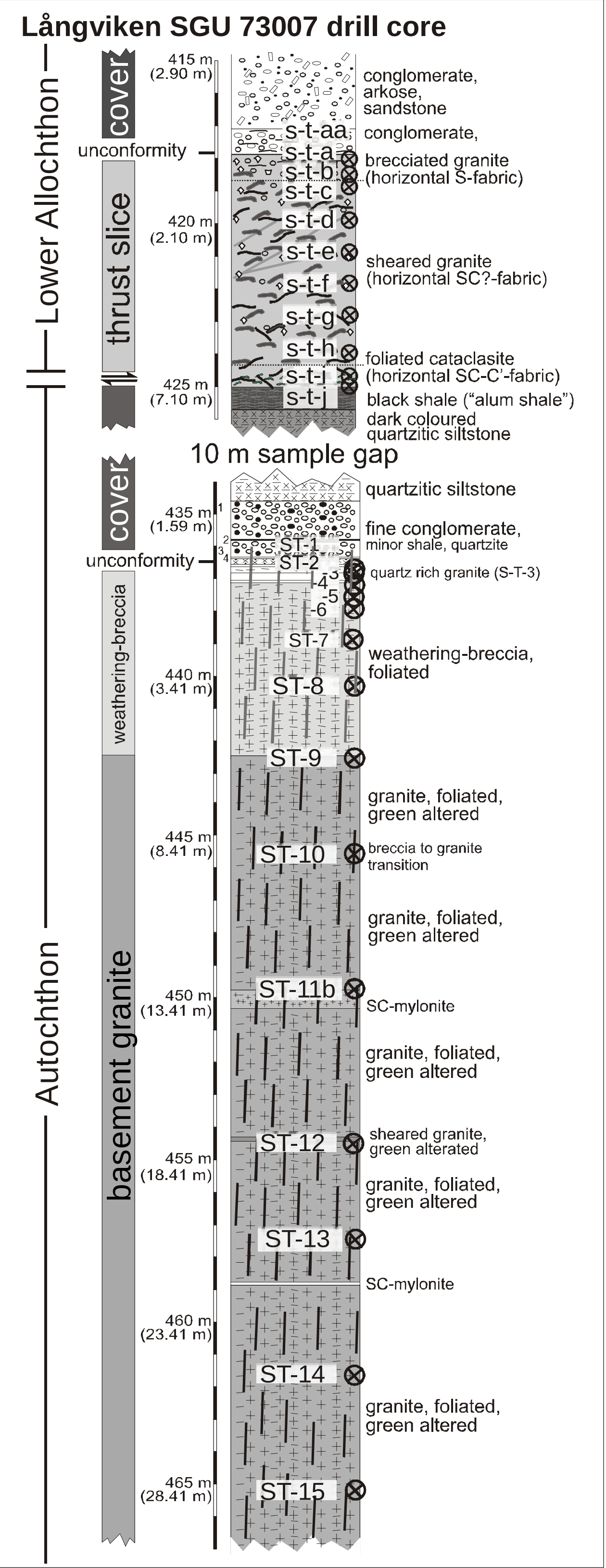

Figure 4.2: SGU 73007 Långviken drill core section of the autochthonous basement and allochthonous basement slice with structural domains, lithologies, foliation orientation and sample locations. (metre in brackets means distance from unconformity)

A brecciated quartz-rich granite (sample ST-3) is present very close to the unconformity within the brecciated zone. It may be interpreted as an unweathered lens (corestone) or a clast sedimented into the weathering zone.

4.2.1.2 Porphyroclastic mylonite

A few thin zones of a fine-grained porphyroclastic quartz-feldspatic rock are crosscutting the granite. The porphyroclastic appearance is given by large magnetites, comparable in size with those of the wall rock granite, and feldspar grains. The phyllosilicate fraction is chlorite dominated (sample ST-11.a). Chlorites define by their SPO / LPO one main and one secondary foliation. These two fabrics are vertically oriented, paralleling the orientation of the foliation sets in the granite. Delta- or sigma-clast elongation of magnetites is observed, possibly facilitated by pressure-solution transfer towards the strain shadows (Plate 4.1.c).

This lithology is a SC-mylonite (*sensu* Passchier & Trouw 1996, Platt 1984). C-surfaces are represented by the main set of chlorite SPO and S-surfaces by the secondary set, which is frequently sigmoidally curved into C. The SC-mylonites are from the mineralogical point of view the fine-grained equivalents of the wall-rock granite. Matrix minerals quartz, feldspar and chlorite suffered grain size reduction by brecciation and recrystallization. This produced a fine-grained porphyroclastic matrix, in which magnetites and feldspars remnants remain larger than the recrystallized part.

4.2.1.3 Overprinted weathering-breccia

The rock in the uppermost 6 metres beneath the unconformity (samples ST-2, ST-4 to -8) is a breccia (Plate 4.1.f). The attribution of the brecciated zone to pedogenesis is based in the first place on its location in the drill core sequence just beneath the unconformity (Gee et al. 1978). Anticipating further interpretations, the term weathering-brecciation is used here. The weathering-breccia is clay-matrix-supported (Plate 4.1.g,h). Clasts are muscovite-biotite-stacks, quartz and feldspar. Quartz and feldspar are characterized by the same intracrystalline deformations, which are observed in the granite beneath.

The weathering-breccia exhibits iron-hydroxide-rich spaced pressure solution seams, which are subhorizontally oriented, hence unconformity-parallel (Plate 4.1.g). Cleavage seams are developed in clay-domains, partly overprinting almost completely altered albite.

These cleavage seams are crenulated by a subvertical cleavage, which is pervasively imprinted in weathering breccia. This macroscopically detectable subvertical cleavage is defined by the preferred orientation (SPO/ LPO) of muscovite-biotite-stacks (Plate 4.1.h). The distinct orientation of the cleavages suggests a formation later than weathering-brecciation, although they are only locally developed at the thin section scale.

4.2.1.4 Transitional lithology

Sample ST-10 represents an intermediate position between unweathered granite and weathering-breccia. Situated within the intact granite zone, it shows mineralogical alteration features but does not show brecciation.

4.2.1.5 Cover rocks

The immediate overlying cover bed (Gärdsjön Fm.: Gee et al. 1978) is a 2 metres thick, hard, ill-sorted, ill-rounded quartzitic conglomerate, which gradually becomes finer-grained and well-sorted going upwards. It represents a basal conglomerate (Gee et al. 1978). Above the conglomerate, a 10 metres thick sequence of siltstones with intercalated conglomerate beds is present. A vertical tectonic foliation is evident in the cover rock.

4.2.1.6 Ore petrology in the autochthonous section

The large magnetites (average 2 mm in diameter) have euhedral shapes when situated in feldspar-dominated zones (Plate 4.3.a). Magnetites can be highly flattened up to 5 : 1 (long : short axis), when located in domains of quartz, which is elongated parallel with the schistosity surfaces, (Plate 4.1.b). Small areas of leucoxene (rutile, titanite and carbonate) are present in the magnetite (Plate 4.3.a).

In the porphyroclastic mylonite, strained magnetites can have an elevated long / medium-axis ratio (Plate 4.1.d), but shapes are generally oblate, as observed in thin sections parallel with the foliation.

Magnetite is frequently fragmented and altered to chlorite, stilpnomelane and (Fe-) carbonate (Plate 4.3.d-e). This network-like alteration affects magnetites grains in feldspar more often than grains in quartz domains.

Pyrite coating or replacement of (fragmented) magnetite is a secondary precipitation observed in the granite and transitional lithology (Plate 4.3.b,c). The weathering-breccia is free of magnetite, but chlorite-pyrite pseudomorphs replacing large iron-oxides point to a previous presence of magnetite (Plate 4.3.f).

Small pyrite grains are disseminated in the matrix of the weathering-breccia. These pyrite grains have idiomorphic shapes and overprint the matrix minerals (Plate 4.4.e).

4.2.2 Lower Allochthon section

A 0.7 metre thick layer of black shale marks the lower boundary of the tectonic slice and the top of the autochthonous sequence at metre 425.05 (Gee et al. 1978). Above the black shale, a green coloured cataclastically deformed granite continues over 7.32 metres. The upper boundary of the granite part is located at metre 417.73, and represents an unconformity to a conglomerate (sample st-aa). The cover rock is weakly cataclastically deformed, as well. The upper boundary of the tectonic slice, about 10 metres higher, is marked by another black shale layer. These black shales of the Cambrian Alum Shale Fm. (Andersson et al. 1985, Gee et al. 1974) are ubiquitously used as shear horizons facilitating Caledonian nappe stacking (e.g. Bierlein & Greiling 1993, Gee et al. 1974, Gee et al. 1978, Warr et al. 1996).

The granite in the allochthonous tectonic slice is cataclastically deformed. Most obvious characteristics are grain size reduction of the rock forming clasts (quartz, feldspar, muscovite and pyrite) and cataclastic flow together with formation of a pressure-solution cleavage. The predominantly flat-lying cleavage parallels the structural boundary of the slice (Gee et al. 1978), and therefore it corresponds to the tectonic imbrication of the thrust slice. A gradient of cataclasis, mainly characterized by progressive grain size reduction and shear fabric formation, is evident within the basement part. Deformation intensity increases downwards. Weak, moderate and intense cataclasis are distinguished. The floor thrust is localized in the black shale horizon beneath the granite part.

4.2.2.1 Weak cataclasis (breccia)

The weak cataclasis is characteristic for the uppermost metre of the granite (st-a, -b) and the cover beds (st-aa). It is defined as a breccia, showing cataclastic grain size reduction, a texture with low petrographic anisotropy with minimum cataclastic flow. The brecciated texture is dominated by large relic clast (up to 2 mm in size) of quartz, feldspar and mica in an illite-chlorite network (Plate 4.2.a). The illite-chlorite network represents a cleavage, which is approximately horizontally oriented. Because of the high content of quartz and feldspar clasts, cleavage is not pervasively imprinted in the matrix but rather restricted to seams in the matrix. The cleavage is a pressure solution cleavage, defined by an accumulation of microcrystalline opaque residual matter (mainly rutile, pyrite and graphite?).

The pre-deformational lithology is best preserved in this part, since the degree of cataclasis is low here. The primary mineralogy was granitic and the rock was supposedly already brecciated, which is indicated by a relatively clay-rich matrix. This rock may be interpreted as the equivalent to the autochthonous weathering-breccia, showing the same matrix components (mainly illite) and clastic components (quartz, feldspar, biotite-muscovite stacks). The matrix-supported breccia above the unconformity in the slice does not resemble the lowermost cover beds (conglomerate) of the Autochthon, which is much richer in quartz.

4.2.2.2 Moderate cataclasis (strongly foliated cataclasite)

Moderate cataclasis is observed in the 5.5 metres thick middle part of the slice (st-c to st-h). The moderate cataclasis is characterized by an intermediate stage of grain size reduction and by the generation of flat-lying cataclastic SC-cleavages. The cataclastic texture is porphyroclastic, defined by relic quartz and feldspar clasts (clasts size: 0.2 - 0.5 mm) and large pyrite grains (up to 2 mm; see chapter 4.2.2.4). Important feature are the secondary cleavage surfaces, crenulating asymmetrically a primary cleavage or producing a rudimentary SC-fabric. The degree of illitization is advanced, analogue to the fragmentation of feldspars and micas. Zircons and large pyrites are heavily brecciated due to the cataclastic deformation (Plate 4.2.d.e). Micas in the medium cataclasite are kinked or crenulated between cleavage seams and fragmented at their short sides to sericite (Plate 4.2.c). Discrete clay-rich faults are subordinately developed. These surfaces are reactivated S-surfaces, as they are medium steeply inclined dipping in the same direction as the crenulated cleavage or the S of the SC-fabrics.

4.2.2.3 Intense Cataclasis (SC-C’-protomylonite)

Intense Cataclasis is the most advanced stage of granite-cataclasis and affected the lowermost 0.5 metre of the imbricate basement slice (sample st-i and st-j). Directly beneath the intense cataclasite, the black shale defines the lower shear surface of the tectonic slice. The intense cataclasis produced a cataclastic protomylonite showing intense grain size reduction (clasts size: 0.02 - 0.2 mm), cataclastic flow and the formation of a penetrative and anastomising cleavage surfaces. Crystalplastic deformation of quartz, mainly subgrain formation, is evident in this zone. Recrystallization remains in its incipient stage (Plate 4.2.d). The grain sizes of the texture are relatively uniform, causing a loss of the porphyroclastic appearance, which is typical for moderate cataclasis. Large pyrites are almost entirely destroyed and fragments are disseminated in the cataclastic matrix. The cleavage domain spacing is much denser than in the weak and moderate cataclastic zones. An anastomising network of cleavage surfaces is the dominant textural feature. It represents very likely a combination of SC and C’-fabric and thus indicates progressive shear deformation (Meschede 1994, Passchier & Trouw 1996). The thickness of the clayey cleavage domains, already developed in the moderate cataclasis zone, is enhanced and reflects an increased clay formation. Thin undeformed veins filled with a pyrite-pyrrhotite-chalcopyrite association are observed in the intense cataclasis (see following chapter).

4.2.2.4 Ore petrology in the allochthonous section

The paragenesis of ore phases is complex in the lower allochthonous basement slice. At least two phases of sulphide-ore precipitation are recognized, namely 1) a phase of large pyrites, which are cataclastically deformed and 2) a pyrrhotite-pyrite-chalcopyrite paragenesis post-dating cataclasis. The distribution of both generations within the slice does not follow a distinct trend.

The occurrence of large pyrites (< 2 mm) is scarce. The minerals are observed in the medium cataclasite. Large pyrites parallel crenulated S-surfaces, showing mimetic growth next to micas and are intensely brecciated. Such large pyrites are neither recognized in the autochthonous granite nor in the autochthonous weathering-breccia. They resemble likely a phase that was present in the entire basement slice, since their formation is associated with the crenulated cleavage, therefore not connected to cataclasis. In the more intense cataclasite, pyrites may have been heavily shattered and disseminated, hence not observed.

The pyrrhotite-pyrite-chalcopyrite paragenesis is pervasively distributed in all cataclastic matrixes within the slice, showing a significant increase of modal fraction with intensity of cataclasis. Pyrite of the pyrrhotite-pyrite-chalcopyrite paragenesis dominates in the weak to moderate cataclasites, whereas in the intense cataclasite monoclinic pyrrhotite is the major phase (compare with $\kappa(T)$ curves in chapter 4.5.1.4). Pyrite (FeS_2) is in reflected light bright yellow-white. Monoclinic pyrrhotite (Fe_7S_8; 4C; or Weiss-type) (Vaughan &

Craig 1978) can be distinguished from pyrite by its anisotropy in polarized reflected light, by a distinctively lower reflectance and bronze-yellow tint. Chalcopyrite ($CuFeS_2$) is always an accessory mineral; it is recognised by an intensive but darker yellow reflectance against pyrite (Plate 4.4.c). Rutile crystals, quite large (0.1 mm long) and elongated, are associated with the sulphide aggregates. Rutile has a low reflectance and strong colourful interior-reflection. Euhedral or lobate grain shapes and polygonization with foam texture characterize the ore (Plate 4.4.a). The pyrrhotite-pyrite-chalcopyrite paragenesis characteristically overgrows mostly all phyllosilicate generations. Only seldomly, intergrowths of sulphides and matrix phyllosilicates are observed. Subordinately, the post-cataclasis pyrrhotite-pyrite-chalcopyrite association precipitates along linear intersection segments of extensional fissures paralleling shear direction (Plate 4.4.b).

Magnetite and haematite are recognized in $\kappa(T)$ curves (see chapter 4.5.1.4), but are accessory phases and are not recognized by petrographic analysis.

4.3 XRD results

4.3.1 Autochthonous section

4.3.1.1 Granite and porphyroclastic mylonite

The whole-rock spectrum of a granite sample (ST-13) confirms the petrographic observations (Figure 4.3.c). XRD peaks at ca. 3.24 Å and at ca. 3.19 Å evidence K-feldspar and (calcian) albite, respectively. Biotite and chlorite dominate over white-mica. A very Fe-rich chamosite is indicated by weakly developed chlorite-001 and -003 peaks in comparison to 002 peaks (c.f. Moore & Reynolds 1997). Fe-rich chamosite is the dominant chlorite phase in the clay fraction of the granite, mylonite and transition lithology; it dominates against illite (Figure 4.4.a). Stilpnomelane is observed in the clay spectra of the granite samples (characteristic low-angle 001 peak at ca. 12.1 Å in Figure 4.3.d).

The illite FWHM in the granite and transition lithology (ST-10) is low (0.21 to 0.23 °2θ), the mylonite (ST-11a) shows a higher value (ca. 0.37 °2θ) (Figure 4.4.b). Chlorite FWHM range between 0.31 and 0.33 °2θ.

4.3.1.2 Weathering-breccia

The whole-rock spectrum of a weathering-breccia (ST-2) shows an increased intensity of quartz against feldspar. K-feldspar dominates against albite (Figure 4.3.c), shown by the relation of intensities of peaks at ca. 3.24 Å and at ca. 3.19 Å (representing K-feldspar and (calcian) albite, respectively). White-mica and biotite is evidenced by characteristic peaks.

The clay fraction of the weathering-breccia resembles more or less the whole-rock constituents. The clayey matrix constituent of the weathering-breccia is predominantly well-crystallized illite (*sensu* Meunier & Velde 2004), whereas the chlorite content is reduced (Figure 4.3.d). This change is visualized by the ratio of chlorite and illite 002-peak intensities (Figure 4.4.a).

The repetition of XRD measurements under ethylene-glycol saturation does not show significantly different results. Vermiculite and smectite phases incorporated in chlorite and illite, respectively, can therefore be ruled out (Moore & Reynolds 1997). Illite 5 Å (002) FWHM is higher in the weathering-breccia (0.42 to 0.44 °2θ) than in the granite (Figure 4.4.b). This may indicate a decrease of crystals maturation (crystallinity) due to weathering-brecciation (e.g. Arkai et al. 1996, Kübler 1967, Warr & Rice 1994). Chlorite FWHM, on the other side, show with 0.35 °2θ only a slight increase with weathering-brecciation.

4.3.1.3 Cover rock

The 002-peak of chlorite in the autochthonous cover (ST-1) shows unusual low FWHM of ca 0.26 °2θ, which is attributed to a strong influence of detrital mica with higher degree of crystallinity. Therefore, the chlorites of the cover rocks are not comparable with those from the other rocks. Nevertheless, the chlorite to illite ratio (Figure 4.4.a) and the illite FWHM (Figure 4.4.b) are comparable to the underlying weathering-breccia.

4.3.2 Lower Allochthonous section

The whole-rock and clay fraction in the tectonic slice indicates an alteration trend with depth, which is similar to the autochthonous weathering-breccia: Albite is present in the lower part (st-e, st-j) but not in the upper part (st-aa, st-a) of the cataclasis-zone (Figure 4.3.a). Microcline does not show such a trend, having a relative

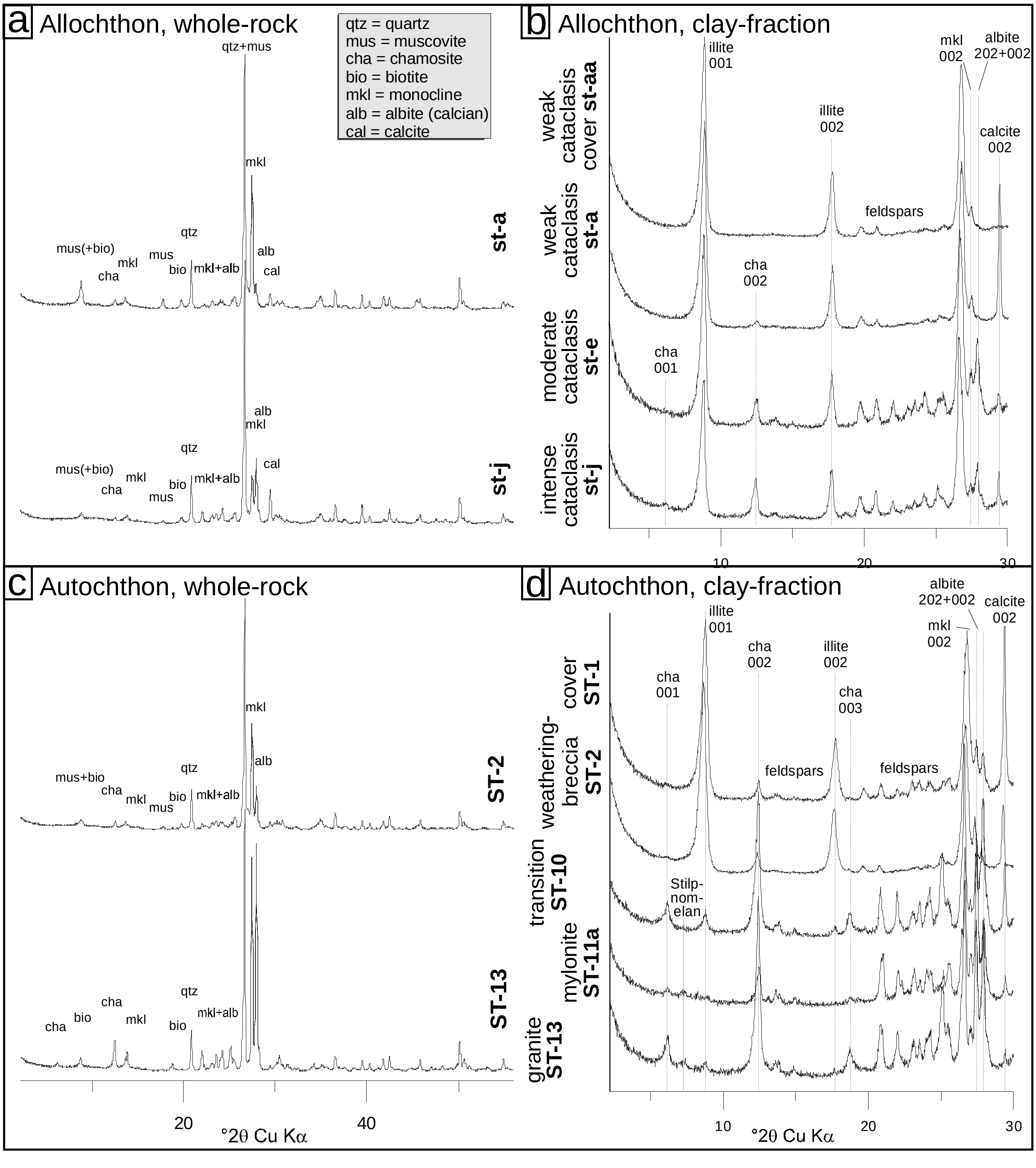

Figure 4.3: XRD-spectra of the whole-rock and clay fraction (2° - 30° 2θ) from allochthonous (a, b) and autochthonous (c,d) sections. Whole-rock spectra are on the left are, clay fraction spectra on the right are. Shown are characteristic peaks of specific minerals.

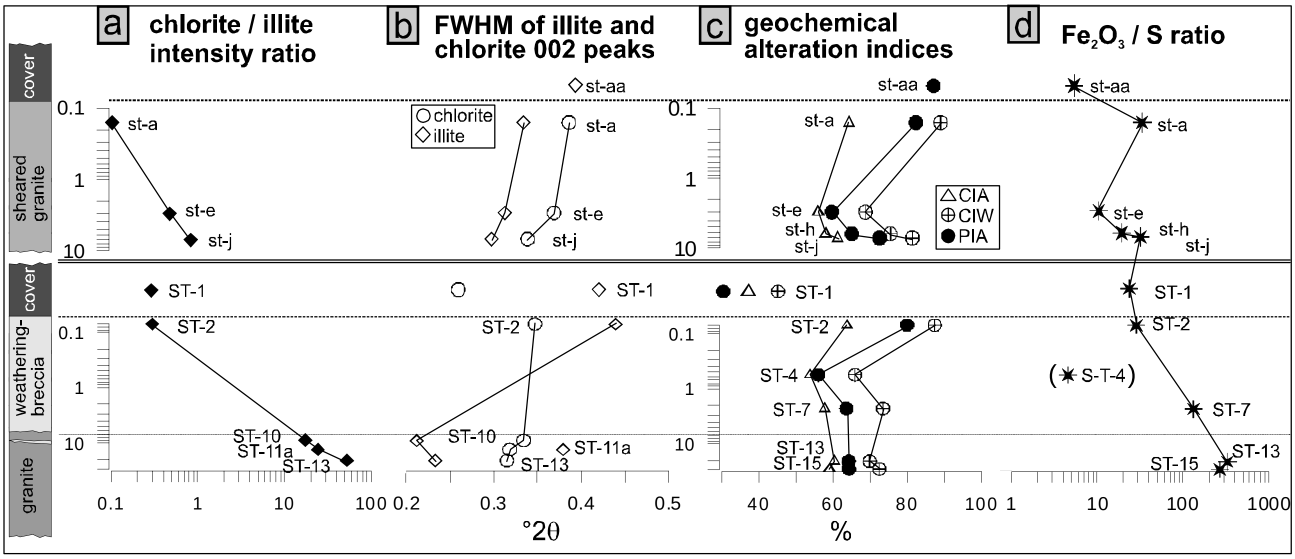

Figure 4.4: XRD and geochemistry trends in the Lower Allochthon basement slice and the autochthonous basement section. a) 002-peak intensity ratio of chamosite and illite, b) FWHM of chlorite-002 peaks and illite-002 peaks, c) Three chemical alteration indices, *PIA* (Fedo et al 1995), *CIW* (Harnois 1988) and *CIA* (Nesbitt & Young 1982). d) ratio of total iron oxide and total sulphur content in the whole-rock.

stable peak intensity. The ratio of chlorite and illite changes, as well (Figure 4.4.a). Towards intense cataclasis a continuous increase of the chlorite-002 / illite-002 peak-intensity-ratio from 0.1 to 0.8 is apparent. A decreasing trend of FWHM of both illite-002 and chlorite-002 is detectable with increasing cataclasis (Figure 4.4.b). This may indicate an increase of crystals maturation (crystallinity) with cataclasis intensity.

4.4 *Whole-rock geochemistry results*

4.4.1 *Autochthonous section*

Enrichment and depletion of major element oxides and trace elements is investigated by a normalization of values to the values from sample ST-15, which is considered as least weathered being the lowermost sample in the profile (Figure 4.5). Si, Al, Ti, Zr and P are stable elements (15 % relative variation from ST-15). Na, Ca, Fe, Mg, Mn and Sr are depleted elements. K, Ba and Nb and LOI are enriched. Sample SH-4 shows with low Al and high Ca, C_{total}, S_{total} and LOI concentrations abnormal values, which are probably due to a high amount of carbonate and organogenic material in the matrix replacing the common rock constituents. Data of this sample are excluded from the graphs (see Appendix I.b).

Chemical alteration indices *CIW* (Harnois 1988) and *PIA* (Fedo et al. 1995) (equations 11 and 12 in chapter 1.2.1) indicate an unconformity-related alteration (Figure 4.4.c), considering ST-4 as not representative. Index values of the granite are already relatively high with 64 (*PIA*) and 72 (*CIW*). *CIW* shows maximum value of ca. 87 in sample ST-2, PIA is slightly lower with 79. *CIA* (Nesbitt & Young 1982; equation 10 in chapter 1.2.1) does not indicate any clear alteration trend, showing values between 59 and 64.

4.4.2 *Lower Allochthonous section*

PIA and *CIW* indicate a gradient of alteration (weathering) through the allochthonous tectonic slice (Figure 4.4.c). Index values of st-a (allochthonous) and ST-2 (autochthonous) are in quantitative accordance, pointing to similar alteration degree of the weakly deformed allochthonous granite and the autochthonous weathering-breccia. Deviations of the indices, however, are evident towards the more intensely cataclastically deformed (lower) part of the slice in comparison to the Autochthon. Regarding the cover rocks, there is no correlation between the autochthonous and lower allochthonous beds.

Towards the bottom part of the slice, the alteration trend of the Na_2O and K_2O whole-rock geochemistry is

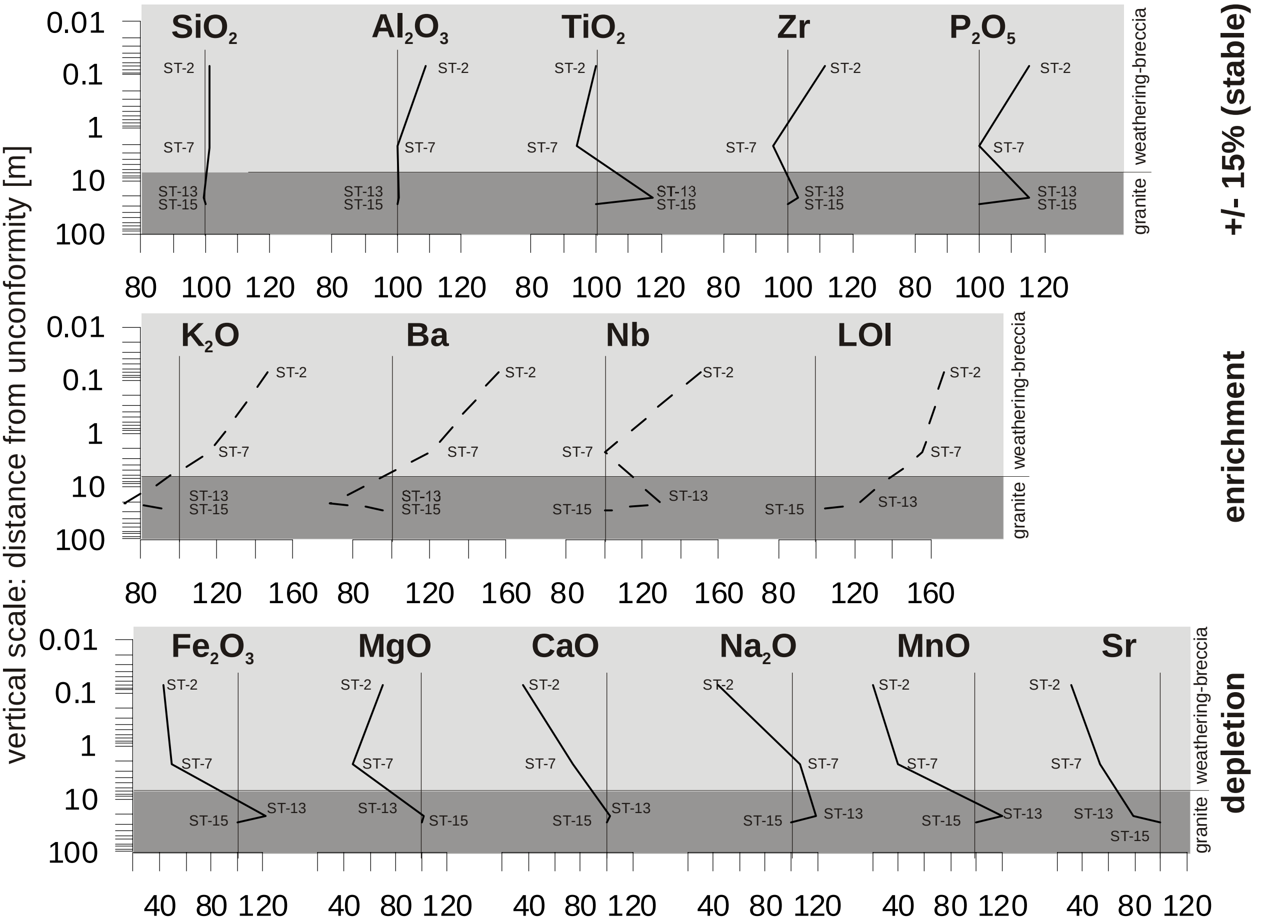

Figure 4.5: Element (-oxide) variations with proximity to the unconformity of the autochthonous basement. Upper row: relatively stable elements; middle row: elements that are enriched; lower row: elements that are depleted. All values are normalized to the lowermost granite sample ST-15. Horizontal dashed lines mark the boundary between granite and weathering-breccia.

inverted compared to the autochthonous section.

4.4.3 *Fe_2O_3 / S - ratio*

Plotting Fe_2O_3 / S ratio, a decrease of total sulphur in comparison to total iron downward both allochthonous and autochthonous sections is shown (Figure 4.4.d). The comparison corresponds to the iron sulphide content, especially pyrite, in the rocks. In the autochthonous magnetite-rich granite, S content is very low with respect to Fe. This behaviour does change towards the weathering-breccia, where pyrite is abundant. A slight change towards S-enrichment is exhibited in the basement slice. Here pyrite content (st-e in particular) is high. Pyrrhotite modification (as observed in st-j, chapter 4.2.2.4) has minor influence on the Fe / S ratio.

4.5 Magnetic susceptibility analyses

4.5.1 Bulk susceptibility κ_{bulk} and temperature dependent susceptibility $\kappa(T)$

4.5.1.1 Autochthonous granite

The granite samples from the autochthonous section show κ_{bulk} values in the range of 10^{-3} and 10^{-2} [SI] (Figure 4.6.c). The temperature dependent susceptibility measurements of the granite point to multi-domain magnetite as the dominant magnetic mineral contributing to the bulk susceptibility (Figure 4.7). Multi-domain magnetite is identified by the pronounced characteristic Verwey transition (T_{Verwey}) near -150 °C and by T_{Curie} at about 575 °C (e.g. Dunlop & Özdemir 1997). No Hopkinson peak is evident. The existence of just one multi-domain magnetite species is supported by the discreteness of T_{Curie} (extremely steep decrease of κ). The findings by $\kappa(T)$ measurements are supported by the dispersed large euhedral to anhedral magnetite crystals in the matrix. A good reversibility of the $\kappa(T)$-curves during heating and cooling run is evident and indicates the absence of magnetically important phase transitions during heating. Fresh magnetite is thus the dominant iron oxide and underwent no or only few martitization (c.f. case study Negev, Figure 2.25).

4.5.1.2 Autochthonous weathering breccia

The samples of the weathering-breccia show very low susceptibilities of $\kappa_{bulk} = 20$ to $100 \cdot 10^{-6}$ [SI] (Figure 4.6.b). This is because the deficiency in magnetite. A weakly defined decreasing trend of κ_{bulk} is observed within the weathering-brecciation zone with proximity to the unconformity (Figure 4.15.a).

$\kappa(T)$-curves exhibit a mixture of paramagnetic minerals (petrographically observed: illite, muscovite, pyrite) and magnetite as the dominant magnetic carriers, by showing 1) hyperbolically decreasing paramagnetic heating curve (well developed in the transition zone, less well in the breccia) and 2) characteristic discrete T_{Curie} of magnetite at ca. 575 °C and T_{Verwey} at ca. -150 °C (Figure 4.7.b). κ_{bulk} is carried by very small amounts of primary magnetite crystals, which, as described in chapter 4.2.1.6, were principally almost completely dissolved during weathering and by an increased amount of paramagnetic phases, like (phengitic?) illite and chlorite. An absence of reversibility during the cooling run is evident in the weathering zone and transitional lithology. Susceptibility is enhanced along the cooling path from temperatures below 600 °C. This points to magnetite formation during high temperatures (above T_{Curie} of magnetite), presumably due to clay mineral alteration (e.g. Just 2005).

4.5.1.3 Quartzitic granite and conglomerate

The κ_{bulk} of the quartzitic granite is extremely low (-10 to 18 · $4 \cdot 10^{-6}$ [SI]). Susceptibility is carried by diamagnetic quartz and minor feldspar (intrinsic volume susceptibility is -13 to $-17 \cdot 10^{-6}$ [SI]: Hunt et al. 1995). A positive κ_{bulk} is present in just one single specimen and due to minor presence of illite and muscovite/chlorite stacks. However modal fraction remains less than 6 vol%, as it is determined by κ_{bulk} addition (after Daly & Henry 1983; see equation 2 in chapter 4.5.2).

κ_{bulk} is enhanced to 184 to $192 \cdot 10^{-6}$ [SI] in the basal conglomerate. Besides quartz and minor feldspar, muscovite, metamorphic chlorite (different from the granitic chlorite, see XRD in chapter 4.3.1.3) and small accessory magnetite grains contribute to the bulk susceptibility.

An array of T_{curie} of magnetite is caused by a variety of grain sizes and supposedly considerable variation of Ti-content (Hunt et al. 1995). This is characteristically displayed by an unusually shallow decrease of κ_{bulk} within the temperature range of 500 to 585 °C (Figure 4.7.a). The Verwey transition of magnetite at ca. -150 °C is pronounced.

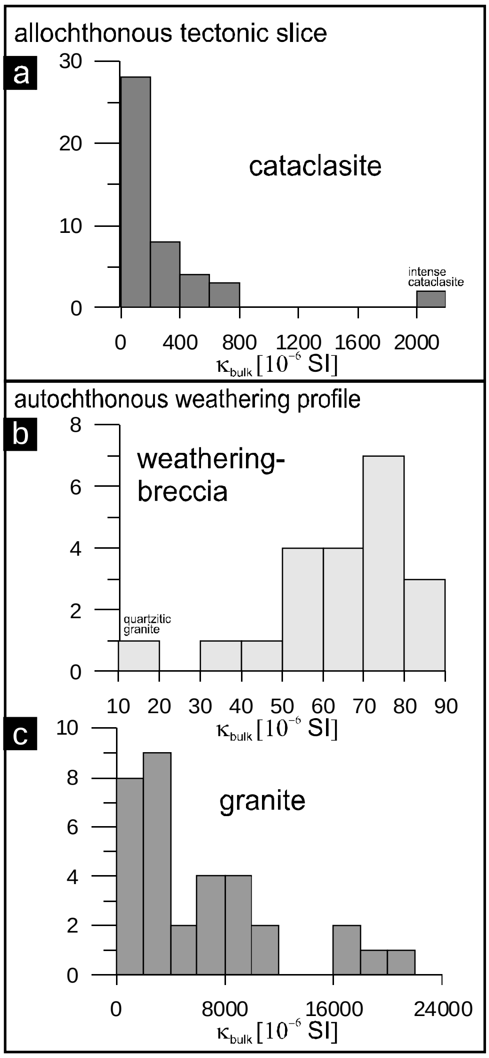

Figure 4.6: Histograms showing the κ_{bulk} of granites, weathering-breccias and cataclasites within the Långviken drill core.

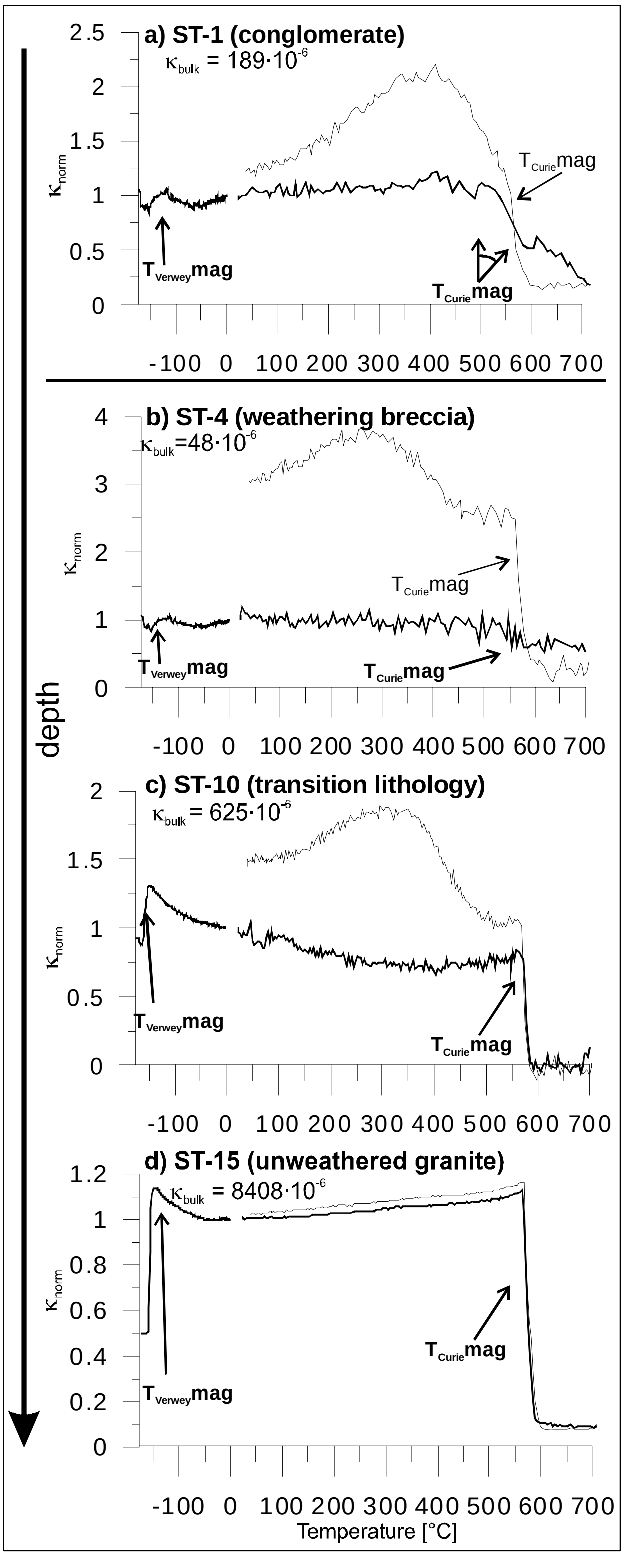

Figure 4.7: Temperature dependence of bulk susceptibility κ(T) (normalized to κ at room temperature) in the autochthonous section. Bold lines are heating curves, thin lines are cooling curves, a) is the cover conglomerate, b) is a weathering-breccia c) is the transition lithology and d) is the intact granite.

4.5.1.4 Allochthonous slice

The magnetomineralogy of the tectonic slice exhibits both iron sulphides (pyrite and monoclinic pyrrhotite) together with ferric (Fe^{3+} in haematite) and ferrous (Fe^{2+} in magnetite) iron oxides.

In the cataclastically deformed granitic slice, κ_{bulk} extends from 60 to 2000·10^{-6} [SI] (Figure 4.6.a). Highest susceptibility values are developed in the strongest deformed lower part; however, there is no other systematic distribution of low-κ and high-κ samples through the tectonic slice. Almost all κ(T) curves of the basement part of the slice point to the existence of haematite by a steady decrease of κ from 600 °C to 680 °C. This range of T_{Curie} indicates different haematite modifications (or grain sizes) (Hunt et al. 1995).

In low-κ samples (< 200·10^{-6} [SI]) of the weak and moderate cataclasis zone (represented by sample st-a and st-g , respectively), the κ(T)-curves display paramagnetic paths (hyperbolic decrease during heating) until ca. 575 °C, where κ decreases abruptly, because T_{Curie} of magnetite has been reached (Figure 4.8.c,d). Since heating-induced formation of magnetite is not indicated by a κ increase during the heating run, it can be inferred that magnetite is present in the rock. Magnetite is supposedly in single domain state, because the characteristic Verwey transition of multi domain magnetite at T_{Verwey} of - 150 °C (Dunlop & Özdemir 1997) is not recognisable. It is possibly masked by the, during the measurements in low T-range, enhanced paramagnetic susceptibility. Although detected, the amount of magnetite must be insignificant in comparison to the paramagnetic components, as κ_{bulk} is low (Tarling & Hrouda 1993; see also chapter 4.5.2 and Figure 4.9.b).

The irreversibility of heating curves while cooling down to ambient temperatures is evident in the low-κ samples and must be attributed to additional magnetite formation in high-T range (above T_{Curie} of magnetite) during the experiment. Reactants are possibly the paramagnetic iron bearing clay phases, which may encounter phase transition to magnetite in argon atmosphere above 600 °C (Just et al. 2004). During the cooling run haematite T_{Curie} is not reproduced, i.e. the curve is irreversible in the high-T range. This points to a transformation of haematite to magnetite at high temperatures.

A ferrimagnetic pyrrhotite modification with a T_{Curie} of 320 °C is in both moderate and intense cataclasis zone an important carrier of susceptibility (represented by sample st-j and st-e , respectively) (Figure 4.8.b,e). The characteristic T_{Curie} of 320 °C indicates monoclinic (Fe_7S_8; 4C or Weiss-type) pyrrhotite (Kontny et al. 2000). Its intrinsic volume susceptibility can reach 3.2 SI (Hunt et al. 1995). κ_{bulk} of pyrrhotite *sensu lato* shows strong variations with composition and crystal structure and ranges between $1.2 \cdot 10^{-3}$ SI ($Fe_{11}S_{12}$), $1.7 \cdot 10^{-3}$ SI ($Fe_{10}S_{11}$), $170 \cdot 10^{-3}$ SI (Fe_7S_9) and 3.2 SI (Fe_7S_8) (Hunt et al. 1995). The κ(T) heating path of the intense

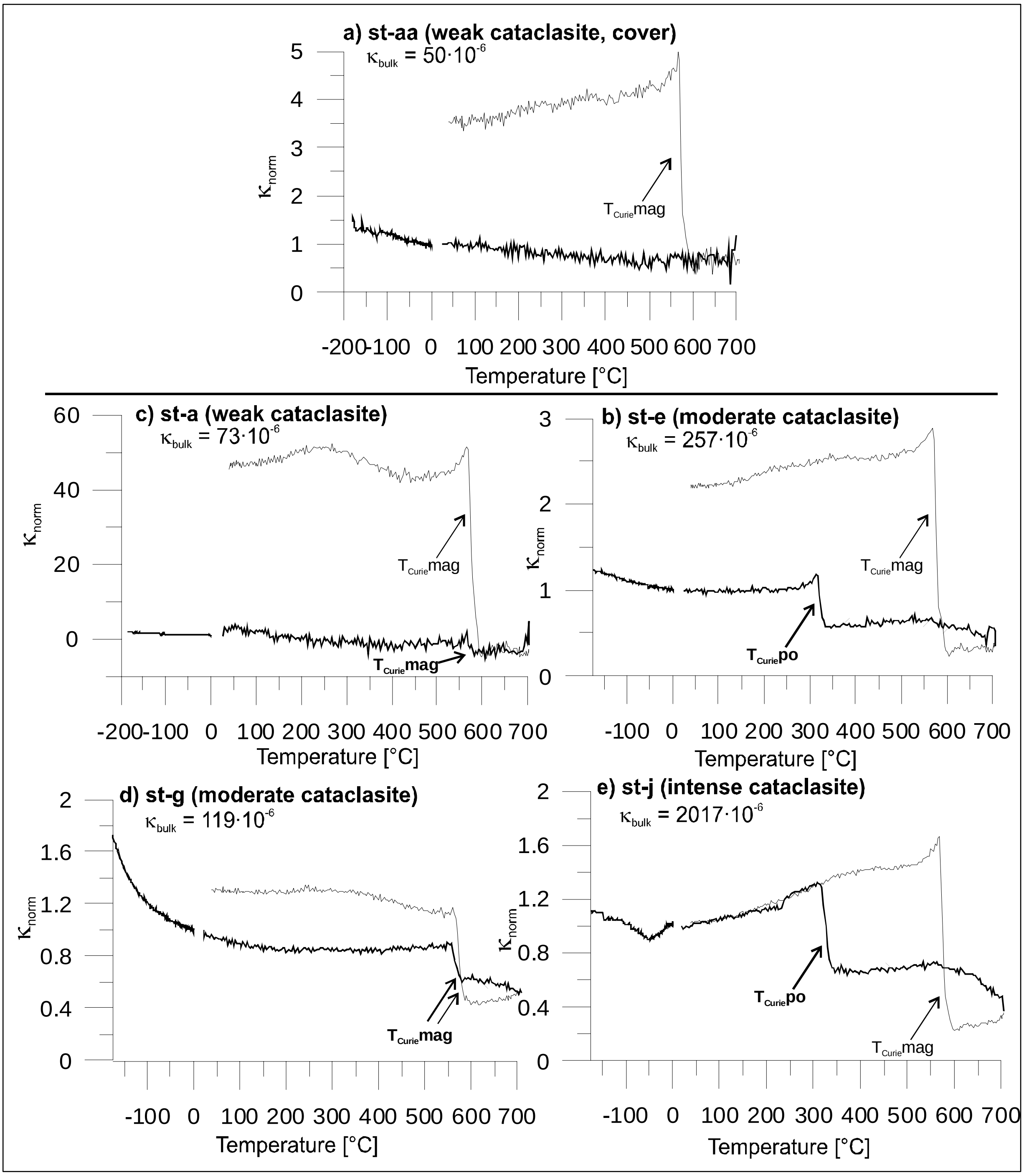

Figure 4.8: Temperature dependence of bulk susceptibility κ(T) (normalized to κ at room temperature) of the rocks in the autochthonous section of the Långviken drill core. Bold lines are heating curves, light lines are cooling curves. a) shows a weak cataclasite of the cover section; b) a weak basement cataclasite; c, d) moderate cataclasites and e) an intense cataclasite.

cataclasite st-j exhibits a small peak at about 220 °C (Figure 4.8.e). This reflects the so-called λ-transition from antiferromagnetic to ferrimagnetic behaviour (Kontny et al. 2000). By this, the additional presence of an antiferromagnetic modification (5C hexagonal type: c.f. Kontny et al. 2000) in the cataclasites can be inferred.

The ferrimagnetic Weiss-type modification dominates against antiferromagnetic modification. The final susceptibility after one heating-cooling cycle in sample st-j equals the initial value. Reactions occurring during experimental heating compensate each other with respect to bulk susceptibility: magnetite, which is evident by a T_{Curie} of 575 °C, has been formed and ferrimagnetic pyrrhotite has vanished (no T_{Curie} during cooling run). Oxidation of pyrrhotite to magnetite during experiments (even in Ar-atmosphere) has been described (e.g. Kontny et al. 2000) but must be questioned here, because magnetite T_{Curie} (ca. at 575 °C) is only evident in the cooling path. Thus, a transformation to magnetite in a high-T range above T_{Curie} of magnetite is more likely. Reactant may be clay and/or haematite. The fate of pyrrhotite during heating is the transition (oxidation and de-sulphidation) to antiferromagnetic pyrrhotite modifications (c.f. Kontny et al. 2000).

A pyrrhotite bearing sample from the moderate cataclasite zone (st-e) shows the following temperature dependence of susceptibility (Figure 4.8.e): a very weak λ-transition (?) is recognisable at ca 200 °C, a Hopkinson peak is developed just before the Weiss-type T_{Curie} of 320 °C and an irreversibility of the curve during cooling is evident by an increase of susceptibility (by the factor of ca. 2.3). Magnetite formation during heating induces an increase of κ_{bulk}, witch is higher than the κ-decrease due to the loss of ferrimagnetic pyrrhotite.

A coexistence of both ferrimagnetic iron modifications (magnetite and pyrrhotite) cannot be absolutely inferred from the κ(T)-curves. It rather appears that magnetite is only present, when pyrrhotite is absent.

The measurements of the cover-bed in the slice show very low susceptibilities (approximately $50 \cdot 10^{-6}$ [SI]). κ(T) curves are of paramagnetic type (Figure 4.8.a). This corresponds to the petrographic observation of pyrite, muscovite and illite.

4.5.2 *Calculation of the magnetite grain number in the autochthonous granite*

The observed range of κ_{bulk} in the high-κ granitic specimens (high standard variations) suggests a high variability of magnetite content in the specimens (error bars in Figure 4.15.a). Considering a shape-anisotropy of the magnetite grains, different specimens of the granite bearing only a few grains with non-uniformly shaped magnetites will result in a scattered AMS fabrics, whereas specimens rich in many uniformly shaped magnetites will cause well defined AMS patterns. Therefore, an estimation of the amount of the magnetite grains of each specimen is considered as crucial for the interpretation of the AMS fabrics.

The (ideal) magnetite grain number n_{mag} can be calculated by:

$$(1) \qquad c_{mag} = n_{mag} \cdot vol_{mag} / vol_{bulk}$$

where c_{mag} is the modal fraction of magnetite; vol_{mag} is the idealized (for simplicity) spherical volume of one single magnetite crystal with the petrographically observed mean radius of 0.68 mm (vol_{mag} = 1.33 mm^3) and vol_{bulk} the specimens' volume (cylinder of 25 mm basis diameter and 22 mm height, vol_{bulk} = 10798.9 mm^3).

c_{mag} is calculated by image analysis of thin sections: c_{mag} is 1.39 % for the granite specimen ST-13_iv ($\kappa_{bulk} = 21960 \cdot 10^{-6}$ SI), and 1.48 % for the porphyroclastic mylonite specimen ST-11a_ii ($\kappa_{bulk} = 18060 \cdot 10^{-6}$ SI). Applying equation (1), n_{mag} for the granite specimen is 113 and n_{mag} is 121 for the porphyroclastic mylonite specimen. The thin sections bear an uncertainty for estimating the magnetite content considering the very scarce occurrence of magnetite grains in the granite texture.

Alternatively, the number of magnetites n_{mag} in each granite specimen is calculated with the specific specimen κ_{bulk}. For this, the κ_{bulk}-addition (Daly & Henry 1983) is employed:

$$\kappa_{bulk} = c_{mag}\kappa_{mag} + c_{para}\kappa_{para} + c_{dia}\kappa_{dia} \tag{2}$$

where $c_{mag} + c_{para} + c_{dia} = 1$. κ_{mag} is the intrinsic volume susceptibility of magnetite.

Since an analytical determination of the true κ_{mag} is not possible, published minimum and maximal data of 1 and 5.7 [SI] (Hunt et al. 1995) are taken and calculations are performed with $\kappa_{mag} = 1$, $\kappa_{mag} = 5.7$ and $\kappa_{mag} = 1.37$ (latter value obtained by calibration, as described below). Therefore, n_{mag} ranges between minimum and maximum values.

Equivalent to equation 1, c_{para} and c_{dia} can be written as $c_{para} = vol_{para}/\ vol_{bulk}$ and $c_{dia} = vol_{dia}/\ vol_{bulk}$, respectively.

Considering equations (1) and (2), following function is obtained to describe n_{mag} as function of κ_{bulk}:

$$n_{mag}(\kappa_{\text{bulk}}) = \frac{vol_{bulk}}{vol_{mag}} \cdot \frac{\kappa_{\text{bulk}} - \kappa_{matrix}}{\kappa_{mag} - \kappa_{matrix}} \tag{3}$$

The low-κ-phases in the matrix were added up to $\kappa_{matrix} = c_{para}\kappa_{para} + c_{dia}\kappa_{dia}$. κ_{matrix} is defined here as $100 \cdot 10^{-6}$ [SI]. This value is calculated with $c_{para} = 20$ %, $c_{dia} = 80$ %, $\kappa_{\text{para}} = 560 \cdot 10^{-6}$ [SI] as an average of the present phyllosilicates chlorite and muscovite and a $\kappa_{dia} = -15 \cdot 10^{-6}$ [SI] from quartz and feldspar (Hunt et al. 1995). κ_{matrix} can be considered more or less constant with changing n_{mag}, because $c_{para} + c_{dia}$ remain almost 1 ($c_{para} + c_{dia} = 1 - \text{c}_{\text{mag}} > 0.98$, as determined by the thin section analyses). κ_{matrix} is assumed, but according to equation (3) not as important, since κ_{mag} is dominating over κ_{matrix} by several orders of magnitude.

The resulting n_{mag} vs. κ_{bulk} plot is displayed in Figure 4.9.a and shows that the number of magnetite grains n_{mag} is linearly dependent on κ_{bulk}.

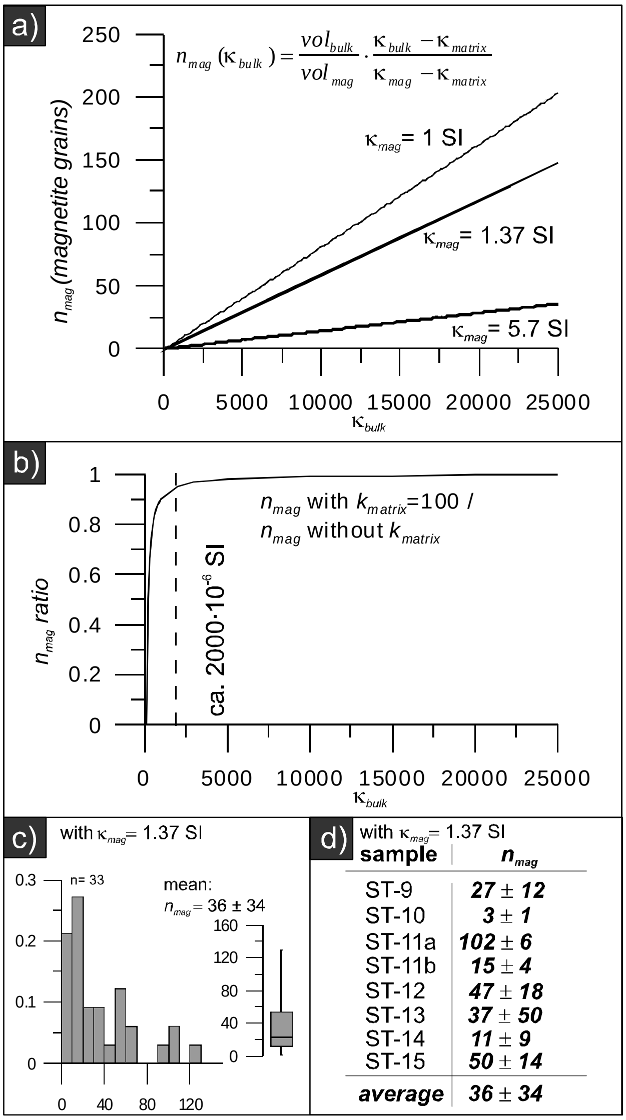

sample	n_{mag}
ST-9	***27*** ± ***12***
ST-10	***3*** ± ***1***
ST-11a	***102*** ± ***6***
ST-11b	***15*** ± ***4***
ST-12	***47*** ± ***18***
ST-13	***37*** ± ***50***
ST-14	***11*** ± ***9***
ST-15	***50*** ± ***14***
average	***36*** ± ***34***

Figure 4.9: Model for calculation of the magnetite grain number n_{mag} in the granite of the Långviken drill core. a) n_{mag} in dependence of measured bulk susceptibility; b) shows the theoretical ratio of n_{mag} with and without contribution of the matrix (κ_{matrix}) in dependence of κ_{bulk}; c) histogram and box-whisker diagram of n_{mag} for the granite sample set (calculation with intrinsic susceptibilities of magnetite $\kappa_{\text{mag}} = 1.37$ SI; value determined by modal fraction estimation in thin section); d) table of n_{mag} with standard deviation of the granite samples.

A calibration of the intrinsic susceptibility of magnetite (between 1 and 5.7 SI) in the granite may be possible employing equation (3), with the modal fraction estimated from thin section observation. A simplification of equation (3) to:

$$\kappa_{mag} = \kappa_{\text{bulk}} / c_{mag} \tag{3a}$$

provides sufficient results. It is based on the realistic assumption that κ_{bulk} is exclusively carried by magnetite in the samples with high κ_{bulk}: the ratio of n_{mag} (equation (1)) calculated with $\kappa_{matrix} = 100 \cdot 10^{-6}$ against n_{mag} calculated with $\kappa_{matrix} = 0$ shows the changing significance of κ_{matrix} contributing to κ_{bulk} (Figure 4.9.b). A ratio of near 1, which is typical for high susceptibilities, means that κ_{matrix} has no significant input on κ_{bulk}. But below a medium-κ of ca. $2000 \cdot 10^{-6}$ [SI] the importance of the paramagnetic + diamagnetic matrix as a magnetic carrier increases strongly against magnetite (ratio lower than 0.95). This ratio is independent from

κ_{mag} (between 1 or 5.7 SI).

Calculated κ_{mag} for the granite sample is 1.58 SI and for the mylonite sample 1.17 SI. The mean intrinsic susceptibility of magnetite in the granite is 1.37 SI. This calibration can be used as a base for the n_{mag} of the samples (Figure 4.9.d).

It can be stated that the number of (ideal) magnetites in the granitic sample set is generally low and highly scattered (mean-n_{mag} = 36 ± 34; for κ_{mag} = 1.37 SI) (Figure 4.9.c). The calculated n_{mag} for the high-κ granite specimen, represented by a thin section, is 129.5 (thus a difference from values determined by image analysis: 129.5 - 113 = 16.5). For the high-κ porphyroclastic mylonite n_{mag} = 106.4 (difference from values determined by image analysis: 106.4 - 121 = -14.6).

The generally low number of magnetite in the rocks implies that AMS fabrics of mylonite and granite, which are almost purely defined by magnetite shapes, may show considerable deviation from the petrographic fabric. This has to be considered when interpreting AMS data (chapter 4.6.1.1).

4.5.3 κ-field dependence of pyrrhotite in the allochthonous slice

Field dependence of bulk susceptibility is recognized in 7 of the 10 selected specimens by an increase of κ with field strength (Figure 4.10). Those samples represent mostly the moderate and intense cataclasite zones. The weak cataclasites st-aa, st-a and the moderate cataclasite st-g do not indicate any changes of κ with field strength. κ-increase is described by a power law function $\kappa = H_{ac}^{X}$ with x being specific for each sample and ranging between 0 and 1.

Field dependence parameter κ_{Hd} (de Wall 2000a, see equation 7 in chapter 1.3.7.4) reaches maximal values of 23 % (sample st-e), whereas high κ_{Hd} value generally corresponds with high κ_{bulk} values (Figure 4.11 and Table 4.1). By the data distribution in the $\kappa_{Hd}(\kappa_{bulk})$ diagram, samples can be divided into three groups. (a) specimens with low κ_{bulk} and no field dependence, (b) specimens with medium κ_{bulk} defining a steep positive slope of, i.e. strong increase of field dependence from 6 and 19 % at a moderate increase of κ_{bulk}, and (c) specimens defining a plateau, or a slightly decrease (see sample st-j) of the field dependence at high κ_{bulk}.

The distribution of κ_{Hd} within the slice is shown in Figure 4.18.a. The κ_{Hd}-trend is characterized by an absent κ_{Hd}-increase in the intense cataclasite, which is in contrast to the strong increase of κ_{bulk} (Figure 4.15.a). This represents the just described modified relation of κ_{bulk} to κ_{Hd}, i.e. the plateau of section c of the $\kappa_{Hd}(\kappa_{bulk})$ diagram.

4.5.3.1 Pyrrhotite grain size

The grain size distribution of two selected samples are determined to test the dependencies of κ_{Hd} on grain size and grain density in the samples (de Wall 2000b, Dekkers 1988, Worm et al. 1993), For the present study, samples with high κ_{Hd} of 17.8 (st-j) and 23 (st-e) are selected, having a significantly differing κ_{bulk} at 300 A/m ($2009 \cdot 10^{-6}$ SI and $407 \cdot 10^{-6}$ SI, respectively).

Pyrrhotite is the only detected ferrimagnetic phase in both samples. The appearance of pyrrhotite grains and their distribution is different for the considered samples: st-e shows relatively few grains (ca. 500 in a standard 28x48 thin section) with an average size of 39.6 μm (1. quartile at 10 μm and 3. quartile at 50 μm: Figure 4.12.a,c). Sample st-j has a much higher grain number, ca. 14000 in one section. Here, pyrite is not differentiated from pyrrhotite. However, pyrite grains, present as inclusions within pyrrhotite, are smaller than pyrrhotite and much lesser abundant. The average size of ca. 9.2 μm is much smaller and the Gaussian distribution narrower (1. quartile at 3.8 μm and 3. quartile as low as 10.8 μm) (Figure 4.12.b,c). Considering that field dependency of pyrrhotite is not significant below a minimum grain size of ca. 30 μm (Worm et al. 1993), statistics of grain size distributions of grains ≥ 30 μm are calculated as well: for st-e, average size

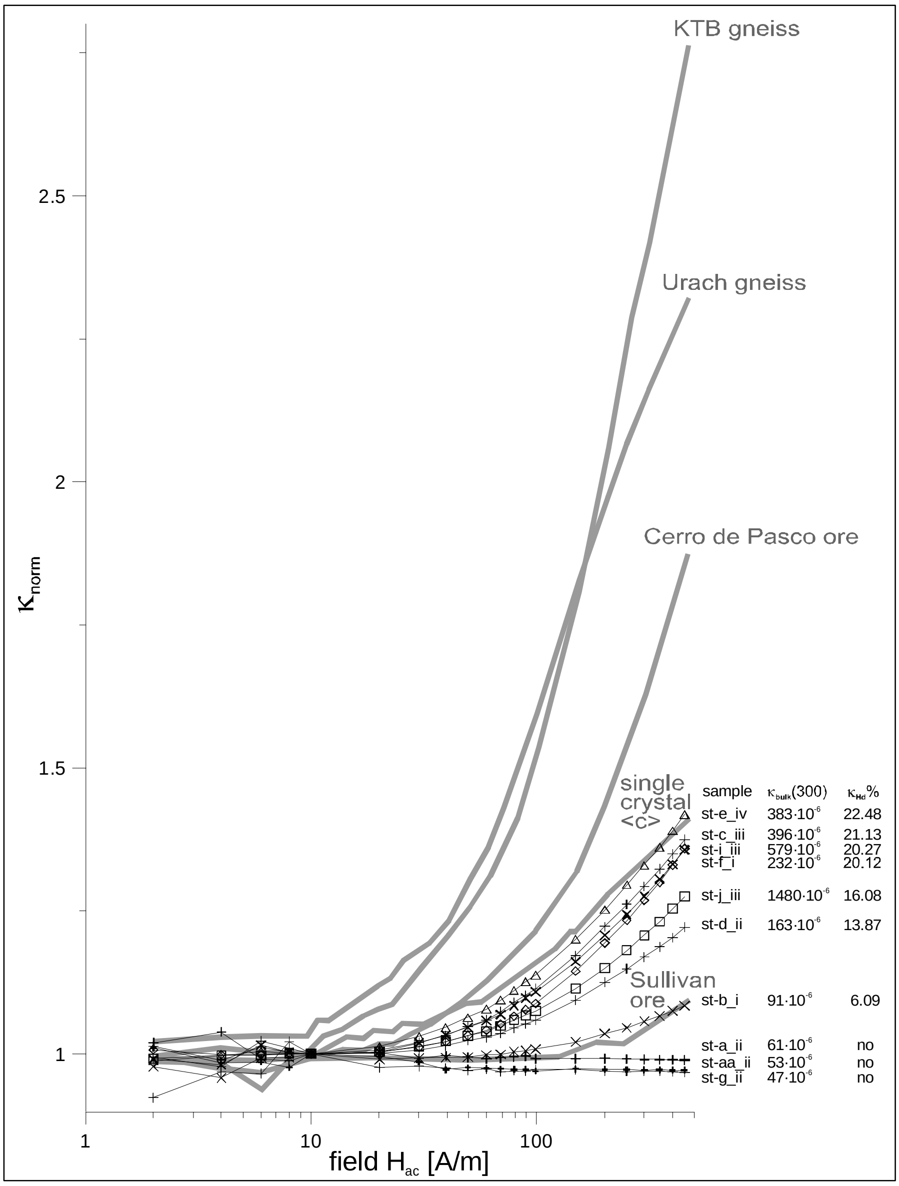

sample	$\kappa_{bulk}(300)$	κ_{Hd}%
st-e_iv	$383 \cdot 10^{-6}$	22.48
st-c_iii	$396 \cdot 10^{-6}$	21.13
st-i_iii	$579 \cdot 10^{-6}$	20.27
st-f_i	$232 \cdot 10^{-6}$	20.12
st-j_iii	$1480 \cdot 10^{-6}$	16.08
st-d_ii	$163 \cdot 10^{-6}$	13.87
st-b_i	$91 \cdot 10^{-6}$	6.09
st-a_ii	$61 \cdot 10^{-6}$	no
st-aa_ii	$53 \cdot 10^{-6}$	no
st-g_ii	$47 \cdot 10^{-6}$	no

Figure 4.10: κ_{norm} vs. H_{ac} diagram, showing the applied magnetic field dependence of κ_{bulk}. Samples are selected from the allochthonous slice. H_{ac}-field range from 2 to 450 A/m. Normalization was carried out with κ(10A/m). Data of pyrrhotite bearing rocks and ores are shown for comparison (in courtesy of de Wall, *unpubl. data*).

increases to 64.5 µm, for st-j average size becomes 52.1 µm. Additionally, statistics of grain size distributions of grains ≥ 6 µm is determined: for st-e, average size increases to 64.5 µm, for st-j average size becomes 9.2 µm.

The calculated modal fraction of ferrimagnetic pyrrhotite is ca. 0.147 vol% in sample st-e (≥ 6 fraction: 0.147 %; ≥ 30 fraction: 0.144). In st-j the modal fraction is about 1.35 % (≥6 fraction: 0.128 ; ≥ 30 fraction: 0.770).

4.5.3.2 Comparison of κ_{Hd} and pyrrhotite grain size with the EOR-standard

Together with corresponding κ_{Hd} values, grain size data are compared with the EOR sample collection (de Wall 2000b, Dekkers 1988, Worm et al. 1993). The EOR collection is a standard for the field dependency of ferrimagnetic pyrrhotite with respect to pyrrhotite grain size. It comprises sieved grain-size fractions from 5 to 250 µm.

Plotting grain size vs. κ_{Hd} the data can be compared with the published EOR-standard (Figure 4.12.d). The measured data are in good agreement with the standard, when the small grain spectra (< 30 µm) is excluded. The lower κ_{Hd} of st-j corresponds to a smaller average grain size, relative to st-e.

The quotient of average grain size (in µm) and κ_{Hd} (in %) is for st-e: 39.6 / 23 = 1.73 and for st-j: 9.2 / 17.8 = 0.52. For the grain size spectra ≥ 30 µm, the quotients are similar: st-e: 64.5 / 23 = 2.8 and st-j: 52.1 / 17.8 = 2.94. These similar quotients indicate a linear relation of the average grain size and κ_{Hd}, fitting well to the linear correlation exhibited in the EOR sample set in the grain size spectra between ca. 20 and 80 µm (c.f. Pokorný et al 2005).

The quotient of κ_{bulk} (in 10^{-6}) and modal fraction (in %) is for st-e: 407 / 0.147 = 2768.7 and for st-j: 2009 / 1.35 = 1488.2. Particles < 6 µm lack a significant ferrimagnetic character (O'Reilly et al. 2000). Excluding grains < 6 µm from the calculation the quotient for st-j increases to 1569.5. For st-e the ratio does not change. The differences of the ratios show that sample st-e bears a higher bulk susceptibility compared to pyrrhotite modal fraction than st-j.

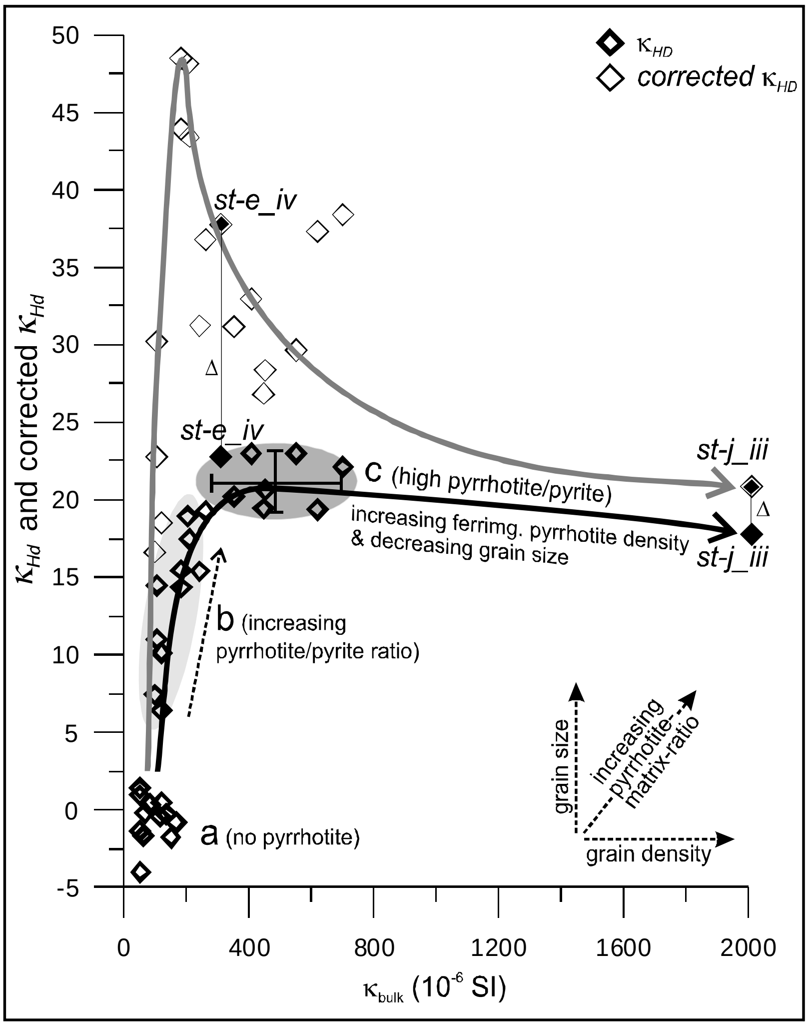

Figure 4.11: Field dependence of pyrrhotite in the Långviken Allochthon basement slice vs. κ_{bulk}. Displayed are normal κ_{Hd} (de Wall 2000a) and corrected κ_{Hd} values. Three groups of κ_{Hd} vs. κ_{bulk} are recognisable (a-c), which are defined by distinct magnetic properties of pyrrhotite. These properties are influenced by the factors density of pyrrhotite, grain size distribution and pyrite/pyrrhotite ratio. Specimen, whose grain size distribution are analysed (st-e, st-j) are marked in dark grey.

4.5.3.3 Corrected field dependence parameter κ_{Hd}corr

κ_{Hd} is a measure to characterize and compare the specific field dependence of κ of magnetic minerals in rocks (de Wall 2000a). In the calculation of κ_{Hd}, it is not considered that the non-field dependent rock matrix, influences κ_{Hd} substantially, if its contribution to κ_{bulk} is high, relative to the field dependent mineral. This is manifested by the bulk susceptibility formula (Daly & Henry 1983):

$$(1) \qquad \kappa_{bulk} = c_{po}\cdot\kappa_{po} + c_{M}\cdot\kappa_{M.}$$

where κ_{po} = intrinsic susceptibility of field dependent ferrimagnetic pyrrhotite and $\kappa_{M.}$ = the non-field dependent matrix phases; and c_{po}, c_M are their modal fractions. Only factor κ_{po} changes with field strength, thus with a small c_{po} and a large term $c_M\cdot\kappa_M$, the difference between κ_{bulk} at 300 A/m and of 30 A/M will be small. Therefore, a correction, which eliminates the effect of $(c_M\cdot\kappa_M)$ on κ_{bulk} in formula (1) by considering the relative susceptibility strength of the paramagnetic matrix components (predominantly pyrite and chlorite)

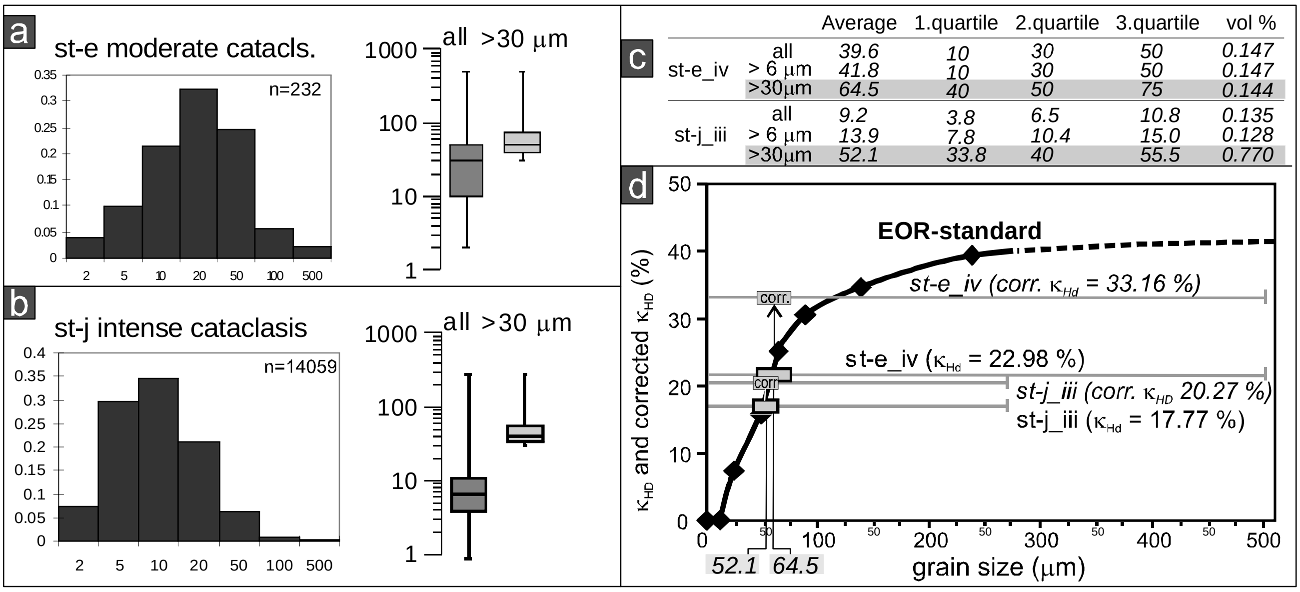

		Average	1.quartile	2.quartile	3.quartile	vol %
st-e_iv	all	39.6	10	30	50	0.147
	> 6 μm	41.8	10	30	50	0.147
	>30μm	64.5	40	50	75	0.144
st-j_iii	all	9.2	3.8	6.5	10.8	0.135
	> 6 μm	13.9	7.8	10.4	15.0	0.128
	>30μm	52.1	33.8	40	55.5	0.770

Figure 4.12: Dependence of κ_{Hd} of pyrrhotite-samples on grain size. a-c) Results of pyrrhotite grain size determination by image analysis of two samples (moderate and intense cataclasite). Statistical results of all grains and of the grain spectrum > 30 μm are shown in box-whisker diagrams and in a table. d) Dependency of k_{Hd} to grain size and comparison with EOR standard (de Wall 2000b, Dekkers 1988, Worm et al. 1993) of pyrrhotite. Only grains > 30 μm are considered. In addition, the corrected k_{Hd} (k_{Hd}corr) are displayed (see text for details).

is applied to the calculation of the field dependence parameter. The corrected κ_{Hd}, referred to as $\kappa_{Hd}corr$, is based on following equation:

$$(2) \qquad \kappa_{HD}corr[\%] = \frac{\kappa_{300}corr - \kappa_{30}corr}{\kappa_{300}corr} \cdot 100$$

with $\kappa_{300}corr$ and $\kappa_{30}corr$ deriving from susceptibility equation of Daly & Henry (1983):

$$(3) \qquad \kappa_{300}corr = \kappa_{300} - c_M \cdot \kappa_M$$

$$(4) \qquad \kappa_{30}corr = \kappa_{30} - c_M \cdot \kappa_M$$

As a result, following term for calculation of the corrected κ_{Hd} can be used:

$$(5) \qquad \kappa_{HD}corr[\%] = \frac{\kappa_{300} - \kappa_{30}}{\kappa_{300} - c_M \cdot \kappa_M} \cdot 100$$

c_M is near 1, since pyrrhotite is an accessory phase with a modal fraction of below ca. 1.5 %. c_M can be calculated in cases, where c_{po} has already been determined by image analysis (see chapter 4.5.3.1), by:

$$(6) \qquad c_M = 1 - c_{po}$$

κ_M is estimated by the assumption that those samples showing no field dependence (weak cataclasis zone: st-a, st-aa; moderate cataclasis zone: st-g, st-h) are characterized by $\kappa_M = \kappa_{bulk}$. These κ_{bulk} values are taken as κ_M. In the intense cataclasis zone, κ_M is higher than in the moderate cataclasis zone, because of the intensified deformation-related illite and chlorite precipitation. However, non-field dependent samples are missing as references for the intense cataclasis zone. κ_M of the intense cataclasis zone is considered double as high as in the moderate cataclasis zone. In Table 4.1 and Figure 4.11 the results of $\kappa_{Hd}corr$ are shown. In all samples, $\kappa_{Hd}corr$ is higher than κ_{Hd} (up to 35 % difference, see Δ in Table 4.1). Δ is positively dependent on κ_{bulk}. For example, it is evident that $\kappa_{Hd}corr$ of st-j does not vary significantly from κ_{Hd}, whereas $\kappa_{Hd}corr$ of st-e is much higher than κ_{Hd} (33.16 %). This is an effect of the stronger influence of ferrimagnetic pyrrhotite in st-j in comparison to the matrix. $\kappa_{Hd}corr$ of st-e deviates from the EOR standard graph (Figure 4.12), which is based on κ_{Hd} (uncorrected).

$\kappa_{Hd}corr$ is introduced here for all field dependence low-κ_{bulk} rocks (ca. $k_{bulk} < 2000 \cdot 10^{-6}$ SI). It allows

Table 4.1: Bulk susceptibility data of the samples of the basement slice with calculated κ_{Hd} and $\kappa_{Hd}corr$. (po = pyrrhotite)

sample	cataclasis	distance	K_m30	K_m300	k_{Hd}	po-content	c_m	k_m	c_M*k_M	corr k_{Hd}	Δ
st-aa_30_I	weak	-0.22	48.04	48.50		no-po	0.95	60	57		
st-aa_30_II	weak	-0.18	55.17	53.05		no-po	0.95	60	57		
st-aa_30_IV	weak	-0.10	50.41	49.75		no-po	0.95	60	57		
st-aa_30_II	weak	0.13	62.71	61.68		no-po	0.95	60	57		
st-aa_30_III	weak	0.16	65.01	64.88		no-po	0.95	60	57		
st-a_30_V	weak	0.22	81.20	81.50		no-po	0.95	60	57		
st-b_30_I	weak	0.60	90.19	97.42	7.42	po	0.95	60	57	17.89	10.47
st-b_30_II	weak	0.63	107.20	119.30	10.14	po	0.95	60	57	19.42	9.28
st-b_30_III	weak	0.66	93.02	104.50	10.99	po	0.95	60	57	24.17	13.18
st-b_30_IV	weak	0.69	88.99	104.10	14.51	po	0.95	60	57	32.08	17.57
st-c_30_I	moderate	0.97	164.70	203.10	18.91	po	0.999	125	124.825	49.06	30.15
st-c_30_II	moderate	1.00	239.90	310.70	22.79	po	0.999	125	124.825	38.09	15.3
st-c_30_III	moderate	1.03	359.30	445.90	19.42	po	0.999	125	124.825	26.97	7.55
st-c_30_IV	moderate	1.06	153.00	181.00	15.47	po	0.999	125	124.825	49.84	34.37
st-d_30_I	moderate	2.01	205.70	243.10	15.38	po	0.999	125	124.825	31.62	16.24
st-d_30_II	moderate	2.04	156.70	182.90	14.32	po	0.999	125	124.825	45.11	30.79
st-d_30_III	moderate	2.07	110.40	117.90	6.36	po	0.999	125	124.825		
st-d_30_IV	moderate	2.10	358.80	452.00	20.62	po	0.999	125	124.825	28.49	7.87
st-d_30_V	moderate	2.13	424.60	551.50	23.01	po	0.999	125	124.825	29.74	6.73
st-e_30_IV	moderate	3.06	313.30	406.80	**22.98**	po	0.999	125	124.825	**33.16**	10.18
st-f_30_I	moderate	3.94	209.20	259.20	19.29	po	0.999	125	124.825	37.21	17.92
st-f_30_II	moderate	3.99	170.30	206.40	17.49	po	0.999	125	124.825	44.25	26.76
st-f_30_III	moderate	4.03	280.50	351.60	20.22	po	0.999	125	124.825	31.35	11.13
st-g_30_I	moderate	4.89	167.60	166.30		no-po	0.999	125	124.825		
st-g_30_II	moderate	4.92	48.58	49.27		no-po	0.999	125	124.825		
st-g_30_III	moderate	4.95	113.00	112.50		no-po	0.999	125	124.825		
st-g_30_IV	moderate	4.98	151.60	149.00		no-po	0.999	125	124.825		
st-h_30_I	moderate	6.15	119.70	120.30		no-po	0.999	125	124.825		
st-h_30_II	moderate	6.18	137.20	136.80		no-po	0.999	125	124.825		
st-i_30_I	intense	6.80	498.20	617.90	19.37	po	0.99	250	247.5	32.32	12.95
st-i_30_III	intense	6.84	545.90	701.00	22.13	po	0.99	250	247.5	34.2	12.07
st-j_30_III	intense	7.10	1652.00	2009.00	**17.77**	po	0.99	250	247.5	**20.27**	2.5

interpretation of the true field dependence of present pyrrhotite phases, which is hidden by the dominant matrix phases. It should be discussed, whether $\kappa_{Hd}corr$ allows a better comparison of rocks with relatively low κ_{Hd} due to κ_{M} with those showing “abnormal” high field dependencies, like Urach or KTB gneisses (Figure 4.10; *in courtesy of* de Wall). Crucial for meaningful calculations of $\kappa_{Hd}corr$ is the proper estimation of the κ_{M}. Some $\kappa_{Hd}corr$ values may be exaggerated because κ_{M} is estimated too high. A correction is not important for high-κ_{bulk}, ranging in a purely ferrimagnetic field (> 10^{-2} SI), because the effect of the matrix on κ_{bulk} is negligible. Here, κ_{Hd} as defined by de Wall (2000a) is sufficient.

4.6 AMS results

4.6.1 Autochthonous section

Two main AMS-patterns, $\mathrm{AMS}_{\mathrm{granite}}$ and $\mathrm{AMS}_{\mathrm{breccia}}$, are distinguishable in the autochthonous section with respect to their distinct AMS-parameters and κ_1-orientations. $\mathrm{AMS}_{\mathrm{granite}}$ is associated with the intact granite and $\mathrm{AMS}_{\mathrm{breccia}}$ with the weathering-breccia. The fabric of the porphyroclastic mylonite (sample ST-11a), $\mathrm{AMS}_{\mathrm{mylonite}}$, is similar to $\mathrm{AMS}_{\mathrm{granite}}$. The very quartz-rich granite (ST-3) near the unconformity bears a unique inverse fabric, $\mathrm{AMS}_{\mathrm{quartzite}}$. The AMS-type of the cover-conglomerate (ST-1) is labelled as $\mathrm{AMS}_{\mathrm{conglomerate}}$. The AMS stereoplots of autochthonous section are shown in the Appendix II.c.

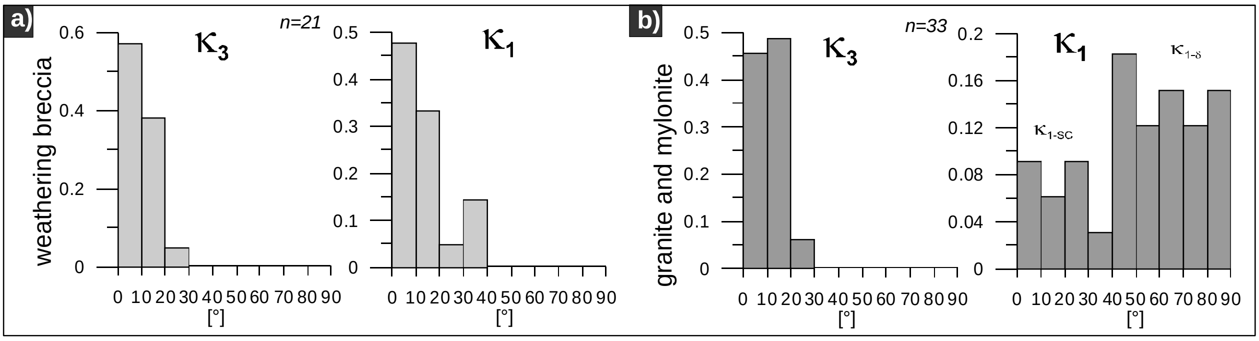

Figure 4.13: Histograms of the inclination of principal AMS axes k_1 and k_3. a) weathering-breccia, b) intact granite and mylonite. In b) the two evident classes of magnetic lineation k_1-SC and k_1-d are distinguishable by their inclination.

4.6.1.1 *AMS$_{granite}$ and AMS$_{mylonite}$*

The granitic magnetic fabric, AMS$_{\text{granite}}$, shows very high anisotropy degrees (P' = 1.2 to 1.6) (Figure 4.15.b). Shape factor T scatters in the oblate zone ($0 < T > 0.8$) (Figure 4.15.c). P' values are positively correlated with κ_{bulk} (see κ_{bulk}(P') plot in Figure 4.16.a), whereas T(P') does not show distinctive pattern (Figure 4.16.a). The κ_3-axes are shallowly inclined between 0 - 20°, the declination scatters at a minimum angle of 55°. The inclination of the magnetic foliation represent well the subvertical orientation of the petrographic foliations S_{1a} and S_{1b}. Magnetic lineations, κ_1-axes, are medium to steeply inclined (40 to 90°) (Figure 4.13).

In the porphyroclastic SC-type mylonite, P'-values are very high, reaching 2 in sample ST-11.a (Figure 4.15.b) (AMS$_{\text{mylonite}}$). Shapes are prolate (T ca. 0.5). κ_3 resemble the directions observed in granite, whereas κ_1-axes are shallowly inclined (20-30°). A good correspondence of AMS$_{\text{mylonite}}$ and petrographic fabrics is given in the mylonite: a) magnetic foliation parallels dominant petrographic foliation, which is the subvertical C-surface, and b) magnetic lineation resembles the horizontal shear direction.

Regarding the distance to the unconformity, there is no uniform trend of any AMS-parameters (P', T) and axes-orientations developed (Figure 4.15). Only the transitional lithology (specimens of samples ST-10, ST-14) shows changes in AMS parameters, which indicate a progressive change to AMS$_{\text{breccia}}$.

4.6.1.2 *Weathering-breccia (AMS$_{breccia}$)*

A decrease towards the unconformity of the anisotropy factor P' from about 1.09 down to 1.03 is evident in the weathering-breccia (Figure 4.15). This trend corresponds to the decreasing trend of κ_{bulk}. Shape factor T is initially positive (oblate shapes) but scatters more with proximity to the unconformity ($-0.5 < T < 0.7$). The magnetic foliation of AMS$_{\text{breccia}}$ is subvertically oriented (subhorizontal κ_3), persisting in the same position as

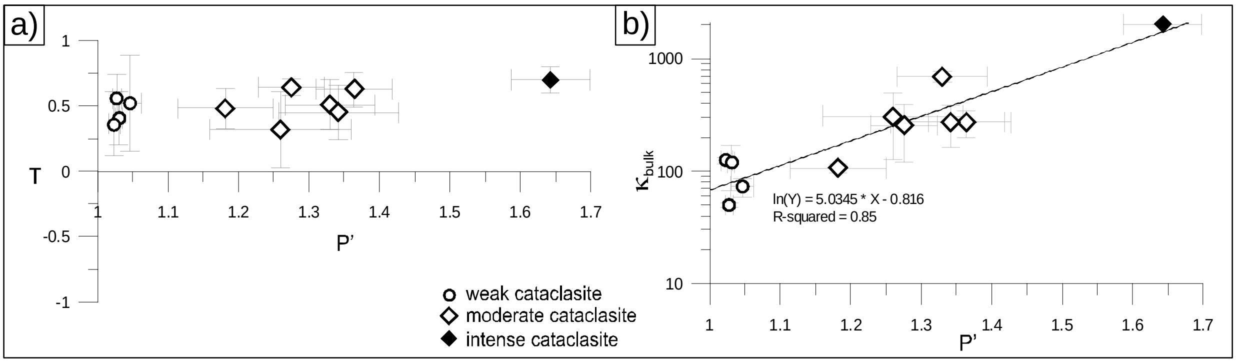

Figure 4.14: Relation of AMS parameters in the basement slice. a) The Jelinek diagram T vs. P' exhibit constantly oblate shapes throughout the slice; b) κ_{bulk} vs. (P') points to an exponential dependency of P' on κ_{bulk}. (Measurements in a field of 300 A/m)

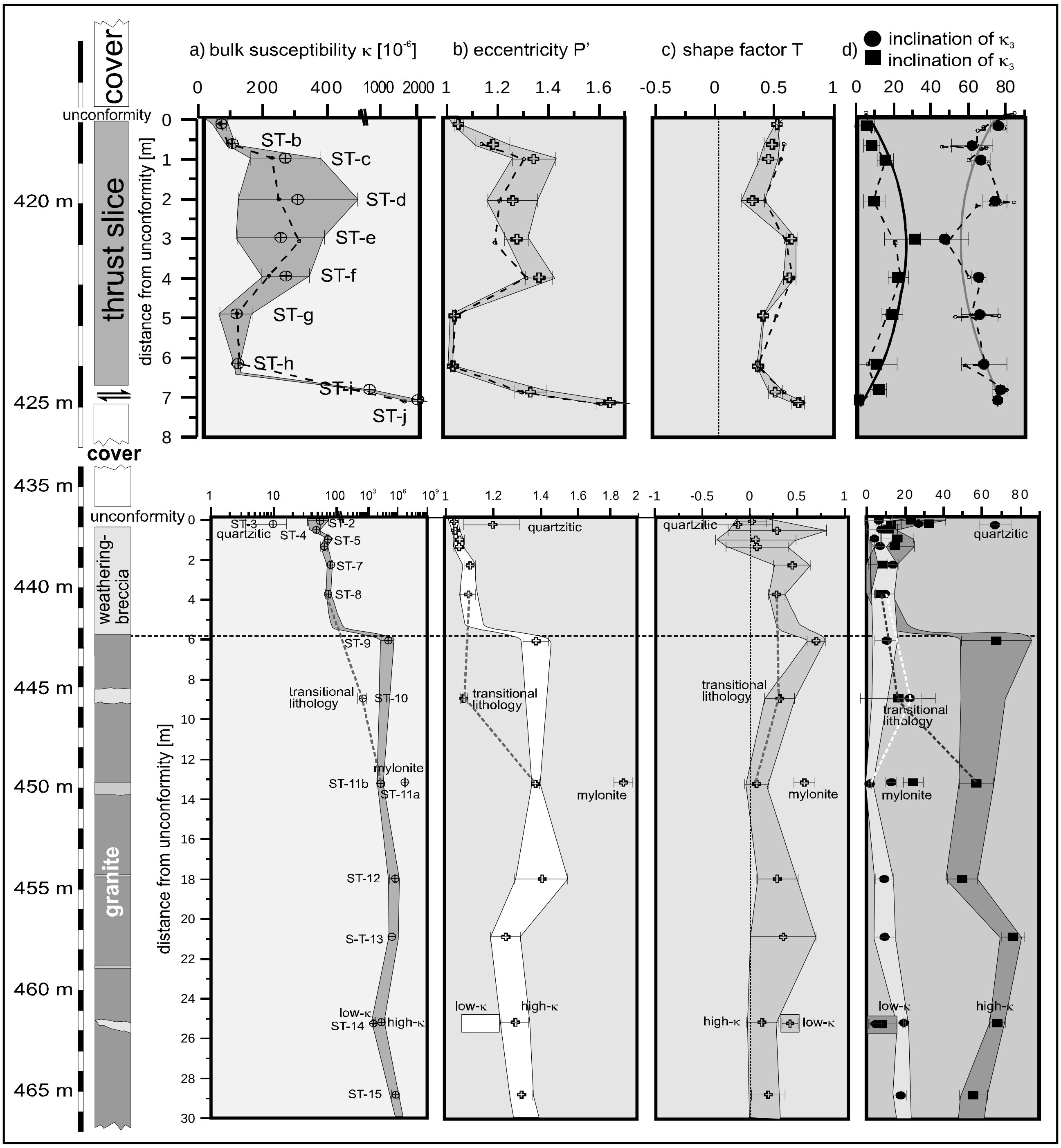

Figure 4.15: AMS-parameters κ_{bulk}, P', T and principal susceptibility axes κ_1 and κ_3 of the autochthonous section (lower part) and lower allochthonous tectonic slice (upper part). In the slice, results are displayed of analyses carried out at magnetic field of 300 A/m (large symbols and range in grey-tones) and at 30 A/m (small dots and dashed lines). Dashed lines in the Autochthon represent weathering trend through a hypothetical transitional lithological zone.

in the granite ($AMS_{granite}$) (Figure 4.13). The magnetic lineation, κ_1, is well clustered in a subhorizontal orientation (Figure 4.16).

4.6.1.3 Quartzitic granite ($AMS_{quartzite}$)

The magnetic fabric represented by the quartzitic granite is characterized by high anisotropies (P' = 1.06 to 1.35) and rather prolate ellipsoid shapes scattering between - 0.5 and 0.25. The axes' orientations show an unusual fabric with steep κ_3 and horizontal κ_1, which may be considered an inverse fabric compared to

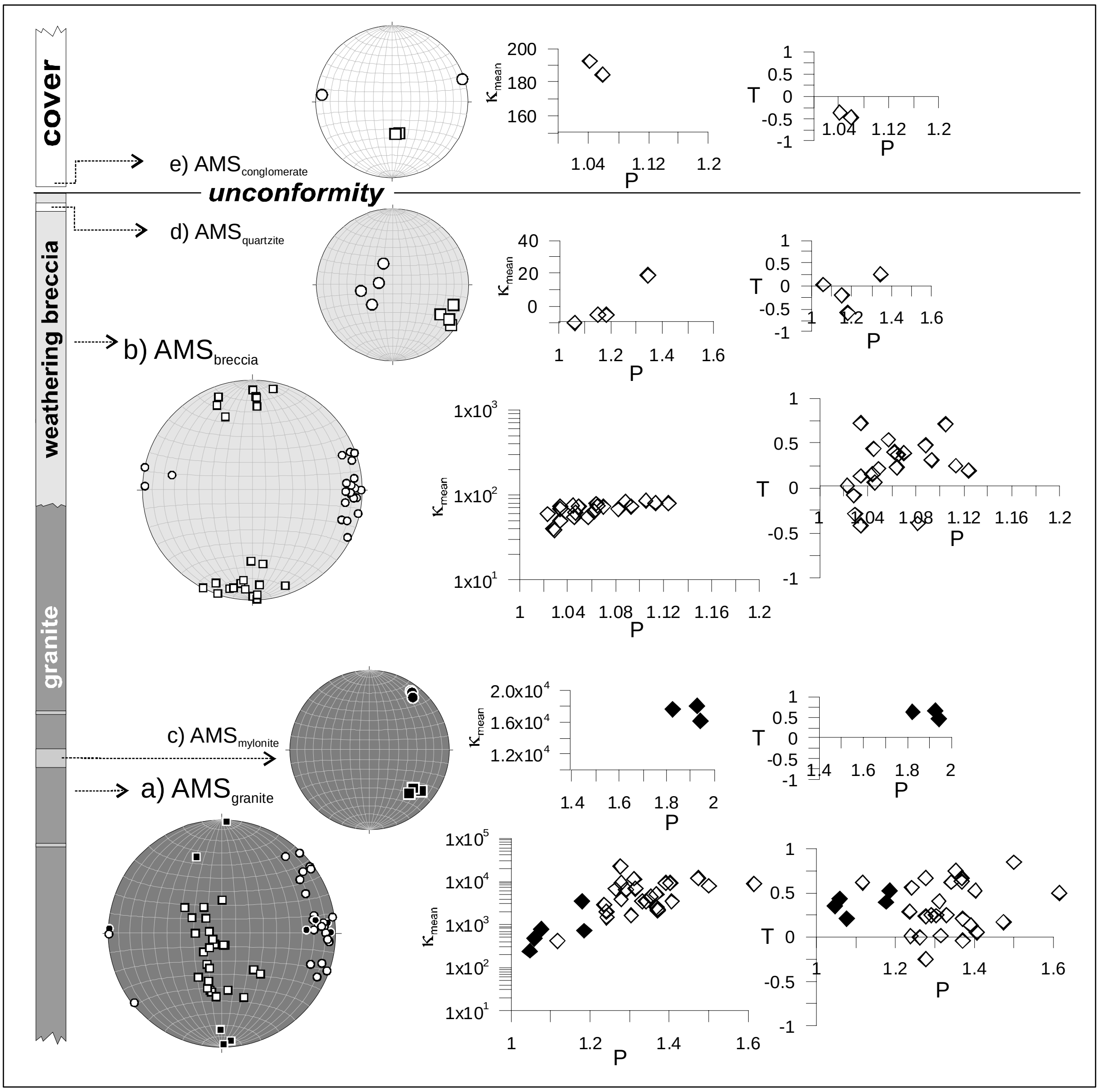

Figure 4.16: AMS fabric types in the Långviken drill core. AMS fabrics are distinguished by k_{bulk}, P' and κ_1-inclination. The two main fabric types correspond to the high-k-granite (a) and the low-k weathering-breccia (b). Minor fabrics are the porphyroclastic mylonite (c), the quartzitic low-k-granite (d) and the cover-conglomerate (e).

AMS$_{granite}$. In fact, the way of how principal axes orientations were calculated using signed (negative) values by AGICO's software SUFAR and ANISOFT results in case of diamagnetism in inverse fabrics (Hrouda 2004), i.e. κ_1 and κ_3 are exchanged with respect to the bulk crystallographic preferred orientation of quartz. The interpretation of this magnetic fabric is even more difficult, considering possible superposition of diamagnetic and paramagnetic fabrics. Since κ_{bulk} of AMS$_{quartzite}$ is near zero, it is suggested by Hrouda (2004), not to take the associated AMS-parameters for interpretations of petrographic fabric. Hence, these specimens are not interpreted here.

κ_{bulk} reaches $18.5 \cdot 10^{-6}$ [SI] in one specimen due to a slightly increased amount of paramagnetic contributors. Apparently, the paramagnetic fabric dominates in this specimen and resembles the characteristic axes-orientations of the wall rock (AMS$_{breccia}$). P' is, however, high with 1.35.

4.6.1.4 Conglomerate (AMS$_{conglomerate}$)

The AMS fabric shown by the conglomerate, AMS$_{conglomerate}$, is characterized by a vertical magnetic foliation, paralleling the orientation of $AMS_{breccia}$ beneath the unconformity (Figure 4.16). κ_1 is medium steeply inclined; not resembling the orientations of magnetic lineations in the basement. Anisotropies are moderately prolate, showing T of -0.25 and -0.5 and P’ of 1.04 and 1.06.

4.6.2 Lower Allochthonous section

The AMS pattern in the lower allochthonous basement slice (AMS_{slice}) are associated with the cataclasis. AMS_{slice} can be divided into subfabrics corresponding to the progressive cataclasis (weak, moderate, intense). The AMS stereoplots of the allochthonous section are shown in the Appendix II.c.

4.6.2.1 Cataclasite (AMS_{slice})

The AMS parameters of the samples from the allochthonous basement slice signify strong magnetic anisotropies. The three zones of cataclasis intensity in the slice are represented by AMS fabrics ($AMS_{slice-wc}$, $AMS_{slice-mc}$ and $AMS_{slice-ic}$), which are mainly defined by their degree of anisotropy (Figure 4.17). P’ is relatively low in the weak cataclasite zone ($AMS_{slice-wc}$), ranging between 1.02 and 0.07. Anisotropies of the moderate cataclasites range between 1.1 to 1.4, but showing also very low values in samples of low κ_{bulk} (st-g, st-h) (Figure 4.15.b) ($AMS_{slice-mc}$). P’-values of 1.3 to 1.7 are reached in the intense cataclasite ($AMS_{slice-ic}$). Shape factor T is with a few exceptions positive, indicating oblate shapes. There is no distinct correlation between T and P’ displayed (Figure 4.14.a). A general dependence of P’ to cataclasis intensity seems to be evident, but the dependency of P’ on κ_{bulk} is also shown by the κ_{bulk}(P’)-diagram (Figure 4.14.b). Therefore,

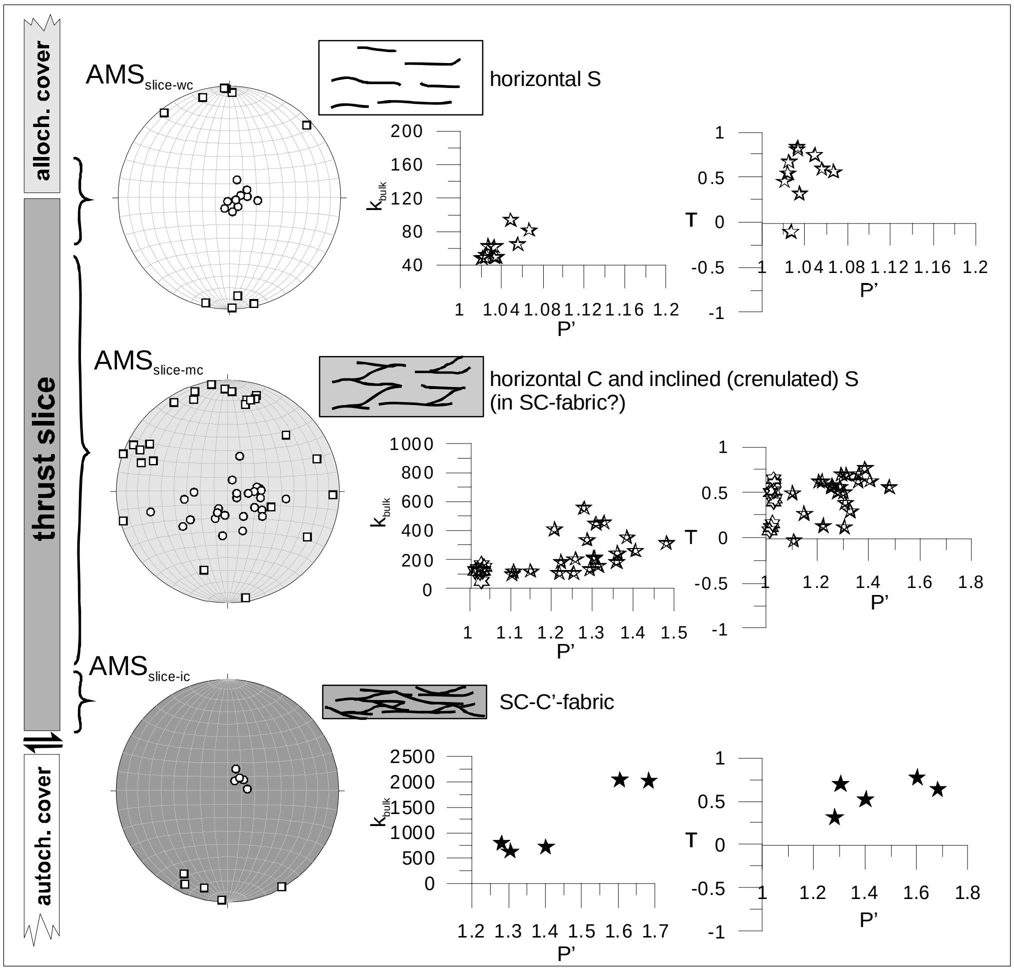

Figure 4.17: AMS-types of the cataclastic basement slice in the Långviken core. Abbreviations wc, mc and ic mean weak, moderate and intense cataclasis zone, respectively. Cataclasis intensity has no distinct influence on the characteristics of AMS sub-types.

P’ appears not as an adequate cataclastic strain marker in the slice, because κ_{bulk} itself is a function of pyrrhotite precipitation (see chapter 4.5.3).

The magnetic foliations are shallowly to medium-steeply inclined (κ_3 between 46° and 87°, average inclination is 70°; Figure 4.15), roughly paralleling the subhorizontal planar fabric, namely the C surfaces of the shear fabric. A slight decrease of κ_3-inclination to the centre of the slice is exhibited.

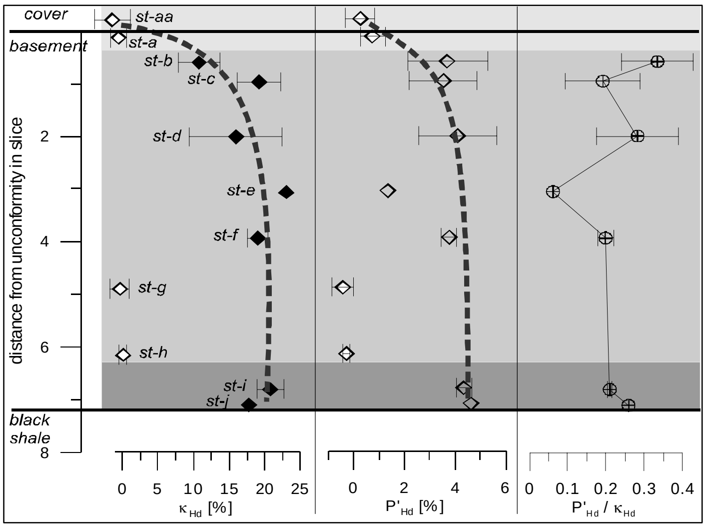

Figure 4.18: Field dependence κ_{Hd} of bulk susceptibility and *P’*$_{Hd}$ of anisotropy factor P’ through the tectonic slice of SGU 73007 Långviken (grey fields correspond to cataclasis zones weak, moderate and intense). c) ratio *P’*$_{Hd}$ / κ_{Hd} of field dependent samples.

Magnetic lineations κ_1 are subhorizontally inclined and cluster in two directions. Most specimens exhibit a flat-lying κ_1 perpendicular to the dip direction of magnetic foliation (cluster 1). A secondary direction (cluster 2) deviating by ca. 70° from cluster 1, resembles more or less the dip direction of magnetic foliations. A few specimens show a shallow κ_1 orientation in between both clusters.

4.6.2.2 P’$_{Hd}$ - Field dependence of P’

AMS parameters and ellipsoid axes are determined in applying field strength of 30 A/m and 300 A/m.

An anisotropy field dependence P’$_{Hd}$ is calculated analogously to κ_{Hd} (de Wall 2000a):

$$(1) \qquad P'_{Hd}\ [\%] = \frac{(P'_{300} - P'_{30})}{P'_{300}} \cdot 100$$

A significant field dependence of the anisotropy factor P’ is evident (Figure 4.19.a). P’$_{Hd}$ displays a weak proportional correlation with the degree of anisotropy (P’$_{300}$). P’$_{Hd}$ shows a similar pattern like κ_{Hd} throughout the cataclasis zones of the tectonic slice, yet not as well defined (Figure 4.18.b). P’$_{Hd}$ is generally weaker than κ_{Hd} with values of maximal 6.3 % (Figure 4.19.b). A proportional increase of P’$_{Hd}$ and κ_{Hd} is evident up to medium high κ_{Hd}-values of ca. 15 %. Samples with higher κ_{Hd} (corresponding roughly to higher κ_{bulk} indicated by bubble sizes) show significant deviations from that trend by showing rather lower P’$_{Hd}$.

Shape factor T does not show any significant dependence on κ_{Hd} and on P’$_{Hd}$. Regarding AMS axes

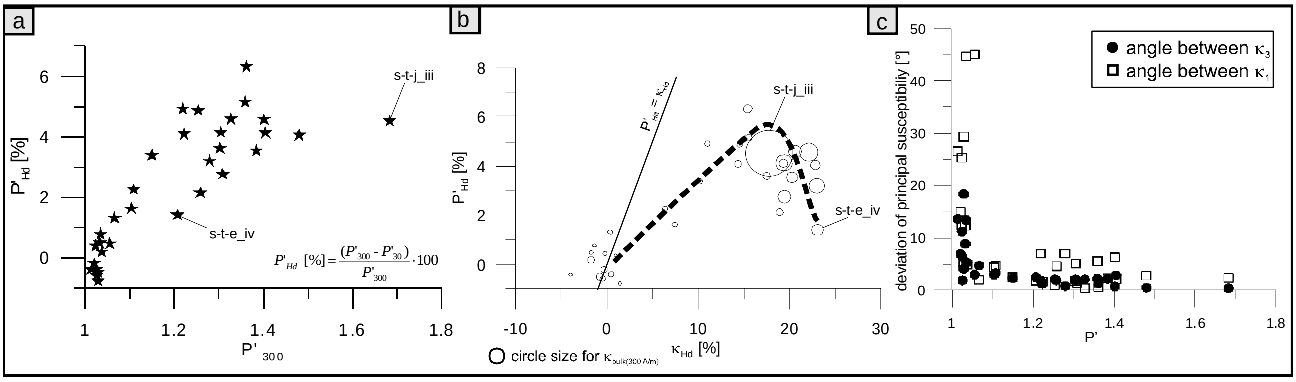

Figure 4.19: Field dependency of P’. a) *P’*$_{Hd}$, vs. P’$_{300}$; b) *P’*$_{H}$*d* versus k_{Hd}. Bubble size indicates κ_{bulk}-values; c) angles between principal susceptibilities measured in magnetic fields of 30 and at 300 A/m.

directions, there are no remarkable changes evident between measurements in 30 and 300 A/m (Figure 4.19.c). The high variations of orientations at very low P’ are possibly due to measurement errors, because of the near-spherical shape of the ellipsoid. The stability of the specimen axes distribution increases with increase of anisotropy (P’).

4.7 Data interpretation and establishing an alteration and deformation sequence

The autochthonous section together with the overlying lower allochthonous slice of the Långviken SGU 73007 drill core, recorded a sequence of basement deformation and alteration (stage numbers refer to Figure 4.20). This sequence is discussed in the following chapters.

4.7.1 D_1 - granite deformation and metamorphism in the Autochthon (stage 1)

A lower greenschist facies mineral assemblage (chlorite zone: chlorite, muscovite, epidote, stilpnomelane) is evident in the granite, thus metamorphic conditions reached at least lower greenschist facies. The intracrystalline feldspar and magnetite deformation (Plate 4.1.b) indicate an earlier deformation event in the granite, accompanied by medium to high metamorphic conditions. The two main sets of vertical schistosities, named S_{1a} and S_{1b}, are together with the intracrystalline deformations of quartz and feldspar, evidences for metamorphic deformation in the granite. In the mylonite, the vertical SC-shear fabric (Plate 4.1.d) parallels the orientation of the S_{1a} and S_{1b} foliations in the granite. Therefore, granite and mylonite are interpreted as deformed within the same tectonic phase. Deformation is heterogeneously distributed into zones of highly localized strain, the mylonites, and zones of lower strain, the granite. The oblate magnetite shapes of the mylonite indicate a pure shear component in addition to the simple-shear SC-fabric. Therefore, the granite / mylonite section may be interpreted as a vertical shear zone with strike-slip kinematics under transpressional regime.

The described deformation in the basement is not associated with Caledonian tectonic cycle, as maximum metamorphism was anchimetamorphic along the Caledonian margin during the Caledonian orogenic cycle (Warr et al. 1996). The imprint of an early pre-Caledonian tectonometamorphic event must be assumed. This event can attributed to transpressive shear zones of Proterozoic age, such as Storsjön-Edsbyn shear zone SESZ (Mattsson & Elming 2001), which are observed in the basement E of the Caledonian margin and are mostly NW-SE trending (see also case study Hara, chapter 3.6.1).

The serizitisation of Na-plagioclase took place in the granite in a hydrothermal environment, which supposedly coincided with low-grade metamorphism and deformation. Cracked microcline grains that altered along their cleavage-surfaces (comparable with feldspars in the Hara case study, Plate 3.1.c) may indicate serizitisation coeval to a late stage of D_1 under maximum greenschist facies temperatures, where feldspar deforms brittle. Similarly, fragmentation of magnetite, followed by precipitation of chlorite, stilpnomelane and Fe-carbonate along the fragment-networks, may be related to this deformation.

Since the age of the transpressive basement shear zones is slightly younger than the Revsund Granite intrusion (Mattsson & Elming 2001), metamorphism, alteration and deformation may have been taken place during initial granite cooling, subsequent to its emplacement. The intracrystalline to brittle deformation sequence of feldspar supports a retrograde path during deformation.

4.7.2 Palaeoweathering (stage 2)

The brecciation is attributed to a moderate physicochemical sub-aerial weathering phase in Neoproterozoic time. The attribution of the brecciated zone to pedogenesis is based in the first place on its location in the drill core sequence just beneath the unconformity (Gee et al. 1978). Characterization of specific pedogenetic phases is not straightforward due to the overprint by anchizonal metamorphism. Nevertheless, distinct differences between intact granite and weathering-breccia are observed by petrography, XRD-measurements and whole-rock geochemistry (chapters 4.2.1.3, 4.3.1 and 4.4.1) and can be attributed to weathering. Main chemical weathering processes were feldspar hydrolysis, chlorite breakdown and magnetite dissolution. Illite or I/S minerals are the weathering clays (see also cases study Hara), whereas smectite transformed to illite due to diagenetic overprint (Weaver 1989) (see following chapter). The zone of chemical weathering begins discretely with the onset of weathering-brecciation; therefore, both processes facilitated each other. A sedimentary genesis of the breccia zone is not inferred in the Långviken weathering-breccia, as relic peaces of primary granite are present in the matrix with a slightly decreasing modal fraction upwards. This is similar to the case study Hara, although the gradual trend of weathering-brecciation is not as well defined in Långviken and the transition zone from granite to breccia much thinner. The process of weathering-brecciation is presumable the same as interpreted for the Hara drill core, as the spatial distances between both locations is just 100 km (see chapter 3.6.2). Similar cold and humid weathering conditions are inferred.

Increased illite peak FWHM in the weathering-breccia, in comparison to the granite (Figure 4.4.a), point to different illite modifications between granite and breccia. The peak broadening in the breccia is likely due to poorly crystallized illite (Meunier & Velde 2004), as smectite is not observed in the breccia.

The enrichment and depletion trends of the element oxides are in a good accordance to published element enrichment and depletion patterns of weathering (e.g. Middelburg et al. 1988). The stability of Al_2O_3, TiO_2 and Zr through the profile indicates iso-volumetric weathering, in the sense that these immobile elements were not passively enriched by dissolution and exit of mobile minerals (c.f. White 1995). This points to moderate weathering conditions. The iso-volumetric weathering suggests that porosity increased because of feldspar, chlorite and magnetite dissolution and the associated leaching of Na, Ca, Fe, Mg (Figure 4.5).

Mobilization and exit of Na and Ca is a result of hydrolysis of Na-plagioclase, which increased progressively

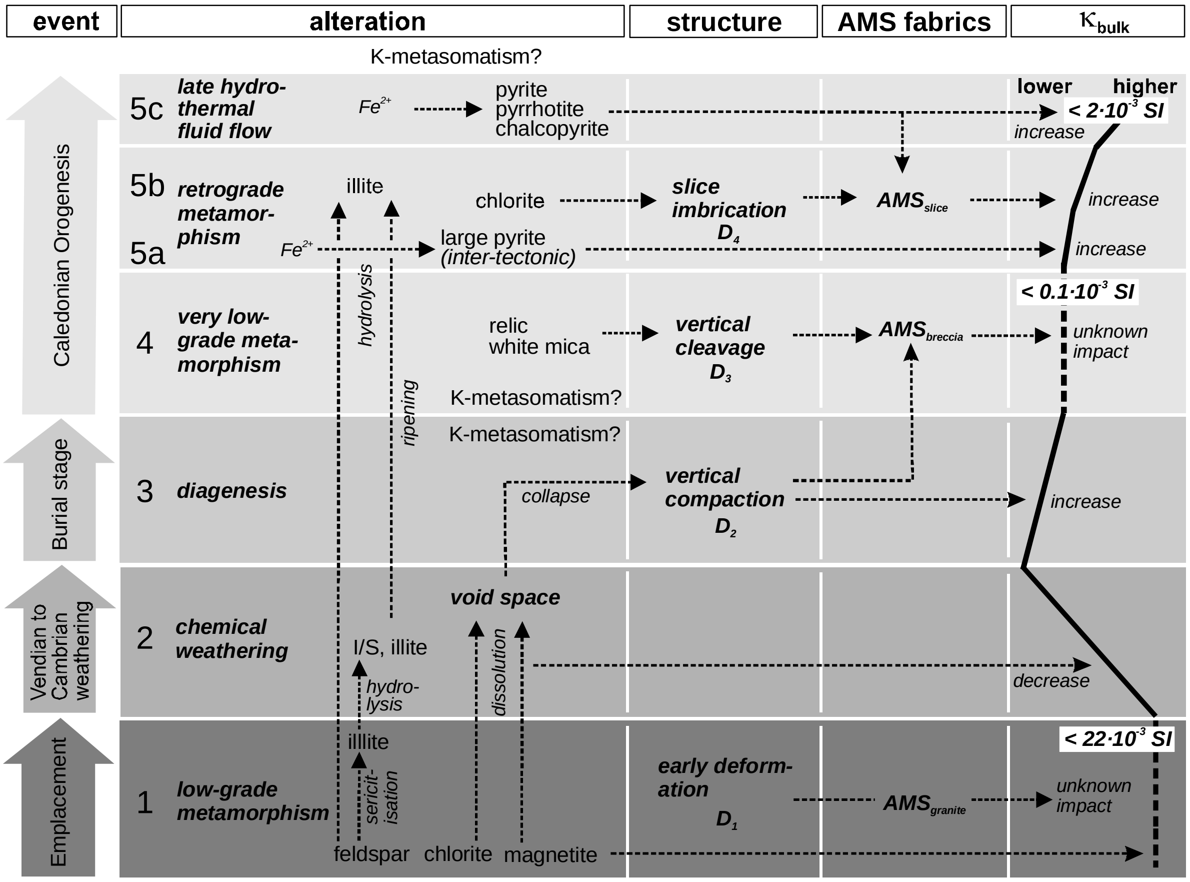

Figure 4.20: Process chart as a synthesis of tectonometamorphic stages, corresponding alterations and AMS features observable in the Långviken drill core near the autochthonous basement-cover-interface and lower allochthonous sections.

with proximity to the unconformity. The enrichment of K (and Ba, being a common substitute of K in feldspars and micas, (Figure 4.5) is partly attributed to a moderate degree of chemical weathering, where Na-plagioclase depleted while mica whereas and K-feldspars persisted and enriched relatively. While Na decreases, K increases in the profile. Therefore *CIA* (Figure 4.4.c), treating K as Na, does not represent a weathering trend. *PIA* and *CIW*, on the other hand, represent the weathering trend quite well. The increase of K, is not only a relative effect of Na-depletion, but may rather indicate absolute enrichment associated with a later fluid stage (see following chapter).

The depletion trend of Mg is mainly associated with chlorite breakdown during weathering. Products of this incongruent dissolution (hydrolysis) are mainly clay minerals and iron phases.

4.7.3 D_2 - unconformity parallel compaction in the Autochthon (stage 3)

Porosity that had been produced during iso-volumetric weathering was reduced during burial compaction, since no large void space is observed in the rocks. By this compaction, a horizontal cleavage formed (Plate 4.1.g). The associated pressure-solution cleavage seams are referred to as S_2. The stability of elements Si, Al, Ti, Zr, P between granite and weathering-breccia (Figure 4.5) shows that compaction did not involve leaching of elements. The evident pressure solution caused only minor SiO_2 mobilization.

Presumable, clay minerals underwent a preferred orientation paralleling S_2 by this vertical compaction. The importance of horizontal S_2 as an anisotropy factor is not constrained. Crenulation of this planar clay fabric in S_3-microlithons is evident and causes a horizontal intersection lineation of both surface sets parallel with the unconformity. It has to be considered that S_2 imprint gradually increases with brecciation intensity towards the unconformity (compare to the Negev and Hara cases, 2.5.6 and 3.7.2.4, respectively).

The increase of K, as described in the previous chapter, is not only a relative effect of Na-depletion, but may rather indicate absolute enrichment associated with a later fluid stage. K-enrichment is observed in many ancient fossil weathering profiles (Dott Jr. 2003, Medaris et al. 2003, Sutton & Maynard 1996, Ziegler & Longstaffe 2000) and related to metasomatism during burial stage (Fedo et al. 1995; see case study Negev).

4.7.4 D_3 - vertical cleavage in the weathering breccia and lower cover (stage 4)

The dominant vertical cleavage in the weathering-breccia (Plate 4.1.h) cannot be an expression of D_1. This is inferred by the textural destruction of the granite in the weathering-breccia, taking place after D_1. The vertical cleavage surfaces locally crenulate S_2-seams. This vertical cleavage generation is therefore referred as S_3. White mica-biotite stacks define the S_3-surfaces, which is in contrast to the chlorite schistosity in the granite. Micas enriched passively as relic minerals during weathering, whereas chlorite altered. Due to the unoriented core, it cannot be stated, whether S_3 is parallel with S_1. D_3 may be related to the overthrusting of the Lower Allochthon, as inferred in the Hara case. The formation of a vertical S_3 is also observed in the Hara case, thus, a regional extension of similar basement-deformation is suggested. The cover rocks also show a vertical foliation imprint. The vertical S_3-cleavage is not evident in the basement-slice. A mechanical decoupling between autochthonous cover sediments and basement rocks is not likely, considering the similar and tectonometamorphic D_3 overprint.

4.7.5 D_4 - slice formation and cataclasis within the allochthonous slice (stages 5a-c)

Remnants of deformed micas are observed in the weak and moderate cataclasites. Locally, mica defines a crenulated cleavage in microlithons and cataclastic cleavage domains. The mica generation is comparable to micas, which define S_3 in the autochthonous weathering-breccia. This is one indication that the pre-cataclasis lithology in the slice was a weathering-breccia, too. A common pre-thrusting evolution of the slice rocks and the autochthonous rocks is discussed in chapter 4.7.7. The tectonic imbrication and associated shear fabrics, crenulating S_3 surfaces, took place following D_3. Consequently, the deformation is referred to as D_4, in accordance to the deformation sequence in the autochthonous basement below.

S_3 surfaces are relatively well preserved in the moderate cataclasis zone and asymmetrically crenulated between newly developed C_4 shear surfaces. This S_3 preservation, comparison to entire obliteration in the breccia above, may be attributes to the dominant simple-shear-like cataclastic flow.

The imbrication is an expression of the advanced Caledonian nappe stacking forming the Lower Allochthon (e.g. Roberts & Stephens 2000, Warr et al. 1996). D_4 is thus comparable to D_4 in the Hara case study. The proposed thrusting is visualized as a sketch in Figure 4.21. Most likely, the thrust base was within the weathering-breccia and the black shale acted as a shear surface. The pre-deformational spatial distance between rocks in the two drill core sections is indicated by a particle path.

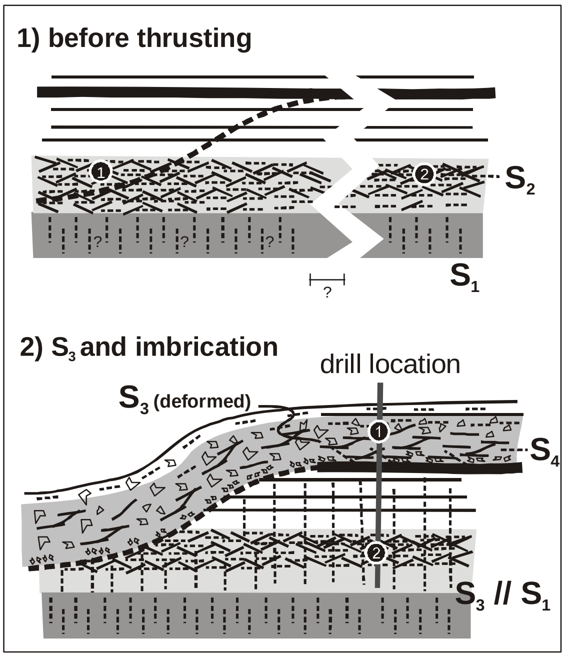

Figure 4.21: Sketch explaining the proposed development of the thrusting, which is exposed in the SGU 73007 Långviken drill core.

Cataclasis in the allochthonous basement slice was accompanied by massive sericite and illite precipitation (Plate 4.2.d), due to cataclastic mica break down and sericitization of feldspar and mica. The stronger alteration in the moderate and intense cataclasis towards the bottom part of the slice is indicated by *PIA* and *CIW*, which show an inverted depth-function, compared to the autochthonous section (Figure 4.4.c). This shows, that Na leaching, accommodated by fluid-flow, took place during cataclasis.

Fine-grained chlorite formation in the matrix occurred coeval with this fluid event. Both chlorite and illite produced a fine-grained network around brecciated quartz and feldspars (Plate 4.2.c). A continuous increase of the ratio chlorite-002 / illite-002 peak-intensity from 0.1 to 0.8 displays an increasing importance of chlorite precipitation with stronger deformation (Figure 4.4.a).

The depth-function of FWHM shows an association of crystal maturity of illite and chlorite to cataclasis intensity (Figure 4.4.b). This may be an expression of the frequently described link between crystallinity and cleavage intensity (e.g. Flehmig & Langheinrich 1974). The good FWHM correlation of chlorite and illite shows a growth within the same regime of temperature and fluid-flow.

The fluid was hydrothermal, considering that quartz underwent incipient recrystallization in the intense cataclasite zone (protomylonite). Maximum sub-greenschist facies conditions (maximum 270 °C: Meschede 1994) during cataclasis are indicated for the lower part of the slice, possibly cataclasis-induced frictional heat caused locally enhanced temperatures.

4.7.6 Evolution of the magnetomineralogy

4.7.6.1 Magnetite dissolution during palaeoweathering

Magnetite, as the major source-minerals of the 3.3 wt% content of Fe_2O_3 (total Fe) in the granite, is almost completely absent in the brecciated zone. Therefore, weathering facilitated dissolution of magnetite (Rowan & Roberts 2006). The physical destruction of magnetite increased the surface area, which facilitated dissolution. The transition from ferrimagnetic magnetite zone (granite) to paramagnetic weathering zone is narrow; there is no broad zone of gradual change of magnetomineralogy. Iron and manganese are depleted in the weathering-breccia by more than 50 % (Figure 4.5). This must be considered as the result of the magnetite dissolution.

The distinct partitioning of the stability of magnetite between granite and breccia suggests a weathering-induced change of the Eh-pH-environment in the rocks, towards a condition that allowed almost complete magnetite dissolution to form dissolved ferrous ions. These conditions must have been oxidizing and acidic (stage 1 and 2 in Figure 4.22, numbers refer to Figure 4.20). The ratio of Fe_2O_3 / S (Figure 4.4.d) gives an approximation for the magnetite / pyrite ratio in the Autochthon. The high ratio in the granite is associated with magnetite content and the low ratio in the weathering breccia to leached Fe by dissolved magnetite.

4.7.6.2 First sulphide formation prior to D_4

Since the first sulphide generation, the large pyrites, is cataclastically deformed and asymmetrically crenulated with S_3 into D_4 shear fabrics (Plate 4.3.c,d), Such large pyrites are not recognized in the autochthonous granite and weathering-breccia. Therefore, the pyrite-generating hydrothermal alteration infiltrated exclusively rocks in the slice. Its formation is considered as syn-D_4, or inter-tectonic, between D_3 and D_4. The required reducing alteration environment facilitating precipitation of pyrite subsequent to D_3, before thrusting, must be the result of sulphur-rich fluids passing through easy pathways of the rock. These pathways are mainly planar structural features. The low ratio of Fe_2O_3 / S (Figure 4.4.d) in the slice indicates the influence of S-rich fluids. The nearest possible sources of sulphur are the Cambrian black shales defining the floor-thrust of the tectonic slice. Cambrian black-shales in the upper parts of the drill core are also a possible source. P/T-conditions are not deducible directly by pyrite, because it is a ubiquitous mineral observable in all metamorphic facies; however, the unusual large size (up to 2 mm) indicates elevated temperatures.

4.7.6.3 Second sulphide formation after D_4

Considering size and shape of the grains, the pyrites of the pyrite-pyrrhotite-chalcopyrite assemblage in the tectonic slice resembles the pyrites observed also in the autochthonous basement (Plate 4.3.a,e). A post-D_4 genesis of the autochthonous pyrite and the allochthonous pyrrhotite-pyrite-chalcopyrite-association is interpreted, because the sulphide grains overprint matrix minerals. Precipitation of sulphide reached down into the autochthonous granite, where magnetite was pseudomorphously replaced by pyrite (Plate 4.4.c,d,h). This pyrite formation in the Autochthon may also be associated with the first sulphide generation (see previous chapter).

Thin undeformed veins filled with a pyrite-pyrrhotite-chalcopyrite assemblage in the intense cataclasis (Allochthon) may have resulted from extension during stress release subsequent to the cataclastic shear.

The ratio of Fe_2O_3 / S (Figure 4.4.d) gives an approximation for the pyrrhotite to pyrite ratio in the tectonic slice. Principally, the pyrrhotite (almost FeS, sulphur-deficient) / pyrite (FeS_2 - sulphur-rich) ratio increases with cataclastic intensity. Pyrrhotite requires slightly lower Eh-conditions to precipitate than pyrite, with respect to redox-conditions in the fluid-rock system (Hall 1986). Thus, the hydrothermal fluid passing through the slice subsequent to D_4 was of more reducing nature, than the inter-tectonic fluid, which caused the first generation of pyrites. The changing fluid conditions leads to an Eh-pH-path, which may be valid for the entire core section (Figure 4.22). The phase boundaries shown in this diagram are based on ambient temperatures, which is not realistic condition in the section. The pyrrhotite field is larger at anchizonal hydrothermal temperatures, reaching to less alkaline conditions (*pers. comm.* A. Kontny).

The coexistence of pyrrhotite and pyrite is common (Vaughan & Craig 1978). Thermal stabilities of both modifications, monoclinic pyrrhotite and pyrite, are similar in low-T: The upper thermal stability of hydrothermal monoclinic pyrrhotite ranges from 225 to 280 °C, depending on characteristics of lithology and fluids (summarized in Kontny et al. 2000). Pyrite is considered as insensitive to temperature and is stable above and below the stability range of pyrrhotite. Hence, the pyrrhotite-pyrite-paragenesis may have been precipitated in a very-low grade hydrothermal environment subsequent to the D_4. This points to a retrograde path, considering that temperatures of 270 °C were established locally during D_4.

It cannot be definitely stated, whether a true paragenesis or a genetic succession involving replacements of older phases occurred. A sequential precipitation of pyrrhotite after pyrite is possible: In addition to the post-D_4 pyrite, a pyrite precipitation stage during, or after D_4 may have occurred, which subsequently changed to a pyrrhotite stage because of decreasing temperature and/or redox-conditions. Small individuals of these pyrites may have been replaced by monoclinic pyrrhotite during the post-D_4 hydrothermal alteration. One possible pyrite-to-pyrrhotite reaction is:

$$(1) \qquad 2\,FeS_2 + 2\,FeO + C_{(aq)} = 4\,FeS + CO_{2(aq)}$$

During this reaction 2 mol pyrrhotite are generated at the expense of 1 mol pyrite and 1 mol Fe-oxide. This may have caused low pyrite and also lower magnetite content in the pyrrhotite-rich samples. The Fe-oxide might have been provided by chlorite or oxide remnants, like magnetite or haematite. The source providing C are the Cambrian black-shales in upper parts of the drill core. These black-shales also supplied the sections with S to precipitate sulphides.

4.7.7 Genetic relation of the autochthonous and allochthonous basement parts

In the allochthonous tectonic slice, a weathering-breccia capped by cover rocks is shown. This section is therefore similar to the autochthonous part. A common genesis prior to D_4-imbrication is suggested by the following indications: (a) tectonic clasts formed by D_4, bear inherited early petrographic features, which are observed also in the Autochthon, such as primary mica clasts and intracrystalline deformation in quartz and feldspars; (b) Mica clasts in the slice resemble petrographically those observed in autochthonous basement (primary mica defining S_3-surfaces); (c) a very close petrographic relationship between autochthonous and allochthonous basement is displayed by XRD and whole-rock geochemistry: Samples just below both unconformities, ST-2 and st-a, show very similar XRD spectra (Figure 4.3 and Figure 4.4.a) and similar values of *PIA*, *CIW* and *CIA* (Figure 4.4.c). XRD-patterns show in both sections a dominance of illite against Fe-chlorite and a similar quartz, feldspar and calcite content.

In both weathering-breccia sections, the low chlorite content can be correlated with the low whole-rock $Fe_2O_3^{total}$ + MgO content (0.9 to 2.67 wt%). Within the tectonic slice, however, the moderately enhanced chlorite-content (compared to illite) with increasing cataclasis intensity (Figure 4.4.a) appears to be independent from the bulk-rock geochemistry: sample st-j as an intense cataclasite has a very low $Fe_2O_3^{total}$ + MgO content of 1.05 wt%, but shows the highest chlorite / illite peak intensity ratio (0.8).

Accessory magnetite and haematite in the allochthonous weathering-breccia, evidenced by κ(T) curves (Figure 4.8), can be interpreted as relic minerals of the granite, as they are observed in the

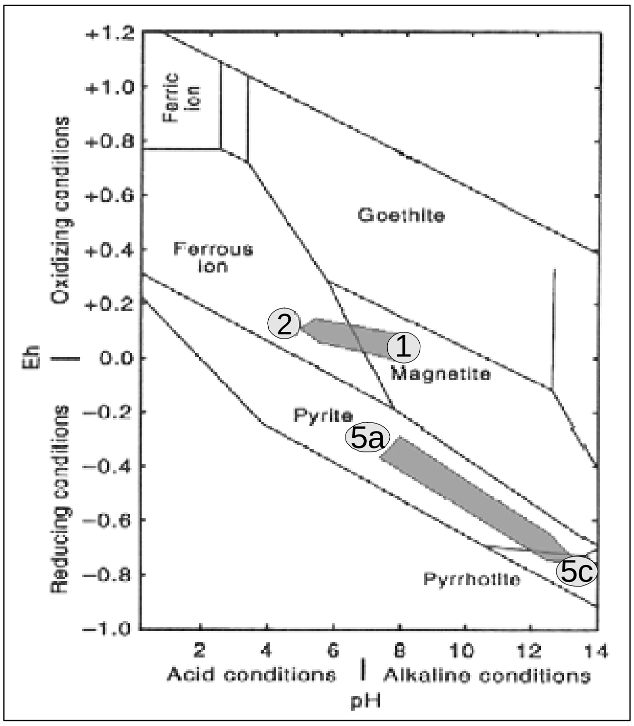

Figure 4.22: Proposed Eh-pH path through the alteration processes in the Långviken basement (numbers refer to evolution-stages in Figure 4.20): 1) initial pre-weathering condition; 2) weathering with magnetite dissolution; 5a) pyrite precipitation before and during Caledonian thrusting; 5c) pyrrhotite precipitation subsequent to thrusting. Stability zones for natural anoxic waters at the earth's surface at 25 °C are indicated (in courtesy C. Vahle, modified).

autochthonous basement.

A certain spatial distance between both autochthonous and allochthonous weathering-breccias prior to imbrication is required, but the exact transport distance cannot be inferred (reference points 1 and 2 of a particle path in Figure 4.21). Regarding the cover rocks, there is no lithological correlation between the autochthonous and lower allochthonous beds. This may be due to a facies change of the siliciclastic sediments. The inter-tectonic (between D_3 and D_4) pyrite-generating hydrothermal alteration must have acted exclusively in the slice. Thus, in this timeframe, the nappe stacking was not yet completed, i.e. a considerable spatial separation of both sections is likely the case during D_3.

4.8 *Development of κ_{bulk} and AMS in relation to petrogenesis*

The texture-defining D_1 is the earliest fabric in the section. The bulk susceptibility and AMS fabrics in the Långviken drill core section are subject to change due to progressive alterations and structural imprints. The three main structural domains of the section, (a) autochthonous granite, (b) autochthonous weathering-breccia and (c) allochthonous cataclastic basement slice, are represented by distinct magnetic fabrics (Figure 4.16 and Figure 4.17).

4.8.1 Evolution of κ_{bulk}

The comparison of κ_{bulk} with the total Fe content in the rocks is a qualitative tool to track those mineral phase changes, which have an impact on bulk susceptibility (Figure 4.23). The three principal alteration stages are: (1) magnetite-alteration from granite to weathering-breccia; (2) pre-D_4 pyrite formation in the slice and (3) post-D_4 pyrrhotite formation. In the ferrimagnetic granite, highest κ_{bulk} of $22 \cdot 10^{-3}$ SI are evident. The alteration of magnetite during palaeoweathering led to a loss of κ_{bulk} by two orders of magnitude, which is observed in the weathering-breccia. Most iron was leached during weathering and burial stage.

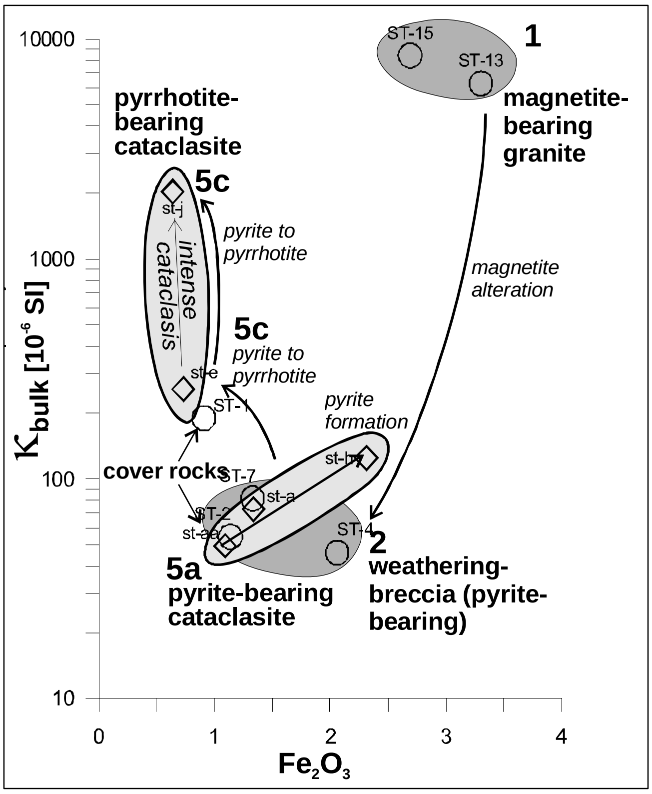

Figure 4.23: Dependence of κ_{bulk} on iron content in the SGU 73007 Långviken core. Light grey field: allochthonous basement slice, dark grey: autochthonous basement. Numbers correspond to evolution stages summarized in chapter 4.7.

A paramagnetic and ferrimagnetic behaviour of the κ(T)-curves in combination with a Verwey transition, is shown in the autochthonous weathering-breccia and transition zone (Figure 4.7). The presence of magnetite, contributing slightly to κ_{bulk}, is interpreted as small and disseminated remnants of palaeoweathering in the rock matrix. These magnetite remnants are not identified by petrography. Such a paramagnetic-ferrimagnetic behaviour of the κ(T)-curves in combination with a Verwey transition, is also observed in the autochthonous weathering-breccia (Figure 4.7), and thus points to a similar genesis of both lithologies prior D_4. A loss of reversibility of κ(T)-curves during the cooling run is evident in the weathering zone and transitional lithology. Susceptibility enhances along the cooling path from temperatures below 600 °C. Such a non-reversibility is a result of magnetite formation occurring during experimental heating (e.g. Kontny et al. 2000). Magnetite is formed from weathering products, which were relatively increased in the weathering zone. These minerals are paramagnetic Fe-bearing (phengitic) illites, chamosite and possibly carbonates.

In the Allochthon, the weakly cataclastic equivalents of the autochthonous weathering-breccia show similar κ_{bulk} / $Fe^{total}O$ ratios (area 2 and 5a in Figure 4.23). This indicates that a) iron was not mobilized and b) no important iron phase changes occurred during D_3 and D_4.

A weak positive (exponential) correlation of κ_{bulk} and $Fe^{total}O$ is indicated by some pyrite bearing cataclasites. This may be explained by the increase of the modal fraction of pyrite. A major increase of κ_{bulk} coeval with a slight decrease of $Fe^{total}O$ corresponds to the generation of pyrrhotite in the slice. Between specimen st-e, which is a moderate cataclasite, and st-j, an intense cataclasite, κ_{bulk} increases strongly due to an enhanced (ferrimagnetic) pyrrhotite to (paramagnetic) pyrite ratio.

4.8.2 *Factors defining the field dependency of κ_{bulk} in the allochthonous slice*

Field dependence of κ of pyrrhotite is evidenced for the samples in the slice. The results show that in the samples st-e and st-j a decrease of the statistical grain size causes a lowering of κ_{Hd} by a degree, which quantitatively agrees with published sample sets (EOR-standard) of pyrrhotite ores (Figure 4.12).

Magnetomineralogical characteristics of the sample set can be explained with the $\kappa_{Hd}(\kappa_{bulk})$ diagram (Figure 4.11). κ_{Hd} depends mainly on grain density (modal fraction) and grain size of pyrrhotite (Dekkers 1988, Worm et al. 1993) and κ_{bulk} increases with grain density of pyrrhotite (see inset in Figure 4.11). A shallow slope may represent an increase of grain density in a set of lithological comparable samples. Such a trend is exhibited by subgroup c. Grain size, on the other hand, positively influences field dependence (Dekkers 1988, Worm et al. 1993), leading to a steep positive slope. Such a positive slope is also an effect of the dependency of effective grain density on grain size. The samples of subgroup b define a linear correlation of κ_{Hd} and κ_{bulk} with a steep slope (κ_{Hd} from 6 to 19 %: Figure 4.11). This trend, is not completely explainable with just change of pyrrhotite grain size, because there are no petrographic indications for enhanced grain sizes accompanying this trend. Hence, another factor defines the linear relation of κ_{bulk} and κ_{Hd}. The samples of subgroup b are distributed rather in the upper part of the tectonic basement slice and are moderately cataclastically deformed. A weak and quite irregular trend of increasing κ_{Hd} is developed with cataclasis intensity (as shown in Figure 4.18, excluding the pyrrhotite-deficient samples st-g and st-h). The successive change in the ratio of modal fractions of weakly susceptible (paramagnetic) pyrite and strongly susceptible (ferrimagnetic) pyrrhotite is an important factor defining the relation between κ_{bulk} and κ_{Hd}. Within the cataclasis zone, pyrite to pyrrhotite alteration or enhanced pyrrhotite precipitation neighbouring pyrite (as discussed in chapter 4.7.6) was intensified with depth and cataclasis.

Petrographically, the strong enhancement of κ_{bulk} from st-e to st-j by the factor 5.27 is directly connected to the enhanced pyrrhotite / pyrite ratio (Figure 4.23). Consequently, an increase of κ_{Hd} in st-j is expected. However, this is not the case; in contrary, a decrease from 23 % down to 17.8 % is observed (Figure 4.11). The decreased value lies slightly outside the range of the standard deviation of subgroup c (grey bar in Figure 4.11). Since the samples in the tectonic slice are in transitional range to ferrimagnetisms (ca. 100 to $2000 \cdot 10^{-6}$ SI), the pyrrhotite / matrix ratio is an effective factor influencing the slope of κ_{Hd} vs. κ_{bulk}. However, the corrected field dependency parameter $\kappa_{Hd}corr$ (chapter 4.5.3.3) shows an even higher reduction of $\kappa_{Hd}corr$ from st-e to st-j (Figure 4.11). Therefore, this abnormal behaviour cannot be explained with the high matrix susceptibility over the small modal fraction of ferrimagnetic pyrrhotite. Instead, the appearance of pyrrhotite itself has to be considered. Pyrrhotite shows ferrimagnetic behaviour already at grain sizes above ca. 6 μm, but field dependency does not occur in pyrrhotite below 30 μm (Worm et al. 1993). The ratios of the modal fractions of grains size classes *>6μm / >30μm* show a difference (values for vol% of > 6μm and > 30μm in

Figure 4.12.c): for st-e, the ratio > *6μm / > 30μm* = 1.02 and for st-j, > *6μm / > 30μm* = 1.67. The higher ratio in st-j leads consequentially to a higher κ_{bulk} / κ_{Hd} ratio. In fact, this higher ratio can be observed in st-j (κ_{bulk} [$\cdot 10^{-6}$] / κ_{Hd} [%] = 92.8), compared to st-e (κ_{bulk} / κ_{Hd} = 13.6).

Furthermore, it is important to have in mind that besides the presence of monoclinic, i.e. ferrimagnetic pyrrhotite (Weiss-type Fe_7S_8), a certain fraction of antiferromagnetic pyrrhotite is present in st-j (see chapter 4.5.1). The intrinsic susceptibility of antiferromagnetic pyrrhotite can be high with about 0.17 SI for (λ-type Fe_9S_{10}: Hunt et al. 1995), but a significant field dependence is absent (de Wall & Worm 1993; also *Sullivan* in Figure 4.10, in courtesy of de Wall). Such a pyrrhotite assemblage may have contributed to the higher κ_{bulk} /κ_{Hd} ratio in sample st-j, compared to assemblages with a higher monoclinic pyrrhotite fraction, present in other samples (e.g. st-e).

Three factors influencing κ_{bulk} and κ_{Hd} can be summarized: (a) pyrrhotite grain size distribution, (b) pyrrhotite-to-matrix ratio and (c) modal fraction ratio of ferrimagnetic pyrrhotite to antiferromagnetic modification.

4.8.3 AMS fabrics

4.8.3.1 AMS in the autochthonous granite

The granite exhibits the magnetic fabric type $\mathrm{AMS}_{\mathrm{granite}}$, which is attributed to the vertical schistosity. $\mathrm{AMS}_{\mathrm{granite}}$ and $\mathrm{AMS}_{\mathrm{mylonite}}$ are defined by large disseminated magnetite crystals with an intrinsic susceptibility of about 1.3 SI (as modelled in chapter 4.5.2). Magnetites have a rather small number between 11 and 102, reflected by k_{bulk} (chapter 4.5.2). They are mostly passive elements of the deformation process without being subject of rotation and change in aspect ratio. Both factors, small number and irregular shape, cause a rather weak definition of the magnetic fabric, indicated by scattered principal AMS axes. The contradicting high anisotropy degree P' of almost 2 (100 %) (in the porphyroclastic mylonite) is a result of the positive correlation of P' with κ_{bulk} (see κ_{bulk}(P') plot in Figure 4.16.a). This is a common observation in ferrimagnetic rocks (Tarling & Hrouda 1993). Orientation and length of principal axes (κ_1, κ_2, κ_3) are defined by the resultants of susceptibility tensors of all magnetite grains (Tarling & Hrouda 1993). Distribution-anisotropy of magnetite (Archanjo et al. 1995a, Archanjo et al. 1995b, Cañon-Tapia 2001, Gaillot et al. 2006, Gaillot et al. 2002, Grégoire et al. 1998, Hargraves et al. 1991) induced by magnetic interaction of closely neighbouring crystals may be considered in those magnetite grains, which were altered to a network of chlorite, stilpnomelane and Fe-carbonates surrounding relic magnetite (Plate 4.3.b,d).

The preferred oblate AMS shapes and the clustering of κ_3 are attributed to predominantly oblate shaped magnetites. Magnetites are predominantly flattened parallel S_{1a} (in the granite) or C_1 (mylonite). However, because of their large size exceeding schistosity-domains, magnetites can also be oriented with long axes in an intermediate position between granitic sub fabrics S_{1a} and S_{1b} and mylonitic S and C. The possible petrographic factors leading to the observed scattering of κ_3-declination in the granite (Figure 4.16 and Figure 4.24.c) are: (a) rotated magnetites paralleling exclusively S_{1a} surfaces, (b) deviation of magnetite shapes from the preferred flattening surface S_{1a} and (c) the superposition of S_{1a} and S_{1b}, displayed by an intermediate positions of κ_3 between both subfabrics.

The bimodal distribution of the κ_1-inclination (Figure 4.13) can be explained considering the deformed granite and mylonite as parts of one vertically oriented transpressional SC-zone with strike-slip kinematics (see chapter 4.7.1). κ_1-inclination maxima correspond to a) the subhorizontal simple shear direction, referred to as $\kappa_{1\text{-str}}$ and b) the subvertical intersection lineation of the SC-fabric, $\kappa_{1\text{-}\delta}$ (Figure 4.24.c) (similar distribution are described by e.g. Aranguren 1996, Henry 1988, Pares & van der Pluijm 2002a, Tomezzoli et al. 2003). In the mylonite, large magnetites are paralleling C_2 and are elongated in simple shear direction

(Plate 4.1.d). Therefore, κ_1 is horizontally oriented ($\kappa_{1\text{-str}}$) in the mylonite. S_1-surfaces are subordinately developed and defined by small chlorite seams. They are affecting neither the orientation nor the shape of magnetites.

Sub-fabrics S and C in a monoclinic SC-fabric system (where stretching lineation in the C-surface and intersection lineation are perpendicular to each other) define a commonly composite AMS fabrics. The relative strength of the sub-fabrics define, whether the magnetic lineation resembles stretching or intersection lineation (Housen et al. 1993, Pares & van der Pluijm 2002a), figure on page 296 therein). In the present case, magnetic lineations scatter between stretching and intersection lineation with an angle α. This scattering is attributed to the sum of three statistical errors in the grain- to specimen-scale: a) the small number of irregularly shaped magnetite clasts. A statistical “averaging out” effect (Hrouda & Ježek 1999b), i.e. the decrease of standard deviation with increasing amount of magnetic grains (statistic sample set), is therefore hardly given for granite and mylonite; b) the principal oblate shapes of the magnetites cause in total a considerable deviation of long axes from the mean values (girdling around κ_3) and c) the statistical deviation of magnetites’ long axes from stretching lineation prior to strain is to a certain extend preserved, because in comparison to the strong pure shear component perpendicular to S_2, the simple shear strain parallel with stretching lineation in C_2 is low, even in the mylonite (Figure 4.24.c).

The deformed granite is, as stated in chapter 4.7.1, part of a vertical transpressional shear zone, similar to the granite in the Hara location. The magnetic fabric, characterized by vertical κ_1, of the granite shows also similarities to the AMS in the Hara granite, hence in the SEDZ (Mattsson & Elming 2001). The anisotropy degrees are not comparable, since the magnetic carriers are different (paramagnetic in Hara, ferrimagnetic in Långviken).

4.8.3.2 AMS in the autochthonous weathering-breccia

The partly developed transitional lithology indicates a change from $AMS_{granite}$ to $AMS_{breccia}$ showing low κ_{bulk}, low P’ and shallowly plunging κ_1, (Figure 4.15). The dashed lines in Figure 4.15 visualizes a gradually increasing (hypothetical) trend of weathering-brecciation. This trend may be developed in a transitional zone, which, however, is not observed in the drill core.

The weathering-breccia, as already stated, is deformed in two phases. S_2, documenting collapse by weathering-brecciation and diagenetic burial compaction (see chapter 4.7.3). The second overprint is the vertical early Caledonian cleavage, which produced S_{3a} and S_{3b} (see chapter 4.7.4). Burial compaction fabrics (diagenetic fabrics) in sediments are oblate, induced by sub-horizontal mineral SPO (Hrouda & Ježek 1999a), an observation that may be transferred to the weathering-breccia. Thus, in this zone, a horizontal oblate AMS subfabric paralleling the burial compaction cleavage S_2 can be assumed. However, a compaction AMS fabric, having presumable an oblate shape factor and horizontal foliation, is not preserved, because of the overprint by S_{3a} and S_{3b} cleavages. The magnetic foliation κ_3 of $AMS_{breccia}$ parallels roughly subvertical mica SPO/LPO parallel with S_{3a} or S_{3b} surfaces. This shows that the SPO/LPO of the phyllosilicates is the most important carrier of the magnetic anisotropy (e.g. Archanjo et al. 1995a, Archanjo et al. 1995b, Borradaile & Sarvas 1990, Tarling & Hrouda 1993).

Magnetic lineations are flat-lying in the weathering-breccia. Therefore, the vertical S_{3a}/S_{3b}-intersection lineation is apparently not important for defining the magnetic lineation of $AMS_{breccia}$. This can be explained by the scale of S_{3a}/S_{3b}-fabric, exceeding mostly specimen size, and hence providing either subfabric S_{3b} or S_{3a} as a carrier of anisotropy. The orientation of κ_1 is a result of the overprint of S_2 by S_3, which led to a composite AMS fabric with κ_1-axes clustering in the direction of the subfabrics intersection lineation (Figure 4.24.b). This intersection lineation is sub-horizontally oriented. As a result of the overprint, bulk anisotropy P’ decreased (c.f. Housen et al. 1993). A gradual decrease of the P’ to 1.01 and T towards 0 (Figure 4.15 and

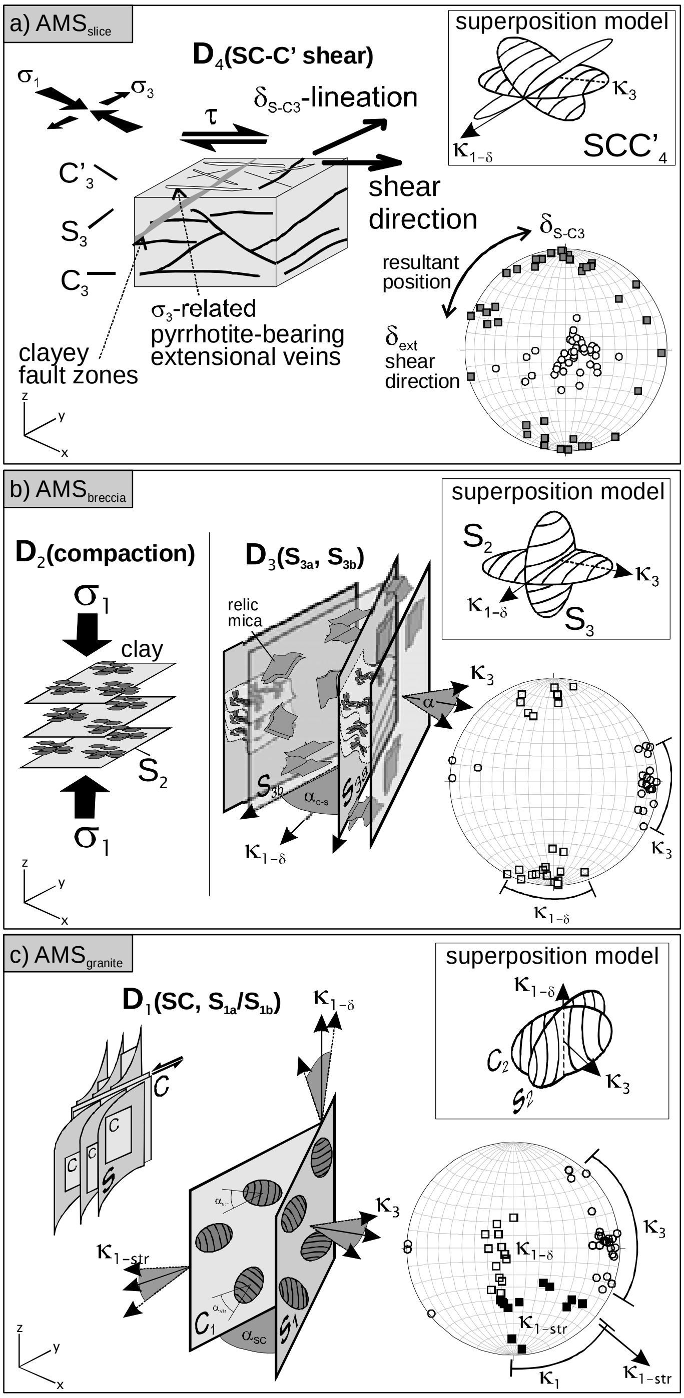

Figure 4.24: Sketches of deformation in the autochthonous basement section (b: weathering-breccia, c: granite) and allochthonous slice (a: cataclasite) and the corresponding AMS fabrics. Principal AMS axes κ_1 (squares) and κ_3 (circles) are shown in the stereonets.

Figure 4.16) indicates a gradual increase of the S_2 imprint with proximity to the unconformity. This is inferred, under the assumption that S_3 and related AMS subfabric stay constant within the brecciated zone, or decrease slightly in intensity with proximity to the unconformity. This assumption is confirmed by petrographic observation. In addition, the slight decrease of κ_{bulk} approaching the unconformity (Figure 4.15.a) effects P' negatively. As the petrographic indications do not show those trends of fabric intensity, AMS proofs to be a sensitive marker of petrofabric intesity.

In what extent the small amounts of magnetite remnants (observed in k(T) curves: Figure 4.7.b) contribute to the AMS is not quite clear and not examined by analytical methods. Supposedly, weathering-brecciation caused a statistical dissemination of relic magnetite grains in the matrix. These magnetite grains may have more or less isotropic shapes (similar to the magnetite remnants shown in Plate 4.3.c). Thus, their shape-anisotropy results in lowering of P'.

The paramagnetic AMS$_{breccia}$ shows a better-defined clustering of axes than the ferrimagnetic AMS$_{granite}$, although having much weaker ellipsoid definitions (expressed in low P' and scattering T). A high P' in the granite is an effect of the positive correlation of κ_{bulk} and P'. κ_1-axes are usually well clustered defining the intersection lineation of subfabrics; this is the case in AMS$_{breccia}$, whereas the irregular magnetite shapes in AMS$_{granite}$ do not produce such an intersection lineation. A well defined magnetic fabric is expected for a phyllosilicate matrix, such as in the weathering-breccia, because the "averaging out effect" (Hrouda & Ježek 1999b) is a typical feature at this high number of aligned grains contributing to the bulk AMS. This is observed typically in strained fine-grained sediments (e.g. Borradaile & Sarvas 1990, Debacker et al. 2004).

The AMS fabric in the weathering-breccia is highly comparable to the equivalent lithology in case study Hara. It is suggested that a common burial-compaction deformation of the palaeoweathered basement took place along the Caledonian margin in pre-Caledonian time.

4.8.3.3 AMS in the autochthonous cover

The vertical magnetic foliation in the cover conglomerate resembles the fabric of the rocks beneath the interface. κ_1, however, is medium steeply inclined, not resembling the sub-horizontal orientations of magnetic lineations in the basement. This is considered as a result of the different rock texture of the cover sediments and their deficiency in weathering.

The mechanical stability along the unconformity resulted in similar imprints of basement and cover and corresponding AMS fabrics adjacent to the unconformity.

4.8.3.4 AMS in the allochthonous cataclasite

The rocks in the lower allochthonous slice and the autochthonous weathering-breccia underwent a common pre-D_4 genesis, as discussed in chapter 4.7.7. D_4-cataclasis in the slice destroyed the affected the weathering-breccia texture and $AMS_{breccia}$.

In the pyrrhotite-free samples, paramagnetic chlorite/mica assemblage defines the petrographic cleavage and the flat-lying oblate AMS_{slice} is controlled by chlorite-mica SPO/LPO (Figure 4.17). Paramagnetic pyrite paralleling the petrographic surfaces may contribute to the AMS, as well. Pyrrhotite is the main magnetic carrier in most of the medium and intense cataclasites. Syn- to post-D_4 grown pyrrhotite crystals impregnate predominantly D_4-surfaces as individuals or elongated aggregates (Plate 4.4.a). The modal fraction of ferrimagnetic pyrrhotite controls the medium high κ_{bulk} (Figure 4.23) and the relatively high degree of anisotropy P' (up to 1.68), which is indicated by the correlation of κ_{bulk} and P' ($AMS_{slice\text{-}mc}$ and $AMS_{slice\text{-}ic}$ in Figure 4.17). Each ferrimagnetic pyrrhotite grain has a shape-anisotropy. Magnetic interaction in aggregates of pyrrhotite may induce a distribution-anisotropy. The aggregate shape will define the distribution-anisotropy (Archanjo et al. 1995, Cañon-Tapia 2001, Gaillot et al 2006, Grégoire et al. 1998, Hargraves et al. 1991). The strong pyrrhotite field dependence is not an important factor for defining the field dependence of anisotropy (P'_{Hd}) and axes orientation (see chapter 4.8.3.5).

Axes distribution is controlled by the intersection pattern of crenulated S_3 with cataclastic C_4 or SC_4 fabric and locally developed C'_4 (Figure 4.24.a). The progressive development of shear fabric with depth can be traced by the changes of κ_3-inclination: (1) in the weak cataclasis, κ_3 is subvertical and related to the dominant subhorizontal dominated planar fabric. (2) In the moderate cataclasis zone to the centre of the slice, preserved and asymmetrically crenulated S_3 surfaces between well developed C_4 shear surfaces causes a resultant magnetic foliation, which is slightly steeper (Figure 4.17). Higher scattering is due to large porphyroclastic pyrites. (3) With progressive shear in the intense cataclasis zone, C' are present producing an anastomising fabric with surfaces dipping in shear direction. This leads to horizontally oriented magnetic foliations; thus, the magnetic foliation is a resultant of magnetic subfabrics induced by S, C and C'.

The direction of κ_1, dominantly perpendicular to the dip direction of magnetic foliations, is caused by the intersection of the sub-fabrics C_3, S_3 and C'_3. Ideally, these planar fabrics intersect in one axis, the zone axis. Magnetic lineations of composite AMS fabrics positioned parallel with the intersection lineation of (oblate) planar sub-fabrics is a common feature (e.g. Borradaile & Tarling 1981, Debacker et al. 2004, Housen et al. 1993, Pares & van der Pluijm 2002a). The subordinate case of κ_1 positioned near the dip direction of the magnetic foliation is attributed to samples with an absence of planar cataclastic fabrics by a deficiency of matrix phyllosilicates (e.g. sample st-d). In these cataclasites, deformation is rather localized along discrete clay rich-fault zones. By the absence of phyllosilicates, cleavages surfaces are not prominent enough to influence the bulk AMS. Consequently, the resulting intersection lineation does not influence the magnetic lineation. κ_1 paralleling the dip direction of the magnetic foliation is most likely related to the pyrite-pyrrhotite-chalcopyrite formations along linear intersection segments of extensional fissures paralleling shear direction (Plate 4.4.b). The 10 to 20° deviation of κ_1-declination from the ideal simple shear (90° to SC-intersection) direction must be attributed to an interference with the sub-fabric caused by SC-C'-intersection.

4.8.3.5 Significance of AMS field dependency in the allochthonous slice

Two petrographic factors in the cataclastic lithology influence P': a) increase of the ferrimagnetic pyrrhotite-carried κ_{bulk} leads to an amplification of P' (Figure 4.14.b) and κ_{Hd} (enhanced by the pyrrhotite grain size), and b) the actual petrographic anisotropy. The magnetic anisotropy defined by the petrographic fabric anisotropy is superposed in high-κ_{Hd} samples by the magnetic anisotropy of pyrrhotite, but becomes more prominent by measurements in low A/m field, when the magnetic subfabric of pyrrhotite less intensely influence bulk AMS (Pokorny et al. 2004).

It is suggested that the petrographic fabric is better shown by the AMS, regarding P', in low field strengths of 30 A/m. The finding that AMS axes directions and shape factor T are not subject to profound changes are in accordance to the literature (e.g. Pokorny et al. 2004).

4.9 Conclusions

The autochthonous Revsund granite section together with the overlying lower allochthonous basement slice of the Långviken SGU 73007 drill core recorded a sequence of basement deformation and alteration:

(Stage 1) genesis of the magnetite-bearing granite and subsequent deformation in a transpressional regime under greenschist metamorphism generating porphyroclastic mylonites (S_{1a} and S_{1b} and mylonitic SC_1); (stage 2) a moderate subaerial chemical and moderate physical weathering-brecciation during Vendian (Cryogenian?) peneplanation forming an autochthonous weathering-breccia zone beneath; (stage 3) a compaction in the weathering-breccia with development of a unconformity-parallel planar fabrics, S_2, during burial stage; (stage 4) a first Caledonian deformation phase forming a pervasive vertical cleavage fabric (S_{3a} and S_{3b}) in the weathering-breccia, possibly induced by reactivating S_1 beneath; (stage 5) formation of the lower allochthonous slice by imbrication, producing a cataclasis zone with shear deformation and S_4-cleavage and SC-C'-fabric development under maximum very-low grade metamorphism; associated are inter-tectonic precipitation (between D_3 and D_4) of a large pyrite generation and a late to post deformational pyrrhotite-pyrite-chalcopyrite association, which overgrew the cataclastic texture.

The earliest deformation in the granite point to a relation to vertical transpressional shear zones, which are frequently described in the Svecofennian Domain (see Hara case study and Mattsson & Elming 2001). Palaeoweathering trend is despite very-low grade metamorphic overprint preserved in geochemical signatures of alkali and alkaline earth element oxides (well represented by alteration indices *CIW*, *PIA*). The rocks in the allochthonous slice (part of the Lower Allochthonous) are closely related to the autochthonous weathering-breccia, with respect to pre-deformational lithology, geochemistry and magnetic susceptibility.

A ferrimagnetic alteration sequence from primary magnetite to paramagnetic clay to pyrite and finally to ferrimagnetic pyrrhotite is evident. The Fe/S ratio (whole-rock geochemistry) and the relation of κ_{bulk} with Fe traces these iron phase transitions. The modifications are the important factor changing magnitudes of κ_{bulk} and P', petrographic fabric carries in all magnetic fabrics the intrinsic AMS shape factor and axes distribution. Composite magnetic fabrics are produced in the granite, weathering-breccia and basement slice cataclasite. Magnetic lineations are sensitive markers for these composite fabrics. In the granite and porphyroclastic mylonite, a change between vertical and horizontal κ_1 displays varying relative intensity of a horizontal simple shear direction and a vertical intersection lineation of the S_{1a}/S_{1b}-fabric. In the weathering-breccia, the subhorizontally oriented magnetic lineation is defined by the intersection of the flat-lying S_2, showing an increasing imprint strength with proximity to the unconformity, and the vertical S_3 foliation sets. Cataclasis in the lower allochthonous basement slice destroyed pre-existing magnetic fabrics and produced predominantly horizontal magnetic lineation defined by the superposition of AMS sub-fabrics of the SC-C'-

fabric.

The AMS fabric in the weathering-breccia is highly comparable to the equivalent lithology in case study Hara. A common pre-Caledonian compaction deformation of the palaeoweathered basement is suggested, occurring along the Caledonian margin. Unlike the Hara case, there are no indications of a mechanical decoupling along the autochthonous basement-cover-interface in the Långviken drill core. However, the existence of the lower allochthonous basement slice, exhibiting a floor thrust cutting through the weathering crust, indicates local rock failure within the weathering-breccia zone.

The field dependence κ_{Hd} (de Wall 2000b) of monoclinic (ferrimagnetic) pyrrhotite is evident and the grain size dependency of κ_{Hd} matches the EOR standard for analysed samples. A corrected field dependence parameter $\kappa_{Hd}corr$ is introduced, in order to overcome the influence of strong matrix susceptibility to investigate the mineralogy-controlled field dependence of ferrimagnetic pyrrhotite. $\kappa_{Hd}corr$ is considerably higher than κ_{Hd} for rocks characterized by a dominant influence of the paramagnetic matrix on κ_{bulk}, but negligible in clearly ferrimagnetic rocks (due to monoclinic pyrrhotite) ($\kappa_{bulk} > 2000 \cdot 10^{-6}$ SI).

Plate 4.1: (Textures in the Autochthon, plate on following page) a) AMS-cylinder of the unweathered granite displaying an SC-fabric (sample ST-11b, diameter 2.5 cm); **b)** texture of the foliated granite with preferred shape orientation of quartz and magnetite paralleling C-surface (ST-13, long side 4.85 mm); **c)** fine crystalline SC-mylonite, green colour due to chlorite (ST-11a, diameter 2.5 cm); **d)** texture of the SC-mylonite with magnetite porphyroclasts (ST-11a, 4.85 mm); **e)** AMS-cylinder of a quartzitic granite (ST-3, diameter 2.5 cm); **f)** AMS-cylinder of a weathering-breccia displaying weak S_2 (ST-5, diameter 2.5 cm); **g)** clay/sericite-rich texture of the weathering-breccia with seams of horizontal S_1 in the κ_3-section (ST-2, 4.85 mm); **h)** same weathering-breccia showing an SC-fabric of D_2 in the κ_2-section (ST-2, 4.85 mm)

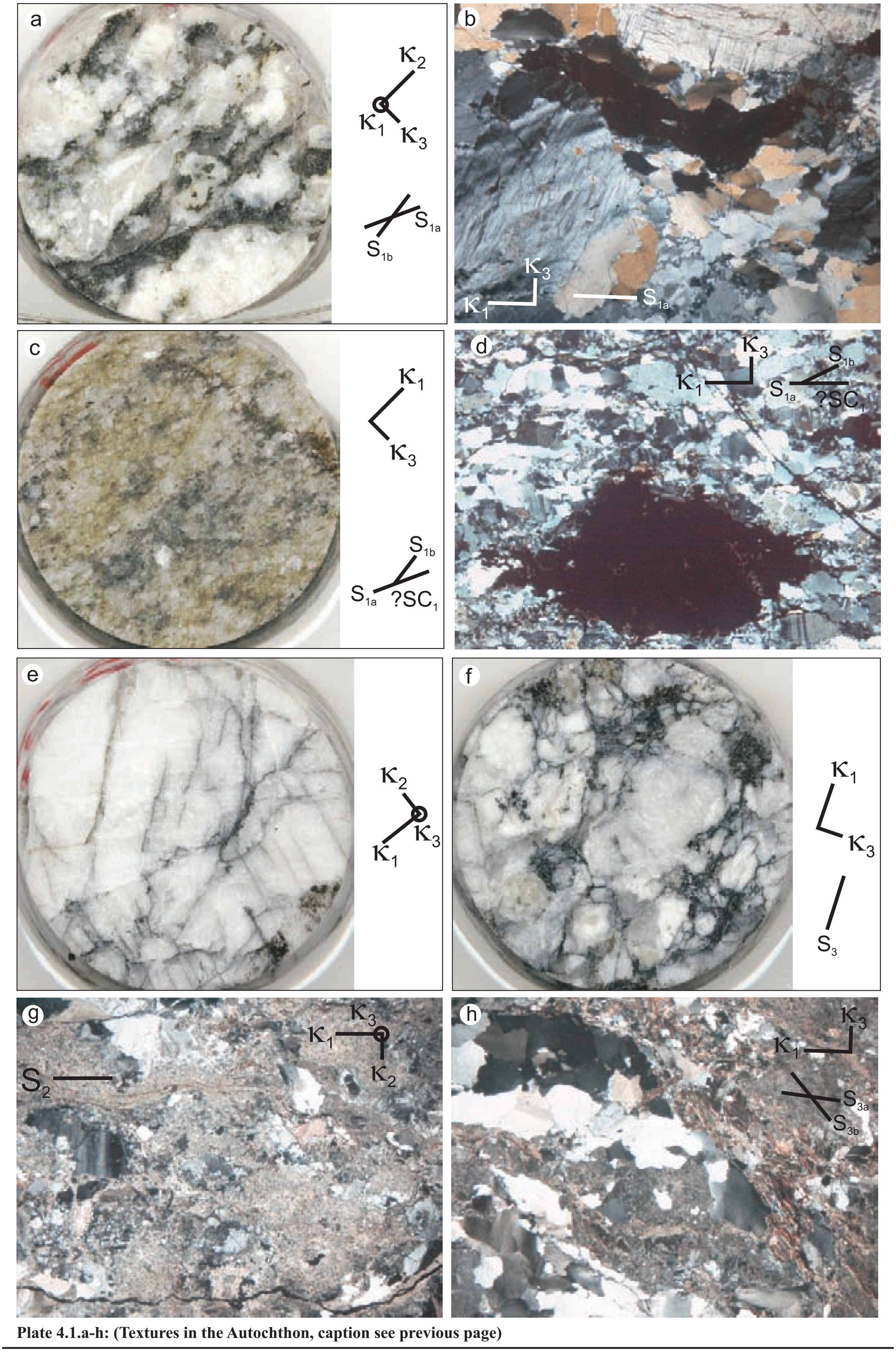

Plate 4.1.a-h: (Textures in the Autochthon, caption see previous page)

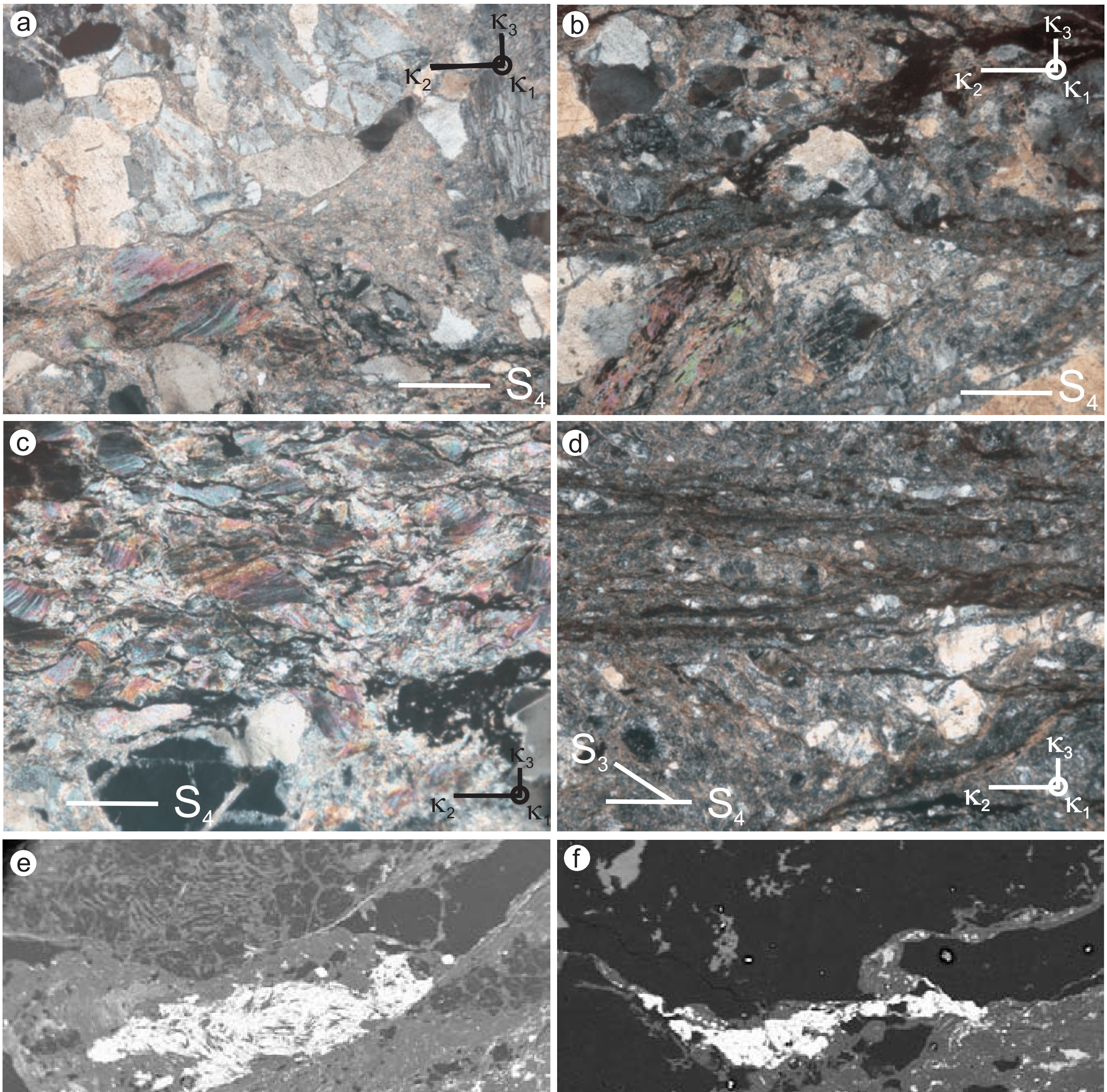

Plate 4.2: (Textures in the tectonic slice) a) weak cataclasis (sample st-a, long side 2.2 mm); **b)** moderate cataclasis with SC-fabric (st-e, 2.2 mm); **c)** moderate cataclasis with mica brecciation and crenulation (st-e, 2.2 mm); **d)** intense cataclasis with SC-C'-fabric (st-j, 2.2 mm) **e)** SEM-micrograph of a large pyrite in a crenulated S_3-surface in the moderate cataclasis zone (st-e); **f)** broken zircon in the moderate cataclasis zone (st-e, SEM).

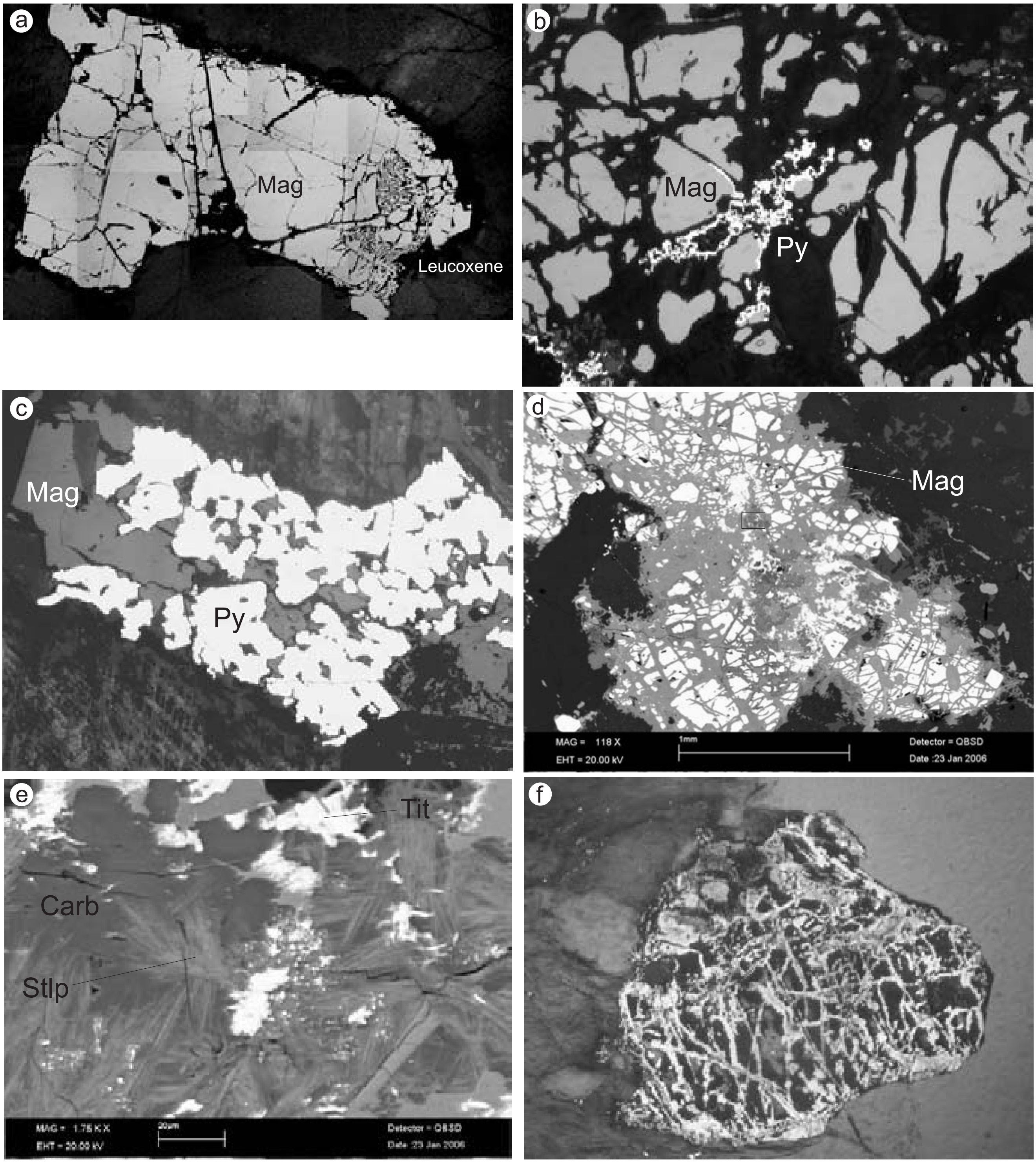

Plate 4.3: (Magnetite alteration in the Autochthon) a) fresh magnetite in the unweathered granite with local titaniferous phases (leucoxene: rutile, carbonate, titanite) (sample ST-13, long side is 1 mm); **b)** incipient stage of pyrite alteration (ST-13, 0.69 mm); **c)** pyrite pseudomorphism after magnetite (?) (ST-10, 0.69 mm); **d)** SEM-micrograph of chlorite, replacing magnetite along its crystallographic surfaces (ST-13); **e)** detail of d, displaying fibrous chlorite, stilpnomelane, carbonate and titanite as replacement of magnetite (ST-13); **f)** intensive magnetite alteration stage in the weathering breccia, with a chlorite-pyrite pseudomorphism after magnetite (ST-2, 0.69 mm)

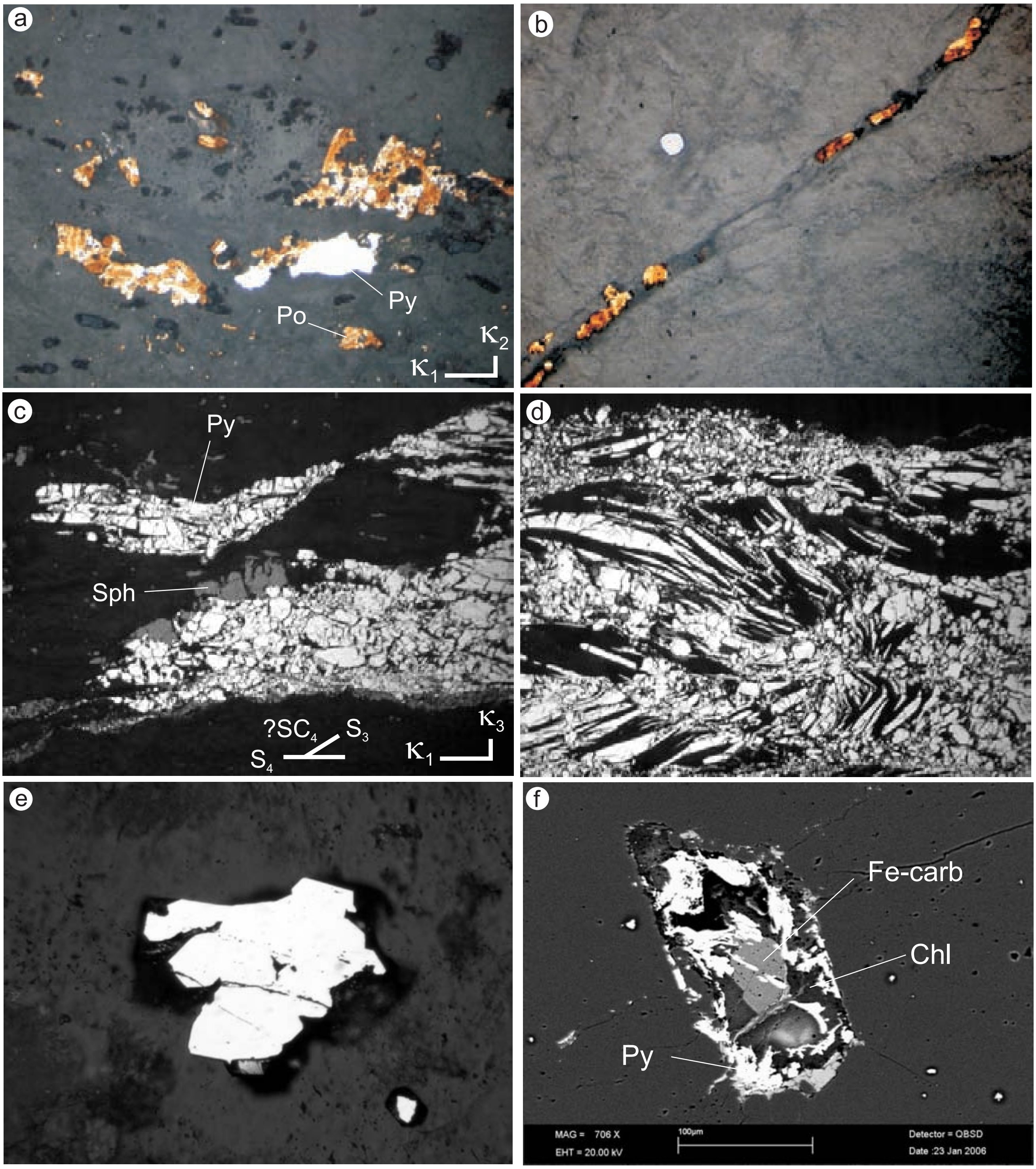

Plate 4.4. (Fe-sulphides) a) micrograph of secondary pyrrhotite-pyrite assemblage in the intense cataclasite of the allochthonous slice (sample st-j, long side 0.69 mm, reflected light and ferrofluid on pyrrhotite); **b)** pyrrhotite as filling of fissures in the cataclasite of the allochthonous slice, which are often oriented parallel with κ_1 (st-j, 0.69 mm, reflected light and ferrofluid); **c)** deformed large pyrite (with dark grey sphalerite, reflected light) in the SC-fabric of D_3, allochthonous slice (st-e, 0.69 mm, reflecting light); **d)** detail of large pyrite, demonstrating the late precipitation of pyrite mimicking crenulated mica (black), allochthonous slice (st-e, 0.69 mm, reflected light); **e)** secondary pyrite in autochthonous weathering-breccia (ST-2, 0.42 mm); **f)** SEM-micrograph showing a late alteration of secondary pyrite in the weathering-breccia (ST-2).

5 CASE STUDY NARCEA ANTIFORM, SPAIN

Moderate weathering in a deformed sedimentary basement (Cantabrian Mountains, North Spain)

5.1 Introduction

The tectonometamorphic evolution of rocks adjacent to a basement-cover interface is studied in this case with particular consideration of the structural reactivation of the interface during orogenic deformation. The geological setting is the Narcea Antiform (NA) in the Cantabrian Zone (CZ) of the Cantabrian Mountains in North Spain. Here, a folded Neoproterozoic sedimentary basement (Mora Formation) is unconformably overlain by Cambrian sediments (Herrería Fm.).

Eight outcrops along the unconformity are chosen displaying a broad variety of alteration and deformation spatially related to the unconformity. The effects of Neoproterozoic-Cambrian palaeoweathering, Palaeozoic hydrothermal alteration and metamorphism as well as pre-existing structures and Variscan deformation on rocks and unconformity are studied. The understanding of the basement-cover relation between Mora Fm. and Herrería Fm. is considered crucial for solving the complicated evolution of the NA and the entire CZ.

Measuring of structures and sampling of sections across the unconformities is carried out in order to investigate gradients of metamorphism, alteration and deformation. The analytical study comprises XRD, whole-rock geochemistry, magnetic susceptibility and microprobe analyses. The sampled rocks (shales, siltstones, greywackes, sublitharenites and conglomerate) are cleaved and show very low grade metamorphism.

5.1.1 Regional setting

The Narcea Antiform (NA) is located in the northern Iberian Variscan Orogen as a prominent arcuate structure in the inner part of the Iberian-Armorican arc. In the NA, parts of the Variscan foreland-hinterland transition are exposed (Julivert 1971, Perez-Estaún 1991). The foreland, to the east, is the Cantabrian Zone (CZ: Lotze et al. 1945), consisting mostly of non metamorphic Cambrian to Lower Carboniferous successions, which are deformed in a thin-skinned tectonic style fold and thrust belt (Julivert 1971). The Westasturian-Leonese Zone (WALZ), which is part of the hinterland, is located to the west and comprises low-grade metamorphic lower Palaeozoic sequences. The rocks in the Narcea Antiform are combined to the Narcea group, first described by Lotze (1956) as Narcea Schists; the stratigraphic term Mora Formation (Fm.) by Comte (1959) will be used in the present study.

Three units are distinguished in the Mora Fm. (Pérez-Estaún 1973, Pérez-Estaún & Martinez 1978). The lower (Tineo group) comprises sandstones and shales with interbedded porphyritic rhyodacites and acidic volcanoclastics. The intermediate group consists of turbiditic greywackes, siltstones and shales and the upper group is composed of shales with interbedded sandstones. Reconstructing a complete stratigraphic column of the Mora Fm. seems to be impossible due to its monotonous lithology deficient in stratigraphic markers and due to the complex deformation by Variscan thrust tectonics.

The Mora Fm. represents the basement of the Palaeozoic successions, which begin with the Cambrian Herrería / Cándana Fm. (Cándana Fm. is the stratigraphic WALZ equivalent of the CZ’s Herrería Fm.). A crystalline basement below the NA is indicated by the deep crustal seismic profile ESCICANTABRICA-1.2 (Gutiérrez-Alonso 1995, Pérez-Estaún 1994), but does not crop out anywhere.

A lower Cambrian age of the Herrería Fm. was confirmed by acritarch, trilobite and archaeocyathan faunas (Palacios & Vidal 1992, Vidal et al. 1994). This is the minimum age for the erosion of the basement.

The Neoproterozoic rocks in the Narcea Antiform are among the oldest in the NW Iberian Peninsula. However, an exact sedimentation age has not been determined yet. Authigenic zircons of the Pola de Allende

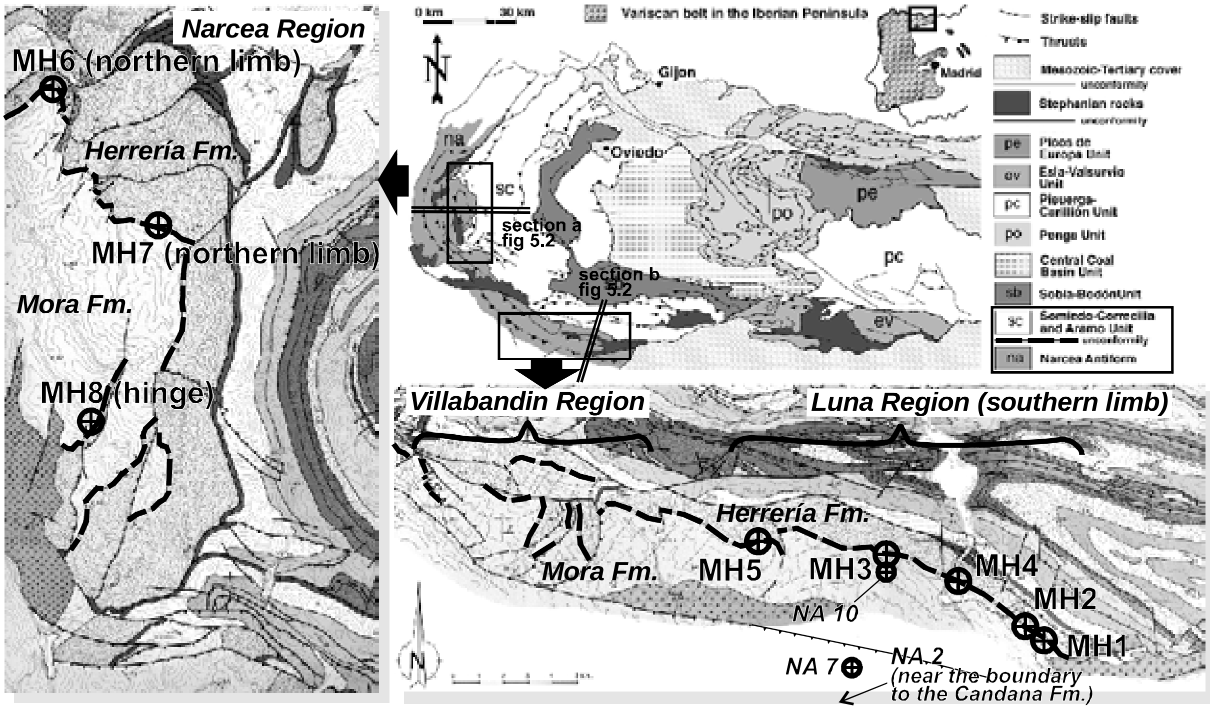

Figure 5.1: Overview of the regional geology of the northern rim of Narcea Antiform. The angular unconformity (dashed line) divides the Neoproterozoic Mora Fm. from the basis of the Palaeozoic Herrería Fm. Three regions Narcea, Villabandin and Luna region are indicated (see text). The outcrop localities are marked. (Compiled and modified after Pérez-Estaún 1994 and Grimmer 2000).

Granitoid, which intruded into the Tineo group at the western most part of the NA, give an intrusion/cooling age of 580 ± 15 Ma (Fernández-Suárez 1998). Slightly younger are intercalated rhyolites (zircon ages 559 ± 3 Ma: Gutiérrez-Alonso et al. 2004b). Sm/Nd crustal residence ages (Nägler et al. 1995) and ^{40}Ar/^{39}Ar dating of detrital muscovites (Gutiérrez-Alonso et al. 2005) showed that the Neoproterozoic Mora Fm. has a higher input of juvenile crust than the Cambrian Herrería sediments, which shows detrital ages as high as late Palaeoproterozoic.

Numerous studies exist on the overall structure of the NA. The studies concentrate on the three different geographical parts of the Antiform (Figure 5.1): the *Narcea region* (in the Region of Asturias) is situated north of the Stephanian Villablino Coal Basin (Aller 1987, de Sitter 1962, Diaz Garcia 2006, Julivert & Martínez-García 1967, Keller & Krumm 1992, Keller & Krumm 1993, Pérez-Estaún 1973), the *Villabandin Region* (Region Leon) is the complex thrust domain southwest of the Villablino Coal Basin (Aller 1987, Pérez-Estaún 1971) and the *Luna region* (Region Leon) reaches the eastern rim of the Antiform, which is defined by Cretaceous cover sediments (Aller 1987, de Sitter 1962, Diaz Garcia 2006, Julivert & Martínez-García 1967, Keller & Krumm 1992, Keller & Krumm 1993, Pérez-Estaún 1973). In the present study, outcrops in the Narcea and the Luna region are investigated.

Variscan deformation led to an antiformal stacking of the Mora Fm. (Figure 5.2). Major Variscan structures in the Antiform, *La Espina thrust* in the Narcea region and the *Cornombre-La Urz thrust* in Villabandin and Luna region, define the tectonic boundary between the CZ and WALZ (Gutiérrez-Alonso 1992, Marcos 1973, Perez-Estaún 1991, Pérez-Estaún 1994). The most recent study of Diaz Garcia (2006) suggested the existence and regional importance of large scale Cadomian structures for the Luna region.

The term tectonic window is applicable for the whole CZ part of the Mora Fm. (Gutiérrez-Alonso 1996). In the Narcea region its western, northern and southern boundary is defined by the La Espina thrust. The eastern rim is located along the structurally reactivated angular unconformity between Mora Fm. and Herrería Fm. In the Villabandin and Luna regions the southern rim is the Cornombre-La Urz thrust, and on their western and

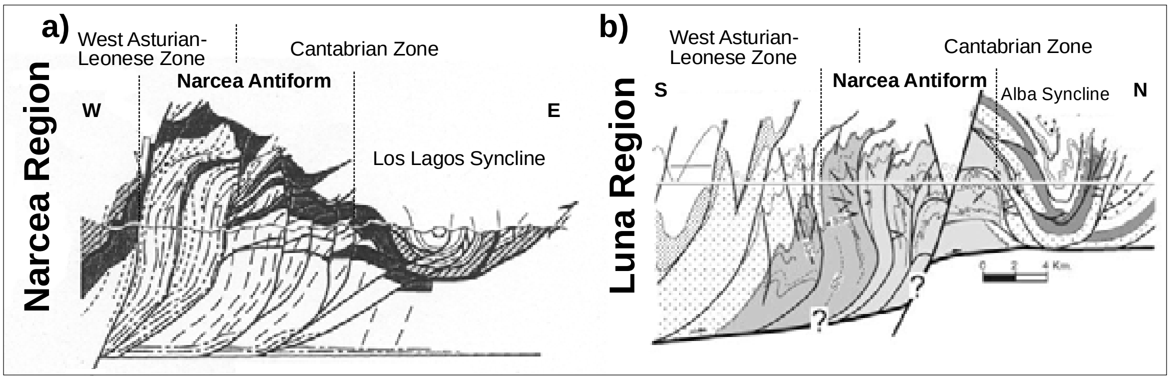

Figure 5.2: Schematic sections across the Narcea Antiform in the Narcea and the Luna regions, respectively. The location is indicated in Figure 5.1. (modified after Gutiérrez-Alonso 1996 and Díaz García 2006)

eastern sides the rocks are covered with post-Variscan sediments. The angular unconformity between Mora Fm. and Herrería Fm. defines the northern limit (see below).

A metamorphic gradient can be traced across the NA, beginning with early anchimetamorphic conditions (Aller 1987, Gutierrez-Alonso & Nieto 1996) in the eastern area (CZ), and increasing to greenschist facies (chlorite zone) in the western area (WALZ) (Marcos 1973, Pérez-Estaún & Bastida 1990). According to these authors the maximum metamorphism has Variscan age. Van den Bosch (1969a) proposed a major Precambrian metamorphic event in the Mora Fm., which is supported by Keller & Krumm (1992) and Keller & Krumm (1993), who suggested a metamorphic hiatus by illite crystallinity between Mora and Herrería Fm. Díaz García (2006) pointed out that Cadomian structures developed under greenschist-facies biotite and chlorite zones.

The genesis of the arcuate structure of the central Iberian-Armorican arc is still in debate. The concept of an orocline, resulting in bending of a linear orogenic belt, is favoured by most authors (Gutiérrez-Alonso et al. 2004b). Principally, there is an agreement about a late to post Variscan origin of the final curvature, since several palaeomagnetic studies indicated Permian rotation at least in upper crust around subvertical axes in NW Spain (e.g. Hirt et al. 1992, Pares et al. 1994, van der Voo et al. 1997, van der Voo et al. 2000, Weil et al. 2000a, 2001, Weil et al. 2000b). A pre-existing curvature of the orogen, e.g. due to indentation of irregular convergent plate boundaries, prior to a late-orogenic tightening, is also proposed (Hirt et al. 1992, Julivert 1971, Perez-Estaún 1988). Recently, a unifying theory was introduced (Gutiérrez-Alonso et al. 2004b), explaining late Variscan oroclinal bending of a linear Variscan Orogen in combination with crustal thinning in the outer part (WALZ) and thickening in the inner part (CZ), having the NA in between, in a so-called neutral zone. A late to post-Variscan change of compressional regime from E-W to N-S (present day direction) is considered to be the driving force for rotational kinematics (van der Voo et al. 2000).

The unconformity between the Neoproterozoic Mora Fm. and the lower Cambrian Herrería Fm. follows the arcuate-shaped eastern rim of the NA for about 100 km. Since first descriptions of this contact in the Narcea region by Lotze (1956) and in the Luna region by de Sitter (1962), a controversial discussion is ongoing concerning its nature and regional significance for the NA and the CZ. Lotze (1956) inferred an erosional contact, taking the angular unconformity as evidence. He explained the discordant contact as a result of Cadomian folding of the Mora Fm. Based on similar lithological facies, a concordant succession of Mora and Herrería Fm., which was subsequently tectonically reactivated, was suggested by Llopis Lladó & Martínez Álvarez (1961) and Llopis Lladó & Torre (1961).

(van den Bosch 1969b) first described a purple-red alteration zone in the uppermost part of the Mora Fm., down to ca. 20 m below the contact. It is interpreted since then as a Neoproterozoic-Cambrian subaerial palaeoweathering horizon. This ubiquitous haematite oxidation zone parallels the unconformity and crosscuts the Mora Fm. bedding in most outcrops (latest review by Gutiérrez-Alonso et al. 2004a).

Since Llopis Lladó & Martínez Álvarez (1961) and Llopis Lladó & Torre (1961), it is manifested that brittle reactivation of at least parts of the Mora-Herrería interface occurred. Gutiérrez Alonso (1996) proclaimed this unconformity as a regional detachment surface. According to that author, the unconformity is the upper decollement surface of an early Variscan “slip transfer zone”, a laterally shortened structural body (the Mora Fm.) between the crustal root zone (the crystalline basement) and the hanging-wall Palaeozoic successions of the CZ (the Herrería Fm.). The Herrería Fm. was subject of layer-parallel shortening and cleavage development as a reaction to the lateral compression of the Mora Fm. The more prominent basal thrust horizon of the Variscan thin-skinned tectonics is located stratigraphically higher in the Lower to Middle Cambrian Láncara Fm. (Julivert 1971).

5.1.2 Sampling and applied methods

Eight field outcrops are chosen, in which the unconformity is exposed. Five outcrops in the Luna region and three in the Narcea region are studied (Figure 5.1). From each outcrop, oriented samples are taken in profiles from the basal cover beds across the unconformity 10 to 20 metres down into the basement, locally down to 70 m depending on outcrop scale. The sampling interval increases approximately logarithmically with distance from the unconformity. The following methods are used: thin section petrography employing optical microscopy and backscattering SEM in combination with EDX analyses, XRD on whole-rock and oriented preparation of the clay fraction (< 2µm), whole-rock geochemistry employing ICP-MS and ICP-ES.

Outcrops in the Luna region:

MH 1 (Julivert & Martínez García 1967) is a long road cut between km 75 and 76 of CL 626 (federal road) – *La Magdalena* to *Los Barrios de Luna*, just south of the bridge across the *Río Portilla*. (Mapa Topográfico Nacional 1:50 000, no. 129-I, *Carrocera*)

MH 2 (Julivert & Martínez García 1967) is located 1 km north of MH 1 following the CL 626 (between km 74 and 75). The unconformity is exposed close to the bridge to *La Vega de Los Caballeros*. (Mapa Topográfico Nacional 1:50 000, no. 129-I, *Carrocera*)

MH 3 (Julivert & Martínez García 1967) is ca. 300 m S of the cemetrey of *Irede de Luna*, a village 3 km W of *Los Barrios de Luna*. The unconformity is exposed in the river valley (Plate 5.1.c). (Mapa Topográfico Nacional 1:50 000, no. 102-IV, *Los Barrios de Luna*)

MH 4 is located, as MH 1 and MH 2, at the CL 626 (*La Magdalena* to *Los Barrios de Luna*), 2 km S of *Los Barrios de Luna* (between km 69 and 70). (Mapa Topográfico Nacional 1:50 000, no. 128-II, *Riello*)

MH 5 is 2 km NE of *Curueña*, along a pathway at the north flank of the small river that flows into the *Arroyo de Río major*. (Mapa Topográfico Nacional 1:50 000, no. 102-IV, *Los Barrios de Luna*)

Outcrops in the Narcea region:

MH 6 is located along the national road AS-15 (Cornellana-Degaña), 500 m N de *Villar de Lantero*. This outcrop is well known as the type locality of the Mora-Herrería unconformity in Asturias (de Sitter, 1962; Lotze, 1956; Gutiérrez-Alonso, 1992; Gutierrez, 2003; Gutiérrez-Alonso, 2004). (Mapa topográfico nacional 1:50 000, no. 51-I, *Soto de la Barca*)

MH 7 is a road cut along the road from *Mieldes* to *Tabladiello*, 200 m north of the cemetary of *Mieldes*. (Mapa Topográfico Nacional 1:50 000, no. 51-III, *Tebongo*)

MH 8 is a road cut at the road from *Onón* to *Parada la Vieja*, 1 km east of *Cerezaliz*. (Mapa Topográfico Nacional 1:50 000, no. 76-I, *Carballo*)

5.2 Description of lithologies

5.2.1 Mora Formation

The Mora Fm. appears as a monotonous sequence of alternating greywacke and siltstone or shale. It is a typical turbiditic sequence (Pérez-Estaún 1973, Pérez-Estaún & Martinez 1978). The lateral continuity of the sediment layers is usually good. They are 0.1 to 0.5 metre thick, whereas locally coarse-grained beds reach thicknesses of 1.5 metres. Sedimentary structures are well preserved. Graded bedding is often observable, as well as crossbedding, longitudinal ripples, flute and load casts.

The siliciclastics can be classified as shales, siltstones, arenites and microconglomerates (detrital grain size 2 to 5 mm). The relative amount of quartz, feldspar and lithic components is determined by mineral counting in thin section, which allows a grouping after Folk (1980) (Figure 5.3). The detritus in the greywackes and microconglomerates is poorly sorted, quartz grains show angular shapes. In many cases, the detrital grain shapes are masked because of pressure solution. Quartz single grains and quartzitic polycrystalline grains (recrystallized and microcrystalline aggregates) are dominating the clastic composition. Lithic materials are mostly clayey aggregates or microcrystalline symplectites. Feldspar content is low, in fine-grained rocks not exceeding accessory quantities, in coarse-grained lithologies up to 5 %, occasionally exceeding 10 %. Rounded twinned (albite law) Na-plagioclase dominates the feldspar spectrum. The content of phyllosilicate clasts is generally low. White micas dominate and biotites and detrital chlorite are accessory components. The low feldspar and detrital mica content is to some extent a result of secondary alteration and/or mechanical destruction. Accessory detrital materials are biotite, zircon, tourmaline (not zoned), carbonates and opaque phases, such as Fe-oxides.

The lithologies of the Mora Fm. are of the same kind in the Narcea and the Leon region. A coarse-grained litharenite of the Mora Fm. is observed in outcrop MH 8 of the Narcea region.

The classification after Herron (1988), employing whole-rock geochemical data (Figure 5.4), roughly reflects the lithological classes (*sensu* Folk 1974). The data from the shale and siltstone samples plot partly into the Fe-sandstone and (grey-)wacke area. This might be a result of the weathering (see chapter 5.7.2). The greywacke samples plot well into the corresponding class (*wacke*). The intermediate to low SiO_2/Al_2O_3 of the fine and medium-grained Mora sediments (shale, siltstone and greywackes) indicates a relatively high maturity.

5.2.2 Herrería Formation

The lowermost 10 m of the Herrería Fm. stratigraphic column are studied. The bedding always parallels the unconformity surface. Herrería Fm. bedding orientations vary between outcrops. The stratigraphic differences are significant between Narcea and Luna region.

5.2.2.1 Luna region

The basal beds are either a coarse-grained quartzitic (micro-) conglomerate or a sublitharenite (Figure 5.3). Beds of the lithic sublitharenite have thicknesses of 0.5 up to 2.5 metres and are hard and massive (Plate 5.1.c). The lower bedding surface defining the unconformity to the Mora Fm. is coated with a thin layer of clay material. In outcrop MH 4, the two or three lowermost cm are brecciated. Sericite and clay phases are the constituents of the weakly defined matrix of the sublitharenite. The cement is SiO_2, partially sericitic + clayey, or made of secondary Fe-hydroxides (Plate 5.2.a,b). An ill-sorted grain spectrum of single crystalline and polycrystalline quartz dominates over other lithic components, which comprise clayey concretions, greywackes and volcanic clasts. Feldspars are only accessory phases. The quartz grains are elongated (up to 2:1) by pressure solution processes, often planar to weakly lobate grain boundaries are observed (Plate 5.1.e). In some sublitharenites, a bedding parallel shear zone shows intense quartz elongation and recrystallization

(Plate 5.1.f-h). Quartz grains are very rich in fluid inclusions. This causes the white rock colour. The sublitharenites are spotted with reddish brown haematite and iron hydroxide dots. These are, together with rutile, replacement products of altered detrital iron oxides. The quartzitic conglomerate of MH 2 shows a partial impregnation of interparticle space with iron hydroxide.

With its high quartz content, the sublitharenite is either a terrigenous sediment with high maturity, or a relic sediment. The clayey lithic components and greywacke fragments may well be relics of the eroded Mora Fm.

A few shale beds intercalated in the sublitharenite are present in outcrops MH 1. In the easternmost outcrops (MH 1, MH 2, MH 4) a thick sequence (between 10 and 15 m) of fine layered green siltstone follows above the basal sublitharenite. Some thin beds (ca. 0.3 m) of sublitharenite are intercalated. This siltstone is very poor in detrital grains, such as quartz. Detrital white micas are moderately abundant (up to 10 vol%). They were subject of partial or entire cataclasis and alteration to form fine grain mica (sericite). Biotites are rarely observed.

A type of interlaminated dark green siltstone and light green greywacke occurs in all sections. It becomes dominant above the basal sublitharenite in the outcrops further to the West (MH 3, MH 5). The anastomising layering has a spacing of 1 mm to 1 cm. It does not show graded bedding. Internal quartz detritus are mostly single crystalline grains, which usually do not show intracrystalline deformation.

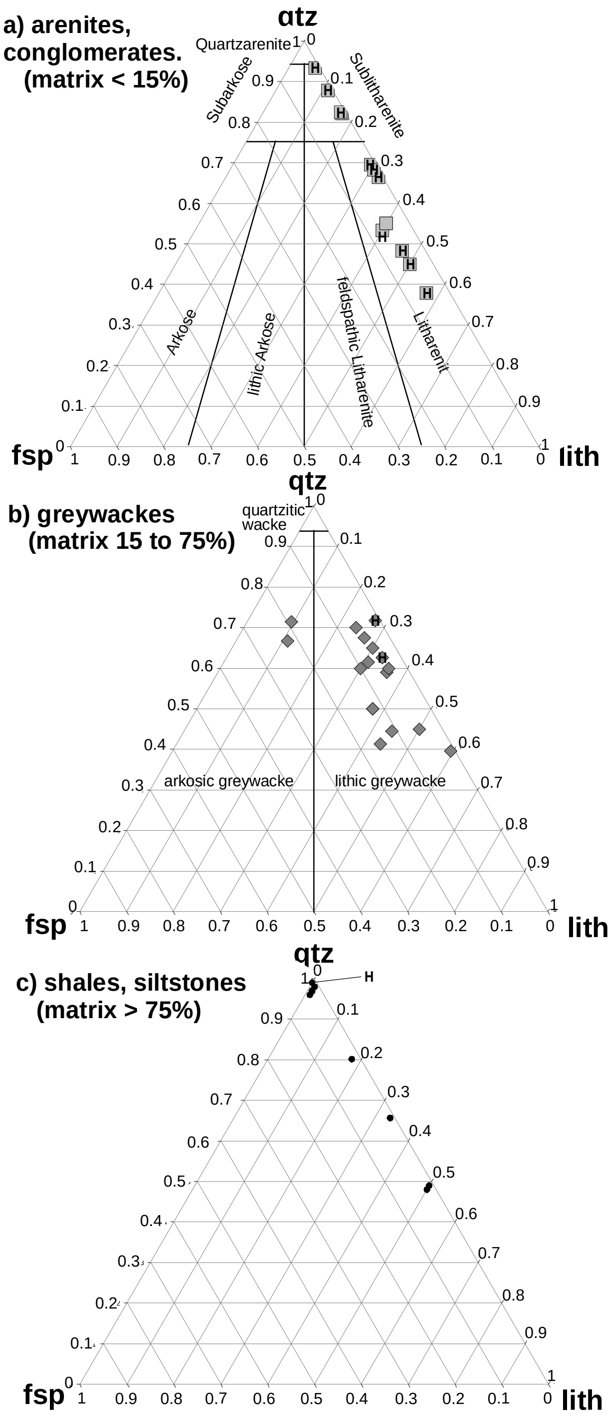

Figure 5.3: Lithological classification of the siliciclastic samples of the Mora Fm. and Herrería Fm (H) after Folk (1974).

5.2.2.2 Narcea Region

An alternating sequence of thick-bedded sericitic sandstone and green siltstones is observed in outcrop MH 6 from the Herrería-Fm. basis upwards. Although the clayey to sericitic matrix reaches 35 vol%, the lithology is often hard, due to the quartzitic cement component. Fe-Mg-carbonates are important constituents of a bedding-parallel shear zone in sample MH 6-2, occurring as lenses and precipitations in pressure shadows of brecciated quartz (Plate 5.1.h). With microprobe analyses, the carbonates can geochemically be characterized as $(Mg,Ca)CO_3$ and $FeCO_3$ (see Appendix I.c).

The basal part of the Herrería Fm. in outcrops MH 7 and MH 8 consists of ca. 20 cm thick beds of brownish red coarse-grained litharenites. In MH 8 after 0.5 m a green sublitharenite-siltstone sequence follows and in MH 7 a tens of metres thick litharenite-conglomerate sequence follows. Detrital components, up to dm-sizes, are frequently red, well rounded siliciclastics, quartzites and volcanic rocks. The conglomerate is a mixture of the reworked sedimentary (Mora Fm.) basement with (Neoproterozoic) volcanic material.

The siltstones of the Narcea region are similar to those in Leon.

After Herron (1988), the sampled Herrería Fm. samples are (sub-) litharenites, which fits well to the petrographical classification according to Folk (1974). The SiO_2/Al_2O_3 values are higher than the finer-grained Mora rocks. This is due to the small fraction of Al-rich clay-matrix and high quartz content.

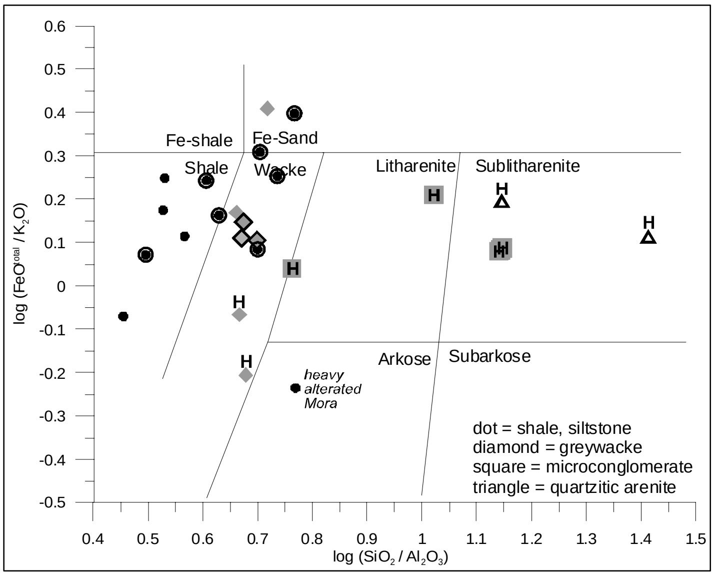

Figure 5.4: The grouping of rock samples (Mora Fm. and Herrería Fm. (H)) after Herron (1988) employing whole-rock geochemical data. Lithologies are grouped after Folk (1974). Differences between Herron and Folk classification are due to alteration (weathering) and metamorphism. Data points with dark boundaries are samples rich in haematite.

5.3 Description of structures

The sequence and nomenclature of the structures in the outcrops follows as far as possible the regional literature (Diaz Garcia 2006, Gutiérrez-Alonso 1992, 1996, Julivert & Martínez-García 1967, Pérez-Estaún & Martinez 1978).

5.3.1 Folding of Mora Fm. - B_{1M}

The earliest folding event B_{1M} (M means Mora Fm., H means Herrería) took place before the Neoproterozoic-Cambrian erosion of the Mora Fm. and the sedimentation of the Herrería Fm. B_{1M} is manifested in the changing angle between Mora Fm. strata and the unconformity (e.g. Lotze 1956, Pérez-Estaún & Martinez 1978). The unconformity surface and the Herrería Fm. strata in the *Luna* region dip steeply to the SSW (MH 1, MH 4, Figure 5.5.a,d). Beds have a vertical orientation or are overturned (MH 2, Figure 5.5.b). Beds change to a moderately steep NNE dipping with upright position in the more western outcrops (MH 3 and 5, Figure 5.5.c,e).

In MH 1, the orientation of Mora Fm. beds are folded by B_{3M} (see chapter 5.3.5). They had presumably a subhorizontal orientation before B_{3M}, thus approximately perpendicular to Herrería Fm. beds. Angles between Mora Fm. beds and the unconformity are 60°-70° in MH 2 and MH 5. Angles are gentle (10-20°) in outcrops MH 3 and MH 4. In the *Narcea* region, the Herrería Fm. bedding surfaces dip steeply to the NE or more gently to the NNE (outcrop MH 6, Figure 5.5.f). A dip to the N is observed in MH 7 (Figure 5.5.g). In MH 8 (Figure 5.5.h), the orientation of bedding surfaces of the hanging wall Herrería Fm. and footwall Mora Fm. are subparallel, dipping SSE. The interface between both formations is a para-unconformity. The dip direction of the Mora Fm. beds is moderately steep or steep SE to E in outcrop MH 6. Bedding surfaces in MH 7 dip steeply to the ENE and moderately steep to the N.

5.3.2 Bedding-parallel cleavage - S_{1M}

A cleavage (S_{1M}) is apparent in all Mora Fm. rocks, approximately bedding-parallel. It is considered as the earliest tectonic foliation in the rocks of the NA. This weak rough cleavage is more often observed in the greywackes than in the siltstones. The cleavage is defined by short, thin and discontinuous pressure solution seams, which are defined by passively enriched mica and heavy minerals (zircon, rutile, tourmaline, limonite

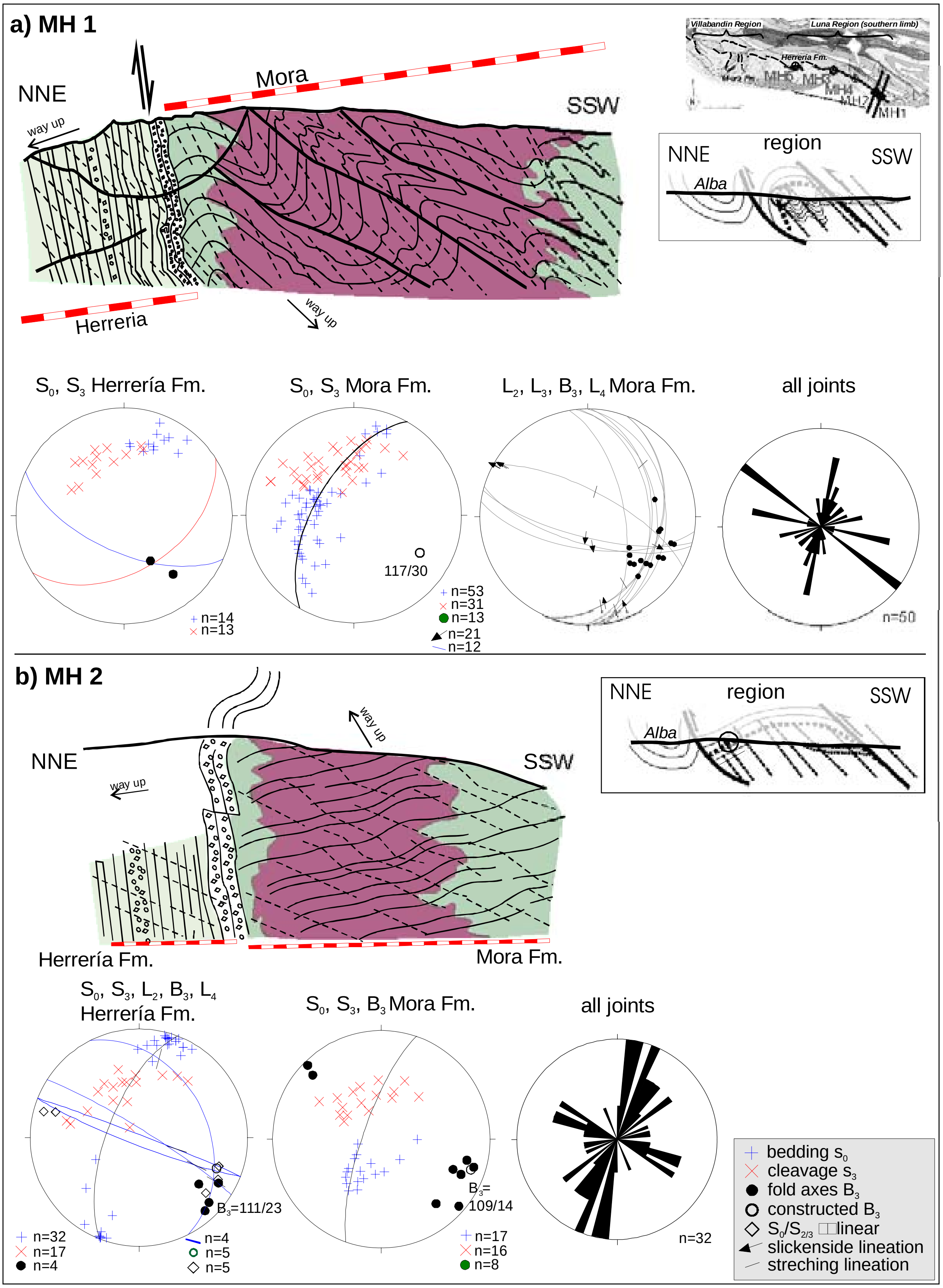

Figure 5.5.a-b: Field structures from outcrops in the Luna Region. Shown are the outcrop locations in map and in section. Stereoplots are equal area projections of the lower hemisphere.

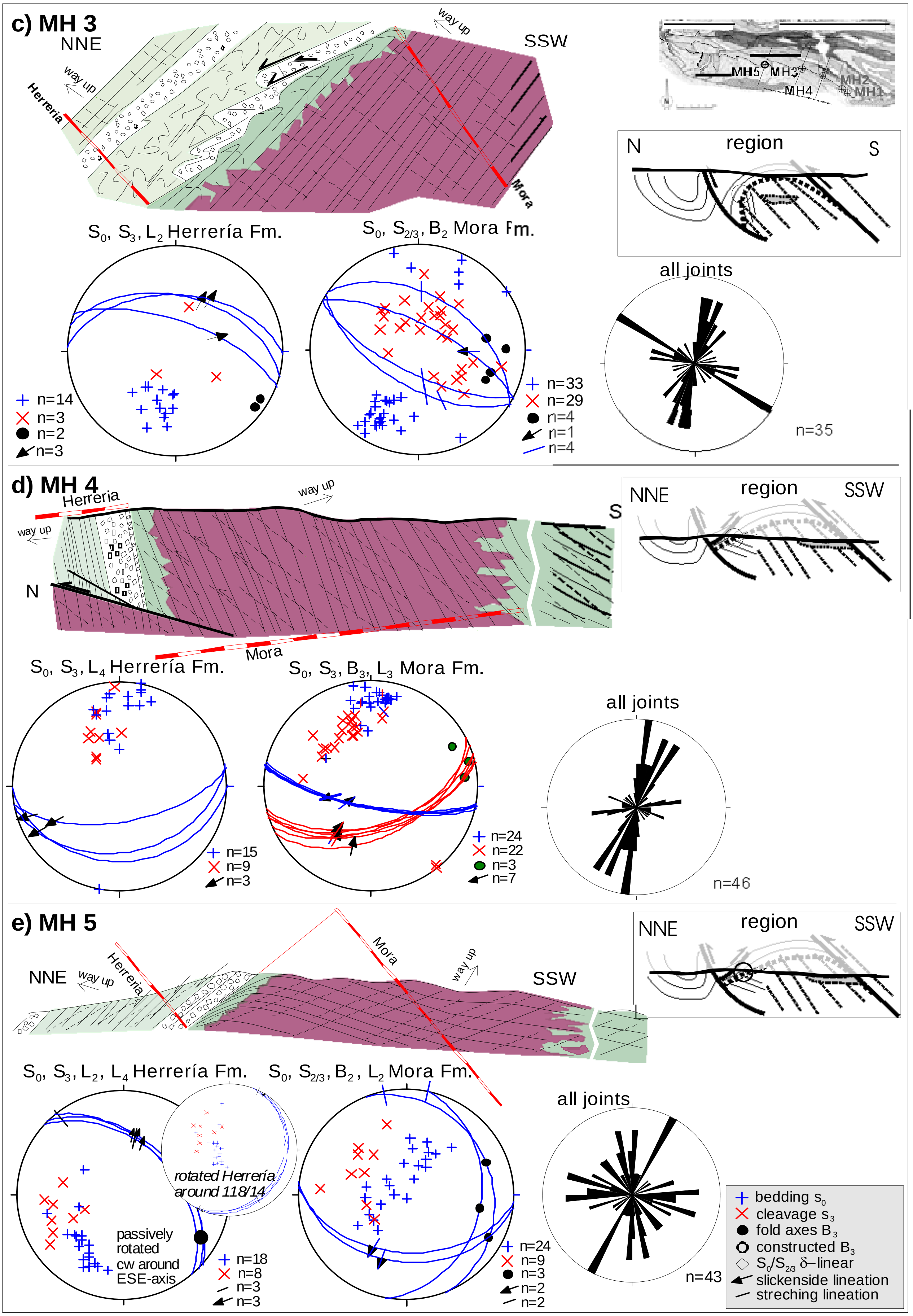

Figure 5.5.c-e: see a-b

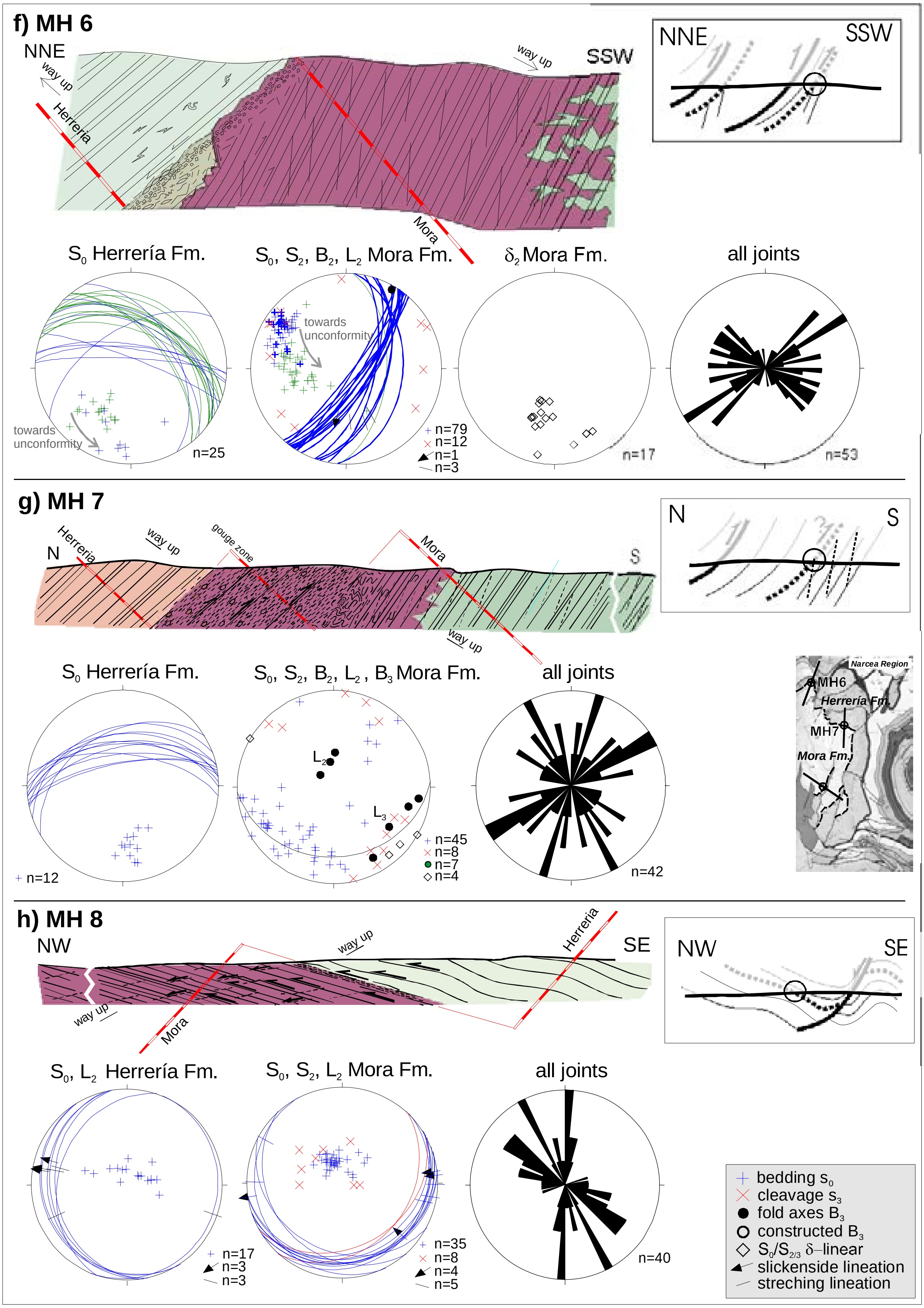

Figure 5.5.f-h: Outcrops in the Narcea Region

and opaque phases) due to the dissolution of quartz and feldspar. Cleavage seams generated strain caps around detrital quartz and feldspar grains. In some cases, quartz grains show a lateral fibrous intergrowth with mica grains parallel with the cleavage domains (mica beards; Plate 5.3.c). Clayey matrix-dominated shales and siltstones rarely show pressure solution seams. In these lithologies, the important mechanism of foliation development is the rotational alignment of elongated detrital micas into the bedding surface.

Locally, early bedding-perpendicular quartz veins are crenulated between S_{1M} (Plate 5.3.b).

5.3.3 Isoclinal folding of the Mora Fm. bedding - B_{2M}

The subhorizontal Mora Fm. beds are inverted between outcrops MH 1 and MH 2 (Luna region). This is an indicator for tight (isoclinal) folding of Mora Fm. beds. Consequently, fold axes are supposedly subhorizontal in the Luna region. B_{2M} axes are not identified in the outcrops of the Luna region. This assumed isoclinal folding is referred to as B_{2M} and has possibly the same orientation of B_{1M}.

Bedding-parallel slip is the dominant folding mechanism in the Mora Fm. producing L_2 slickenside and stretching lineations in slip direction (perpendicular to the B-axes). Lineation involves quartz and phyllosilicate deformation and precipitation.

B_{2M}-axes are subvertical and perpendicular to Herrería Fm. beds in the Narcea region, as observed in outcrops MH 6 and MH 7 and in the internal NA (Gutiérrez-Alonso 1992, 1996). Prior to tilting of the Herrería Fm. in the Luna region (see below), B_{2M} may have had a vertical orientation, resembling the B_{2M} orientation in the Narcea region.

5.3.4 Cleavage in Mora and Herrería Fm. - S_2

The tight B_{2M} folding of the Mora Fm. produced an axial surface-parallel cleavage S_{2M}. S_{2M} is defined by two conjugated surfaces, S_{2a} and S_{2b}; each set has an angle of ca. 20° to the bedding surface (Plate 5.3.c and Figure 5.16). Theses low angles with the bedding indicate a main compression direction perpendicular to bedding surfaces. Locally, only one set of S_{2M} is developed (Plate 5.2.e and Plate 5.3.e). This cleavage generation is defined by white mica and chlorite. Development of S_{2M} depends on the lithology: the cleavage rarely develops in coarse-grained siliciclastic rocks but is often recognized in greywackes and siltstones. S_{2M} is non-pervasively developed in the Mora rocks near the unconformity, but pervasively in the interior parts of the NA.

Cleavage development in the Herrería Fm. of the Luna region is restricted to a narrow zone of a few decametres from the unconformity (c.f. Aller et al. 1987). Both single set and conjugate sets of mica cleavages are developed in the Herrería Fm. rocks, similar to the Mora Fm. (Plate 5.3.c,d).

All Herrería Fm. sublitharenites near the unconformity display a distinct bedding-parallel preferred orientation of slightly elongated quartz grains. Locally, grains are elongated up to 5:1 (relation long to short axis). Mechanisms of defining quartz SPO are mainly pressure solution transfer and extensional cracking (Plate 5.1.e). An oblate strain ellipsoid with short axis (z) at high angle to the bedding surface is shown by strain estimation with perpendicular thin sections results. This indicates a high angle to the bedding orientation of the main compression direction. A coaxial compression in the lower Herrería Fm. rocks is indicated.

5.3.5 Subhorizontal folding in the Mora Fm. (Luna region) - B_{3M}

A set of second order B_{3M} folds affecting the Mora Fm. sequence is the dominant structure in outcrop MH 1 (Plate 5.1.b). Very gentle folds with minor amplitudes (buckling) can be observed also in MH 2. These secondary B_3 folds are absent in the more western outcrops of the Luna region and in the Narcea region. B_{3M} fold wavelengths reach a few metres in MH 1. Fold-axes are gently ESE plunging. The fold type is monoclinic and asymmetrical. The vergence is NNE-directed with an angle of ca. 30°; steep limbs are locally overturned. Class 1B (*parallel*) folds are dominating in greywackes and class 1C or class 2 (*similar*) in siltstone. A prominent spaced fracture cleavage (S_{3M}) is developed with the folds.

5.3.6 Fracture cleavage in Mora and Herrería Fm. (Luna region) - S_3

S_{3H} and S_{3M} are developed in the Luna region, but not in the Narcea region. S_{3M} is a fold axis-parallel cleavage in B_{3M}-affected parts of the Mora Fm. In the less deformed parts, S_{3M} is a pencil cleavage with similar orientation. Siltstones preferentially break along S_{3M} cleavage surfaces.

S_{3M} continues in the fine-grained Herrería Fm. rocks (S_{3H}) with the same orientation (red crosses in stereoplots of Figure 5.5.a-e). This may indicate a simultaneous deformation in both formations. A direct transition of S_{3M} to S_{3H} is, however, not observed, since the basal Herrería Fm. sublitharenites and conglomerates are not affected by S_{3H}.

S_3 dips moderately towards ESE to SE, hence parallel in both Herrería and Mora Fm. A deviation of S_{3H} (ENE dipping) was observed only in outcrop MH 5 (Figure 5.5.e). In this outcrop, the cleavages in Herrería and Mora Fm. are distributed on one great circle, indicating a rotation of beds around a steeply plunging axis subsequent to S_3 development.

Intersection lineations δ_3 on bedding surfaces defined by S_3 are abundant. δ_{3M} has the same horizontal orientation as B_{3M}, demonstrating the genetic association of monoclinic folding and cleavage. Stretching and slickenside lineations L_{3M} are developed on bedding surfaces and indicate flexural-slip deformation. They can be distinguished from the deformed L_2 by their distribution on the π-circle of B_3 and not on a small circle (Figure 5.15).

S_3 surfaces are reactivated as reverse faults near the unconformity, showing displacements of a few centimetres (Plate 5.3.h). This reactivation of S_3 surfaces is a ubiquitous feature in the outcrops of the Luna region. An L_{3M} lineation on S_3 surfaces is observed in outcrop MH 4 (Figure 5.5.d).

5.3.7 Vertical folding - B_4

In outcrops MH 6 and MH 7, the bedding poles of both Mora and Herrería Fm. girdle along a common flat-lying great circle. This implies folding around steeply plunging axes.

In the outcrops of the Luna region, Mora and Herrería Fm. bedding poles girdle on a common great circle, as well. Here, the fold axis is subhorizontally oriented, thus not related to the vertical axis of the Narcea region. Subhorizontal stretching lineations and slickensides on surfaces of the basal sublitharenites (L_4) are observed in outcrops MH 1, MH 2 and MH 5. L_4 may have been produced by flexural slip with strike-slip kinematics during vertical folding.

5.3.8 Deformation at the unconformity in the Luna region

The unconformity itself is a discrete and typically planar surface in the Luna region. In outcrop MH 2, it is slightly buckled at the metre scale around a B-axis, which is parallel with the unconformity strike (ca. WNW-ESE) (Figure 5.5.b).

Mora Fm. rocks directly below the interface (down to half a metre) in MH 3 and 5 are deformed. Both bedding and S_{2M} surfaces are folded around gently WSW to SW plunging B_{3M} axes, paralleling the Herrería Fm. strike (Figure 5.5.c, e). Such an unconformity-related modification of the bedding orientation is not observed in MH 1 and MH 4, but intra-foliation folding is evident (Plate 5.3.g).

The lowermost centimetres of the Herrería Fm. sublitharenites are locally brecciated, either showing a clayey (MH 2, 3) or quartzitic cement (MH 4). Scarce decimetre-scale ptygmatic folds B_{2H} involving entire beds of the sublitharenite are developed in MH 1 and MH 3. Long fold limbs are subparallel with the bedding surfaces and axes are parallel with the unconformity strike.

In MH 1, the NNE block, i.e. the Herrería Fm., is internally sheared showing a reverse fault kinematic (S_{0H}-

bedding-parallel slip). Due to the slightly overturned unconformity, shear kinematics appear as normal.

Reverse faults with thin clayey gouge zones and brittle reactivation of S_{3M} as reverse slip surfaces are observed in MH 4. There are several indications for slip along bedding surfaces in the lowermost Herrería Fm. Chlorite, illite and quartz slickensides and stretching lineations on bedding surfaces of the sublitharenite are present. Occasionally, deformation is concentrated in cm-thin clay horizons with cataclastically deformed quartz clasts.

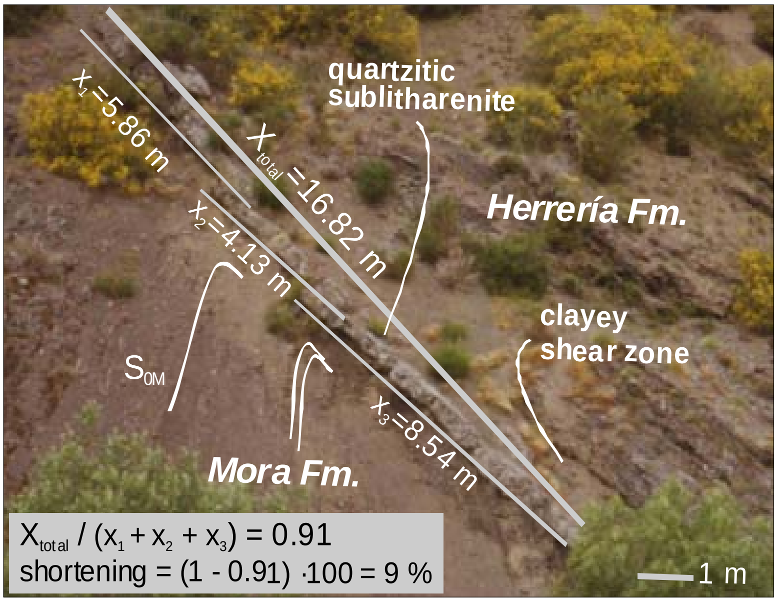

Figure 5.6: Outcrop MH 3. The basal quartzitic sublitharenite is bedding-parallel shortened by imbrication. Estimated shortening is 9 %, which is a minimum value, since internal shortening and small scale folding are not taken into account.

The sublitharenite beds in outcrop MH 3 are deformed in an imbricate fan Figure 5.5.c). A 9 % layer-parallel shortening is estimated from the deformation of the sublitharenite (Figure 5.6). The inferred layer-parallel shortening is a minimum estimation, since it does not take small scale folding and internal deformation (Plate 5.1.c,f,h) into account. A shear zone of 70 centimetres thickness is developed in siltstone layers directly above the sublitharenite. Sedimentary fabrics are mostly destroyed here; locally, remnants of bedding are bent into newly developed shear surfaces, slightly steeper than the unconformity surface. These shear surfaces show stretching and slickenside lineations pointing to a NE to NNE shear direction. In MH 3 and MH 5, the NNE (Herrería Fm.) block is sheared downwards. The imbricate fan in MH 3 is clearly a compressional feature, thus, the imbrication of the sublitharenite took place before the tilting of the unconformity (B_{3H}), and consequently indicates top-N shear. The same sequence of deformations can be suggested for MH 5. The folded cleavage S_{2M} in the flexure-zone of the uppermost Mora Fm. is therefore older. The shear zone in the siltstone beds above the imbricate fan possibly occurred during or after imbrication. Both deformations have the same N-directed shear sense and might be the result of a progressive deformation sequence.

5.3.9 *Deformation at the unconformity in the Narcea region*

In MH 6, the uppermost two metres of the consolidated Mora Fm. rocks are sheared and buckled. The original sedimentary structures are destroyed and the zone is lithified by clayey cement. Large dispersed asymmetric facoids in the sheared matrix beneath the interface are shear-sense indicators, displaying a top to the N normal faulting. Small intra-foliated quartz veins are ptygmatically and isoclinally folded in the quartzitic sandstones. The limbs are subparallel with bedding surfaces suggesting a relation to bedding parallel simple shear deformation. Bedding parallel shear zones along bedding surfaces are abundant. Quartz veins and quartz detritus are incorporated into the shear zones and are elongated and dynamically recrystallized (Plate 5.1.f,h).

The unconformity is not preserved in MH 7, but tectonically replaced by a thick gouge zone (see below). The Mora Fm. beds beneath that gouge zone are affected by internal ptygmatic and isoclinal folding, as in the Luna area. Fold axes B_{2M} plunge gently towards ESE to SE and display an N-S to NE-SW direction of movement. B_{2M} folds can be observed down to eight metres beneath the gouge zone. Slip along bedding surfaces is indicated in the basement by chlorite and quartz lineations. These deformations indicate an unconformity-related shear deformation, which occurred prior to the development of the gouge zone, as the gouge zone capped the folded zone.

The unconformity in outcrop MH 8 is interpreted as a para-unconformity located in an antiformal stack in the centre of the NA (Figure 5.2.a). Bedding-parallel slip occurred here in both Herrería and Mora Fm., but a distinct reactivation of the unconformity is not evident (Figure 5.5.h). The shear sense is top to WNW and WSW.

Zones of brittle grain size reduction just beneath the lowermost Herrería Fm. rocks are observed only in the Narcea region. Cataclasis affected mostly the Mora Fm. rocks, crosscutting bedding and internal deformation features. The cataclasis zone in outcrop MH 6 is thin (two decimetres) (Figure 5.5.f). It shows just beneath the basal Herrería Fm. beds a zone of imbricate sandstone facoids, each approximately one decimetre long (Plate 5.1.a).

The 8 m thick gouge and cataclasis zone in MH 7 overprinted the erosional interface between the Mora and Herrería Fm. Cataclastic relics of Herrería Fm. conglomerates, as well as purple Mora Fm. greywackes are present within the gouge zone. The gouge zone boundary to the hanging wall rocks is relatively discrete and dips moderately steep towards N. The orientation of the shear zone boundary and the Herrería Fm. beds are parallel. A repetition of one discrete (a few centimetres thin) purple horizon parallel with the boundary is observed (Figure 5.5.g). This indicates a doubling or tripling of the whole zone, likely due to compressional imbrication. The purple horizons in the gouge zone are not overprinted by later deformation.

5.4 Characterization of the weathering profile in the Mora Formation

5.4.1 Petrography

The alteration of the rocks beneath the unconformity are similar in all studied outcrops. The colour of rocks in the Mora Fm. is usually green (lower green zone). A purple red colour dominates in the upper ca. 16 m beneath the unconformity (red zone). Rock colour turns green again in the uppermost one or two metres beneath the unconformity (upper green zone). There is a transition zone of a few metres between red and lower green zone showing decolourization from red to green preferentially along bedding, cleavage and joint surfaces (Plate 5.2.c). The colour in the transitional stage depends also on lithology: coarse-grained rocks tend to have green colour more frequently than fine-grained rocks. The lower transition zone in outcrop MH 6 extends to a thickness of ca. 10 m. The weathering zones, being parallel with the unconformity, crosscuts in most outcrops the Mora Fm. bedding beneath the unconformity.

The red colour is a result of a high haematite content. Microcrystalline haematite occurs as coatings around grains (Plate 5.4). Haematite occupies the space of quartz and phyllosilicates, which are subject to dissolution. A progressive haematite precipitation, either contemporaneous or subsequent to the disintegration of clasts is inferred. Haematite precipitation associated with chlorite weathering is described in the literature (Ji et al. 2002). Typically, haematite accumulates in zones, which are parallel with rock foliations, i.e. bedding and cleavage surfaces (Plate 5.4.f). These affected cleavage surfaces may be younger than the weathering stage (S_2, S_3) (see chapter 5.3.4). Thus, Fe remobilization occurred. The green alteration horizon just beneath the unconformity and mm-thick green zones along the joint network in the purple-red weathering profile indicate Fe-dissolution processes (Plate 5.2.c,d). This is discussed in detail in chapter 5.7.4.

The Herrería rocks are not affected by secondary haematite precipitation.

5.4.2 XRD

XRD analyses of the whole-rock and the clay fraction (< 2µm) show that the rocks of the Mora Fm. are similar throughout the examined outcrops. The spectra do not show evidences pointing to significant

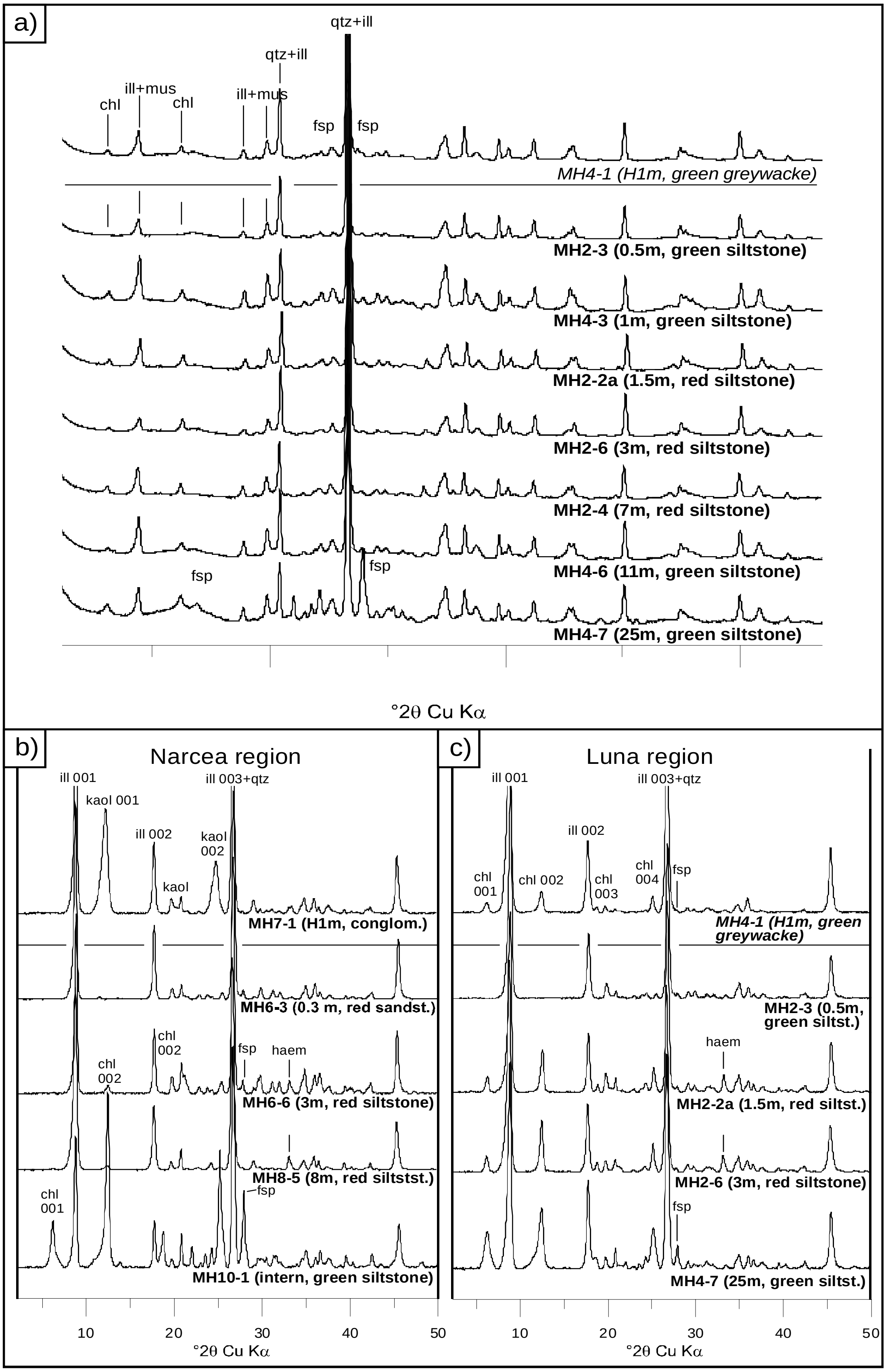

Figure 5.7: a) XRD spectra of whole-rock showing changes in mineralogy in the Luna region; b+c) XRD spectra of clay fractions (< 2 μm) showing the changes within the weathering profiles in the Narcea and the Luna region, respectively. Profiles are compiled from different outcrops.

differences in the mineralogy between Narcea and Luna region. It can be stated that the principal mineralogical characteristics of the weathering crust are similar at the regional scale. Combined profiles of fine-grained samples of the Luna region (whole-rock and clay fraction) and the Narcea region (clay fraction) are shown in Figure 5.7.a-c.

The major minerals are quartz, muscovite and illite. Illite in the clay fraction is dominantly well crystallized (*sensu* Meunier & Velde 2004), shown by relatively sharp and symmetric 10 Å peaks (Figure 5.7.b,c). Chlorite in the clay fraction is a Fe-dominated Fe-Mg-chamosite, indicated by the dominant 002 peak relative to 001 and 003 peaks (Moore & Reynolds 1997). Changes of the illite crystal maturity are traceable throughout the weathering profile by the FWHM (Figure 5.8.j). Illite 001 peak FWHM ranges between 0.34 and 0.38° °2θ in the lower green zone beneath the weathering profile. A general peak broadening to 0.42 °2θ is evident in the red zone. In the upper green horizon, a reversed trend is displayed. Here, FWHM of the 10 Å peak narrows to values below 0.34 °2θ.

Chlorite is the major matrix constituents, together with white mica, within and beneath the red zone and in the internal part of the NA (sample MH 10-1), but it is absent in the upper green horizon (see sample MH 6-3, MH 2-3).

The feldspar content (microcline and albite) is of considerable amount only beneath the red zone, away from the unconformity (see sample MH 4-7, MH 10-1). The primary feldspar content variations due to the lithology differences (0 to 2 vol% in fine-grained siliciclastics) are evident but do not mask the general decrease of feldspar.

The whole rock spectra of the Herrería Fm. rocks do not show significant differences to the Mora Fm. rocks. The clay fraction spectra partly reveal chlorite or, as in sample MH 7-1 (Figure 5.7.b), kaolinite, which is represented by the strong 7 Å peak, while 14 Å peak (chlorite 001) is missing.

5.4.3 Whole-rock geochemistry

As it is indicated by XRD, also the geochemistry show relative similar trends of element oxides through out outcrops. Therefore, combined trends, compiled from different outcrops, are shown.

The element oxides SiO_2, Al_2O_3 and TiO_2 remain stable through the profile (Figure 5.8.a-c). The lithological variations and the regional selection of samples cause a relative high scattering of data and the subsequent Palaeozoic alterations (see below and chapter 5.6) may have reset the weathering trends.

Fe_2O_3 (total iron, Fe^{II} + Fe^{III}) shows an increasing trend from 4 to 9 wt% from lower green throughout the red zone. It decreases again in the upper green horizon (Figure 5.8.d).

Na_2O shows an unconformity-related depletion trend (Figure 5.8.e). Beginning from a content of 2-3 wt% in the unweathered zone, Na_2O concentration decreases to almost complete absence (< 0.1 wt%) near the unconformity.

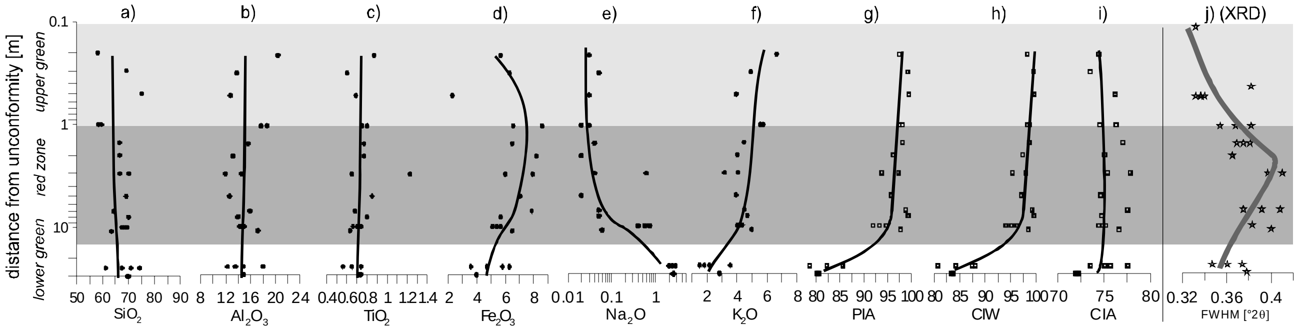

Figure 5.8: Whole-rock geochemistry (ICP-MS) and FWHM (XRD) data (compiled from different outcrops). a-c) selected elements oxides showing stable trends during weathering; d-f) elements oxides, which are subject to change during weathering; g-h) geochemical alteration indices *PIA* (Fedo et al. 1995), *CIW* (Harnois 1988) and *CIA* (Nesbitt & Young 1982); j) FWHM of illite 10 Å peak.

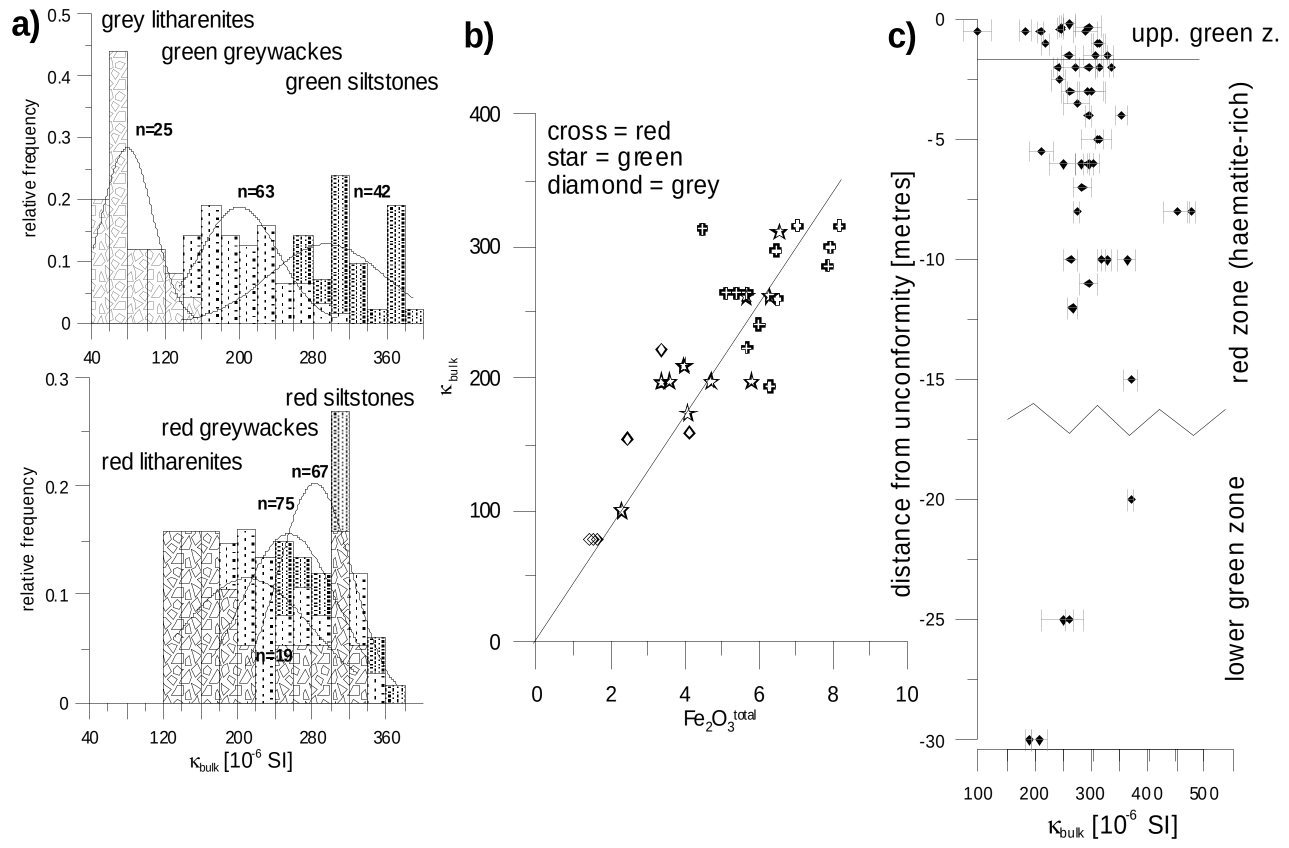

Figure 5.9: Dependence of κ_{bulk} on a) lithology and b) Fe_2O_3-content; c) shows the distribution of κ_{bulk} through the weathering profile (compiled from all outcrops).

K_2O shows an inverse trend relative to Na_2O: it increases from 2 in the lower part up to 6 wt% just beneath the unconformity (Figure 5.8.f).

The predominantly intermediate Fe_2O_3/K_2O ratios in the Mora Fm. samples (Herron plot: Figure 5.4) are defined by (1) high iron content (haematization) and (2) the high white micas to chlorite ratio.

Selected chemical alteration indices display an alteration, predominantly affecting alkali and alkaline earth elements (Figure 5.8.g-i). *PIA* (Fedo et al. 1995) and *CIW* (Harnois 1988) (equation 11 and 12 in chapter 1.2.1) show good approximations of weathering. Potassium increases in the profile due to an alteration event, possibly event not related to weathering. In *CIA* (Nesbitt & Young 1982; equation 10 in chapter 1.2.1), all alkali elements, including K, are treated equivalent and therefore the result does not provide useful information.

5.4.4 Bulk susceptibility κ_{bulk}

A further characterization of lithology and alterations in the weathering profile is possible with bulk susceptibility. κ_{bulk} is generally low in the rocks reaching values of maximum $500 \cdot 10^{-6}$ SI. Highest κ_{bulk} is shown in siltstones (mostly Mora Fm.) (average of $300 \cdot 10^{-6}$ SI), lowest in grey litharenites of the Herrería Fm. (average of $80 \cdot 10^{-6}$ SI), values of greywackes (mostly Mora Fm.) and red (micro-) conglomerates (mostly Herrería Fm.) ranges in between (Figure 5.9.a). There is a dependence on the haematite content in the greywackes: red coloured greywackes show with $280 \cdot 10^{-6}$ SI a higher average than green coloured ($200 \cdot 10^{-6}$ SI). This dependence, however, is not indicated by the finer-grained lithology (siltstones).

The κ_{bulk} vs. Fe_2O_3 diagram displays a good positive correlation (Figure 5.9.b). This points to paramagnetic (mostly chlorite, illite) and antiferromagnetic (haematite) magnetic minerals, as there is no significant deviation from the trend indicated, due to ferrimagnetic minerals (magnetite). The diagram also shows that red haematite-bearing rocks are most Fe-enriched, as already indicated in Figure 5.8.d, and grey litharenites of the Herrería Fm. least Fe-enriched.

The κ_{bulk} vs. depth diagram (Figure 5.9.c) weakly shows the relation of κ_{bulk} to haematite-richness within the weathering profile. In the red zone from 2 to ca. 16 m below the unconformity, κ_{bulk} is slightly higher than in both upper and lower green zone due to haematite richness. The scattering is due to different lithologies.

5.5 Illite- and chlorite crystallinity (IC, ChC)

5.5.1 IC and ChC section across the NA in the Luna region

By means of XRD, the illite and chlorite crystallinity (IC and ChC, respectively) in the clay fraction (< 2 μm) are estimated. The Kübler indices of fine-grained samples along a profile across the NA in the Luna region are shown in Figure 5.10. The section comprises samples from (a) the Herrería Fm., (b) the Mora Fm. of the weathering profile, (c) the Mora Fm. of the internal CZ and (d) the WALZ part of the NA. The IC of Herrería and Mora Fm. in the Cantabrian zone (CZ) indicate late diagenetic to anchimetamorphic conditions ($0.36 \leq IC \leq 0.48$). In the weathering profile, the IC display a trend of increase with distance from the unconformity: near the unconformity, in the upper green horizon IC is slightly below 0.42. In the red altered zone IC-values of 0.48 are reached. With further distance (beneath the weathering zone and in the internal part of the NA) IC are again below 0.42. In sample NA 2 (phyllite), taken from the southern limb of the NA (WALZ), IC of 0.25 indicates temperature of the incipient greenschist facies. σ lies between 0.00 and 0.02, an error of ±8 % must be considered for each sample.

Chlorite appears to have similar crystallinity values (ChC < 0.42) as illite in the internal part of the Mora and in the WALZ (samples NA7, NA2). In the weathering profile (red and upper green horizons), ChC values are between 0.37 and 0.42, showing as well anchimetamorphism. An increasing trend is not evident in ChC, unlike IC, indicating separate growth behaviour of chlorite and illite in the weathering zone.

5.5.2 XRD-spectra and IC of the clayey gouge zone in outcrop MH 7

The XRD (clay fraction) of three samples from the ca. 8 metes thick clayey gouge zone in outcrop MH 7 are

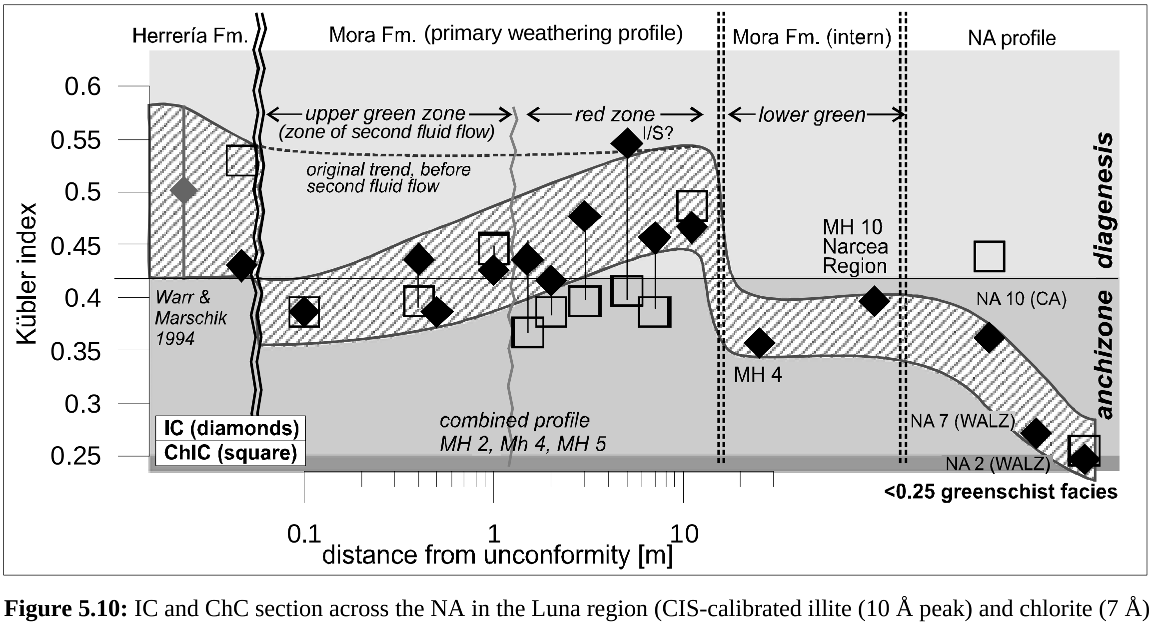

Figure 5.10: IC and ChC section across the NA in the Luna region (CIS-calibrated illite (10 Å peak) and chlorite (7 Å) crystallinity of shales and siltstones). Weathering profile is combined from outcrops MH 2, MH 4 and MH 5. Samples NA 2, NA 7, NA 10 represent a profile through the Narcea Antiform in the Luna region (NA 2: phyllite at southern boundary of Mora, part of the WALZ ; NA 7: siltstone south of Conobre-La Urz fault, WALZ; NA 10: siltstone 1,2 km South of outcrop MH 3, CA). Herrería data from Warr & Marschik (1996). The hatched zone covers the IC variation.

measured (Figure 5.11). The samples represent different zones: Sample (a) is a gouge from the uppermost part, just below the Herrería Fm. conglomerate. It shows well-crystallized illite as the dominant clay constituent. Gypsum is a minor constituent. Sample (b) is a deep red gouge and exhibits illite, chamosite and lepidocrocite. Lepidocrocite ($Fe^{III}O(OH)$) in the red gouge is a hydrated iron oxide modification (“hydrohaematite”) and gives the red colour to the gouge. Sample (c) is a rock fragment of red Mora Fm. siltstone from inside the gouge zone. Its constituents are dominantly quartz and illite and to a minor extend chamosite. IC value (CIS-corrected) in Mora Fm. rock fragment is with 0.49 ± 0.02 similar to the IC in the red weathering zone of the Luna region (chapter 5.5.1). IC values of the gouges are with 0.52 to 0.55 ± 0.01 relatively high, probably due to superposition with a smectite-peak.

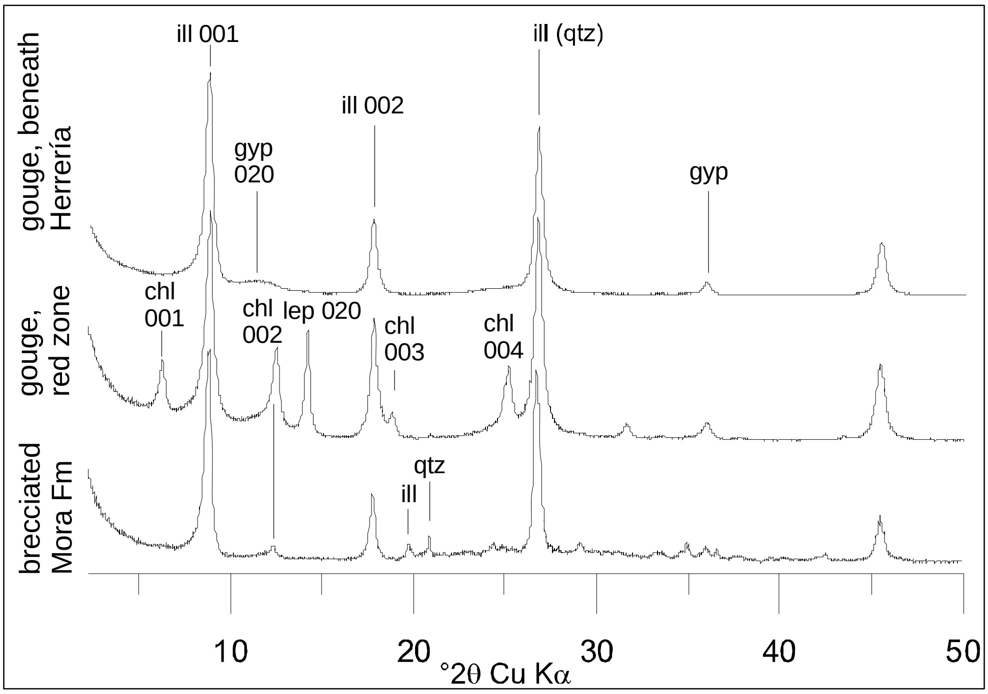

Figure 5.11: XRD spectra of three samples in a gouge zone of outcrop MH 7. a) is a gouge at the upper boundary of the zone, b) is a deeply red gouge and c) is a from a fragment of a Mora Fm siltstone inside the gouge zone.

5.5.3 *Illite crystallinity in a bedding-plane slickenside*

Illite and quartz precipitation on a bedding-parallel slickenside in outcrop MH 8, reveals an illite crystallinity (illite/muscovite 10 Å-peak, measured with a whole-rock sample) of 0.35 ± 0.01.

5.6 Chlorite classification and geothermometry

Some selected samples of different parts of the NA are analysed by the microprobe in order to collect information about the chlorite chemistry and to apply a geothermometer.

The chlorite formula is

$$(1) \qquad [Al, Mg, Fe]^{VI}_{6}\ [Si_{4-x}\ (Al, Fe)_{x}]^{IV} O_{10}\ (OH)_{8}$$

where indices VI symbolizes the octahedral vacancies and IV the tetrahedral vacancies. Al^{3+} and Fe^{3+} are substitutes for Si in the tetrahedral vacancy, whereas Fe^{3+} is with typically 5 wt% maximum not as important (Foster 1962, Zane & Weiss 1998).

After the classification system of Foster (1962), the measured chlorites are rhipidolites and brunsvigites (Figure 5.13.a). A more recent categorization (Zane & Weiss 1998) classifies the chlorites as Type I Fe-chlorites (Type I: $x_{Mg} + x_{Fe\text{-}total} \geqslant x_{Al} + x_{V}$; Type II: $x_{Mg} + x_{Fe\text{-}total} < x_{Al} + x_{V}$; x is the number of atoms per

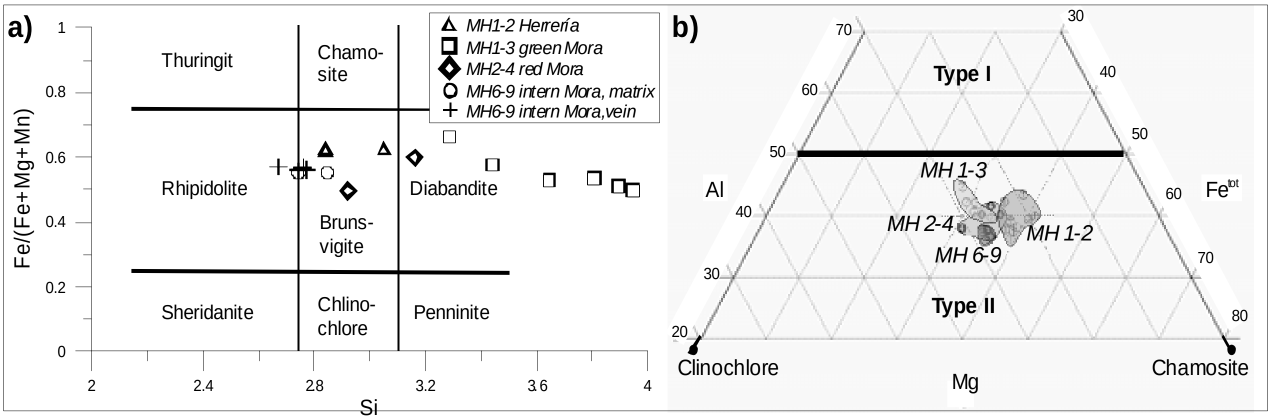

Figure 5.13: Chemical characterization of chlorites after Zane & Weiss (1998). Data are derived from microprobe measurements.

formula unit, x_V are the vacancies) (Figure 5.13.b).

Chlorites of the Mora Fm. are aligned parallel with S_2-cleavage surfaces (see chapter 5.3.4), but are also disseminated and deformed in the microlithons. Herrería Fm. greywackes show similar distribution of chlorite parallel S_2 (Plate 5.3.d). Those chlorites that are crenulated in microlithons between S_2-cleavage surfaces, may be detrital or authigenic phases, precipitated prior to D_2. Since these crenulated chlorites differ from cleavage-parallel chlorites, with respect to geochemistry, showing smaller Si^{IV} content (average 3.28 against 3.02 atoms per formula) and much less contamination with K (0.09 against 0.24), these crenulated species are

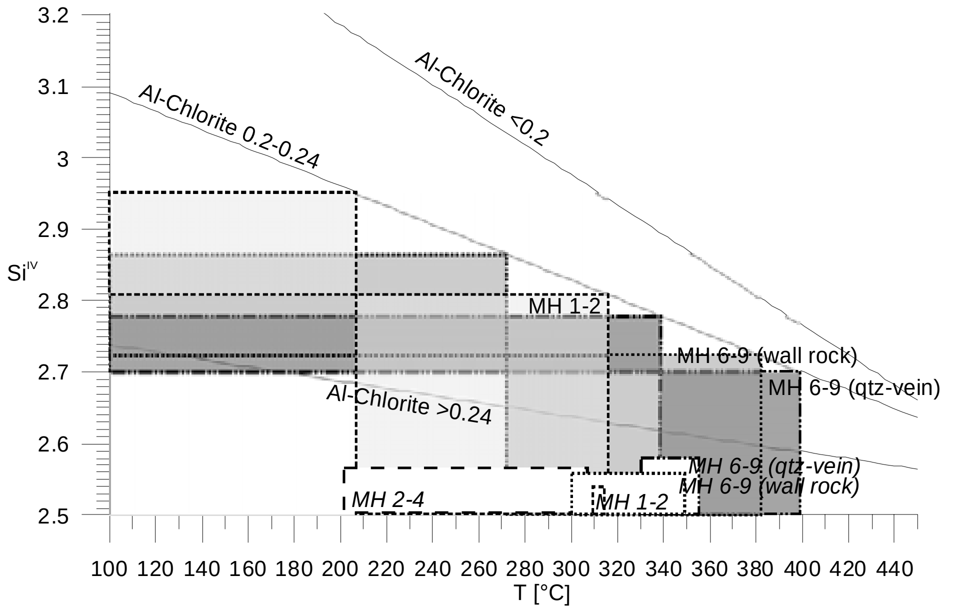

		"Al-Chlorite"	De Caritat et al.	Cathelineau
Luna Region	MH 1-2 (Herrería Fm.; n=3)	**0.253 +/- 0.017**	**261.4 +/- 54.6**	**298.4 +/- 22.8**
	MH 1-3 (green Mora Fm.; n=6)	**(0.378 +/- 0.046)**	**n.n (K-contamination)**	**n.n**
	MH 2-4 (red Mora Fm; n=2)	**(0.291 +/- 0.035)**	**n.n**	**254.6 +/- 54.1**
Narcea Region	MH 6-9 (Mora Fm. wall rock; n=2)	**0.248 +/- 0.010**	**327.9 +/- 56.1**	**326.2 +/- 23.48**
	MH 6-9 (Mora Fm. qtz-vein; n=5)	**0.233 +/- 0.010**	**369.1 +/- 30.9**	**343.47 +/- 12.9**

Figure 5.12: The chlorite thermometers of De Caritat et al (1993) and of Cathelineau (1988). For the De Caritat thermometer the Al-content of the chlorites is an important factor. Al-content is between 0.2 and 0.24. (n.n. means no reasonable results).

considered rather as detritus.

Two chlorite geothermometers (Cathelineau 1988, de Caritat et al. 1993); see chapter 1.3.3) are applied to (a) a Herrería siltstone (MH 1-2) directly above and (b) a weathered Mora siltstone (MH 1-3, 0.5 m) directly beneath the unconformity, (c) a red Mora siltstone of the weathering horizon (MH 2-4) and d) a Mora greywacke of the internal NA, bearing chlorite in the matrix and hydrothermal chlorite in a quartz vein (Plate 5.2.e,f). Similar chlorite-bearing veins were described in greenschist facies pelites in an accretionary prism setting in Chile (Marioth 2001) and interpreted as local remobilization.

The results of the De Caritat and the Cathelineau thermometers are listed in Figure 5.12. The De Caritat thermometer is fully applicable, in a strict way, only for the quartz vein chlorites in MH 6-9. The chlorites of other samples cause difficulties: chlorites of MH 1-2 and matrix chlorites of MH 6-9 have “Al-chlorites”-content of > 0.24, but the specific thermometer for “Al-chlorites” content > 0.24 shows unrealistic results. Instead, the 0.2 to 0.24 equation is used and provides interpretable results. Chlorites have very high “Al-chlorite”-content of 0.378 and 0.291 in MH 1-3 and MH 2-4, respectively, resulting in unrealistic data with all De Caritat thermometers. Chlorites of MH 1-3 are substantially contaminated with alkali elements and depleted in Fe and Mg. K_2O reaches up to 2.15 wt%, which is about ten times higher than normal chlorite (Deer et al. 1966). An intergrowth with white mica phases is likely the case, and therefore none of the thermometers is applicable for MH 1-3. All results of the Cathelineau thermometer have to be taken with care. For MH 1-3 it produces unrealistic temperature, but results from MH 1-2 and MH 6-9 may be taken to verify the De Caritat thermometer.

The quartz vein chlorites in MH 6-9 indicate low-grade temperatures of 369.1 ± 30.9 °C (343.47 ± 12.9 °C using Cathelineau). The average temperatures for the matrix chlorite are slightly lower: 327.9 ± 56.1 °C (326.2 ± 23.48 °C using Cathelineau).

In the Mora rocks of the Luna region, those quartz-chlorite veins are not observed. Here, only weakly constrained thermometer can be used for interpretation. The red, altered Mora sample MH 2-4 displays a chlorite temperature of 254.6 ± 54.1 °C (Cathelineau). The Herrería Fm. sample MH 1-2 shows a similar temperature of 261.4 ± 54.6 (De Caritat) and 298.4 ± 22.8 °C using Cathelineau. These temperatures indicate anchizonal metamorphism, which is in accordance to IC and ChC in that region (Figure 5.10). There is no indication pointing to different chlorite-growth characteristics in Herrería and Mora Fm.

5.7 Data interpretation and establishing a tectonometamorphic and alteration sequence

5.7.1 Cadomian deformation in the Mora Fm. - D_{1M}

The earliest folding event B_{1M} took place before the Neoproterozoic-Cambrian erosion of the Mora Fm. and the sedimentation of the Herrería Fm., which is manifested in the changing angle between Mora Fm. strata and the unconformity. The deformation is therefore assigned to the Cadomian Orogeny (e.g. Lotze 1956, Pérez-Estaún & Martinez 1978).

S_{1M} may have been associated with B_{1M}. However, this is not verified, as there are no relation observed, showing B_{1M} hinge zones crosscut by S_{1M}. Díaz García (2006) proposed Cadomian tight folding with cleavage parallel with or in a low angle to the bedding.

The Cadomian structures were subject to active or passive rotation at least within two stages of late deformations; (1) tilting around a horizontal axis (B_3) and (2) rotation around a vertical axis (B_4). In order to reveal the pre-erosional bedding orientation, caused by Cadomian folding (B_{1M}), S_{0M} are back-rotated in two steps. A more or less passive rotation of both Mora and Herrería Fm. during B_4 is assumed, according to Gutiérrez-Alonso et al. (2004b), who assigned the vertical folding (B_4) to the crustal scale oroclinal bending causing the Asturian Arc (see chapter 5.7.6). Back rotation of bedding poles of each outcrop is achieved by rotation around a vertical axis in order to get an N-S striking unconformity surface (1. step). The original N-S orientation of Herrería beds follows the assumption that an originally linear orogen was subsequently folded around vertical axis (e.g. Hirt et al. 1992, Pares et al. 1994, van der Voo et al. 1997, van der Voo et al. 2000, Weil et al. 2000a, 2001, Weil et al. 2000b). Therefore, an individual degree of rotation is defined for each outcrop corresponding to the individual strike of the unconformity and the position in the orocline (northern limb = MH 6, MH 7), hinge = MH 8, southern limb = MH 1-MH 5). Then, in step 2, the unconformity is tilted back to a horizontal position around the horizontal axis 0/0 to simulate the syn-erosional bedding orientation. The results of the two-phase unfolding are displayed in Figure 5.14.b. A vertical and a horizontal domain of bedding poles are shown. The vertical poles, indicating flat-lying bedding surfaces, are present in outcrops MH 3, MH 4 and MH 8 and the horizontal poles, displaying vertical strata, are represented by outcrops MH 1, MH 2, MH 6 and MH 7. MH 5 is not considered because of its misrepresentation of structures due to an additional late stage tilting.

The bedding orientation of the Mora Fm. reflects a regional scale folding around horizontal axes. The axial surfaces are subject of a syn-Cadomian curvature (sketch in Figure 5.14.b). Cadomian large wave-length folding with E-W oriented axes and vertical axial surfaces has been suggested by Gutiérrez-Alonso (1996) for

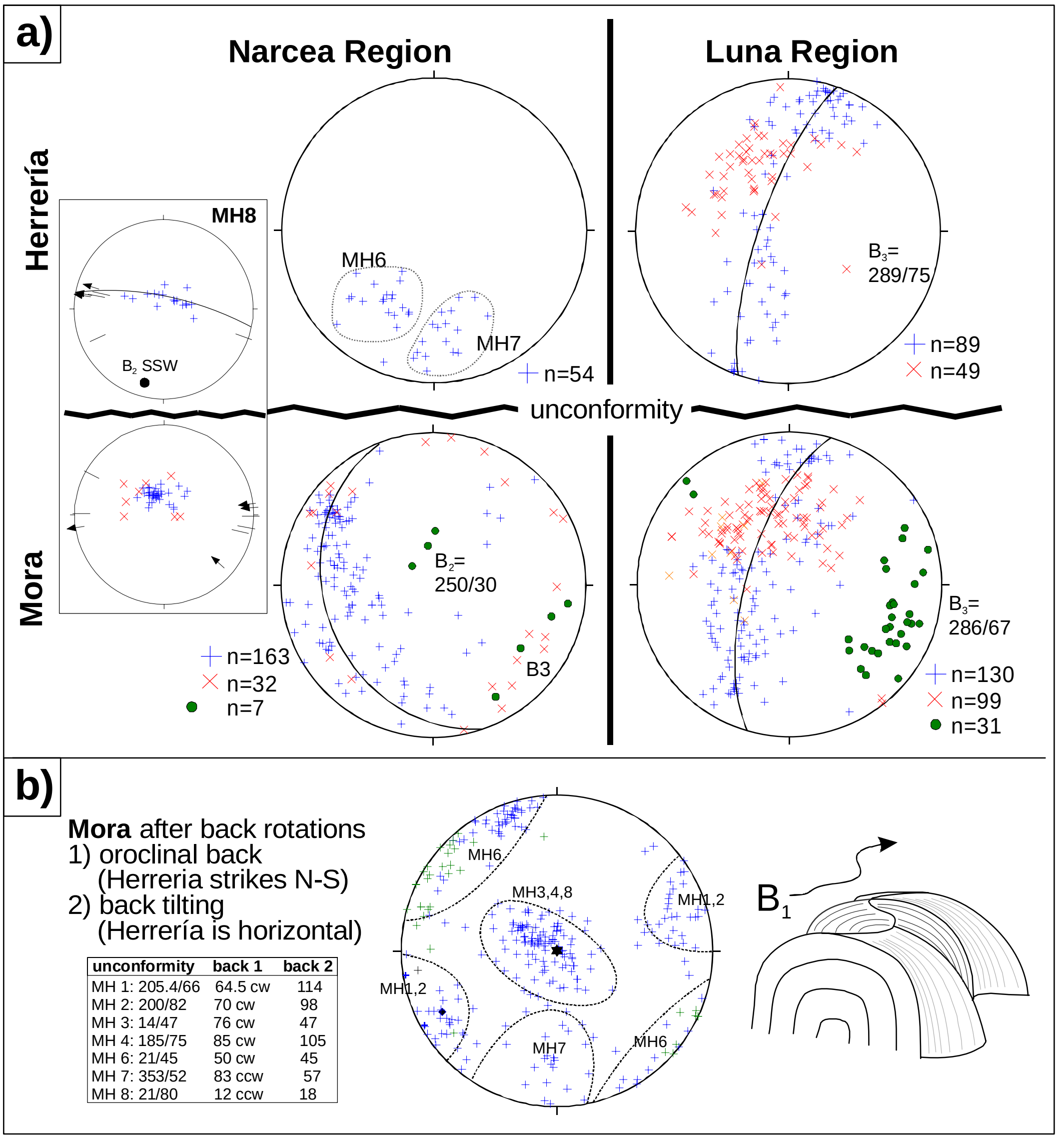

unconformity	back 1	back 2
MH 1: 205.4/66	64.5 cw	114
MH 2: 200/82	70 cw	98
MH 3: 14/47	76 cw	47
MH 4: 185/75	85 cw	105
MH 6: 21/45	50 cw	45
MH 7: 353/52	83 ccw	57
MH 8: 21/80	12 ccw	18

Figure 5.14: a) stereographic projections (lower hemisphere) of bedding S_0 (plus), cleavage S_2 (cross), lineations L_2 (arrow, line), B-axes B_2 / B_3(circle). b) The result of a back rotation of Mora Fm. beds is shown (see text for details). The inferred pre-B_2/B_3 folding structure is visualized in the sketch (in table: cw = clockwise, ccw = counter clockwise).

the Narcea region. Díaz García (2006) proposed Cadomian tight folding with cleavage parallel with or in a low angle to the bedding for the internal NA in the Luna region. The pre-erosional, Cadomian development of large-scale horizontal folds is supported by the described back rotation in this study.

5.7.2 Palaeoweathering in Neoproterozoic-Cambrian time (climatic indications)

Indications of palaeoweathering are (a) haematite precipitation in a zone of ca 16 m thickness parallel with the unconformity (chapter 5.4.1), (b) decrease of feldspar content as revealed by XRD spectra (chapter 5.4.2), (c) illite 10 Å peak broadening (chapters 5.4.2 and 5.5.1), (d) Na depletion from whole-rock geochemistry (chapter 5.4.35.4.2) and (e) the increased κ_{bulk} signature with Fe-and haematite enrichment (chapter 5.4.4).

The haematite precipitation in the Mora Fm. is considered to be a result of subaerial palaeoweathering (Gutiérrez-Alonso et al. 2004a, van den Bosch 1969a). The haematite coating of grains seems to be comparable with red beds, such as the Old Red and the Buntsandstein. Reddening of beds is generally interpreted as a diagenetic process subsequent to sediment deposition in an arid to semi-arid climate (van Houten 1973). Haematite, as a dehydrated Fe^{III}-oxide modification, is typically the most important iron oxide under arid weathering conditions (e.g. Tardy et al. 1990). Goethite may have been the primary weathering product and subject to subsequent dehydration during Palaeozoic burial stage and /or metamorphism.

The Fe_2O_3 (total iron) content corresponds mostly to the haematite occurrence in the profile. Analysis of the ratio of $Fe_2^{III}O_3$ and $Fe^{II}O$ showed a depletion of Fe^{II} and enrichment of Fe^{III} with proximity to the unconformity (Gutiérrez-Alonso et al. 2004a).

κ_{bulk} is an indicator of the Fe- and haematite enrichment, as it shows a slight increase in the red weathering zone. This weathering indication is not as well developed in the fine-grained rocks (siltstone), because κ_{bulk} does not show a clear dependence on haematite content in this lithology (Figure 5.9.a). Instead, the generally higher modal fraction of clay (illite, chlorite) in comparison to diamagnetic quartz and feldspar is more important for defining κ_{bulk}.

Sodium in the whole-rock geochemistry is mainly bound to Na-feldspar and therefore, a decrease with proximity to the unconformity is an expression of the Na-feldspar decomposition. A correlation of illite increase and feldspar decrease is not detectable by XRD, nevertheless, a causal relation can be discussed here: feldspars may have been subject to alteration to form illite. Disseminated clay-aggregates may either be remnants of those altered feldspars (Gutiérrez-Alonso et al. 2004a).

The illite 10 Å peak broadening in the red weathering zone was caused by weathering and is preserved after metamorphic overprint. The broadening of illite peaks is a result of the enhanced precipitation of poorly crystalline illite (*sensu* Meunier & Velde 2004) or I/S mixed-layer minerals. Possibly, smectite were the original alteration products of feldspar hydrolysis and underwent prograde illitization during the burial stage and the Variscan orogeny.

Chlorite is generally not resistant to subaerial weathering. It alters by hydrolysis to vermiculite, smectite or kaolinite causing a peak broadening by interference. Chlorite in the profile, however, does not show any peak broadening due to smectite or vermiculite interlayering. It may therefore be a younger phase, which formed after weathering by metamorphism. Either, early chlorite generations were completely altered during weathering or primary chlorite was not present in the Mora Fm. during palaeoweathering. The latter is more likely, because weathering was presumably never intense enough to alter all chlorite content. This interpretation leads to the suggestion that an early chlorite-generating (Cadomian) metamorphism did not happen.

To summarize, only moderate weathering is indicated in the profiles, not showing features such as weathering-brecciation, element mobilization other than Na (and Ca) and clearly defined trends of mineral depletion. Weathering took place presumably in an arid climate with periodical infiltration of meteoric water, as a consequence chemical weathering was only moderately intense and oxidation of Fe and precipitation of haematite (or goethite) an important process. The stability of the element oxides SiO_2 through the profiles also indicates moderate weathering. Typically, SiO_2 is subject to mobilization in more intense weathering conditions (as observed in the Negev case study). The weathered Mora Fm. (the red haematite-rich zone) is referred to as a saprock (see chapter 1.2). Weakly consolidated weathering horizons (e.g. saprolite) may also have been eroded prior sedimentation of the Herrería Fm.

5.7.3 Main Variscan E-W compression and unconformity reactivation - D_2 and peak metamorphism

5.7.3.1 Regional deformation pattern in the Narcea Antiform

After the crustal thickening, the Variscan deformation cycle in the Cantabrian Mountains began with the folding and thrusting (Top-E-direction, in present day coordinates) of the Palaeozoic sequences (e.g. Julivert 1971, Perez-Estaún 1991) and the antiformal stacking of the underlying Mora Fm. of the NA (Figure 5.2). The metamorphic cleavage S_{2H} (metamorphism see following chapter) is associated with the tightening of the Cadomian folds by B_{2M}. Peak metamorphism during this deformation is indicating (see following chapter) and therefore, it is considered as a features of the regional Variscan deformation phase. In B_{3M}-folded zones (MH 1, see chapter 5.3.5), L_{2M}-lineations lie on a small circle around B_3. L_{2M} are both N-S and E-W trending after un-folding of B_{3M}-folded Mora Fm. beds to a horizontal orientation (Figure 5.15). This may suggest two generations of lineations; one is related to the B_3-folding (the N-S direction, considering the Variscan E-W fold axes and the rotation of ca 90° by oroclinal bending) and the other may be a related to B_{1M}.

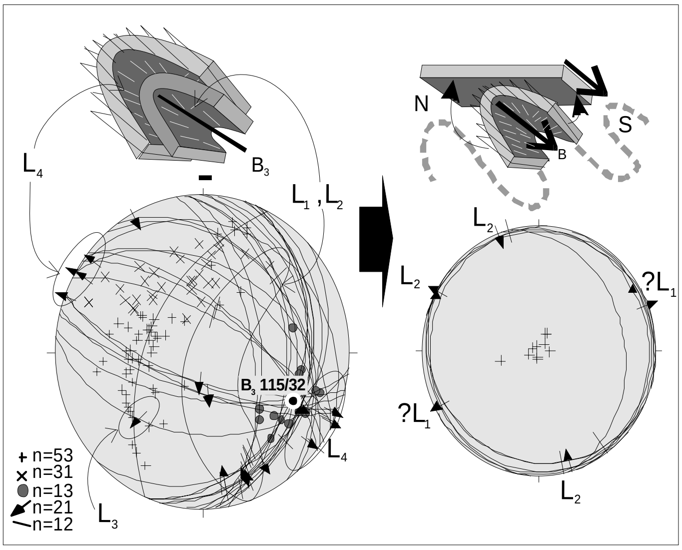

Figure 5.15: Lineation generations in outcrop MH 1 with a back-rotation study of folded (small circle) lineations.

5.7.3.2 Regional metamorphism pattern

The rocks of the studied outcrops show a anchizonal metamorphism by IC and ChC (see chapter 5.5.1) and well preserved primary mineral content and textures.

However, local features indicate lower greenschist facies: (a) a mineral assemblage of quartz + white mica (muscovite, illite) + chlorite, where chlorite grows together with mica parallel with cleavage S_2 (Plate 5.3.c,d). (b) chlorite-thermometer indicating greenschist facies conditions (see chapter 5.6) and (c) quartz recrystallization locally in strained zones at the unconformity. The greenschist facies metamorphism is discussed in the following chapter.

The entire Mora Fm. and lower Herrería Fm. sediments (in the “cleavage zone”: Aller 1987) were buried in Palaeozoic times and underwent maximum burial during the Variscan thrusting. The total thickness of the pre-Variscan Palaeozoic succession (Cambrian to Lower Carboniferous) in the CZ is more than 3 km. With an estimated geothermal gradient of 45 °C/km, very low metamorphic conditions of 160 °C to 200 °C (onset of the anchizone) were reached in the Palaeozoic sediments during the initial Variscan crustal thickening (Warr & Marschik 1996). In combination with the data from the Palaeozoic CZ sediments in the Luna region (Warr & Marschik 1996), the IC show a profile of increasing metamorphism from late diagenesis in the

Palaeozoic formations to greenschist facies in the WALZ part of the NA (Figure 5.10). Chlorite appears to have similar crystallinity values (ChC < 0.42) as illite in the internal part of the Mora and in the WALZ (samples NA7, NA2). This gives evidence for co-genetic growth of both illite and chlorite in theses zones. The sample set is small, nevertheless, the results are in accordance with the literature for both the Luna and the Narcea region (Aller 1987, Gutierrez-Alonso & Nieto 1996, Martin Parra 1989, Pérez-Estaún 1973). The thermal peak was reached in during the Variscan orogeny (or upper Ordovician time *sensu* Keller & Krumm 1992). Although this regional increase of Palaeozoic metamorphism is well constrained, the results show local breaks in IC-values between basal Herrería (late diagenesis, > 0.42) and uppermost Mora Fm. (anchizone, < 0.42). This break is considered as a result of alterations occurring closely to the unconformity, locally changing the IC pattern (discussed in chapter 5.7.4).

The relatively high IC values (> 0.42) in the red weathering zone (Figure 5.10) may be associated with the high amount of poorly crystallized illite, which is typical for weathered rocks (Meunier & Velde 2004). It shows that the overprint was not completed during the Palaeozoic anchizonal metamorpism. This points to a relatively short or weak thermal influence, which seems to be in accordance with Carrière (2006), who inferred a weak thermal overprint from partially annealed apatite fission tracks of Precambrian-age.

ChC values are between 0.37 and 0.42 within the weathering zone, indicating anchimetamorphism, hence higher metamorphism than IC. This may point to a separate growth behaviour of chlorite and illite in the weathering zone. Chlorite is a product of metamorphism during D_2 and probably did not form in pre-Palaeozoic time (neither as a product of palaeoweathering nor of Cadomian metamorphism, as discussed in chapter 5.5.1).

The red, altered Mora sample MH 2-4 displays a chlorite temperature of 254.6 ± 54.1 °C (Cathelineau) (Figure 5.12). The Herrería Fm. sample MH 1-2 shows a similar temperature of 261.4 ± 54.6 (De Caritat) and 298.4 ± 22.8 °C using Cathelineau. These temperatures indicate anchimetamorphic metamorphism and are therefore supported by IC and ChC in that region. A hiatus concerning chlorite growth between Herrería and Mora Fm is not indicated by chlorite geothermometry. This supports the interpretation that chlorite precipitation took place predominantly during peak metamorphism in Palaeozoic time (after palaeoweathering). There is a generation of crenulated and kinked chlorites in the Herrería rocks. These chlorites are indicators of an earlier Palaeozoic growth phase, which occurred together with the maximum crustal thickening in early Variscan time (Warr & Marschik 1996) or already during an older Ordovician event (Keller & Krumm 1992).

5.7.3.3 Hydrothermal greenschist facies metamorphism

Higher temperatures (chlorite zone) are indicated locally by the quartz vein chlorites in MH 6-9 (Narcea region): low-grade temperatures of 369.1 ± 30.9 °C (343.47 ± 12.9 °C using Cathelineau) (Figure 5.12). The matrix chlorite show slightly lower temperatures of 327.9 ± 56.1 °C (326.2 ± 23.48 °C using Cathelineau). Matrix and vein chlorites precipitated in the same low-grade hydrothermal environment, considering standard deviations of temperatures and the fact that element distributions are similar (Figure 5.13). It is possible that quartz and chlorite in these veins derive locally from the wall rock. A similar chlorite-bearing vein, which is folded, is observed in MH 7-4, a red greywacke 1.5 metres beneath the highly deformed unconformity (see chapter 5.3.3). This shows that the hot hydrothermal alteration is regionally distributed at least in the Narcea region. Therefore, a direct relation to geological processes taking place at the unconformity can be ruled out.

The thermal conditions for the veining are incompatible to the pervasive anchizonal matrix metamorphism shown by IC in the CZ of the Narcea region (see chapter 5.5.1). It is possible that thermal imprint of the hydrothermal fluid flow was restricted to the veins and its vicinity, but did not cause pervasive metamorphism in the wall rock. In this case, the veining, regionally restricted to the Narcea region, may have occurred contemporaneously to the anchimetamorphic thermal peak of Palaeozoic time. The chlorite bearing quartz vein beneath the unconformity (MH 7) is folded around Variscan B_2-axes (see chapter 5.3.3). Veining is at least slightly older than D_2. An earlier metamorphism having affected the Mora Fm. and having accompanied the Cadomian deformation is under debate (Díaz García 2006). The present study, however, does not suggest an early metamorphism in the Mora Fm. of the Luna region, because pre-Palaeozoic chlorite, as stated beforehand, is not evident and a hiatus concerning chlorite growth between Herrería and Mora Fm is not indicated.

5.7.3.4 D_2-related detachment along the unconformity

The unconformity was reactivated for the first time during D_2. This is indicated by enhanced S_2-cleavage development, flexuring, facoids or internal (isoclinal) folding of rocks beneath the unconformity and bedding-parallel shortening (folding, imbrication, SC-fabric) and ductile behaviour of quartz in the bed above, such as internal ptygmatic folds (chapters 5.3.8 and 5.3.9). The impact of D_2 on the unconformity and adjacent rocks are similar in both the Luna and Narcea region.

A shortening direction parallel or in a low angle to the unconformity and to the bedding dip direction of the Herrería Fm. is evident in most outcrops. A uniformly E-directed shear is inferred as the pre-oroclinal-bending detachment direction from most outcrops (after back-rotation around a vertical axis, axis: step 1 of back-rotation in Figure 5.14.b). The E-directed shear is in accordance to the proposed Variscan thrusting along regional detachment horizons in the CZ (such as the Cambrian Lancara Fm.) (Julivert 1971).

The indicated W-movement in MH 8 contradicts with the regional pattern. It may be interpreted as flexural slip in large-scale folds, associated with the regional antiformal stacking during Variscan E-W shortening. The illite crystallinity of 0.35 ± 0.01 on a bedding-parallel slickenside (MH 8) can be correlated to the regional IC pattern indicating anchimetamorphic peak conditions in the Mora Fm. of the Narcea region (Gutierrez-Alonso & Nieto 1996). A concurrent development of the bedding parallel shear with slickenside precipitation and D_2, accompanied by the anchizonal peak metamorphism, is indicated.

There are no tectonic basements slices (Mora Fm.) observed in the CZ nappe region (Martin Parra 1989, Sitter & Bosch 1969, van den Bosch 1969a). Basements slices in allochthonous parts are expected in orogenies, given a certain basement topography (e.g. in the Lower Allochthon in the Caledonides, see cases Hara and Långviken). Their absence points to a low basement topography and/or to minor displacement along the unconformity, possibly without involving any considerable imbrication. Outcrop MH 3 shows a imbricate fan at the outcrop scale (Figure 5.6). Here, a layer-parallel shortening of ca. 9 % is evident, inferred by image

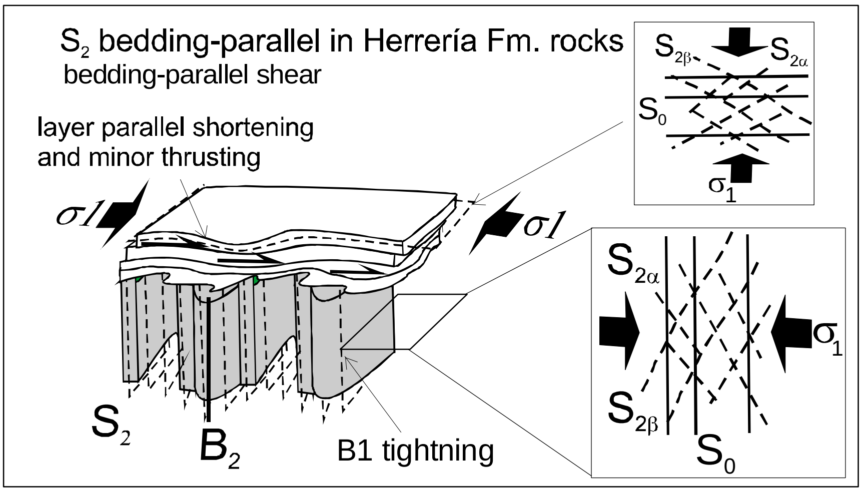

Figure 5.16: Sketch showing the deformations in the Mora and the Herrería Fm. in the vicinity of the unconformity. Structures are considered results of a slip-transfer-zone (after Gutiérrez-Alonso 1996).

analysis. Further implication about total displacement along the basement-cover unconformity cannot be given. Due to the absence of markers at the regional scale it is inferred that the transport distance was rather unimportant with respect to the Variscan nappe emplacement.

The considerations for the Narcea region by Gutiérrez-Alonso (1996) interpreting the system of the folded Mora Fm. and layer-parallel shortened Herrería Fm. as a slip transfer zone between crystalline basement and Palaeozoic CZ can be supported by this study (Figure 5.16). Its extension to the Luna region is supported by (1) the fold style in the Mora Fm. (B_{2M}), (2) the shear activity along the unconformity and (3) layer-parallel shortening of the basal Herrería Fm. beds. Only the lowermost Herrería Fm., where S_{2H} is observed, shows a shortening. The "cleavage zone" (*sensu* Aller et al. 1987) in the Herrería Fm. strata along the northern rim of the NA represents the zone of S_{2H} overprint. It is, however, not reported from the Narcea region. This may be due to the coarse-grained lithology. Alternatively, the "cleavage zone" may also represent the deformation zone in which S_{3H} developed during the tightening of the Alba-Syncline (see chapter 5.7.5).

5.7.4 Fluid-flow during D_2-reactivation of the unconformity

The upper green colour zone just beneath the Herrería Fm. is a macroscopic indication of an unconformity-related alteration, influencing only the uppermost metre of the Mora Fm. Samples in the upper green zone show lowest IC in the weathering profile, comparable to values from the internal Mora zone (Figure 5.10). Therefore, the IC-increase by weathering, as observed in the red-zone beneath, has been overprinted in the upper green zone. This overprint, younger than the palaeoweathering, is attributed to a fluid flow related to the unconformity.

A geochemical indication for the fluid-flow is the mobilization of Fe. Iron is depleted in the upper green horizon (Figure 5.8.d), which is attributed to haematite dissolution and a lower chlorite content (Figure 5.11). Haematite is hardly dissolvable due to it intrinsic Fe^{III}-modification, therefore the dissolution of haematite required a fluid with low pH values and/or reducing nature. Fe^{III} can be transformed to Fe^{II}, which is easily dissolvable, in a reducing fluid. Haematite dissolution can be promoted in $CO_2 + HCO_3^-$ rich fluids (Bruno et al., 1992). According to this author, the ability of haematite dissolution increases with high pCO_2 (CO_2 partial pressure) which itself is positively dependent on the hydrostatic pressure and the concentration of CO_2 in the fluid-rock system.

Temperature is another factor promoting Fe^{III} dissolution: the higher the temperature is, the easier haematite is dissolved. An enhanced thermal imprint is recognized in rocks adjacent to the unconformity. Hot temperatures at the unconformity are inferred by (a) the distinctively low (anchizonal) IC values, (b) by the S_{2H}-chlorite geothermometer (260-300 °C in a greywacke of MH 1, chapter 5.6) and (c) by ductile D_2 deformations close to the unconformity (grain size reduction, flexures, ptygmatic folding, crenulation of older surfaces, quartz elongation and recrystallization). Quartz recrystallization in the sheared Herrería Fm. sublitharenite and sandstone (MH 5, MH 6) indicates temperatures of at least 270 °C.

The spatial relation of hot fluids accompanied by deformation near the unconformity and the CO_2-brines promoting haematite dissolution in the upper green horizon is striking. It has to be discussed, whether both processes occurred contemporaneously. There are several indications for Fe-precipitation in the Herrería Fm. rocks adjacent to the unconformity: (1) the siderite and iron-dolomite (in outcrop MH 6, see chapter 5.2.2 and Plate 5.1.h) in the shear zone just above the unconformity, (2) remnants of hydroxides (limonite) covering the unconformity surface and many bedding surfaces, (3) the typical brown spots in the sublitharenites in the lower Herrería Fm. beds and (4) pervasive alteration with brown Fe-hydroxides in the sandstones direct at the basal Herrería Fm. (MH 6). Rocks are in fresh condition and do not indicate Fe-enrichment just half a metre above the Herrería basis. The iron-carbonate precipitated late syn- to post-deformational by the infiltration of Ca-enriched fluids. This can be inferred by the large amount of euhedral grains overgrowing the deformed matrix (Plate 5.1.h). Possibly, fluids, enriched in Ca, Fe and Mg to precipitate carbonates, arrived from below the unconformity. Iron and magnesium were mobilized in the uppermost weathering zone of the Mora Fm. as it is inferred from the haematite dissolution and Fe-Mg-chamosite hydrolysis. Dissolution of Fe and Mg beneath the unconformity and the nearby precipitation of Fe-Mg-rich phases above the unconformity may therefore be related to the same hot fluid CO_2-rich flow accompanying D_2.

The pathway of the hot brine is traceable by the reduction zones along bedding, S_{2M} and joint surfaces in the purple-red weathering horizon of the Mora Fm. (Plate 5.2.c,d). The fluids may have created a hydraulic overpressure below the unconformity due to impermeable basal litharenites of the Herrería Fm. and changed their path following laterally the unconformity. This caused the pervasive haematite and chlorite alteration, producing the upper green zone. Ultimately, a first brittle reactivation of the unconformity took place because of unconformity-parallel shear stress during D_2 and the overpressure. Shear was accommodated by imbrication of the basal beds. Paths opened for the fluid to escape across the interface into the Herrería. Here, precipitation took place during advanced shear deformation. It might have been the case that friction during D_2-shear released heat increasing the temperature of the fluid-rock system to facilitate intracrystalline quartz deformation.

S_2-surfaces show reduction features (lacking haematite) indicating their development prior to shear along the unconformity.

An input of K into the unconformity-near system is suggested by the gradual increase with proximity to the unconformity (Figure 5.8.f). Highest K-content is in the upper green horizon, where the related alteration was apparently most intensive. K is bound to relic micas and newly grown illite; secondary K-Feldspar is not observed. This geochemical pattern must be a result of alteration superposition, which has been described by Gutiérrez-Alonso et al. (2004) for outcrop MH 6 (*Villar de Lantero*) inferring a combination of sub-aerial weathering in Neoproterozoic-Cambrian time and fluid circulation during Palaeozoic (Variscan) age. The K-enrichment may have been resulted by the infiltration with the hot CO_2-rich Ca-fluid, which accompanied D_2. An increased incorporation of K into illite corresponds with the observed decrease of IC, thus the progressive transformation of illite to muscovite (Hunziker et al. 1986).

5.7.5 Second phase of Variscan compression and unconformity reactivation - D_3

The B_3 folds in the Luna region are parallel with the regional-scale Alba-Syncline (WNW-ESE trending), the dominating structural feature in the CZ North of the Luna area (Figure 5.2.b). Therefore, the local B_3-folding is interpreted as genetically related as a second-order folding to the Alba-Syncline. The fracture cleavages S_{3H} and S_{3M} are associated with this folding. The regional B_3-folding involved locally a reactivation of the basement-cover unconformity.

The dominant Mora Fm. folding in MH 1, the bedding-parallel shear in the Herrería Fm. and the S_3-fracture cleavage (see chapter 5.3.5) are integrated into one single deformation model (Figure 5.17). The progressive rotation of the NNE block (Herrería Fm.) around the subhorizontal rotation axis B_{3H} was accompanied by book-shelf-like slip along bedding surfaces of the Herrería Fm. (S_{0H} = shear surface). In an advanced stage of the S_{0H}-rotation, cleavage S_{2H} paralleling S_{3H}, were flexured by bedding-surface shear. The compressive stress field (in present day coordinates) was SE-NW directed (336/32 in Herrería Fm. and 346/50 in Mora Fm.), which is perpendicular to the Alba Syncline and to the unconformity surface.

Reverse faults with thin clayey gouge zones and brittle reactivation of S_{3M} as reverse slip surfaces, as observed in MH 4, are associated with the same stress fields of B_{3M}. Three stages of deformation intensity are inferred by observations in outcrops MH 2 and MH 1 (see inset “stages of deformation” in Figure 5.17). Moderate compression produced the pencil cleavage and buckling in MH 2 and intense compression produced the narrow folding in MH 1. Temperatures accompanying D_3 shear were lower as D_2-shear, indicated by the fracture cleavage. A relation to Alpine tectonics, which is characterized by a similar N-S compressional regime (c.f. Alonso 1995), is also possible.

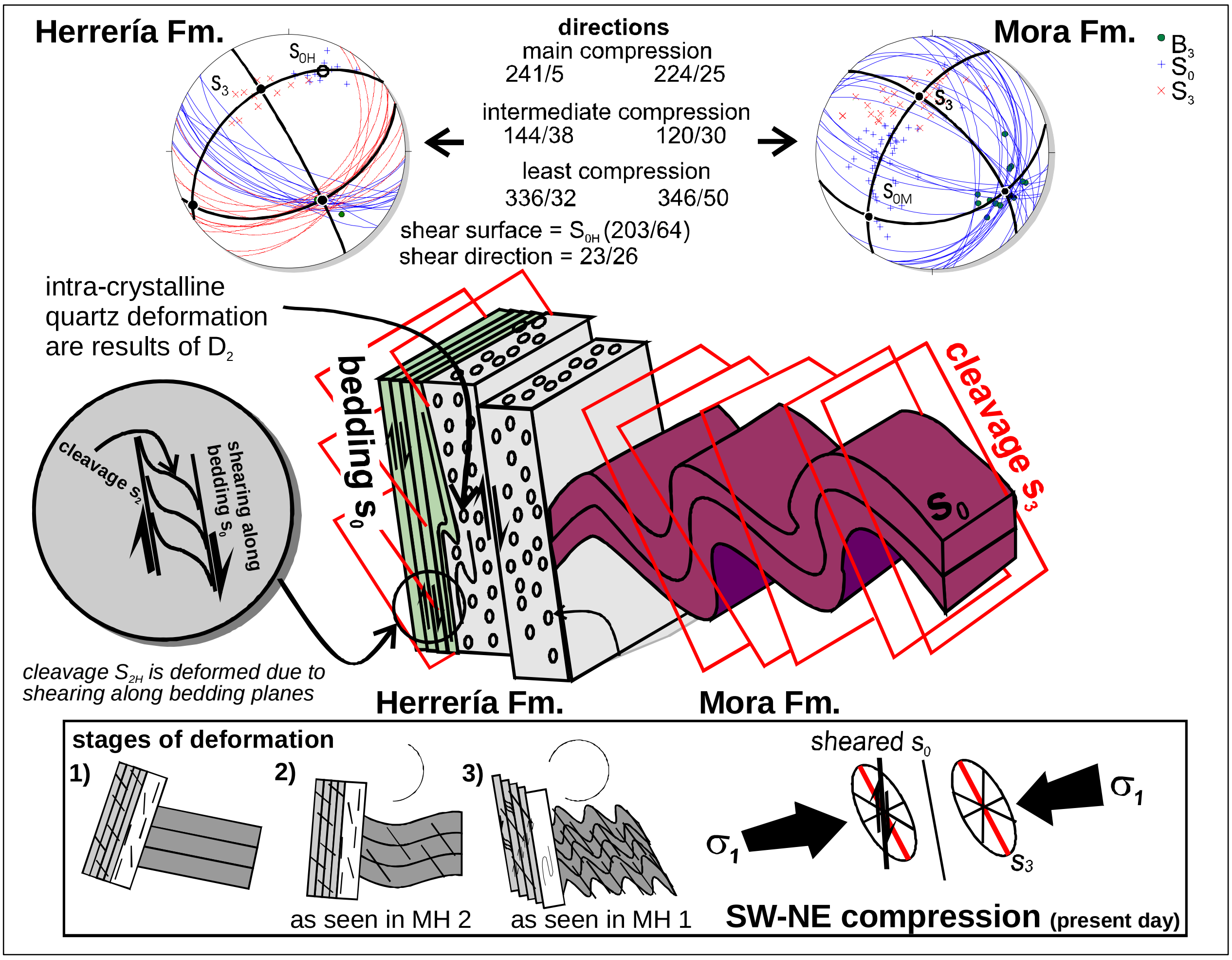

Figure 5.17: Integrated model for the folding and related cleavage development in outcrop MH 1 during D_3. See text for details.

5.7.6 Oroclinal bending and related unconformity reactivation - D_4

Vertical folding B_4 is the result of regional orocline rotation. This crustal-scale oroclinal bending (Gutiérrez-Alonso et al. 2004b and references therein) spatially separated the Luna and Narcea regions. The studied outcrops represent different structural positions in the orocline: MH 1 to MH 5 are situated along the southern limb, MH 6 represents a moderately folded part of the northern limb, MH 7 an intensely deformed part of the northern limb and MH 8 is situated in the weakly affected hinge zone. MH 6 and MH 7 display cataclastic reactivation of the unconformity between Mora Fm and Herrería Fm.

The oroclinal bending affected the Luna region as one block, without causing significant internal deformation. Two deformation features in the Luna region are related to D_4: (1) a rotation around steep NE plunging axis in outcrop MH 5 and (2) subhorizontal stretching lineations and slickensides (L_4) on surfaces of the basal sublitharenites in outcrops MH 1, MH 2 and MH 5. The L_4-lineations on bedding surfaces are caused by flexural slip with strike-slip kinematics. Such a shear may be controlled by regional-scale vertical fold axes of the oroclinal bending (Gutiérrez-Alonso, *pers. comm.*).

Decimetre to several metres thick cataclasis (gouge) zones (MH 6, MH 7) developed in the Narcea region and represent the basement-cover-interfaces. They may be interpreted as late-stage reactivations of the unconformity during oroclinal bending (B_4). Such reactivation of thrust surfaces is common in an orocline and has been recognized by the imbrication of thrusts (like an iris) in the Narcea region (see geological map in Figure 5.1 also Julivert (1971).

Lepidocrocite ($Fe^{III}O(OH)$) in the red gouge (MH 7) is most probably the alteration (hydration) product of haematite from the cataclastically deformed weathering zone in the uppermost Mora Fm. (Figure 5.11). IC value in Mora Fm. rock fragment is with 0.49 similar to the IC in the red weathering zone of the Luna region (chapter 5.5.1). IC values of the gouges are with 0.52 to 0.55 relatively high, probably due to the interference with smectite. Smectite and lepidocrocite precipitation in the gouge may have accompanied the cataclasis, pointing to secondary pulses of very-low-grade fluids along the unconformity. However, a precipitation of these phases as recent weathering products cannot be excluded.

The oroclinal rotation (D_4) and the tightening of the Alba Syncline (D_3) in the Luna region and the Los Lagos Syncline in the Narcea region may have taken place in the same setting. The Alba Syncline in the CZ is in the inner part of the orocline and thus an expression of the crustal scale thickening taken place during oroclinal bending in the inner part (Gutiérrez-Alonso et al. 2004b).

5.8 Conclusions

The tectonometamorphic evolution and related alterations of the rocks adjacent to the basement-cover unconformity (weathering horizon in the Mora Fm. and basal Herrería Fm. beds) can be summarized as follows: (stage 1) large scale horizontal Cadomian folding B_{1M} and bedding-parallel S_{1M} in the Mora Fm. turbidites; (stage 2) erosion, peneplanation and associated moderate weathering with some feldspar alteration (hydrolysis) and clay precipitation and Fe-oxide or -hydroxide precipitation in an arid environment in the Neoproterozoic-Cambrian time interval, (stage 3) sedimentation of Herrería Fm., beginning with basal sublitharenites and conglomerates and diagenesis of Mora weathering zone involving dehydration of iron-hydroxide to haematite; (stage 4) loading of Palaeozoic sediments leading to a maximum anchizonal regional metamorphism; (stage 5) first Variscan folding B_2 accompanied by anchizonal metamorphism and cleavage S_2 formation; (stage 6) subsequent D_2-detachment along the unconformity, facilitated by a hot and overpressured (?) carbonate-, and possibly K-enriched reducing brine; (stage 7) horizontal D_3-folding and reactivation of the unconformity resulting from formation and tightening of the Alba-Syncline; (stage 8) cataclastic reactivation of the unconformity during oroclinal bending D_4.

A Cadomian folding around horizontal axes with curved axial surfaces is suggested by back-rotation of the Mora Fm. beds. S_{1M} is a weakly defined pre-Palaeozoic bedding-parallel foliation, developed under maximum anchizonal regional metamorphism. There are no indications in the studied locations for a chlorite-forming regional Cadomian metamorphism. Regional distributed quartz-chlorite veins older than D_2, indicate hydrothermal greenschist facies metamorphism. They may be related to the Cadomian granitic intrusions (Fernández-Suárez 1998, Gutiérrez-Alonso et al. 2004b), or to local quartz-chlorite mobilization during early stage of the Variscan deformations.

A Palaeozoic age of the anchizonal regional peak metamorphism is inferred by chlorite formation overprinting weathering artefacts and by illite crystallinity. Metamorphic grade increases to lower greenschist facies towards the WALZ. The tectonic overprint of rocks near the unconformity is similar in both Narcea and Luna region, hence throughout the NA. The main tectonometamorphic stage in both regions can be considered as contemporaneous.

Iron-enrichment and associated paramagnetic/antiferromagnetic κ_{bulk} increase, together with Na-depletion and increased FWHM of the illite 10 Å peaks are indicators of the fossil palaeoweathering horizon, which reaches down to 16 metres below the unconformity. A gradual K-enrichment towards the unconformity is not related to weathering, but is rather an indication of later fluid-flow parallel the unconformity (K-metasomatism).

The unconformity has been structurally reactivated, acting as a detachment horizon, within the entire Variscan deformation cycle. Reactivation was more complex than previously thought; three phases of reactivation are interpreted. The first detachment phase (D_2) is associated with the crustal-scale formation of a slip-transfer zone between a crystalline basement and the fold-and-thrust belt of the CZ (Gutiérrez-Alonso

1996), which accommodated the early E-directed thrust tectonics of the CZ. The D_2-detachment was accompanied by low-grade hydrothermal alterations due to the infiltration a carbonate-, possibly also K-enriched, brine, originated from deeper zones of the Mora Fm. A secondary and a tertiary cataclastic reactivation of the unconformity (during D_3 and D_4) took place and might have been accompanied by pulses of very-low-grade fluids (precipitation of lepidocrocite and smectite in gouge zones). Although the compressional stress fields of D_2 and D_3 were the same, a certain pause between both events is inferred by the changed deformation style (ductile to cataclastic), hence thermal hiatus, between D_2 and D_3. The strongest influence of D_3 is observed in the most eastern Luna region (manifested in the combined B_3-folding/bookshelf shear in outcrop MH 1). The tightening of the Alba Syncline (D_3) is an expression of the crustal thickening induced by the oroclinal rotation (D_4), leading to the conclusion that both deformations may have taken place within the same tectonic setting.

Plate 5.1: (unconformity) refers to next page, a) photograph of outcrop MH 6 (Villar de Latero, Narcea region) with purple red weathering zone and tectonic breccia (small picture) in the Mora Fm. and basal sandstones of the Herrería Fm.; **b)** asymmetric B_3-folds in outcrop MH 1 (Luna region, long side is 5 m); **c)** deformations related to the unconformity in outcrop MH 3 (Irede de Luna, Luna): folding and imbrication of Herrería sublitharenite and flexure in Mora greywacke; **d)** micrograph of a deformed Mora siltstone near the unconformity showing an interference pattern of a folded quartz vein (sample MH 11-8, Luna; long side 4.85 mm); **e)** a basal quartzite of the Herrería Fm., compaction was accommodated by pressure solution (MH 1-1, Luna, 2.8 cm) **f)** a bedding-parallel shear zone in a Herrería sandstone with deformed relics of S_1 (MH 3-5, Luna, 4.85 mm); **g)** a deformed zone of the same sample with undulatory quartz clasts in a sericite matrix (MH 6-2, Narcea, 4.85 mm); **h)** a bedding-parallel shear zone in a Herrería sandstone above the unconformity with quartz-recrystallization, quartz sigma-clasts and syn- to post-deform Fe-Mg-carbonate (MH 6-2, Narcea, 4.85 mm).

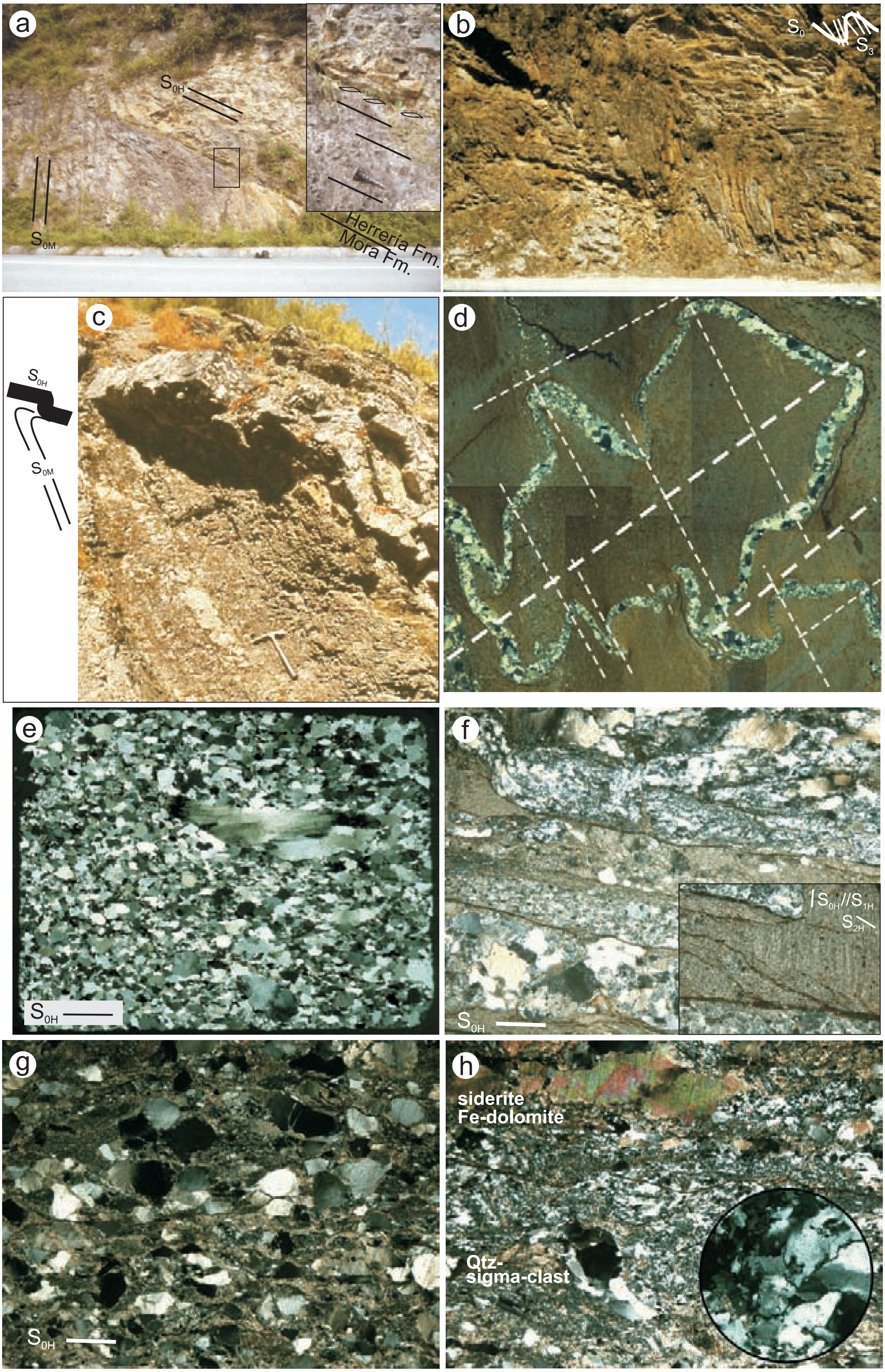

Plate 5.1.a-h: (Unconformity, caption see previous page)

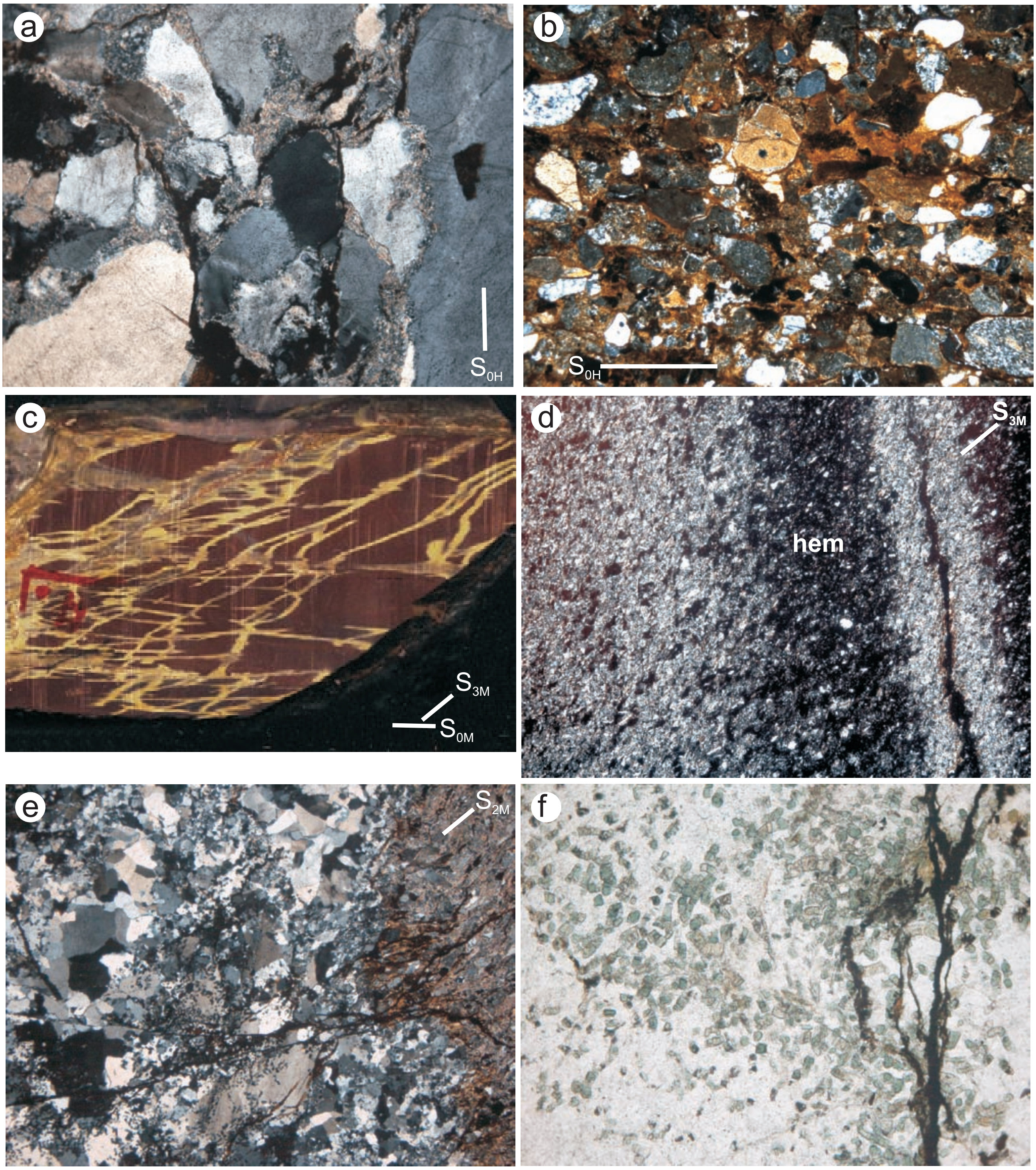

Plate 5.2: (Alterations) a) Micrograph of a Herrería basis conglomerate with clayey cement (sample MH 2-1, long side 4.85 mm, crossed nicols); **b)** Herrería microconglomerate with limonitic cement (MH 7-2, 4.85 mm, crossed nicols); **c)** hand specimen (siltstone) with purple red alteration with subsequent reduction along planar structures (MH 1-9, 11 cm); **d)** micrograph of the same sample, displaying the haematite (dark) remobilization and local reprecipitation (MH 1-9, 4.85 mm); **e)** Mora quartz-chlorite vein, which is oblique to S_2 and shows recrystallized quartz (MH 6-9, 4.85 mm, crossed nicols); **f)** detail of e, chlorite is disseminated in vein matrix or accumulated along fissures (MH 6-9, 1.4 mm).

Plate 5.3: (Structures, plate on the following page) a) Micrograph of a coarse-grained Mora Fm greywacke with S_1 pressure-solution seams paralleling bedding S_{0M} (sample MH 1-15, Luna region, long side 4.85 mm); **b)** oldest quartz vein (diagenetic) in a Mora Fm. siltstone are crenulated by S_{1M}, which parallels S_0 (MH 2-7, Luna, 4.85 mm); **c)** two conjugated sets of S_{2H} in a Herrería Fm. arenites adjacent to the unconformity, growth of mica in quartz pressure shadows (MH 6-2, Luna, 0.54 mm); **d)** SEM-micrograph of a Herrería Fm. greywacke with dominant chlorite growth along S_{2H} (MH 1-2); **e)** asymmetric crenulation of S1 surfaces by S_2 surfaces in a Mora Fm. siltstone (MH 11-7, 1.4 mm); **f)** sedimentary structures (gradated bedding, load casts) in the Mora Fm. (graded bedding, load casts) overprinted by S_{3M} (MH 2-4, 11 cm); **g)** asymmetric D_3-folds and D_3-faults in a Herrería Fm. sandstone near the unconformity (MH 1-2, 15 cm); **h)** reactivation of S_2 surfaces during D_3 or later in a purple-red Mora Fm. siltstone (MH 2-2a, 4.85 mm).

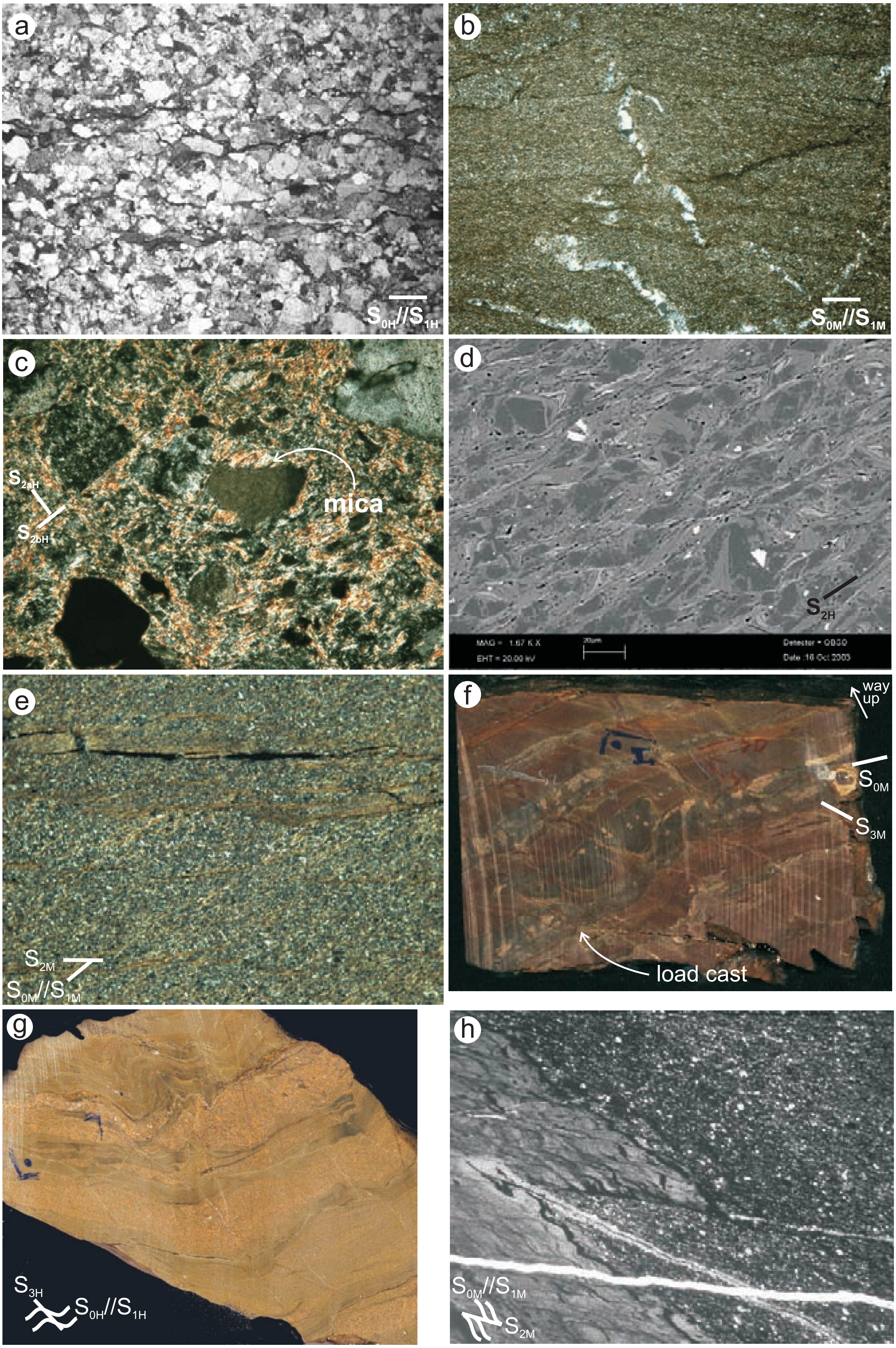

Plate 5.3.a-h: (Structures, caption see previous page)

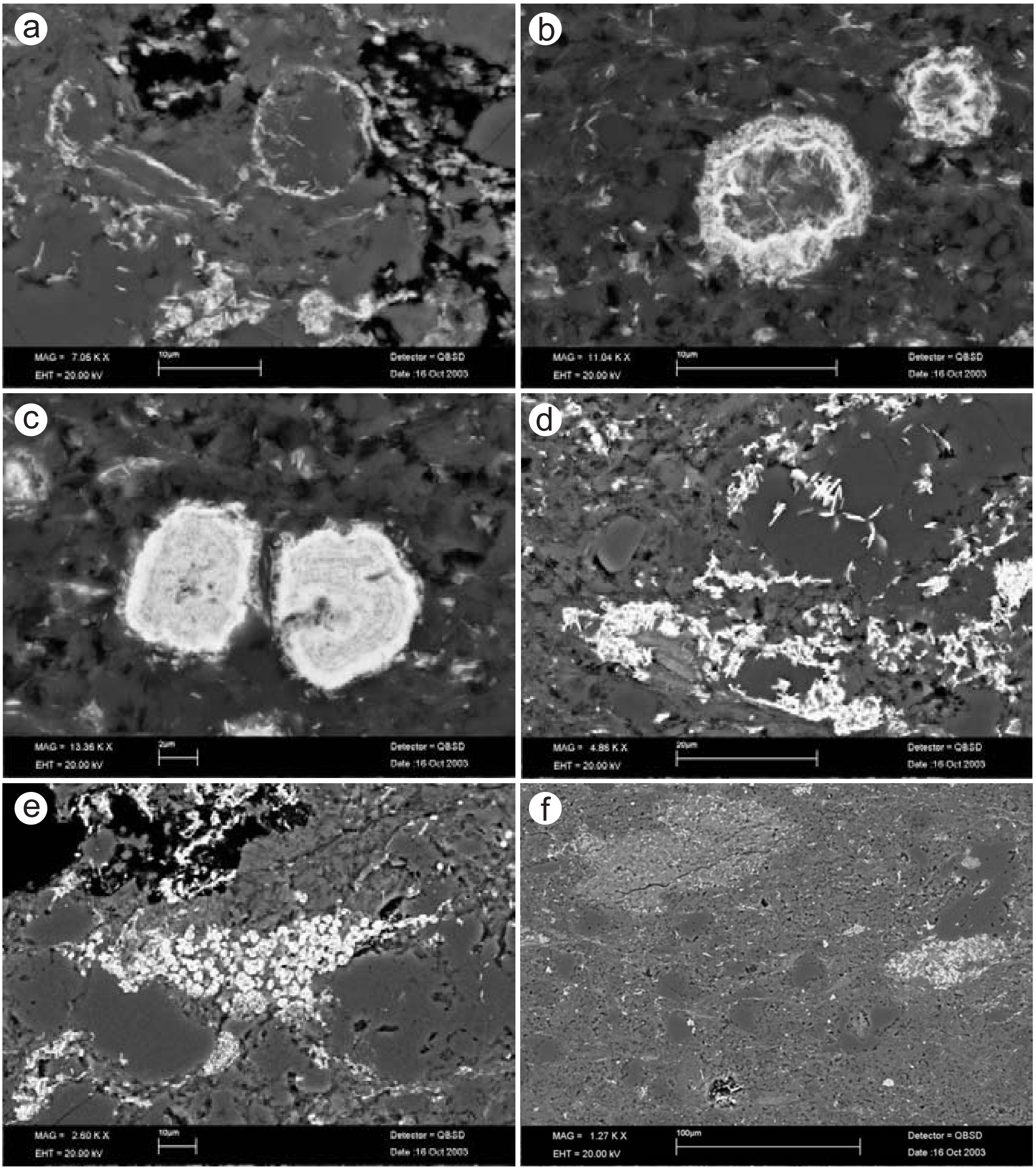

Plate 5.4: (Microcrystalline haematite, sample MH 2-4) a) SEM-micrograph showing coatings of haematite on detrital quartz and mica; **b)** advanced precipitation around quartz grain; **c)** complete replacement of grain (quartz?) led to haematite pseudomorphs; **d)** ubiquitous replacement of the detritus; **e)** accumulation of haematite pseudomorphs in the matrix; **f)** preferred orientation of haematite pseudomorphs and accumulations parallel with planar fabric elements in the texture.

6 SUMMARY OF CASE STUDIES AND DISCUSSION

The following key questions regarding alteration and fabric evolution of rocks adjacent to the unconformity between palaeoweathered basement and sedimentary cover have been addressed:

(1) Is palaeoweathering of Neoproterozoic/Early Cambrian time in the rocks traceable by geochemistry and mineralogy and at the same time distinguishable from overprinting alterations?

(2) Are there specific rock fabrics, such as preferred orientation of minerals, created by palaeoweathering, and are they distinguishable from overprinting deformation?

(3) How do magnetic susceptibility signatures change during palaeoweathering and are there principal relations to specific alterations and fabrics?

(4) Are weathering and subsequent diagenetic features important factors for shear strength modification in the rocks as well as along the unconformity?

6.1 Common palaeoweathering features and trends

In all four case studies, the fossil palaeoweathering is traceable by petrography, XRD and geochemical analyses. In the Negev weathering profile, a sequence of saprock, saprolite (pallid zone) and laterite (ferricrete) formed under warm and humid conditions. A subsequent change to (semi-) arid climate is indicated by several features (see chapter 2.7.2). Main weathering processes were weathering-brecciation (see chapter 2.2.2), I/S mixed-layer mineral formation due to Na-plagioclase hydrolysis, kaolinite formation due to K-feldspar hydrolysis (see chapter 2.2.10 and 2.7.2), quartz dissolution and leaching (see chapter 2.2.11), and magnetite dissolution and oxidation (martitization) (see chapter 2.2.12). In the Swedish examples (Hara, Långviken), chemical weathering and sub-soil weathering-brecciation took place presumably in a cold climate (see chapter 3.6.2.1); chemical weathering mainly involved I/S mixed-layer mineral formation due to hydrolysis of Na-plagioclase (see chapter 3.3 and 4.3.1.2) and SiO_2 dissolution (see chapter 3.2.2). Hydrolysis of silica minerals is an observed phenomenon under cold climates (Anderson et al. 1997, Dietzel 2005, Williams & Walter 2004, Williams et al. 2003). Almost complete magnetite dissolution is observed in the Långviken case, leading to Fe leaching in the weathering-breccia (Figure 4.5). In the Hara case, the uppermost metres of the preserved weathering-breccia profile may represent a soil-sediment, because the texture is sedimentary and relic K-feldspars are occasionally sub-angular (Plate 3.1.d). No weathering-brecciation is observed in the weathered sedimentary basement (Narcea Antiform). Weathering is limited here, showing moderate alteration of Na-plagioclase (see chapter 5.4.2) leading to precipitation of poorly crystallized illite (high FWHM: Figure 5.8.j) and formation of a haematite-enriched zone, characterized by the red colour of weathered rocks (van den Bosch 1969a); and Figure 5.5). Presumably, weathering took place in an arid climate with periodical rain water infiltration, as a consequence, chemical weathering was only moderately intense and oxidation of Fe with precipitation of haematite the important process.

Erosion of the uppermost weathering horizons is assumed in all cases. The physical sub-surface weathering, referred to as weathering-brecciation, is the dominant feature in the palaeoweathering profile with respect to thickness in the granite cases. Weathering-brecciation is the result of different processes: in the Negev case, a weak fragmentation of the granite was presumable due to argilliturbation during periodical water infiltration by groundwater level variation. In the Swedish examples, freeze-thaw-cycles (in a permafrost zone?) (Dietzel 2005 and references therein) is the likely factor for brecciation.

Although palaeoweathering conditions were different, some geochemical and mineralogical features and trends can be correlated across the case studies. The geochemistry of the alkali and alkaline earth elements are very similar, as it can be observed in a general *PIA* increase (Figure 6.1.a). A similar trend is shown by *CIW* (see case studies). *PIA* and *CIW* (equations 11 and 12 in chapter 1.2.1) are dominantly defined by the ubiquitous Na mobilization and depletion, due to the breakdown of plagioclase by hydrolysis (equation 1a in chapter 1.2.1).

The fate of potassium in palaeoweathering profiles appears to be more complex. A regular increase of K is evident in the case studies (Figure 6.1.b). Potassium is predominantly bound to primary mica and K-feldspar. Both minerals were relatively stable during palaeoweathering in the Narcea Antiform and Swedish case studies. In the latter case, feldspar stability is evidenced by abundant clasts in the weathering-breccia matrix (Plate 3.1.d). K-feldspar was subject to hydrolysis in the saprolite and, most extreme, in the laterite of the Roded Granite (Negev). This led to a local K-depletion in the laterite. An absolute enrichment of K in ancient soils beneath basement-cover unconformities is frequently observed (Dott Jr. 2003, Medaris et al. 2003, Sutton & Maynard 1996, Ziegler & Longstaffe 2000) and has been interpreted as related to metasomatism during burial evolution (Fedo et al. 1995; also chapter 2.5.3.2). The K signature is the most significant difference between recent and ancient (Precambrian) soils (Dott Jr. 2003). Secondary illite is in all cases the

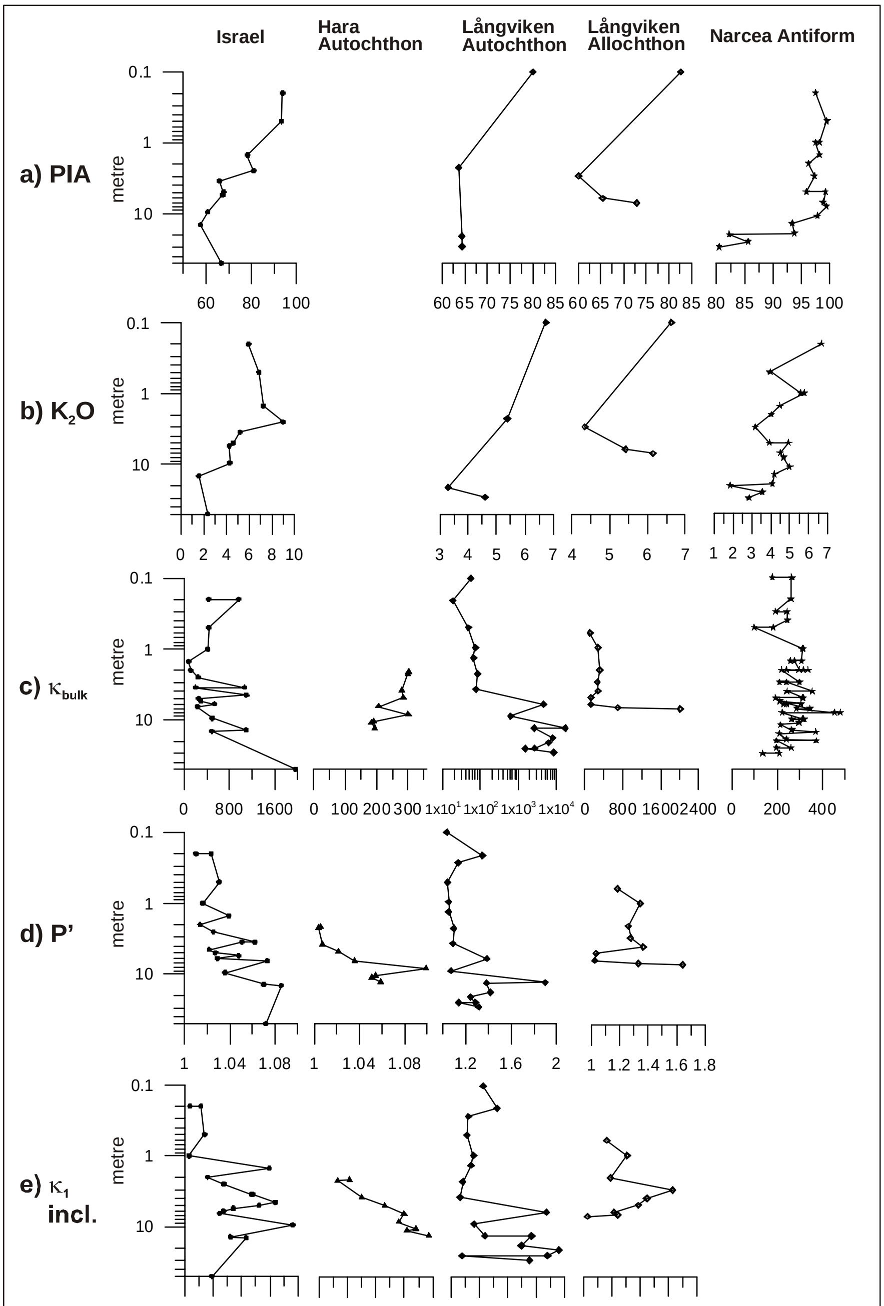

Figure 6.1: Compilation of geochemical and magnetic susceptibility trends through the weathering profiles of the four case studies: a) *PIA* b) K_2O, c) κ_{bulk}, d) P', e) κ_1-inclination.

main mineral incorporating metasomatic enriched K. Illitization of smectite phases, which were presumably the dominant weathering products in all cases, is considered as the most likely process of the diagenetic illite precipitation (c.f. Meunier & Velde 2004). Illite is a ubiquitous mineral and a product of all alteration stages: early hydrothermal stage, palaeoweathering and Palaeozoic diagenesis and up to low grade metamorphism (Meunier & Velde 2004).

Chlorite was subject to gradual alteration with proximity to the unconformity in most studied weathering profiles. Chlorite was subject to hydrolysis during palaeoweathering, and dissolved incongruently to form kaolinite (Negev) and Fe-oxyhydroxides (goethite, haematite) or I/S mixed-layer minerals (Sweden) and Fe-oxyhydroxides. Chlorite appears not as a primary mineral in the Narcea Antiform case. Chlorite alteration in (fossil) palaeoweathering profiles is frequently described (e.g. Braendlein et al. 1994, Craw 1994, Molina et al. 1994, Vicente et al. 1991). Chlorite partly dissolved under very-low grade (hydrothermal) alteration prior to weathering in the case of the Roded Granite (Negev; Plate 2.2.g) and later than weathering the Mora Fm. siliciclastics (Narcea Antiform, see chapter 5.7.4).

6.2 Bulk susceptibility as a tracer of weathering

The bulk susceptibility (κ_{bulk}) is a sensitive tracer for the degree of weathering in most case studies (Figure 6.1.c). This reflects the association of κ_{bulk} with the magnetomineralogy, which altered under varied redox and hydration conditions during weathering. The Negev case shows successive magnetite weathering by oxidation (martitization) and dissolution, which led to a gradual decrease of the ferrimagnetic κ_{bulk} below the laterite. In the laterite, however, a moderate increase is evident because of the relative enrichment of paramagnetic and antiferromagnetic minerals (martite, Fe/Mg-mica and the secondary precipitated microcrystalline haematite). The alteration trend is visualized by the normalization of κ_{bulk} to the whole-rock Fe_2O_3 (Figure 2.17.d) and by the magnetite-martite ratio (Figure 2.17.c and Figure 2.25). In the Långviken (Sweden) example, magnetite decomposition was predominantly facilitated by dissolution and led to a ferrimagnetic κ_{bulk} decrease (Figure 4.23). Here, no martitization took place, presumably due to a reducing weathering agent. In the Swedish Hara case, an increase of the paramagnetic κ_{bulk} towards the unconformity is attributed to the hydrolysis of feldspars and chlorite. In the Narcea Antiform case study, the weathering-induced formation of paramagnetic (illite) to antiferromagnetic (haematite) minerals led to a slight increase of κ_{bulk}. As in the other cases, κ_{bulk} is dependent on the whole-rock Fe_2O_3 content (Figure 5.9.b). The trend in the Narcea Antiform is weakly defined, due to the varying sedimentary mineralogy.

The knowledge about magnetic phases is crucial for interpreting correlations between weathering and susceptibility, e.g. to use susceptibility peaks as an indicator for palaeosoils. It can be summarized that weathering of ferrimagnetic lithologies led to a κ_{bulk} decrease, whereas weathering of paramagnetic lithologies caused an increase of κ_{bulk}. The weathering-induced precipitation of antiferromagnetic phases, such as haematite, caused, locally resticted to horizons (laterite), an additional enhancement of κ_{bulk}. The case of formation of secondary ferrimagnetic phases (magnetite or maghaemite; discussed for red oxidized palaeoweathering profiles by e.g. Dearing et al. 1996, Liu et al. 2001, Liu et al. 2003, Maher 1998, Maher et al. 2003, Retallack et al. 2003, Vidic et al. 2004) is not observed in the case studies.

Subsequent alteration phases or textural changes affected the magnetic susceptibility, overprinting the weathering trend entirely or at least partly. Tectonically precipitated ferrimagnetic pyrrhotite obliterated the paramagnetic weathering trend in the Långviken allochthonous basement slice (Figure 4.23). Burial compaction of the Negev laterite increased in addition κ_{bulk} by the relative enrichment of higher magnetic susceptible minerals (Figure 2.17.a). The upper green horizon in the Narcea profile was subject of haematite and chlorite dissolution, which caused a slight decrease of κ_{bulk} (Figure 5.9.c).

6.3 Textural rearrangement and unconformity-parallel fabrics

The observed rock fabrics adjacent to the unconformities were produced by the superposition of primary rock, weathering, compaction and shear fabrics. Due to this combination of factors, there is a large degree of variety in unconformity-related rock fabrics.

Weathering-brecciation: The weathering-brecciation is a deformation feature, which is developed in the granitic examples (see previous chapter). Brecciation in the weathering zone caused grain size reduction in the Swedish cases, which was intensified by I/S mixed-layer mineral formation by feldspar alteration. This led to an obliteration of the primary fabric (e.g. Plate 3.1.d). In the Negev profile, the breccia is developed, but grain size reduction is in an incipient stage and the granite texture is essentially preserved (see chapter 2.2.2 and Plate 2.1.d).

Unconformity-parallel fabrics: Sedimentary overburden during the Palaeozoic burial stage caused a vertical compaction of the uppermost weathering textures of the weathering crusts. In the granite example, either an incipient (Sweden, see chapters 3.2.2 and 4.2.1.3 and Plate 4.1.g) or an intense (Negev, see chapter 2.2.4 and Plate 2.1.e) unconformity-parallel compaction fabric is developed.

In the laterite (Negev), the vertical compaction of the laterite is macroscopically observed as faulted and rotated quartz veins and microscopically as a crenulation cleavage (Figure 2.4 and Figure 2.6). The formation of a well-built cleavage was accommodated by the rearrangement of relic micas and facilitated by the high porosity (see below) and the easy deformable clay mineral matrix. The maximum overburden was 2.8 ± 0.1 km, estimated by a compaction curve of Sheldon & Retallack (2001) (see chapter 2.5.6.1).

In the Långviken case, the pressure solution is the main deformation process leading to the formation of a foliation, which is hardly macroscopically detectable. In the Hara case, an unconformity-parallel SPO of clay minerals is only detected by means of AMS (see below). Although the Swedish weathering zones underwent a burial of 2.4 to 3.1 kilometres (modelled by Middleton et al. 1996), reaching the late diagenetic to anchizonal grade (Warr et al. 1996), a compaction fabric is not well developed. This may be explained by two factors: (a) low weathering-induced porosity and (b) reaction hardening due to the SiO_2 cement, generated in the weathering-breccia by mobilization and immediate reprecipitation of SiO_2 due to dissolution of quartz or hydrolysis of Na-feldspar during weathering (see chapter 3.6.2).

An unconformity-parallel fabric is not developed in the Narcea Antiform profile, where chemical weathering was moderate and textural breakdown did not occur.

A general covariance between the intensity of chemical weathering and intensity of horizontal cleavage is suggested. This covariance is mainly the result of the porosity produced during chemical weathering (ϕ_w). The evolution of ϕ_w is, simply speaking, a function of the mineral volume strain of the solid material taking place during chemical weathering: a high negative volume strain, i.e. a strong decrease of the solid material volume, leads to a high porosity under the assumption that rock texture-collapse does not occur. The incongruent dissolution (hydrolysis) of albite, producing muscovite (or illite) and dissolved SiO_2, results in a volume loss of 8 to 53 %, depending on the state of SiO_2 (Wintsch et al. 1995 and references therein). High volume loss is observed, when quartz is dissolved and leached and minimum strain occurs at an immediate reprecipitation of quartz. First case is realized in the Roded laterite, thus a high ϕ_w was created while the textural framework was preserved (as seen in Plate 2.1). Weathering-induced porosity (micro- and macro-porosity: Boivin et al. 2005) in the laterite was initially high (at least $\phi_w = 0.37$: see chapter 2.5.6.1). The deformation gradient increases towards the unconformity as a function of ϕ_w increase induced by advancing chemical weathering. This changing degree of chemical weathering affects K-feldspars and is shown by the decreasing trend of K_2O.

ϕ_w in the weathering-breccia of the Revsund Granite cannot be determined, as deformation overprint (D_2 and D_3) was too strong (see chapters 3.6.3, 3.6.4, 4.7.3, 4.7.4). Nevertheless, the observed quartz-cement in the weathering-breccia as a reaction of Na-plagioclase hydrolysis suggests a rather low volume loss, hence low ϕ_w.

To summarize, the factors promoting diagenetic compaction fabrics parallel with the unconformity are: (a) a weakly consolidated weathering texture (strong weathering-brecciation with grain size reduction or with advanced chemical weathering a clayey matrix), (b) a high porosity and (c) a high burial depth. SiO_2 mobilization and reprecipitation forming a cement may have been a strain hardening process (c.f. Wibberley 1999); see also chapter 6.5). The detection of unconformity-parallel fabrics in weathering profiles that encountered at least weathering-brecciation is an important finding with respect to the hydraulic characteristics and the structural strength of the rocks beneath the unconformity (see chapter 6.5).

6.4 AMS as a tracer of fabrics related to weathering and compaction

The AMS method is chosen to trace the fabrics in the granitic weathering profiles. The anisotropy degree P' is a measure of the weathering-brecciation intensity of the primary fabric. A general decrease of P' is recognized approaching the unconformity (Figure 6.1.d). In the ferrimagnetic parent rocks (Negev and Långviken), P' is also influenced by κ_{bulk}, which is evidenced by the positive correlations between both parameters (Figure 2.16 and Figure 4.16). This complicates the interpretation of P'.

The persistence of the primary texture during weathering-brecciation is verified with the stability of the ellipsoid axes through the moderately weathered zone (Negev) (chapter 2.6.4.3).

The magnetic anisotropy is a highly sensitive rock characteristic linked to the development of the unconformity-parallel fabrics (all granite case studies, see chapters 2.6.4.4, 3.7.2.4 and 4.8.3.2). The distribution of the κ_1-axes through the profiles is the most powerful indicator of unconformity-parallel fabrics and the superposition with steep fabrics (Figure 6.1.e). κ_1 inclination is flat-lying, approximately parallel with the unconformity. It represents the intersection lineation between the unconformity-parallel and another, rather steep fabric. This steep fabric is either a partly preserved relic primary foliation, (Negev) or a secondary cleavage overprinting the weathering-breccia (Hara, Långviken). The relative timing between unconformity-parallel and steep fabric is not important for the development of the typical AMS patterns. In the Hara weathering-breccia, a variation of the magnetic lineation from subvertical to subhorizontal orientation with proximity to the unconformity is associated with the gradually increasing influence of the unconformity-parallel cleavage. This gradual increase is associated with the degree of weathering-brecciation. This AMS pattern also features a decrease of P'. A comparable change of the orientation of the magnetic lineation from steep to horizontal is displayed in the Långviken and Negev cases. In these cases, the AMS fabric change is completed within a relatively narrow zone of lithology transformation from granite to weathering-breccia (Långviken) or from saprolite to laterite (Negev).

The orientation of κ_3 is strongly dependent on the relative fabric strengths. Similar strengths of primary and secondary fabrics led to a gradual rotation of magnetic foliation (κ_3) from steep to subhorizontal (Negev: Figure 2.17), whereas a dominance of the steep fabric (defined by mica) leads to a stable steep magnetic foliation paralleling the step petrofabric (Hara: Figure 3.10, Långviken: Figure 4.15). In a case, with no distinct fabric present other than the unconformity-parallel, κ_3 would be vertically oriented and κ_1 would have a flat-lying position. This is inferred by modelling of diagenetic fabrics (Hrouda & Ježek 1999a), however, not realized in any case study.

Although shape factor T is dependent on the superposition degree, it is not easy to interpret, because of its high scattering at low anisotropies.

In the Lower Allochthonous basement slice (Långviken), the weathering texture is obliterated and the AMS only associated with shear fabrics (Figure 6.1.d,e) and the precipitation of ferrimagnetic pyrrhotite (see chapter 4.7.5 and 4.7.6.3).

The onset of flat-lying fabrics and lowered ellipsoid anisotropy in a modern feralitic soil has been documented by Mathe et al. (1997). Here, ferromagnetic neo-formation in a collapsed soil led to horizontal fabrics in a nodular iron crust in soils. In another case (Hus 2003), large deviations of the principal susceptibility directions are caused by bioturbation.

6.5 Structural strength of palaeoweathering zones and shear along the unconformity

All four case studies exhibit deformation adjacent to the basement-cover-interface. This is either frictional sliding along the unconformity or rock failure in the weathering crust.

In the Negev case, the uppermost metre of the preserved laterite is characterized by *plane strain* deformation (compaction in vertical direction (z) and extension in one horizontal direction (x)), associated with the burial compaction (see chapter 2.5.6). Compaction in the cover sediments is less intense, thus a local horizontal reactivation of the unconformity in one horizontal direction beneath the unconformity is inferred (see chapter 2.7.3). At interfaces between the undeformed saprolite and the sedimentary cover, such a reactivation has not occurred.

In the Hara and Långviken case, faulting cutting through the weathering-breccia is inferred (see chapters 3.6.5 and 4.7.5). Faulting is associated to the regional Caledonian process of the emplacement of the Lower Allochthon (c.f Roberts & Stephens 2000). Parts of the weathering-breccia and the basement-cover unconformity itself are repeated as tectonic basement slices of a few metres thickness. The fault inclination might have been unconformity-parallel or in a low angle leading to imbrication and eventually, the formation of the allochthonous basement slices. In Hara, the basement slice is placed on top of the basement, divided by a 1-2 metre thin black shale horizon, which represents the lower thrust surface of the basement slice (Figure 3.13). In Långviken, 10 metres of autochthonous cover strata lie in between (Figure 4.24).

In the Narcea Antiform case, a structural reactivation of the unconformity between the weathered basement and cover rocks took place during the formation of the Variscan fold-and-thrust belt (Cantabrian zone). Layer-parallel shortening (folding, imbrication) and bedding-parallel slip in the lowermost cover rocks accompanied the shear deformation along the unconformity (Gutiérrez-Alonso 1996; also chapter 5.7.3.4 and Figure 5.16). Unlike in the Swedish example, basement slices are absent in the Narcea Antiform case, indicating minor lateral displacements without imbrication. Secondary and tertiary reactivation phases are caused by the tightening of regional anticlines and oroclinal bending.

As inferred from the case studies in this thesis, there are several critical factors for structural reactivation of (i.e. frictional sliding along) unconformities and rock failure within the weathering zone. The following aspects are suggested to be important for lowering the shear strength of the unconformity:

Pre-deformational petrographic contrasts:

a) a low topography relief (peneplain),
b) a lithological and structural contrast between basement and cover,
c) a lithological contrast, generated by weathering of the basement,
d) an unconformity-parallel fabric generated in the weathered basement by diagenetic compaction.

Syn-deformational physicochemical conditions:

e) special hydraulic conditions (overpressure) in rocks beneath the unconformity and
f) an accompanying hydrothermal or regional metamorphism.
g) differential stress σ_1-σ_3

To assess the evolution of lithological contrasts in basement-cover-systems, it is convenient to distinguish between primary and secondary contrasts and the processes that led to these contrasts (Figure 6.2). The primary contrast is defined by the cover sediment and the basement rocks. Secondary processes result either in enhanced or decreased the contrasts between basement and cover rocks, i.e. producing a secondary contrast. Concerning first-stage contrasts, a distinction between unweathered petrographical and structural differences, and those variation caused by palaeoweathering, has to be made.

6.5.1 Primary contrasts and related processes

Topography relief: In principal, the basement morphology, as already discussed, is a large-scale primary contrast. A well developed peneplain in a landscape of low topography relief is a precursor for the formation of a smooth erosional unconformity, which facilitates gliding along the unconformity surface. This is because "mega-scale friction" between basement and cover lithologies is minimized. In the Negev case, the stage of peneplanation took 60 Ma (Stern 2002) during which weathering was intense (Avigad et al. 2005). This suggests a fairly well developed peneplain. The abrasion of the Mora rocks (Narcea Antiform) during weathering is very well developed in the regional scale, as inferred by mapping (Figure 5.1). The peneplain is laterally continuous throughout both the Luna region and the Narcea region (Gutiérrez-Alonso 1996). In the Swedish Caledonides basement slices are a common feature inside the duplex architecture of the Lower Allochthon (Roberts & Stephens 2000). They are considered as the result of abrasion of basement highs during thrust emplacement (pers. comm. Greiling). Such an abrasion of part of the weathered basement and the formation of basement slices is evident in the Långviken and Hara examples ca. 7 to 10 metres beneath the unconformity. The significance of lower allochthonous basement slices for the regional orogenic evolution shows that the absence of planar erosion surfaces, was not a factor of primary importance preventing shear parallel with the unconformity.

Lithological contrasts: Lithological contrasts are generally zones of low shear strength. This is because (a) changes of rheology at the boundary between the lithologies causes different reaction to stress in the lithologies and (b) *grain-scale cohesion* is minimized at lithological boundaries. Such low grain-scale cohesion is expected at basement-cover-interfaces of the upper crust (ca. below 10 km), where rocks did not encounter textural modification at the grain-scale by at least greenschist facies tectonometamorphic overprint. While diagenetic compaction does indeed increase the grain-scale cohesion within the cover rock, the basement rocks remain rather unaffected by diagenesis, as they were already compacted prior to the cover deposition (Narcea Antiform). However, compaction may also affect parts of the basement, if a textural modification caused by palaeoweathering took place in the basement rocks prior to diagenesis. In the granite case studies, the primary granitic textures are replaced by weathering lithologies (intense weathering-brecciation in Hara, moderate brecciation in Långviken and massive clay precipitation in the Negev case). In the Narcea Antiform example, weathering grade is moderate showing intact primary lithology beneath the unconformity. Considering the lithologies on top and beneath the unconformity, the primary lithological contrasts can be classified into three levels of intensity: (1) moderate chemical weathering, high primary contrast due to lithological and structural differences (Narcea Antiform); (2) moderate chemical and intense physical weathering (brecciation), high contrast (Sweden) and (3) strong chemical and physical weathering (brecciation and clay-rich laterite), moderate to high lithological contrast, depending on cover lithology (Negev).

"Reaction softening vs. hardening": Chemical reactions led to a change of the rheological behaviours of the rocks of the weathering zones. The plagioclase decomposition in all weathering profiles is a process of reaction softening and a weakening factor in rock textures (e.g. White & Knipe 1978, with respect to ductile deformation). Weakening of the texture by feldspar alteration is due to the coupled clay (illite, smectite, kaolinite) precipitation. Minerals, i.e. gouges consisting of minerals, are characterized by different frictional strengths, which are expressed as the *coefficient of friction* (μ) (Byerlee 1978). For most earth material (such as quartzo-feldspatic gouges), μ ranges between 0.6 and 0.8 according to Byerlee's Law (Byerlee 1978; equation 2 in chapter 6.5.3). Some clay minerals have lower intrinsic frictional strengths, not following

Byerlee's Law. Montmorillonite gouges have low μ of 0.4, illite gouges show *μ* of ca. 0.5, kaolinite shows with μ of 0.6 to 0.8 no significantly other frictional strengths than quartzo-feldspatic gouges (Byerlee 1978). It has been established by experiments (Morrow et al. 2000) that the effect of water adsorbation on frictional strength can be very high. Water-adsorbing minerals have considerably lower coefficients of friction at water saturation than in dehydrated condition (montmorillonite: 0.2, illite: 0.4, kaolinite 0.6). The coefficients of friction, especially under the consideration of fluid infiltration, which is discussed in chapter 6.5.3, is an important material property of the constituents of the weathering zone.

At least in the Swedish examples, a local quartz precipitation (cement) was presumably a by-product of Na-feldspar hydrolysis (according to equation 1a in chapter 1.2.1) and might have caused a "reaction hardening" (*sensu* Wibberley 1999).

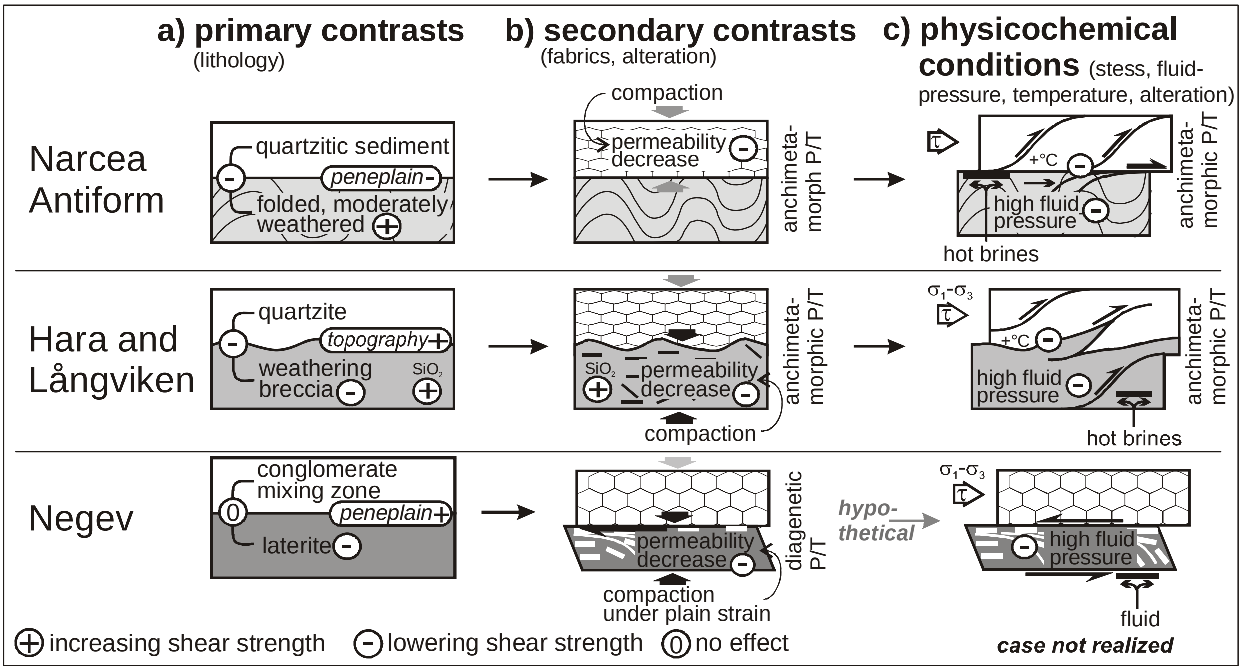

Figure 6.2: The case studies and the individual factors influencing the shear strength in the weathering-zone and the likelihood of shear along or near the unconformity. The three major categories of factors are a) primary contrasts, b) secondary contrasts and c) physicochemical conditions at the unconformity.

6.5.2 *Secondary contrasts and related processes*

Compaction fabric: The main secondary process, which has an effect on basement petrography, is the development of a diagenetic compaction fabric (see chapter 6.3). Such unconformity-parallel fabrics are distinctively formed in the mica and clay-rich laterite (Negev), probably less distinct in the weathering-breccia of the Revsund Granite (Sweden) and not developed in the Mora Fm. (Narcea Antiform). Compaction in the basement rocks (see chapter 6.3) results in a preferred orientation (SPO/LPO) of clays and relic micas parallel with the unconformity and in a reduction of porosity. Associated are a loss of permeability or the generation of a permeability-anisotropy, characterized by an "easy" flow direction parallel with the unconformity. The phyllosilicate SPO/LPO is considered, in addition to the phyllosilicate content, as an important factor lowering the frictional strength in fault zones (Wintsch et al. 1995).

The intense compaction in the Negev laterite was plane strain, which is characterized by a horizontal extension in only one direction (perpendicular to the strike of the relic primary gneissic foliation) (see chapter 2.5.6). Such a plane strain compaction is commonly observed in clastic sediments (Ramsay & Huber 1987). Considering sandstone as the basal cover bed showing not as much of compaction-induced lateral extension, the compaction process itself would have caused a minor reactivation of the laterite-cover unconformity with shear in the same direction as the horizontal extension (x). This reactivation might have intensified the unconformity-parallel fabric in the uppermost dm of the laterite, where the fabric overprint obliterated the entire relic primary fabrics (depth section 4 in the laterite compaction: Figure 2.6). The basal cover bed is a conglomerate-laterite mixture in the outcrop (soil-sediment?), showing petrographic similarities to the underlying laterite, thus, an unconformity-parallel reactivation is not as clearly defined as it would be at a sandstone-laterite interface. The sandstone-saprolite interface (Figure 2.4.a) is not reactivated, since the saprolite is not compacted. The Negev case is an example, where reactivation of the unconformity surface occurred already during the formation the unconformity-parallel fabric (secondary contrast). Any further reactivation, as indicated in Figure 6.2.c, is of hypothetical nature.

Reaction hardening: In addition to the SiO_2-cementation resulting from weathering, a secondary mobilization of quartz and reprecipitation in the matrix, may have taken place in the Swedish weathering-breccias during the burial stage. SiO_2-cementation resulted in a higher structural strength of the weathering-breccias.

Cover rock compaction: In the basal cover rocks of the Swedish and the Narcea Antiform case studies, a process enhancing the secondary contrast was the compaction of the quartzitic matrix of the quartzitic basal cover beds (quartzites and quartzitic sublitharenites), which was accommodated by pressure solution transfer. A bedding-parallel SPO of quartz was generated (Plate 5.1.e), leading to a reduction of porosity and associated loss of permeability.

6.5.3 Physicochemical conditions

Fluid flow: In all case studies, fluid flow in the basement and/or the cover body, as well as along and/or through the interface is evident. The characteristics concerning fluid pathways, heat and fluid-rock-interaction vary. In Israel, the laterite shows a petrographic texture-anisotropy by the unconformity-parallel phyllosilicate cleavage, which caused a permeability-anisotropy. The laterite horizon acted as a hydraulic barrier ("aquitard") for vertical fluid-flow. Element transport into or out of the laterite did not occur after burial compaction: The K decrease in the laterite is considered to be a relic K-feldspar weathering trend (see chapter 2.5.3.2 and Figure 6.1), which was not overprinted by K-metasomatism during burial stage. The fluids in the Negev case study might have originated in the cover rocks (K-rich and reducing basinal brines) infiltrating the highly permeable weathered-brecciated saprolite, which is locally cut by the unconformity (Figure 2.4.b).

The principal sealing character of a highly anisotropic SPO of phyllosilicate has been described (Kopf 2001, Zhu & Wong 1997). The common observation, that permeability is lowest in the immediate hanging wall or footwall of a fault zone (Kopf 2001) can be related to the present case studies. Examples are the black shales on top of the Hara Autochthon and below the Långviken Allochthon basement slice and the quartzitic sublitharenites above the Mora Fm. unconformity (Narcea Antiform).

The situation in the Swedish weathering-breccia is similar, although the permeability-anisotropy is not as well

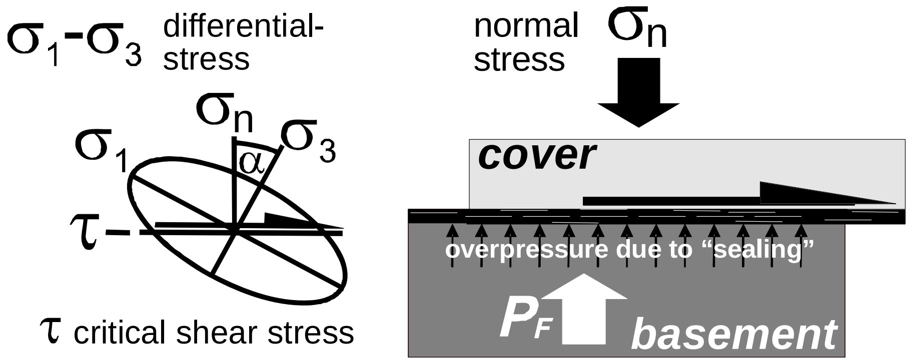

Figure 6.3: Fluid-pressure and stress regime for frictional sliding along the weathered unconformity, facilitated by clays with low coefficient of friction and permeability anisotropy creating fluid-overpressure and water adsorbation.

defined. This is attributed to the quartzitic cement, leading to texture hardening and preventing compaction, as discussed beforehand. The hardened weathering-breccia reaches deep into the profile and has characteristics of a hydraulic barrier. These fluids had a “warm” (< 200 °C) and reducing nature and were enriched in iron (pyrrhotite-pyrite association in Långviken, see chapters 4.7.6.2 and 4.7.6.3), or in carbonate and graphite (upper fault zone in Hara, see chapter 3.6.6). Fluids possibly originated in the cover sediments (black shales).

In the Narcea example, the quartzitic rocks acted in a pre- to syn-shear stage as a hydraulic barrier. The fluids coming from beneath the unconformity were hot, with a high $p\mathrm{CO}_2$, and presumable K-enriched (see chapter 5.7.4). They followed a distinct pathway along the unconformity causing haematite-dissolution. Subsequently, in the syn- to post-deformation stage, fluids crossed the unconformity through fractured basal quartzitic rocks, and caused precipitation of Fe-Mg-carbonate. In the Narcea Antiform case study compaction fabrics play only an inferior role for detachment tectonics. More important for mechanical decoupling at the unconformity are the structural differences between Mora and Herrería Fm. In a given stress-field, differently oriented strata can lead to different strain patterns. While the vertical Mora beds are shortened laterally E-W by reactivation and tightening of Cadomian folds, the horizontal Herrería beds are shortened bedding-parallel by folding or imbrication. As a result, decoupling at the basement cover interface takes place (Gutiérrez-Alonso 1996). Similar reactivations of angular unconformities are observed in the Cantabrian fold-and-thrust belt (Alonso 1989).

The water adsorbation of clay-minerals and the associated lowering of the frictional strength of the material (see chapter 6.5.1), may have been considerably high during fluid-flow, especially in the presence of smectite, as far as infiltration was possible, due to the low permeability.

Depth and normal stress: The normal stress σ_N of a horizontally oriented, hence unconformity-parallel fault equals the lithostatic pressure, which is linearly dependent on depth (ca. 26 MPa/km: Figure 6.4.a). The shear strength (or critical shear stress τ) of rocks in the upper crust increases linearly with σ_N (Byerlee 1978). A precursor for the reactivation of the unconformity is a small angle between the unconformity and shear stress tensor τ. This is given, when the direction of maximal compression (σ_1) has a small to intermediate angle α with σ_N (Figure 6.3).

Shear stress and hydraulic overpressure: Impermeable layers in the crust can increase the fluid pressure P_F, which causes a considerable decrease of the shear strength (Figure 6.4) (Scholz 1990). It has been established that hydraulic overpressure is an important physical state of fluids in rocks, which promotes mechanical decoupling in rocks in a given differential stress field (Handin et al. 1963). The fluid-flow along the unconformities might have induced such a hydraulic overpressure in those cases, where the fluids were driven upwards (e.g. by heat convection). P_F opposes σ_N (Figure 6.3), their difference is the effective stress σ_e (Scholz 1990):

$$(1) \qquad \sigma_e = \sigma_N - P_F$$

The critical shear stress τ, at which the rock deforms, is directly proportional to σ_e, according to the Coulomb Criterion (Coulomb 1773) and Byerlee’s Law (Byerlee 1978).

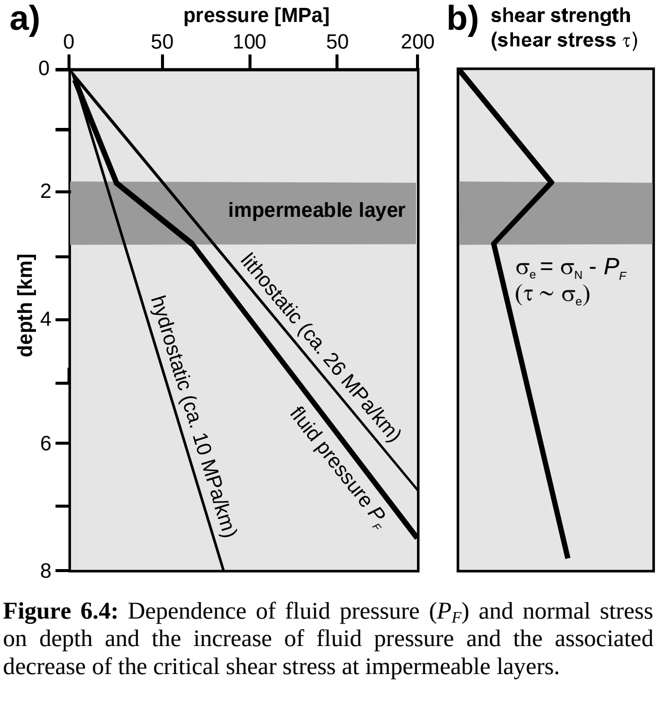

Figure 6.4: Dependence of fluid pressure (P_F) and normal stress on depth and the increase of fluid pressure and the associated decrease of the critical shear stress at impermeable layers.

Byerlee’s Law describes the condition, under which a pre-existing surface will be reactivated by frictional sliding (Byerlee 1978). This can be considered for sliding along the unconformity (Negev, Narcea Antiform). Implementing σ_e, Byerlee’s Law is written as follows (Scholz 1990):

$$(2) \qquad \tau = \mu_F \cdot \sigma_e$$

where μ_F is the coefficient of sliding friction, a critical factor for lowering the shear stress, as discussed in chapter 6.5.1).

The Coulomb Criterion for rock failure is most likely applicable on the faults cutting through the weathering crusts (Sweden cases). Implementing σ_e, the Coulomb Criterion is written as follows (Coulomb 1773, Scholz 1990):

$$(3) \qquad \tau = \tau_0 + \mu_C \cdot \sigma_e$$

where μ_C is the coefficient of cohesion, similar to the coefficient of friction (chapter 6.5.1), and τ_0 the intrinsic shear strength, a parameters depending on the rock characteristics and on physicochemical conditions during rock failure.

Frictional sliding, i.e. the reactivation of pre-existing compositional or fabric heterogeneities or faults in the upper crust has been described from different structural settings (Beacom 2001, Holdsworth et al. 1998, Kopf 2001, Rutter 2001, Stewart et al. 1998, Warr & Cox 2001, Yan 2001).

Temperature: Temperature can be an important factor for enabling shear, when it is high enough to cause plasticity of rock forming minerals (Scholz 1990 and references therein). In unconsolidated to weakly consolidated clayey material (Negev laterite), such conditions are already established at very low temperatures, whereas quartz plasticity requires ca. 270 °C. The temperatures in the fluid-rock system along the unconformity in the Negev case study did not exceed diagenetic conditions. Temperatures accompanying the detachments were enhanced in the Swedish and the Narcea Antiform examples. Deformations were accompanied by local anchizonal metamorphism, i.e. minimum 200 °C (Kisch 1989). Quartz in the basal arenites encountered grain-size reduction by dynamic recrystallization, thus the frictional-plastic transition zone is reached during deformation (under fluid ca. 270 °C). The local increase of temperature was induced by hydrothermal fluids and might have been enhanced by frictional heating.

The flow chart in Figure 6.5 summarizes the processes for the acquisition of primary and secondary lithological contrasts, and the physicochemical conditions, which facilitates frictional sliding along the unconformity and rock failure in the weathering crust.

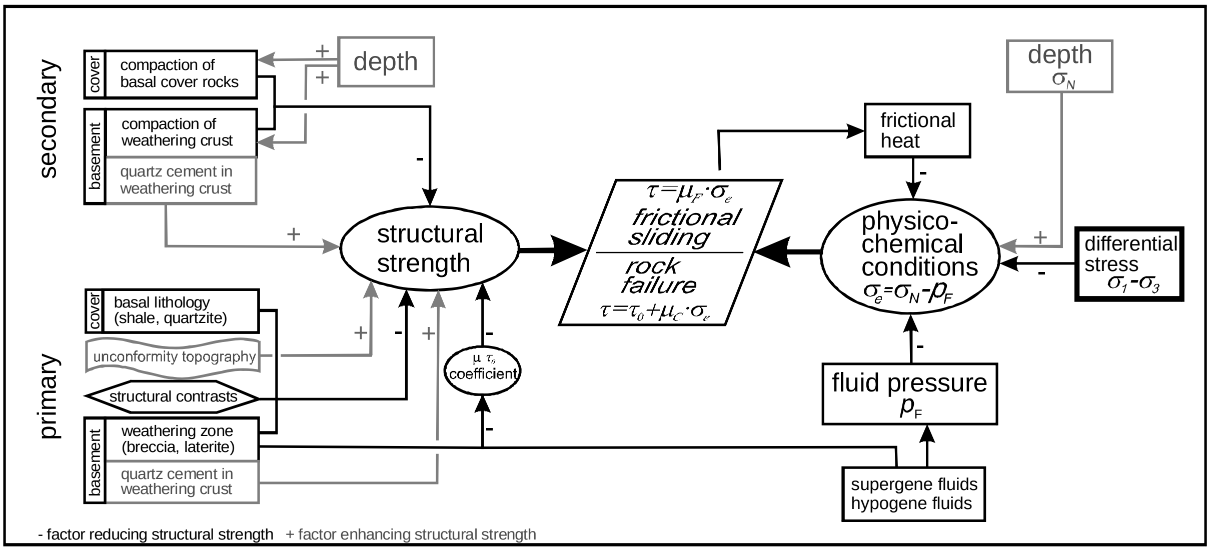

Figure 6.5: Integrated flow-chart combing processes leading to an unconformity-related shear.(+) symbols have an enhancing effect, (-) symbol a negative effect and (o) no effect on the parameters.

7 FINAL CONCLUSIONS

The fabric evolution and alterations that were established in palaeoweathered basement and overlying cover rocks at erosional unconformities of the Neoproterozoic-Cambrian time interval and their relation to deformation at basement-cover-interfaces are the object of this thesis. Following conclusions are drawn on the base of three case studies of weathered granite basement (Negev, Hara and Långviken), and one of folded sedimentary basement (Narcea Antiform).

Fossil palaeoweathering signatures: The geochemical, mineralogical and textural signatures of palaeoweathering are dependent on the climatic conditions during palaeoweathering and on the profile depth. Predominant chemical weathering process, increasing with proximity to the unconformity, was the incongruent Na-feldspar dissolution (hydrolysis). This led to Na_2O leaching and to illite and/or I/S mixed-layer mineral precipitation. Secondary processes were chlorite decomposition producing clay and iron-phases, SiO_2-dissolution and reprecipitation and transformation of specific magnetomineralogies (magnetite dissolution in Långviken and Negev, Partial magnetite dissolution and subsequent martitization in Negev; microcrystalline haematite precipitation in Negev and Narcea Antiform).

Magnetic susceptibility: Weathering of ferrimagnetic lithologies led to κ_{bulk} decrease, whereas weathering of paramagnetic lithologies caused an increase of κ_{bulk}. The weathering-induced precipitation of antiferromagnetic phases, such as haematite, caused enhancement of κ_{bulk}, locally restricted to certain weathering horizons (laterite in Negev case). Thus, when using κ_{bulk} as a tracer of weathering intensity, susceptibility information has to be evaluated regarding the magnetic carriers. Additionally, later alterations may obliterate the weathering signatures (such as the precipitation of ferrimagnetic and field dependent pyrrhotite in the Långviken basement slices).

Field dependence of pyrrhotite: The magnetic field dependence of pyrrhotite-bearing rocks is dependent on pyrrhotite grain size, but also on its modal fraction in the matrix. A corrected field dependence parameter is calculated, to eliminate the strong influence of the paramagnetic matrix susceptibility.

Weathering textures: Primary petrofabrics of the basement were preserved or completely destroyed by the overprint of palaeoweathering. This is mainly dependent on the intensity of physical brecciation and not necessarily on the intensity of chemical alteration. Primary fabrics have been lost in Hara, Långviken due to weathering-brecciation causing grain size reduction. However, in cases of absence of grain size reduction, primary granitic foliations are preserved (saprolite-laterite profile in the Negev case), although extreme hydrolysis and dissolution processes took place.

Compaction fabrics: Unconformity-parallel compaction foliations by pressure solution and rotation of phyllosilicates developed in clay-rich weathering-profiles (weathering-breccia in Hara and Långviken; laterite in the Negev case study) in the diagenetic stage. In the Narcea Antiform, particular anisotropic weathering textures are missing. Intensity of compaction is dependent on the burial depth, the secondary weathering mineralogy (clay-richness) and the porosity. Porosity was mainly achieved by dissolution of quartz and feldspar. An increasing porosity with proximity to the unconformity is evident. A general positive covariance between the intensities of palaeoweathering and horizontal fabric is suggested.

AMS: The fabric anisotropy that is produced by the superposition of the flat-lying unconformity-parallel compaction fabric and a steep (primary or secondary) rock fabric are quantitatively determined by means of AMS. The degree of magnetic anisotropy (P') is inversely covariant with the intensity of the flat-lying fabric, thus P' decreases towards the unconformity. The pole of the magnetic foliation (κ_3) reflects the dominant subfabric, thus it may rotate towards a vertical position (strong horizontal fabric in Negev) or stay stable in a horizontal position (stong vertical fabric in Hara and Långviken). Concurrently, the magnetic lineation (κ_1) is subject of rotation (Hara) or switching (Negev, Långviken) towards a flat-lying position reflecting the intersection lineation ob both fabrics. These flat-lying magnetic lineations, associated with unconformity-parallel fabrics, appear to be a common feature in fossil palaeoweathering profiles, characterized by at least moderate textural rearrangement.

Lithological shear-strength weakening: The palaeoweathered basements and the basement-cover-interfaces show lithological characteristics (primary, secondary contrasts), which, collectively, led to overall shear-strength weakening of the weathered zone. These features are primary structural differences between basement and cover, a low unconformity relief (topography), weathering-brecciation, clay formation (lowering of the coefficients of friction and cohesion) and porosity increase by hydrolysis and unconformity-parallel fabrics in basement and in the cover. An opposing process is SiO_2 cementation in the weathering crust (in Hara, Långviken).

Fluid-flow, metasomatism and fluid overpressure: An absolute K-enrichment in the weathering profiles is attributed to K-metasomatism, as described from numerous ancient fossil palaeoweathering profiles. Fluid-rock interaction gradually increased with proximity to the unconformity. Fluid pressure of the fluid-rock-systems was maximized directly beneath the unconformity or the uppermost weathering horizon, presumably because the clay-rich weathering-breccia (Hara, Långviken), the laterite (Negev) and the compacted quartzitic basal cover beds (Narcea Antiform) sealed the unconformities.

Shear: Structural reactivation of the interface by frictional sliding is observed in the Narcea Antiform case and rock failure in the weathering-breccia is inferred in Hara and Långviken. The lithological shear-strength weakening of the weathering zone as well as overpressured fluid-flow (and associated hydrothermal temperatures in the Narcea Antiform) were important factors facilitating these deformations.

Despite superficial appearance in nature, the studied fossil weathering zones dividing the basement from the cover show common characteristics of textural and fabric evolution, fluid-flow and alteration. It is suggested that these common characteristics leading to associated shear-strength weakening in fossil weathering-profiles are an explanation for the frequently observed localization of detachments along basement-cover-interfaces. This thesis demonstrates the importance of fossil palaeoweathering zones for upper crustal detachment tectonics, as well as for the characteristics of fluid-flow in the basement and related element mobilization and potential ore formation.

Literature

Al Faraj, A. & Harvey, A. M. 1997. Use of desert pavement characteristics to correlate wadi terrace and alluvial fan surfaces; Wadi Al-Bih, United Arab Emirates and Oman. *International Association of Geomorphologists, Fourth international conference on Geomorphology; Abstracts* **3**, 45-46.

Alkmim, F. F., Ribeiro, F. M. & Rolim, V. K. 1999. 3D geometry of a complex thrust system; insights from field mapping physical modeling, and computer simulation. *Abstracts with Programs - Geological Society of America* **31**, 185.

Aller, J., Bastida, F., Brime, C. & Perez-Estaun, A. 1987. Cleavage and its Relation with metamorphic Grade in the Cantabrien Zone (Hercynian of North-West Spain). *Sciences Géologique Bulletin* **40**, 255-272.

Anderson, M. W. & Morris, A. 2004. The puzzle of axis-normal magnetic lineations in folded low-grade sediments (Bude Formation, SW England). In: *Magnetic Fabric: Methods and Applications* (edited by Martín-Hernández, F., Lüneburg, M., Aubourg, C. & Jackson, M.). *Geological Society of London, Special Publications* **238**, 37-47.

Anderson, S. P., Drever, J. I. & Humphrey, N. F. 1997. Chemical weathering in glacial environments. *Geology* **25**, 399-402.

Andersson, A., Dahlman, B., Gee, D. G. & Snall, S. 1985. *The Scandinavian alum shales.* In: *Sveriges Geologiska Undersoekning, Serie Ca: Avhandlingar och Uppsatser i 4:o* **56**. Sveriges Geologiska Undersoekning, Uppsala, 50 p.

Aranguren, A., Cuevas, J., Tubia, J. M. 1996. Composite magnetic fabrics from S-C mylonites. *Journal of Structural Geology* **18**, 863 - 869.

Archanjo, C. J., Launeau, P. & Bouchez, J. L. 1995a. Magnetic fabric vs. magnetite and biotite shape fabrics of the magnetite-bearing granite pluton of Gameleiras (Northeast Brazil). *Physics of the Earth and Planetary Interiors* **89**, 63-75.

Archanjo, C. J., Silva, M. G., Castro, J. C., Launeau, P., Trindade, R. I. F. & Macedo, J. W. P. 1995b. AMS and grain shape fabric of the late Palaeozoic diamictites of the southeastern Parana Basin, Brazil. *Journal of the Geological Society of London* **163**, 95-106.

Arkai, P. 1991. Chlorite crystallinity; an empirical approach and correlation with illite crystallinity, coal rank and mineral facies as exemplified by Palaeozoic and Mesozoic rocks of Northeast Hungary. *Journal of Metamorphic Geology* **9**, 723-734.

Arkai, P., Merriman, R. J., Roberts, B., Peacor, D. R., Toth, M. & Ayora, C. 1996. Crystallinity, crystallite size and lattice strain of illite-muscovite and chlorite; comparison of XRD and TEM data for diagenetic to epizonal pelites. *European Journal of Mineralogy* **8**, 1119-1137.

Aubourg, C., Rochette, P. & Bergmueller, F. 1995. Composite magnetic fabric in weakly deformed black shales. *Physics of the Earth and Planetary Interiors* **87**, 267-278.

Avigad, D., Kolodner, K., McWilliams, M., Persing, H. & Weissbrod, T. 2003. Origin of northern Gondwana Cambrian sandstone revealed by detrital zircon SHRIMP dating. *Geology* **31**, 227-230.

Avigad, D., Sandler, A., Kolodner, K., Stern, R. J., McWilliams, M., Miller, N. & Beyth, M. 2005. Mass-production of Cambro-Ordovician quartz-rich sandstone as a consequence of chemical weathering of Pan-African terranes: Environmental implications. *Earth and Planetary Science Letters* **240**, 818-826.

Barshad, I. 1966. Factors affecting the frequency distribution of clay minerals in soils. *Clays and clay minerals - Natl. Conf., 14th, Berkeley, Calif. [1965], Proc.* **26**, 207.

Behr, H. J. 1989. Crustal Fluids in the Precambrian Basements and the Sedimentay Cover. In: *Niedersächsische Akademische Geowissenschaftliche Veröffentlichungen* **1**, 7-42.

Ben, A. Z. & Lazar, M. 2006. The structure and development of the Dead Sea basin; recent studies. In: *New frontiers in Dead Sea paleoenvironmental research.* (edited by Enzel, Y., Agnon, A. & Stein, M.). *Special Paper - Geological Society of America* **401**, 1-13.

Beyth, M., Longstaffe, F. J., Ayalon, A. & Matthews, A. 1997. Epigenetic alteration of the Precambrian igneous complex at Mount Timna, southern Israel; oxygen-isotope studies. *Israel Journal of Earth-Sciences* **46**, 1-11.

Bierlein, F. P. & Greiling, R. O. 1993. New constraints on the basal sole thrust at the eastern Caledonian margin in northern Sweden. *Geologiska Föreningens i Stockholm Förhandlingar* **115**, 109-116.

Bingen, B., Griffin, W. L., Torsvik, T. H. & Saeed, A. 2005. Timing of late Neoproterozoic glaciation on

Baltica constrained by detrital zircon geochronology in the Hedmark Group, South-east Norway. *Terra Nova* **17**, 250-258.

Blakey, R. 2007. Global Paleogeographic Views of Earth History - Late Precambrian to Recent. *http://jan.ucc.nau.edu/~rcb7/paleogeographic.html*.

Bleeker, W., Ketchum, J. W. F. & Davis, W. J. 1999. The Central Slave Basement Complex; Part II, Age and tectonic significance of high-strain zones along the basement-cover contact. *Canadian Journal of Earth Sciences = Revue Canadienne des Sciences de la Terre* **36**, 1111-1130.

Bobrov, Y. T. & Shchipakina, I. G. 1990. Changes in the mean K content of weathering-crust rocks as a function of age. *Geochemistry International* **27**, 34-41.

Bogoch, R., Avigad, D. & Weissbrod, T. 2002. Geochemistry of the quartz diorite-granite association, Roded area, southern Israel. *Journal of African Earth Sciences* **35**, 51-60.

Boivin, P., Schäffer, B., Temgoua, E., Gratier, M. & Steinman, G. 2005. Assessment of soil compaction using soil shrinkage modelling: Experimental data and perspectives. *Soil and Tillage Research* **88**, 65-79.

Bonijoly, M., Oberlin, M. & Oberlin, A. 1982. A possible mechanism for natural graphite formation. *International Journal of Coal Geology* **1**, 283-312.

Borradaile, G. & Sarvas, P. 1990. Magnetic susceptibility fabrics in slates: structural, mineralogical and lithological influences. *Tectonophysics* **172**, 215 - 222.

Borradaile, G. J. 1988. Magnetic susceptibiliy, petrofabrics and strain. *Tectonophysics* **156**, 1 - 20.

Borradaile, G. J. & Tarling, D. H. 1981. The influence of deformation mechanisms on magnetic fabrics in weakly deformed rocks. *Tectonophysics* **77**, 151 - 168.

Bourman, R. P., Milnes, A. R. & Oades, J. M. 1987. Investigations of ferricretes and related surficial ferruginous materials in parts of southern and eastern Australia. *Zeitschrift für Geomorphologie* **64**, 1-24.

Braendlein, P., Murray, H. H. & Rossner, R. 1994. Petrologie von Verwitterungsprofilen ueber praekambrischen Gesteinen aus dem Minnesota River Valley; Anzeichen einer mehrfachen meso- und kaenozoischen Alteration. *Erlanger Geologische Abhandlungen* **124**, 127-165.

Brasier, M. D. 1992. Global ocean-atmosphere change across the Precambrian-Cambrian transition. *Geological Magazine* **129**, 161-168.

Bronger, A. & Catt, J. A. (Editors), 1989. *Paleopedology: Nature and Application of Paleosoils*. In: *Catena Supplement* **16**, 1-232 p.

Brown, D. J., Helmke, P. A. & Clayton, M. K. 2003. Robust geochemical indices for redox and weathering on a granitic laterite landscape in central Uganda. *Geochimica et Cosmochimica Acta* **67**, 2711-2723.

Buchan, K. L., Mertanen, S., Park, R. G., Pesonen, L. J., Elming, S. A., Abrahamsen, N. & Bylund, G. 2000. Comparing the drift of Laurentia and Baltica in the Proterozoic; the importance of key palaeomagnetic poles. *Tectonophysics* **319**, 167-198.

Byerlee, J. 1978. Friction of rocks. In: *Rock friction and earthquake prediction* (edited by Byerlee, J. D. & Wyss, M.). *Pure and Applied Geophysics* **116**, 615-626.

Callot, J. P. & Guichet, X. 2003. Rock texture and magnetic lineation in dykes; a simple analytical model. *Tectonophysics* **366**, 207-222.

Cañon-Tapia, E. 2001. Factors affecting the relative importance of shape and distribution anisotropy in rocks; theory and experiments. *Tectonophysics* **340**, 117-131.

Carrière, K. 2006. *Neoproterozoic to Holocene tectonothermal evolution of the southern Cantabrian Mountains NW Iberia, as revealed by apatite fission-track thermochronology.* PhD Thesis, Ruprecht-Karls-Universität, Heidelberg, 289 p.

Cathelineau, M. 1988. The chlorite and illite geothermometers. In: *International congress of geochemistry and cosmochemistry.* (edited by Bottinga, Y.). *Chemical Geology* **70**, 182.

Caudill, M. R., Driese, S. G. & Mora, C. I. 1997. Physical compaction of vertic Palaeosols; implications for burial diagenesis and palaeo-precipitation estimates. *Sedimentology* **44**, 673-685.

Claesson, S. & Lundqvist, T. 1995. Origins and ages of Proterozoic granitoids in the Bothnian Basin, central Sweden; isotopic and geochemical constraints. *Lithos* **36**, 115-140.

Clark, D. A. 1984. Hysteresis properties of sized dispersed monoclinic pyrrhotite grains. In: *Rock magnetism.* (edited by Banerjee, S. K.). *Geophysical Research Letters* **11**, 173-176.

Comte, P. 1959. Recherches sur les terrains anciens de la Corillère Cantabrique. *Mem. Inst. Geol. Min. España* **60**, 440.

Coulomb, C. A. 1773. Sur une application des règles de Maximis et Minimis a quelques problèmes de statique relatifs à l'Architeture. *Academie Royale des Sciences Memoires de mathematique et de physique par divers savans* **7**, 343-382.

Craw, D. 1994. Contrasting alteration mineralogy at an unconformity beneath auriferous terrestrial sediments, central Otago, New Zealand. *Sedimentary Geology* **92**, 17 - 30.

Daly, L. & Henry, B. 1983. Separation d'anisotropies magnetiques composantes en vue d'applications a l'etude quantitative de la deformation des roches. *Comptes-Rendus des Seances de l'Academie des Sciences, Serie 2: Mecanique-Physique, Chimie, Sciences de l'Univers, Sciences de la Terre* **296**, 153-156.

Das, F. 1982. Geologic significance of laterite. *Bhu-Vidya* **40**, 23-24.

de Boer, C. B., Mullender, T. A. T. & Dekkers, M. J. 2001. Low-temperature behaviour of haematite; susceptibility and magnetization increase on cycling through the Morin transition. *Geophysical Journal International* **146**, 201-216.

de Caritat, P., Hutcheon, I. & Walshe, J. L. 1993. Chlorite geothermometry; a review. *Clays and Clay Minerals* **41**, 219-239.

de Sitter, L. U. 1962. The structure of the southern slope of the Cantabrian Mountains. *Leidse Geologische Mededelingen* **26**, 255-264.

de Wall, H. 2000a. The field-dependence of AC susceptibility in titanomagnetites; implications for the anisotropy of magnetic susceptibility. *Geophysical Research Letters* **27**, 2409-2411.

de Wall, H. 2000b. *Strukturgeologische und mineralogische Anwendungsmöglichkeiten von magnetischen Suszeptibilitätsmessungen.* Habilitationsschrift, Universität Heidelberg, 267 p.

de Wall, H., Bestmann, M. & Ullemeyer, K. 2000. Anisotropy of diamagnetic susceptibility in Thassos marble; a comparison between measured and modeled data. In: *Textures and physical properties of rocks.* (edited by Leiss, B., Ullemeyer, K. & Weber, K.). *Journal of Structural Geology* **22**, 1761-1771.

de Wall, H. & Worm, H. U. 1993. Field dependence of magnetic anisotropy in pyrrhotite; effects of texture and grain shape. In: *Magnetic characteristics of well defined samples.* (edited by Heider, F. & Moskovitz, B.). *Physics of the Earth and Planetary Interiors* **76**, 137-149.

Dearing, J. A., Hay, K. L., Baban, S. M. J., Huddleston, A. S., Wellington, E. M. H. & Loveland, P. J. 1996. Magnetic susceptibility of soil; an evaluation of conflicting theories using a national data set. *Geophysical Journal International* **127**, 728-734.

Debacker, T. N., Robion, P. & Sintubin, M. 2004. The anisotropy of magnetic susceptibility (AMS) in low-grade, cleaved pelitic rocks; influence of cleavage/ bedding angle and type and relative orientation of magnetic carriers. In: *Magnetic Fabric; Methods and Applications.* (edited by Martín-Hernández, F., Lueneburg, M., Aubourg, C. & Jackson, M.). *Geological Society of London, Special Publications* **238**, 77-107.

Deer, W. A., Howie, R. A. & Zussmann, J. 1966. *An introduction to the Rock Forming Minerals.* Longman, Essex, 528 p.

Dekkers, M. J. 1988. Some rockmagnetic parameters for natural goethite, pyrrhotite and fine-grained hematite. *Geologica Ultraiectina* **51**, 231.

Diaz Garcia, F. 2006. Geometry and regional significance of Neoproterozoic (Cadomian) structures of the Narcea Antiform, NW Spain. *Journal of the Geological Society of London* **163**, 499-508.

Dietzel, M. 2005. Impact of cyclic freezing on precipitation of silica in Me-SiO (sub 2) -H (sub 2) O systems and geochemical implications for cryosoils and sediments. *Chemical Geology* **216**, 79-88.

Dott Jr., R. H. 2003. The Importance of Eolian Abrasion in Supermature Quartz Sandstone and the Paradox of Weathering on Vegetation-Free Landscapes. *The Journal of Geology* **111**, 387-405.

Druckman, Y., Weissbrod, T. & Garfunkel, Z. 1993. *Geological map of Israel 1:100.000 sheet 25, 26 Yotvata and Elat.* Geological Survey of Israel, Jerusalem.

Dunlop, D. J. & Özdemir, Ö. 1997. *Rock Magnetism: Fundamentals and frontiers.* Cambridge University Press, Cambridge, 596 p.

Eggleton, R. A. & Banfield, J. F. 1985. The alteration of granitic biotite to chlorite. *American Mineralogist* **70**, 902-910.

Elming, S. A., Pesonen, L. J., Leino, M. A. H., Khramov, A. N., Mikhailova, N. P., Krasnova, A. F., Mertanen, S., Bylund, G. & Terho, M. 1993. The drift of the Fennoscandian and Ukrainian shields during the Precambrian; a palaeomagnetic analysis. *Tectonophysics* **223**, 177-198.

Elvhage, C. & Lidmar-Bergström, K. 1987. Some working hypotheses on the geomorphology of Sweden in the light of a new relief map. *Geografiska Annaler, Series A, Physical Geography* **69**, 343-358.

Essex, R. M. & Gromet, L. P. 2000. U-Pb dating of prograde and retrograde titanite growth during the Scandian Orogeny. *Geology* **28**, 419-422.

Essex, R. M., Gromet, L. P., Andreasson, P. G. & Albrecht, L. 1997. Early Ordovician U-Pb metamorphic ages of the eclogite-bearing Seve nappes, northern Scandinavian Caledonides. *Journal of Metamorphic Geology* **15**, 665-676.

Eyal, M., Eyal, Y., Bartov, Y. & Steinitz, G. 1981. The tectonic development of the western margin of the Gulf of Elat (Aqaba) Rift. *Tectonophysics* **80**, 39-66.

Fedo, C. M., Nesbitt, H. W. & Young, G. M. 1995. Unraveling the effects of potassium metasomatism in sedimentary rocks and Paleosols, with implications for paleoweathering conditions and provenance. *Geology* **23**, 921-924.

Fernández-Suárez, J., Gutiérrez-Alonso, G., Jenner, G.A. & Jackson, S.E. 1998. Geochronology and geochemestry of the Pola de Allende granitoids (NW Spain): their bearing on the Cadomian-Avalonian evolution of northwest Iberia. *Canadian Journal of Earth Sciences* **35**, 1 - 15.

Ferre, E. C. & Ameglio, L. 2000. Preserved magnetic fabrics vs. annealed microstructures in the syntectonic recrystallised George granite, South Africa. *Journal of Structural Geology* **22**, 1199-1219.

Firman, J. B. 1994. Paleosols in laterite and silcrete profiles: evidence from the south east margin of the Australian Precambrian shield. *Earth Science Reviews* **36**, 149-179.

Flehmig, W. & Langheinrich, G. 1974. Beziehung zwischen tektonischer Deformation und Illit-Kristallinitaet. The relationship between tectonic deformation and illite crystallinity. *Neues Jahrbuch fuer Geologie und Palaeontologie. Abhandlungen* **146**, 325-346.

Florindo, F., Roberts, A. P. & Palmer, M. R. 2003. Magnetite dissolution in siliceous sediments. *Geochemistry, Geophysics, Geosystems - G (super 3)* **4**, 1053.

Folk, R. L. 1980. *Petrology of sedimentary rocks.* Hemphill Publications Co., Austin, Texas, 184 p.

Foster, M. D. 1962. Interpretation of the composition and a classification of the chlorites. *U. S. Geological Survey Professional Paper, Report P 0414-A*, A1-A33.

Freyssinet, P. & Farah, A. S. 2000. Geochemical mass balance and weathering rates of ultramafic schists in Amazonia. In: *Laterites and paleoclimates; weathering processes and anthropogenic impact.* (edited by Probst, J. L., Chivas, A. R. & Wilson, J.). *Chemical Geology* **170**, 133-151.

Gaillot, P. J., de Saint-Blanquat, M. & Bouchez, J. L. 2006. Effects of magnetic interactions in anisotropy of magnetic susceptibility: Models, experiments and implications for igneous rock fabrics quantification. *Tectonophysics* **418**, 3-19.

Gaillot, P. J., de Saint Blanquat, M. & Bouchez, J. L. 2002. Numerical modelling of magnetic susceptibility in ferromagnetic rocks; the role of magnetic interactions. *Abstracts with Programs - Geological Society of America, 2002 annual meeting* **34**, 52.

Garfunkel, Z. 1980. Contribution to the geology of the Precambrian of the Elat area. *Israel Journal of Earth-Sciences* **29**, 25-40.

Garfunkel, Z. 1999. History and paleogeography during the Pan-African orogen to stable platform transition; reappraisal of the evidence from Elat area and the northern Arabian-Nubian Shield. *Israel Journal of Earth-Sciences* **48**, 135-157.

Garfunkel, Z. 2002. Early Paleozoic sediments of NE Africa and Arabia; products of continental-scale erosion, sediment transport, and deposition. *Israel Journal of Earth-Sciences* **51**, 135-156.

Garfunkel, Z. & Greiling, R. O. 1996. Influence of the geometry of orogenic loads on foreland basins; preliminary results. *Zeitschrift der Deutschen Geologischen Gesellschaft* **147**, 415-425.

Garfunkel, Z. & Greiling, R. O. 1998. A thin orogenic wedge upon thick foreland lithosphere and the missing foreland basin. *Geologische Rundschau* **87**, 314-325.

Gattacceca, J., Orsini, J. B., Bellot, J. P., Henry, B., Rochette, P., Rossi, P. & Cherchi, G. 2004. Magnetic fabric of granitoids from southern Corsica and northern Sardinia and implications for late Hercynian tectonic setting. *Journal of the Geological Society of London* **161**, 277-289.

Gee, D. G. 1978. Nappe displacement in the Scandinavian Caledonides. In: *Structural characteristics of tectonic zones.* (edited by Burns, L. & Rutland, R. W. R.). *Tectonophysics* **47**, Elsevier, Amsterdam, Netherlands, 393-419.

Gee, D. G. 1980. Basement-cover relationships in the central Scandinavian Caledonides. *Geologiska Foereningen i Stockholm Foerhandlingar* **102**, 455-474.

Gee, D. G., Karis, L., Kumpulainen, R. & Thelander, T. 1974. A summary of Caledonian front stratigraphy, northern Jamtland/ southern Vasterbotten, central Swedish Caledonides. *Geologiska Foereningen i Stockholm Foerhandlingar* **96**, 389-397.

Gee, D. G., Kumpulainen, R. & Thelander, T. 1978. *The Tåsjön Decollement, central Swedish Caledonides.* In: *Sveriges Geologiska Undersoekning, Serie C, Avhandlingar och Uppsatser.* Sveriges Geologiska Undersoekning, Uppsala, 35 p.

Gee, D. G., Snäll, S. & Stejskal, V. 1982. *Alunskifferprojektet, Prospekteringsrapport: Undersökningar mellan Östersund och Svenstavik.* Sveriges Geologiska Undersökning, Report, Uppsala, 48 p.

German, K., Fischer, K., Schwarz, T. & Wipki, M. 1996. Early Paleozoic lateritic weathering of Proterozoic basement rocks in the northwestern Sudan. *Travaux du Comite International pour l'Etude des Bauxites, de l'Alumine, et de l'Aluminium* **26**, 13-23.

Gleizes, G., Leblanc, D., Olivier, P. & Bouchez, J. L. 2001. Strain partitioning in a pluton during emplacement in transpressional regime; the example of the Neouvielle Granite (Pyrenees). *International Journal of Earth Sciences* **90**, 325-340.

Gleizes, G., Leblanc, D., Santana, V., Olivier, P. & Bouchez, J. L. 1998. Sigmoidal structures featuring dextral shear during emplacement of the Hercynian granite complex of Cauterets-Panticosa (Pyrenees). In: *Extraction, transport and emplacement of granitic magmas.* (edited by Benn, K., Cruden, R., Sawyer, W. & Evans, J. P.). *Journal of Structural Geology* **20**, 1229-1245.

Goldich, S. S. 1938. A study in rock weathering. *Journal of Geology* **46**, 17-58.

Grégoire, V., Darrozes, J., Gaillot, P., Nedelec, A. & Launeau, P. 1998. Magnetite grain shape fabric and distribution anisotropy vs rock magnetic fabric; a three-dimensional case study. *Journal of Structural Geology* **20**, 937-944.

Grégoire, V., de Saint Blanquat, M., Nedelec, A. & Bouchez, J.-L. 1995. Shape anisotropy versus magnetic interactions of magnetite grains; experiments and application to AMS in granitic rocks. *Geophysical Research Letters* **22**, 2765-2768.

Greiling, R. O., Garfunkel, Z. & Zachrisson, E. 1998. The orogenic wedge in the central Scandinavian Caledonides; Scandian structural evolution and possible influence on the foreland basin. *Geologiska Föreningens i Stockholm Förhandlingar (GFF)* **120**, 181-190.

Greiling, R. O., Garfunkel, Z. & Zachrisson, E. 1999a. Evolution of the orogenic wedge in the central Scandinavian Caledonides and its interaction with the foreland lithosphere; reply. *Geologiska Föreningens i Stockholm Förhandlingar (GFF)* **121**, 154.

Greiling, R. O., Gayer, R. A. & Stephens, M. B. 1993. A basement culmination in the Scandinavian Caledonides formed by antiformal stacking (Bangonaive, northern Sweden). *Geological Magazine* **130**, 471-482.

Greiling, R. O., Jensen, S. & Smith, A. G. 1999b. Vendian-Cambrian subsidence of the passive margin of western Baltica; application of new stratigraphic data from the Scandinavian Caledonian margin. *Norsk Geologisk Tidsskrift* **79**, 133-144.

Greiling, R. O. & Verma, P. K. 2000. Strike-slip tectonics and granitoid emplacement: an AMS fabric study from the Odenwald Crystalline Complex, SE-Germany. *Mineralogy and Petrology* **72**, 165-184.

Grimmer, J. O. W. 2000. *Fluidassoziierte Brekzien als Monitor dolomitisierender und dedolomitisierender Lösungsströme in der Kantabrischen Zone (Nord Spanien).* Inaugural-Dissertation, Ruprecht-Karls-Universität, Heidelberg, 148 p.

Gutiérrez-Alonso, G. 1992. *La Estructura del Antiforme del Narcea y su relacion con los Mantos Occidentales de la Zona Cantabrica.* Universidad de Oviedo, Oviedo, 321 p.

Gutiérrez-Alonso, G. 1996. Strain partitioning in the footwall of the Somiedo Nappe; structural evolution of Narcea tectonic window, NW Spain. *Journal of Structural Geology* **18**, 1217-1229.

Gutiérrez-Alonso, G., Blanco, J. A., Macfarlane, A. & Fernández-Suárez, J. 2004a. Paleometeorización vs. Paleoalteración en la superficie de discordancia Proterozoico-Cámbrico en el Antiforme del Narcea. *Geogaceta* **36**, 7-10.

Gutiérrez-Alonso, G., Fernández-Suárez, J. & Weil, A. B. 2004b. Orocline triggered lithospheric delamination. *GSA Special Paper* **383**, 121-130.

Gutiérrez-Alonso, G., Fernandez, S. J., Collins, A. S., Abad, I. & Nieto, F. 2005. Amazonian Mesoproterozoic basement in the core of the Ibero-Armorican Arc; (super 40) Ar/ (super 39) Ar detrital mica ages complement the zircon's tale. *Geology* **33**, 637-640.

Gutiérrez-Alonso, G., Fernandez, S. J., Jeffries, T. E., Jenner, G. A., Tubrett, M. N., Cox, R. & Jackson, S. E. 2003. Terrane accretion and dispersal in the northern Gondwana margin; an early Paleozoic analogue of a long-lived active margin. In: *Collisional orogenesis in the geological record and modern analogues.* (edited by Murphy, B. & Keppie, D.). *Tectonophysics* **365**, 212-232.

Gutierrez-Alonso, G. & Nieto, F. 1996. White-mica 'crystallinity', finite strain and cleavage developement across a large Variscan structure, NW Spain. *Journal of the Geological Society, London* **153**, 287 - 299.

Gutkin, V. & Eyal, Y. 1998. Geology and evolution of Precambrian rocks, Mt. Shelomo, Elat area. *Israel Journal of Earth-Sciences* **47**, 1-17.

Hamer, M., Graham, R. C., Amrhein, C. & Bozhilov, K. N. 2003. Dissolution of ripidolite (Mg, Fe-chlorite) in organic and inorganic acid solutions. *Soil Science Society of America Journal* **67**, 654-661.

Handin, J., Hager, R. V., Jr., Friedman, M. & Feather, J. N. 1963. Experimental deformation of sedimentary rocks under confining pressure; pore pressure tests. *Bulletin of the American Association of Petroleum Geologists* **47**, 717-755.

Hargraves, R. B., Johnson, D. & Chan, C. Y. 1991. Distribution anisotropy; the cause of AMS in igneous rocks? *Geophysical Research Letters* **18**, 2193-2196.

Harnois, L. 1988. The CIW index; a new chemical index of weathering. *Sedimentary Geology* **55**, 319-322.

Harrison, R. J. & Putnis, A. 1996. Magnetic properties of the magnetite-spinel solid solution: Curie temperatures, magnetic susceptibilities, and cation ordering. *American Mineralogist* **81**, 375-384.

Hartz, E. & Andresen, A. 1995. Caledonian sole thrust of central East Greenland; a crustal-scale Devonian extensional detachment? *Geology* **23**, 637-640.

Hartz, E., Andresen, A. & Andersen, T. B. 1994. Structural observations adjacent to a large-scale extensional detachment zone in the hinterland of the Norwegian Caledonides. In: *Terranes in the Arctic Caledonides, Lund, Sweden, Aug. 12-16, 1991* (edited by Andreasson, P.-G. & Andresen, A.). *Tectonophysics* **231**, 123-137.

Harvey, P. K. & Laxton, R. R. 1980. The estimation of finite strain from the orientation distribution of passively deformed linear markers; eigenvalue relationships. *Tectonophysics* **70**, 285-307.

Henry, B. 1988. The magnetic fabric of the Egleton granite (France): separation and structural implications. *Physics of the Earth and Planetary Interiors* **51**, 253-263.

Hirt, A. M., Lowrie, W., Julivert, M. & Arboleya, M. L. 1992. Paleomagnetic results in support of a model for the origin of the Asturian Arc. *Tectonophysics* **213**, 321-339.

Hölting, B. 1996. *Hydrogeologie. Einführung in die Allgemeine und Angewandte Hydrogeologie.* Enke, Stuttgart, 441 p.

Housen, B. A., Richter, C. & van der Pluijm, B. A. 1993. Composite magnetic anisotropy fabrics; experiments, numerical models, and implications for the quantification of rock fabrics. *Tectonophysics* **220**, 1-12.

Housen, B. A., Tobin, H. J., Labaume, P., Leitch, E. C., Maltman, A. J., Shipley, T., Ogawa, Y., Ashi, J., Blum, P., Brueckmann, W., Felice, F., Fisher, A., Goldberg, D., Henry, P., Jurado, M. J., Kastner, M., Laier, T., Meyer, A., Moore, J. C., Moore, G., Peacock, S., Rabaute, A., Steiger, T., Underwood, M., Xu, Y., Yin, H., Zheng, Y. & Zwart, G. 1996. Strain decoupling across the decollement of the Barbados accretionary prism. *Geology* **24**, 127-130.

Housen, B. A. & van der Pluijm, B. A. 1991. Slaty cleavage development and magnetic anisotropy fabrics. *Journal of Geophysical Research, B, Solid Earth and Planets* **96**, 9937-9946.

Hrouda, F. 2004. Problems in interpreting AMS parameters in diamagnetic rocks. In: *Magnetic fabric; Methods and Applications.* (edited by Martín-Hernández, F., Lueneburg, M., Aubourg, C. & Jackson, M.). *Geological Society of London, Special Publications* **238**, 49-59.

Hrouda, F., Jelinek, V., Pokorny, J. & Vejmelek, L. 2000. Field-dependence of low-field magnetic susceptibility and its effect on magnetic anisotropy. In: *AGU 2000 fall meeting. Eos, Transactions, American Geophysical Union* **81**, F372.

Hrouda, F. & Ježek, J. 1999a. Magnetic anisotropy indications of deformations associated with diagenesis. In: *Palaeomagnetism and diagenesis in sediments.* (edited by Tarling, D. H. & Turner, P.). *Geological Society of London, Special Publications* **151**, 127-137.

Hrouda, F. & Ježek, J. 1999b. Theoretical models for the relationship between magnetic anisotropy and strain: effect of triaxial magnetic grains. *Tectonophysics* **301**, 183 - 190.

Hrouda, F., Pokorny, J. & Quade, H. 1998. Magnetic anisotropy and low temperature susceptibility of hematite single crystals from Minas Gerais, Brazil. *AGU 1998 fall meeting.* **79**, 236.

Hunt, C. P., Moskowitz, B. M. & Banerjee, S. K. 1995. Magnetic properties of rocks and minerals. In: *Rock* *physics & phase relations; a handbook of physical constants.* (edited by Ahrens, T.). *AGU Reference Shelf* **3**, 189-204.

Hunziker, J. C., Frey, M., Clauer, N., Dallmeyer, R. D., Friedrichsen, H., Flehmig, W., Hochstrasser, K., Roggwiler, P. & Schwander, H. 1986. The evolution of illite to muscovite; mineralogical and isotopic data from the Glarus Alps, Switzerland. *Contributions to Mineralogy and Petrology* **92**, 157-180.

Hus, J. J. 2003. The magnetic fabric of some loess-Palaeosol deposits. In: *Paleo, rock and environmental magnetism 2002.* (edited by Petrovsky, E., Urbat, M. & von Dobeneck, T.). *Physics and Chemistry of the Earth* **28**, 689-699.

Isambert, A., Valet, J. P., Gloter, A. & Guyot, F. 2003. Stable Mn-magnetite derived from Mn-siderite by heating in air. *Journal of Geophysical Research, B, Solid Earth and Planets* **108**.

Jackson, M., Moskowitz, B. M., Rosenbaum, J. G. & Kissel, C. 1998. Field-dependence of AC susceptibility in titanomagnetites. *Earth and Planetary Science Letters* **157**, 129-139.

Jarrar, G. H., Wachendorf, H. & Zachmann, D. 1993. A Pan-African alkaline pluton intruding the Saramuj Conglomerate, South-west Jordan. *Geologische Rundschau* **82**, 121-135.

Jelinek, V. 1981. Characterization of the magnetic fabric of rocks. *Tectonophysics* **79**, T63-T67.

Jenny, H. 1994. *Factors of soil formation; a system of quantitative pedology.* Dover Publications, New York, 281 p.

Ji, J., Chen, J., Xu, H. & Chen, T. 2002. Chemical weathering of chlorite in the Chinese loess; Paleosol stratigraphy and climate change. *Abstracts with Programs - Geological Society of America Northeastern Section, 2002 annual meeting.* **34**, 353.

Julivert, M. 1971. Decollement tectonics in the Hercynian Cordillera of Northwest Spain. *American Journal of Science* **270**, 1-29.

Julivert, M. & Martínez-García, E. 1967. Sobre el contacto entre el Cambrico y el Precámbrico en la parte meridonal de la Cordillera y el papel del Precámbrico en la orognesis herciniana. *Acta Geologica de Hispaña* **2**, 107-110.

Just, J. 2005. *Modification of magnetic properties in granite during hydrothermal alteration (EPS-1 borehole, Upper Rhine Graben).* PhD Thesis, Ruprecht-Karls-Universität, Heidelberg, 92 p.

Just, J., Kontny, A., de Wall H., Hirt, A. M. & Martin, H. F. 2004. Development of magnetic fabrics during hydrothermal alteration in the Soultz-sous-Forets granite from the EPS-1 borehole, Upper Rhine Graben. In: *Magnetic Fabric; Methods and Applications.* (edited by Martín-Hernández, F., Lueneburg, M., Aubourg, C. & Jackson, M.). *Geological Society of London, Special Publications* **238**, 509-526.

Katz, O., Avigad, D., Matthews, A. & Heimann, A. 1998. Precambrian metamorphic evolution of the Arabian-Nubian Shield in the Roded area, southern Israel. *Israel Journal of Earth-Sciences* **47**, 93-110.

Keller, M. & Krumm, S. 1992. Evidence of an Upper Ordovician thermo-metamorphic event in the SW corner of the Cantabrian Mountains (N. Spain). *Estudios Geologicos (Madrid)* **48**, 289-296.

Keller, M. & Krumm, S. 1993. Variscan versus Caledonian and Precambrian metamorphic events in the Cantabrian Mountains, northern Spain. *Zeitschrift der Deutschen Geologischen Gesellschaft* **144**, 88-103.

Kisch, H. J. 1989. Discordant relationship between degree of very low-grade metamorphism and the development of slaty cleavage. In: *Evolution of metamorphic belts; proceedings of the 1987 joint meeting of the Metamorphic Studies Group and IGCP project 235.* (edited by Daly, S., Cliff, A. & Yardley, B. W. D.). *Geological Society of London, Special Publications* **43**, 173-185.

Kontny, A., de Wall, H., Sharp, T. G. & Posfai, M. 2000. Mineralogy and magnetic behavior of pyrrhotite from a 260 degrees C section at the KTB drilling site, Germany. *American Mineralogist* **85**, 1416-1427.

Kousa, J., Lukkarinen, H. & Lundqvist, T. 2000. Proterozoic crystalline rocks. In: *Description to the bedrock map of central Fennoscandia (Mid-Norden)* (edited by Lundqvist, T. & Autio, S.). *Special Paper - Geological Survey of Finland* **28**, 25-75.

Kruhl, J. H. 1996. Prism- and basal-plane parallel subgrain boundaries in quartz; a microstructural geothermobarometer. *Journal of Metamorphic Geology* **14**, 581-589.

Kübler, B. 1967. La cristallinite de l'illite et les zones tout a fait superieures du metamorphisme. In: *Etages tectoniques*. *Colloque de Neuchatel, 18-21 avril 1966*, 105-121.

Kumpulainen, R. & Nystuen, J. P. 1985. Late Proterozoic basin evolution and sedimentation in the westernmost part of Baltoscandia. In: *The Caledonide Orogen; Scandinavia and related areas* (edited by Gee, D. G.) **1**, 213-232.

Lagoeiro, L. E. 1998. Transformation of magnetite to hematite and its influence on the dissolution of iron oxide minerals. *Journal of Metamorphic Geology* **16**, 415-423.

Launeau, P. & Cruden, A. R. 1998. Magmatic fabric acquisition mechanisms in a syenite; results of a combined anisotropy of magnetic susceptibility and image analysis study. *Journal of Geophysical Research, B, Solid Earth and Planets* **103**, 5067-5089.

Launeau, P. & Robin, P. Y. F. 1996. Fabric analysis using the intercept method. *Tectonophysics* **267**, 91-119.

Launeau, P. & Robin, P. Y. F. 2005. Determination of fabric and strain ellipsoids from measured sectional ellipses; implementation and applications. *Journal of Structural Geology* **27**, 2223-2233.

Lindsley, D. H. 1991. Experimental studies of oxide minerals. In: *Oxide minerals; petrologic and magnetic significance.* (edited by Donald, L.). *Reviews in Mineralogy* **25**, 69-106.

Liu, X. M., Hesse, P., Beget, J. & Rolph, T. 2001. Pedogenic destruction of ferrimagnetics in Alaskan loess deposits. In: *Aeolian dust symposium.* (edited by Greene, R., Gatehouse, R. D., Scott, K. & Chen, L.). *Australian Journal of Soil Research* **39**, 99-115.

Liu, X. M., Rolph, T., An, Z. & Hesse, P. 2003. Paleoclimatic significance of magnetic properties on the red clay underlying the loess and Paleosols in China. *Palaeogeography, Palaeoclimatology, Palaeoecology* **199**, 153-166.

Llopis Lladó, N. & Martínez Álvarez, J. A. 1961. Reseña crítica del "Precámbrico de España" por F. Lotze. *Breviora Geológica Asturica* **V**, 48-51.

Llopis Lladó, N. & Torre, S. d. l. 1961. Sobre la existencia de una orogenia arcaica en el centro de España y sus relaciones con Asturias. *Breviora Geológica Asturica* **V**, 53.

Lotze, F. 1956. Das Präkambrium Spaniens. *Neues Jahrbuch für Geologie und Paläontologie, Monatsheft* **8**, 373 - 380.

Lotze, F., Carle, W. & Schmidt, T. P. 1945. *Zur Geologie der iberischen Meseta, I.* In: *Geotektonische Forschungen* **6**. Schweizerbart'sche Verlagsbuchhandlung, Stuttgart, 92 p.

Maher, B. A. 1998. Magnetic properties of modern soils and Quaternary loessic Paleosols; paleoclimatic implications. *Palaeogeography, Palaeoclimatology, Palaeoecology* **137**, 25-54.

Maher, B. A., Alekseev, A. & Alekseeva, T. 2003. Magnetic mineralogy of soils across the Russian Steppe; climatic dependence of pedogenic magnetite formation. *Palaeogeography, Palaeoclimatology, Palaeoecology* **201**, 321-341.

Marcos, A. 1973. Las series del Paleozoico inferior y la estructura herciniana del occidente de Asturias (NW de Espana). *Trabajos de Geologia de Universidad de Oviedo* **6**, 113.

Marioth, R. 2001. *Characterisierung und Quantifizierung thermischer und diagenetischer Prozesse im karbonischen Akkretionskeil in Nordchile.* Inaugural-Dissertation, Ruprecht-Karls-Universität, Heidelberg, 145 p.

Martin Parra, L. M. 1989. Mapa Geologico de Espana. Escala 1:50 000. 128 (Riello).

Martini, I. P. & Chesworth, W. 1992. Reflections on soils and Paleosols. In: *Weathering, soils & Paleosols.* (edited by Martini, P. & Chesworth, W.). *Developments in Earth Surface Processes* **2**, 3-16.

Mathe, P. E., Rochette, P., Collin, F. & Richter, A. K. 1997. The origin of magnetic susceptibility and its anisotropy in some weathered profiles. *Physics and Chemistry of the Earth* **22**, 183-187.

Mathe, P. E., Rochette, P., Vandamme, D. & Colin, F. 1999. Volumetric changes in weathered profiles; iso-element mass balance method questioned by magnetic fabric. *Earth and Planetary Science Letters* **167**, 255-267.

Mattsson, H. J. & Elming, S. A. 2001. Magnetic fabrics and paleomagnetism of the Storsjon-Edsbyn deformation zone, central Sweden. *Precambrian Research* **107**, 265-281.

McCrea, A. F., Anand, R. R. & Gilkes, R. J. 1990. Mineralogical and physical properties of lateritic pallid zone materials developed from granite and dolerite. *Geoderma* **47**, 33-57.

McFadden, L. D., Eppes, M. C., Gillespie, A. R. & Hallet, B. 2005. Physical weathering in arid landscapes due to diurnal variation in the direction of solar heating. *Geological Society of America Bulletin* **117**, 161-173.

Medaris, L. G., Jr., Singer, B. S., Dott, R. H., Jr., Naymark, A., Johnson, C. M. & Schott, R. C. 2003. Late Paleoproterozoic climate, tectonics, and metamorphism in the southern Lake Superior region and proto-North America; evidence from Baraboo interval quartzites. *Journal of Geology* **111**, 243-257.

Meschede, M. 1994. *Methoden der Strukturgeologie: Ein Leitfaden zur Aufnahme und Auswertung* *strukturgeologischer Daten im Gelände und Labor*. Ferdinand Enke Verlag, Stuttgart, 169 p.

Meunier, A. & Velde, B. 2004. *Illite: Origin, Evolution and Metamorphism.* Springer, Berlin, Heidelberg, New York, 286 p.

Middelburg, J. J., van der Weijden, C. H. & Woittiez, J. R. W. 1988. Chemical processes affecting the mobility of major, minor and trace elements during weathering of granitic rocks. *Chemical Geology* **68**, 253-273.

Middleton, M. F., Tullborg, E. L., Larson, S. A. & Bjorklund, L. 1996. Modelling of a Caledonian foreland basin in Sweden; petrophysical constraints. *Marine and Petroleum Geology* **13**, 407-413.

Migon, P. & Lidmar, B. K. 2001. Weathering mantles and their significance for geomorphological evolution of Central and Northern Europe since the Mesozoic. *Earth-Science Reviews* **56**, 285-324.

Molina, E., Garcia Talegon, J. & Vicente, M. A. 1994. Las paleoalteraciones sobre el zocalo hercinico-iberico; aproximacion a una interpretacion regional a partir de perfiles espanoles. The paleo-alterations on the Hercynian-Iberian basement; approximation of a regional interpretation using Spanish profiles. *Cuadernos do Laboratorio Xeoloxico de Laxe* **19**, 261-271.

Moore, D. M. & Reynolds, J., R.C. 1997. *X-Ray Diffraction and the Identification and Analysis of Clay Minerals.* Oxford University Press, 378 p.

Morrow, C. A., Moore, D. E. & Lockner, D. A. 2000. The effect of mineral bond strength and adsorbed water on fault gouge frictional strength. Geophysical Research Letters **27**, 815-818.

Nägler, T. F., Schaefer, H.-J. & Gebauer, D. 1995. Evolution of the western European continental crust; implications from Nd and Pb isotopes in Iberian sediments. *Chemical Geology* **121**, 345-357.

Nakamura, N. & Nagahama, H. 2001. Changes in magnetic and fractal properties of fractured granites near the Nojima Fault, Japan. *The Island Arc* **10**, 486-494.

Nesbitt, H. W. 1992. Diagenesis and metasomatism of weathering profiles, with emphasis on Precambrian Paleosols. In: *Weathering, soils & Paleosols* (edited by Martini, P. & Chesworth, W.). *Developments in Earth Surface Processes* **2**, 127-152.

Nesbitt, H. W. & Young, G. M. 1982. Early Proterozoic climates and plate motions inferred from major element chemistry of lutites. *Nature* **299**, 715-717.

Nesbitt, H. W. & Young, G. M. 1989. Formation and diagenesis of weathering profiles. *Journal of Geology* **97**, 129-147.

O'Reilly, W., Hoffmann, V., Chouker, A. C., Soffel, H. C. & Menyeh, A. 2000. Magnetic properties of synthetic analogues of pyrrhotite ore in the grain size range 1-24 µm. *Geophysical Journal International* **142**, 669-683.

Okudaira, T., Takeshita, T., Toriumi, M. & Kruhl, J. H. 1998. Prism- and basal-plane parallel subgrain boundaries in quartz; a microstructural geothermobarometer; discussion and reply. *Journal of Metamorphic Geology* **16**, 141-146.

Palacios, T. & Vidal, G. 1992. Lower Cambrian acritarchs from northern Spain; the Precambrian-Cambrian boundary and its biostratigraphic implications. *Geological Magazine* **129**, 421-436.

Pares, J. M. & Dinares-Turell, J. 1993. Magnetic fabric in two sedimentary rock-types from the southern Pyrenees. *Journal of Geomagnetism and Geoelectricity* **45**, 193-205.

Pares, J. M. & van der Pluijm, B. A. 2000. Is magnetic anisotropy a bulk strain gauge? *Abstracts with Programs - Geological Society of America* **32**, 97-98.

Pares, J. M. & van der Pluijm, B. A. 2002a. Evaluating magnetic lineations (AMS) in deformed rocks. *Tectonophysics* **350**, 283-298.

Pares, J. M. & van der Pluijm, B. A. 2002b. Phyllosilicate fabric characterization by low-temperature anisotropy of magnetic susceptibility (LT-AMS). *Geophysical Research Letters* **29**, 4.

Pares, J. M., van der Pluijm, B. A. & Dinaras-Turell, J. 1999. Evolution of magnetic fabrics during incipient deformation of mudrocks (Pyrenees, northern Spain). *Tectonophysics* **307**, 1-14.

Pares, J. M., van der Voo, R. & Stamatakos, J. 1994. Paleomagnetic results from Upper Permian and Triassic red beds of the Cantabrian Arc, Spain; implications for post-Variscan rotations in the arc. In: *AGU 1994 fall meeting. Eos, Transactions, American Geophysical Union* **75**, 199.

Passchier, C. W. & Trouw, R. A. J. 1996. *Microtectonics.* Springer, Berlin, Heidelberg, New York, 289 p.

Pérez-Estaún, A. 1971. La ventana tectonica de Villabandin (Antiforme del Narcea, Leon). *Brevioro Geologica Asturica* **XV**, 7-13.

Pérez-Estaún, A. 1973. Datos sobre la sucesion estratigrafica del Precambrico y la estructura del extremo sur del Antiforme del Narcea (NW de España). *Breviora Geológica Asturica* **XVII**, S. 367 - 375.

Pérez-Estaún, A. & Bastida, F. 1990. Cantabrian Zone. In: *Pre-Mesozoic geology of Iberia*. (edited by Dallmeyer, D. & Martinez, G.), Springer-Verlag, Berlin, Heidelberg, New York, 55-66.

Perez-Estaún, A., Bastida, F., Alonso, J.L., Marquinez, J., Aller, J., Alvarez-Marron, J., Marcos, A., Pulgar, J.A. 1988. A Thin-skinned Tectonics model for an arcuate Fold and Thrust belt: The Cantabrian Zone (Variscan Ibero-Amorican Arc). *Tectonics* **7**, 517 - 537.

Perez-Estaún, A., Martinez-Catalan, J.R. & Bastida, F. 1991. Crustal thickening and deformation sequences in the footwall to the suture of the Variscan belt of northwest Spain. *Tectonophysics* **191**, 243 - 253.

Pérez-Estaún, A. & Martinez, F. J. 1978. El Precambrico del Antiforme del Narcea en el sector de Tineo-Cangas de Narcea (NW de Espana). *Trabajos de Geologia de Universidad de Oviedo* **10**, 367 - 375.

Pérez-Estaún, A., Pulgar, J.A., Banda, E., Alvarez-Marrùn, J. & ESCI-N Research Group. 1994. Crustal structure of the external variscides in northwest Spain from deep seismic reflection profiling. *Tectonophysics* **232**, 91 - 118.

Pitcairn, I. K., Roberts, S., Teagle, D. A. H. & Craw, D. 2005. Detecting hydrothermal graphite deposition during metamorphism and gold mineralization. *Journal of the Geological Society of London* **162**, 429-432.

Platt, J. P. 1984. Secondary cleavages in ductile shear zones. *Journal of Structural Geology* **6**, 439 - 442.

Pokorny, J., Suza, P. & Hrouda, F. 2004. Anisotropy of magnetic susceptibility of rocks measured in variable weak magnetic fields using the KLY-4S Kappabridge. In: *Magnetic Fabric; Methods and Applications*. (edited by Martín-Hernández, F., Lueneburg, M., Aubourg, C. & Jackson, M.). *Geological Society of London, Special Publications* **238**, 69-76.

Potter, D. K., Corbett, P. W. M., Barclay, S. A. & Haszeldine, R. S. 2004. Quantification of illite content in sedimentary rocks using magnetic susceptibility; a rapid complement or alternative to X-ray diffraction. *Journal of Sedimentary Research* **74**, 730-735.

Price, J. R. & Velbel, M. A. 2002. Chemical weathering indices applied to weathering profiles developed on heterogenous felsic metamorphic parent rocks. *Chemical Geology* **202**, 397-416.

Pueyo, E. L., Roman, B. M. T., Bouchez, J. L., Casas, A. M. & Larrasoana, J. C. 2004. Statistical significance of magnetic fabric data in studies of paramagnetic granites. In: *Magnetic Fabric: Methods and Applications*. (edited by Martín-Hernández, F., Lueneburg, M., Aubourg, C. & Jackson, M.). *Geological Society of London, Special Publications* **238**, 395-420.

Raja, R. C. S. 2001. The geological control for formation of laterite in western Maharashtra. *Memoir - Geological Society of India*. **47**, 773-778.

Ramdohr, P. 1975. *Die Erzmineralien und ihre Verwachsungen*. Akademischer Verlag, Berlin, 1277 p.

Ramsay, J. G. & Huber, M. I. 1987. *The Techniques of Modern Structural Geology, Volume 1: Strain Analysis*. Academic Press, London, 307 p.

Rebertus, R. A., Weed, S. B. & Buol, S. W. 1986. Transformations of biotite to kaolinite during saprolite-soil weathering. *Soil Science Society of America Journal* **50**, 810-819.

Retallack, G. J. 1991. Untangling the effects of burial alteration and ancient soil formation. *Annual Review of Earth and Planetary sciences* **19**, 183-206.

Retallack, G. J., Sheldon, N. D., Cogoini, M. & Elmore, R. D. 2003. Magnetic susceptibility of early Paleozoic and Precambrian Paleosols. *Palaeogeography, Palaeoclimatology, Palaeoecology* **198**, 373-380.

Richard, G., Cousin, I., Sillon, J. F., Bruand, A. & Guerif, J. 2001. Effect of compaction on the porosity of a silty soil; influence on unsaturated hydraulic properties. *European Journal of Soil Science* **52**, 49-58.

Riller, U., Schwerdtner, W. M. & Robin, P. Y. F. 1998. Low-temperature deformation mechanisms at a lithotectonic interface near the Sudbury Basin, eastern Penokean Orogen, Canada. *Tectonophysics* **287**, 59-75.

Roberts, D. 2003. The Scandinavian Caledonides; event chronology, palaeogeographic settings and likely modern analogues. *Tectonophysics* **365**, 283-299.

Roberts, D. & Gee, D. G. 1985. An introduction to the structure of the Scandinavian Caledonides. In: *The Caledonide Orogen; Scandinavia and Related Areas* (edited by Gee, D. G. & Sturt, B. A.), John Wiley & Sons, Chichester, 55-68.

Roberts, D. & Stephens, M. B. 2000. Caledonian orogenic belt. In: *Description to the bedrock map of central Fennoscandia (Mid-Norden)*. (edited by Lundqvist, T. & Autio, S.). *Special Paper - Geological Survey of Finland, Espoo* **28**, 78-104.

Robin, P. Y. F. 2002. Determination of fabric and strain ellipsoids from measured sectional ellipses; theory.

Journal of Structural Geology **24**, 531-544.

Rowan, C. J. & Roberts, A. P. 2006. Magnetite dissolution, diachronous greigite formation, and secondary magnetizations from pyrite oxidation: Unravelling complex magnetizations in Neogene marine sediments from New Zealand. *Earth and Planetary Science Letters* **241**, 119-137.

Ruhe, R. V. 1956. Geomorphic surfaces and the nature of soils [Iowa]. *Soil Science* **82**, 441-455.

Saint-Bezar, B., Hebert, R. L., Aubourg, C., Robion, P., Swennen, R. & Frizon de Lamotte, D. 2002. Magnetic fabric and petrographic investigation of hematite-bearing sandstones within ramp-related folds; examples from the South Atlas Front (Morocco). *Journal of Structural Geology* **24**, 1507-1520.

Scholz, C. 1990. *The mechanics of earthquakes and faulting.* Cambridge University Press, Cambridge, 439 p.

Schönborn, G. S., M.E. 1994. Controls on thrust tectonics along basement-cover detachment. *Schweizerische Mineralogische Petrographische Mitteilungen* **74**, 421 - 436.

Sheldon, N. D. & Retallack, G. J. 2001. Equation for compaction of Paleosols due to burial. *Geology* **29**, 247-250.

Sitter, L. U. d. & Bosch, W. J. v. d. 1969. The structure of the SW part of the Cantabrian mountains (explanation of a provisional geological 1:100,000 scale map). *Leidse Geologische Mededelingen* **43**, 213-215.

Slack, J. F., Passchier, C. W. & Zhang, J. S. 1996. Metasomatic tourmalinite formation along basement-cover decollements, Orobic Alps, Italy. *Schweizerische Mineralogische und Petrographische Mitteilungen = Bulletin Suisse de Mineralogie et Petrographie* **76**, 193-207.

Smith, H. (Editor), 1999. *Soil Taxonomy: A Basic System of Soil Classification for Making and Interpreting Soil Surveys*. In: *Agriculture Handbook* **436**. Soil Survey Staff, United States Department of Agriculture, Natural Resources Conservation Service, 871 p.

Sobolev, S. V., Petrunin, A., Garfunkel, Z., Babeyko, A. Y. & Desert Group. 2005. Thermo-mechanical model of the Dead Sea Transform. *Earth and Planetary Science Letters* **238**, 78-95.

Stephens, C. G. 1946. Pedogenesis following the dissection of lateritic regions in southern Australia. *Bulletin of the Council for Scientific and Industrial Research - Australia, Commonwealth* **206**, 1-21.

Stephenson, A. 1994. Distribution anisotropy; two simple models for magnetic lineation and foliation. *Physics of the Earth and Planetary Interiors* **82**, 49-53.

Stern, R. J. 2002. Crustal evolution in the East African Orogen; a neodymium isotopic perspective. *Journal of African Earth Sciences (1994)* **34**, 109-117.

Subramanian, K. S. 2002. Laterites; an overview. *Memoir - Geological Society of India* **49**, 109-116.

Sutton, S. J. & Maynard, J. B. 1996. Basement unconformity control on alteration, St. Francois Mountains, SE Missouri. *Journal of Geology* **104**, 55-70.

Tardy, Y. 1971. Characterization of the principal weathering types by the geochemistry of waters from some European and African crystalline massifs. *Chemical Geology* **7**, 253-271.

Tardy, Y. 1992. Diversity and terminology of lateritic profiles. In: *Weathering, soils & Paleosols.* (edited by Martini, P. & Chesworth, W.). *Developments in Earth Surface Processes* **2**, Elsevier, Amsterdam-Oxford - New York - Tokyo, 379-405.

Tardy, Y. 1993. Climates, paleoclimates and world wide laterite distribution. In: *1993 SEPM meeting abstracts with program; Stratigraphic record of global change*, Society for Sedimentary Geology, United States, 28-29.

Tardy, Y., Boeglin, J. L., Novikoff, A. & Roquin, C. 1995. Petrological and geochemical classification of laterites. In: *Clays; controlling the environment.* (edited by Churchman, J., Fitzpatrick, W. & Eggleton, R. A.). *Proceedings of the International Clay Conference* **10**, Association Internationale pour l'Etude des Argiles, International, 481-486.

Tardy, Y., Trolard, F., Roquin, C. & Novikoff, A. 1990. Distribution of hydrated and dehydrated minerals in lateritic profiles and landscapes. *Geochemistry of the Earth's surface and of mineral formation. 2nd International Symposium* **84**, 133-136.

Tarling, D. H. & Hrouda, F. 1993. *The magnetic anisotropy of rocks.* Chapman & Hall, London, 217 p.

Taylor, G. & Eggleton, R. A. 2001. *Regolith geology and geomorphology.* John Wiley & Sons. Chichester, 375 p.

Tomezzoli, R. N., MacDonald, W. D. & Tickyj, H. 2003. Composite magnetic fabrics and S-C structure in granitic gneiss of Cerro de los Viejos, La Pampa province, Argentina. *Journal of Structural Geology* **25**, 159-169.

Torsvik, T. H., Smethurst, M. A., Meert, J. G., van der Voo, R., McKerrow, W. S., Brasier, M. D., Sturt, B.

A. & Walderhaug, H. J. 1996. Continental break-up and collision in the Neoproterozoic and Palaeozoic; a tale of Baltica and Laurentia. *Earth-Science Reviews* **40**, 229-258.

Tröger, W. E. 1969. *Optische Bestimmung der Gesteinsbildenden Minerale, Teil 2: Textband.* Schweizerbart'sche Verlagsbuchhandlung, Stuttgart, 822 p.

van den Bosch, W. J. 1969a. Geology of the Luna-Sil region, Cantabrian mountains (NW Spain). *Leidse Geologische Mededelingen* **44**, 137-225.

van den Bosch, W. J. 1969b. The relationship between orogenesis and sedimentation in the SW part of the Cantabrian mountains (NW Spain). *Leidse geologische Mededelingen* **44**, 227-233.

van der Voo, R., Stamatakos, J. A. & Pares, J. M. 1997. Kinematic constraints on thrust-belt curvature from syndeformational magnetizations in the Lagos del Valle Syncline in the Cantabrian Arc, Spain. *Journal of Geophysical Research, B, Solid Earth and Planets* **102**, 10105-10119.

van der Voo, R., van der Pluijm, B. A. & Weil, A. B. 2000. The evolution of the Cantabrian-Asturian orocline with implications for late Paleozoic Gondwana-Laurussia convergence. *Abstracts with Programs - Geological Society of America* **32**, 234.

van Houten, F. B. 1973. Origin of red beds: a review; 1961-1972. *Annual Review of Earth and Planetary Sciences* **1**, 39-61.

Vicente, M. A., Molina, E. & Espejo, R. 1991. Clays in paleoweathering processes; study of a typical weathering profile in the Hercynian basement in the Montes de Toledo (Spain). *Clay Minerals* **26**, 81-90.

Vidal, G. & Bylund, G. 1981. Late Precambrian boulder beds in the Visingsoe Beds, South Sweden. In: *Earth's pre-Pleistocene glacial record* (edited by Hambrey, J. & Harland, W. B.), Cambridge University Press, Cambridge, 629-631.

Vidal, G. & Moczydlowska, M. 1996. Vendian-Lower Cambrian acritarch biostratigraphy of the central Caledonian fold belt in Scandinavia and the palaeogeography of the Iapetus-Tornquist Seaway. *Norsk Geologisk Tidsskrift* **76**, 147-168.

Vidal, G., Palacios, T., Gámaz-Vintaned, J. A., Díez Balda, M. A. & Grant, S. W. F. 1994. Neoproterozoic-early Cambrian geology and palaeontology of Iberia. *Geological Magazine* **131**, 729-765.

Vidic, N. J., Singer, M. J. & Verosub, K. L. 2004. Duration dependence of magnetic susceptibility enhancement in the Chinese loess-Palaeosols of the past 620 ky. *Palaeogeography, Palaeoclimatology, Palaeoecology* **211**, 271-288.

Warr, L. N., Greiling, R. O. & Zachrisson, E. 1996. Thrust related very low grade metamorphism in the maginal part of an orogenic wedge, Scandinavian Caledonides. *Tectonics* **15**, 1213-1229.

Warr, L. N. & Marschik, R. 1996. The growth of illite in the Palaeozoic rocks of the Cantabrian Zone, NW Spain: Evidence for fluid activity? *Graduiertenkolleg 237 " Einwirkung fluider Phasen auf Locker- und Festgesteine", Symposium Poster.*

Warr, L. N. & Rice, A. H. N. 1994. Interlaboratory standardization and calibration of clay mineral crystallinity and crystallite size data. *Journal of Metamorphic Geology* **12**, 141-152.

Watson, A. 1992. Desert soils. In: *Weathering, soils & Paleosols.* (edited by Martini, P. & Chesworth, W.). *Developments in Earth Surface Processes* **2**, Elsevier, Amsterdam - Oxford - New York - Tokyo, 225-260.

Weaver, C. E. 1989. *Clays, muds, and shales.* In: *Developments in Sedimentology* **44**. Elsevier, Amsterdam-Oxford-New York, 819 p.

Weil, A. B., van der Voo, R. & van der Pluijm, B. A. 2000a. New paleomagnetic data from the southern Cantabria-Asturias Arc, northern Spain; implications for true oroclinal rotation and the final collisional adjustments within Pangea. In: *AGU 2000 fall meeting. Eos, Transactions, American Geophysical Union* **81**, 1237.

Weil, A. B., van der Voo, R. & van der Pluijm, B. A. 2001. Oroclinal bending and evidence against the Pangea megashear; the Cantabria-Asturias Arc (northern Spain). *Geology* **29**, 991-994.

Weil, A. B., van der Voo, R., van der Pluijm, B. A. & Pares, J. M. 2000b. The formation of an orocline by multiphase deformation; a paleomagnetic investigation of the Cantabria-Asturias Arc (northern Spain). *Journal of Structural Geology* **22**, 735-756.

West, A. J., Bickle, M. J., Collins, R. & Brasington, J. 2002. Small-catchment perspective on Himalayan weathering fluxes. *Geology* **30**, 355-358.

White, A. F. 1995. Chemical weathering rates of silicate minerals in soils. In: *Chemical weathering rates of silicate minerals.* (edited by White, A. F. & Brantley, S.). *Reviews in Mineralogy* **31**, 407-461.

White, A. F. & Brantley, S. L. (Editors), 1995a. *Chemical weathering rates of silicate minerals*. In: *Reviews in Mineralogy* **31**, 1-583 p.

White, A. F. & Brantley, S. L. 1995b. Chemical weathering rates of silicate minerals; an overview. In: *Chemical weathering rates of silicate minerals.* (edited by White, A. F. & Brantley, S.). *Reviews in Mineralogy* **31**, 1-22.

White, S. H. & Knipe, R. J. 1978. Transformation- and reaction-enhanced ductility in rocks. *Journal of the Geological Society of London* **135**, 513-516.

Wibberley, C. 1999. Are feldspar-to-mica reactions necessarily reaction-softening processes in fault zones? *Journal of Structural Geology* **21**, 1219-1227.

Willdén, M. Y. 1980. Paleoenvironment of the autochthonous sedimentary rock sequence at Laisvall, Swedish Caledonides. *Stockholm Contributions in Geology* **33**, 1-100.

Williams, E. L. & Walter, L. M. 2004. Controls on carbonate and silicate weathering fluxes in two forested watersheds, northern Michigan. *Abstracts with Programs - Geological Society of America, 2004 annual meeting.* **36**, 86.

Williams, E. L., Walter, L. M., Ku, T. C. W., Budai, J. M. & Kling, G. W. 2003. The weathering of silicate minerals in the glaciated Mid-Continent U. S.; results from natural and experimental field studies. *Abstracts with Programs - Geological Society of America, 2003 annual meeting.* **35**, 104.

Wimmenauer, W. 1985. *Petrographie der magmatischen und metamorphen Gesteine.* Enke, Stuttgart, 382 p.

Wintsch, R. P., Christofferson, R. & & Kronenberg, A. K. 1995. Fluid-rock reaction weakening of fault zones. *Journal of Geophysical Research* **100**, 13021 - 13032.

Wood, Y. A., Graham, R. C. & Wells, S. G. 2005. Surface control of desert pavement pedologic process and landscape function, Cima volcanic field, Mojave Desert, California. *Catena (Giessen)* **59**, 205-230.

Worm, H. U. 1991. Multidomain susceptibility and anomalously strong low field dependence of induced magnetization in pyrrhotite. *Physics of the Earth and Planetary Interiors* **69**, 112-118.

Worm, H. U. 1995. Frequency- and field-dependence of k-T curves for pyrrhotite. *International Union of Geodesy and Geophysics; XXI general assembly; abstracts.* **21**, 93.

Worm, H. U., Clark, D. & Dekkers, M. J. 1993. Magnetic susceptibility of pyrrhotite; grain size, field and frequency dependence. *Geophysical Journal International* **114**, 127-137.

Zane, A. & Weiss, Z. 1998. A procedure for classifying rock-forming chlorites based on microprobe data. *Atti della Accademia Nazionale dei Lincei. Rendiconti Lincei. Scienze Fisiche e Naturali* **9**, 51-56.

Ziegler, K. & Longstaffe, F. J. 2000. Multiple episodes of clay alteration at the Precambrian / Paleozoic unconformity, Appalachian Basin: Isotopic evidence for long-distance and local fluid migrations. *Clays and Clay Minerals* **48**, 474 - 493.

SYMBOLS, ABBREVIATIONS, EQUATIONS

Petrography

vol%	modal fraction in % of the total volume
D_1, D_2,...	first deformation, second deformation, ...
S_1, S_2...	foliation generated by first deformation
L_1, L_2...	lineation generated by first deformation
δ_1,.δ_2…	delta lineation (intersection lineation)
SPO, LPO	shape preferred orientation / lattice preferred orientation

Geochemistry & Mineralogy

wt%	concentration in % of the total mass
ICP-MS	Inductively-coupled-plasma mass-spectrometry
LOI	Lost on ignition (volatile substances)
CIA	Chemical index of alteration (Nesbitt & Young 1982)
	$CIA = [Al_2O_3/ (Al_2O_3+CaO+Na_2O+ K_2O)\cdot 100]$
CIW	Chemical index of weathering (Harnois 1988)
	$CIW = [Al_2O_3)/(Al_2O_3+CaO+Na_2O)\cdot 100]$
PIA	Plagioclase alteration index (Fedo et a. 1995)
	$PIA = [(Al_2O_3-K_2O)/(Al_2O_3+CaO+Na_2O-K_2O)\cdot 100]$
XRD	X-Ray Diffraction
EG	Ethylene-glycol
FWHM	Full Width at Half Maximum
I/S	Illite/smectite (mixed-layer mineral)
IC	Illite crystallinity
ChC	Chlorite crystallinity

Magnetic susceptibility

T_{Curie} [°C]	Curie temperature
T_{Morin} [°C]	temperature of Morin transition
T_{Vervey} [°C]	temperature of Vervey transition
$T_{Néel}$ [°C]	Néel temperature
κ_{bulk} [SI]	bulk rock magnetic susceptibility in SI unities
	$\kappa_{bulk} = c_f\kappa_f + c_p\kappa_p + c_d\kappa_d$ (after Daly & Henry 1983)
κ_1, κ_2, κ_3	principal susceptibility axes (maximum, intermediate and minimum)
P'	corrected anisotropy degree of the AMS ellipsoid (Jelinek 1981, Tarling & Hrouda 1993) (also referred to as *eccentricity*)
	$P' = exp\ [2(ln\ \kappa_{max} - ln\ \kappa_{bulk})^2 + 2(ln\ \kappa_{int} - ln\ \kappa_{bulk})^2 + 2(ln\ \kappa_{min} - ln\ \kappa_{bulk})^2]^{1/2}$
T	shape factor of the AMS ellipsoid (Jelinek 1981, Tarling & Hrouda 1993)
	$T = (2\ ln\ \kappa_{int} - ln\ \kappa_{max} - ln\ \kappa_{min})\ (ln\ \kappa_{max} - ln\ \kappa_{min})^{-1}$
κ_{Hd} [%]	field dependence parameter in percentage (de Wall 2000a)
	$\kappa_{Hd}\ [\%] = \frac{(\kappa_{300} - \kappa_{30})}{\kappa_{300}} \cdot 100$
$\kappa_{Hd}corr$ [%]	corrected field dependence parameter in percentage
	$\kappa_{HD}corr[\%] = \frac{\kappa_{300} - \kappa_{30}}{\kappa_{300} - c_M \cdot \kappa_M} \cdot 100$
P'_{Hd} [%]	anisotropy field dependence parameter in percentage analogue to κ_{Hd}
	$P'_{Hd}\ [\%] = \frac{(P'_{300} - P'_{30})}{P'_{300}} \cdot 100$

APPENDIX

I – Whole-rock geochemistry

  a. Negev, b. Långviken, c. Narcea Antiform

II – AMS (all κ values in 10^{-6})

  a. Negev, b. Hara, c. Långviken, d. Narcea Antiform

III – Microprobe

  a. Narcea Antiform

IV – XRD parameters

  a. Negev, b. Hara, c. Långviken, d. Narcea Antiform

V – Image analyses

  a. Negev

Whole-rock geochemistry

Israel

sample	distance	SD	WS	SiO2 [%]	Al2O3 [%]	Fe2O3 [%]	MgO [%]	CaO [%]	Na2O [%]	K2O [%]	TiO2 [%]	P2O5 [%]
RA3-1	50.0	micro-foliated	unweathered	73.19	13.36	2.43	0.86	1.44	4.1	2.34	0.43	0.14
RA3-1.ii	50.0	micro-foliated	unweathered	72.64	13.27	2.41	0.86	1.45	4.14	2.67	0.41	0.12
RA1-1A	14.5	foliated	moderately	64.96	14.06	2.9	1.16	4.16	5.08	1.56	0.58	0.19
RA1-2 (aplite)	9.5	cataclasite	moderately	66.72	13.97	1.99	1.41	2.21	4.04	4.29	0.32	0.1
RA1-3B	5.5	w-breccia	moderately	72.24	14.07	1.79	0.38	0.64	4.14	4.25	0.28	0.06
RA1-4B	5.0	w-breccia	moderately	75.75	12.75	1.17	0.24	0.88	3.03	4.6	0.22	0.04
RA1-5A	3.5	foliated	unweathered	68.77	14.99	1.91	0.74	1.59	3.48	5.21	0.35	0.08
RA1-6A	2.5	cataclasite	Saprolite	67.88	15.4	1.83	0.34	1.25	0.26	8.99	0.38	0.11
RA1-7	1.5	w-breccia	Saprolite	72.34	13.11	1.28	0.33	1.41	0.22	7.25	0.26	0.05
RA2-3	1.0	compacted	Laterite	58.53	17.49	6.42	1.98	0.74	0.03	6.88	1.04	0.36
RA2-1A	0.2	compacted	Laterite	51.24	21.03	8.62	2.01	0.9	0.09	5.95	1.41	0.52
STD SO-17/CSB				61.64	13.82	5.86	2.37	4.71	4.1	1.41	0.59	0.99

sample	MnO [%]	Cr2O3 [%]	Ba [ppm]	Ni [ppm]	Sc [ppm]	LOI [%]	TOT/C [%]	TOT/S [%]	SUM [%]
RA3-1	0.06	0.005	528.7	< 20	4	1.5	0.11	< .01	99.85
RA3-1.ii	0.06	0.004	558.3	< 20	4	1.2	0.1	< .01	99.24
RA1-1A	0.11	0.002	314.9	35	9	5.2	1.09	0.01	99.96
RA1-2 (aplite)	0.11	0.005	915.5	< 20	4	4.2	0.81	0.01	99.36
RA1-3B	0.04	0.002	1161.4	< 20	2	1.4	0.12	0.01	99.29
RA1-4B	0.02	< .001	695.2	< 20	2	1.3	0.09	0.01	100
RA1-5A	0.06	0.003	1204.5	< 20	4	2.3	0.33	0.01	99.49
RA1-6A	0.06	0.002	1151.5	< 20	4	3.2	0.26	0.02	99.71
RA1-7	0.07	0.003	983.1	< 20	2	3.5	0.32	< .01	99.82
RA2-3	0.06	< .001	706.3	< 20	14	6.6	0.01	< .01	100.14
RA2-1A	0.08	0.002	405.8	29	17	7.9	0.02	0.01	99.76
STD SO-17/CSB	0.53	0.441	395	35	23	3.4	2.4	5.39	99.87

sample	Mo [ppm]	Cu [ppm]	Pb [ppm]	Zn [ppm]	Ni [ppm]	As [ppm]	Cd [ppm]	Sb [ppm]	Bi [ppm]	Ag [ppm]	Au [ppm]	Hg [ppm]
RA3-1	0.3	12.2	2.6	60	3.7	0.6	< .1	0.1	< .1	0.1	1	< .01
RA3-1.ii	0.4	11.6	2.5	59	3.8	0.7	< .1	0.1	< .1	0.1	< .5	< .01
RA1-1A	0.2	4.4	1.6	32	3.3	< .5	< .1	0.2	< .1	< .1	< .5	< .01
RA1-2 (aplite)	0.3	2	2.1	26	2.4	< .5	< .1	< .1	0.1	< .1	0.7	0.02
RA1-3B	0.2	1.3	3.1	17	1.9	0.6	< .1	< .1	0.1	< .1	1.5	< .01
RA1-4B	0.2	2	1.5	8	1.1	0.5	< .1	0.1	0.1	< .1	0.5	< .01
RA1-5A	0.3	12.6	1.2	35	3.8	< .5	< .1	< .1	0.1	< .1	0.8	< .01
RA1-6A	0.3	13.7	2.6	8	2.6	1.8	< .1	0.1	0.2	< .1	< .5	0.02
RA1-7	0.4	13.3	3.5	10	2.5	2.2	0.1	< .1	< .1	< .1	0.5	< .01
RA2-3	0.1	3.3	14.4	12	3.3	7.2	< .1	0.1	0.1	0.1	< .5	< .01
RA2-1A	0.1	5.2	8.3	67	12.2	6.6	< .1	0.3	0.1	0.2	< .5	< .01
STD SO-17/CSB	12.4	140.6	24.1	139	23.3	17.8	5.8	3.5	6	0.3	42	0.17

I.a – Whole-rock geochemistry – Israel

sample	Tl [ppm]	Se [ppm]	Be [ppm]	Co [ppm]	Cs [ppm]	Ga [ppm]	Hf [ppm]	Nb [ppm]	Rb [ppm]	Sn [ppm]	Sr [ppm]	Ta [ppm]
RA3-1	< .1	< .5	3	63.3	2	16.3	4.7	8	63.9	2	261.4	1.2
RA3-1.ii	< .1	< .5	3	73.4	2.1	19.6	5.6	8.8	72.6	3	299.5	1.1
RA1-1A	< .1	< .5	1	31.1	2.3	19.6	4.5	7.7	58.8	2	132.8	0.5
RA1-2 (aplite)	< .1	< .5	< 1	54.3	2.2	16.9	4.1	6.8	98.3	3	274	0.7
RA1-3B	< .1	< .5	3	31.8	5.8	16	2.9	4.5	101.4	< 1	234.5	0.6
RA1-4B	< .1	< .5	3	40.2	3.2	15.1	3.1	5.9	100.3	1	260.6	0.6
RA1-5A	< .1	< .5	3	36.3	2.5	20.2	4.8	6.8	103.7	2	357.2	0.6
RA1-6A	< .1	< .5	1	27.6	3.2	19	4.8	6.6	186.4	1	121.7	0.6
RA1-7	< .1	< .5	< 1	20.1	3.5	16.3	4.1	4.3	160.8	< 1	125.7	0.4
RA2-3	0.1	< .5	4	20.3	17.2	24.6	7.4	10.8	211.4	3	103.1	0.7
RA2-1A	0.3	< .5	4	19.3	29.3	34.8	7.7	11.1	263.4	2	37.6	0.6
STD SO-17/CSB	1	4.6	1	17.9	3.8	19.1	13.3	24.9	24.4	11	308.7	4.3

sample	Th [ppm]	U [ppm]	V [ppm]	W [ppm]	Zr [ppm]	Y [ppm]	La [ppm]	Ce [ppm]	Pr [ppm]	Nd [ppm]	Sm [ppm]	Eu [ppm]
RA3-1	6.3	1.5	25	963.3	125.8	13	28.7	55.4	6.03	20.3	3.3	0.76
RA3-1.ii	10	1.3	30	1088.6	173.9	14.6	33.8	61.9	6.39	21.3	3.3	0.8
RA1-1A	3.5	1.4	60	336.6	171.1	15.9	29.5	54.7	6.65	25.6	4.6	1.12
RA1-2 (aplite)	7.4	1.1	29	728.1	110.4	13.9	23.9	45.5	5.22	19.4	3.3	0.79
RA1-3B	1.5	0.5	20	435.5	87.6	4.3	9.1	17.3	2.02	7.5	1.6	0.42
RA1-4B	7.2	0.8	14	500.2	85.5	11.7	9.1	18.9	2.04	8.5	1.4	0.39
RA1-5A	3.1	1.4	28	470.1	145.7	12.8	18.3	35.8	4.02	17.1	3.1	0.68
RA1-6A	3.7	1.4	35	343.4	143.8	9.8	6	13.5	1.46	5.7	1.2	0.36
RA1-7	3.7	1.3	31	217.3	128.1	6.9	6.1	19.8	2.02	7.8	1.7	0.36
RA2-3	2	2.4	54	67.8	250	10.9	11.8	43.2	3.69	14.6	3.1	0.67
RA2-1A	1.7	3.1	82	41.6	268.7	12.8	11.5	39.7	2.95	13.9	3.4	0.68
STD SO-17/CSB	13.2	10.9	132	11	363.7	28.8	10.7	23.7	3.05	13.7	3.2	1.05

sample	Gd [ppm]	Tb [ppm]	Dy [ppm]	Ho [ppm]	Er [ppm]	Tm [ppm]	Yb [ppm]	Lu [ppm]
RA3-1	2.64	0.38	2.24	0.37	1.14	0.16	1.17	0.16
RA3-1.ii	2.59	0.41	2.59	0.42	1.3	0.18	1.38	0.23
RA1-1A	4.2	0.48	2.84	0.54	1.24	0.21	1.33	0.24
RA1-2 (aplite)	2.69	0.36	2.64	0.41	1.24	0.16	1.37	0.21
RA1-3B	1.16	0.14	0.78	0.1	0.38	0.07	0.43	0.06
RA1-4B	1.59	0.26	1.98	0.34	1.04	0.18	1	0.2
RA1-5A	2.49	0.33	2.19	0.4	1.14	0.17	0.89	0.17
RA1-6A	1.89	0.23	1.85	0.38	1.11	0.21	1.14	0.21
RA1-7	1.53	0.26	1.5	0.24	0.67	0.12	0.82	0.12
RA2-3	2.6	0.35	2.03	0.36	1.11	0.18	1.15	0.2
RA2-1A	3.6	0.43	2.44	0.44	1.18	0.15	1	0.17
STD SO-17/CSB	3.83	0.66	4.32	0.95	2.8	0.44	2.92	0.42

calculations

sample	**Porosity**	**bulk density [g/cm3]**	**solid density [g/cm3]**	**R_{0_Loss}**	**R_{0_Gain}**	**ε (Al2O3)**	**ε (TiO2)**	**ε (Hf)**	**CIA**	**CIW**	**PIA**
RA3-1	0.04	2.46	2.56	1.00	1.00	**1**	**1**	1	62.9	70.7	66.5
RA3-1.ii	--	--	--	--	--	--	--	--	--	--	--
RA1-1A	0.08	2.53	2.72	0.95	1.11	**0.92**	**0.72**	**1.02**	56.6	60.3	57.5
RA1-2 (aplite)	0.14	2.41	2.75	1.08	1.20	**0.98**	**1.37**	**1.17**	57	69.1	60.8
RA1-3B	0.27	2.46	3.12	1.58	1.55	**0.95**	**1.54**	**1.62**	60.9	74.6	67.3
RA1-4B	0.08	2.47	2.67	1.56	1.29	**1.04**	**1.95**	**1.51**	60	76.5	67.6
RA1-5A	0.27	2.49	3.16	0.93	1.05	**0.88**	**1.21**	**0.97**	59.3	74.7	65.9
RA1-6A	0.07	2.4	2.56	0.87	1.04	**0.89**	**1.16**	**1.00**	59.5	91.1	80.9
RA1-7	0.27	2.32	2.95	1.11	1.03	**1.08**	**1.75**	**1.22**	59.6	88.9	78.2
RA2-3	*0.43*	2.25	*3.31*	0.46	0.96	**0.84**	**0.45**	**0.68**	69.6	95.8	93.2
RA2-1A	0.24	2.32	2.94	0.37	1.10	**0.67**	**0.32**	**0.63**	75.2	95.5	93.8
STD SO-17/CSB	--	--	--	--	--	--	--	--	--	--	--

Langviken

sample	unit	lithology	distance	SiO2 [%]	Al2O3 [%]	Fe2O3 [%]	MgO [%]	CaO [%]	Na2O [%]	K2O [%]	TiO2 [%]	P2O5 [%]	MnO
ST-1	autoch.cover	quartz conglomerate	-0.5	52.05	12.92	0.91	0.39	13.45	2.19	6.01	0.61	0.62	0.08
ST-2	au.basement	low-k granite	0.07	71.56	15.83	1.14	0.55	0.66	1.61	6.73	0.34	0.15	0.01
ST-4	au.basement	low-k granite	0.56	71.19	12.34	2.06	0.5	3.88	2.47	4.21	0.23	0.08	0.05
ST-7	au.basement	low-k granite	2.3	71.49	14.57	1.33	0.37	1.36	3.88	5.38	0.32	0.13	0.02
ST-13	au.basement	high-k granite	20.93	70.31	14.58	3.3	0.79	1.89	4.36	3.3	0.4	0.15	0.06
ST-15	au.basement	high-k granite	28.86	70.69	14.53	2.69	0.78	1.85	3.64	4.6	0.34	0.13	0.05
st-aa	allocht.cover	conglom, weak catals.	-0.5	73.57	14.5	1.09	0.29	0.92	0.29	6.58	0.28	0.05	0.02
st-a	all.basement	weak cataclasite	0.16	71.34	15.59	1.34	0.35	1.19	0.7	6.63	0.51	0.07	0.03
st-e	all.basement	moderate caraclasite	3.02	73.23	13.39	0.73	0.17	2.51	3.5	4.34	0.17	0.02	0.03
st-h	all.basement	moderate cataclasite	6.21	72.15	13.76	2.31	0.36	1.12	3.29	5.42	0.31	0.08	0.03
st-j	all.basement	intense cataclasite	7.08	72.34	15.52	0.64	0.41	0.71	2.79	6.14	0.37	0.16	0.01
STANDARD SO-18/CSB				58.03	14.35	7.65	3.34	6.37	3.82	2.13	0.71	0.84	0.37

sample	Cr2O3	Ba ppm	Ni ppm	Sr ppm	Zr ppm	Y ppm	Nb ppm	Sc ppm	LOI	TOT/C	TOT/S	SUM
ST-1	0.001	1701	8	225	326	30	14	6	10.6	3.13	0.04	100.1
ST-2	0.001	1054	6	107	235	30	15	5	1.5	0.11	0.04	100.26
ST-4	0.001	572	5	133	185	25	6	5	3.1	0.88	0.45	100.22
ST-7	0.001	818	5	181	202	25	10	4	1.4	0.28	0.01	100.4
ST-13	0.001	460	14	271	218	44	13	6	1.1	0.12	0.01	100.37
ST-15	0.001	677	38	342	211	29	10	5	0.9	0.05	0.01	100.35
st-aa	0.001	1005	18	62	374	57	11	6	2.5	0.73	0.2	100.28
st-a	0.001	926	47	86	441	102	13	9	2.3	0.27	0.04	100.25
st-e	0.001	541	5	117	127	34	7	3	2.2	0.54	0.07	100.39
st-h	0.001	897	5	139	251	26	10	5	1.4	0.36	0.12	100.4
st-j	0.001	896	9	157	220	30	19	6	1	0.12	0.02	100.25
STANDARD SO-18/CSB	0.557	533	40	421	283	32	24	24	1.9	2.39	5.33	100.24

calculations **sample**	**CIA**	**CIW**	**PIA**	**Fe_2O_3/S**
ST-1	37.4	45.2	30.6	22.75
ST-2	63.8	87.5	80	28.5
ST-4	53.9	66	56.1	4.58
ST-7	57.8	73.5	63.7	133
ST-13	60.4	70	64.3	330
ST-15	59	72.6	64.4	269
st-aa	65.1	92.3	86.7	5.45
st-a	64.7	89.2	82.6	33.5
st-e	56.4	69	60.1	10.43
st-h	58.3	75.7	65.4	19.25
st-j	61.7	81.6	72.8	32
STANDARD SO-18/CSB	--	--	--	

Narcea Antiform

sample	outcrop	distance	Fm.	lithology	farbe	SiO2 [%]	Al2O3 [%]	Fe2O3 [%]	MgO [%]	CaO [%]	Na2O [%]	K2O [%]	TiO2 [%]
MH2-3 (altered)	MH2	0.5	Mora	siltstone, alterated	green	75.19	12.79	2.3	0.65	0.02	0.03	3.95	0.69
MH2-2a	MH2	1.5	Mora	siltstone	red	66.46	15.6	6.49	1.65	0.17	0.04	4.46	0.77
MH2-6	MH2	3	Mora	siltstone	red	70.05	11.97	7.92	1.38	0.21	0.04	3.17	0.65
MH2-4	MH2	7	Mora	siltstone	red	64.36	15.92	7.86	1.81	0.09	0.05	4.49	0.68
MH4-1	MH4	-1	Herrería	greywacke	green	69.33	14.93	4.08	1.55	0.06	0.05	4.76	0.82
MH4-3	MH4	1	Mora	siltstone	green	58.36	18.64	6.56	2.12	0.22	0.03	5.56	0.75
MH4-6	MH4	11	Mora	siltstone	red	63.37	17.19	6.48	2.14	0.22	0.06	4.98	0.63
MH4-7	MH4	25	Mora	shale	green	61.13	18.02	6.29	2.44	0.4	2.04	3.55	0.74
MH5-2	MH5	-1.5	Herrería	greywacke	green	70.2	14.71	3.37	1.57	0.07	0.03	5.41	0.74
MH5-1.I	MH5	-0.1	am	lithic quartz arenite	gray	90.57	3.44	1.62	0.4	0.06	0.09	1.22	0.15
MH5-1.II	MH5	-0.1	Herrería	lithic quartz arenite	gray	91.38	3.58	1.43	0.44	0.1	0.08	1.15	0.18
MH5-1.avg	*MH5*	*-0.1*	*Herrería*	*lithic quartz arenite*	*gray*	*90.975*	*3.51*	*1.525*	*0.42*	*0.08*	*0.085*	*1.185*	*0.165*
MH5-3a	MH5	0.2	Mora	siltstone	green	58.07	20.36	5.66	2.23	0.33	0.03	6.65	0.87
MH5-4	MH5	1	Mora	siltstone	red	59.51	17.67	8.59	2.16	0.29	0.02	5.75	0.8
MH5-5a	MH5	2	Mora	siltstone	red	66.57	13.16	8.18	2.17	0.34	0.02	4.02	0.77
MH5-6	MH5	5	Mora	siltstone	red	68.99	12.66	7.04	2.05	0.36	0.02	3.93	0.85
MH5-7.I	MH5	10	Mora	greywacke	red	69.53	14.29	5.11	1.73	0.18	0.72	4.02	0.66
MH5-7.II	MH5	10	Mora	greywacke	red	67.4	14.93	5.68	1.94	0.2	0.39	4.35	0.74
MH5-7.avg	*MH5*	*10*	*Mora*	*greywacke*	*red*	*68.465*	*14.61*	*5.395*	*1.835*	*0.19*	*0.555*	*4.185*	*0.7*
MH5-8.I	MH5	30	Mora	fine greywacke	green	69.5	14.88	3.99	1.52	0.43	2.54	2.85	0.74
MH5-8.II	MH5	30	Mora	fine greywacke	green	70.06	14.78	3.98	1.52	0.35	2.51	2.83	0.72
MH5-8.avg	*MH5*	*30*	*Mora*	*fine greywacke*	*green*	*69.78*	*14.83*	*3.985*	*1.52*	*0.39*	*2.525*	*2.84*	*0.73*
MH6-2	MH6	-1.5	Herrería	sandstone, carb.	gray	82.01	5.85	3.37	1.24	0.97	0.07	2.17	0.24
MH6-3	MH6	0.3	Mora	greywacke	red	69.03	13.81	6.3	0.78	0.02	0.05	4.93	0.6
MH7-1	MH7	-3	Herrería	microcongl.	red	73.72	12.72	4.47	0.7	0.02	0.04	4.07	0.53
MH7-5	MH7	3	Mora	greywacke	red	66.64	14.55	6.01	1.74	0.09	0.61	4.07	1.23
MH7-8.I	MH7	25	Mora	greywacke	green	74.32	12.33	3.59	1.21	0.15	2.79	1.51	0.56
MH7-8.II	MH7	25	Mora	greywacke	green	67.45	14.81	5.81	1.79	0.09	2.04	2.16	0.74
MH7-8.avg	*MH7*	*25*	*Mora*	*greywacke*	*green*	*70.885*	*13.57*	*4.7*	*1.5*	*0.12*	*2.415*	*1.835*	*0.65*
MH8-1.I	MH8	-0.5	Herrería	microcongl.	gray	86.3	6.24	2.45	0.33	0.01	0.04	2.04	0.26
MH8-1.II	MH8	-0.5	Herrería	microcongl.	gray	86.5	6.17	2.45	0.33	0.02	0.04	2	0.26
MH8-1.avg	*MH8*	*-0.5*	*Herrería*	*microcongl.*	*gray*	*86.4*	*6.205*	*2.45*	*0.33*	*0.015*	*0.04*	*2.02*	*0.26*
MH8-2	MH8	-0.1	Herrería	microcongl.	gray	81.82	7.79	4.12	0.53	0.01	0.04	2.54	0.3
MH8-5	MH8	8	Mora	siltstone	red	69.99	13.97	5.68	1.02	0.01	0.05	4.68	0.8
STANDARD SO-17/CSB						61.45	13.8	5.89	2.35	4.66	4.17	1.41	0.59

I.c – Whole-rock geochemistry – Narcea Antiform

sample	**P2O5 [%]**	**MnO [%]**	**Cr2O3 [%]**	**Ba [ppm]**	**Ni [ppm]**	**Sc [ppm]**	**LOI [%]**	**TOT/C [%]**	**TOT/S [%]**	**SUM [%]**
MH2-3 (altered)	0.13	< .01	0.011	530	< 20	12	4	0.26	0.04	99.82
MH2-2a	0.17	0.01	0.012	426	33	16	4	0.15	< .01	99.89
MH2-6	0.19	0.01	0.01	449	49	11	4.2	0.17	< .01	99.85
MH2-4	0.13	0.02	0.012	499	40	15	4.4	0.12	0.01	99.88
MH4-1	0.07	0.01	0.009	805	37	14	4.1	0.09	< .01	99.86
MH4-3	0.17	0.01	0.011	1299	33	16	7.3	0.11	< .01	99.89
MH4-6	0.11	0.01	0.012	649	34	15	4.6	0.12	0.01	99.88
MH4-7	0.18	0.03	0.011	665	41	16	5	0.21	0.01	99.91
MH5-2	0.09	0.01	0.01	451	47	14	3.5	0.09	< .01	99.77
MH5-1.I	0.06	0.03	0.003	174	21	4	1.8	0.1	< .01	99.47
MH5-1.II	0.08	0.02	0.003	151	< 20	4	1.1	0.06	< .01	99.56
MH5-1.avg	*0.07*	*0.025*	*0.003*	*162.5*	*21*	*4*	*1.45*	*0.08*	< .01	*99.515*
MH5-3a	0.34	0.01	0.013	616	64	20	5.3	0.14	0.02	99.95
MH5-4	0.28	0.01	0.012	485	51	18	4.8	0.07	< .01	99.95
MH5-5a	0.29	0.02	0.011	351	50	12	4.3	0.19	< .01	99.89
MH5-6	0.31	0.02	0.015	329	40	11	3.6	0.07	0.01	99.88
MH5-7.I	0.16	0.02	0.01	483	36	10	3.3	0.1	< .01	99.79
MH5-7.II	0.18	0.02	0.011	496	38	12	4	0.18	< .01	99.9
MH5-7.avg	*0.17*	*0.02*	*0.0105*	*489.5*	*37*	*11*	*3.65*	*0.14*	< .01	*99.845*
MH5-8.I	0.15	0.03	0.011	1016	28	12	3	0.09	0.03	99.75
MH5-8.II	0.16	0.02	0.011	1203	27	11	2.8	0.05	0.03	99.88
MH5-8.avg	*0.155*	*0.025*	*0.011*	*1109.5*	*27.5*	*11.5*	*2.9*	*0.07*	*0.03*	*99.815*
MH6-2	0.1	0.08	0.002	216	< 20	6	3.6	0.82	0.01	99.73
MH6-3	0.07	0.01	0.01	586	< 20	13	4.2	0.49	0.08	99.88
MH7-1	0.02	0.01	0.005	253	< 20	10	3.6	0.17	< .01	99.93
MH7-5	0.16	0.04	0.016	343	37	16	4.6	0.04	< .01	99.8
MH7-8.I	0.12	0.03	0.007	259	23	10	3.2	0.22	0.01	99.85
MH7-8.II	0.14	0.05	0.009	356	31	13	4.8	0.27	< .01	99.92
MH7-8.avg	*0.13*	*0.04*	*0.008*	*307.5*	*27*	*11.5*	*4*	*0.245*	*0.01*	*99.885*
MH8-1.I	0.07	< .01	0.002	525	< 20	5	1.9	0.03	0.01	99.7
MH8-1.II	0.08	< .01	0.002	526	< 20	5	1.8	0.04	0.02	99.71
MH8-1.avg	*0.075*	< .01	*0.002*	*525.5*	< 20	*5*	*1.85*	*0.035*	*0.015*	*99.705*
MH8-2	0.06	0.01	0.003	1493	< 20	6	2.4	0.04	0.04	99.79
MH8-5	0.07	< .01	0.009	202	32	12	3.6	0.04	< .01	99.91
STANDARD SO-17/CSB	1	0.52	0.436	394	36	23	3.4	2.41	5.29	99.73

I.c – Whole-rock geochemistry – Narcea Antiform

sample	**Mo [ppm]**	**Cu [ppm]**	**Pb [ppm]**	**Zn [ppm]**	**Ni [ppm]**	**As [ppm]**	**Cd [ppm]**	**Sb [ppm]**	**Bi [ppm]**	**Ag [ppm]**	**Au [ppm]**	**Hg [ppm]**	**Tl [ppm]**
MH2-3 (altered)	0.2	1.4	1.8	2	1.3	18.1	< .1	1.2	0.1	< .1	1.8	5.9	< .1
MH2-2a	0.1	1.1	2	48	43.6	0.7	< .1	4.2	0.1	0.4	< .5	0.28	< .1
MH2-6	0.2	1	1.2	74	57.2	0.5	< .1	2.5	0.1	< .1	28.9	0.3	< .1
MH2-4	0.2	64.1	3.1	69	44	0.8	< .1	5.8	0.1	0.1	2.8	0.09	0.1
MH4-1	0.1	68.7	3.7	36	28.3	5.8	< .1	1	0.8	< .1	1.5	0.07	0.1
MH4-3	< .1	3	1.9	51	36.3	0.9	< .1	1.2	0.2	< .1	1.3	0.02	0.1
MH4-6	0.1	1.2	1.9	50	33.8	< .5	< .1	1.3	0.1	< .1	2.9	0.05	0.1
MH4-7	0.2	28.4	8.2	54	41.5	9.8	< .1	1.5	0.3	0.1	0.6	0.07	0.1
MH5-2	0.2	15.1	1.3	35	39.1	3.3	< .1	1	0.5	< .1	2.7	0.01	0.1
MH5-1.I	0.7	14.4	1.1	11	12.3	1.5	< .1	0.9	0.2	< .1	4.3	< .01	< .1
MH5-1.II	0.6	11.3	0.8	13	13.4	1.5	< .1	0.6	0.2	< .1	1.9	0.02	< .1
MH5-1.avg	*0.65*	*12.85*	*0.95*	*12*	*12.85*	*1.5*	< .1	*0.75*	*0.2*	< .1	*3.1*	*0.02*	< .1
MH5-3a	0.1	45.6	2.7	39	39.4	10.6	< .1	1.7	1.5	< .1	< .5	0.02	0.1
MH5-4	0.2	2.1	10.7	43	44.9	3.5	< .1	12.6	0.4	< .1	0.9	0.01	0.1
MH5-5a	0.2	1.6	6.4	61	51.7	2.3	< .1	8	0.2	0.1	1.5	0.02	0.1
MH5-6	0.2	2.2	4.3	55	44.6	2.1	< .1	4.4	0.1	< .1	1	0.01	0.1
MH5-7.I	0.2	1.2	1.4	45	31.4	0.9	< .1	1.9	0.1	< .1	1	0.01	0.1
MH5-7.II	0.2	1.2	1.4	49	35.9	0.8	< .1	1.6	0.1	< .1	0.6	< .01	< .1
MH5-7.avg	*0.2*	*1.2*	*1.4*	*47*	*33.65*	*0.85*	< .1	*1.75*	*0.1*	< .1	*0.8*	*0.01*	*0.1*
MH5-8.I	0.2	11.8	1.4	39	31.2	3.6	< .1	0.5	0.1	< .1	2.6	< .01	< .1
MH5-8.II	0.2	14.9	1.3	43	31.5	3.9	< .1	0.4	0.1	< .1	2.4	< .01	< .1
MH5-8.avg	*0.2*	*13.35*	*1.35*	*41*	*31.35*	*3.75*	< .1	*0.45*	*0.1*	< .1	*2.5*	< .01	< .1
MH6-2	0.3	6.5	0.8	16	8.4	1.1	< .1	0.6	< .1	0.1	2.3	0.03	< .1
MH6-3	0.5	29.2	5.9	13	9.9	23.4	< .1	3.6	0.2	0.1	12.7	0.47	0.1
MH7-1	0.3	1.3	3.2	4	1.4	1.7	< .1	1.6	0.1	< .1	1.7	< .01	< .1
MH7-5	< .1	1.8	1.4	53	37	0.6	< .1	0.8	0.1	< .1	1.8	0.03	0.1
MH7-8.I	0.3	92.4	4.8	28	25.3	15.6	< .1	0.5	0.1	0.1	1.7	0.05	< .1
MH7-8.II	0.3	147.7	5.3	43	37.5	17.8	< .1	0.9	0.1	0.1	2.1	0.06	< .1
MH7-8.avg	*0.3*	*120.05*	*5.05*	*35.5*	*31.4*	*16.7*	< .1	*0.7*	*0.1*	*0.1*	*1.9*	*0.055*	< .1
MH8-1.I	0.4	11.3	1.1	15	2.2	0.8	< .1	0.3	< .1	< .1	1	0.05	< .1
MH8-1.II	0.4	11.1	1.1	15	2	0.9	< .1	0.3	< .1	< .1	2.3	0.05	< .1
MH8-1.avg	*0.4*	*11.2*	*1.1*	*15*	*2.1*	*0.85*	< .1	*0.3*	< .1	< .1	*1.65*	*0.05*	< .1
MH8-2	0.3	6.9	2	39	6.3	1.4	< .1	0.7	0.1	< .1	1.4	< .01	< .1
MH8-5	0.1	21.1	4.4	27	7.8	1.8	< .1	1	0.1	< .1	2.1	0.02	0.1
STANDARD SO-17/CSB	12.2	141.1	23.5	138	24.7	18.8	5.2	3.7	5.7	0.3	41.5	0.16	0.9

sample	**Se [ppm]**	**Co [ppm]**	**Cs [ppm]**	**Ga [ppm]**	**Hf [ppm]**	**Nb [ppm]**	**Rb [ppm]**	**Sn [ppm]**	**Sr [ppm]**	**Ta [ppm]**	**Th [ppm]**	**U [ppm]**	**V [ppm]**
MH2-3 (altered)	< .5	107.1	13	18.2	6.6	10.1	158.4	2	42	0.8	8.2	2.3	99
MH2-2a	< .5	116.7	15.3	21.2	7	11.3	189.1	2	23.5	0.8	11.8	3.7	118
MH2-6	< .5	149	13.2	15	5.5	8.7	124.7	2	21.3	0.7	8.2	2.6	80
MH2-4	< .5	112.1	15	21.1	5	9.5	184.6	3	18.3	0.8	10.9	3.2	123
MH4-1	< .5	56.8	19.6	20.3	7.2	15.4	191.4	9	22.9	1.2	14.7	3.4	86
MH4-3	< .5	53.7	22	27.7	8.7	39	230.9	5	16.5	2.2	17.6	5.2	110
MH4-6	< .5	81.6	21.1	23.5	4.8	9.8	202.7	3	16.7	0.8	10.8	3.4	114
MH4-7	< .5	73.5	11.2	24	5	11.7	140.6	3	63.4	0.9	14.2	3.1	107
MH5-2	< .5	34.3	21.8	20.4	6.3	12.5	181.3	6	23.3	1.2	12.1	3.7	76
MH5-1.I	< .5	131	5.9	4.5	1.9	2.8	41.8	3	10.1	1.1	3.1	1	15
MH5-1.II	< .5	124.3	5.7	4.5	1.9	3.5	42.6	2	13.3	1.2	3.3	0.9	16
MH5-1.avg	< .5	*127.65*	*5.8*	*4.5*	*1.9*	*3.15*	*42.2*	*2.5*	*11.7*	*1.15*	*3.2*	*0.95*	*15.5*
MH5-3a	< .5	15.2	34	30.5	5.7	14	253.3	4	14.5	1.1	13	5.8	123
MH5-4	< .5	16.2	28.9	24.6	5.4	12.4	214.8	3	16.8	0.9	12.1	3.7	109
MH5-5a	< .5	27.2	19.8	17.7	6.1	11.7	147.9	3	21.8	0.9	11.1	2.8	73
MH5-6	< .5	36.2	19.8	17.1	11.9	12.6	147	3	20.2	1	12	3	74
MH5-7.I	< .5	36.4	17.3	16.5	5.7	9.5	127.5	2	28.2	0.8	10	2.3	66
MH5-7.II	< .5	34.6	18.4	18.5	7.1	11.1	147.8	3	22.5	0.9	9.7	2.5	78
MH5-7.avg	*< .5*	*35.5*	*17.85*	*17.5*	*6.4*	*10.3*	*137.65*	*2.5*	*25.35*	*0.85*	*9.85*	*2.4*	*72*
MH5-8.I	< .5	30.2	6.6	18.8	7.8	10.5	97.8	4	113.5	1	11.2	2.8	79
MH5-8.II	< .5	29	6.5	19	7.4	10.6	94.6	2	104.6	0.9	11	2.5	77
MH5-8.avg	*< .5*	*29.6*	*6.55*	*18.9*	*7.6*	*10.55*	*96.2*	*3*	*109.05*	*0.95*	*11.1*	*2.65*	*78*
MH6-2	< .5	82.8	8.8	7.8	3	5.6	68.8	2	55.3	1	5.3	2.1	31
MH6-3	< .5	26.7	16.1	19.1	4.9	9.5	168.5	2	78.7	0.8	8	2.8	74
MH7-1	< .5	22.4	7.2	15.1	6	8.4	138.7	4	9.2	0.8	10.7	2.3	56
MH7-5	< .5	33.1	8.8	20.1	14.2	16.4	114	3	20.1	1.2	18.6	3.5	131
MH7-8.I	< .5	28	1.7	14.1	4.2	7.6	44.4	2	140.6	0.8	8.6	2	60
MH7-8.II	< .5	20.2	2.9	18.4	4.8	10.8	71.8	5	88.5	0.9	8.4	2.5	85
MH7-8.avg	*< .5*	*24.1*	*2.3*	*16.25*	*4.5*	*9.2*	*58.1*	*3.5*	*114.55*	*0.85*	*8.5*	*2.25*	*72.5*
MH8-1.I	< .5	72.1	3.7	7	3.2	5.1	69.5	2	36.6	1	6.2	2.1	32
MH8-1.II	< .5	80.6	4.6	7	3.9	5.8	75.7	2	40.7	1	7	2.1	33
MH8-1.avg	*< .5*	*76.35*	*4.15*	*7*	*3.55*	*5.45*	*72.6*	*2*	*38.65*	*1*	*6.6*	*2.1*	*32.5*
MH8-2	< .5	56.3	8.7	9.7	4.5	6.5	96.5	3	54.5	0.9	8.3	2.4	33
MH8-5	< .5	19.4	35.7	19	6.1	12.1	194.4	4	32.6	0.9	11.3	3.4	79
STANDARD SO-17/CSB	4.9	18.9	3.7	19.1	12	24.7	22.4	11	306	4.3	11.8	11.3	125

sample	**W [ppm]**	**Zr [ppm]**	**Y [ppm]**	**La [ppm]**	**Ce [ppm]**	**Pr [ppm]**	**Nd [ppm]**	**Sm [ppm]**	**Eu [ppm]**	**Gd [ppm]**	**Tb [ppm]**	**Dy [ppm]**	**Ho [ppm]**
MH2-3 (altered)	568.5	194.7	28.6	22.5	47.5	5.76	23.1	4.5	0.98	4.28	0.64	3.96	0.83
MH2-2a	229.7	216.5	40.4	37.5	79.4	9.26	37.6	7.4	1.31	6.78	1.12	6.37	1.09
MH2-6	527.8	182	27.2	20.9	43.9	5.03	21	5.2	1.06	4.92	0.74	4.08	0.76
MH2-4	247.6	164.4	27.7	31.2	64.9	7.53	29.8	5.5	0.99	4.73	0.75	4.28	0.88
MH4-1	275.5	238.1	37	35.2	70	8.39	35.9	5.6	1.2	5.63	0.98	5.57	1.09
MH4-3	74.5	302	54.7	42.3	85.4	10.01	44.4	8.5	1.67	8.28	1.42	8.02	1.64
MH4-6	144	149.1	31.7	30	64.6	7.75	33.7	6.3	1.08	5.26	0.84	5.04	0.94
MH4-7	189.8	154.7	27.8	33.8	70.3	8.39	31.9	5.4	1.11	4.75	0.85	4.67	0.95
MH5-2	450.5	218.4	31.7	37.1	81.6	8.67	32.7	6.4	1.12	5.1	0.83	5.04	0.97
MH5-1.I	1760.3	57.6	11.6	16.9	36	3.98	14.9	3.1	0.6	2.4	0.42	2.09	0.4
MH5-1.II	1855.9	54.6	12.7	23.4	50.9	5.77	22.9	3.8	0.73	2.99	0.44	2.21	0.41
MH5-1.avg	*1808.1*	*56.1*	*12.15*	*20.15*	*43.45*	*4.875*	*18.9*	*3.45*	*0.665*	*2.695*	*0.43*	*2.15*	*0.405*
MH5-3a	30.3	187.3	55.7	26.5	61	7.6	32.8	8	1.84	9.04	1.52	8.71	1.67
MH5-4	35.6	174.7	45.5	33.6	72.9	8.82	37.1	8.8	1.67	7.99	1.34	7.6	1.41
MH5-5a	125.4	204.1	39.1	47.4	101.4	11.65	43.6	9.7	2.06	8.31	1.22	6.62	1.14
MH5-6	244.9	432.9	24.6	44.5	92.9	9.66	38.4	7.5	1.61	5.82	0.8	4.36	0.81
MH5-7.I	339.4	200.3	23.7	26.4	57.2	6.48	25.4	5.3	1.09	4.54	0.72	3.92	0.78
MH5-7.II	294.6	245.7	29.7	33	70.5	7.89	29.9	5.9	1.38	5.31	0.83	4.4	0.77
MH5-7.avg	*317*	*223*	*26.7*	*29.7*	*63.85*	*7.185*	*27.65*	*5.6*	*1.235*	*4.925*	*0.775*	*4.16*	*0.775*
MH5-8.I	339.4	259.7	31.4	33.8	72.4	8.37	34.1	6.6	1.32	5.67	0.9	4.74	0.89
MH5-8.II	291.7	238.8	28.1	35.1	76.2	8.58	33.2	6.6	1.24	5.32	0.88	4.84	0.88
MH5-8.avg	*315.55*	*249.25*	*29.75*	*34.45*	*74.3*	*8.475*	*33.65*	*6.6*	*1.28*	*5.495*	*0.89*	*4.79*	*0.885*
MH6-2	1047.7	94.5	25.7	15.4	34.8	4.18	16.9	3.9	0.81	3.95	0.75	4.03	0.79
MH6-3	268.2	155.2	23.9	39.3	71	7.14	24.6	4.7	0.94	3.39	0.57	3.41	0.75
MH7-1	246.8	170.1	35.7	36.1	74.9	8.4	32.7	6.4	1.04	5.48	1.04	5.6	1.03
MH7-5	263	479.2	28.4	33.4	79.2	8.83	35	6.1	1.24	5.09	0.84	4.84	0.89
MH7-8.I	434.4	130.4	22.8	21.9	48.2	5.84	23.1	4.5	1.11	3.91	0.62	3.66	0.64
MH7-8.II	166.1	159.7	28.3	27.4	59.4	6.83	28.7	5.3	1.3	4.52	0.79	4.42	0.87
MH7-8.avg	*300.25*	*145.05*	*25.55*	*24.65*	*53.8*	*6.335*	*25.9*	*4.9*	*1.205*	*4.215*	*0.705*	*4.04*	*0.755*
MH8-1.I	1200.8	96.4	25.1	19.6	46.1	5.16	21	4	0.73	3.71	0.72	3.64	0.75
MH8-1.II	1286.5	109.1	27	21.6	48.7	5.47	23.6	3.8	0.65	3.81	0.68	4.21	0.77
MH8-1.avg	*1243.65*	*102.75*	*26.05*	*20.6*	*47.4*	*5.315*	*22.3*	*3.9*	*0.69*	*3.76*	*0.7*	*3.925*	*0.76*
MH8-2	773.2	133.1	31.6	19.9	46.4	5.4	23.4	4.2	0.72	4.37	0.81	4.49	0.9
MH8-5	136	200.5	39	29.4	63.1	6.97	31.4	5.8	1.24	6.14	1.02	6.08	1.16
STANDARD SO-17/CSB	10.6	351	26.8	10	23.6	3.02	13.4	3.2	1.02	3.85	0.64	4.23	0.88

sample	**Er [ppm]**	**Tm [ppm]**	**Yb [ppm]**	**Lu [ppm]**	**LOG(Fe2O3/K2O)**	**LOG(SiO2/Al2O3)**	**CIA**	**CIW**	**PIA**
MH2-3 (altered)	2.57	0.39	2.82	0.37	-0.2	0.8	76.2	99.6	99.4
MH2-2a	3.33	0.47	3.44	0.49	0.2	0.6	77	98.7	98.1
MH2-6	2.27	0.32	2.39	0.34	0.4	0.8	77.8	98	97.2
MH2-4	2.83	0.38	2.74	0.45	0.2	0.6	77.5	99.1	98.8
MH4-1	3.34	0.47	3.53	0.49	-0.1	0.7	75.4	99.3	98.9
MH4-3	4.8	0.7	5.37	0.68	0.1	0.5	76.2	98.7	98.1
MH4-6	2.98	0.41	3.21	0.44	0.1	0.6	76.6	98.4	97.8
MH4-7	2.7	0.42	2.81	0.42	0.2	0.5	75.1	88.1	85.6
MH5-2	2.97	0.45	3.5	0.52	-0.2	0.7	72.7	99.3	98.9
MH5-1.I	1.03	0.18	0.94	0.16	0.1	1.4	71.5	95.8	93.7
MH5-1.II	1.08	0.16	1.02	0.17	0.1	1.4	72.9	95.2	93.1
MH5-1.avg	*1.055*	*0.17*	*0.98*	*0.165*	0.1	1.4	72.2	95.5	93.4
MH5-3a	5.19	0.73	4.96	0.68	-0.1	0.5	74.4	98.3	97.4
MH5-4	3.86	0.51	3.62	0.54	0.2	0.5	74.5	98.3	97.5
MH5-5a	2.98	0.4	3.11	0.46	0.3	0.7	75	97.3	96.2
MH5-6	2.35	0.35	2.42	0.36	0.3	0.7	74.6	97.1	95.8
MH5-7.I	2.26	0.31	2.49	0.33	0.1	0.7	74.4	94.1	91.9
MH5-7.II	2.48	0.41	2.64	0.38	0.1	0.7	75.1	96.2	94.7
MH5-7.avg	*2.37*	*0.36*	*2.565*	*0.355*	0.1	0.7	74.8	95.1	93.3
MH5-8.I	2.65	0.36	2.63	0.4	0.1	0.7	71.9	83.4	80.2
MH5-8.II	2.53	0.35	2.52	0.36	0.1	0.7	72.2	83.8	80.7
MH5-8.avg	*2.59*	*0.355*	*2.575*	*0.38*	0.1	0.7	72	83.6	80.4
MH6-2	2.15	0.33	2.08	0.32	0.2	1.1	64.6	84.9	78
MH6-3	2.08	0.3	2.18	0.32	0.1	0.7	73.4	99.5	99.2
MH7-1	3.24	0.45	3.14	0.46	0	0.8	75.5	99.5	99.3
MH7-5	2.92	0.42	3.39	0.48	0.2	0.7	75.3	95.4	93.7
MH7-8.I	2.06	0.28	2.1	0.27	0.4	0.8	73.5	80.7	78.6
MH7-8.II	2.64	0.36	2.66	0.37	0.4	0.7	77.5	87.4	85.6
MH7-8.avg	*2.35*	*0.32*	*2.38*	*0.32*	0.4	0.7	75.6	84.3	82.2
MH8-1.I	2.27	0.31	2.37	0.32	0.1	1.1	74.9	99.2	98.8
MH8-1.II	2.38	0.33	2.52	0.36	0.1	1.1	75	99	98.6
MH8-1.avg	*2.325*	*0.32*	*2.445*	*0.34*	0.1	1.1	74.9	99.1	98.7
MH8-2	2.63	0.4	3.02	0.39	0.2	1	75	99.4	99.1
MH8-5	3.55	0.47	3.82	0.56	0.1	0.7	74.7	99.6	99.4
STANDARD SO-17/CSB	2.77	0.4	2.93	0.42					

AMS

Israel

specimen	sample	lithology	ams type	distance	k_{bulk} 10^{-6}	k1	k2	k3	L	F	P	P'	T	U	dK1 geo	iK1 geo	dK2 geo	iK2 geo	dK3 geo	iK3 geo
RA3-1_I	RA3-1	granite	0	50	1650	1691	1668	1590	1.014	1.049	1.063	1.067	0.557	0.546	97	12.6	300.4	76.3	188.2	5.3
RA3-1_II	RA3-1	granite	0	50	1291	1324	1295	1252	1.022	1.035	1.058	1.059	0.216	0.203	87.4	34.9	269	55.1	177.9	0.7
RA3-1_III	RA3-1	granite	0	50	2092	2183	2096	1996	1.041	1.05	1.094	1.094	0.092	0.07	87.6	22.9	331.3	46.4	194.7	34.7
RA3-1_IV	RA3-1	granite	1	50	629	641.4	629.2	617	1.019	1.02	1.04	1.04	0.016	0.006	16.2	27.5	272.3	24.8	146.9	51.5
RA3-1_V	RA3-1	granite	0	50	2810	2883	2839	2709	1.016	1.048	1.064	1.067	0.506	0.495	284.5	5	17.8	33.1	186.9	56.4
RA3-1_VI	RA3-1	granite	1	50	608	627.3	599.1	598	1.047	1.003	1.05	1.056	-0.893	-0.895	208.9	4.3	115.7	36.4	304.7	53.3
RA1-1A_I	RA1-1A	fol granite	1	14.5	457	471.7	458.7	442	1.028	1.039	1.068	1.068	0.153	0.137	239.1	31.9	350.7	30.6	113.9	42.7
RA1-1A_II	RA1-1A	fol granite	1	14.5	573	603.4	573.1	542	1.053	1.057	1.112	1.112	0.034	0.007	250.6	48.3	356.7	13.9	98	38.3
RA1-1A_III	RA1-1A	fol granite	1	14.5	672	708.3	667.3	641	1.061	1.04	1.104	1.105	-0.201	-0.225	250.7	55.9	21.1	23.7	121.8	23
RA1-1A_IV	RA1-1A	fol granite	1	14.5	225	229.6	226.4	219	1.015	1.032	1.047	1.048	0.367	0.358	236.3	40.5	30.3	46.5	134.7	13.3
RA1-1A_V	RA1-1A	fol granite	1	14.5	501	520.8	504.9	477	1.031	1.058	1.091	1.093	0.292	0.272	253.3	40.1	4.3	23.1	116.1	41.1
RA1-1B_I	RA1-1B	fol granite	1	14	898	922.7	901.6	870	1.023	1.036	1.06	1.061	0.211	0.197	230.3	8.1	109	74.8	322.2	12.8
RA1-1B_II	RA1-1B	fol granite	1	14	1255	1296	1245	1223	1.04	1.018	1.059	1.061	-0.382	-0.395	235.4	36	69.7	53.2	330.4	6.9
RA1-1B_III	RA1-1B	fol granite	1	14	1099	1128	1108	1060	1.018	1.045	1.064	1.066	0.417	0.404	235.7	34.3	68.3	55	329.8	5.9
RA1-1B_IV	RA1-1B	fol granite	1	14	1536	1596	1559	1452	1.024	1.073	1.099	1.103	0.498	0.48	240.9	48.4	77.1	40.5	340.1	8.1
RA1-1B_V	RA1-1B	fol granite	1	14	689	705.2	694.4	667	1.016	1.041	1.057	1.059	0.438	0.427	236.2	33.6	57.8	56.4	326.7	0.7
RA1-2_I	RA1-2	cataclasite	3	9.5	489	497.7	487.3	480	1.021	1.014	1.036	1.036	-0.193	-0.202	205.9	66.4	82.2	13.6	347.5	18.9
RA1-2_III	RA1-2	cataclasite	3	9.5	419	426	417.7	413	1.02	1.01	1.03	1.031	-0.315	-0.321	291	82.8	71.4	5.6	161.9	4.6
RA1-2_IV	RA1-2	cataclasite	3	9.5	463	471.8	463.4	452	1.018	1.024	1.043	1.043	0.146	0.136	44.3	77	260.7	10.5	169.3	7.5
RA1-2_V	RA1-2	cataclasite	3	9.5	612	625.7	617.3	593	1.013	1.04	1.054	1.056	0.493	0.483	250	77.9	64	12.1	154.3	1.2
RA1-3A_I	RA1-3A	w-breccia	0/1w	6.5	170	179.2	168.3	162	1.065	1.039	1.106	1.107	-0.245	-0.269	344.9	29.1	246.5	14.7	133.1	56.7
RA1-3A_II	RA1-3A	w-breccia	0/1w	6.5	145	149.7	144.1	141	1.039	1.019	1.058	1.06	-0.341	-0.354	340.4	52	95.9	18.6	198	31.8
RA1-3A_III	RA1-3A	w-breccia	0	6.5	141	143.2	142.2	137	1.007	1.039	1.047	1.051	0.69	0.684	287	17.9	25.6	25	165.2	58.5
RA1-3A_IV	RA1-3A	w-breccia	0/1w	6.5	288	296.2	287.4	282	1.031	1.021	1.052	1.052	-0.192	-0.205	178	3.9	323.2	85.3	87.8	2.7
RA1-3A_V	RA1-3A	w-breccia	0/1w	6.5	333	343.5	334.8	321	1.026	1.045	1.072	1.073	0.264	0.247	323.4	12.7	57	15.3	195.3	70
RA1-3A_VI	RA1-3A	w-breccia	0	6.5	193	198.5	192.1	189	1.033	1.019	1.053	1.053	-0.282	-0.294	115.9	2.4	25.2	17.5	213.6	72.3
RA1-3C_I	RA1-3C	w-breccia	0/1w	6	619	626.6	623	608	1.006	1.024	1.03	1.032	0.615	0.61	358.2	20.9	107.6	40.9	248.3	41.7
RA1-3C_II	RA1-3C	w-breccia	0/1w	6	577	586.5	575.8	569	1.019	1.011	1.03	1.03	-0.247	-0.254	148.2	12	52.8	24	262.6	62.8
RA1-3C_III	RA1-3C	w-breccia	0/1w	6	483	488.1	485.2	476	1.006	1.02	1.026	1.027	0.524	0.52	4.8	19.5	119.3	49.6	261.1	33.8
RA1-3C_IV	RA1-3C	w-breccia	0/1w	6	404	406.9	403.3	401	1.009	1.006	1.015	1.015	-0.241	-0.244	352.3	0.4	82.7	39.6	261.8	50.3
RA1-3C_V	RA1-3C	w-breccia	0/1w	6	691	702.3	693.6	678	1.013	1.023	1.035	1.036	0.285	0.277	358.6	56.9	124.5	21	224.5	24.4
RA1-3C_VI	RA1-3C	w-breccia	0/1w	6	417	424.5	415.7	411	1.021	1.011	1.033	1.033	-0.315	-0.322	337.4	53.5	102.6	23.1	204.9	26.6
RA1-3B_I	RA1-3B	w-breccia	0/1w	5.5	257	261.5	257.4	251	1.016	1.027	1.044	1.044	0.254	0.244	36.2	0.3	304.4	80	126.2	10
RA1-3B_III	RA1-3B	w-breccia	0/1w	5.5	240	246.5	240.6	233	1.025	1.033	1.059	1.059	0.145	0.131	25	60	227.7	28.1	132.4	9.8
RA1-3B_IV	RA1-3B	w-breccia	0/1w	5.5	302	305.7	303.6	297	1.007	1.022	1.029	1.03	0.516	0.511	16.2	32.5	234.1	51	118.9	19
RA1-3B_V	RA1-3B	w-breccia	0/1w	5.5	320	331.4	317.6	310	1.044	1.024	1.068	1.069	-0.289	-0.304	348.4	25.3	206.1	59.2	86.4	16.4
RA1-3B_VI	RA1-3B	w-breccia	0/1w	5.5	239	246	237.9	232	1.034	1.027	1.062	1.063	-0.105	-0.12	40.9	52.1	284.6	19	182.5	31.4
RA1.4B_III	RA1-4B	w-breccia	0/1w	5	89	89.71	88.53	89	1.013	1	1.014	1.016	-0.947	-0.947	30.4	64.3	188.3	24	282.2	8.6
RA1-4B_I	RA1-4B	w-breccia	0/1w	5	96	97.59	95.7	94	1.02	1.013	1.033	1.033	-0.202	-0.21	42.9	51.9	294.4	14	194.6	34.6
RA1-4B_II	RA1-4B	w-breccia	0/1w	5	122	124.9	122.2	119	1.023	1.026	1.05	1.05	0.072	0.06	16.4	48.9	113	5.7	207.8	40.5
RA1-4B_IV	RA1-4B	w-breccia	0/1w	5	103	103.7	102.7	102	1.01	1.011	1.02	1.02	0.034	0.028	62.3	54.6	233.6	35.1	326.5	4.1
RA1-4B_V	RA1-4B	w-breccia	0/1w	5	100	100.5	100.2	99	1.003	1.009	1.012	1.013	0.474	0.471	61.3	56.3	175.5	15.3	274.3	29.2
RA1-4B_VI	RA1-4B	w-breccia	0/1w	5	183	184.5	183.5	180	1.006	1.019	1.025	1.026	0.535	0.531	353.4	50.5	117.1	24.6	221.7	28.8
RA1-4A_I	RA1-4A	cataclasite	3	4.5	936	946.4	934.4	926	1.013	1.009	1.022	1.022	-0.176	-0.181	190.3	56.6	98.7	1.1	8	33.4
RA1-4A_II	RA1-4A	cataclasite	3	4.5	1322	1339	1325	1301	1.011	1.018	1.029	1.03	0.24	0.233	162.3	69	260.8	3.3	352.1	20.7

II.a – AMS – Israel

specimen	sample	lithology	ams type	Dist-ance	K_{bulk} 10^{-6}	k1 10^{-6}	k2 10^{-6}	k3 10^{-6}	L	F	P	P'	T	U	dK1	iK1	dK2	iK2	dK3	iK3
RA1-4A_III	RA1-4A	cataclasite	3	4.5	847	856.2	845	841	1.013	1.005	1.019	1.019	-0.427	-0.431	290.8	72.8	36	4.6	127.4	16.5
RA1-4A_V	RA1-4A	cataclasite	3	4.5	1232	1243	1229	1223	1.012	1.005	1.017	1.017	-0.423	-0.426	275	41.6	174.1	12	71.5	46
RA1-4A_VI	RA1-4A	cataclasite	3	4.5	1242	1262	1239	1226	1.019	1.01	1.029	1.029	-0.301	-0.308	186.3	79	0.6	10.9	90.8	1.1
RA1-5A_I	RA1-5A	fol granite	0/1	3.5	893	929.6	885.8	863	1.05	1.027	1.078	1.079	-0.291	-0.308	53.2	56.9	154.4	7.2	249	32.1
RA1-5A_II	RA1-5A	fol granite	0/1	3.5	1260	1319	1239	1223	1.065	1.013	1.078	1.084	-0.662	-0.672	49.7	33.7	169.9	37	291.8	35
RA1-5A_III	RA1-5A	fol granite	0/1	3.5	1178	1202	1179	1154	1.02	1.022	1.042	1.042	0.048	0.038	43.9	44.4	134.8	0.9	225.7	45.6
RA1-5A_IV	RA1-5A	fol granite	0/1	3.5	832	846.4	836.6	814	1.012	1.028	1.04	1.041	0.408	0.4	61.6	53.2	318	10	221	35
RA1-5A_V	RA1-5A	fol granite	0/1	3.5	1173	1215	1156	1147	1.051	1.008	1.059	1.064	-0.73	-0.737	75.6	46.9	167.8	2.1	259.8	43
RA1-5B_I	RA1-5B	w-breccia	0/1w	3.5	170	175.1	170.1	166	1.029	1.026	1.056	1.056	-0.053	-0.067	37	23.8	247.9	62.8	132.6	12.4
RA1-5B_III	RA1-5B	w-breccia	0/1w	3.5	173	179.6	171.2	169	1.049	1.012	1.062	1.065	-0.595	-0.604	31.2	55.6	232.4	32.6	136	9.9
RA1-5B_IV	RA1-5B	w-breccia	0/1w	3.5	196	198.4	196.3	194	1.01	1.011	1.022	1.022	0.051	0.046	25.5	47.3	173.5	38	276.9	16.4
RA1-5B_V	RA1-5B	w-breccia	0/1w	3.5	281	291	282.9	269	1.029	1.053	1.083	1.084	0.291	0.272	55	59.3	163	10.4	258.7	28.5
RA1-5B_VI	RA1-5B	w-breccia	0/1w	3.5	261	267.5	262.9	254	1.017	1.036	1.054	1.055	0.347	0.335	2.2	53.9	264.7	5.4	170.8	35.5
RA1-6A_I	RA1-6A	cat saprolite	3/2	2.5	176	178.8	176.5	172	1.013	1.026	1.039	1.04	0.317	0.309	87.6	31.8	346.3	17.5	231.9	52.7
RA1-6A_II	RA1-6A	cat saprolite	3/2	2.5	348	349.1	348.5	347	1.002	1.004	1.006	1.006	0.396	0.395	107.8	0.9	265.8	89	17.8	0.4
RA1-6A_III	RA1-6A	cat saprolite	3/2	2.5	297	298.7	297.3	294	1.005	1.01	1.015	1.015	0.372	0.369	73.2	19	226.8	68.9	340.2	8.7
RA1-6A_IV	RA1-6A	cat saprolite	3	2.5	238	239.9	237.8	236	1.009	1.007	1.016	1.016	-0.106	-0.11	170.3	72.6	331.6	16.6	63.2	5.3
RA1-6A_V	RA1-6A	cat saprolite	3/2	2.5	262	264.1	263.2	260	1.003	1.012	1.015	1.016	0.542	0.539	90.1	44	255.6	45.1	353	7.3
RA1-6A_VI	RA1-6A	cat saprolite	3/2	2.5	154	157.9	154.1	150	1.024	1.025	1.05	1.05	0.025	0.013	132.2	41	281.7	44.8	28	15.8
RA1-6B_I	RA1-6B	cat saprolite	3	2	142	143.7	140.7	140	1.022	1.003	1.025	1.027	-0.733	-0.735	33.9	82.1	268	4.6	177.5	6.4
RA1-6B_II	RA1-6B	cat saprolite	0/1w	2	103	103.5	102.9	102	1.007	1.009	1.016	1.016	0.14	0.136	23.3	20.1	289.1	11.1	171.8	66.8
RA1-6B_III	RA1-6B	cat saprolite	3/2	2	134	135.4	133.5	133	1.014	1.001	1.015	1.017	-0.833	-0.834	117.8	5.6	222.4	68.8	25.7	20.3
RA1-6B_IV	RA1-6B	cat saprolite	3/2	2	109	109.5	108.9	109	1.006	1.002	1.008	1.008	-0.464	-0.464	76.9	23.4	327.6	37.2	191.2	43.6
RA1-6B_V	RA1-6B	cat saprolite	0/1w	2	125	125.5	124.6	124	1.007	1.009	1.016	1.016	0.149	0.145	36.5	59.9	304.8	1	214.2	30
RA1-6B_VI	RA1-6B	cat saprolite	3/2	2	105	106	104.9	104	1.01	1.006	1.016	1.016	-0.263	-0.266	102.1	19	322.5	65.7	197.3	14.6
RA1-7_I	RA1-7	cat saprolite	0/1w	1.5	72	74.36	71.99	71	1.033	1.019	1.053	1.053	-0.259	-0.271	164.3	75.7	65	2.4	334.4	14.1
RA1-7_II	RA1-7	cat saprolite	0/1w	1.5	83	83.88	82.91	82	1.012	1.005	1.017	1.018	-0.374	-0.378	343.9	29.8	246.5	12.7	136.1	57
RA1-7_III	RA1-7	cat saprolite	0/1w	1.5	50	51.6	49.51	49	1.042	1.009	1.051	1.055	-0.659	-0.666	2.7	46.5	151.1	39	254.8	16.3
RA1-7_IV	RA1-7	cat saprolite	0/1w	1.5	53	54.16	52.26	52	1.036	1.011	1.048	1.05	-0.524	-0.532	347.2	52.9	156.1	36.6	250.1	5.3
RA1-7_V	RA1-7	cat saprolite	0/1w	1.5	92	93.59	92.42	90	1.013	1.026	1.039	1.04	0.351	0.343	52.9	79.8	295.4	4.7	204.6	9
RA1-7_VI	RA1-7	cat saprolite	0/1w	1.5	104	104.7	103.4	103	1.013	1.005	1.017	1.018	-0.464	-0.467	37.1	72.5	244.5	15.7	152.3	7.7
RA2-3_i	RA2-3	fol laterite	1_lat	1	417				1.006	1.011	1.016	1.016	0.305	0.302	136	3	231	64	44	26
RA2-2_I	RA2-2	fol laterite	2a	0.5	424	429	426	417	1.007	1.021	1.028	1.029	0.487	0.482	209.4	15.7	305	19.1	82.5	64.9
RA2-2_II	RA2-2	fol laterite	2a	0.5	446	450	448	440	1.004	1.018	1.022	1.024	0.639	0.636	7.5	23.4	265.5	25.8	133.9	53.9
RA2-2_III	RA2-2	fol laterite	2a	0.5	416	421	419	408	1.005	1.027	1.032	1.035	0.701	0.697	16.3	2.4	285.2	25	111.4	64.8
RA2-2_IV	RA2-2	fol laterite	2a	0.5	430	435	432	423	1.008	1.021	1.029	1.03	0.456	0.451	8.6	15.8	270.8	25.5	127	59.4
RA2-2_V	RA2-2	fol laterite	2a	0.5	451	456	454	442	1.005	1.026	1.032	1.034	0.66	0.656	4.7	12.2	267.5	30.2	114.2	56.9
RA2-1A_I	RA2-1A	fol laterite	1_lat	0.2	1145	1157	1151	1127	1.005	1.021	1.026	1.028	0.598	0.594	100.3	6.7	198.1	48.9	4.6	40.3
RA2-1A_II	RA2-1A	fol laterite	1_lat	0.2	967	973.2	971.4	955	1.002	1.017	1.019	1.021	0.803	0.802	293.1	13	187	50.2	33.1	36.8
RA2-1A_III	RA2-1A	fol laterite	1_lat	0.2	862	869.1	866.7	851	1.003	1.018	1.021	1.023	0.743	0.741	297.4	8.4	196.9	51	33.9	37.8
RA2-1A_IV	RA2-1A	fol laterite	1_lat	0.2	879	886	882	868	1.005	1.016	1.021	1.022	0.561	0.558	115.3	17.1	239.9	61.6	18.2	22
RA2-1B_I	RA2-1B	fol laterite	2b	0.2	389	390.7	388.8	387	1.005	1.005	1.01	1.01	0.035	0.032	46.9	2.2	137.5	15.1	309	74.7
RA2-1B_II	RA2-1B	fol laterite	2b	0.2	433	434.7	433.4	431	1.003	1.005	1.008	1.008	0.237	0.235	13.3	4.4	283	3.5	154.7	84.4
RA2-1B_III	RA2-1B	fol laterite	2b	0.2	437	439.5	437	434	1.006	1.008	1.014	1.014	0.153	0.149	28.6	7	118.9	2.5	228.1	82.5
RA2-1B_IV	RA2-1B	fol laterite	2b	0.2	469	470.8	470.1	467	1.002	1.006	1.008	1.008	0.587	0.586	359.4	0.5	269.3	4	96.5	85.9

Averagve and standard deviation

sample	Kbulk-mean	K1-mean	K2-mean	K3-mean	L-mean	F-mean	P-mean	P'-mean	T-mean	U-mean	dK1geo-mean	iK1geo-mean	dK3geo-mean	iK3geo-mean
RA3-1	1960.75	2020.25	1974.50	1886.75	1.02	1.05	1.07	1.07	0.34	0.33	139.13	18.85	186.93	24.28
RA1-1A	485.60	506.76	486.08	464.42	1.04	1.05	1.08	1.09	0.13	0.11	246.00	43.34	116.90	31.68
RA1-1B	1095.40	1129.58	1101.60	1054.50	1.02	1.04	1.07	1.07	0.24	0.22	235.70	32.08	329.84	6.88
RA1-2	495.75	505.30	496.43	484.85	1.02	1.02	1.04	1.04	0.03	0.02	197.80	76.03	208.25	8.05
RA1-3AI	234.00	242.15	233.65	226.35	1.04	1.03	1.07	1.07	-0.13	-0.15	296.68	24.43	153.55	40.30
RA1-3C	531.83	539.15	532.77	524.00	1.01	1.02	1.03	1.03	0.10	0.10	259.92	27.20	243.87	39.93
RA1-3B	271.60	278.22	271.42	264.46	1.03	1.03	1.05	1.05	0.10	0.09	93.34	34.04	129.28	17.32
RA1-4B	256.67	259.60	256.45	253.39	1.01	1.01	1.03	1.03	0.12	0.12	107.26	52.44	244.98	27.44
RA1-4A	1115.80	1129.32	1114.48	1103.32	1.01	1.01	1.02	1.02	-0.22	-0.22	220.94	63.80	129.96	23.54
RA1-5A	1067.20	1102.40	1059.28	1040.02	1.04	1.02	1.06	1.06	-0.25	-0.26	56.80	47.02	249.46	38.14
RA1-5B	216.20	222.32	216.68	210.28	1.03	1.03	1.06	1.06	0.01	0.00	30.18	47.98	195.00	20.54
RA1-6A_I	247.40	249.72	247.92	244.78	1.01	1.02	1.03	1.03	0.33	0.33	98.18	27.34	194.18	16.98
RA1-6B_I	116.00	116.97	115.77	115.47	1.01	1.00	1.01	1.01	-0.52	-0.52	98.93	16.00	138.07	26.17
RA1-7_I	75.67	77.05	75.42	74.47	1.02	1.01	1.04	1.04	-0.32	-0.33	158.02	59.53	193.10	18.52
RA2-3_i	417				1.006	1.011	1.016	1.016	0.305	0.302	136	3	44	26
RA2-2_I	433.32	438.24	435.72	426.08	1.01	1.02	1.03	1.03	0.59	0.58	49.30	13.90	113.80	59.98
RA2-1A_I	963.25	971.33	967.78	950.28	1.00	1.02	1.02	1.02	0.68	0.67	201.53	11.30	22.45	34.23
RA2-1B_I	432.00	433.93	432.33	429.73	1.0040	1.0060	1.01	1.01	0.25	0.25	112.05	3.53	197.08	81.88

sample	Kbulk-σ	K1-σ	K2-σ	K3-σ	L-σ	F-σ	P-σ	P'-σ	T-σ	U-σ	dK1geo-σ	iK1geo-σ	dK3geo-σ	iK3geo-σ
RA3-1_I	654.11	674.29	662.77	626.90	0.01	0.01	0.02	0.02	0.22	0.23	97.02	12.97	6.92	26.18
RA1-1A_I	166.85	179.03	165.04	156.62	0.02	0.01	0.03	0.03	0.22	0.23	7.72	9.11	13.30	12.91
RA1-1B_I	325.48	342.11	330.01	304.27	0.01	0.02	0.02	0.02	0.36	0.36	3.76	14.70	6.59	4.35
RA1-2_I	82.71	85.57	85.60	77.39	0.00	0.01	0.01	0.01	0.36	0.36	108.07	6.90	93.04	7.68
RA1-3A_I	90.80	92.56	92.03	88.06	0.02	0.01	0.02	0.02	0.27	0.27	79.66	21.14	53.10	29.65
RA1-3C_I	115.66	118.11	117.12	112.42	0.01	0.01	0.01	0.01	0.42	0.42	149.33	22.90	24.01	14.77
RA1-3B_I	37.22	38.43	36.87	36.84	0.01	0.00	0.02	0.02	0.31	0.32	142.91	23.54	34.63	8.83
RA1-4B_I	334.37	338.04	333.72	331.03	0.01	0.01	0.01	0.01	0.32	0.32	138.85	3.01	54.70	13.89
RA1-4A_I	210.08	213.63	210.94	205.50	0.00	0.01	0.01	0.01	0.28	0.27	57.84	14.86	131.51	17.05
RA1-5A_I	191.25	203.05	184.17	187.55	0.02	0.01	0.02	0.02	0.48	0.48	12.31	8.95	28.61	5.82
RA1-5B_I	51.51	53.35	52.86	48.04	0.01	0.02	0.02	0.02	0.38	0.37	19.16	14.20	68.42	11.00
RA1-6A_I	81.57	80.53	81.69	82.71	0.01	0.01	0.02	0.02	0.19	0.19	22.64	17.70	163.32	20.70
RA1-6B_I	15.72	16.06	15.49	15.69	0.00	0.00	0.00	0.00	0.29	0.29	20.63	9.27	97.36	15.36
RA1-7_I	21.49	21.28	21.67	21.42	0.01	0.01	0.02	0.02	0.36	0.36	155.03	19.69	73.54	19.43
RA2-2_I	14.72	14.61	14.78	14.83	0.00	0.00	0.00	0.00	0.11	0.11	89.60	7.62	19.77	4.85
RA2-1A_I	129.61	131.92	130.59	126.36	0.00	0.00	0.00	0.00	0.12	0.12	108.41	4.69	13.92	8.28
RA2-1B_I	32.88	32.96	33.39	33.02	0.00	0.00	0.00	0.00	0.24	0.24	165.47	2.81	92.02	4.98

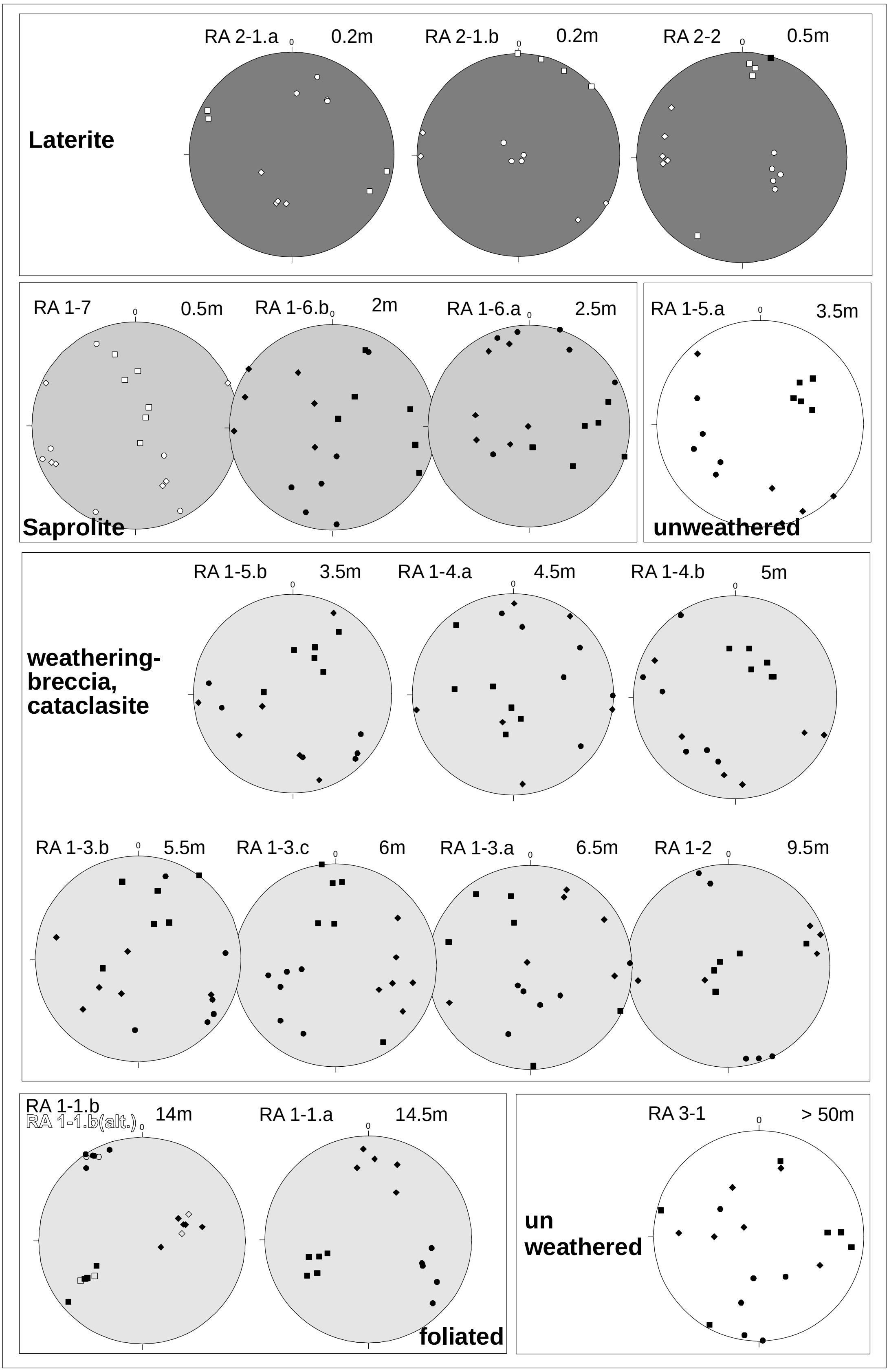

Compilation of AMS stereoplots. Numbers are depth measured from the unconformity (equal area projection of the lower hemisphere).

Hara Autochthon & Allochthon

specimen	lithology	ams-type	section*	log	distance	K_{bulk}	K1	K2	K3	L	F	P	P'	T	U
SH-1_I	siltstone	upperfault	mh0	182.77	-0.18	295.30	300.00	295.40	290.40	1.016	1.017	1.033	1.033	0.04	0.032
SH-1_II	siltstone	upperfault	mh0	182.80	-0.15	264.80	268.50	265.20	260.70	1.013	1.017	1.03	1.03	0.154	0.147
SH-2_I	brecc.granite	upperfault	mh1	184.08	0.13	110.50	111.20	110.80	109.40	1.004	1.013	1.016	1.017	0.547	0.544
SH-2_II	brecc.granite	upperfault	mh1	184.11	0.16	101.20	102.10	101.70	99.96	1.004	1.017	1.021	1.023	0.605	0.601
SH-2_III	brecc.granite	upperfault	mh1	184.15	0.20	156.90	158.00	157.40	155.30	1.004	1.014	1.017	1.018	0.588	0.586
SH-2_IV	brecc.granite	upperfault	mh1	184.19	0.24	141.70	142.50	142.10	140.50	1.003	1.012	1.015	1.015	0.573	0.57
SH-3_I	brecc.granite	upperfault	mh1	184.79	0.84	143.60	144.90	143.60	142.40	1.009	1.008	1.017	1.017	-0.04	-0.044
SH-3_II	brecc.granite	upperfault	mh1	184.85	0.90	128.70	130.20	129.00	126.90	1.009	1.017	1.026	1.027	0.323	0.317
SH-3_II	brecc.granite	upperfault	mh1	184.90	0.95	128.40	129.90	128.80	126.50	1.009	1.018	1.027	1.027	0.324	0.318
SH-4_I	brecc.granite	upperfault	mh2	186.96	3.01	175.70	179.00	175.40	172.70	1.021	1.016	1.037	1.037	-0.126	-0.135
SH-4_II	brecc.granite	upperfault	mh2	187.00	3.05	235.20	239.10	236.50	230.00	1.011	1.028	1.039	1.04	0.44	0.432
SH-4_III	brecc.granite	upperfault	mh2	187.03	3.08	189.60	191.50	189.80	187.30	1.009	1.013	1.022	1.022	0.215	0.21
SH-4_IV	brecc.granite	upperfault	mh2	187.06	3.11	193.10	195.50	192.60	191.30	1.015	1.007	1.022	1.022	-0.381	-0.386
SH-5_I	brecc.granite	xxxx	mh2	187.66	3.71	203.10	204	203	202.4	1.005	1.003	1.008	1.008	-0.275	-0.276
SH-5_II	brecc.granite	detachment	mh2	187.69	3.74	174.90	175.5	175	174.4	1.003	1.004	1.006	1.006	0.166	0.165
SH-5_III	brecc.granite	upperfault	mh2	187.72	3.77	179.00	180.1	179.3	177.6	1.005	1.009	1.014	1.015	0.324	0.32
SH-5_IV	brecc.granite	detachment	mh2	187.75	3.80	173.00	173.7	172.8	172.4	1.005	1.002	1.008	1.008	-0.365	-0.367
SH-6_I	granite grus	detachment	mh2	188.62	4.67	211.20	211.60	211.30	210.80	1.001	1.003	1.004	1.004	0.438	0.437
SH-6_II	granite grus	detachment	mh2	188.66	4.71	214.00	215.10	214.60	212.20	1.002	1.011	1.014	1.015	0.668	0.666
SH-6_III	granite grus	detachment	mh2	188.69	4.74	199.30	200.30	199.80	197.80	1.002	1.01	1.013	1.014	0.611	0.609
SH-6_IV	granite grus	detachment	mh2	188.72	4.77	213.30	214.30	213.40	212.20	1.004	1.006	1.01	1.01	0.179	0.176
SH-8_I	cat. w-breccia	detachment	mh3	192.27	2.12	311.90	313.50	311.40	310.60	1.007	1.003	1.009	1.01	-0.445	-0.447
SH-8_II	cat. w-breccia	detachment	mh3	192.31	2.16	291.20	291.60	291.50	290.50	1	1.004	1.004	1.004	0.788	0.787
SH-8_III	cat. w-breccia	w-breccia	mh3	192.36	2.21	299.20	299.70	299.40	298.50	1.001	1.003	1.004	1.004	0.523	0.522
SH-9_I	w-breccia	w-breccia	mh3	193.95	3.80	422.10	423.20	422.40	420.60	1.002	1.004	1.006	1.006	0.444	0.443
SH-9_II	w-breccia	w-breccia	mh3	193.98	3.83	260.90	261.70	260.90	260.10	1.003	1.003	1.006	1.006	0.054	0.053
SH-9_III	w-breccia	w-breccia	mh3	194.02	3.87	270.90	272.00	271.20	269.60	1.003	1.006	1.009	1.009	0.312	0.31
SH-9_IV	w-breccia	xxxx	mh3	194.05	3.90	247.60	248.50	248.20	246.20	1.001	1.008	1.01	1.01	0.721	0.72
SH-9_V	w-breccia	w-breccia	mh3	194.09	3.94	202.60	203.30	202.40	202.00	1.004	1.002	1.007	1.007	-0.268	-0.269
SH-10_I	w-breccia	w-breccia	mh3	195.03	4.88	232.50	235.20	232.30	229.90	1.013	1.01	1.023	1.023	-0.097	-0.102
SH-10_II	w-breccia	w-breccia	mh3	195.06	4.91	327.70	331.40	327.40	324.30	1.012	1.01	1.022	1.022	-0.124	-0.129
SH-10_III	w-breccia	w-breccia	mh3	195.09	4.94	320.20	321.90	321.00	317.80	1.003	1.01	1.013	1.014	0.563	0.56
SH-10_IV	w-breccia	trans	mh3	195.12	4.97	257.30	261.10	255.90	254.70	1.02	1.005	1.025	1.027	-0.626	-0.63
SH-11_I	w. granite	cleavage	mh3	196.66	6.51	125.60	127.90	126.10	122.70	1.014	1.028	1.042	1.043	0.331	0.322
SH-11_II	w. granite	cleavage	mh3	196.69	6.54	213.90	218.00	212.70	210.90	1.025	1.008	1.034	1.035	-0.502	-0.508
SH-11_III	w. granite	cleavage	mh3	196.72	6.57	260.90	264.60	261.30	256.90	1.013	1.017	1.03	1.03	0.151	0.144
SH-11_IV	w. granite	cleavage	mh3	196.75	6.60	219.80	223.90	219.40	216.20	1.02	1.015	1.036	1.036	-0.144	-0.152
SH-12_I	w. granite	trans	mh3	198.52	8.37	329.70	343.80	331.90	313.40	1.036	1.059	1.097	1.098	0.239	0.217
SH-12_II	w. granite	trans	mh3	198.55	8.40	267.00	275.40	272.70	252.80	1.01	1.079	1.089	1.098	0.771	0.762
SH-12_III	w. granite	trans	mh3	198.58	8.43	327.00	341.80	330.20	308.90	1.035	1.069	1.107	1.108	0.319	0.296
SH-12_IV	w. granite	trans	mh3	198.61	8.46	278.10	287.90	281.70	264.80	1.022	1.064	1.088	1.091	0.479	0.463
SH-13_I	w. granite	cleavage	mh3	200.69	10.54	202.30	206.50	204.20	196.30	1.012	1.04	1.052	1.055	0.544	0.535
SH-13_II	w. granite	cleavage	mh3	200.72	10.57	194.80	198.80	196.80	188.80	1.01	1.042	1.053	1.056	0.606	0.598
SH-13_III	w. granite	cleavage	mh3	200.75	10.60	173.10	176.70	174.40	168.20	1.013	1.037	1.051	1.052	0.465	0.456
SH-14_I	w. granite	cleavage	mh5	201.26	11.11	192.10	196.60	194.80	184.80	1.009	1.054	1.064	1.069	0.697	0.689
SH-14_II	w. granite	cleavage	mh5	201.31	11.16	221.30	226.40	223.40	214.20	1.013	1.043	1.057	1.059	0.526	0.516
SH-14_III	w. granite	cleavage	mh5	201.36	11.21	162.90	165.30	163.70	159.70	1.01	1.025	1.036	1.037	0.425	0.418
SH-14_IV	w. granite	cleavage	mh5	201.41	11.26	154.10	156.70	154.80	150.70	1.012	1.027	1.039	1.04	0.391	0.383
SH-15_I	granite	cleavage	mh6	203.29	13.14	188.00	191.70	190.40	181.90	1.007	1.046	1.054	1.058	0.741	0.735
SH-15_II	granite	cleavage	mh6	203.33	13.18	175.40	178.80	178.50	168.90	1.002	1.057	1.059	1.067	0.936	0.934

specimen	lithology	ams-type	section*	log	distance	Kbulk	K1	K2	K3	L	F	P	P'	T	U
SH-15_III	granite	cleavage	mh6	203.38	13.23	226.00	229.90	228.70	219.30	1.005	1.043	1.049	1.053	0.782	0.777
SH-15_IV	granite	cleavage	mh6	203.42	13.27	188.80	192.40	191.20	182.70	1.007	1.046	1.053	1.058	0.743	0.737

specimen	dK1geo	iK1geo	dK2geo	iK2geo	dK3geo	iK3geo
SH-1_I	37.9	48.2	192.9	39	293.4	12.6
SH-1_II	37.3	40.5	202.4	48.5	300.9	7.4
SH-2_I	184.3	1.1	275.6	48.4	93.3	41.5
SH-2_II	199.6	24.9	319.5	47	92.4	32.4
SH-2_III	211	30.6	327.5	37.1	93.6	37.9
SH-2_IV	190.8	22.7	310.9	50.1	86.3	30.8
SH-3_I	286.2	37.5	192.7	4.5	96.8	52.1
SH-3_II	266.5	38	171.1	6.9	72.4	51.1
SH-3_II	270.6	38.8	173.8	8.4	73.7	49.9
SH-4_I	316	46.4	95.4	35.9	201.8	21.3
SH-4_II	190.5	71.8	293.2	4.1	24.6	17.7
SH-4_III	319	60.9	109.8	25.9	205.9	12.3
SH-4_IV	326.4	52.6	78.1	15.9	178.7	32.9
SH-5_I	297.9	6.7	28.1	1.9	133.6	83.1
SH-5_II	306.8	6.9	194.6	72.3	38.9	16.2
SH-5_III	333.5	72.9	105.4	11.6	198	12.4
SH-5_IV	302.8	15.4	82.2	70.1	209.4	12.3
SH-6_I	238.7	20.1	120.9	52	341.3	30.8
SH-6_II	232.5	44	97.4	36.3	348.2	24.2
SH-6_III	218.7	54.6	90.6	23.7	349	24.6
SH-6_IV	222.6	33.3	110.2	30.2	348.7	41.9
SH-8_I	276.8	22.4	175.9	24.7	43.7	55.6
SH-8_II	277.8	29.2	159.5	40.3	31.7	35.8
SH-8_III	139.4	12.7	279.7	73.6	47.1	10.1
SH-9_I	325.3	1.8	66.2	80.4	235	9.4
SH-9_II	148.4	12.9	328.1	77.1	58.3	0.1
SH-9_III	143.3	42.5	328	47.4	235.5	2.3
SH-9_IV	122.3	65.7	343.8	18.7	248.6	15
SH-9_V	143.1	26.6	350.1	60.6	238.9	11.5
SH-10_I	281	30.8	114	58.6	14.5	5.8
SH-10_II	270.6	40.6	97	49.2	3.3	3.2
SH-10_III	292.3	58.2	101.7	31.4	194.6	4.8
SH-10_IV	307.4	55.7	76	23.1	176.9	23.9
SH-11_I	283.5	57.6	91.7	31.8	185.1	5.3
SH-11_II	308.1	58.1	74.7	20.4	174	23.4
SH-11_III	307.3	69.8	107.8	19.1	199.9	6.3
SH-11_IV	292.7	54.5	88.9	33.1	186.4	11.3
SH-12_I	37.9	46.1	218.6	43.9	128.3	0.3
SH-12_II	197.8	66.1	45.9	21.4	311.8	10.2
SH-12_III	38.1	50.6	231.1	38.7	136	6.4
SH-12_IV	216.9	62.6	51.3	26.6	318.4	5.9
SH-13_I	143.8	76.8	292.7	11.3	24	6.6
SH-13_II	91.5	60.1	292.3	28.3	197.4	9
SH-13_III	106.7	67.4	291.9	22.5	201.1	1.8
SH-14_I	223.2	57.3	64	31	328.2	9.4
SH-14_II	200.7	79.9	66.1	7.1	335.2	7.1
SH-14_III	64.3	58.3	237.5	31.5	329.4	3

specimen	dK1geo	iK1geo	dK2geo	iK2geo	dK3geo	iK3geo
SH-14_IV	68	51.5	235	37.8	330	6.3
SH-15_I	215.4	74.3	355	12.1	87.1	9.9
SH-15_II	205.3	74	8.3	15.3	99.5	4.5
SH-15_III	291.6	84	179.1	2.3	88.8	5.6
SH-15_IV	234.5	78	355.8	6.3	86.9	10.1

average and standard deviation σ

sample	Kbulk-mean	K1-mean	K2-mean	K3-mean	L-mean	F-mean	P-mean	P'-mean	T-mean	U-mean	dK1geo-mean	iK1geo-mean	dK2geo-mean	iK2geo-mean	dK3geo-mean	iK3geo-mean
SH-1_I	280.05	284.25	280.30	275.55	1.01	1.02	1.03	1.03	0.10	0.09	37.60	44.35	197.65	43.75	297.15	10.00
SH-2_I	127.58	123.77	123.30	121.55	1.00	1.01	1.02	1.02	0.58	0.58	198.30	18.87	307.53	44.17	93.10	37.27
SH-3_I	133.57	135.00	133.80	131.93	1.01	1.01	1.02	1.02	0.20	0.20	274.43	38.10	179.20	6.60	80.97	51.03
SH-4_I	198.40	201.28	198.58	195.33	1.01	1.02	1.03	1.03	0.04	0.03	287.98	57.93	144.13	20.45	152.75	21.05
SH-5_I	182.50	183.33	182.53	181.70	1.00	1.00	1.01	1.01	-0.04	-0.04	310.25	25.48	102.58	38.98	144.98	31.00
SH-6_I	209.45	210.33	209.78	208.25	1.00	1.01	1.01	1.01	0.47	0.47	228.13	38.00	104.78	35.55	346.80	30.38
SH-8_I	300.77	301.60	300.77	299.87	1.00	1.00	1.01	1.01	0.29	0.29	231.33	21.43	205.03	46.20	40.83	33.83
SH-8_III	299.20	299.70	299.40	298.50	1.001	1.003	1.004	1.004	0.523	0.522	139.4	12.7	279.7	73.6	47.1	10.1
SH-9_I	280.82	281.74	281.02	279.70	1.00	1.00	1.01	1.01	0.25	0.25	176.48	29.90	283.24	56.84	203.26	7.66
SH-10_I	284.43	287.40	284.15	281.68	1.01	1.01	1.02	1.02	-0.07	-0.08	287.83	46.33	97.18	40.58	97.33	9.43
SH-11_I	205.05	208.60	204.88	201.68	1.02	1.02	1.04	1.04	-0.04	-0.05	297.90	60.00	90.78	26.10	186.35	11.58
SH-12_I	300.45	312.23	304.13	284.98	1.03	1.07	1.10	1.10	0.45	0.43	122.68	56.35	136.73	32.65	223.63	5.70
SH-13_I	190.07	194.00	191.80	184.43	1.01	1.04	1.05	1.05	0.54	0.53	114.00	68.10	292.30	20.70	140.83	5.80
SH-14_I	182.60	186.25	184.18	177.35	1.01	1.04	1.05	1.05	0.51	0.50	139.05	61.75	150.65	26.85	330.70	6.45
SH-15_I	194.55	198.20	197.20	188.20	1.01	1.05	1.05	1.06	0.80	0.80	236.70	77.58	224.55	9.00	90.58	7.53

sample	Kbulk- σ	K1-σ	K2-σ	K3-σ	L-σ	F-σ	P-σ	P'-σ	T-σ	U-σ	dK1geo-σ	iK1geo-σ	dK2geo-σ	iK2geo-σ	dK3geo-σ	iK3geo-σ
SH-1_I	21.57	22.27	21.35	21.00	0.00	0.00	0.00	0.00	0.08	0.08	0.42	5.44	6.72	6.72	5.30	3.68
SH-2_I	26.12	29.99	29.88	29.60	0.00	0.00	0.00	0.00	0.03	0.03	13.40	15.65	27.94	6.16	0.62	4.58
SH-3_I	8.69	8.57	8.49	9.07	0.00	0.01	0.01	0.01	0.21	0.21	10.39	0.66	11.77	1.97	13.73	1.10
SH-4_I	25.66	26.18	26.38	24.46	0.01	0.01	0.01	0.01	0.36	0.36	65.13	10.99	100.22	13.62	86.27	8.72
SH-5_I	13.96	14.04	13.91	13.97	0.00	0.00	0.00	0.00	0.33	0.33	15.92	31.88	69.37	37.43	78.20	34.78
SH-6_I	6.87	6.85	6.79	7.00	0.00	0.00	0.00	0.00	0.22	0.22	9.13	14.77	13.48	12.11	3.68	8.26
SH-8_I	10.44	11.07	10.02	10.12	0.00	0.00	0.00	0.00	0.65	0.65	79.62	8.29	65.18	24.98	8.09	22.81
SH-9_I	83.18	83.31	83.29	82.91	0.00	0.00	0.00	0.00	0.38	0.38	83.80	25.15	121.72	25.12	81.22	6.28
SH-10_I	46.85	46.70	47.31	46.66	0.01	0.00	0.01	0.01	0.49	0.49	15.77	12.94	15.83	16.22	102.46	9.71
SH-11_I	56.94	57.65	56.75	56.52	0.01	0.01	0.01	0.01	0.36	0.36	11.93	6.72	13.57	7.37	10.61	8.31
SH-12_I	32.55	35.68	31.31	30.67	0.01	0.01	0.01	0.01	0.23	0.24	98.08	9.53	101.91	10.43	105.71	4.08
SH-13_I	15.16	15.47	15.52	14.55	0.00	0.00	0.00	0.00	0.07	0.07	26.90	8.37	0.40	8.64	101.20	3.67
SH-14_I	30.49	31.79	31.27	28.49	0.00	0.01	0.01	0.02	0.14	0.14	84.69	12.47	98.85	13.53	3.09	2.65
SH-15_I	21.85	22.04	21.79	21.68	0.00	0.01	0.00	0.01	0.09	0.09	38.55	4.65	166.41	5.82	6.01	2.89

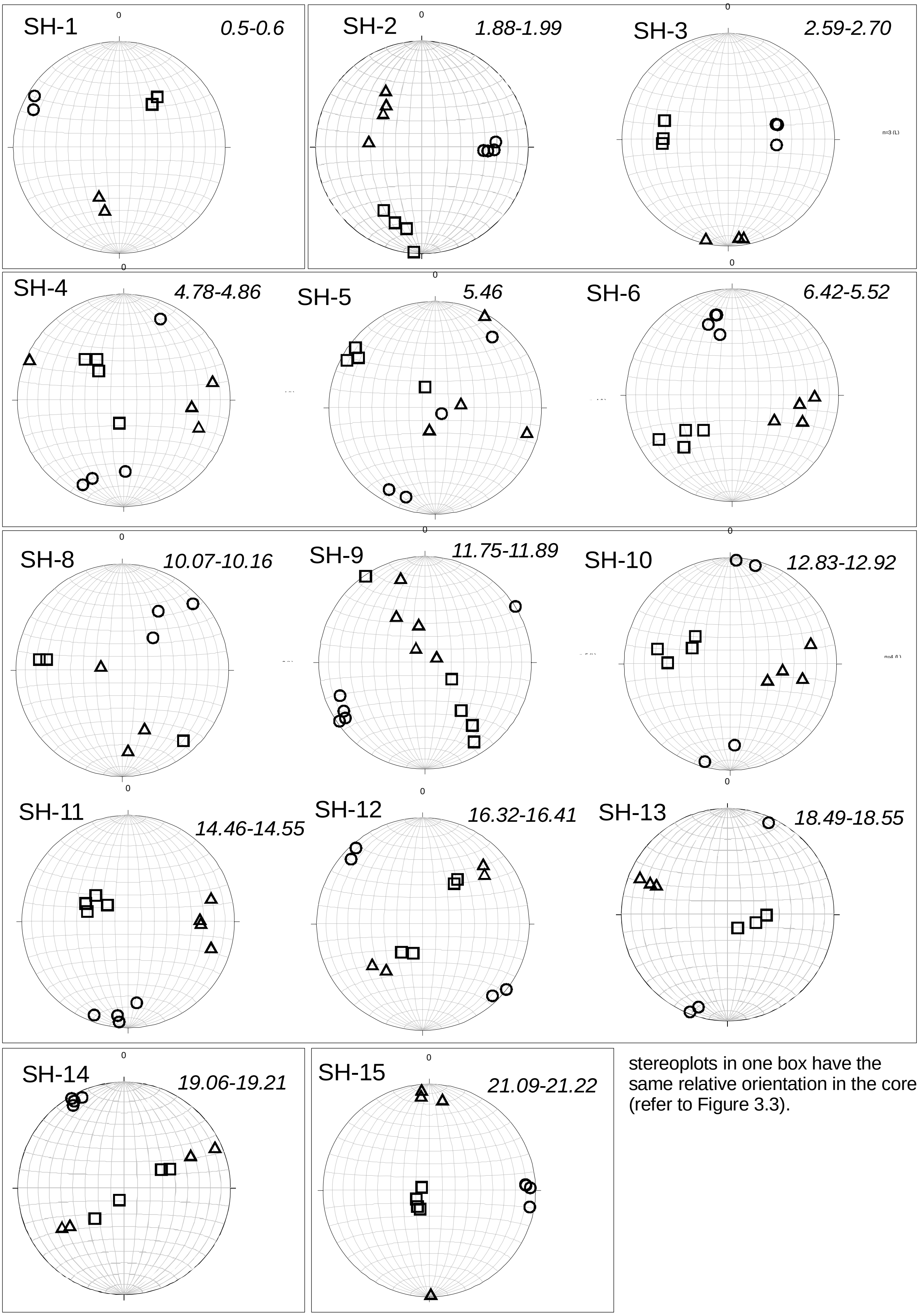

stereoplots in one box have the same relative orientation in the core (refer to Figure 3.3).

Compilation of AMS stereoplots in the Hara drill core section. (shown data are not correction-rotated). Numbers are depth measured from the unconformity (equal area projection of the lower hemisphere).

Langviken Autochthon

specimen	lithology	ams-type	section*	log	distance	Kbulk	K1	K2	K3	L	F	P	P'	T	U
ST-1_I	qtz. congl.	conglomerate	mt1	436.42	-0.17	184.70	190.70	183.10	180.40	1.041	1.015	1.057	1.059	-0.468	-0.478
ST-1_II	qtz. congl.	conglomerate	mt1	436.55	-0.04	192.40	196.80	191.40	189.00	1.028	1.013	1.041	1.042	-0.365	-0.374
ST-2_I	w-breccia	breccia	mt1	436.63	0.04	40.34	40.91	40.31	39.81	1.015	1.013	1.028	1.028	-0.084	-0.09
ST-2_II	w-breccia	breccia	mt1	436.68	0.09	68.74	69.83	68.84	67.55	1.014	1.019	1.034	1.034	0.134	0.126
ST-3_I	qtz. granite	qtz granite	mt1	436.80	0.21	18.47	20.97	18.80	15.63	1.116	1.203	1.342	1.346	0.256	0.187
ST-3_III	qtz. granite	qtz granite	mt1	436.86	0.27	-5.21	-4.87	-5.15	-5.60	1.088	1.057	1.15	1.151	-0.205	0.238
ST-3_IV	qtz. granite	qtz granite	mt1	436.89	0.30	-5.38	-5.03	-5.20	-5.90	1.135	1.033	1.173	1.183	-0.592	0.617
ST-3_V	qtz. granite	qtz granite	mt1	436.91	0.32	-9.94	-9.64	-9.94	-10.23	1.029	1.031	1.061	1.061	0.038	-0.023
ST-4_I	w-breccia	breccia	mt1	437.09	0.50	38.71	39.31	38.60	38.22	1.018	1.01	1.029	1.029	-0.29	-0.297
ST-4_III	w-breccia	breccia	mt1	437.15	0.56	50.04	50.62	50.41	49.10	1.004	1.027	1.031	1.034	0.719	0.716
ST-4_IV	w-breccia	breccia	mt1	437.21	0.62	54.79	55.78	55.11	53.47	1.012	1.031	1.043	1.045	0.435	0.427
ST-5_I	w-breccia	breccia	mt2	437.55	0.96	74.18	75.57	73.84	73.13	1.023	1.01	1.033	1.034	-0.416	-0.423
ST-5_II	w-breccia	breccia	mt2	437.59	1.00	72.39	74.47	72.98	69.72	1.02	1.047	1.068	1.07	0.389	0.375
ST-5_IV	w-breccia	breccia	mt2	437.67	1.08	73.29	74.92	73.53	71.43	1.019	1.029	1.049	1.049	0.213	0.202
ST-6_I	w-breccia	breccia	mt2	437.92	1.33	75.20	76.74	75.36	73.51	1.018	1.025	1.044	1.044	0.157	0.147
ST-6_II	w-breccia	breccia	mt2	437.95	1.36	59.84	60.51	59.85	59.16	1.011	1.012	1.023	1.023	0.029	0.023
ST-6_III	w-breccia	breccia	mt2	437.98	1.39	55.32	56.52	55.83	53.62	1.012	1.041	1.054	1.057	0.537	0.528
ST-6_IV	w-breccia	breccia	mt2	438.01	1.42	62.37	63.74	62.42	60.95	1.021	1.024	1.046	1.046	0.064	0.053
ST-6_V	w-breccia	breccia	mt2	438.04	1.45	68.14	71.13	67.42	65.86	1.055	1.024	1.08	1.082	-0.393	-0.409
ST-7_I	w-breccia	breccia	mt6	438.84	2.25	74.34	76.35	74.88	71.80	1.02	1.043	1.063	1.065	0.368	0.355
ST-7_II	w-breccia	breccia	mt6	438.87	2.28	81.10	85.06	81.75	76.50	1.041	1.069	1.112	1.113	0.251	0.226
ST-7_III	w-breccia	breccia	mt6	438.90	2.31	86.32	89.34	88.13	81.48	1.014	1.082	1.096	1.105	0.705	0.694
ST-7_IV	w-breccia	breccia	mt6	438.94	2.35	83.90	86.77	84.94	79.98	1.022	1.062	1.085	1.088	0.475	0.459
ST-8_I	w-breccia	breccia	mt6	440.30	3.71	79.68	84.01	80.20	74.82	1.048	1.072	1.123	1.124	0.198	0.17
ST-8_II	w-breccia	breccia	mt6	440.34	3.75	65.21	66.88	65.70	63.05	1.018	1.042	1.061	1.062	0.396	0.383
ST-8_III	w-breccia	breccia	mt6	440.38	3.79	73.68	76.59	74.31	70.14	1.031	1.059	1.092	1.093	0.312	0.292
ST-8_IV	w-breccia	breccia	mt6	440.41	3.82	79.35	81.60	79.70	76.76	1.024	1.038	1.063	1.064	0.229	0.214
ST-9_I	granite	granite	mt12	442.64	6.05	7879.00	8864.00	8615.00	6158.00	1.029	1.399	1.439	1.5	0.844	0.816
ST-9_II	granite	granite	mt12	442.67	6.08	4462.00	4917.00	4746.00	3724.00	1.036	1.274	1.32	1.353	0.745	0.713
ST-9_III	granite	granite	mt12	442.70	6.11	3418.00	3789.00	3595.00	2872.00	1.054	1.252	1.319	1.342	0.621	0.577
ST-9_IV	granite	granite	mt12	442.73	6.14	5113.00	5682.00	5411.00	4245.00	1.05	1.275	1.339	1.367	0.665	0.623
ST-9_V	granite	granite	mt12	442.77	6.18	2481.00	2766.00	2617.00	2060.00	1.057	1.27	1.343	1.368	0.624	0.577
ST-10_I	trans	granite	mt12	445.53	8.94	773.70	800.40	777.20	743.40	1.03	1.046	1.077	1.077	0.205	0.187
ST-10_II	trans	granite	mt12	445.60	9.01	476.70	488.00	480.30	461.70	1.016	1.04	1.057	1.059	0.429	0.418
ST-11A_I	mykonite	mylonite	mt14	449.74	13.15	17670.00	21470.00	19330.00	12200.00	1.111	1.585	1.76	1.825	0.629	0.538
ST-11A_II	mykonite	mylonite	mt14	449.77	13.18	18060.00	22220.00	19950.00	12020.00	1.114	1.66	1.849	1.928	0.649	0.554
ST-11A_III	mykonite	mylonite	mt14	449.79	13.20	16160.00	20510.00	17190.00	10780.00	1.193	1.594	1.902	1.943	0.451	0.318
ST-11B_I	granite	granite	mt14	449.81	13.22	3351.00	3924.00	3341.00	2789.00	1.175	1.198	1.407	1.407	0.057	-0.028
ST-11B_II	granite	granite	mt14	449.84	13.25	2288.00	2662.00	2259.00	1942.00	1.178	1.163	1.371	1.371	-0.041	-0.119
ST-11B_III	granite	granite	mt14	449.86	13.27	2111.00	2422.00	2139.00	1771.00	1.132	1.208	1.368	1.371	0.207	0.131
ST-12_I	granite	granite	mt14	454.57	17.98	9137.00	10340.00	9581.00	7487.00	1.079	1.28	1.381	1.402	0.526	0.467
ST-12_II	granite	granite	mt14	454.60	18.01	6821.00	7767.00	6791.00	5906.00	1.144	1.15	1.315	1.315	0.019	-0.05
ST-12_III	granite	granite	mt14	454.63	18.04	11700.00	13860.00	11820.00	9428.00	1.172	1.254	1.47	1.473	0.174	0.08
ST-12_IV	granite	granite	mt14	454.66	18.07	8710.00	10360.00	9235.00	6536.00	1.122	1.413	1.585	1.615	0.502	0.412
ST-12_V	granite	granite	mt14	454.69	18.10	3818.00	4250.00	3872.00	3332.00	1.098	1.162	1.275	1.278	0.233	0.175
ST-13A_I	granite	granite	mt14	457.48	20.89	417.30	434.50	425.90	391.40	1.02	1.088	1.11	1.117	0.619	0.603

II.c – AMS – Långviken

specimen	lithology	ams-type	section*	log	distance	Kbulk	K1	K2	K3	L	F	P	P'	T	U
ST-13A_II	granite	granite	mt14	457.50	20.91	1604.00	1799.00	1629.00	1383.00	1.104	1.177	1.3	1.304	0.243	0.181
ST-13A_III	granite	granite	mt14	457.53	20.94	2874.00	3146.00	2921.00	2553.00	1.077	1.144	1.232	1.236	0.29	0.242
ST-13A_IV	granite	granite	mt14	457.55	20.96	21960.00	23880.00	22990.00	19000.00	1.039	1.21	1.257	1.277	0.666	0.633
ST-13B_I	trans	granite	mt14	457.57	20.98	9275.00	10520.00	9044.00	8256.00	1.164	1.095	1.275	1.278	-0.249	-0.305
ST-13B_II	trans	granite	mt14	457.60	21.01	1465.00	1587.00	1516.00	1292.00	1.047	1.174	1.229	1.242	0.557	0.521
ST-14_I	granite	granite	mt16	461.77	25.18	3427.00	3876.00	3485.00	2920.00	1.112	1.193	1.327	1.331	0.248	0.181
ST-14_II	granite	granite	mt16	461.80	25.21	1987.00	2203.00	1981.00	1776.00	1.112	1.115	1.24	1.24	0.012	-0.042
ST-14_III	granite	granite	mt16	461.83	25.24	3460.00	3700.00	3526.00	3153.00	1.049	1.118	1.173	1.178	0.399	0.365
ST-14_IV	granite	granite	mt16	461.85	25.26	706.40	753.70	725.00	640.60	1.04	1.132	1.176	1.185	0.522	0.493
ST-14_V	granite	granite	mt16	461.87	25.28	245.60	250.50	246.90	239.50	1.015	1.031	1.046	1.047	0.355	0.345
ST-15_I	granite	granite	mt18	465.40	28.81	6468.00	7223.00	6570.00	5612.00	1.1	1.171	1.287	1.291	0.248	0.189
ST-15_II	granite	granite	mt18	465.43	28.84	9129.00	10590.00	9181.00	7619.00	1.153	1.205	1.389	1.391	0.135	0.053
ST-15_III	granite	granite	mt18	465.46	28.87	11440.00	12740.00	11780.00	9789.00	1.082	1.204	1.302	1.311	0.406	0.35
ST-15_IV	granite	granite	mt18	465.49	28.90	6593.00	7376.00	6561.00	5842.00	1.124	1.123	1.263	1.263	-0.004	-0.062

specimen	dK1geo	iK1geo	dK2geo	iK2geo	dK3geo	iK3geo
ST-1_I	160.3	54.6	333.1	35.2	65.5	3.4
ST-1_II	166.7	54.5	4	34.3	268.4	8.2
ST-2_I	173.9	35.3	351.5	54.6	83.1	1.1
ST-2_II	353.5	10.3	221.8	74.8	85.5	11.1
ST-3_I	164.8	32.3	34.5	45.6	273.4	26.8
ST-3_III	117.8	6.7	23.9	30.2	219	59
ST-3_IV	114.6	13.4	23.2	6	269.7	75.3
ST-3_V	101.7	16.9	197	17.1	329.7	65.6
ST-4_I	4.8	7.2	182.7	82.8	274.7	0.3
ST-4_III	355.3	16.4	198.9	72.2	87.3	6.8
ST-4_IV	194.3	9.8	315.7	71.7	101.6	15.3
ST-5_I	153.5	14.3	304.9	73.8	61.6	7.4
ST-5_II	170.9	8.4	340.3	81.5	80.7	1.5
ST-5_IV	341.2	25.2	154.4	64.6	250	2.6
ST-6_I	157.7	3.3	272	82	67.2	7.3
ST-6_II	317.9	30.1	152.3	59.1	51.6	6.3
ST-6_III	315.3	18	151.7	71.3	46.9	5
ST-6_IV	317.9	11.3	145.2	78.6	48.2	1.4
ST-6_V	139	8.4	260.1	74	47	13.5
ST-7_I	87.5	0.3	179.3	79.3	357.4	10.7
ST-7_II	95.6	18.3	241.1	68.1	1.7	11.6
ST-7_III	94	10	214.7	71	1.1	16
ST-7_IV	87.3	4.6	193.5	74	356	15.3
ST-8_I	96.9	15.3	247.6	72.6	4.7	8.1
ST-8_II	100.7	9.9	222.1	71.5	7.9	15.5
ST-8_III	116.6	0.2	209.7	86.7	26.6	3.3
ST-8_IV	108.3	0.7	202.4	79.8	18.2	10.2
ST-9_I	204.9	76.4	114.8	0	24.8	13.6
ST-9_II	146.3	39.9	292	44.7	40.6	17.9
ST-9_III	150.5	80.9	307.3	8.4	37.9	3.5
ST-9_IV	158.1	81.3	308.8	7.6	39.3	4.2
ST-9_V	289.2	57.6	134.6	29.8	37.9	11.5
ST-10_I	164	2.3	258.6	63.4	72.9	26.5
ST-10_II	326.5	29.9	183.8	54.1	67.2	17.9
ST-11A_I	128.8	18	275.5	68.8	35.2	10.9

II.c – AMS – Långviken

specimen	dK1geo	iK1geo	dK2geo	iK2geo	dK3geo	iK3geo
ST-11A_II	131.4	27.6	286	59.9	35.6	10.9
ST-11A_III	137.7	26.6	282	58.4	39.6	15.9
ST-11B_I	139.2	54.7	322.7	35.2	231.5	1.6
ST-11B_II	136.6	49.1	312.4	40.8	44.2	2.1
ST-11B_III	0.8	66.4	179.3	23.6	269.5	0.6
ST-12_I	191.6	47.5	343.5	39	85.4	14.3
ST-12_II	189.8	46.2	351.3	42.3	89.9	9.4
ST-12_III	185.1	43.1	342.9	44.7	84.3	11.3
ST-12_IV	174	48	350	41.9	81.8	2
ST-12_V	198.8	63.2	359.7	25.5	93.4	7.7
ST-13A_I	223.9	71.3	14.3	16.4	106.9	8.7
ST-13A_II	325.4	67.7	203.6	12.2	109.5	18.4
ST-13A_III	276.3	80.9	24.4	2.8	114.8	8.6
ST-13A_IV	212.5	80.5	19.5	9.2	109.8	2.1
ST-13B_I	313.1	74.4	178.6	11.1	86.4	10.9
ST-13B_II	234	82.1	4.1	5.1	94.6	6
ST-14_I	290	65.2	54.5	14.7	149.9	19.6
ST-14_II	354.2	70.9	255.4	3	164.3	18.8
ST-14_III	87.4	2.1	242.2	87.6	357.4	1
ST-14_IV	266	16.1	68.4	73.2	174.6	4.8
ST-14_V	260.1	5.4	26.3	80.9	169.4	7.3
ST-15_I	204.7	48.6	352.7	36.8	95.3	16.3
ST-15_II	306.7	65.8	186.3	12.8	91.6	20.2
ST-15_III	217.8	53.6	356.5	29	98.2	20
ST-15_IV	205.4	53.9	357.7	32.8	96.4	13.3

average and standard deviation σ

specimen	Kbulk-mean	K1-mean	K2-mean	K3-mean	L-mean	F-mean	P-mean	P'-mean	T-mean	U-mean	dK1geo-mean	iK1geo-mean	dK2geo-mean	iK2geo-mean	dK3geo-mean	iK3geo-mean
ST-1_I	188.55	193.75	187.25	184.70	1.03	1.01	1.05	1.05	-0.42	-0.43	163.50	54.55	168.55	34.75	166.95	5.80
ST-2_I	54.54	55.37	54.58	53.68	1.01	1.02	1.03	1.03	0.03	0.02	263.70	22.80	286.65	64.70	84.30	6.10
ST-3_I	18.47	20.97	18.80	15.63	1.116	1.203	1.342	1.346	0.256	0.187	164.8	32.3	34.5	45.6	273.4	26.8
ST-3_III	-6.84	-6.51	-6.76	-7.24	1.08	1.04	1.13	1.13	-0.25	0.28	111.37	12.33	81.37	17.77	272.80	66.63
ST-4_I	47.85	48.57	48.04	46.93	1.01	1.02	1.03	1.04	0.29	0.28	184.80	11.13	232.43	75.57	154.53	7.47
ST-5_I	73.29	74.99	73.45	71.43	1.02	1.03	1.05	1.05	0.06	0.05	221.87	15.97	266.53	73.30	130.77	3.83
ST-6_I	64.17	65.73	64.18	62.62	1.02	1.03	1.05	1.05	0.08	0.07	249.56	14.22	196.26	73.00	52.18	6.70
ST-7_I	81.42	84.38	82.43	77.44	1.02	1.06	1.09	1.09	0.45	0.43	91.10	8.30	207.15	73.10	179.05	13.40
ST-8_I	74.48	77.27	74.98	71.19	1.03	1.05	1.08	1.09	0.28	0.26	105.63	6.53	220.45	77.65	14.35	9.28
ST-9_I	4670.60	5203.60	4996.80	3811.80	1.05	1.29	1.35	1.39	0.70	0.66	189.80	67.22	231.50	18.10	36.10	10.14
ST-10_I	625.20	644.20	628.75	602.55	1.02	1.04	1.07	1.07	0.32	0.30	245.25	16.10	221.20	58.75	70.05	22.20
ST-11A_I	17296.67	21400.00	18823.33	11666.67	1.14	1.61	1.84	1.90	0.58	0.47	132.63	24.07	281.17	62.37	36.80	12.57
ST-11B_I	2583.33	3002.67	2579.67	2167.33	1.16	1.19	1.38	1.38	0.07	-0.01	92.20	56.73	271.47	33.20	181.73	1.43
ST-12_I	8037.20	9315.40	8259.80	6537.80	1.12	1.25	1.41	1.42	0.29	0.22	187.86	49.60	349.48	38.68	86.96	8.94
ST-13A_I	6265.88	6894.42	6420.98	5479.23	1.08	1.15	1.23	1.24	0.35	0.31	264.20	76.15	74.08	9.47	103.67	9.12
ST-14_I	2707.00	3039.50	2733.00	2348.00	1.11	1.15	1.28	1.29	0.13	0.07	322.10	68.05	154.95	8.85	157.10	19.20
ST-14_III	1470.67	1568.07	1499.30	1344.37	1.03	1.09	1.13	1.14	0.43	0.40	204.50	7.87	112.30	80.57	233.80	4.37
ST-15_I	8407.50	9482.25	8523.00	7215.50	1.11	1.18	1.31	1.31	0.20	0.13	233.65	55.48	313.30	27.85	95.38	17.45

specimen	Km-σ	K1-σ	K2-σ	K3-σ	L-σ	F-σ	P-σ	P'-σ	T-σ	U-σ	dK1geo-σ	iK1geo -σ	dK2geo -σ	iK2geo-σ	dK3geo-σ	iK3geo-σ
ST-1_I	5.44	4.31	5.87	6.08	0.01	0.00	0.01	0.01	0.07	0.07	4.53	0.07	232.71	0.64	143.47	3.39
ST-2_I	20.08	20.45	20.17	19.62	0.00	0.00	0.00	0.00	0.15	0.15	127.00	17.68	91.71	14.28	1.70	7.07
ST-3_III	2.68	2.71	2.75	2.59	0.05	0.01	0.06	0.06	0.32	0.32	8.52	5.18	100.14	12.11	55.42	8.20
ST-4_I	8.26	8.42	8.51	7.85	0.01	0.01	0.01	0.01	0.52	0.52	175.44	4.74	72.56	6.27	104.31	7.52
ST-5_I	0.90	0.55	0.44	1.71	0.00	0.02	0.02	0.02	0.42	0.42	103.71	8.52	98.71	8.46	103.70	3.14
ST-6_I	7.71	8.16	7.53	7.50	0.02	0.01	0.02	0.02	0.33	0.33	92.63	10.35	63.91	8.80	8.61	4.41
ST-7_I	5.18	5.63	5.66	4.30	0.01	0.02	0.02	0.02	0.19	0.20	4.32	7.76	26.90	4.78	205.13	2.64
ST-8_I	6.77	7.58	6.74	6.10	0.01	0.02	0.03	0.03	0.09	0.09	8.72	7.36	19.84	7.07	9.99	5.06
ST-9_I	2055.26	2326.61	2288.79	1553.39	0.01	0.06	0.05	0.06	0.09	0.10	60.31	18.09	97.97	18.55	6.42	6.19
ST-10_I	210.01	220.90	209.94	199.19	0.01	0.00	0.01	0.01	0.16	0.16	114.90	19.52	52.89	6.58	4.03	6.08
ST-11A_I	1003.51	857.15	1448.08	773.13	0.05	0.04	0.07	0.06	0.11	0.13	4.58	5.28	5.30	5.62	2.43	2.89
ST-11B_I	670.68	806.87	662.06	545.13	0.03	0.02	0.02	0.02	0.12	0.13	79.17	8.83	79.98	8.77	120.61	0.76
ST-12_I	2930.83	3565.47	3032.40	2232.18	0.04	0.11	0.12	0.13	0.22	0.22	9.18	7.84	6.84	7.64	4.64	4.59
ST-13A_I	8316.88	9072.68	8679.00	7201.15	0.05	0.05	0.07	0.07	0.34	0.36	47.94	5.91	91.23	4.94	10.83	5.45
ST-14_I	1018.23	1182.99	1063.49	808.93	0.00	0.06	0.06	0.06	0.17	0.16	45.40	4.03	142.06	8.27	10.18	0.57
ST-14_III	1738.15	1863.37	1771.38	1579.11	0.02	0.05	0.07	0.08	0.09	0.08	101.45	7.32	114.45	7.21	107.07	3.17
ST-15_I	2364.37	2669.62	2496.98	1935.93	0.03	0.04	0.05	0.05	0.17	0.18	49.07	7.30	84.69	10.53	2.79	3.30

Langviken Allochthon
300 A/m

specimen	group	ams-type	section*	log	distance	Kbulk	K1	K2	K3	L	F	P	P'	T	U
st-aa_I	slice-cover	c-weak	mts0	417.68	-0.22	48.50	48.94	48.69	47.86	1.005	1.017	1.023	1.024	0.544	0.54
st-aa_II	slice-cover	c-weak	mts0	417.72	-0.18	53.05	53.53	53.33	52.30	1.004	1.02	1.024	1.025	0.668	0.664
st-aa_III	slice-cover	c-weak	mts0	417.76	-0.14	48.16	48.56	48.30	47.61	1.005	1.014	1.02	1.021	0.452	0.448
st-aa_IV	slice-cover	c-weak	mts0	417.80	-0.10	49.75	50.50	49.92	48.82	1.012	1.022	1.034	1.035	0.314	0.307
st-aa_V	slice-cover	c-weak	mts0	417.84	-0.06	48.94	49.47	49.33	48.02	1.003	1.027	1.03	1.033	0.802	0.799
st-a_I	slice-basement	c-weak	mts1	418.00	0.10	62.32	63.18	62.26	61.53	1.015	1.012	1.027	1.027	-0.107	-0.114
st-a_II	slice-basement	c-weak	mts1	418.03	0.13	61.68	62.34	62.18	60.52	1.003	1.027	1.03	1.033	0.826	0.823
st-a_III	slice-basement	c-weak	mts1	418.06	0.16	64.88	66.23	65.52	62.88	1.011	1.042	1.053	1.056	0.588	0.58
st-a_IV	slice-basement	c-weak	mts1	418.09	0.19	93.40	94.93	94.40	90.86	1.006	1.039	1.045	1.049	0.741	0.736
st-a_V	slice-basement	c-weak	mts1	418.12	0.22	81.50	83.54	82.41	78.56	1.014	1.049	1.063	1.067	0.557	0.546
st-b_I	slice-basement	c-mod	mts1	418.50	0.60	97.42	101.30	98.86	92.12	1.024	1.073	1.099	1.104	0.49	0.471
st-b_II	slice-basement	c-mod	mts1	418.53	0.63	119.30	126.80	120.60	110.50	1.052	1.091	1.148	1.15	0.264	0.232
st-b_III	slice-basement	c-mod	mts1	418.56	0.66	104.50	112.20	108.20	93.07	1.036	1.163	1.205	1.219	0.618	0.589
st-b_IV	slice-basement	c-mod	mts1	418.59	0.69	104.10	113.20	107.90	91.24	1.049	1.182	1.241	1.254	0.553	0.515
st-c_I	slice-basement	c-mod	mts1	418.87	0.97	203.10	220.90	210.90	177.60	1.047	1.188	1.244	1.258	0.577	0.54
st-c_II	slice-basement	c-mod	mts1	418.90	1.00	310.70	357.30	328.70	246.00	1.087	1.336	1.452	1.48	0.554	0.487
st-c_III	slice-basement	c-mod	mts1	418.93	1.03	445.90	497.20	458.40	382.20	1.085	1.199	1.301	1.309	0.382	0.325
st-c_IV	slice-basement	c-mod	mts1	418.96	1.06	181.00	201.40	190.60	150.90	1.057	1.263	1.335	1.359	0.616	0.57
st-c_V	slice-basement	c-mod	mts1	418.98	1.08	212.50	240.00	213.50	184.00	1.124	1.16	1.304	1.305	0.118	0.052
st-d_I	slice-basement	c-mod	mts2	419.91	2.01	243.10	269.10	257.90	202.20	1.044	1.275	1.331	1.361	0.7	0.663
st-d_II	slice-basement	c-mod	mts2	419.94	2.04	182.90	200.70	183.90	164.10	1.091	1.12	1.223	1.223	0.129	0.079
st-d_III	slice-basement	c-mod	mts2	419.97	2.07	117.90	124.10	117.70	112.00	1.055	1.051	1.108	1.108	-0.036	-0.061
st-d_IV	slice-basement	c-mod	mts2	420.00	2.10	452.00	509.40	461.30	385.20	1.104	1.197	1.322	1.328	0.29	0.225
st-d_V	slice-basement	c-mod	mts2	420.03	2.13	551.50	605.50	570.90	478.10	1.061	1.194	1.267	1.279	0.501	0.455
st-e_I	slice-basement	c-mod	mts2	420.87	2.97	129.90	141.70	136.60	111.60	1.037	1.225	1.27	1.294	0.695	0.664

II.c – AMS – Långviken

specimen	group	ams-type	section*	log	distance	Kbulk	K1	K2	K3	L	F	P	P'	T	U
st-e_II	slice-basement	c-mod	mts2	420.90	3.00	156.30	171.30	164.70	132.90	1.04	1.239	1.289	1.314	0.691	0.657
st-e_III	slice-basement	c-mod	mts2	420.93	3.03	334.30	366.60	347.70	288.40	1.054	1.206	1.271	1.287	0.559	0.517
st-e_IV	slice-basement	c-mod	mts2	420.96	3.06	406.80	435.30	420.70	364.50	1.035	1.154	1.194	1.207	0.616	0.588
st-f_I	slice-basement	c-mod	mts3	421.84	3.94	259.20	291.40	274.50	211.60	1.062	1.297	1.377	1.405	0.626	0.576
st-f_II	slice-basement	c-mod	mts3	421.89	3.99	206.40	228.30	214.10	177.00	1.066	1.21	1.29	1.303	0.495	0.446
st-f_III	slice-basement	c-mod	mts3	421.93	4.03	351.60	389.60	375.90	289.20	1.036	1.3	1.347	1.384	0.76	0.727
st-g_I	slice-basement	c-modw	mts4	422.79	4.89	166.30	168.10	167.30	163.60	1.005	1.023	1.027	1.029	0.644	0.64
st-g_II	slice-basement	c-modw	mts4	422.82	4.92	49.27	49.87	49.45	48.50	1.008	1.02	1.028	1.029	0.396	0.39
st-g_III	slice-basement	c-modw	mts4	422.85	4.95	112.50	113.90	112.60	111.00	1.011	1.015	1.026	1.026	0.155	0.149
st-g_IV	slice-basement	c-modw	mts4	422.88	4.98	149.00	151.30	149.80	146.10	1.01	1.025	1.035	1.037	0.429	0.421
st-h_I	slice-basement	c-modw	mts4	424.05	6.15	120.30	121.10	120.30	119.50	1.006	1.007	1.014	1.014	0.078	0.075
st-h_II	slice-basement	c-modw	mts4	424.08	6.18	136.80	137.90	137.20	135.20	1.005	1.015	1.02	1.021	0.496	0.492
st-h_III	slice-basement	c-modw	mts4	424.11	6.21	120.30	121.40	120.40	119.00	1.009	1.011	1.02	1.02	0.114	0.11
st-h_IV	slice-basement	c-modw	mts4	424.14	6.24	124.30	125.80	124.90	122.20	1.007	1.022	1.03	1.031	0.516	0.51
st-h_V	slice-basement	c-modw	mts4	424.17	6.27	118.80	120.30	119.50	116.50	1.006	1.026	1.032	1.034	0.599	0.594
st-i_I	slice-basement	c-int	mts4	424.70	6.80	617.90	675.50	650.60	527.60	1.038	1.233	1.28	1.305	0.695	0.663
st-i_III	slice-basement	c-int	mts4	424.74	6.84	701.00	794.20	734.40	574.40	1.081	1.279	1.383	1.402	0.517	0.456
st-i_II	slice-basement	c-int	mts4	424.78	6.88	771.40	856.30	787.30	670.70	1.088	1.174	1.277	1.282	0.312	0.256
st-j_I	slice-basement	c-int	mts4	424.96	7.06	2025.00	2335.00	2223.00	1517.00	1.05	1.465	1.539	1.603	0.772	0.726
st-j_III	slice-basement	c-int	mts4	425.00	7.10	2009.00	2385.00	2179.00	1463.00	1.094	1.49	1.63	1.682	0.631	0.554
30 A/m															
st-aa_30_I	slice-cover	c-weak	mts0	417.68	-0.22	48.04	48.40	48.23	47.49	1.003	1.016	1.019	1.02	0.633	0.63
st-aa_30_II	slice-cover	c-weak	mts0	417.72	-0.18	55.17	55.82	55.39	54.29	1.008	1.02	1.028	1.029	0.45	0.445
st-aa_30_III	slice-cover	c-weak	mts0	417.76	-0.14	48.79	49.42	48.59	48.37	1.017	1.005	1.022	1.023	-0.562	-0.565
st-aa_30_IV	slice-cover	c-weak	mts0	417.80	-0.10	50.41	50.94	50.65	49.65	1.006	1.02	1.026	1.027	0.551	0.546
st-a_30_I	slice-basement	c-weak	mts1	418.00	0.10	63.84	64.99	63.48	63.04	1.024	1.007	1.031	1.032	-0.549	-0.554
st-a_30_II	slice-basement	c-weak	mts1	418.03	0.13	62.71	63.34	63.08	61.71	1.004	1.022	1.026	1.028	0.687	0.683
st-a_30_III	slice-basement	c-weak	mts1	418.06	0.16	65.01	66.09	65.78	63.15	1.005	1.042	1.047	1.051	0.797	0.793
st-a_30_V	slice-basement	c-weak	mts1	418.12	0.22	81.20	82.67	82.12	78.80	1.007	1.042	1.049	1.053	0.719	0.714
st-b_30_I	slice-basement	c-mod	mts1	418.50	0.60	90.19	92.94	91.59	86.03	1.015	1.065	1.08	1.086	0.621	0.609
st-b_30_II	slice-basement	c-mod	mts1	418.53	0.63	107.20	112.00	108.50	101.10	1.032	1.073	1.108	1.111	0.378	0.356
st-b_30_III	slice-basement	c-mod	mts1	418.56	0.66	93.02	98.12	95.55	85.40	1.027	1.119	1.149	1.159	0.619	0.597
st-b_30_IV	slice-basement	c-mod	mts1	418.59	0.69	88.99	94.49	92.24	80.25	1.024	1.149	1.177	1.193	0.704	0.683
st-c_30_I	slice-basement	c-mod	mts1	418.87	0.97	164.70	177.20	171.00	145.80	1.036	1.173	1.215	1.231	0.634	0.604
st-c_30_II	slice-basement	c-mod	mts1	418.90	1.00	239.90	271.70	253.20	194.80	1.073	1.299	1.394	1.42	0.575	0.518
st-c_30_III	slice-basement	c-mod	mts1	418.93	1.03	359.30	396.00	369.00	313.00	1.073	1.179	1.265	1.273	0.401	0.351
st-c_30_IV	slice-basement	c-mod	mts1	418.96	1.06	153.00	167.50	159.70	131.80	1.049	1.212	1.271	1.289	0.603	0.564
st-d_30_I	slice-basement	c-mod	mts2	419.91	2.01	205.70	222.40	216.50	178.00	1.028	1.216	1.249	1.275	0.756	0.731
st-d_30_II	slice-basement	c-mod	mts2	419.94	2.04	156.70	168.20	158.20	143.60	1.063	1.102	1.171	1.173	0.231	0.194
st-d_30_III	slice-basement	c-mod	mts2	419.97	2.07	110.40	114.60	110.70	105.80	1.035	1.046	1.082	1.083	0.126	0.107
st-d_30_IV	slice-basement	c-mod	mts2	420.00	2.10	358.80	396.10	366.50	313.90	1.081	1.167	1.262	1.267	0.331	0.278
st-d_30_V	slice-basement	c-mod	mts2	420.03	2.13	424.60	457.60	441.50	374.60	1.037	1.178	1.222	1.238	0.641	0.611
st-e_30_IV	slice-basement	c-mod	mts2	420.96	3.06	313.30	333.70	323.00	283.20	1.033	1.14	1.178	1.19	0.601	0.574
st-f_30_I	slice-basement	c-mod	mts3	421.84	3.94	209.20	231.70	220.70	175.30	1.05	1.259	1.322	1.347	0.653	0.612
st-f_30_II	slice-basement	c-mod	mts3	421.89	3.99	170.30	185.50	176.20	149.20	1.053	1.181	1.243	1.256	0.526	0.486
st-f_30_III	slice-basement	c-mod	mts3	421.93	4.03	280.50	307.30	298.30	236.00	1.03	1.264	1.302	1.335	0.777	0.75
st-g_30_I	slice-basement	c-modw	mts4	422.79	4.89	167.60	169.70	168.60	164.50	1.006	1.025	1.032	1.034	0.59	0.584
st-g_30_II	slice-basement	c-modw	mts4	422.82	4.92	48.58	49.16	49.02	47.56	1.003	1.031	1.034	1.037	0.824	0.821
st-g_30_III	slice-basement	c-modw	mts4	422.85	4.95	113.00	114.60	113.20	111.10	1.013	1.018	1.031	1.032	0.175	0.167
st-g_30_IV	slice-basement	c-modw	mts4	422.88	4.98	151.60	153.80	152.40	148.70	1.009	1.025	1.034	1.035	0.465	0.458
st-h_30_I	slice-basement	c-modw	mts4	424.05	6.15	119.70	120.80	119.80	118.70	1.008	1.01	1.018	1.018	0.114	0.109

II.c – AMS – Långviken

specimen	group	ams-type	section*	log	distance	Kbulk	K1	K2	K3	L	F	P	P'	T	U
st-h_30_II	slice-basement	c-modw	mts4	424.08	6.18	137.20	138.40	137.80	135.40	1.004	1.018	1.022	1.023	0.615	0.612
st-i_30_I	slice-basement	c-int	mts4	424.70	6.80	498.20	538.80	519.10	436.80	1.038	1.189	1.234	1.251	0.646	0.614
st-i_30_III	slice-basement	c-int	mts4	424.74	6.84	545.90	608.70	568.60	460.40	1.071	1.235	1.322	1.338	0.512	0.459
st-j_30_III	slice-basement	c-int	mts4	425.00	7.10	1652.00	1925.00	1791.00	1238.00	1.075	1.447	1.555	1.606	0.673	0.609

300 A/m

specimen	dK1geo	iK1geo	dK2geo	iK2geo	dK3geo	iK3geo
st-aa_I	238.2	3	328.3	1.5	84.7	86.7
st-aa_II	237.3	2.2	147.1	4.3	354	85.1
st-aa_III	241.4	6.5	150.7	6.3	17.2	80.9
st-aa_IV	202.3	4.3	292.9	7.8	83.8	81.1
st-aa_V	287	5.8	196.1	9.2	48.5	79.1
st-a_I	317.8	3.4	48.6	12.4	212.8	77.1
st-a_II	292	2.3	22.5	13.5	192.3	76.3
st-a_III	300.3	12.3	31.7	6.4	148.4	76.1
st-a_IV	303.7	1.2	33.9	8	205.3	81.9
st-a_V	110.1	8	17.3	19.1	221.8	69.2
st-b_I	116.3	3.5	24.7	24.2	214	65.5
st-b_II	123.3	9	24.9	42.5	222.7	46.1
st-b_III	106.6	6.6	14.5	17.9	215.9	70.8
st-b_IV	104.4	13.6	9.3	19.9	226.4	65.6
st-c_I	141.7	11.7	45.2	28.8	251.4	58.5
st-c_II	127.3	11.6	33.2	19.4	246.4	67.2
st-c_III	141.5	14.7	47.3	15.5	272.9	68.3
st-c_IV	136.8	17.7	46.3	1.5	311.6	72.2
st-c_V	136.5	21.7	228.3	4.7	329.8	67.8
st-d_I	57	6.4	325.6	12.8	173.1	75.6
st-d_II	261	6.5	170.9	1.2	70.2	83.4
st-d_III	260.2	14.3	169	4.7	61.4	75
st-d_IV	338.9	17.1	69.9	3.3	170.5	72.6
st-d_V	135.5	3.4	43.9	24.4	232.8	65.3
st-e_I	75.3	55.8	319.5	16.5	220	29
st-e_II	11.1	28.1	109.3	15	224.3	57.5
st-e_III	69.9	23	328.7	24.6	197.4	55.2
st-e_IV	84.9	19	340.3	36.3	197	47.5
st-f_I	22.1	28.6	113.7	2.9	208.9	61.2
st-f_II	31.1	19.3	296.6	12.5	175.5	66.7
st-f_III	18.1	19.3	285.1	8.7	172	68.7
st-g_I	175.4	24	82.3	6.9	337.2	64.9
st-g_II	123.9	11.1	33.2	4	283.8	78.2
st-g_III	185.4	21.9	83.9	26.4	309.8	54.5
st-g_IV	171.2	20.5	77.4	10.2	322.5	66.9
st-h_I	320.1	16.2	221.3	27.8	76.7	57
st-h_II	144.2	2.8	235.9	31.1	49.6	58.8
st-h_III	218.7	7.7	128.3	3	17.1	81.8
st-h_IV	179.5	0.4	89.4	8.8	272.4	81.2
st-h_V	86.8	27.1	177.3	0.9	269	62.8
st-i_I	94.5	8.5	184.8	1.9	287.1	81.3
st-i_III	83.5	11.1	174.7	6	292.8	77.3
st-i_II	97.7	16.8	7.1	2	270.7	73.1

specimen	dK1geo	iK1geo	dK2geo	iK2geo	dK3geo	iK3geo
st-j_I	40.5	1.1	130.8	14.1	306.2	75.9
st-j_III	73.2	1.9	163.7	14.3	335.7	75.5
30 A/m						
st-aa_30_I	47.7	3.6	317.4	3.8	180.9	84.8
st-aa_30_II	261.5	10.1	351.6	0.5	84.3	79.9
st-aa_30_III	69.6	4.2	161	19.1	327.7	70.4
st-aa_30_IV	66.6	1.9	336.2	11.1	166.2	78.7
st-a_30_I	136.8	1.1	227.1	18.4	43.5	71.5
st-a_30_II	300.3	11.5	34.2	18.2	179.7	68.2
st-a_30_III	255.8	3.2	346.4	10.4	149.1	79.1
st-a_30_V	111.5	6.6	18.6	24	215.8	65.1
st-b_30_I	120.5	4.8	28.2	24.8	220.8	64.7
st-b_30_II	123.9	11.4	23.6	41.7	226	46
st-b_30_III	100.7	10.4	7.4	17.4	220.1	69.6
st-b_30_IV	105.5	13.5	11	18.2	230	67.1
st-c_30_I	137.5	13.8	40.7	25.8	253	60.2
st-c_30_II	124.8	12.9	30.3	18.8	247.3	66.9
st-c_30_III	142.1	16	47.9	14.3	278.1	68.3
st-c_30_IV	142.5	19.1	51.9	1.7	317.1	70.8
st-d_30_I	56.5	6.1	325.2	11.5	173.9	76.9
st-d_30_II	262.3	5.4	172.3	0.6	75.5	84.5
st-d_30_III	263.6	10.9	172.3	6.8	51	77.1
st-d_30_IV	338.7	16.7	70.3	5.4	177.6	72.4
st-d_30_V	129.3	6.6	36.2	24.5	233.4	64.5
st-e_30_IV	84.2	20.8	339.7	33.6	200	49
st-f_30_I	20	29.6	110.8	1.4	203.2	60.3
st-f_30_II	32.9	20	298.6	11.6	180.2	66.6
st-f_30_III	19	21.4	285.6	8.6	174.8	66.8
st-g_30_I	181	25.3	85.2	12.2	331.6	61.6
st-g_30_II	96.1	0.9	5.9	13.4	190	76.6
st-g_30_III	191.2	21.1	89	28.7	312	53.1
st-g_30_IV	176.3	19.1	80.3	16.9	311.7	64
st-h_30_I	159	2.6	250	20.8	62.2	69
st-h_30_II	316.3	10	220.5	29.5	63.1	58.5
st-i_30_I	99.6	8.8	190.1	3.2	300	80.6
st-i_30_III	89.9	11.2	180.7	4.3	291.4	77.9
st-j_30_III	75.4	2.9	166.2	14.4	334.2	75.3

average and standard deviation σ

300 A/m

specimen	Km-mean	K1-mean	K2-mean	K3-mean	L-mean	F-mean	P-mean	P'-mean	T-mean	U-mean	dK1geo-mean	iK1geo-mean	dK2geo-mean	iK2geo-mean	dK3geo-mean	iK3geo-mean
st-aa_I	49.68	50.20	49.91	48.92	1.01	1.02	1.03	1.03	0.56	0.55	241.24	4.36	223.02	5.82	117.64	82.58
st-a_I	72.76	74.04	73.35	70.87	1.01	1.03	1.04	1.05	0.52	0.51	264.78	5.44	30.80	11.88	196.12	76.12
st-b_I	106.33	113.38	108.89	96.73	1.04	1.13	1.17	1.18	0.48	0.45	112.65	8.18	18.35	26.13	219.75	62.00
st-c_I	270.64	303.36	280.42	228.14	1.08	1.23	1.33	1.34	0.45	0.39	136.76	15.48	80.06	13.98	282.42	66.80
st-d_I	309.48	341.76	318.34	268.32	1.07	1.17	1.25	1.26	0.32	0.27	210.52	9.54	155.86	9.28	141.60	74.38
st-e_I	256.83	278.73	267.43	224.35	1.04	1.21	1.26	1.28	0.64	0.61	60.30	31.48	274.45	23.10	209.68	47.30
st-f_I	272.40	303.10	288.17	225.93	1.05	1.27	1.34	1.36	0.63	0.58	23.77	22.40	231.80	8.03	185.47	65.53
st-g_I	119.27	120.79	119.79	117.30	1.01	1.02	1.03	1.03	0.41	0.40	163.98	19.38	69.20	11.88	313.33	66.13
st-h_I	124.10	125.30	124.46	122.48	1.01	1.02	1.02	1.02	0.36	0.36	189.86	10.84	170.44	14.32	136.96	68.32

II.c – AMS – Långviken

specimen	Km-mean	K1-mean	K2-mean	K3-mean	L-mean	F-mean	P-mean	P'-mean	T-mean	U-mean	dK1geo-mean	iK1geo-mean	dK2geo-mean	iK2geo-mean	dK3geo-mean	iK3geo-mean
st-i_I	696.77	775.33	724.10	590.90	1.07	1.23	1.31	1.33	0.51	0.46	91.90	12.13	122.20	3.30	283.53	77.23
st-j_I	2017.00	2360.00	2201.00	1490.00	1.07	1.48	1.58	1.64	0.70	0.64	56.85	1.50	147.25	14.20	320.95	75.70
30 A/m																
st-aa_30_I	50.60	51.15	50.72	49.95	1.01	1.02	1.02	1.02	0.27	0.26	111.35	4.95	291.55	8.63	189.78	78.45
st-a_30_I	68.19	69.27	68.62	66.68	1.01	1.03	1.04	1.04	0.41	0.41	201.10	5.60	156.58	17.75	147.03	70.98
st-b_30_I	94.85	99.39	96.97	88.20	1.02	1.10	1.13	1.14	0.58	0.56	112.65	10.03	17.55	25.53	224.23	61.85
st-c_30_I	229.23	253.10	238.23	196.35	1.06	1.22	1.29	1.30	0.55	0.51	136.73	15.45	42.70	15.15	273.88	66.55
st-d_30_I	251.24	271.78	258.68	223.18	1.05	1.14	1.20	1.21	0.42	0.38	210.08	9.14	155.26	9.76	142.28	75.08
st-e_30_IV	313.30	333.70	323.00	283.20	1.033	1.14	1.178	1.19	0.601	0.574	84.2	20.8	339.7	33.6	200	49
st-f_30_I	220.00	241.50	231.73	186.83	1.04	1.23	1.29	1.31	0.65	0.62	23.97	23.67	231.67	7.20	186.07	64.57
st-g_30_I	120.20	121.82	120.81	117.97	1.01	1.02	1.03	1.03	0.51	0.51	161.15	16.60	65.10	17.80	286.33	63.83
st-h_30_I	128.45	129.60	128.80	127.05	1.01	1.01	1.02	1.02	0.36	0.36	237.65	6.30	235.25	25.15	62.65	63.75
st-i_30_I	522.05	573.75	543.85	448.60	1.05	1.21	1.28	1.29	0.58	0.54	94.75	10.00	185.40	3.75	295.70	79.25
st-j_30_III	1652.00	1925.00	1791.00	1238.00	1.075	1.447	1.555	1.606	0.673	0.609	75.4	2.9	166.2	14.4	334.2	75.3

300 A/m

specimen	Km-σ	K1-σ	K2-σ	K3-σ	L-σ	F-σ	P-σ	P'-σ	T-σ	U-σ	dK1geo-σ	iK1geo-σ	dK2geo-σ	iK2geo-σ	dK3geo-σ	iK3geo-σ
st-aa_30_I	3.20	3.29	3.29	3.03	0.01	0.01	0.00	0.00	0.56	0.56	100.57	3.57	88.15	8.27	101.30	5.98
st-a_30_I	8.72	9.00	9.08	8.11	0.01	0.02	0.01	0.01	0.64	0.64	91.28	4.54	158.14	5.59	74.21	6.01
st-b_30_I	8.40	8.68	7.88	8.98	0.01	0.04	0.04	0.05	0.14	0.14	11.29	3.72	9.93	11.28	4.66	10.75
st-c_30_I	94.88	106.23	96.63	82.32	0.02	0.06	0.08	0.08	0.10	0.11	8.27	2.76	9.48	10.14	31.77	4.53
st-d_30_I	134.60	148.20	140.38	115.45	0.02	0.07	0.07	0.08	0.27	0.27	114.29	4.74	112.75	9.11	76.39	7.34
st-f_30_I	55.89	61.49	61.79	44.53	0.01	0.05	0.04	0.05	0.13	0.13	7.75	5.19	104.88	5.24	15.08	3.70
st-g_30_I	52.96	53.69	53.21	52.01	0.00	0.01	0.00	0.00	0.27	0.27	43.81	10.78	39.63	7.54	64.89	9.72
st-h_30_I	12.37	12.45	12.73	11.81	0.00	0.01	0.00	0.00	0.35	0.36	111.23	5.23	20.86	6.15	0.64	7.42
st-i_30_I	33.73	49.43	35.00	16.69	0.02	0.03	0.06	0.06	0.09	0.11	6.86	1.70	6.65	0.78	6.08	1.91
30 A/m																
st-aa_I	1.98	2.00	2.01	1.94	0.00	0.00	0.01	0.01	0.19	0.19	30.15	1.81	83.20	3.02	135.06	3.18
st-a_I	14.11	14.51	14.44	13.39	0.01	0.01	0.02	0.02	0.37	0.37	86.97	4.63	12.02	5.00	28.78	4.54
st-b_I	9.24	10.45	8.93	9.21	0.01	0.05	0.06	0.07	0.15	0.15	8.78	4.26	7.74	11.23	5.80	10.89
st-c_I	109.88	124.19	113.34	92.90	0.03	0.07	0.08	0.08	0.21	0.21	5.84	4.29	83.06	11.10	36.90	5.04
st-d_I	184.40	206.29	191.19	156.00	0.03	0.09	0.09	0.10	0.29	0.29	112.58	5.84	110.83	9.53	73.61	6.50
st-e_I	135.04	144.40	138.57	122.23	0.01	0.04	0.04	0.05	0.07	0.07	33.38	16.64	110.43	9.76	14.51	12.93
st-f_I	73.49	81.28	81.76	57.46	0.02	0.05	0.04	0.05	0.13	0.14	6.66	5.37	102.44	4.83	20.37	3.88
st-g_I	51.77	52.43	52.14	50.81	0.00	0.00	0.00	0.00	0.20	0.20	27.37	5.70	24.16	10.01	22.64	9.71
st-h_I	7.39	7.36	7.43	7.39	0.00	0.01	0.01	0.01	0.24	0.24	87.48	10.92	61.77	14.16	123.90	12.22
st-i_I	76.84	91.86	68.93	72.96	0.03	0.05	0.06	0.06	0.19	0.20	7.45	4.25	99.81	2.34	11.47	4.10
st-j_I	11.31	35.36	31.11	38.18	0.03	0.02	0.06	0.06	0.10	0.12	23.12	0.57	23.26	0.14	20.86	0.28

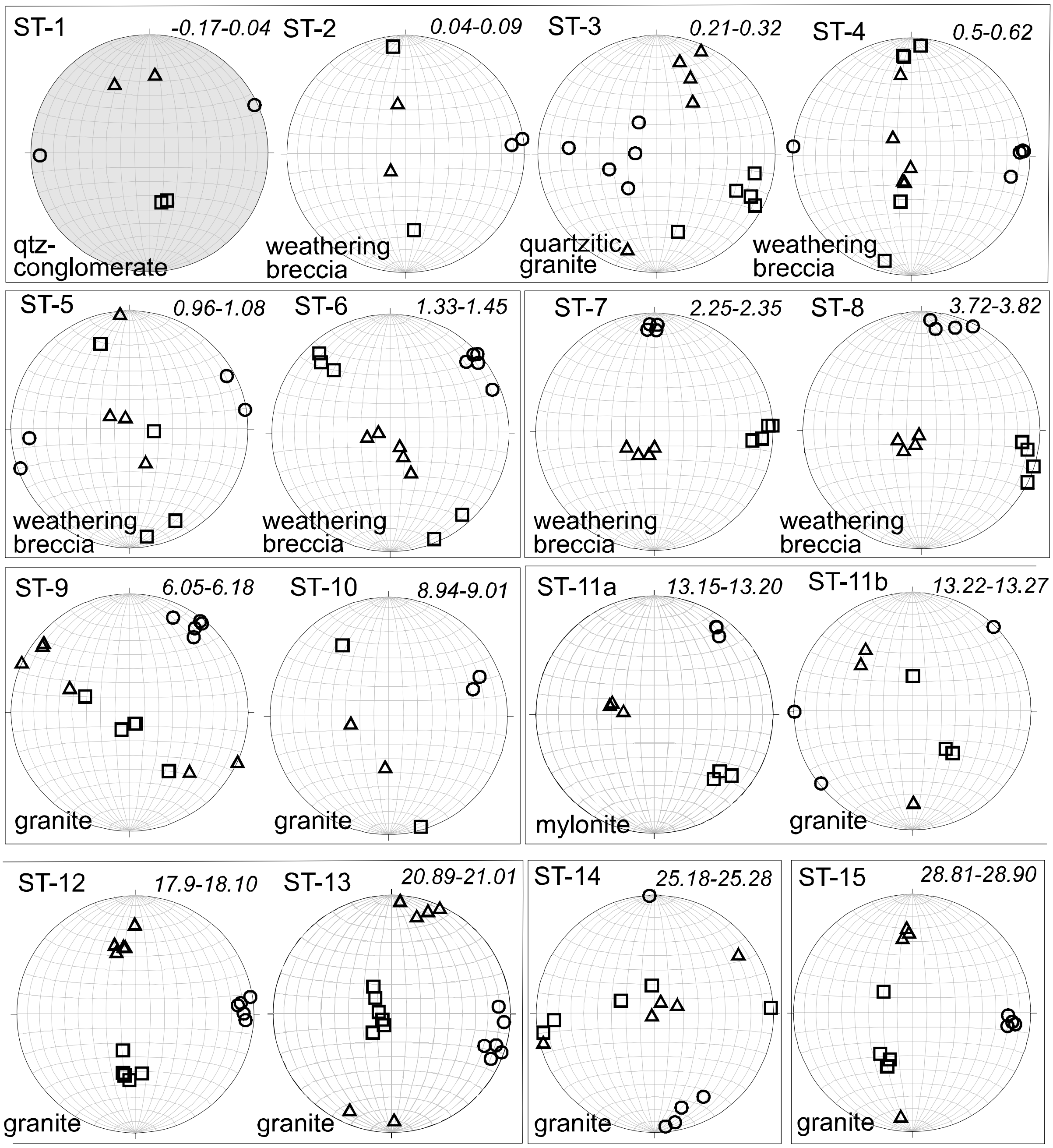

AMS stereoplots of the autochthonous basement section of the Långviken core. Numbers are depth measured from the unconformity. Stereoplots in on box have the same relative orientation in the core. (equal area projection of the lower hemisphere)

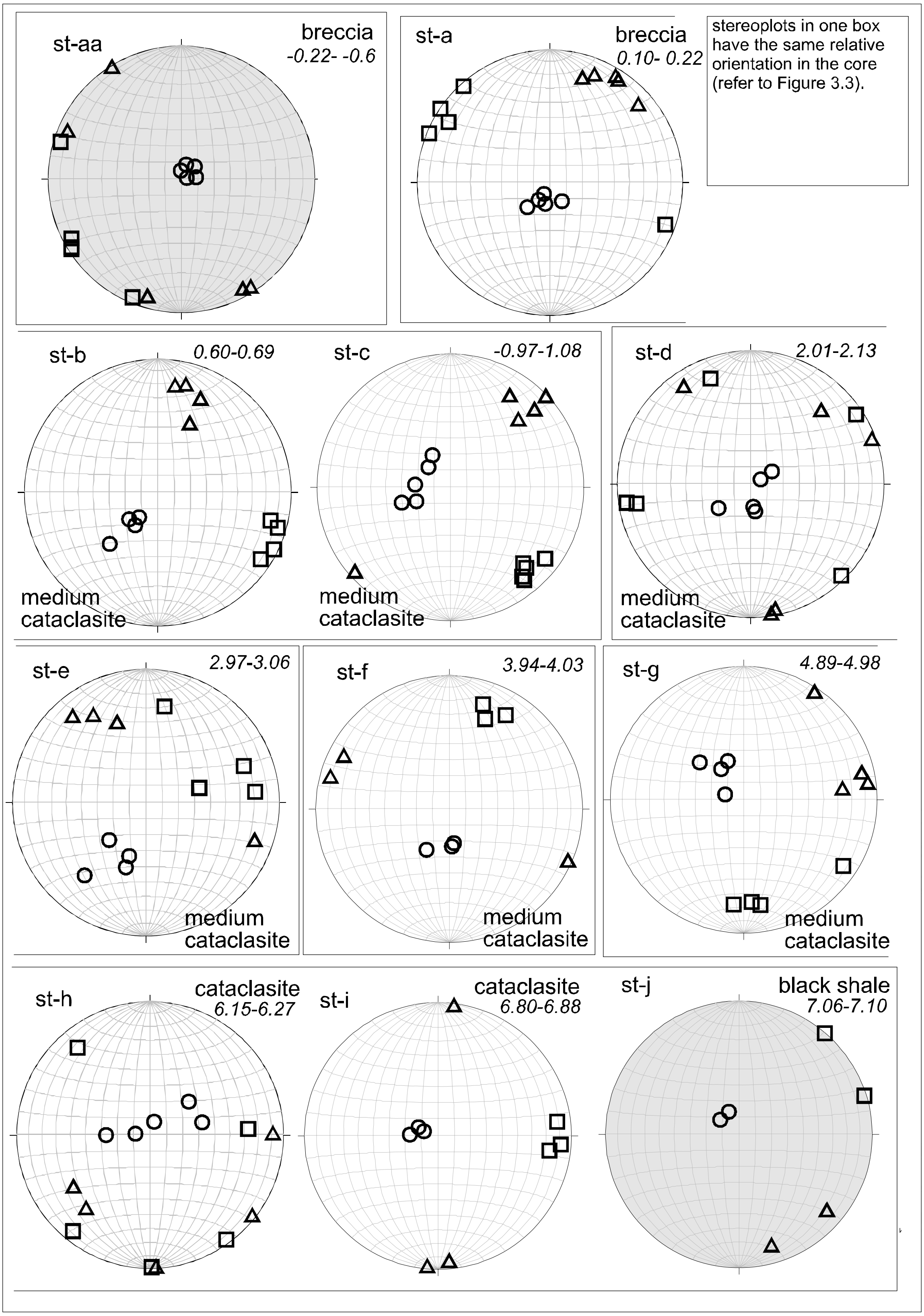

Compilation of AMS stereoplots of the allochthonous basements slice in the Långviken core. Numbers are depth measured from the unconformity (equal area projection of the lower hemisphere).

Narcea Antiform

specimen	mean	L	F	P	P'	T	U	dK1geo	iK1geo	dK2geo	iK2geo	dK3geo	iK3geo
mh1-1_i	26.55	1.008	1.012	1.02	1.02	0.187	0.183	115.5	42.4	23.5	2.1	291.2	47.5
mh1-1_ii	17.57	1.008	1.005	1.013	1.013	-0.206	-0.209	137.7	17.8	231.6	12	353.8	68.4
mh1-1_iii	18.37	1.006	1.012	1.018	1.019	0.351	0.347	156.1	18.7	52.5	34.7	269.1	49.2
mh1-1_iv	20.09	1.004	1.007	1.011	1.011	0.265	0.263	90.5	49.9	342.4	14.6	241.4	36.3
mh1-1_v	24.05	1.008	1.012	1.02	1.02	0.176	0.171	78.4	46.9	338.8	8.8	240.8	41.8
MH1-2_i	169.70	1.009	1.01	1.019	1.019	0.079	0.1	128.2	43.5	37	1	306.3	46.4
MH1-2_ii	198.70	1.019	1.016	1.035	1.035	-0.075	-0.1	144.2	42.7	351	44	247.4	13.9
MH1-2_iii	180.10	1.015	1.004	1.019	1.02	-0.587	-0.6	120.8	39.5	4	28	249.9	37.4
MH1-2_iv	178.60	1.017	1.003	1.021	1.022	-0.666	-0.7	140.1	46	258	24	5.4	34.2
MH1-2_v	173.30	1.014	1.004	1.017	1.018	-0.585	-0.6	143	43	255	22	4	39
MH1-3_i	202.80	1.012	1.007	1.018	1.019	-0.282	-0.3	178.5	46.5	278	9	16.5	42.1
MH1-3_ii	183.50	1.01	1.005	1.015	1.015	-0.359	-0.4	143.2	30.1	38	24	275.9	49.4
MH1-3_iii	175.60	1.011	1.004	1.015	1.016	-0.471	-0.5	168.8	47.7	61	15.8	318.1	38
MH1-3_iv	176.10	1.01	1.004	1.014	1.014	-0.46	-0.5	168.1	50.1	13.4	37	273.8	12.7
MH1-3_v	174.80	1.013	1.004	1.017	1.018	-0.522	-0.5	205.1	51.9	81.8	23	338.6	28.4
MH1-4_i	304.70	1.012	1.021	1.033	1.034	0.271	0.3	167.6	68.8	291	12	24.6	17.2
MH1-4_ii	303.10	1.022	1.019	1.042	1.042	-0.073	-0.1	166.4	59.8	286.2	16.6	24.1	24.7
MH1-4_iii	287.10	1.019	1.022	1.041	1.042	0.077	0.1	176.6	68.8	297.9	11.8	31.6	17.6
MH1-4_iv	299.40	1.016	1.02	1.036	1.036	0.119	0.1	144.9	56.1	280	25	20.5	20.7
MH1-4_v	344.50	1.015	1.033	1.049	1.05	0.36	0.4	159.6	67.5	269.5	17	31.5	14.3
MH1-5a_i	313.80	1.019	1.029	1.049	1.049	0.199	0.2	134.7	50.5	42	2	310.5	39.5
MH1-5a_ii	308.10	1.016	1.028	1.045	1.046	0.266	0.3	134.3	46.4	41	3	308.9	43.5
MH1-5a_iii	281.30	1.023	1.032	1.055	1.055	0.159	0.1	140.8	45.4	42	9	303.4	43.3
MH1-5a_iv	284.10	1.025	1.026	1.052	1.052	0.024	0	150.9	38.2	48	15	300.7	47.7
MH1-5b_i	239.10	1.017	1.02	1.037	1.037	0.088	0.1	177.8	52.1	75	10	337.6	36.2
MH1-5b_ii	250.80	1.024	1.018	1.043	1.043	-0.136	-0.1	166.9	57.1	70	5	337	32.5
MH1-5b_iii	248.70	1.015	1.013	1.028	1.028	-0.06	-0.1	163.6	51	258	3	350	38.9
MH1-8_i	227.30	1.005	1.003	1.008	1.008	-0.163	-0.2	114.8	7.4	206	6	335.5	80.3
MH1-8_ii	237.00	1.006	1.007	1.013	1.013	0.025	0	124.3	18.5	33	3	292.9	71.2
MH1-8_iii	193.70	1.003	1.002	1.004	1.004	-0.199	-0.2	207.4	1.7	111	72.9	289	17
MH1-8_iv	186.10	1.003	1.004	1.007	1.007	0.063	0.1	108.9	11	203	22	354.3	64.9
MH1-8_v	214.30	1.002	1.01	1.011	1.012	0.706	0.7	146.3	22.8	56	1	324	67.1
MH1-9_i	299.30	1.016	1.021	1.037	1.037	0.141	0.1	142.8	15.1	233	1	328	74.9
MH1-9_ii	314.90	1.022	1.028	1.051	1.051	0.104	0.1	161.5	14.9	69	9	310.3	72.7
MH1-9_iii	291.90	1.021	1.025	1.046	1.046	0.074	0.1	156.6	20.5	63	10	307.2	66.7
MH1-9_iv	312.10	1.025	1.027	1.053	1.053	0.051	0	147.5	17.3	55.4	6.7	305.5	71.4
MH1-10_i	317.60	1.009	1.045	1.055	1.059	0.655	0.6	129.7	25.9	225	11	337.2	61.3
MH1-10_ii	309.60	1.008	1.037	1.046	1.049	0.628	0.6	136.6	39.4	230	4	324.7	50.3
MH1-10_iii	324.70	1.013	1.059	1.073	1.078	0.632	0.6	151.2	36.1	59	4	323.6	53.7
MH1-10_iv	321.10	1.012	1.043	1.055	1.058	0.569	0.6	131.7	34.6	235	19	348.3	49.3
MH1-11_i	361.70	1.029	1.052	1.082	1.083	0.286	0.3	138.8	43.1	34	15	289.6	43
MH1-11_ii	389.00	1.032	1.056	1.09	1.091	0.261	0.2	133.2	45.8	33	10	293.4	42.5
MH1-11_iii	364.60	1.029	1.054	1.085	1.086	0.292	0.3	161	31	54	27	291.2	47
MH1-11_iv	368.50	1.034	1.053	1.089	1.09	0.216	0.2	151.1	36.4	46	19	294.1	47.2
MH1-13_i	305.80	1.019	1.006	1.026	1.027	-0.495	-0.5	166.9	55.9	283.7	17	23.4	28.5
MH1-13_ii	156.60	1.014	1.006	1.019	1.02	-0.421	-0.4	148.2	68.3	9	17	274.9	13.4
MH1-13_iii	163.40	1.008	1.008	1.016	1.016	0.027	0	180.9	34.1	14	55	275.1	6.1

II.d – AMS – Narcea Antiform

specimen	mean	L	F	P	P'	T	U	dK1geo	iK1geo	dK2geo	iK2geo	dK3geo	iK3geo
MH1-13_iv	189.80	1.015	1.004	1.019	1.02	-0.53	-0.5	185.3	51.4	288	10	25.4	36.8
MH1-13_v	254.40	1.014	1.005	1.019	1.019	-0.456	-0.5	176.8	58.1	289.3	13	26.1	28.5
MH1-15_i	152.90	1.012	1.017	1.028	1.029	0.176	0.2	215.8	33.9	110	22	354.1	48
MH1-15_ii	137.40	1.011	1.015	1.027	1.027	0.138	0.1	236.1	25.6	132	28	2	50.7
MH1-15_iii	135.40	1.005	1.012	1.018	1.018	0.401	0.4	224.1	23.7	121	27	349.1	52.5
MH1-15_iv	148.20	1.012	1.022	1.035	1.035	0.286	0.3	224.6	23.4	119.3	31.5	344.4	48.9
MH1-15_v	139.70	1.004	1.013	1.017	1.018	0.49	0.5	89.4	3.7	182	35	354.3	54.4
mh1-16a_i	435.30	1.03	1.025	1.056	1.056	-0.096	-0.109	159.6	38.8	64	6.9	325.6	50.3
mh1-16a_ii	459.10	1.034	1.02	1.055	1.055	-0.27	-0.283	162	38.7	64	9.9	322.2	49.6
mh1-16a_iii	475.00	1.018	1.043	1.062	1.064	0.396	0.383	175.9	43.9	80.4	5.7	344.5	45.5
mh1-16a_iv	421.40	1.025	1.03	1.056	1.056	0.09	0.077	160.7	43.7	254.6	4	348.7	46
mh1-16a_v	472.60	1.022	1.042	1.064	1.065	0.309	0.294	174.8	46.8	78.8	5.6	343.6	42.6
mh1-16b_i	468.50	1.026	1.019	1.046	1.046	-0.153	-0.164	142.6	46.8	241.3	8.1	338.6	42
mh1-16b_ii	483.50	1.027	1.016	1.044	1.044	-0.238	-0.248	153.1	44.2	62.6	0.5	332.1	45.8
mh1-16b_iii	481.20	1.026	1.017	1.043	1.044	-0.212	-0.222	151.3	40.1	61.1	0.2	330.8	49.9
mh1-17_i	356.40	1.022	1.015	1.037	1.037	-0.186	-0.195	143.9	47.9	259.7	21.5	5.2	34.2
mh1-17_ii	342.60	1.021	1.017	1.039	1.039	-0.087	-0.097	147	53	259.9	16.4	0.6	32.2
mh1-17_iii	333.00	1.02	1.015	1.036	1.036	-0.139	-0.148	155	50.9	258.2	10.5	356.2	37.2
mh1-17_iv	345.90	1.018	1.016	1.034	1.034	-0.063	-0.072	148.1	48.3	247.9	8.6	345.2	40.4
mh1-18_i	181.30	1.012	1.014	1.027	1.027	0.075	0.069	131.2	14.1	338.7	74.2	222.9	7
mh1-18_ii	177.20	1.009	1.019	1.028	1.028	0.337	0.331	134.2	28.7	309.7	61.3	43.1	1.9
mh1-18_iii	178.50	1.01	1.008	1.018	1.018	-0.091	-0.095	131.5	13.1	354.5	72.4	224.2	11.6
MH2-1_i	65.31	1.002	1.004	1.006	1.006	0.263	0.3	206.8	64.3	6	24	99.4	8.2
MH2-1_ii	112.50	1.004	1.002	1.007	1.007	-0.262	-0.3	147.7	54	308	34	44.6	9.3
MH2-1_iii	70.12	1.005	1.004	1.009	1.009	-0.118	-0.1	173.9	65.2	288	11	22.2	22.1
MH2-1_iv	82.18	1.006	1.005	1.011	1.011	-0.03	0	357.9	21.4	148	66	263.5	11
MH2-1_v	70.99	1.003	1.002	1.005	1.005	-0.055	-0.1	147.7	52.3	30	20	287.3	30.4
MH2-2a_i	244.80	1.013	1.025	1.039	1.039	0.309	0.3	88.6	28.9	183	8	286.7	59.9
MH2-2a_ii	272.00	1.011	1.022	1.034	1.035	0.332	0.3	95.2	29.5	186	1	278.2	60.5
MH2-2a_iii	262.40	1.012	1.026	1.039	1.04	0.366	0.4	92.1	29.4	185	5	283	60.2
MH2-2a_iv	260.60	1.011	1.023	1.034	1.035	0.364	0.4	89.3	27	185	11	295.7	60.4
MH2-3_i	78.40	1.004	1.007	1.011	1.011	0.316	0.3	165.8	45.6	69	7	332.2	43.6
MH2-3_ii	113.10	1.002	1.004	1.005	1.005	0.336	0.3	143.9	41.9	244	11	345.8	46
MH2-3_iii	75.44	1.005	1.003	1.008	1.008	-0.322	-0.3	191.7	40	94	9	354.2	48.7
MH2-3_iv	94.89	1.003	1.002	1.005	1.005	-0.122	-0.1	151.6	49.9	51	9	314.1	38.7
MH2-3_v	134.20	1.004	1	1.004	1.004	-0.863	-0.9	158.8	43.5	251	3	344.3	46.4
MH2-4_i	303.20	1.011	1.025	1.036	1.037	0.395	0.4	294.4	22.3	27	5	129.7	67
MH2-4_ii	293.70	1.009	1.03	1.04	1.042	0.524	0.5	287.6	18.8	21	9	135.9	68.9
MH2-4_iii	289.80	1.008	1.033	1.041	1.044	0.588	0.6	283.3	19.9	14	3	113.6	69.8
MH2-4_iv	272.30	1.011	1.03	1.042	1.043	0.444	0.4	286	19.6	196	1	101.6	70.4
MH2-4_v	267.20	1.01	1.026	1.036	1.037	0.457	0.4	284.4	20.5	194	1	102.1	69.4
MH2-6_i	309.20	1.006	1.027	1.032	1.035	0.653	0.6	220.3	13.3	119	39	325.3	47.6
MH2-6_ii	335.70	1.006	1.022	1.028	1.029	0.598	0.6	211.9	18.8	106	38	322.4	45.8
MH2-6_iii	280.00	1.001	1.028	1.029	1.033	0.918	0.9	215.1	14.6	115	35	324	51.2
MH2-6_iv	295.50	1.003	1.026	1.029	1.032	0.779	0.8	61.2	11.9	161	39	317.4	48.5
MH2-6_v	276.00	1.012	1.021	1.033	1.034	0.29	0.3	205.9	24.2	101	31	327.3	49.3
MH2-7_i	362.90	1.018	1.022	1.04	1.04	0.118	0.1	11.1	0.9	101	21	278.7	68.9
MH2-7_ii	374.30	1.016	1.019	1.036	1.036	0.085	0.1	7.6	5.7	99	17	259.9	71.8
MH2-7_iii	370.40	1.013	1.021	1.034	1.034	0.216	0.2	2.3	8.5	94	11	234.3	76.4
MH2-7_iv	371.60	1.016	1.016	1.032	1.032	0.017	0	2.2	4.5	93	7	240.9	81.4
MH2-7_v	379.70	1.018	1.023	1.041	1.041	0.115	0.1	2.9	1.6	94	32	270.2	58.3

II.d – AMS – Narcea Antiform

specimen	mean	L	F	P	P'	T	U	dK1geo	iK1geo	dK2geo	iK2geo	dK3geo	iK3geo
MH3-1_i	333.00	1.001	1.021	1.022	1.025	0.876	0.9	141.6	10.1	235	20	25.8	67.6
MH3-1_ii	339.80	1.006	1.019	1.025	1.026	0.526	0.5	160.4	18.6	255	15	21.2	66
MH3-1_iii	331.30	1.005	1.021	1.026	1.027	0.61	0.6	159.7	20.3	256	15	20.2	64
MH3-1_iv	341.40	1.006	1.018	1.024	1.025	0.51	0.5	156.1	15.2	251	16	24.6	67.7
MH3-1_v	333.30	1.009	1.018	1.027	1.028	0.342	0.3	158.1	22.1	261	28	35.6	52.9
MH3-2_i	64.57	1.002	1.012	1.014	1.015	0.765	0.8	322.8	8.7	72	66	229.2	22.7
MH3-2_ii	62.71	1.007	1.017	1.025	1.025	0.428	0.4	303.3	33.3	42	13	149.4	53.8
MH3-2_iii	64.28	1.006	1.004	1.01	1.01	-0.175	-0.2	312	34	70	35	191.4	37.1
MH3-2_iv	66.49	1.005	1.008	1.013	1.013	0.202	0.2	349.8	39.8	113	33	228	32.3
MH3-2_v	65.16	1.007	1.005	1.011	1.011	-0.148	-0.2	313.1	44.4	94	38	201.6	20.5
MH3-3_i	350.00	1.004	1.017	1.021	1.023	0.601	0.6	148.6	8.3	240	8	12.3	78.6
MH3-3_ii	373.00	1.01	1.01	1.02	1.02	0.035	0	325.5	11.4	229	31	73.2	56.5
MH3-3_iii	351.80	1.003	1.022	1.025	1.027	0.76	0.8	182.4	14.3	278	20	58.4	65.4
MH3-3_iv	357.70	1.006	1.014	1.02	1.02	0.42	0.4	319.7	8.9	225	27	66.3	61.2
MH3-3_v	340.20	1.007	1.015	1.022	1.022	0.329	0.3	150.9	6.5	243	18	41.8	70.8
MH3-4_i	224.80	1.003	1.031	1.035	1.038	0.813	0.8	107.1	3	13	55	199.3	35.1
MH3-4_ii	202.60	1.004	1.032	1.036	1.04	0.763	0.8	114.1	2.6	21	45	206.6	44.4
MH3-4_iii	329.10	1.008	1.056	1.064	1.07	0.752	0.7	298.7	9.1	39	48	200.7	40.9
MH3-4_iv	341.30	1.003	1.056	1.06	1.067	0.893	0.9	299.9	11.1	43	49	200.9	38.7
MH3-4_v	334.50	1.003	1.05	1.054	1.06	0.888	0.9	297.8	8.5	37	48	200.5	40.6
MH3-5_i	155.80	1.004	1.023	1.027	1.029	0.715	0.7	1.2	35.6	101	14	208.9	51.1
MH3-5_ii	120.90	1.007	1	1.007	1.009	-0.946	-0.9	320.1	17.6	55	15	182.5	66.8
MH3-5_iii	113.90	1.005	1.003	1.008	1.008	-0.35	-0.4	348.5	33.4	87	13	195.9	53.4
MH3-5_iv	122.20	1.005	1.004	1.009	1.009	-0.172	-0.2	327.1	26	71	27	199.9	51.1
MH3-5_v	116.50	1.004	1.002	1.006	1.006	-0.418	-0.4	311.3	17	187	61	48.6	22.4
MH3-6_i	329.30	1.009	1.007	1.016	1.016	-0.122	-0.1	144.2	13.2	239	21	24.3	64.7
MH3-6_ii	266.90	1.01	1.003	1.013	1.014	-0.568	-0.6	136	32.2	246	28	7.4	44.8
MH3-6_iii	332.60	1.005	1.012	1.017	1.017	0.402	0.4	164.9	31	262	11	9.4	56.6
MH3-6_iv	310.50	1.009	1.007	1.017	1.017	-0.134	-0.1	125.6	13.2	33	9	269.7	73.8
MH3-6_v	313.70	1.014	1.008	1.022	1.022	-0.286	-0.3	123.7	10.2	238	67	29.8	20.9
MH3-8_i	315.30	1.016	1.006	1.023	1.023	-0.431	-0.4	141.2	6.8	49	21	248.4	68
MH3-8_ii	322.80	1.016	1.008	1.025	1.025	-0.316	-0.3	324.9	11.7	68	47	224.7	40.5
MH3-8_iii	317.10	1.019	1.001	1.02	1.022	-0.872	-0.9	319.9	1.9	229	31	53.1	59.2
MH3-8_iv	319.90	1.016	1.003	1.019	1.02	-0.672	-0.7	309.3	3.1	40	19	210.5	70.3
MH3-8_v	299.90	1.018	1.001	1.018	1.021	-0.917	-0.9	312.5	2.4	50	73	221.8	16.7
MH5-1_i	72.29	1.003	1.004	1.007	1.008	0.192	0.2	174.3	27.4	56	42	286.1	35.6
MH5-1_ii	79.00	1.004	1.006	1.01	1.01	0.13	0.1	148.4	27.7	52	12	301.6	59.5
MH5-1_iii	81.31	1.004	1.003	1.007	1.007	-0.043	0	136.9	25.2	35	24	266.6	53.7
MH5-1_iv	80.83	1.007	1.003	1.009	1.01	-0.427	-0.4	109.2	31.1	201	3	297	58.7
MH5-1_v	78.79	1.01	1.002	1.012	1.013	-0.601	-0.6	168.8	48.4	284	21	29.5	33.9
MH5-2_i	208.50	1.002	1.023	1.026	1.029	0.83	0.8	332.3	24	80	34	215.1	45.8
MH5-2_ii	188.10	1.007	1.021	1.028	1.029	0.507	0.5	75.5	43.4	325	20	217.4	39.7
MH5-2_iii	201.50	1.003	1.022	1.024	1.027	0.777	0.8	322.3	16.9	64	35	210.7	50.4
MH5-2_iv	193.40	1.002	1.025	1.027	1.03	0.86	0.9	356.2	41.5	105	20	214.3	41.7
MH5-2_v_new	192.39	1.003	1.02	1.023	1.025	0.75	0.7	42	41	305	8	207	48
MH5-3a_i	250.60	1.012	1.039	1.052	1.054	0.517	0.5	154.6	0.3	65	16	245.8	74
MH5-3a_ii	267.60	1.008	1.045	1.054	1.058	0.677	0.7	1.9	6.8	93	12	243.9	75.9
MH5-3a_iii	266.90	1.009	1.045	1.054	1.058	0.673	0.7	3.5	7	95	13	245.2	75.4
MH5-3b_i	247.80	1.006	1.042	1.048	1.053	0.75	0.7	184.1	0.2	94	5	276.8	85
MH5-3b_ii	251.30	1.01	1.047	1.058	1.062	0.64	0.6	160.8	3.8	70	9	272.8	80.1
MH5-3b_iii	241.50	1.005	1.05	1.055	1.062	0.824	0.8	8.5	1.6	99	5	262.5	84.4

specimen	mean	L	F	P	P'	T	U	dK1geo	iK1geo	dK2geo	iK2geo	dK3geo	iK3geo
MH5-3b_iv	243.60	1.009	1.046	1.055	1.059	0.682	0.7	165.4	0.9	75	0	323.4	89
MH5-5a_i	314.60	1.007	1.028	1.036	1.038	0.588	0.6	171	7.8	263	14	52	74.3
MH5-5a_ii	305.40	1.005	1.031	1.037	1.04	0.719	0.7	177.4	17	270	10	29.4	70.1
MH5-5a_iii	312.30	1.008	1.027	1.036	1.038	0.531	0.5	159.3	12.1	253	15	32	70.6
MH5-5a_iv	316.60	1.009	1.026	1.035	1.037	0.505	0.5	168.3	14.1	261	10	25	72.7
MH5-5a_v	327.60	1.003	1.032	1.036	1.039	0.821	0.8	180.3	25.8	271	1	3.2	64.2
MH5-6_i	314.80	1.009	1.022	1.031	1.032	0.424	0.4	182.7	11.9	276	16	57.3	70
MH5-6_ii	318.10	1.01	1.019	1.03	1.03	0.287	0.3	189.8	15.8	283	11	45.4	70.8
MH5-6_iii	322.50	1.01	1.021	1.031	1.031	0.349	0.3	180.8	10	272	7	37.2	77.7
MH5-6_iv	303.70	1.009	1.02	1.029	1.03	0.364	0.4	179	11.6	270	6	26.3	77
MH5-6_v	318.40	1.005	1.021	1.026	1.027	0.642	0.6	193.9	9.3	104	0	12.1	80.7
MH5-7_i	263.20	1.012	1.013	1.025	1.025	0.062	0.1	191.1	5.5	100	10	308.4	78.2
MH5-7_ii	275.40	1.016	1.012	1.028	1.028	-0.162	-0.2	191.4	5.6	100	12	305.8	76.5
MH5-7_iii	273.40	1.015	1.013	1.028	1.028	-0.075	-0.1	191.5	5.4	101	7	317.9	81
MH5-7_iv	247.10	1.011	1.013	1.024	1.024	0.11	0.1	188.4	3.3	98	14	291.3	75.6
MH5-8_i	196.40	1.009	1.021	1.03	1.031	0.413	0.4	221.6	29.3	312	1	43	60.7
MH5-8_ii	207.70	1.013	1.016	1.029	1.029	0.13	0.1	231.7	25.5	138	7	33.9	63.4
MH5-8_iii	194.40	1.009	1.02	1.029	1.03	0.353	0.3	213.1	31.4	304	2	37.7	58.5
MH5-8_iv	222.30	1.013	1.017	1.03	1.03	0.138	0.1	220.3	32	311	2	44.2	58
MH5-8_vi	226.70	1.012	1.014	1.027	1.027	0.061	0.1	224.3	31.7	133	2	39.6	58.2
MH6-1_i	154.20	1.009	1.005	1.015	1.015	-0.285	-0.3	333.9	26.1	103	52	230.2	25.7
MH6-1_ii	156.10	1.003	1.007	1.009	1.01	0.409	0.4	334.3	43.1	145	47	239.8	4.8
MH6-1_iii	144.90	1.008	1.003	1.012	1.012	-0.422	-0.4	18	50.3	144	26	249.1	27.6
MH6-1_iv	149.60	1.002	1.008	1.01	1.011	0.638	0.6	337.5	34.8	147	55	244.1	4.8
MH6-1_v	138.00	1.003	1.009	1.012	1.013	0.473	0.5	346.6	51.1	143	36	241.6	11.8
MH6-2_i	225.90	1.013	1.005	1.018	1.018	-0.482	-0.5	171.9	27.4	338	62	79	5.6
MH6-2_ii	211.40	1.017	1.003	1.02	1.022	-0.716	-0.7	160.7	11.1	40	69	254.3	18
MH6-2_iii	206.20	1.013	1.005	1.019	1.019	-0.446	-0.4	344.6	1.5	251	69	75.2	21.3
MH6-2_iv	239.90	1.012	1.004	1.015	1.016	-0.534	-0.5	157.7	25.7	30	52	261.3	26
MH6-2_v	225.10	1.01	1.005	1.016	1.016	-0.31	-0.3	172.9	18	36	66	268.1	15.5
MH6-3_i	192.30	1.006	1.009	1.014	1.014	0.212	0.2	349.7	12.3	96	51	250.6	35.8
MH6-3_ii	195.30	1.005	1.008	1.013	1.013	0.288	0.3	336.4	4.9	72	47	241.8	42.9
MH6-3_iv	194.10	1.008	1.005	1.013	1.013	-0.281	-0.3	336.6	10.6	90	65	242.1	22.6
MH6-6_i	231.80	1.008	1.017	1.025	1.026	0.367	0.4	162.3	39.2	46	29	291.1	37.5
MH6-6_ii	203.90	1.012	1.007	1.019	1.019	-0.261	-0.3	163.8	32.8	38	42	276.1	30.5
MH6-6_iii	219.70	1.007	1.014	1.022	1.022	0.318	0.3	155.9	40.4	40	27	287	37.7
MH6-6_iv	193.20	1.01	1.011	1.021	1.021	0.05	0	149.6	37.9	29	33	272.3	34.8
MH6-6_v	204.00	1.007	1.012	1.019	1.019	0.287	0.3	149.8	45.8	35	22	288.1	36
MH6-8_i	286.80	1.009	1.011	1.02	1.02	0.083	0.1	204.3	43.1	71	36	320.8	25.6
MH6-8_ii	315.90	1.008	1.004	1.012	1.012	-0.271	-0.3	192.4	55.2	77	17	337.2	29.6
MH6-8_iii	308.70	1.011	1.002	1.013	1.014	-0.674	-0.7	193.9	54.6	99	4	6.2	35.1
MH6-8_iv	330.60	1.009	1.002	1.011	1.012	-0.567	-0.6	191.5	61.9	310	14	46.5	23.6
MH6-8_v	314.30	1.011	1.001	1.012	1.013	-0.858	-0.9	191.7	54.2	287	4	19.3	35.6
MH7-1_i	330.50	1.014	1.016	1.03	1.03	0.084	0.1	54.6	56	316	5	222.8	33.4
MH7-1_ii	302.70	1.014	1.015	1.03	1.03	0.032	0	89.9	47.6	325	27	218.4	29.6
MH7-1_iii	312.90	1.007	1.012	1.019	1.019	0.3	0.3	26.9	62.5	134	9	227.8	25.9
MH7-1_iv	290.80	1.013	1.018	1.032	1.032	0.17	0.2	70.4	58.1	320	12	222.9	28.9
MH7-1_v	329.30	1.006	1.019	1.025	1.026	0.508	0.5	88.5	45.8	326	28	217.2	31.3
MH7-2_i	295.00	1	1.015	1.016	1.018	0.945	0.9	10.8	47.7	276	5	181.8	41.9
MH7-2_ii	314.50	1.006	1.009	1.014	1.014	0.214	0.2	314.4	43.1	73	27	183.3	35.1
MH7-2_iii	329.20	1.005	1.016	1.021	1.022	0.538	0.5	313.3	36.6	56	17	166.1	48.5

II.d – AMS – Narcea Antiform

specimen	mean	L	F	P	P'	T	U	dK1geo	iK1geo	dK2geo	iK2geo	dK3geo	iK3geo
MH7-2_iv	311.20	1.003	1.008	1.011	1.012	0.467	0.5	319.2	38.5	59	12	163.9	48.8
MH7-2_v	303.50	1.005	1.005	1.01	1.01	-0.032	0	324.6	34.7	75	26	193.2	43.8
MH7-3a_i	262.20	1.01	1.013	1.023	1.023	0.117	0.1	311.9	5.5	53	62	219.1	27
MH7-3a_ii	258.20	1.014	1.011	1.025	1.025	-0.121	-0.1	310.6	28.7	166	56	49.9	16.5
MH7-3a_iii	201.10	1.014	1.008	1.021	1.022	-0.289	-0.3	311.4	12.6	91	74	219.1	10.2
MH7-3a_iv	246.40	1.01	1.009	1.02	1.02	-0.04	0	309	7.4	52	60	214.9	29.1
MH7-3a_v	251.30	1.017	1.004	1.022	1.023	-0.626	-0.6	321.1	33.8	127	55	226.7	6.6
MH7-4_i	273.60	1.011	1.004	1.015	1.015	-0.502	-0.5	82.9	64.6	315	16	219.3	19
MH7-4_ii	283.80	1.006	1.007	1.012	1.012	0.088	0.1	91.9	38.9	298	48	192.7	13.1
MH7-4_iii	294.80	1.005	1.012	1.018	1.018	0.421	0.4	306.3	69.9	98	18	191	8.9
MH7-4_iv	267.30	1.008	1.006	1.014	1.014	-0.19	-0.2	71.3	64	319	11	223.9	23.4
MH7-4_v	266.50	1.004	1.014	1.019	1.019	0.534	0.5	107.3	55	313	32	214.9	11.9
MH7-5_i	292.20	1.015	1.004	1.019	1.02	-0.554	-0.6	134.8	52.3	40	4	306.8	37.4
MH7-5_ii	214.40	1.01	1.006	1.015	1.016	-0.278	-0.3	144.9	27.9	272	49	38.7	27.7
MH7-5_iii	256.50	1.01	1.005	1.015	1.015	-0.28	-0.3	126.5	39.3	233	19	343.1	44.5
MH7-5_iv	219.70	1.011	1.005	1.016	1.016	-0.39	-0.4	141.3	30	243	19	359.7	53.5
MH7-5_v	219.80	1.01	1.004	1.014	1.015	-0.427	-0.4	149.6	36	271	36	30	34.2
MH7-6_i	241.10	1.012	1.009	1.022	1.022	-0.119	-0.1	149.6	37.3	27	35	269.5	33.2
MH7-6_ii	231.10	1.008	1.007	1.016	1.016	-0.047	-0.1	138.8	31.4	24	35	258.9	39.5
MH7-6_iii	212.60	1.007	1.007	1.014	1.014	0.015	0	147.4	17.4	37	47	251.2	37.4
MH7-6_iv	237.30	1.007	1.01	1.018	1.018	0.148	0.1	137.7	38.6	11	37	255.1	29.9
MH7-7a_i	221.60	1.013	1.012	1.026	1.026	-0.04	0	135.2	21.9	10	55	236.4	25.7
MH7-7a_ii	213.60	1.011	1.011	1.022	1.022	0.021	0	136.1	27.1	2	53	238.4	22.6
MH7-7a_iii	221.00	1.012	1.012	1.024	1.024	0.002	0	138.5	18.6	338	70	230.6	6.2
MH7-7a_iv	203.80	1.013	1.014	1.027	1.027	0.027	0	133.2	21.6	3	59	232.2	21.6
MH7-8_i	157.40	1.011	1.013	1.025	1.025	0.071	0.1	298.4	79.1	194	3	103.9	10.5
MH7-8_ii	227.80	1.018	1.008	1.026	1.027	-0.383	-0.4	12.3	63	148	20	244.2	17.5
MH7-8_iii	231.20	1.02	1.008	1.027	1.028	-0.439	-0.4	14.2	60	142	19	240	21.9
MH7-8_iv	172.30	1.013	1.01	1.024	1.024	-0.117	-0.1	325.1	76.6	185	10	93.7	8.4
MH8-1_i	141.10	1.005	1.014	1.02	1.021	0.452	0.4	313.1	1.6	44	26	219.7	64.1
MH8-1_ii	153.50	1.007	1.003	1.01	1.011	-0.406	-0.4	315.3	32.9	177	49	59.9	21.3
MH8-1_iii	166.40	1.009	1.003	1.012	1.013	-0.51	-0.5	327.2	17.3	196	64	63	18.2
MH8-1_iv	148.60	1.01	1.007	1.017	1.017	-0.17	-0.2	330	31.7	225	23	106.2	49.4
MH8-1_v	160.30	1.008	1.002	1.011	1.011	-0.58	-0.6	329.9	16	83	53	229.6	32
MH8-2_i	160.80	1.012	1.006	1.018	1.018	-0.29	-0.3	139	30.9	340	57	234.9	9.7
MH8-2_ii	164.70	1.013	1.003	1.017	1.018	-0.586	-0.6	133.8	26.8	3	52	237.1	24.4
MH8-2_iii	160.10	1.011	1.002	1.013	1.014	-0.702	-0.7	144.7	22.6	44	25	271.8	55.3
MH8-2_iv	150.20	1.008	1.003	1.01	1.011	-0.502	-0.5	154.1	24.8	9	61	251.1	14.9
MH8-2_v	157.10	1.007	1.005	1.012	1.012	-0.193	-0.2	134.6	24.5	10	51	238.8	28.2
MH8-3_i	194.60	1.012	1.007	1.019	1.019	-0.25	-0.3	135.7	16.4	31	41	242.4	44.3
MH8-3_ii	250.40	1.012	1.006	1.018	1.018	-0.344	-0.3	128.5	24.4	25	27	253.6	51.7
MH8-3_iii	202.30	1.015	1.007	1.022	1.023	-0.348	-0.4	137.3	12.9	41	25	251.8	61.1
MH8-3_iv	191.40	1.015	1.007	1.022	1.022	-0.35	-0.4	129.8	14.4	32	26	245.6	59.4
MH8-3_v	263.80	1.013	1.005	1.018	1.019	-0.422	-0.4	133.9	22.9	26	36	248.7	44.9
MH8-4_i	238.10	1.003	1.024	1.028	1.03	0.771	0.8	295.2	1.7	205	15	31.8	75
MH8-4_ii	245.40	1.004	1.022	1.026	1.028	0.676	0.7	282.2	1.8	192	14	19.7	76.2
MH8-4_iii	248.10	1.003	1.024	1.027	1.029	0.744	0.7	142.5	2.1	233	17	45.6	73.2
MH8-4_iv	241.80	1.003	1.026	1.029	1.032	0.801	0.8	136	6.9	227	12	16.5	76.2
MH8-5_i	222.10	1.012	1.016	1.028	1.028	0.117	0.1	148.6	8.4	239	4	356.9	80.4
MH8-5_ii	227.10	1.005	1.023	1.028	1.029	0.643	0.6	136.1	10	226	1	320.4	80
MH8-5_iii	230.00	1.004	1.023	1.028	1.03	0.671	0.7	138.2	6.3	228	0	322.3	83.7

II.d – AMS – Narcea Antiform

specimen	mean	L	F	P	P'	T	U	dK1geo	iK1geo	dK2geo	iK2geo	dK3geo	iK3geo
MH8-5_iv	219.40	1.006	1.021	1.027	1.028	0.58	0.6	137.4	8.5	228	1	323.2	81.5
MH8-5_v	215.80	1.006	1.021	1.027	1.029	0.568	0.6	127.7	8.1	218	1	314.8	81.8
MH8-7_i	132.30	1.008	1.007	1.015	1.015	-0.079	-0.1	354.3	15.1	108	56	255.5	29.7
MH8-7_ii	136.10	1.007	1.009	1.017	1.017	0.116	0.1	353.6	14.9	103	51	252.7	35.5
MH8-7_iii	142.70	1.009	1.009	1.018	1.018	0.002	0	354.7	23.5	120	53	252	26.8
MH8-7_iv	135.50	1.008	1.007	1.016	1.016	-0.063	-0.1	357.2	15.1	109	54	257.4	32.3
MH8-8_i	253.90	1.007	1.022	1.029	1.031	0.531	0.5	156.6	8.2	247	5	10.4	80.2
MH8-8_ii	240.20	1.003	1.027	1.03	1.033	0.789	0.8	148	9.2	238	2	339	80.7
MH8-8_iii	239.70	1.003	1.026	1.029	1.032	0.761	0.8	148.7	10.1	57	7	291.5	77.4
MH8-8_iv	245.50	1.005	1.021	1.026	1.028	0.639	0.6	156.6	4.3	66	2	307.5	85
MH8-8_v	234.00	1.003	1.022	1.026	1.028	0.738	0.7	133.4	9	224	2	327	80.8
MH10-1_i	256.50	1.046	1.024	1.071	1.072	-0.311	-0.3	235.4	83	19	6	109.8	4.1
MH10-1_ii	237.00	1.038	1.027	1.066	1.067	-0.163	-0.2	192.6	82.1	21	8	290.9	1.1
MH10-1_iii	257.60	1.047	1.032	1.081	1.081	-0.191	-0.2	196.5	80.4	21	10	290.6	0.7
MH10-1_iv	251.80	1.05	1.03	1.081	1.082	-0.244	-0.3	181.7	81.5	15	8	284.8	1.9
MH10-1_v	268.50	1.053	1.028	1.083	1.084	-0.304	-0.3	187.1	82.1	18	8	288.1	1.5
MH10-2_i	315.20	1.03	1.054	1.086	1.087	0.283	0.3	203.3	78.4	16	11	106	1.5
MH10-2_ii	287.60	1.025	1.05	1.076	1.078	0.323	0.3	206	77	13	3	103.9	2.8
MH10-2_iii	301.70	1.028	1.048	1.077	1.078	0.266	0.2	180	76.6	13	13	282.7	3
MH10-2_iv	305.90	1.028	1.038	1.068	1.068	0.154	0.1	195.4	79.4	10	11	104.9	0.1
MH10-2_v	310.60	1.033	1.04	1.075	1.075	0.086	0.1	176.3	79	15	11	279.4	2.5
MH11-1_i	186.70	1.003	1.033	1.036	1.04	0.832	0.8	228.9	41	101	35	347.7	29
MH11-1_ii	138.30	1.002	1.048	1.05	1.057	0.919	0.9	118.6	29.3	237	40	4.9	35.7
MH11-1_iii	167.80	1.003	1.026	1.029	1.032	0.793	0.8	147.3	44.7	253	15	357.1	41.2
MH11-1_iv	179.50	1.001	1.038	1.038	1.044	0.957	1	228.6	49.3	106	25	0.5	29.9
MH11-1_v	194.50	1.002	1.035	1.038	1.042	0.878	0.9	220.3	38.8	102	30	346.5	36.4
MH11-2_i	48.49	1.008	1.009	1.016	1.016	0.084	0.1	35.3	70.7	299	2	208.4	19.1
MH11-2_ii	42.28	1.005	1.003	1.007	1.007	-0.241	-0.2	122.4	52.1	271	34	11.4	15.7
MH11-2_iii	50.79	1.004	1.007	1.01	1.011	0.321	0.3	318.1	42.5	98	40	206.9	21.5
MH11-2_iv	46.62	1.009	1.005	1.014	1.014	-0.307	-0.3	118	34	295	56	27.1	1.4
MH11-2_v	48.44	1.008	1.007	1.015	1.015	-0.075	-0.1	58.6	72	303	8	210.8	16
MH11-3_i	319.40	1.015	1.033	1.048	1.05	0.383	0.4	162.1	86.3	268	1	358.3	3.5
MH11-3_ii	305.10	1.015	1.031	1.047	1.048	0.348	0.3	137.7	82.7	271	5	1.4	5.3
MH11-3_iii	297.50	1.014	1.029	1.044	1.045	0.34	0.3	158.5	72.9	269	6	0.9	15.9
MH11-3_iv	307.20	1.016	1.031	1.047	1.048	0.332	0.3	156.6	76.7	271	5	1.8	12
MH11-3_v	325.30	1.02	1.031	1.052	1.053	0.204	0.2	201.6	78.6	88	5	356.9	10.4
MH11-6_i	299.50	1.003	1.049	1.053	1.059	0.872	0.9	185.4	44.3	80	15	335.6	41.6
MH11-6_ii	308.60	1.008	1.045	1.053	1.057	0.703	0.7	175.9	51.7	72	11	334.2	36.2
MH11-6_iii	273.20	1.008	1.05	1.058	1.063	0.731	0.7	165.3	45.9	70	5	334.9	43.6
MH11-6_iv	304.60	1.004	1.047	1.051	1.057	0.846	0.8	113.7	50.1	236	24	340.3	29.9
MH11-7_i	261.00	1.015	1.05	1.066	1.069	0.533	0.5	236.9	16.1	139	26	355.3	58.7
MH11-7_ii	263.00	1.011	1.043	1.055	1.058	0.587	0.6	229.4	33.6	121	25	1.9	45.5
MH11-7_iii	266.80	1.008	1.05	1.059	1.064	0.71	0.7	248.5	13.6	150	31	359.3	55.7
MH11-7_iv	266.00	1.008	1.048	1.056	1.06	0.72	0.7	239.3	27.7	134	27	7.3	49.5
MH11-7_v	252.10	1.008	1.054	1.063	1.069	0.725	0.7	234.3	19.7	135	24	358.8	57.7
mh11-8 i	263.70	1.007	1.028	1.034	1.036	0.604	0.599	187.8	74.2	94.2	1	4	15.8
mh11-8_ii	256.60	1.014	1.035	1.05	1.051	0.412	0.402	127.5	65.8	273.9	20.5	8.5	12.3
mh11-8_iii	275.50	1.009	1.037	1.046	1.049	0.604	0.597	136.8	63.1	264.8	17.3	1.3	19.9

Microprobe – Narcea Antiform

sample	point	phase	comment	Na2O	MgO	Al2O3	SiO2	K2O	CaO	MnO	FeO	TiO2	Cr2O3	Total
chlorite														
MH1-2	P1-2-4	chlorite	crenulated in S1	0.009	10.695	20.013	25.962	0.166	0.057	0.025	30.589	0.022	0.009	87.545
MH1-2	P1-2-7	chlorite	crenulated in S1	0.013	10.254	20.453	25.836	0.224	0.031	0.054	30.272	0.065	0.02	87.222
MH1-2	P1-2-8	chlorite	crenulated in S2	0.035	9.794	20.625	28.239	0.999	0.063	0.027	28.598	0.065	0	88.446
MH1-2	P1-2-9	chlorite	crenulated in S3	0.005	9.575	20.321	26.792	0.426	0.045	0.015	29.565	0.097	0	86.841
MH1-2	P1-2-10	chlorite	S1	0.094	7.355	19.302	29.503	1.711	0.087	0.034	28.115	2.691	0.042	88.934
MH1-2	P1-2-11	chlorite	S1	0.092	7.645	21.83	31.279	2.307	0.26	0.034	26.867	0.082	0.007	90.403
MH1-2	P1-2-12	chlorite	crenulated in S1	0.084	9.197	19.525	30.658	1.154	0.201	0.018	26.803	0.025	0.016	87.681
MH1-2	P1-2-13	chlorite	in microlithon	0.1	10.207	19.847	28.318	0.983	0.05	0.034	28.079	0.013	0	87.629
MH1-2	P1-2-14	chlorite	in s1	0.113	8.872	21.052	33.135	1.921	0.292	0	24.985	0.078	0.009	90.458
MH2-4	P2-4-4	chlorite	matrix	0.123	11.412	21.553	29.922	0.859	0.05	0.263	25.184	0.048	0	89.416
MH2-4	P2-4-6	chlorite	altered	0.155	9.864	20.85	31.221	0.583	0.109	0.006	24.057	0.245	0	87.09
MH2-4	P2-4-7	chlorite	altered	0.098	10.293	21.719	29.935	0.407	0.104	0.022	27.408	0.093	0.037	90.117
MH2-4	P2-4-8	chlorite	matrix	0.127	10.748	18.809	30.979	0.847	0.201	0.012	24.99	0.314	0.053	87.079
MH2-4	P2-4-11	chlorite	qtz coating	0.027	13.59	21.124	27.37	0.399	0.039	0.283	24.174	0.07	0	87.075
MH1-3	P1-3-1	chlorite	detrital	0.102	7.81	19.11	29.437	1.921	0.081	0.074	27.617	0.052	0	86.202
MH1-3	P1-3-2	chlorite	qtz coating	0.069	10.54	19.384	33.803	1.641	0.344	0.115	21.128	0.052	0.019	87.094
MH1-3	P1-3-3	chlorite	qtz coating	0.088	9.915	19.52	35.551	2.157	0.15	0.003	20.283	0.038	0	87.705
MH1-3	P1-3-4	chlorite	detrital	0.093	10.028	19.629	31.888	1.508	0.076	0.067	24.398	0.072	0.047	87.805
MH1-3	P1-3-17	chlorite	detrital	0.066	9.522	19.289	35.405	2.148	0.074	0.152	17.025	0.068	0.025	83.776
MH1-3	P1-3-19	chlorite	detrital	0.09	10.126	18.994	36.295	1.862	0.241	0.075	18.856	0.979	0.045	87.564
MH6-9	P6-9-1	chlorite	vein	0.04	12.13	0	25.462	0.104	0.022	0.103	27.619	0.017	0.02	86.63
MH6-9	P6-9-2	chlorite	vein	0.008	12.286	20.825	24.55	0.006	0.011	0.097	29.104	0.032	0	86.92
MH6-9	P6-9-3	chlorite	vein	0	12.266	20.678	25.436	0.011	0.007	0.124	28.595	0.023	0.054	87.195
MH6-9	P6-9-4	chlorite	vein	0	12.704	20.515	25.028	0.001	0	0.045	28.974	0.023	0	87.291
MH6-9	P6-9-7	chlorite	vein	0.003	12.664	20.36	25.271	0.008	0.021	0.112	28.584	0.013	0.02	87.06
MH6-9	P6-9-18	chlorite	wall rock, 10 μm	0.03	12.162	20.888	26.142	0.236	0.017	0.112	26.781	0.13	0	86.498
MH6-9	P6-9-19	chlorite	wall rock	0.015	12.668	21.245	25.547	0.142	0	0.139	27.882	0.033	0.001	87.673
chlorite-illite mix														
MH2-4	P2-4-9	chlorite+illite	matrix	0.105	9.153	22.017	34.917	1.797	0.118	0.139	21.579	0.092	0.012	89.929
MH2-4	P2-4-15	chlorite+illite	matrix	0.154	11.165	20.504	35.153	1.117	0.194	0	20.756	0.055	0.01	89.109
MH1-3	P1-3-9	chlorite+illite	at qtz	0.1	1.147	24.045	47.948	7.214	0.062	0.009	14.406	0.048	0.057	95.036
MH1-3	P1-3-14	chlorite+illite	matrix	0.073	9.504	19.55	33.871	1.773	0.097	0.049	21.837	0.212	0.085	87.049
MH1-3	P1-3-15	chlorite+illite	matrix	0.089	7.465	23.333	38.636	3.003	0.076	0.009	16.238	0.09	0.08	89.018
MH6-9	P6-9-11	chlorite+illite	wall rock	0.337	10.013	22.339	33.826	2.332	0.102	0.111	19.801	0.025	0.015	88.902
Fe-Mg-carbonate														
MH6-2	P6-2-1	Fe-Mg-carbonate	Fe-rich	0.034	18.879	0.967	1.512	0.284	0.69	0.262	34.685	0	0	57.314
MH6-2	P6-2-3	Fe-Mg-carbonate	Fe-rich	0.016	16.876	0	0.03	0.02	0.084	1.37	38.47	0	0.02	56.887
MH6-2	P6-2-5	Fe-Mg-carbonate	MgCa-rich	0	13.188	0.004	0.13	0.005	28.554	0.678	12.782	0	0.022	55.364
MH6-2	P6-2-8	Fe-Mg-carbonate	Fe-rich	0.03	16.78	0.567	1.512	0.02	1.117	0.42	36.846	0.02	0.023	57.334
Fe-oxide														
MH6-9	P6-9-8	Fe-oxide	wall at vein bound	0.062	0.686	0.964	5.466	0.051	0.322	0.155	70.141	0.003	0	77.85
MH8-2	P8-2-7	Fe-oxide	in qtz with Illite	0.305	0.534	12.198	11.317	0.554	0.574	0.012	57.014	0.082	0.015	82.603
MH8-2	P8-2-10	Fe-oxide		0.155	0.279	10.881	11.146	0.823	0.341	0	59.799	0.025	0.003	83.452
illite/sericite														
MH1-2	P1-2-5	illite/sericite	with chlorite	0.12	2.636	28.918	53.934	9.067	0	0.015	3.355	0.222	0.042	98.309
MH1-2	P1-2-6	illite/sericite	matrix	0.069	1.444	30.72	51.634	8.808	0.034	0	3.315	0.007	0.022	96.052
MH1-2	P1-2-15	illite/sericite	20 μm, in s1	0.074	2.441	29.7	53.491	9.368	0	0.013	2.864	0.02	0.029	98

III.a – Microprobe – Narcea Antiform

sample	point	phase	comment	Na2O	MgO	Al2O3	SiO2	K2O	CaO	MnO	FeO	TiO2	Cr2O3	Total
MH1-2	P1-2-16	illite/sericite	15 µm	0.311	1.555	30.898	50.342	9.647	0	0	4.548	0.509	0.044	97.853
MH1-2	P1-2-17	illite/sericite	matrix	0.106	1.52	30.055	52.603	8.602	0.032	0.019	3.185	0.105	0.006	96.235
MH1-2	P1-2-18	illite/sericite	detrital	0.031	2.59	29.45	54.633	9.051	0.018	0.006	2.098	0.127	0.007	98.012
MH1-2	P1-2-19	illite/sericite	s1 at chlorite	0	2.829	27.523	53.677	9.139	0.141	0.052	3.646	0.032	0.067	97.106
MH2-4	P2-4-1	illite/sericite	matrix	0.062	1.985	29.549	51.734	8.26	0.05	0	3.537	0.143	0.032	95.351
MH2-4	P2-4-2	illite/sericite	matrix	0.092	1.698	30.607	50.447	8.855	0.008	0.009	3.235	0.247	0.056	95.253
MH2-4	P2-4-13	illite/sericite	matrix	0.078	2.026	29.917	51.292	8.527	0.064	0	3.4	0.12	0.032	95.457
MH2-4	P2-4-14	illite/sericite	matrix	0.117	1.915	26.705	57.558	8.3	0.066	0.003	3.659	0.158	0.038	98.518
MH1-3	P1-3-11	illite/sericite	matrix	0.08	2.2	28.519	53.067	7.901	0.087	0	3.885	0.148	0.058	95.945
MH1-3	P1-3-16	illite/sericite	matrix	0.109	1.511	29.054	50.583	8.942	0.02	0	4.423	0.055	0	94.696
MH8-2	P8-2-1	illite/sericite	matrix	0.082	1.597	30.231	50.853	9.501	0	0.032	5.257	0.115	0.028	97.696
MH8-2	P8-2-2	illite/sericite	matrix	0.069	1.229	32.362	52.669	9.125	0.029	0.103	2.392	0.047	0.026	98.05
MH8-2	P8-2-3	illite/sericite	matrix	0.044	1.496	29.923	49.338	9.592	0.013	0.039	5.528	0.22	0.031	96.223
MH8-2	P8-2-4	illite/sericite	in qtz strain cap	0.082	1.447	29.957	50.181	9.148	0.039	0.013	5.128	0.16	0	96.156
MH8-2	P8-2-11	illite/sericite	matrix	0.026	1.52	29.511	49.595	9.151	0.014	0	5.114	0.172	0.001	95.103
MH8-2	P8-2-6	illite/sericite	at qtz (P8-2-5)	0.049	1.587	29.532	50.693	9.609	0.028	0	5.17	0.135	0	96.802
MH8-2	P8-2-8	illite/sericite	at qz (P8-2-5)	0.069	1.701	29.864	50.648	9.148	0.017	0	4.63	0.123	0	96.199
MH8-2	P8-2-9	illite/sericite	at qtz (P8-2-5)	0.046	1.585	30.885	50.868	9.001	0.045	0.052	4.472	0.175	0	97.128
MH6-2	P6-2-2	illite/sericite	matrix	0.14	1.63	31.121	50.372	9.332	0.018	0	4.419	0.145	0	97.176
MH6-2	P6-2-4	illite/sericite	matrix	0.115	1.713	28.753	50.973	9.461	0	0	4.338	0.26	0	95.612
MH6-2	P6-2-6	illite/sericite		0.175	1.655	31.145	50.733	9.764	0.017	0.003	3.893	0.105	0.047	97.537
MH6-2	P6-2-7	illite/sericite		0.129	1.703	30.102	49.826	9.953	0	0	4.602	0.145	0.035	96.496
MH6-2	P6-2-9	illite/sericite	in qtz press. shadow	0.123	1.575	29.968	48.737	8.978	0.011	0.019	4.004	0.103	0	93.519
MH6-2	P6-2-10	illite/sericite	in qtz press. shadow	0.148	1.633	29.997	49.326	9.205	0.011	0.028	4.226	0.085	0.031	94.691
MH6-2	P6-2-11	illite/sericite	in qtz strain cap	0.113	1.771	30.412	51.495	9.392	0	0.006	4.369	0.105	0.019	97.682
MH6-2	P6-2-13	illite/sericite	matrix	0.112	1.587	30.769	51.075	8.95	0.018	0	4.02	0.112	0.004	96.648
MH6-2	P6-2-14	illite/sericite	matrix	0.162	1.497	31.754	50.404	9.55	0.007	0	3.85	0.152	0.034	97.409
MH6-2	P6-2-15	illite/sericite	matrix	0.171	1.424	32.232	49.811	9.455	0	0.013	3.287	0.122	0.015	96.53
MH6-2	P6-2-17	illite/sericite	at recrystallised qtz	0.135	1.708	30.595	50.742	9.374	0.01	0	4.213	0.165	0.038	96.981
MH6-9	P6-9-9	illite/sericite	wall rock, vein bound	0.098	1.794	30.289	50.718	9.28	0.022	0.015	4.588	0.205	0.025	97.035
MH6-9	P6-9-13	illite/sericite	matrix, ligth BSE	0.112	1.913	28.921	51.101	9.062	0.004	0.039	5.433	0.275	0.019	96.879
MH6-9	P6-9-14	illite/sericite	matrix, dark BSE	0.306	0.743	36.114	48.69	9.611	0.011	0.015	1.765	0.479	0	97.736
MH6-9	P6-9-15	illite/sericite	matrix, ligth BSE	0.1	2.02	29.528	51.578	9.276	0	0	4.959	0.135	0	97.596
MH6-9	P6-9-16	illite/sericite	matrix, dark BSE	0.368	0.754	35.357	48.215	9.175	0.063	0.045	1.788	0.529	0.019	96.312
MH6-9	P6-9-20	illite/sericite	matrix	0.084	1.779	30.042	49.122	8.814	0	0.028	4.828	0.175	0.026	94.899
muscovite														
MH1-3	P1-3-5	detrital white mica	detrital	0.162	2.026	29.668	52.558	8.595	0	0.048	3.211	0.113	0.02	96.401
MH1-3	P1-3-6	detrital white mica	detrital	0.101	2.751	26.229	51.17	9.622	0	0.003	6.364	0.265	0.022	96.527
MH1-3	P1-3-7	detrital white mica	detrital	0.1	1.761	30.391	51.974	8.269	0.064	0.003	3.261	0.077	0.018	95.918
MH1-3	P1-3-8	detrital white mica	detrital	0.12	1.567	32.047	51.277	9.038	0.039	0	2.721	0.15	0	96.958
MH1-3	P1-3-13	detrital white mica	detrital	0.105	1.554	30.628	51.253	8.868	0.021	0.022	4.359	0.192	0.015	97.016
MH1-3	P1-3-18	detrital white mica	at chlorite (P1-3-17)	0.104	1.819	30.958	49.646	8.453	0.025	0.041	3.274	0.113	0.003	94.437
MH1-2	P1-2-1	detrital white mica	detrital	0.155	2.199	29.639	52.254	9.185	0.011	0.013	3.997	0.157	0.013	97.624
MH1-2	P1-2-2	detrital white mica	detrital	0.342	1.303	32.972	49.888	9.641	0.024	0	2.655	0.412	0.015	97.253
MH1-2	P1-2-3	detrital white mica	detrital	0.295	1.088	33.628	49.304	9.228	0.024	0.032	2.462	0.389	0	96.45

XRD parameters

Israel

Feldspars		K-feldspar				Na-plagioclase				ratios		
sample	distance	Peak(Å)	Intensity	Area	FWHM	Peak(Å)	Intensity	Area	FWHM	ratio Intens	ratio Area	ratio FWHM
RA 3-1	50	3.237	788	14030	0.303	3.19	2128	28616	0.24	2.7	2.04	0.79
RA 1-1.a	14.5					3.192	4238	45746	0.167			
RA 1-1.b	14	3.241	1028	8825	0.137	3.192	3101	39563	0.194	3.02	4.48	1.42
RA 1-2	9.5	3.243	1160	13915	0.187	3.196	2223	25846	0.181	1.92	1.86	0.97
RA 1-3.a	6.5	3.239	1495	17811	0.194	3.196	2138	26154	0.198	1.43	1.47	1.02
RA 1-3.c	6	3.242	1373	16492	0.191	3.195	2233	24478	0.168	1.63	1.48	0.88
RA 1-3.b	5.5	3.241	1692	19601	0.191	3.195	3197	33781	0.168	1.89	1.72	0.88
RA 1-4.b	5	3.242	3417	34042	0.165	3.195	1321	11038	0.146	0.39	0.32	0.88
RA 1-4.a	4.5	3.24	2286	22615	0.184	3.19	1831	20416	0.183	0.8	0.9	0.99
RA 1-5.a	3.5	3.237	2520	27380	0.191	3.189	1999	21014	0.176	0.79	0.77	0.92
RA 1-5.b	3.5	3.238	1364	15830	0.191	3.189	1778	22787	0.21	1.3	1.44	1.1
RA 1-6.a	2.5	3.238	1615	17708	0.181	3.191	1388	14977	0.175	0.86	0.85	0.97
RA 2-3	1	3.246	80	944	0.192							
RA 1-7	0.5	3.241	2511	28984	0.209							
RA 2-2	0.5	3.237	190	3396	0.328							
RA 2-1.b	0.2	3.239	156	2730	0.319							
RA 2-1.a	0.2	3.233	78	1449	0.347							

Hara

Illite, chlorite (CIS calibration : CIS=1.1463·Lab-0.0066)

sample	distance	ill001 peak	ill001 int	ill001 area	ill001 FWHM	001-CIS caibrated	ill002 peak	ill002 int	ill002 area	ill002 FWHM
SH2	0.13	10.278	2231	101949	0.793		5.006	494	16986	0.567
SH2-gle	0.13	10.045	1619	75382	0.76		5.026	553	19758	0.622
SH5	3.71	10.159	710	27895	0.677		4.994	197	5801	0.474
SH8	8.32	10.115	2247	85210	0.667		4.974	593	24763	0.659
SH10	11.08	10.041	2722	86907	0.535		4.978	951	25921	0.426
SH11	12.71	10.012	1781	56393	0.517		4.98	782	19935	0.406
SH15	19.34	10.051	878	22624	0.418		4.996	336	6289	0.314

sample	chl001 peak	chl001 int	chl002 area	chl001 FWHM	chl002 peak	chl002 int	chl002 area	chl002 FWHM	chl003 peak	chl003 int	chl003 area	chl003 FWHM
SH2	14.269	89	2844	0.586	7.088	881	22701	0.398	4.735	176	7763	0.733
SH2-gle	14.391	79	2453	0.566	7.104	1047	25727	0.372	4.738	206	8597	0.678
SH5	14.192	328	9167	0.435	7.089	2303	58320	0.387	4.725	380	9151	0.38
SH8	14.049	514	12594	0.397	7.05	3055	75911	0.372	4.71	712	17182	0.392
SH10	14.14	763	17023	0.358	7.074	3148	71668	0.347	4.716	793	16864	0.35
SH11	14.167	852	22013	0.422	7.075	3452	88458	0.391	4.719	936	20253	0.346
SH15	14.243	331	8205	0.392	7.101	1567	35493	0.355	4.729	319	6036	0.295

calculations

sample	Int ill001+chl002	Int ill001/chl002	ill-peak distance	Int chl002/chl001	Int ill002 / chl002	clay-cont
SH2	3112	2.532	5.272	9.899	0.561	33.58
SH2-gle	2666	1.546	5.019	13.253	0.528	
SH5	3013	0.308	5.165	7.021	0.086	46.47
SH8	5302	0.736	5.141	5.944	0.194	74.3
SH10	5870	0.865	5.063	4.126	0.302	70.45
SH11	5233	0.516	5.032	4.052	0.227	51.78
SH15	2445	0.56	5.055	4.734	0.214	49.31

Långviken

Illite, chlorite, feldspars (CIS calibration : CIS=1.1463·Lab-0.0066)

sample	distance	ill001 Peak	ill001 Int	ill001 Area	ill001 FWHM	001 CIS-calibration	ill002 Peak	ill002 Int	ill002 Area	ill002 FWHM
st-aa	-0.5	10.073	3489	85759	0.392	**0.46**	5.007	1192	25714	0.345
st-a	0.16	10.059	3620	90308	0.391	**0.45**	5.003	1110	23495	0.333
st-e	3.02	10.028	1711	39610	0.363	**0.42**	4.997	487	9385	0.312
st-j	7.08	10.066	1526	35334	0.367	**0.43**	5.002	553	10205	0.297
ST-1	-0.5	10.087	1954	55178	0.451	**0.52**	5.001	686	17315	0.42
ST-2	0.07	10.221	4103	120414	0.48	**0.56**	5.03	1413	37655	0.439
ST-10	9.01	10.064	158	3497	0.323	**0.38**	5.01	72	969	0.212
ST-11a	13.15	9.957	30	550	0.325	**0.38**	4.975	13	284	0.379
ST-13	20.93	10.051	60	1214	0.306	**0.36**	5.02	23	301	0.233

sample	chl001 Peak	chl001 Int	chl001 Area	chl001 FWHM	chl002 Peak	chl00 Int	chl002 Area	chl002 FWHM
st-aa								
st-a					7.084	115	2759	0.385
st-e		21			7.092	232	5275	0.368
st-j		64			7.117	451	9891	0.338
ST-1	14.65	28	284	0.177	7.101	205	3621	0.26
ST-2	14.347	44	533	0.21	7.156	415	9527	0.347
ST-10	14.37	199	5033	0.398	7.119	1239	26769	0.334
ST-11a	14.255	65	837	0.181	7.093	313	6327	0.318
ST-13	14.275	193	4186	0.334	7.119	1225	26134	0.315

sample	Ksp Peak	Ksp Int	Ksp Area	Ksp FWHM	Alb Peak	Alb Int	Alb Area	Alb FWHM	chl002/ill002	alb/kfsp
st-aa	3.248	401	5952	0.246						
st-a	3.252	379	5558	0.26					0.1	
st-e	3.247	292	6150	0.385	3.195	596	10223	0.267	0.48	2.04
st-j	3.252	172	4249	0.5	3.199	434	7096	0.245	0.82	2.52
ST-1	3.25	461	6336	0.264	3.196	359	5662	0.245	0.3	0.78
ST-2	3.262	994	14036	0.252	3.207	372	3684	0.18	0.29	0.37
ST-10	3.252	590	11207	0.269	3.195	596	10223	0.267	17.21	1.01
ST-11a	3.247	1395	17551	0.206	3.192	629	9941	0.241	24.08	0.45
ST-13	3.253	948	12505	0.198	3.196	943	14005	0.212	53.26	0.99

Narcea Antiform

Illite and chlorite (incl. IC/ChC)

sample	kind	LIthology	distance	Ill001 Peak	Ill001 Intensity	Ill001 Area	Ill001 FWHM	Ill002 Peak	Ill002 Intensity	Ill002 Area	Ill002 FWHM
MH1-12	sample	shale	10	10.009	3592	85049	0.368	4.989	1390	28006	0.309
MH2-3.I_altered	sample	Siltstone	0.5	10.045	7483	168321	0.34	5.003	2256	45082	0.319
MH2-3.II_altered	sample	Siltstone	0.5	10.156	5255	115557	0.337	5.032	1961	37014	0.3
MH2-3.I-gly_altered	sample	Siltstone	0.5	9.965	3764	83090	0.332	4.988	1294	25727	0.316
MH2-3 altered	*average*	*Siltstone*	*0.5*	--	--	--	*0.3363*	--	--	--	*0.312*
MH2-2b	sample	Siltstone	1.5	10.012	4137	101135	0.381	4.99	1392	25880	0.301
MH2-2b-gly	sample	Siltstone	1.5	9.973	2092	49451	0.369	4.985	685	13446	0.317
MH2-2b	*average*	*Siltstone*	*1.5*	--	--	--	*0.375*	--	--	--	*0.309*
MH2-6	sample	Siltstone	3	10.162	4773	125704	0.423	5.026	1542	32962	0.353
MH2-6-gly	sample	Siltstone	3	9.998	2508	64325	0.397	4.993	903	19353	0.348
MH2-6	*average*	*Siltstone*	*3*	--	--	--	*0.41*	--	--	--	*0.3505*
MH2-4	sample	Siltstone	7	10.016	3880	100333	0.408	4.987	1669	31939	0.31
MH2-4-gly	sample	Siltstone	7	9.974	2049	49845	0.375	4.984	748	14083	0.295
MH2-4	*average*	*Siltstone*	*7*	--	--	--	*0.3915*	--	--	--	*0.3025*
MH4-8	sample	shale	0.1	10.025	3917	83664	0.332	4.995	1374	24903	0.293
MH4-3	sample	Siltstone	1	10.068	7468	179543	0.382	5.001	2302	47149	0.329
MH4-3-gly	sample	Siltstone	1	9.947	3556	82974	0.354	4.981	1190	24433	0.332
MH4-3	*average*	*Siltstone*	*1*	--	--	--	*0.368*	--	--	--	*0.3305*
MH4-6	sample	Siltstone	11	9.973	6028	140293	0.4	4.987	1727	32728	0.303
MH4-7	sample	Siltstone	25	9.972	3781	90979	0.374	4.984	1619	30503	0.306
MH4-7	sample	Siltstone	25	9.951	1763	40414	0.347	4.985	699	13948	0.315
MH4-7	sample	Siltstone	25	--	--	--	0.3605	--	--	--	0.3105
MH5-3	sample	Siltstone	0.4	10.018	4793	117817	0.382	4.995	1665	33049	0.321
MH5-5.a	sample	Siltstone	2	9.979	1249	30327	0.365	4.985	412	7452	0.299
MH5-6	sample	Siltstone	5	10.047	2073	59634	0.471	4.996	715	15825	0.374
MH6-13	sample	Siltstone	0.5	10.013	2288	42115	0.276	4.998	942	17176	0.28
MH10-2	sample	Siltstone	100	9.95	2821	57573	0.346	4.973	1230	20376	0.278
NA10	sample	Siltstone	Intern NA	10.046	3515	79945	0.3167	5.003	1313	26780	0.324
NA10	sample	Siltstone	Intern NA	10.081	3176	75511	0.331	5.01	1359	26386	0.316
NA10	*average*	*Siltstone*	Intern NA	--	--	--	*0.3237*	--	--	--	*0.32*
NA7	sample	Siltstone	Intern NA	9.984	3068	53177	0.2451	4.987	1840	26344	0.238
NA2	sample	Phyllite	Intern NA	10.044	2534	39181	0.21	5	1430	16634	0.191
NA2	sample	Phyllite	Intern NA	9.956	2627	42412	0.2321	4.98	1147	16068	0.234
NA2	*average*	*Phyllite*	Intern NA	--	--	--	*0.224*	--	--	--	*0.213*
mh8-9-slickenside	sample	slickenside		10.02	1289	24379	0.296	4.996	400	6787	0.272
7-9a	sample	Clay	0	10.188	12923	387361	0.476	5.029	4640	121180	0.424
7-9b	sample	Clay	0	9.971	4704	142964	0.452	4.983	2556	63874	0.409
7-9c	sample	Clay	0	10.027	3165	84505	0.422	4.991	990	23106	0.37
MH1-13	sample	Greywacke	10	10.013	889	21695	0.397	4.995	412	8692	0.337
MH5-2	sample	Greywacke	1.5	10	2817	68769	0.402	4.988	1077	21769	0.332
MH4-1	sample	Greywacke	1	9.974	3745	102571	0.426	4.986	1289	28888	0.36
MH5-7	sample	Greywacke	10	10.05	2810	72701	0.383	5.004	1052	20892	0.327
MH5-8	sample	Greywacke	30	10.059	5116	121162	0.378	5.004	1479	30352	0.34

IV.d – XRD parameters – Narcea Antiform

sample	kind	LIthology	distance	Ill001 Peak	Ill001 Intensity	Ill001 Area	Ill001 FWHM	Ill002 Peak	Ill002 Intensity	Ill002 Area	Ill002 FWHM
MH6-3.II altered	sample	Greywacke	0.3	10.007	6116	109999	0.269	4.994	2212	35745	0.254
MH6-3.I altered	sample	Greywacke	0.3	9.951	7287	131694	0.277	4.98	2846	45793	0.25
MH6-3 altered	*average*	*Greywacke*	*0.3*	--	--	--	*0.273*	--	--	--	*0.252*
MH6-6.II	sample	Greywacke	3	10.161	3202	57843	0.288	5.031	1050	16607	0.24
MH6-6.I	sample	Greywacke	3	9.946	3445	58067	0.257	4.979	1263	19600	0.24
MH6-6	*average*	*Greywacke*	*3*	--	--	--	*0.2725*	--	--	--	*0.24*
MH7-1	sample	lith-arenite	3	9.958	5755	120564	0.331	4.985	2024	36361	0.276
MH7-11	sample	Greywacke	70	10.02	1309	33579	0.383	5	386	6624	0.269
MH8-5	sample	Greywacke	8	10.042	6055	162448	0.422	4.997	2142	47660	0.362
MH10-1	sample	Greywacke	100	9.962	2350	43457	0.306	4.984	921	13226	0.224

sample	chl001 Peak	chl001 Int	chl001 Area	chl001 FWHM	chl002 Peak	chl002 Int	chl002 Area	chl002 FWHM	chl003 Peak	chl003 Int	chl003 Area	chl003 FWHM	CIS Ill001	σ	CIS chl002	σ	intIll001 /chl002	Ill002/ chl003
MH1-12	--	--	--	--	7.131	278	7368	0.454	--	--	--	--	**0.43**		**0.53**		12.92	
MH2-3.I_altered	--	--	--	--	--	--	--	--	--	--	--	--	**0.40**					
MH2-3.II_altered	--	--	--	--	--	--	--	--	--	--	--	--	**0.39**					
MH2-3.I-gly_altered	--	--	--	--	--	--	--	--	--	--	--	--	**0.39**					
MH2-3 altered	--	--	--	--	--	--	--	--	--	--	--	--	***0.39***	***0.00***				
MH2-2b	14.154	355	7790	0.373	7.075	1011	21893	0.327	4.714	181	2623	0.249	**0.44**		**0.38**		4.09	7.69
MH2-2b-gly	14.082	183	3104	0.287	7.065	541	11509	0.309	4.708	110	1743	0.29	**0.43**		**0.36**		3.87	6.23
MH2-2b	--	--	--	*0.33*	--	--	--	*0.318*	--	--	--	*0.2695*	***0.44***	***0.01***	***0.37***	***0.01***		
MH2-6	14.433	355	7619	0.348	7.137	1180	26071	0.342	4.742	227	3970	0.296	**0.49**		**0.40**		4.04	6.79
MH2-6-gly	14.112	159	4035	0.43	7.077	691	15982	0.35	4.718	145	2769	0.298	**0.46**		**0.41**		3.63	6.23
MH2-6	--	--	--	*0.389*	--	--	--	*0.346*	--	--	--	*0.297*	***0.48***	***0.02***	***0.40***	***0.01***		
MH2-4	14.174	456	10147	0.375	7.08	811	17766	0.337	4.722	243	3879	0.276	**0.47**		**0.39**		4.78	6.87
MH2-4-gly	14.137	230	4566	0.306	7.071	468	10573	0.331	4.714	117	1712	0.263	**0.44**		**0.39**		4.38	6.39
MH2-4	--	--	--	*0.3405*	--	--	--	*0.334*	--	--	--	*0.2695*	***0.46***	***0.02***	***0.39***	***0.00***		
MH4-8	14.182	234	5154	0.341	7.105	766	17014	0.337	4.732	158	2930	0.337	**0.39**		**0.39**		5.11	8.7
MH4-3	14.266	880	21045	0.376	7.121	1272	31995	0.386	4.742	279	5802	0.324	**0.44**		**0.45**		5.87	8.25
MH4-3-gly	14.089	348	8782	0.404	7.067	650	16852	0.381	4.715	137	2888	0.351	**0.41**		**0.44**		5.47	8.69
MH4-3	--	--	--	*0.39*	--	--	--	*0.384*	--	--	--	*0.3375*	***0.43***	***0.02***	***0.45***	***0.00***		
MH4-6	14.108	494	14111	0.467	7.092	849	22608	0.423	4.741	185	4639	0.408	**0.47**		**0.49**		7.1	9.34
MH4-7	14.123	645	25708	0.668	7.108	1043	34640	0.539	4.769	192	8006	0.716	**0.44**		**0.62**		3.63	8.43
MH4-7	14.353	234	10733	0.791	7.112	364	16330	0.724	4.795	43	2298	0.961	**0.40**		**0.84**		4.84	16.26
MH4-7	--	--	--	0.668	--	--	--	0.539	--	--	--	0.716	**0.42**		**0.62**			
MH5-3	14.227	401	8187	0.324	7.1	779	16843	0.339	4.729	197	3506	0.299	**0.44**		**0.40**		6.15	8.45
MH5-5.a	14.09	243	5073	0.332	7.088	521	11331	0.332	4.714	119	1541	0.201	**0.42**		**0.39**		2.4	3.46
MH5-6	14.223	486	10613	0.347	7.109	1115	25039	0.356	4.733	244	4490	0.315	**0.55**		**0.41**		1.86	2.93
MH6-13	--	--	--	--	--	--	--	--	--	--	--	--	**0.32**					
MH10-2	13.82	333	11084	0.574	7.098	479	20630	0.709	4.83	203	5482	0.445	**0.40**		**0.82**		5.89	6.06
NA10	--	--	--		--	--	--		--	--	--		**0.36**					
NA10	14.191	551	25203	0.805	7.246	415	18900	0.696	--	--	--		**0.37**		**0.79**		7.65	
NA10	--	--	--	*0.463*	--	--	--		--	--	--	*0.342*	***0.37***	***0.01***				
NA7	14.107	910	33722	0.607	7.177	817	30433		4.791	394	11619	0.541	**0.28**				3.76	4.67

IV.d – XRD parameters – Narcea Antiform

sample	**chl001 Peak**	**chl001 Int**	**chl001 Area**	**chl001 FWHM**	**chl002 Peak**	**chl002 Int**	**chl002 Area**	**chl002 FWHM**	**chl003 Peak**	**chl003 Int**	**chl003 Area**	**chl003 FWHM**	**CIS Ill001**	**σ**	**CIS chl002**	**σ**	**intIll001 /chl002**	**Ill002/ chl003**
NA2	14.292	1087	29056	0.448	7.101	4271	73474	0.23	4.727	1474	24864	0.241	**0.24**		**0.26**		0.59	0.97
NA2	--	--	--		--	--	--	--	--	--	--	--	**0.26**					
NA2	--	--	--	*0.448*	--	--	--	--	--	--	--	*0.241*	***0.25***	***0.02***				
mh8-9-slickenside	--	--	--										**0.35**					
MH7-9a	--	--	--										**0.55**					
MH7-9b	14.108	1090	24646	0.378	7.1	1745	46918	0.443	4.714	413	16261	0.61	**0.52**		**0.51**		2.7	6.19
MH7-9c	--	--	--		7.174	176	4190	0.352	--	--	--	--	**0.49**		**0.41**		17.98	
MH1-13	14.103	60	1374	0.425	7.104	463	9373	0.339	4.736	55	936	0.319	**0.46**		**0.40**		1.92	7.49
MH5-2	14.239	491	18852	0.616	7.093	618	13050	0.34	4.725	126	2844	0.396	**0.47**		**0.40**		4.56	8.55
MH4-1	14.156	256	5943	0.39	7.077	445	11909	0.398	4.717	109	2534	0.371	**0.49**		**0.46**		8.42	11.83
MH5-7	14.276	380	7130	0.318	7.115	1589	28671	0.275	4.735	299	4306	0.24	**0.45**		**0.32**		1.77	3.52
MH5-8	14.232	696	15088	0.355	7.102	2893	59070	0.316	4.728	429	8251	0.315	**0.44**		**0.37**		1.77	3.45
MH6-3.II altered	--	--	--	--	--	--	--	--	--	--	--	--	**0.31**					
MH6-3.I altered	--	--	--	--	--	--	--	--	--	--	--	--	**0.32**					
MH6-3 altered	--	--	--	--	--	--	--	--	--	--	--	--	***0.32***					
MH6-6.II	--	--	--	--	--	--	--	--	--	--	--	--	**0.34**					
MH6-6.I	--	--	--	--	--	--	--	--	--	--	--	--	**0.30**					
MH6-6	--	--	--	--	--	--	--	--	--	--	--	--	***0.32***					
MH7-1	--	--	--	--	--	--	--	--	--	--	--	--	**0.39**					
MH7-11	14.224	389	10603	0.449	--	--	--	--	4.769	74	1484	0.366	**0.45**					5.22
MH8-5	14.208	41	1159	0.503	7.124	149	4997	0.495	--	--	--	--	**0.49**		**0.57**		40.64	
MH10-1	14.123	771	18496	0.372	7.08	2977	63833	0.335	4.722	653	14696	0.332	**0.36**		**0.39**		0.79	1.41

CIS calibration: CIS=1.1463·Lab-0.0066

	Ill 001 (10Å) FWHM		**chl002 (7Å) FWHM**	
CIS sample	**CIS (Illites)**	**Lab**	**CIS (Chlorites)**	**Lab**
SW1-TA	0.63	**0.563**	0.34	**0.458**
TA-SW1II	0.63	**0.568**	0.34	**0.443**
TASW1GLY	0.57	**0.468**	0.34	**0.285**
SW2-TA	0.47	**0.358**		
TA-SW2I	0.47	**0.397**		
TASW2GLY	0.44	**0.371**		
TA-SW4II	0.38	**0.339**	0.32	**0.293**
SW4-TA	0.38	**0.338**	0.32	**0.299**
TASW4GLY	0.38	**0.357**	0.32	**0.313**
TA-SW6	0.25	**0.209**	0.25	**0.202**
TASW6GLYL	0.25	**0.228**	0.25	**0.226**

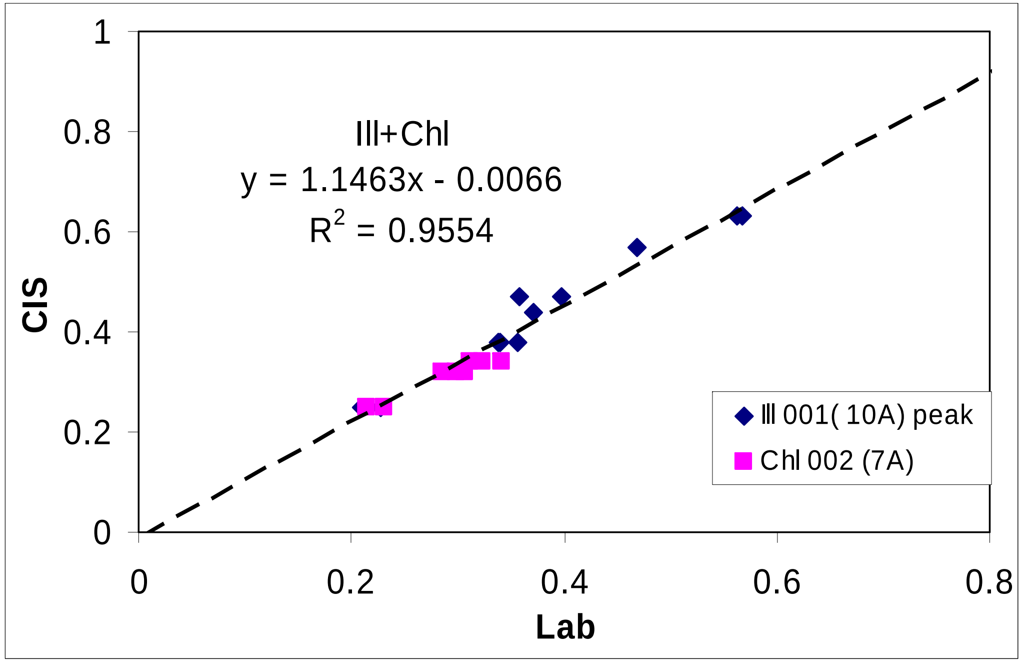

V.a – Image Analysis – Israel

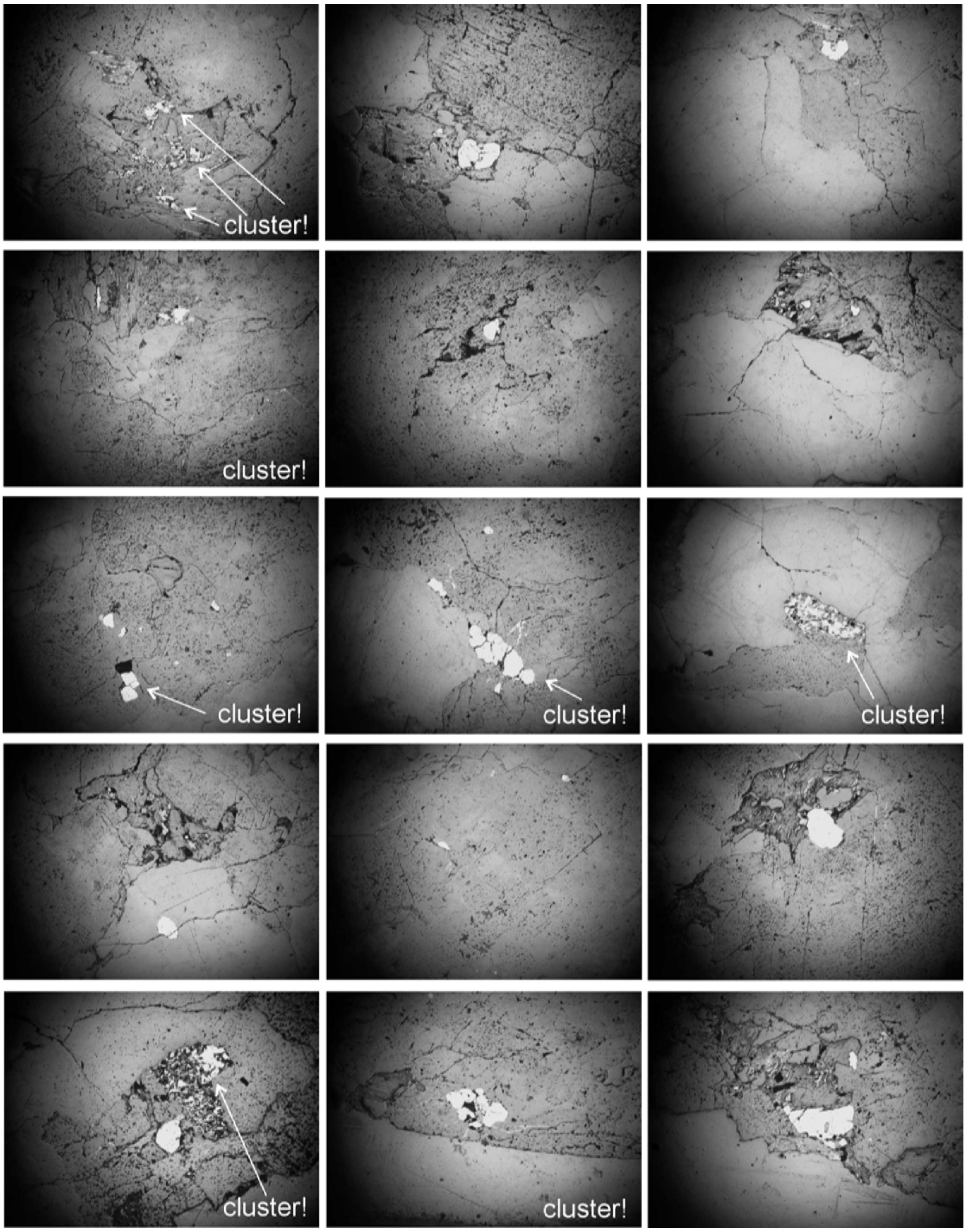

RA3-1_v

$\kappa_1\kappa_2$

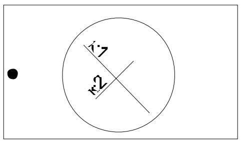

2.8 mm

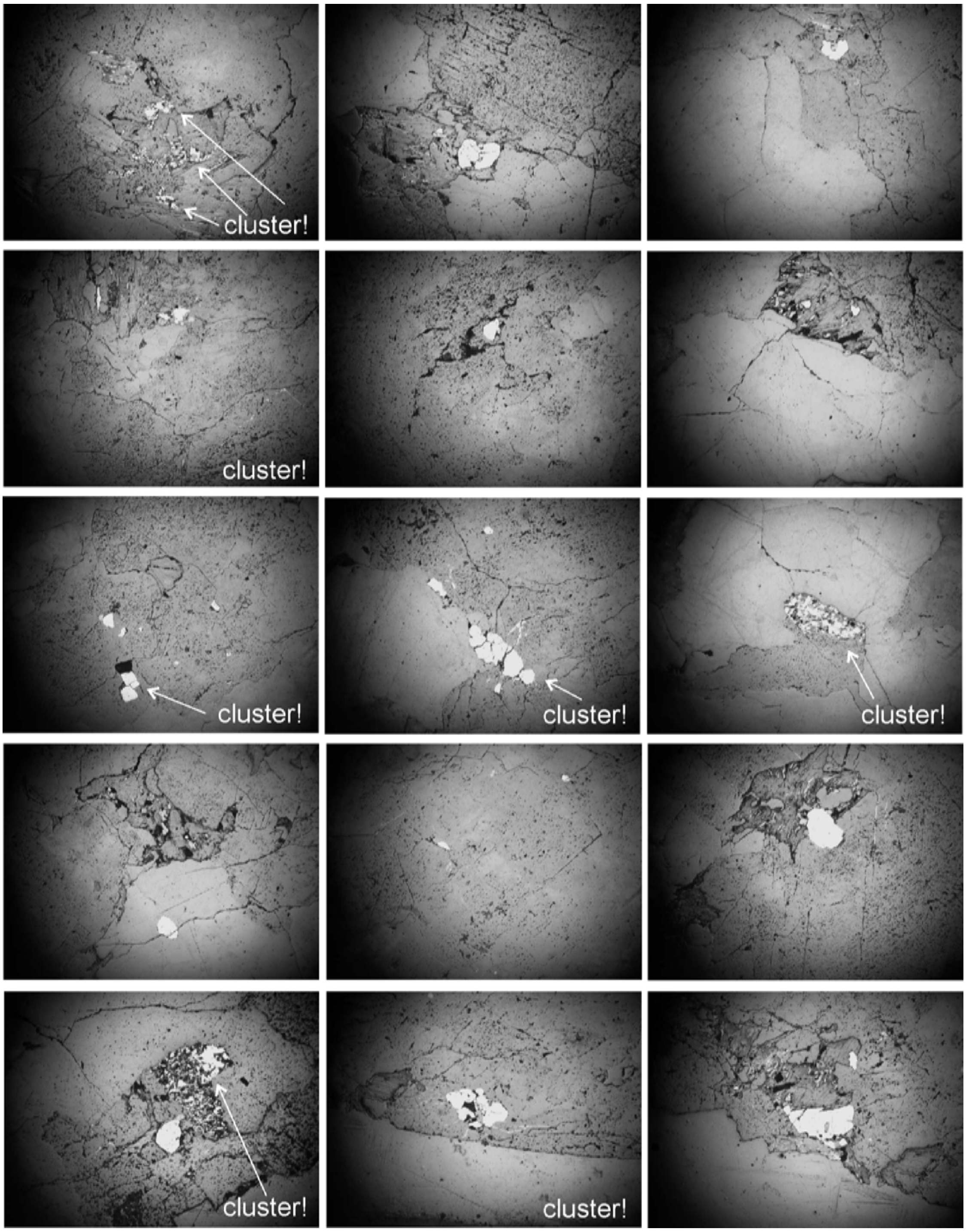

RA3-1_v

$\kappa_1\kappa_2$

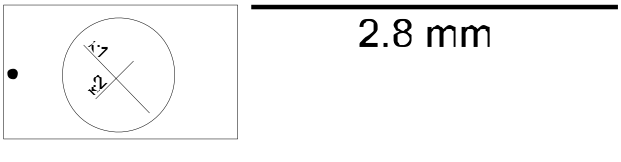

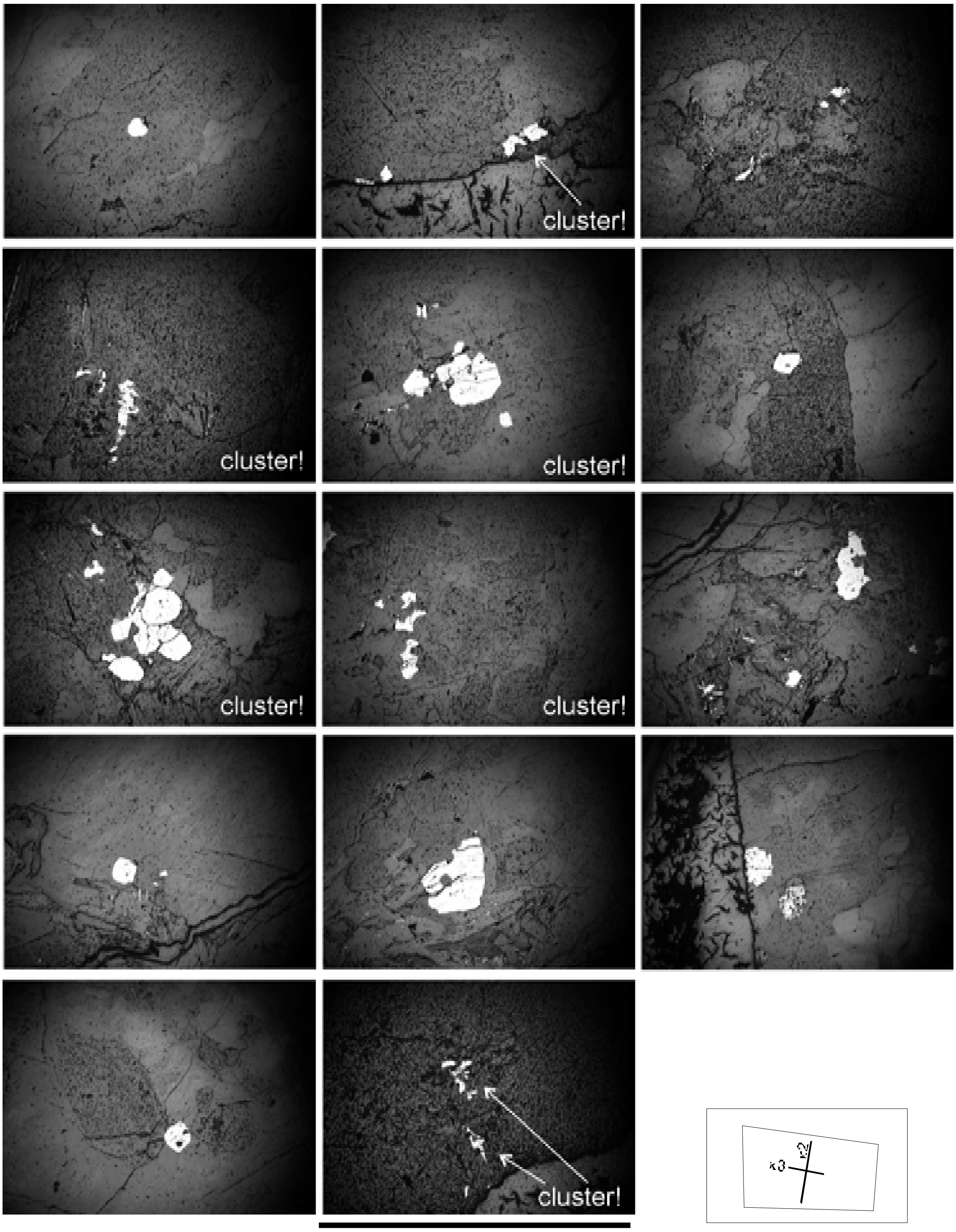

RA3-1_v

$\kappa_2\kappa_3$

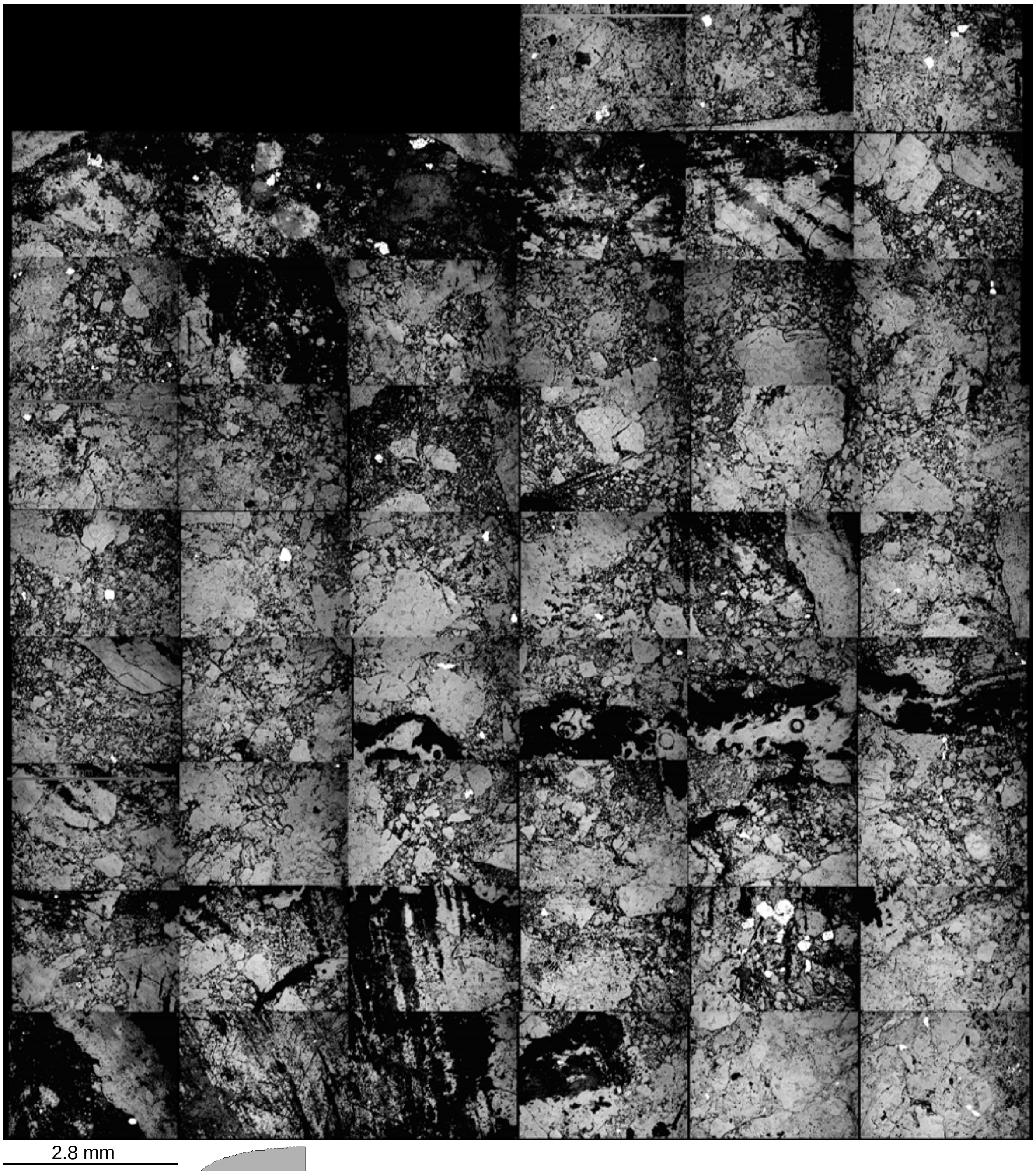

RA1-4a_vi

$\kappa_1\kappa_2$

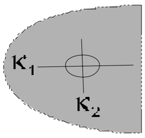

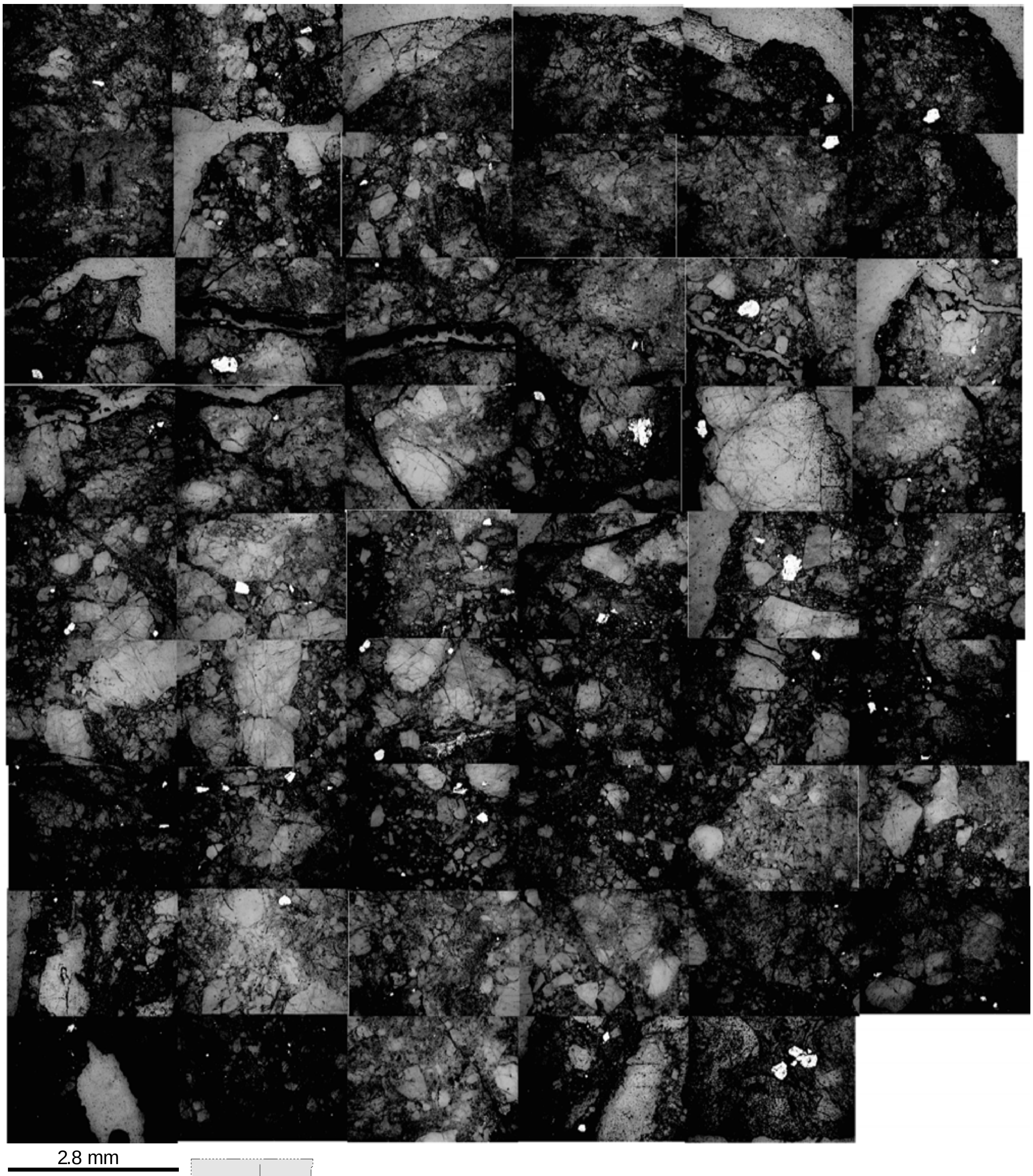

RA1-4a_vi

$\kappa_2\kappa_3$

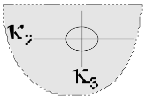

RA2-1b_vi

$\kappa_1\kappa_2$

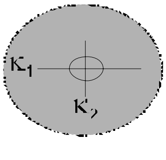

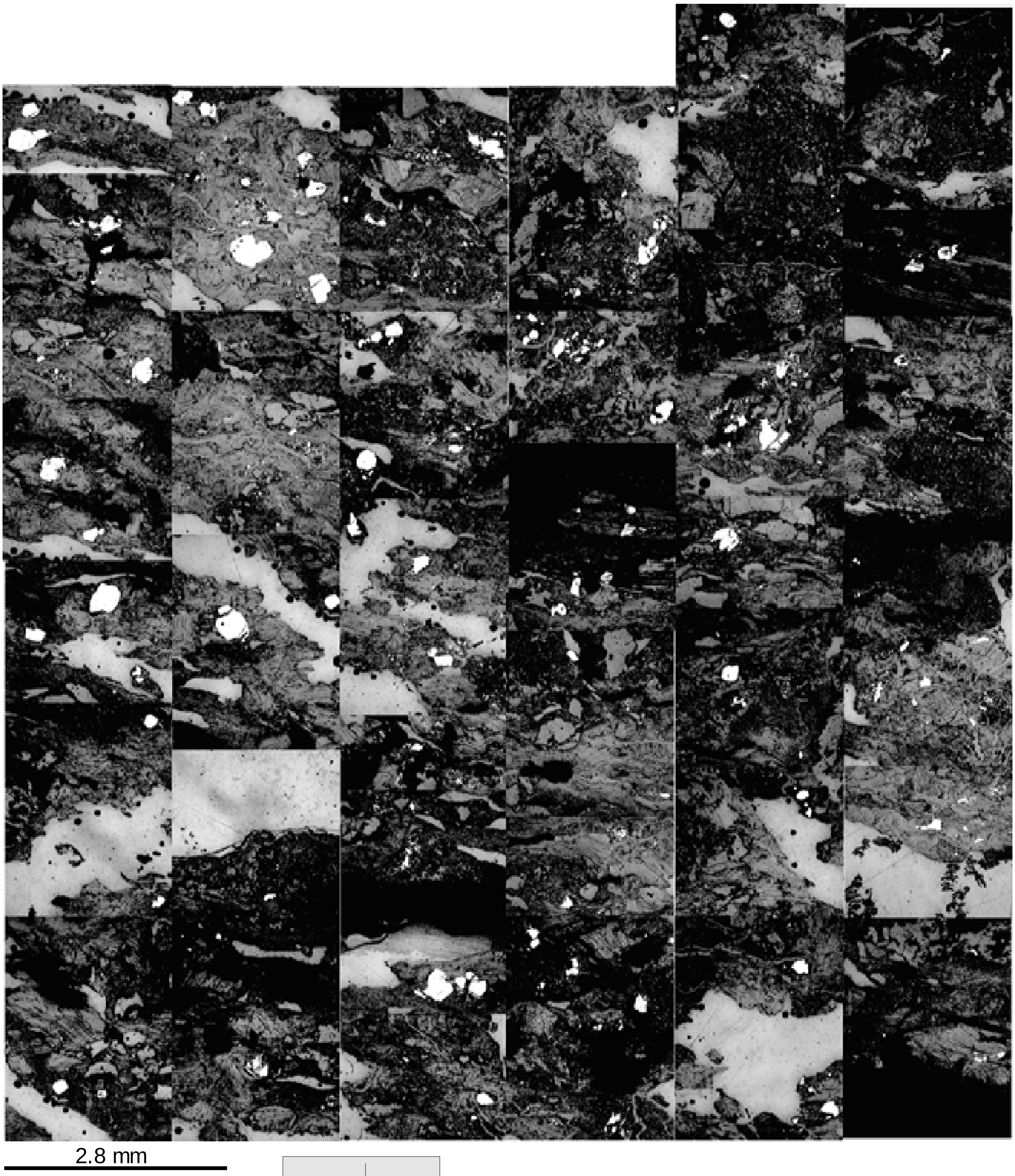

RA2-1b_vi

$\kappa_2\kappa_3$